Gravity Waves and Ripples near the Mesopause above Davis Station, Antarctica, 1999-2013

National University of Ireland, Maynooth

A thesis submitted in fulfilment of the requirements
for the degree of Doctor of Philosophy by

Sharon Rourke

Department of Experimental Physics,
Faculty of Science and Engineering

Research Supervisor:	Dr. Frank Mulligan
Head of Department	Prof. J. Anthony Murphy

May 2018

CONTENTS

ABSTRACT

Ground-based observations of infrared OH* airglow emissions made during the period February-October from 1999-2013 at Davis Station, Antarctica (68.6 ° S, 78 ° E) are analysed to construct a climatology of the horizontal characteristics of short-period gravity waves (GWs) and ripples near the mesopause (~87 km altitude). The main findings are as follows:

1. Two distinct distributions of horizontal wavelength were observed both obeying the relation $\lambda_h\,(\mathrm{km}) \approx 2.5\,T\,(\mathrm{min.})^{1.05}$. This is consistent with previous studies at various locations, but is extended to shorter wavelengths in the present study.

2. GWs showed a particular pattern of propagation directions with an almost complete absence of northward-propagating waves. Ripples, on the other hand, tended not to propagate eastward. A seasonal-dependent anisotropy in the zonal direction was discovered in the observed GW propagation directions, whose timing corresponds to the annual formation (in autumn) and break-up (in spring) of the polar vortex. Results suggest that seasonal variability of GW sources (such as the polar vortex) around the station appears to be a more likely explanation of this pattern than critical level filtering.

3. The majority of waves were observed in winter, with peaks in April/May and August, in good agreement with an earlier study of GWs at Davis Station by *Dowdy et al.* (2007).

4. Application of a ray-tracing technique to the observed GWs facilitated the determination of the approximate geographical and altitudinal location from which the waves originated. Four groups of sources were identified, each with a distinct geographical origin and a predominant observed propagation direction. Only about 15% of GWs were found to originate at tropospheric altitudes. These waves occurred consistently

throughout the year with a preferred source region approximately $100 - 200$ km north-west of the station and a preferred southward propagation direction. Two similar-sized groups (approximately 9.5% and 15% of the total number of observed waves) were found to originate in the altitude range 45−55 km (just above the polar jet) and 70−80 km respectively. Atmospheric conditions for the remainder of the GWs detected were found to be unsuitable for vertical propagation and these waves could not be traced significantly below the mesopause region.

5. Up to 278 potential mesospheric frontal events were identified (~ 25 events/year, in good agreement with event frequency observed at south Pole Station by *Pautet et al.* (2018)), five of which are compared and verified with images from a co-located all-sky infrared camera operated by Utah State University since 2012. Distributions of event persistence, phase speed, wavelength and period do not vary substantially from those of band-type GWs within the dataset. Propagation directions, which exhibited a seasonal dependency, were predominantly eastward and westward. Just 5% of these events (compared to 15% of all GWs) had tropospheric origin.

ACKNOWLEDGEMENTS

Ní heolas go haontíos

(There is no knowledge without unity)

I am very privileged to be in the position to sincerely say that my journey as a PhD student has been immensely fulfilling, and that I'm sad to see it come to an end. Throughout the past few years, I have been honoured to work with and be supported by some truly remarkable people. I do not have the vocabulary or the required reams of paper to do the generosity of all of these people justice, but I do hope to at least acknowledge those who have contributed to my project and who have made the whole experience such a pleasure.

First and foremost, I would like to express my deepest gratitude to my supervisor, Dr. Frank Mulligan, whose energy and enthusiasm far outweighs that of anyone else I know. I have thoroughly enjoyed the well-rounded educational experience that Frank embodies, and have been very lucky to have such a supportive supervisor who is so willing to freely share his time, skills and wisdom. I hope that we will continue to work together in our spare time.

I would also like to thank some external colleagues who have been of great help to me during my research. Firstly, I would like to thank Dr. Damian Murphy and Dr. John French of the Australian Antarctic Division for all their work on the instrumentation at Davis Station, for making this work possible, and for responding to my (many!) questions and requests with such fine detail and thought. I would also like to thank Prof. Mike Taylor and Dr. Dominique Pautet of Utah State University who were so open and efficient about sharing and discussing their Davis all-sky camera data, as well as analysis techniques. The UWOSCR instrument would not exist, of course, if not for Prof. Bob Lowe (R.I.P.) and his colleagues Ms. Kelly Ward, Mr. Ron De Serrano, and Dr. Bob Stockwell. I would like to express my gratitude to them for the use of the instrument and the analysis software which they developed. Big thanks also goes to the organisers and attendees of the meetings that I have been to, as they have led to some very interesting conversations, sparking off new ideas and collaborations.

I have been blessed to have had the opportunity to work in the Experimental Physics Department, and I cannot thank the staff enough for their help,

support, and the positive working environment which they create. Nobody in the department has escaped without helping me out in some shape or form during my time here. In particular, I would like to extend a special thanks to Mr. John Kelly who seemed to always be helping me with something that wasn't working and to Ms. Gráinne Roche for her constant administrative support. I would also like to thank the other members of staff with whom I have had many very useful conversations: Prof. Anthony Murphy, Dr. Créidhe O'Sullivan, Dr. Dan Nickström, Mr. David Watson, Mr. Derek Gleeson, Dr. Emma Whelan, Dr. Ian McAuley, Dr. Marcin Grądziel, Ms. Marie Galligan, Dr. Michael Cawley, Dr. Neil Trappe, Mr. Pat Seery, and Dr. Peter van der Burgt. I am so thankful also to the department for funding me on numerous occasions.

I would like to express a very heartfelt appreciation to my fellow postgraduate students (past and present) for being so wonderful; I don't know where I would be without their friendship and daily chats. Special thanks go to my proof-readers – (*i*) my very kind office-mate, Julianne Kealy, who somehow read through my whole thesis in two days (in tremendous detail!) and who has always been so willing to offer help (and Mooju!) when it is needed most (*ii*) Dr. Eimantė Kalinauskaitė, with whom I treasure our many shared experiences and who has become a very dear friend to me during the past eight years, and (*iii*) Joe Brennan, who I will especially miss for our early-morning 'beefcakes' and who has provided tonnes of emotional support via whiteboard drawings! I would also like to give a special thanks to my previous office-mates, Andrew Wilson and Niall Tynan, who made me feel welcome here from the beginning. Finally, I wish to thank all of the other postgrads, for their friendships and for all the good times – Aisling Murphy, Dave Burke, Donnacha Gayer, Eoin Cahill, James Murphy, Mark Deegan, Pauline Ambrosi-Taylor, Adam Byrne, Anthony Donohoe, Bastien Rouzé, Darragh McCarthy, Emma Garnett, Fiachra Cahill, George Walker, Melissa Dunne, Michael Brown, Niamh Tobin, Rory Sheridan, Stephen Scully and Steve Diskin – I hope we keep in touch and I'll probably see most of you in Intel!

Last but not least, I would like to thank my friends and family, who have always been a great source of comfort and encouragement for me. In particular, I would like to thank my father, Seamus, and my two brothers, Stephen and David, who always inspire and support me (and attempt to keep me down to Earth). I would also like to thank their partners Irene, Orla and Elizabeth whose presence bring a very homely feel to our house. I'd like to give a special thank you to (Dr. Queenie) Elizabeth who gave me lots of PhD advice and who spends all her weekend time cooking the Rourkes top-notch meals. A very

special thanks goes to a pair of remarkable nieces, Nóra and Eva, who have the future in their very capable little hands. I am so grateful also to our extended family – all my aunties, uncles and cousins – who always welcome me when I come rambling. I'm especially grateful to Granny Peggy, who never fails to make time on Sunday for chats, tea, sandwiches and apple tart! Huge thanks also to my boyfriend, Seán, for his unending support, philosophical chats, delicious food, *etc.* I would also like to thank the whole MacNamara clan, especially Pat and Mary who have been keeping me fed and sheltered for over a year now – it has been really nice to have been welcomed into the family home. I have been so lucky to have very supportive friends and neighbours, who would be impossible to all mention individually, so I would like to express my appreciation to them all with a very special thanks to Paula, Anna, Mary, Dearbhaile, and Níamh, who have been here for me on a weekly basis over the past few years.

I would like to dedicate my final acknowledgement to Mammy and Granny Whitepark, whose precious memories remain with me and guide me.

NOMENCLATURE

AIRS	Atmospheric Infrared Sounder
ANGWIN	ANtarctic Gravity Wave Instrument Network
ARISE	Atmospheric dynamics Research InfraStructure in Europe
CCD	Charge Couple Device
COSMIC	Constellation Observing System for Meteorology, Ionosphere and Climate
DEEPWAVE	Deep Propagating Gravity Wave Experiment
DFT	Discrete Fourier Transform
FFT	Fast Fourier Transform
FOV	Field of View
FWHM	Full Width Half Maximum
GCM	Global Climate Model
GPS	Global Positioning System
GROGRAT	Gravity-wave Regional Or Global Ray Tracer
GW	Gravity Wave
GWPED	Gravity Wave Potential Energy Density
HIRDLS	High Resolution Dynamics Limb Sounder
HWM	Horizontal Wind Model
MF	Medium Frequency
MIL	Mesospheric Inversion Layer
MLS	Microwave Limb Sounder
MLT	Mesosphere and Lower Thermosphere
MSIS	Mass Spectrometer Incoherent Scatter
NASA	National Aeronautics and Space Administration
NCAR	National Center for Atmospheric Research
NCEP	National Centers for Environmental Prediction
NLC	Noclicuent Cloud
NWP	Numerical Weather Prediction
PSC	Polar Stratospheric Cloud
SAAMER	Southern Argentina Agile Meteor Radar
SABER	Sounding of the Atmosphere using Broadband Emission Radiometry
SCAR	Scientific Committee on Antarctic Research
SSW	Sudden Stratospheric Warming
STFT	Short Time Fourier Transform
TEC	Thermoelectric Cooler
TIMED	Thermosphere Ionosphere Mesosphere Energetics Dynamics
USU	Utah State University
UWO	University of Western Ontario
UWOSCR	University of Western Ontario Scanning Radiometer
VER	Volume Emission Rate
WACCM	Whole Atmosphere Community Climate Model
WKB	Wentzel-Kramers-Brillouin

1. INTRODUCTION

1.1. Project Overview

Atmospheric gravity waves (GWs) are primarily generated at low altitudes (in the troposphere and lower stratosphere) as a result of air convection, wind over mountainous terrain, jet streams, air fronts, and other such disturbances which exist in the lower atmosphere. They can also be generated at higher altitudes (up to the mesosphere and lower thermosphere (MLT)) by secondary sources, including interactions between multiple waves, breaking waves, and wind shear. This variety of sources, in turn, creates a wide variety (or 'spectrum') of GWs throughout the entire atmosphere. Due to their ubiquity, GWs are a major driver of the multi-scale dynamics and the large-scale forcing that exists all the way from the Earth's surface to the MLT (*Fritts et al.*, 2017a).

Many discoveries about GW dynamics (*e.g.* GW sources, GW propagation, instability dynamics, GW spectrum variation with altitude, and GW influence on the large-scale meridional circulation) have been made since *circa* 1950, when GWs first became an active area of research (summarized, *e.g.*, by *Fritts* and *Alexander* (2003); *Nappo* (2002); *Kim et al.* (2003); *Fritts et al.* (2017b)). Nevertheless, although they dominate atmospheric motions above ~ 70 km (*Houghton*, 2006), GWs in the MLT region are still relatively poorly understood as, until recently, the teleconnection between different layers of the atmosphere was not fully appreciated. It is now known that GWs are a major driver for and have a major influence on atmospheric structure and circulation in the MLT region where they often break, depositing momentum and energy. In particular, short-period ($<$1 hour) GWs account for up to 70% of the total momentum transported, and thus they are of particular interest. Since GWs often break there, the MLT region is an important connecting region between the lower and middle atmosphere (where most GW sources reside) and the

thermosphere/ionosphere regions (where the atmosphere connects with space), and so the dynamics within the MLT region have a direct influence on space weather as well as on global circulation and energy balance within the atmosphere (*Pautet et al.*, 2018). Therefore, a detailed understanding of the influence of GWs in the MLT is essential (*e.g. Fritts et al.* (2014)*; Garcia et al.* (2007)).

GW characterisation over Antarctica is particularly important for several reasons. One such reason is the significant role of GWs in the formation of polar stratospheric clouds (PSCs) which, each spring, help create a large ozone hole over the South Pole (*e.g. Moffat-Griffin et al.* (2011); *Alexander et al.* (2013); *Innis* and *Klekociuk* (2006); *Noel et al.* (2008)). In addition, it is known (*Choi* and *Chun*, 2013) that there are very intense stratospheric GW 'hot spots' in Antarctica that are currently missing from global climate models. Another reason why GW studies in this region are so important is because of the sparsity of such research (caused by a lack of accessibility to the continent and a lack of public interest in a predominantly uninhabited area). As a result, sufficient climate model constraints (using observations) are not currently available on the Antarctic continent (*Mihalikova et al.*, 2016). Ground-based optical studies of short-period GWs at high latitudes are particularly infrequent because observation conditions are less than ideal, especially during the summer months when airglow observations cannot be made (*Pautet et al.*, 2011). In this project, an attempt to partially address this issue is made by using ground-based GW observations of the MLT above an Antarctic Station which are available for analysis.

Complex global climate models (GCMs), which are used to create climate change simulations, need to represent the vertical transfer of the mean flow of the atmosphere's momentum and energy due to GWs in order to produce more accurate climate information. The major difficulty in this regard is that the majority of GWs are too small to be resolved by the grids used by these GCMs,

and so GW effects must be parameterised (*e.g. Garcia et al.* (2007)). It is already known that GCMs do not accurately represent the intense stratospheric GW activity which occurs in the southern hemisphere winter. Missing stratospheric GW drag at ~60°S in GCMs cause what is known as the 'cold pole problem', where the modelled southern polar vortex is too cold by $5-10$ K, persists too long into spring, is too strong by ~10 m/s, and is located too far poleward, leading to poor predictions of ozone-hole dissipation timing (*e.g. Choi* and *Chun* (2013); *Mitchell et al.* (2016)).

Global distributions of momentum-flux from GWs have been measured from satellite and balloon observations at certain altitudes (*Alexander et al.*, 2010). However, each observation method is sensitive to only a portion of the GW spectrum and a portion of the atmosphere. The combined set of measurements from different observation methods may provide good spectral and spatial coverage of GW momentum-fluxes. However, a challenge resulting from the very intermittent nature of wave events (*i.e.* they are localized in space and time) presents itself, which can cause local values of momentum-flux to be more than an order of magnitude larger than averaged fluxes. Currently, it is known that local observations are more accurate than global ones (*Alexander et al.*, 2010) because satellite-based instruments have particularly strong observational filter effects, reducing their sensitivity to parts of the GW spectrum (*Preusse et al.*, 2002). A solution to this challenge is a greater number of localized observations to enumerate GW parameterisations (such as horizontal and vertical wavelength, phase velocity, period, and momentum-flux) in atmospheric models.

This project will focus on GW characterisation of a small area (~24 km×24 km) of the mesopause region (~87 km altitude) above Davis Station, Antarctica (68.6 ° S, 78 ° E) during the period 1999-2013. The GW observation technique used is ground-based measurements of airglow emissions from vibrationally excited hydroxyl radicals. An automated analysis method to determine GW

characteristics is used in order to analyse the large amount of data which is available. This characterisation of GWs contributes to the dataset available of ground-based optical studies of short-period GWs at high latitudes.

It will be seen later, in section 2.2, that the instrument used has a very small instantaneous field of view (FOV) of 1° and scans through a small portion of the sky (~24 km×24 km). Therefore, it is most sensitive to short-period, small-scale GWs, which have been estimated theoretically to carry momentum more efficiently than large-scale GWs and to be more effective at changing the velocity of the mean flow. Therefore, these small-scale GWs may be the main contributors to vertical transfer of horizontal momentum in the atmosphere (*e.g. Fritts et al.* (2014); *Tsuda* (2014)). The limitation of the instrument to short-period GWs does, however, have its disadvantages. For example, long-period waves are known to be less susceptible to critical-level wind filtering as they are much faster and can, therefore, propagate to higher altitudes. This makes long-period waves better suited for ray-tracing studies to identify possible GW source regions (*Taylor et al.*, 2009).

1.2. Historical Overview

1.2.1. Early Studies of Atmospheric Waves

The study of atmospheric and oceanic waves is one of the oldest subject areas in fluid dynamics. Some fundamental studies in this area include work by *von Helmholtz* (1868), *Thompson* (1880) (*a.k.a.* Lord Kelvin), *Strutt* (1883) (*a.k.a.* Lord Rayleigh), and *Lamb* (1910).

The most obvious piece of evidence and motivation for the study of atmospheric waves has long since been the effect which they have on clouds. Some early work in atmospheric physics was inspired by these cloud displays. For example, *Trey* (1919) was one of the first to support the idea, first proposed by *Wegener* (1906), that billow clouds (clouds which have a wave-like structure as in Figure 1.1) were caused by atmospheric waves. Although it is now thought that billow

clouds form due to the Kelvin-Helmholtz instability (an instability which occurs when there is a wind velocity difference between two layers of the atmosphere), and not atmospheric waves, billow clouds inspired scientists to study atmospheric waves. Subsequently, the idea that waves could propagate on atmospheric density discontinuities was further considered by *Goldie* (1925) (*Gossard* and *Hooke*, 1975).

Figure 1.1: Billow clouds at Tupper Lake, New York, in the Adirondack Mountains. This type of cloud formation inspired some early work on atmospheric waves. Photo by Paul Chartier (*Imster*, 2014).

Atmospheric GWs can be seen in clouds (including upper atmospheric clouds such as nacreous and noctilucent clouds, as shown in Figure 1.2) and travelling soliton waves may be seen in Morning Glory clouds.

Figure 1.2: (left) GWs visible in noctilucent clouds in the mesosphere above Sweden (*Dalin et al.*, 2004). (right) GWs visible in nacreous clouds in the stratosphere above McMurdo Station, Antarctica – Photo by Deven Stross.

Johnson (1929) studied the fluctuations of air pressure in England using a microbarograph, and created a frequency graph of these oscillations at four different locations. Verifying Goldie's idea, Johnson concluded that the pressure fluctuations were caused by waves travelling on density discontinuities in the atmosphere. After similar frequency distributions were also found in subsequent studies, scientists now had reason to believe that atmospheric waves had a part to play in the weather. This was the start of the quest for the determination of atmospheric wave characteristics (*Gossard* and *Hooke*, 1975).

1.2.2. Early Developments in Numerical Weather Prediction and Climate Modelling

Weather forecasting is done by running computer models which can predict the time evolution of the atmosphere for a few days when given initial conditions (and usually also some boundary conditions). These initial conditions come from weather observations which are made around the globe. Therefore, in order to obtain reliable predictions, the computer models must be a realistic representation of the atmosphere, and the weather observations which are used must be accurate. Since the 1950s, when weather forecasting was first attempted, the reliability of forecasts has improved dramatically. This improvement is as a result of finer numerical resolution (due to the increased processing power of computers), improved representation of small-scale physical processes (*e.g.* clouds, moisture, radiation, and momentum transport), more accurate data assimilation methods, and an increase in availability of accurate weather observations (*Kalnay*, 2003). It was not an easy task to achieve this reliability in weather prediction as there is no simple set of relationships which relate the state of the atmosphere at one instant in time to its state at another.

Some history of the earliest developments in this area will be briefly outlined here but more detailed historical overviews have been written on this topic (*e.g.* *Kalnay* (2003); *Fleming* (2016)) which provide excellent summaries on the developments in atmospheric science since *circa* 1900.

Bjerknes (1904) was the first to come up with the idea that the future state of the atmosphere could be completely determined by an initial state and known boundary conditions. He also knew that the governing equations of motion of the atmosphere needed to be integrated in order to make further progress on this. *Richardson* (1922) showed how these equations could be integrated numerically in his book "Weather Prediction by Numerical Weather Process", and envisaged a weather forecasting factory which included a global model grid that was updated regularly by a large number of parallel processors. Richardson's vision, which is summarised very nicely and represented artistically (as in Figure 1.3) in a recent paper by *Lynch* (2016), showed some remarkable foresight into weather prediction. However, this was too computationally challenging at the time to obtain any successful predictions. Another problem was that there wasn't a large enough network of weather observation stations (*Kalnay*, 2003).

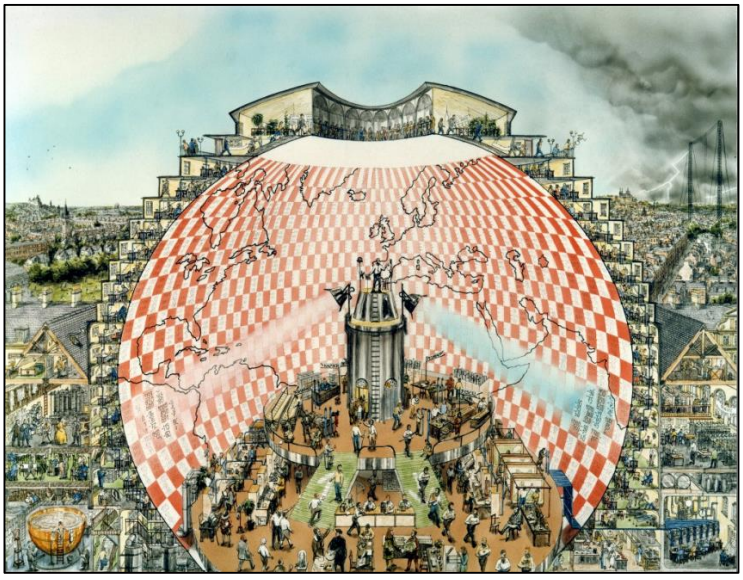

Figure 1.3: The "Weather Forecasting Factory" as described by Richardson in 1922. Picture by artist Stephen Conlin in 1986 (*Lynch*, 2016).

Rather than tackle this daunting numerical challenge, efforts were instead focussed on using simplified models of the atmosphere. These models would approximate what were thought to be the major influences of atmospheric motion. *Charney* (1951) was working on such a meteorology project at the

Institute for Advanced Study at Princeton University. By this point, their models did, at least, bear some resemblance to reality, and with time, they would gradually increase in complexity and accuracy as knowledge of atmospheric influences increased (*Kalnay*, 2003). The first operational numerical weather forecasting started in Sweden in September 1954 using a powerful computer known as BESK (Binary Electronic Sequence Calculator). This was directed by Charney's student; Carl-Gustaf Rossby. Six months later, operational numerical weather forecasting began in the United States (*Kalnay*, 2003).

It was suspected by Charney that, due to model deficiencies, there was some upper limit on the number of days which could be forecast. Model deficiencies were not the only set-back however; *Lorenz* (1965) estimated the upper forecasting limit to be approximately two weeks, but this was purely as a result of chaos and was assuming that there were no model deficiencies. This newly founded chaos theory was disheartening in terms of Bjerknes' idealistic goal of determining any future state of the atmosphere if an initial state and boundary conditions are known.

Despite these challenges, research in atmospheric science was still needed more than ever. Climate change had just become a worldwide concern, an improvement in two-week forecasts was desperately needed by farmers to meet the needs of the growing world population, and weather control (*e.g.* cloud seeding) was an exciting new possibility for military and agricultural purposes. Scientists were beginning to realise that there was much about the atmosphere which they did not understand, and that they could not meet the demand for weather forecasts or weather control without a more complete understanding of the atmosphere as a whole lest they damage the climate permanently in the process. The upper layers of the atmosphere, which had previously been neglected due to lack of accessibility and perceived lack of influence on the weather, were now becoming an active area of research as the space age was

beginning and realisation of the importance of these upper layers was growing (*Fleming*, 2016).

1.2.3. Current State of Research

Since the introduction of man-made satellites in space in the early 1960s, the atmospheric science community have been gaining a huge amount of information from global-scale observations, and have been using it to study the composition, dynamics and evolution of the Earth's atmosphere. In addition, with the improvement of space technology, atmospheric scientists have also begun to study other planetary atmospheres.

GCMs of the atmosphere have now become a very powerful tool for numerical weather prediction and climate monitoring. A GCM consists of a grid (as shown later in Figure 1.22), similar to that in Richardson's hypothetical forecasting factory, with values for various atmospheric parameters associated with each grid. With an increase in Earth-observing satellites, many of these values can now be constrained with real measurements, making them much more comparable to reality. Still, despite the benefits of imagery and detection of various atmospheric parameters from space, both local and global measurements are currently required to achieve the spatial and temporal resolution needed for accurate global models.

With the introduction of large-scale data-collection, atmospheric scientists had the opportunity to branch out in many new directions. In most of these branches, the new emphases have now become data analysis and visualisation, and adequate calibration and resolution of detectors.

In this project, the focus is on the specific topic of the detection and analysis of gravity waves in the Antarctic upper atmosphere. A brief overview of the current state of research in this particular branch of atmospheric science is now given.

Until recently, the atmosphere had been considered a stratified fluid with negligible interactions between the upper layers and the troposphere, where we live. However, more recent studies have shown that middle and upper atmospheric thermal structure, dynamics, and chemistry are important and sensitive indicators of the health of our entire atmosphere. In particular, they have a significant effect on tropospheric climate and weather. Therefore, the perceived societal impact of upper atmospheric research has increased dramatically in recent years. In particular, the Antarctic middle and upper atmosphere is now recognised as one of the least understood regions of the atmosphere, and only recently has this region been investigated with a variety of different instruments (*Dowdy et al.*, 2007).

Atmospheric waves are major components of global atmospheric motions, and are a major driver for interactions which penetrate through layer boundaries. One type of atmospheric wave is a gravity wave, and these waves are ubiquitous in the Earth's atmosphere. Their primary importance comes from their contribution to the mean meridional circulation from the summer to the winter pole. This circulation is driven by (and cannot be explained without) the deposition and extraction of gravity wave momentum-flux (*Lindzen*, 1990). GW-scale ranges from tens to thousands of kilometres, and so it is difficult to represent the smaller scale waves in GCMs as the grid resolution is too coarse. Therefore, parameterisations based on local observations are currently used to represent these small-scale gravity waves in GCMs.

Early studies on using GW drag parameterisations in GCMs was done by *Lindzen* (1981) and *Holton* (1982). The first implementation of these studies was done using mountain waves, which have a horizontal phase speed of zero. Later, when model lid heights increased to altitudes as high as the mesosphere, it became necessary to include GWs which were generated by non-orographic sources (*Alexander et al.*, 2010).

Despite some recent improvements, small-scale GWs are still misrepresented in GCMs (*Dowdy et al.*, 2007) due to a lack of global observations of small-scale, intermittent structures and the coarse grid resolution ($\sim 2-5^{\circ}$ in the horizontal direction and usually $\sim$3 km in the vertical direction in the stratosphere) used in most GCMs. Some assumptions which are common to current GCM GW parameterisations are that GWs propagate only vertically and instantly through an air column, and that GW momentum and energy is conserved up until the altitude where the amplitude grows so large that the wave breaks and GW drag is induced. Recent satellite measurements and other global datasets, with improved spatial and temporal resolution, together with improved analysis methods are now capable of providing better constraints for GCM GW drag parameterisations. In addition, following improvements in computing speed, higher resolution GCMs are now capable of resolving these observations (*Alexander et al.*, 2010).

One problem is that each measurement technique comes with an observational filter, *i.e.* each instrument is only sensitive to a portion of the full GW spectrum, and may be sensitive to features other than just GWs (*e.g.* planetary waves or tides). *Wright et al.* (2016) highlights this problem, explaining that no observational technique combines the spatial, spectral and temporal resolution and coverage which is needed to study the full spectrum and distribution of GWs. In addition, the observational filter can change both the absolute value and the relative global distributions. Since there are missing observations of portions of the spectrum, there still exists some unresolved GW forcing in GCMs. In order to observe the full spectrum of wave properties, a synergy comprised of different measurement techniques, including both local and global measurements, is needed (*e.g. Wright et al.* (2016); *Alexander et al.* (2010)). An example demonstrating the need for synergistic measurements is that, although global data is required to include a large spatial extent of GWs in GCMs, errors in GW momentum-fluxes derived from global observations remains large

compared to local case studies, which are quite accurate (*Alexander et al.*, 2010). Research is now needed in the interpretation of multi-datasets, as each individual observational technique has its own bias, perhaps leading to order of magnitude differences in wave momentum-flux calculations (*Geller et al.*, 2013). This is part of the reason why, in this project, some same-night co-located airglow measurements are compared.

Here, local observations will be used to provide a better understanding of GW activity in a poorly understood region, the Antarctic mesopause, so that climate modelling studies may benefit from more representative model constraints and, thus, better predictions. Long-term changes in GWs contribute significantly to long-term changes in the thermal structure and the chemistry of the mesopause region (*Gruzdev* and *Brasseur*, 2005). In this project, mesopause GW activity is studied using a dataset which dates back to 1999, making long-term trends possible to examine.

1.3. The Earth's Atmosphere

The atmospheres of several planets in our solar system have been observed and studied, but none to a greater extent than our own atmosphere. Observation of the atmospheres of the gas giants is not easy as it is difficult to distinguish where the atmosphere begins. It has been much easier to distinguish the atmospheres of the terrestrial planets Venus, Earth, and Mars (Mercury has no detectable atmosphere). The Earth's atmosphere is an ideal comparison model when studying other atmospheres as its structure is much more complex than that of any other atmosphere in our solar system (*Cole* and *Woolfson*, 2002).

The complexity of our atmosphere's structure comes from both its composition and its interaction with radiation from outside Earth. Section 1.3.1 will focus on Earth's atmosphere's spectroscopy and composition. It will be described that the composition of the atmosphere controls the passage of radiation through it and thus controls the temperature profile. For this reason, the

atmosphere is often classified by the variation of temperature with altitude, and it is this classification on which will be the focus of section 1.3.2.

1.3.1. Atmospheric Composition

The atmosphere is composed of various gases, which can exist in either atomic, molecular, or ionic form. Some of these gases are inert, but some absorb/emit radiation, react chemically with other gases, or are condensable under a certain temperature and pressure. Therefore, atmospheric composition tends to vary spatially and temporally, creating energy sources within the atmosphere. To provide a general idea of the composition of the Earth's atmosphere, the mean values are given in Table 1.1.

A combination of remote sensing and *in situ* mass spectroscopy observations can be used to learn about atmospheric composition at any particular time and place. In other words, one must examine the spectrum of light emitted from a planet (the planetary spectrum) in order to study its atmosphere's composition.

A planetary spectrum is comprised of a reflected sunlight spectrum and a thermal radiation spectrum, as shown in Figure 1.4. The reflected sunlight comes from particles in the atmosphere and reflective surfaces at ground level, and usually falls in the ultraviolet (UV) to near-infrared wavelength range ($\sim 0.1{-}1$ μm). The thermal radiation comes from both the internal energy of the planet and emission of heat of absorbed solar radiation, and usually falls in the infrared to microwave wavelength range ($>1{-}10$ μm).

As a result of their dependence on atmospheric composition and surface structure, the reflected and thermal spectra vary hugely from one planet to another. Therefore, studying the planetary spectrum can provide a vast amount of information about the composition and thermal structure of the atmosphere, as well as information about the physical and chemical processes occurring within it.

Constituent	Formula	Proportion	Notes
Nitrogen	N_2	78.08 %	
Oxygen	O_2	20.95 %	
Carbon Dioxide	CO_2	385 ppm	variable
Methane	CH_4	3 ppm	variable
Water Vapour	H_2O	< 3 %	variable, condensable
Argon	Ar	0.9 %	
Carbon Monoxide	CO	0.2 ppm	
Ozone	O_3	10 ppm	
Acetylene	C_2H_2	8.7 ppb	
Ethane	C_2H_6	13.6 ppb	
Propane	C_3H_8	18.7 ppb	
Ethylene	C_2H_4	11.2 ppb	
Nitric Oxide	NO	< 0.01 ppm	
Nitrous Oxide	N_2O	0.35 ppm	
Nitrogen Dioxide	NO_2	15 ppb	
Sulphur Dioxide	SO_2	< 2 ppb	variable
Hydrogen	H_2	0.5 ppm	
Helium	He	5 ppm	
Neon	Ne	18 ppm	
Krypton	Kr	1 ppm	
Xenon	Xe	0.09 ppm	

Table 1.1: Mean composition of the Earth's atmosphere given as a percentage, ppm (parts per million), or ppb (parts per billion). Constituents at a level < 1 ppb are omitted, and largely variable and major condensable constituents are marked (*Sánchez-Lavega*, 2011).

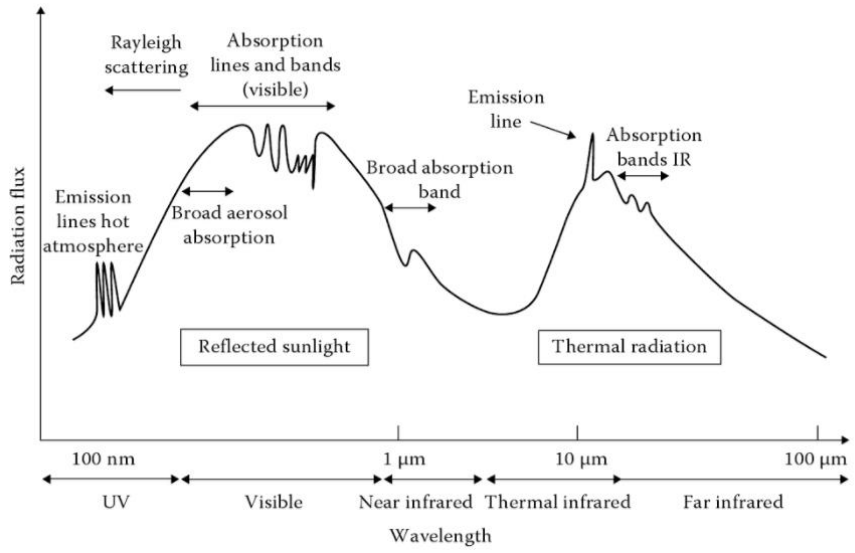

Figure 1.4: A typical planetary spectrum (*Sánchez-Lavega*, 2011).

Within the reflected and thermal spectra (*a.k.a.* the continuum), there are spectral line profiles due to emission and absorption from atoms and molecules. These line profiles can be represented by a wavelength-dependent intensity function, $I(\lambda)$, and are measured with respect to the background intensity of the

continuum, I_0. As shown in Figure 1.4, emission lines have intensity $I > I_0$, whereas absorption lines have intensity $I < I_0$. The abundance of an atom or molecule producing the emission or absorption, along with the temperature and pressure in their vicinity, is what determines the line profile, and thus spectroscopy can be used to derive these parameters. To do this, however, energy perturbations during absorption/emission (*e.g.* due to atomic/molecular collisions or Doppler shifting) need to be taken into account as the shape of the spectral line profile can be affected by them.

Molecular signatures in a planetary line spectrum can be classified into two groups: those with very broad absorption bands which correspond to molecules with no permanent dipole moment, and those with discrete absorptions which correspond to molecules which have undergone a (combination of) rotational, vibrational, or electronic transition(s). A schematic diagram showing the structure of these energy transitions is shown in Figure 1.5.

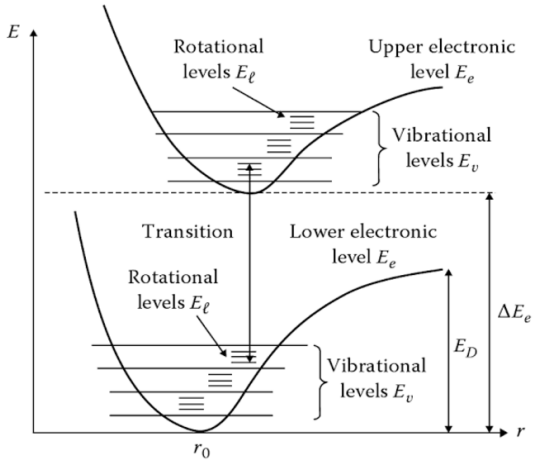

Figure 1.5: Rotational and vibrational energy levels of a molecule associated with two electronic states (*Sánchez-Lavega*, 2011).

1.3.2. The Vertical Structure of the Atmosphere

The vertical structure of any planetary atmosphere is primarily determined by its vertical density distribution. As air density decreases with increasing altitude due to gravity, so too does air pressure, in accordance with the hydrostatic equation. This is described in detail in Appendix B.2.

The vertical temperature structure of the Earth's atmosphere is determined by heating sources coming from outside the Earth's atmosphere, within the atmosphere, and from the Earth itself. It varies both in time and space, as heat is transported throughout the atmosphere via atmospheric dynamics (which will be described in section 1.5), but it is generally categorized into five different vertical layers. Starting from space and moving toward the Earth's surface, these layers are known as the exosphere, thermosphere, mesosphere, stratosphere, and troposphere. By convention, each layer is defined by the temperature gradient in that region (as shown in Figure 1.6), although there are other factors (such as chemical composition, air movement, and air density) which affect the division between the layers.

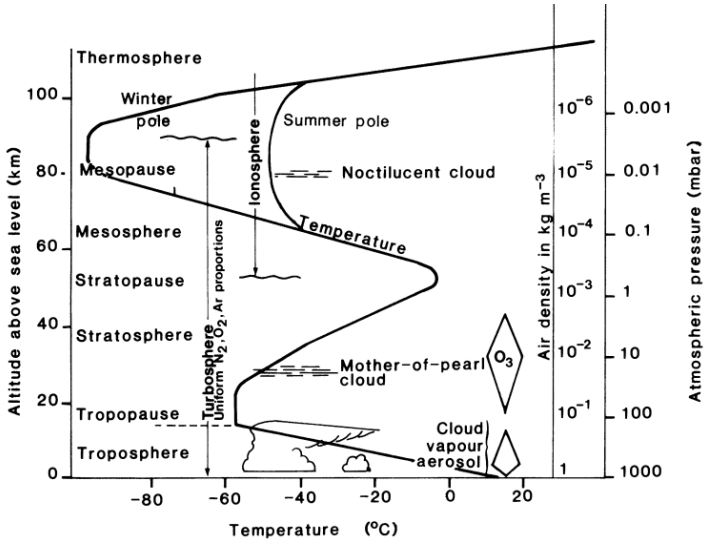

Figure 1.6: A diagram of altitude, air density, and atmospheric pressure as a function of temperature (*McIlveen*, 2010).

The uppermost layer of the atmosphere is known as the exosphere (not shown in Figure 1.6), where particles are so rarefied that they can move about with very large velocities, unaffected by collisions and may sometimes escape the Earth's gravitational pull.

Moving toward the Earth's surface, the next layer is the thermosphere. In this layer, UV radiation from the Sun ionises atoms and breaks bonds between atoms/molecules (photodissociation) to produce a large amount of heat energy.

As it moves down through the thermosphere, the UV radiation is absorbed and hence there is a decrease in temperature with decreasing height in the region. It should be noted that bodies moving through this high temperature region (*e.g.* rockets and meteors) are not heated much by the hot air as the density of air molecules at this height is so low that the heat content per unit volume is very small (*Cole* and *Woolfson*, 2002).

The mesopause, the coldest region of the atmosphere, is the boundary layer between the thermosphere and the mesosphere. It is a very complex and interesting region, which this project will focus on primarily. It is at a difficult altitude for *in situ* observations as it is too high for aircraft or balloon studies and too low for *in situ* satellite studies. It can be studied using remote sensing as will be described later in this chapter in terms of GW measurements.

The mesosphere is the middle layer of the atmosphere. Although there is comparatively little relative to the thermosphere, there is still some ionising radiation all the way down to approximately 60 km, the bottom of the 'ionosphere'. There is also a high proportion of UV radiation not absorbed by the mesosphere which causes dissociation of molecules in the mesosphere. An important dissociation which occurs in this layer breaks molecular oxygen into atomic oxygen. Atomic and molecular oxygen can then react to form ozone, a molecule which absorbs UV radiation. UV radiation decreases with decreasing height due to this absorption by ozone and because it has more molecules per unit volume to act upon as altitude is decreased. As a result of this UV absorption, temperature increases with decreasing height in the mesosphere (*Houghton*, 2006).

The stratopause is the boundary layer between the mesosphere and the stratosphere and occurs at approximately 50 km altitude. At this point, ozone becomes very abundant as there is a runaway effect due to UV absorption, which causes dissociation of molecular oxygen and production of more ozone,

and thus more UV absorption. Temperatures are very high in this ozone layer as a result of the high absorption levels of radiation.

The stratosphere is a highly stratified layer. Temperatures decrease with decreasing height because there is much less UV absorption. Since the density of air increases with a decrease in temperature, a stable stratification of density occurs. The amount of ozone, and hence the temperature profile, varies depending on latitude and time of year, as shown in Figure 1.7.

The tropopause is the boundary layer between the stratosphere and the troposphere. Heat cannot penetrate through the tropopause by convection.

The troposphere, or *turning sphere*, contains ~90% of the atmosphere's mass. As we know from everyday experience, temperature increases with decreasing altitude in this region, as a result of convective heating from the Earth's surface.

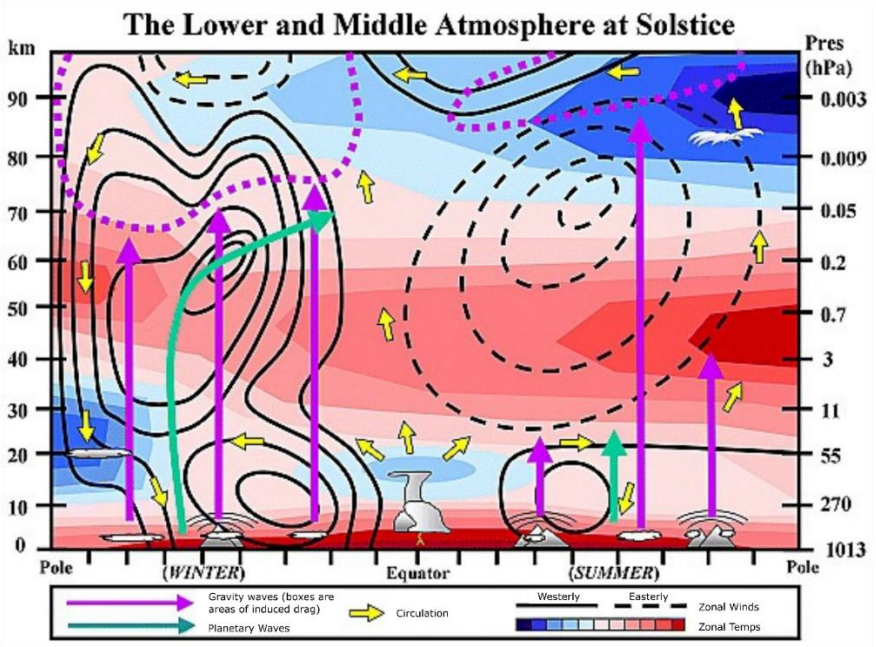

Figure 1.7: A 2-dimensional schematic of the lower and middle atmosphere. Colours indicate relative temperatures, with red being warmer and dark blue being cooler. Ray paths of GWs and planetary waves are also shown in purple and green, respectively. The polar vortex (eastward zonal wind, shown by solid black line) is shown on the left, extending from the upper troposphere into the upper mesosphere at the winter pole. In the upper right corner, clouds can be seen forming in the cold summer mesosphere, and in the lower left, polar stratospheric clouds can be seen forming in the cold polar vortex core (*Meriwether* and *Gerrard*, 2004).

An alternative way to classify different vertical regions within the atmosphere is by composition and mixing, as shown in Figure 1.8 (right). Using this classification scheme, there are two main atmospheric regions: the homosphere (lower region) and the heterosphere (upper region). These two regions are separated by the turbopause, which is located at ∼100 km altitude. In the homosphere, the primary particle transport mechanism is mixing via turbulence and eddy diffusion. This creates a relatively uniform distribution of major atmospheric constituents, with the mean molecular weight of air decreasing very slowly with altitude. Above the turbopause, in the heterosphere, transport of atmospheric constituents is no longer possible. The constituents actually begin to separate according to their masses via a process known as molecular diffusion. The effectiveness of molecular diffusion increases with an increase in the mean free path of the molecules, which increases with altitude (*e.g.* *McCarthy* (2015); *Hobbs* (2000); *Brasseur* and *Solomon* (1986)).

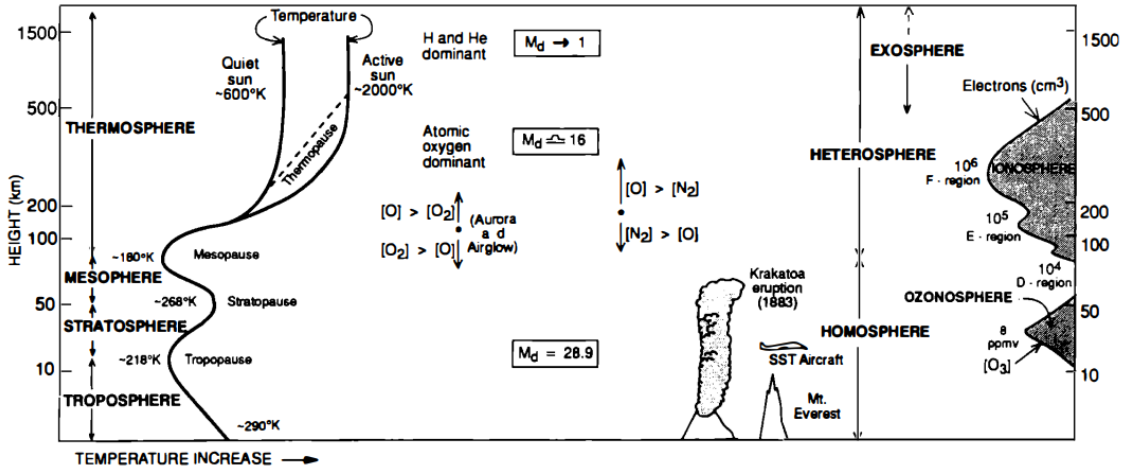

Figure 1.8: The two atmospheric classification schemes described in the text above. The temperature structure scheme is shown on the left, while the composition/mixing scheme is shown on the right. The variable M_d, shown in the centre of the image, denotes the apparent molecular weight of air in grams (*Hobbs*, 2000).

1.4. The Upper Atmosphere

As one approaches the upper atmosphere, atomic and molecular dissociation and ionisation processes become dominant, primarily because of the decrease in density and pressure with altitude. At these high altitudes, optical emission

(known as airglow) due to discrete molecular and atomic transitions at particular altitudes occurs at various wavelengths (*Sánchez-Lavega*, 2011). The passage of GWs through one such airglow layer is observed in this project, and so it will be discussed in detail in section 1.4.3. The aurora is another optical emission which occurs at even higher altitudes in the upper atmosphere due to atoms/molecules which are excited in the polar regions by electrons and ions from the solar wind and magnetosphere (*Sánchez-Lavega*, 2011). The instrument used to detect GWs in this project is also sensitive to aurora emission wavelengths, and so it will be discussed in further detail in section 1.4.4.

The temperature structure of the low-density upper atmosphere (shown in Figure 1.8, for example) results from a balance between heat gain/loss processes, and heat transport mechanisms (*Sánchez-Lavega*, 2011). The major heat sources in the middle atmosphere result from absorption of UV light by O_3 (and to a lesser extent, O_2), whereas the major heat loss processes are infrared emissions due to vibrational relaxation of CO_2, H_2O and O_3. It is also important to note that regions where heating/cooling is dominant do not necessarily correspond to hot/cold regions respectively. Heat transport mechanisms also play an important role. For example, the summer mesopause is the coldest region in the Earth's atmosphere despite significant radiative heating in the region, and this is due to a dynamical uplift of air affecting the temperature structure (*Brasseur* and *Solomon*, 1986).

1.4.1. Photochemistry

Photochemistry occurs when electromagnetic waves (usually from solar sources) are absorbed by molecules/atoms, inducing chemical reactions which produce new compounds. Depending on the wavelength of the incoming radiation, along with the binding energy of the particular chemical bond, different energy levels are excited within the molecules. Low-energy photons, in the radio to far-infrared range ($\lambda \geq 100$ μm), excite electrons in the rotational levels (lowest

quantum states) of molecules, photons in the infrared range (λ~2−20 μm) may excite vibrational levels of molecules, and photons in the visible and UV range ($\lambda \lesssim 1$ μm) may excite higher quantum electronic levels of atoms/molecules. The latter high-energy photons may break up molecules into atoms/ions by a process known as photodissociation. This is part of the process of stratospheric ozone production, for example, where UV photons react with molecular oxygen to produce atomic oxygen. At very high photon energies, electrons may be removed (outer-shell electrons at $\lambda \lesssim 0.1$ μm and inner-shell electrons at $\lambda \lesssim 0.01$ μm) from atoms/molecules by photoionisation (*Sánchez-Lavega*, 2011). Excited molecules may otherwise partake in a direct reaction with another atom/molecule, may fluoresce (*i.e.* emission of airglow as they de-excite), or may undergo collisional deactivation (*Seinfield* and *Pandis*, 1998).

As radiation penetrates deeper into the atmosphere, shorter wavelengths (higher energies) are progressively removed by absorption (mainly with O_2, N_2, and O_3), such that photochemistry in the troposphere is confined to wavelengths greater than ~ 290 nm (*Seinfield* and *Pandis*, 1998). In the lower part of the heterosphere, concentrations of atomic oxygen and hydrogen, hydroxyl, nitric oxide and ozone are relatively high. Photochemical reactions with these molecules create products in excited electronic states, which emit luminescence known as airglow (*Hobbs*, 2000).

1.4.2. The Ionosphere

With a rapid increase in mean free path, a decrease in pressure, and an increase in ion stability with altitude, free electrons which are produced by photoionisation (mainly of O_2 on Earth) have much longer lifetimes in the upper atmosphere ($\gtrsim$60 km altitude) compared to the lower atmosphere. The number density of free electrons in the upper atmosphere is thus very large, creating an electrically conducting layer which can affect radio wave propagation. This region of high free electron density is known as the ionosphere. As it is dependent on photoionisation, the ionosphere diminishes significantly after

sunset. Similarly, solar flares may cause an increase in the abundance of free electrons (*Hobbs*, 2000).

There are three distinct peaks in free electron density in the Earth's atmosphere, as shown in Figure 1.8 (right). These regions are known as the D-region (which extends from approximately 60−90 km) created primarily by x-ray ionisation of O_2 and N_2, the E-region (which extends from approximately 105−160 km) created by photoionisation of O_2, and the F-region (which extends from approximately 160 km up to >1200 km where it merges with the magnetosphere). The F-region is further categorised into the F1- and F2- layers based on two smaller peaks within the region (*Sánchez-Lavega*, 2011).

1.4.3. The Hydroxyl Airglow

A soft airglow, independent of moonlight, aurorae, and artificial lights, is present globally throughout the day/night and throughout the year. As described in section 1.4.1, the airglow is produced by light emissions from electronically or vibration-rotationally excited atoms/molecules at altitudes above 80 km. The airglow spectrum, which is produced by photochemical reactions with different molecules/atoms such as O_2, O, Na, and OH, is shown in Figure 1.9 (visible part only is shown).

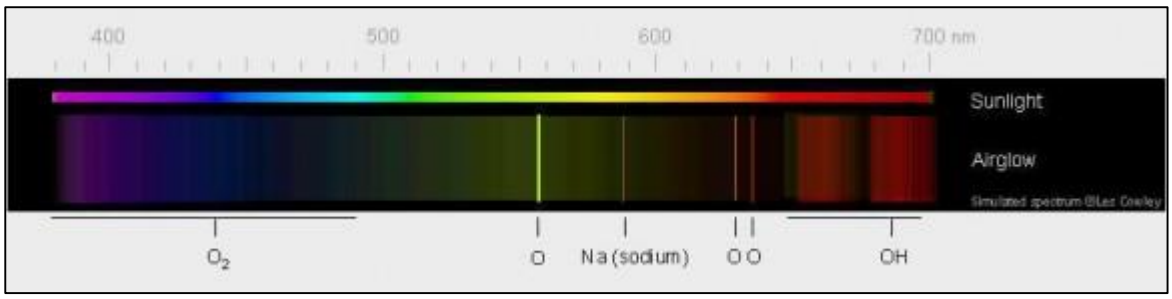

Figure 1.9: The airglow spectrum (*Cowley*, 2016).

Among these excited atoms/molecules are hydroxyl (OH) radicals. Changes in vibrational energy along with smaller changes in rotational energy excite OH molecules, causing them to emit red and infrared light (with wavelengths ranging from ~0.5−4 μm (*Baker* and *Stair*, 1988)). This produces a narrow

(~6−12 km FWHM) airglow layer centred at a peak altitude of ~87 km, which can reach an intensity of up to 10^6 rayleigh (*Baker* and *Stair*, 1988) (*i.e.* they have an emission rate of up to 10^{16} photons per square metre per column per second). The exact thickness and altitude of this layer is time and latitude dependent (*Grygalashvyly et al.*, 2014). Typical values for layer peak altitude and layer thickness are 86.8±2.6 km and 8.6±3.1 km, respectively (*Baker* and *Stair*, 1988).

Since the emission is in the infrared range, daytime observations of these emissions are not possible as the infrared detector would be saturated by sunlight. Additionally, the concentration of excited OH molecules is approximately ten times greater during the night time (*Ern et al.*, 2009b). Therefore, the ground-based airglow observation instrument used in this project makes night time observations only.

The hydroxyl radical is composed of an oxygen atom and a hydrogen atom in a covalent bond. As a radical, it has an unpaired valence electron, making it highly reactive. As a result of this high level of reactivity, it is a very important oxidising agent for the atmosphere. In particular, it plays a fundamental role in the catalytic loss of ozone between ~15 and 90 km altitude As it is involved in so many reactions, OH has very low abundance within the atmosphere and is thus difficult to measure (*Summers et al.*, 1997). In its ground state, it can be found in most atmospheric layers due to the photolysis of ozone and the photodissociation of water by UV light (*McCarthy*, 2015), but excited OH represents only a tiny portion of the atmosphere in comparison (as shown in Figure 1.10).

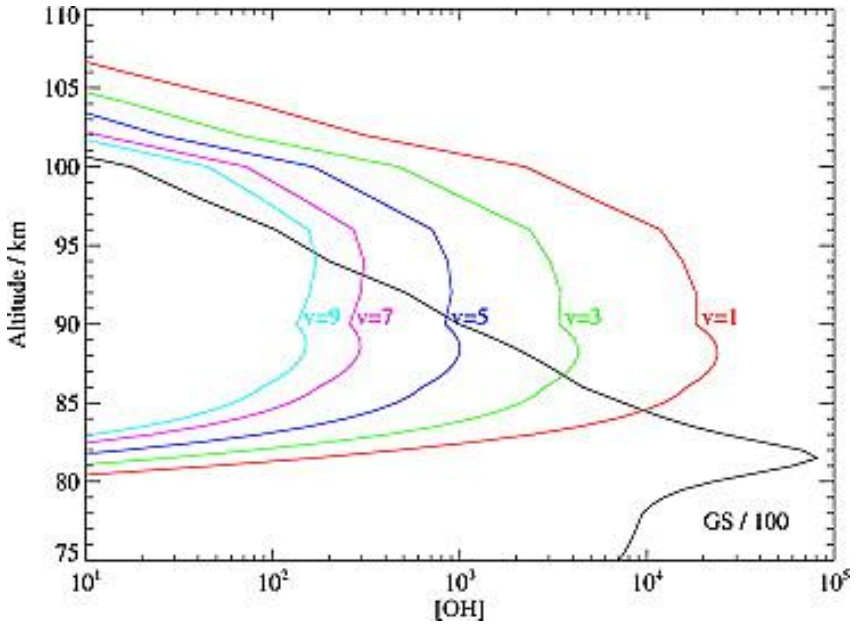

Figure 1.10: Calculated night profiles of OH and excited OH on a particular night. It can be seen that the abundance of OH in its ground state is approximately 100 times greater than the abundance of excited OH (*Pickett et al.*, 2006).

Vibrationally excited hydroxyl (OH*) is produced primarily by an exothermic hydrogen-ozone reaction. This reaction is known as the Bates-Nicolet mechanism, and is shown in Equation 1.1.

The Bates-Nicolet mechanism occurs most frequently in the narrow layer centred at ~87 km and is the main source of heat at this altitude. It is centred at this altitude as it is low enough for a sufficient concentration of ozone and high enough so that rapid quenching of the excited products by collisions does not occur frequently, due to low atmospheric pressure. This gives OH* molecules a relatively long radiative lifetime, with (on average) at least 10 collisions occurring before photons are emitted (*Sivjee*, 1992).

This OH* airglow layer is a useful tool for remote sensing in the study of photochemical and dynamical processes that play a role in the upper atmosphere. By studying OH* intensity variations (*e.g.* like those shown in Figure 1.11), one may infer information about GWs which are passing through the layer, and this is what will be used in this project to study the passage of gravity waves through the mesopause region. This is further illustrated in

Figure 1.12, where it can be seen that a GW passing through the airglow layer changes the OH* emission rate. This is because the GW causes fluctuations in ozone, which changes the rate of production of OH*. In other words, the perturbation of local density and temperature due to GWs can affect the chemical reactions which produce the OH* airglow (*Tang*, 2005).

Figure 1.11: Fluctuations in the night sky airglow due to gravity waves. Red, green and orange emissions are visible from hydroxyl, oxygen and sodium airglow emission layers between ~87 and 97 km altitude (*Claro*, 2016).

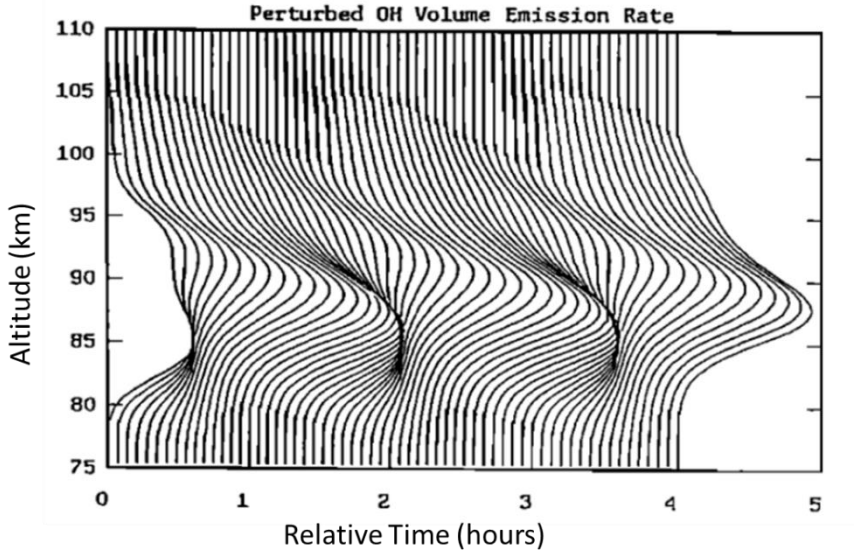

Figure 1.12: OH* volume emission rate perturbations caused by a gravity wave with an amplitude of 10% at z =89 km, λ_z =15 km, T =90 minutes (*Swenson* and *Gardner*, 1998).

The OH* airglow has been a subject of research for many years. In 1948, Aden Meinel discovered that the OH* airglow was rich in infrared emissions and identified high resolution spectra due to different emission bands within the layer. He also identified, with the help of David Bates and Marcel Nicolet, the chemical reaction in the mesopause region which produces the brightest of these emissions (*i.e.* the Bates-Nicolet mechanism, shown in Equation 1.1) due to the abundance of ozone near the mesopause (*Meinel* (1950); *Meinel* and *Meinel* (1983)). *Makhlouf et al.* (1995) provide a full list of possible reactions which cause production and loss of OH*, and these are shown in Equations 1.1−1.11. In these reactions, the vibrational level of the hydroxyl radical is denoted by v.

$$H + O_3 \rightarrow OH^*(v = 6 - 9) + O_2 + 3.34\ eV \quad (1.1)$$

Primary production (Bates-Nicolet mechanism)

$$O + HO_2 \rightarrow OH^*(v \leq 6) + O_2 \quad (1.2)$$

Secondary production (Perhydroxyl reaction)

$$O_3 + HO_2 \rightarrow OH^*(v) + 2O_2 \quad (1.3)$$

Tertiary source ($v = 0$)

$$O + O_2 + M \rightarrow M + O_3 \quad (1.4)$$

O_3 production

$$H + O_2 + M \rightarrow M + HO_2 \quad (1.5)$$

HO_2 production

$$OH^*(v) + O_3 \rightarrow HO_2 + O_2 \quad (1.6)$$

Minor sink ($v = 0$)

$$OH^*(v) + HO_2 \rightarrow H_2O + O_2 \quad (1.7)$$

Minor sink ($v = 0$)

$$OH^*(v) + O \rightarrow H + O_2 \quad (1.8)$$

Chemical quenching by atomic oxygen $(v = 0 - 9)$

$$OH^*(v) + O_2 \leftrightarrow OH^*(v-1) + O_2 \quad (1.9)$$

Collisional quenching/excitation by the molecular species O_2 $(v = 0 - 9)$

$$OH^*(v) + N_2 \leftrightarrow OH^*(v-1) + N_2 \quad (1.10)$$

Collisional quenching/excitation by the molecular species N_2 $(v = 1 - 9)$

$$OH^*(v) \rightarrow OH^*(v-n) + hv \quad (1.11)$$

Radiative decay $(v = 1 - 9), (n = 1 - 6), (v - n \geq 0)$

Some of the reactions shown above are caused by OH* collisional quenching. This is when the OH* molecule collides with another molecule in the atmosphere such as O_2 or N_2 (as in Equations 1.9 and 1.10). Collisional quenching can result in two different outcomes for the OH* molecule: 'sudden death', where the vibrational state, v, is reduced to $v = 0$, and 'collisional-cascade', where the vibrational state, v, is reduced to $v - 1$ (*McDade* and *Llewellyn*, 1987).

Atmospheric hydroxyl is not unique to the Earth's atmosphere; it has also been detected on other planets. For example, *Piccioni et al.* (2008) detected OH* in the Venus night time mesosphere and *Clancy et al.* (2013) detected OH* in Mars' polar winter atmosphere. As a result of these studies, it is now thought that the primary OH* production mechanism in Venus' atmosphere is either the Bates-Nicolet mechanism (Equation 1.1) or the perhydroxyl reaction (Equation 1.2) and the primary OH* production mechanism in Mars' atmosphere is the Bates-Nicolet mechanism (Equation 1.1). While collisional quenching of OH* in the terrestrial atmosphere is primarily through O_2 and N_2, it is more effective through CO_2 in the Martian atmosphere (*Clancy et al.*, 2013).

As mentioned above, it is often implied that measurements derived from OH* variations correspond to an altitude thickness of ~8 km centred at an altitude of ~87 km. However, studies have shown that pressure is often a better coordinate than altitude for both ground state (*Pickett et al.*, 2006) and vibrationally excited (*Grygalashvyly et al.*, 2014) OH layers. Therefore, when using atmospheric hydroxyl to infer information about temperature variations and dynamical processes, it is important to note that the hydroxyl layer, and hence the inferred quantity, changes with altitude; it is not always centred at 87 km altitude. For example, *Grygalashvyly et al.* (2014) showed that temperature trends which are derived from the emission from the OH*(6−2) transition, an emission line which is often used to infer long-term temperature trends, correspond more closely to temperature trends at constant pressure than at constant altitude (as illustrated in Figure 1.13).

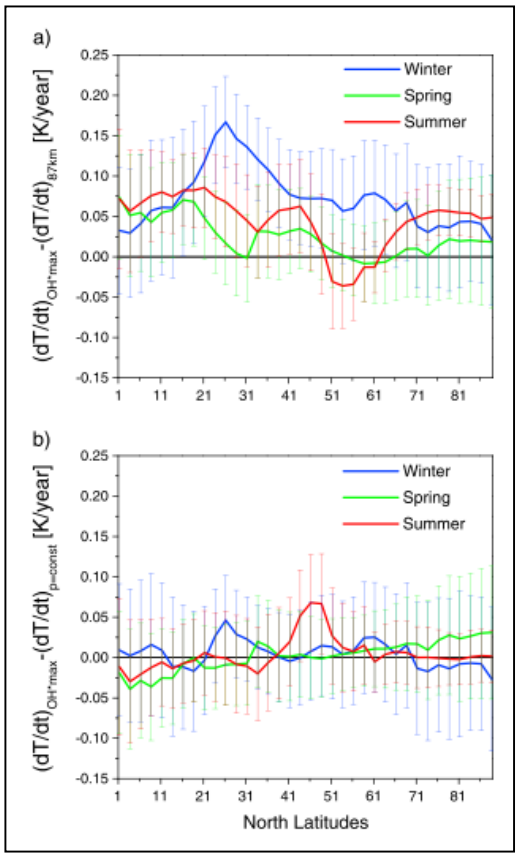

Figure 1.13: Latitudinal distributions in the northern hemisphere of differences between temperature trends inferred from the OH* ($v = 6$) peak and temperature trends at (a) constant altitude (87 km) and (b) constant pressure (0.00185 hPa) (*Grygalashvyly et al.*, 2014).

Finally, in order to understand the OH* layer's long-term behaviour, its functional dependencies were derived by *Grygalashvyly et al.* (2014). This will now be outlined briefly to conclude this section.

The amount of excited hydroxyl produced, P_{OH^*}, is primarily due to the Bates-Nicolet mechanism (shown in Equation 1.1). It follows that

$$P_{OH^*} \approx k_1[H][O_3], \tag{1.12}$$

where

$k_1 = 1.4 \times 10^{-10} e^{-460/T}$ is the reaction rate between H and O_3, and
square brackets denote the number density of the given constituents.

The amount of excited hydroxyl lost, L_{OH^*} is primarily due to quenching by molecular oxygen (as shown in Equation 1.9). Therefore,

$$L_{OH^*} \approx Q[O_2], \tag{1.13}$$

where

Q is the quenching rate of OH* due to collisions with O_2.

Additionally, it is known that the amount of ozone produced is equal to the amount of ozone lost during the night. Ozone is produced via the reaction $O + O_2 + M \rightarrow M + O_3$, where M denotes air, and it is lost primarily due to the Bates-Nicolet mechanism and $O + O_3 \rightarrow 2O_2$. Therefore,

$$k_4[O][O_2][M] \approx k_1[H][O_3] + k_5[O][O_3], \tag{1.14}$$

where the reaction rates for ozone production and loss are

$k_4 = 6 \times 10^{-34} (300/T)^{2.4}$,
$k_1 = 1.4 \times 10^{-10} e^{-460/T}$, and
$k_5 = 8 \times 10^{-12} e^{-2060/T}$.

To simplify, it is known that $k_5 \ll k_4$ at altitudes less than ~95 km, and hence k_5 is neglected. From Equations 1.12 and 1.14, this implies that

$$P_{OH^*} \approx k_4[O][O_2][M]. \tag{1.15}$$

Now, the number density of excited hydroxyl can be written as

$$[OH^*] = \frac{P_{OH^*}}{L_{OH^*}} \approx \frac{k_4[O][O_2][M]}{Q[O_2]} = \frac{6 \times 10^{-34} (300/T)^{2.4} [O][O_2][M]}{Q[O_2]}. \tag{1.16}$$

From the ideal gas law (which will be shown in Equation 1.19), it is known that $[\mathrm{M}] = \rho = p/(kT)$, where k is the Boltzmann constant.

The constants $(6 \times 10^{-34} \cdot 300^{2.4})/(kQ)$ can be written as a single term, B. Thus, the relationship between the number density of excited hydroxyl, pressure, temperature, and the number density of atomic oxygen, derived by (*Grygalashvyly et al.*, 2014), is given by

$$[\mathrm{OH}^*] \approx BpT^{-3.4}[\mathrm{O}]. \qquad 1.17$$

From Equation 1.17, it can be seen that the OH* peak can be derived from any particular set of vertical profiles for temperature, pressure, and atomic oxygen. Figure 1.14 shows an $[\mathrm{OH}^*]$ profile calculated using Equation 1.17, and it is observed that this emission layer is centred at approximately 87 km. A particular $[\mathrm{O}]$ and temperature profile was taken from the Mass Spectrometer Incoherent Scatter (MSIS) model data, a pressure profile was calculated simply using the barometric formula (as shown in Equation 1.18), and the value for OH* quenching rate due to molecular oxygen collisions used was an arbitrary value of $Q = 10^{-4}$ cm^3 molecules^{-1} s^{-1}, as exact values were not needed for the purpose of this project.

$$p(z) = p_0 e^{\frac{-mgz}{kT}} \qquad 1.18$$

where

$p(z)$ = pressure at altitude z,
p_0 = pressure at altitude $z = 0$,
m = mass of one molecule of ideal gas,
g = acceleration due to gravity,
z = altitude,
k = the Boltzmann constant, and
T = temperature.

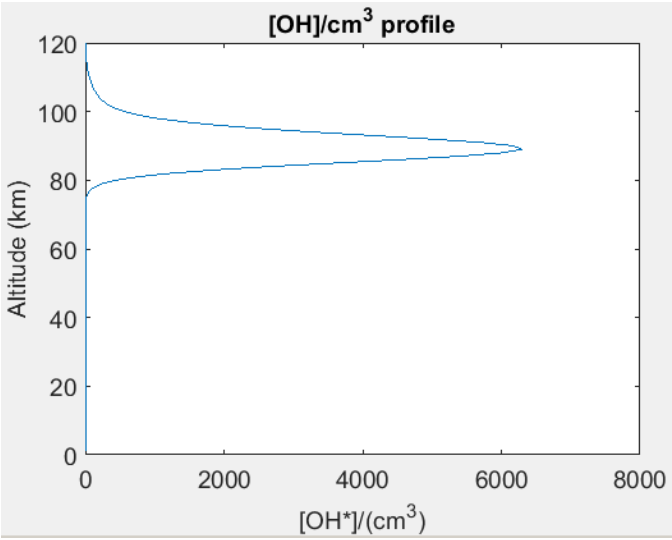

Figure 1.14: Excited hydroxyl number density profile derived from an MSIS [O] profile, a simplified pressure profile, and an arbitrary quenching rate of OH* due to O_2. It can be seen from this approximation that the OH* layer is centred in the mesopause region.

1.4.4. Aurora

Like airglow, aurora is an optical emission which occurs in upper atmospheres. It is distinguished from airglow based on its excitation source, which consists of high-energy ($\sim 1-10$ keV) electrons and ions from the solar wind and magnetosphere precipitating into the atmosphere in the polar regions, guided along the planet's magnetic field lines. These electrons and ions collide with atmospheric atoms/molecules in the region, some of which are excited and subsequently fluoresce as they are de-excited (*Sánchez-Lavega*, 2011).

The Earth's magnetic field acts as a solar wind barrier at low-mid latitudes, as depicted in Figure 1.15. This creates zones, known as the Van Allen belts (located between approximately 3000 and 60000 km from the Earth's surface (*Van Allen* and *Frank* (1959); *Van Allen* (1959); *Akasofu* and *Chapman* (1961))), of charged particles which originate from the solar wind but are held in place by the planet's magnetic field. As mentioned above, high-energy particles can still spiral into the atmosphere along the magnetic field lines (in the cusp regions), which converge at the poles, thus creating two ring-shaped regions of aurora at ~60−80° latitude (although they may rarely extend to the equator in the case of extremely strong magnetic disturbances) in both the

northern and southern hemispheres. Green aurora (557.7 nm) generally occurs at ~110−250 km altitude, while red aurora (630 nm and 636.4 nm) generally occurs at higher altitudes of >800 km where gas density is very low (*Cole* and *Woolfson*, 2002).

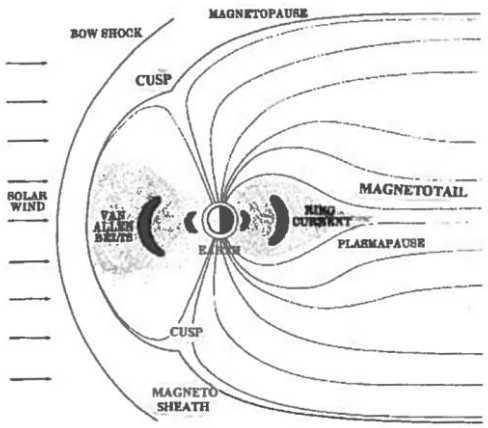

Figure 1.15: A schematic depicting the interaction between the Earth's magnetosphere and the incoming solar wind (*Cole* and *Woolfson*, 2002).

1.5. Atmospheric Dynamics

Motion in the atmosphere is linked to an almost infinite variety of physical and chemical processes. In this section, a simplified view of these motions is provided. Some concepts which will be covered here include the major atmospheric motions, the equations governing these atmospheric motions, and some simple dynamical models.

1.5.1. Major Atmospheric Motions

Solar radiation is the major driver for atmospheric motion. Incoming solar energy is not evenly distributed across all latitudes, and this creates differential heating between low and high latitudes, which gives rise to atmospheric circulation (as shown in Figure 1.16). Low latitudes receive most of the solar radiation which is incident upon the Earth, and then the heat energy is transported poleward. The thermal structure of the atmosphere also varies with season as a result of atmospheric motions. For example, the middle atmosphere at the solstice is not in radiative equilibrium and the differences are due to a

GW-driven mean meridional circulation from the summer to winter pole, with air rising from the summer pole and sinking toward the winter pole (*Vincent* and *Reid*, 1983).

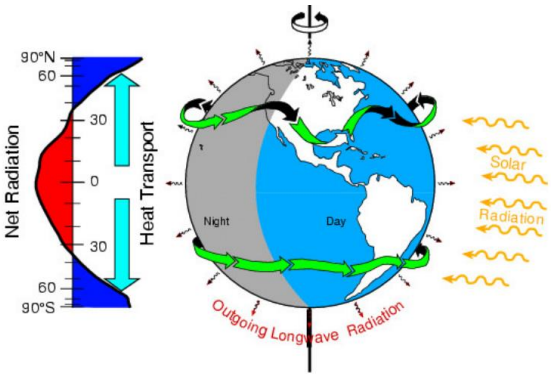

Figure 1.16: Differential solar heating between low and high latitudes (*Serreze*, 2011).

Atmospheric motions occur at a wide range of different scales, both temporally and spatially. Figure 1.17 shows the characteristic scales of some of these motions, and includes micro (~1 km), meso (~10−100 km), and synoptic (~1000 km) scale dynamics. GCMs can usually resolve anything within the meso and synoptic scales. In general, it is observed that large spatial scales are associated with long time scales (*Huang*, 1993).

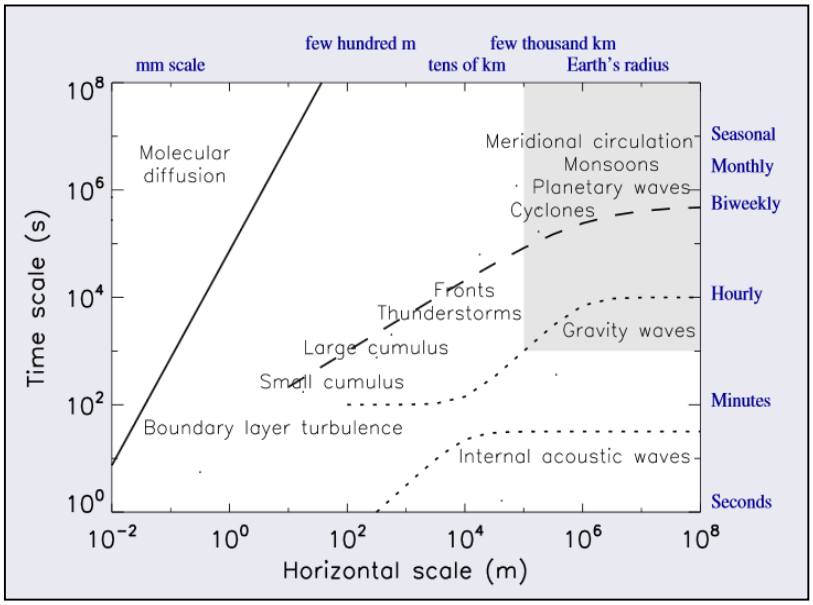

Figure 1.17: A schematic published by *Thurburn* (2011) outlining the spatial and temporal scales of different atmospheric structures and processes. The grey shaded region corresponds to what can generally be resolved by global climate models.

Atmospheric dynamics are governed by atmospheric forces. The major atmospheric forces are pressure, gravity, viscosity, the Coriolis force, and the centrifugal force. Each of these will now be discussed separately before describing how they are combined with fundamental physical laws and approximations to provide a somewhat simplified picture of the atmosphere.

The vertical forces mentioned above are the upward force of pressure and the downward force of gravity. These forces balance out in what is called hydrostatic equilibrium. This is described in detail in Appendix B.2.

The next major atmospheric force which is mentioned above is viscosity, or the frictional force. This is a measure of the resistance in a fluid (due to turbulence). Reynolds number, Re, which is the ratio of inertial forces to viscosity, is a measure of how important it is to include viscosity in a particular situation. A high Reynolds number signifies that viscosity is relatively unimportant. It can be calculated by $Re = \frac{Uh}{v}$, where U is the background wind in the propagation direction of the turbulent motion, h is half the depth of the shear layer, and v is the effective viscosity of the fluid, which can be either kinematic or turbulent (*Fritts et al.*, 2017a).

The Earth's rotation also introduces two fictitious forces; the Coriolis force and the centrifugal force, which are introduced when making Earth observations in a non-inertial reference frame. The apparent centrifugal force acts radially outward on an air parcel, while the apparent Coriolis force deflects a moving air parcel to the left (Southern Hemisphere) or the right (Northern Hemisphere) with a magnitude determined by the latitude, due to the conservation of angular momentum (as shown in Figure 1.18).

A combination of the Earth's rotation and the incoming solar energy generates three major circulation cells in each hemisphere of the atmosphere, as shown in Figure 1.19. At about 30° N/S latitude and at the poles, there are bands of high pressure, whereas at the equator and about $50-60$° N/S latitude, there are

bands of low pressure. These areas of different pressure, combined with the rotation of the Earth cause air to move around the globe in particular patterns. Examples of such air movements in the troposphere are jet streams, which are strong (often >90 m/s) winds typically thousands of kilometres long, a few hundred kilometres wide, and a few kilometres thick (*Wilhelmson* and *Ramamurthy*, 2010). Jet streams have a huge impact on the weather in certain regions, and occur at the pressure boundaries mentioned above. They are strongest in the winter because of larger latitudinal temperature differences (*e.g.* *Evers* and *Haak* (2010)).

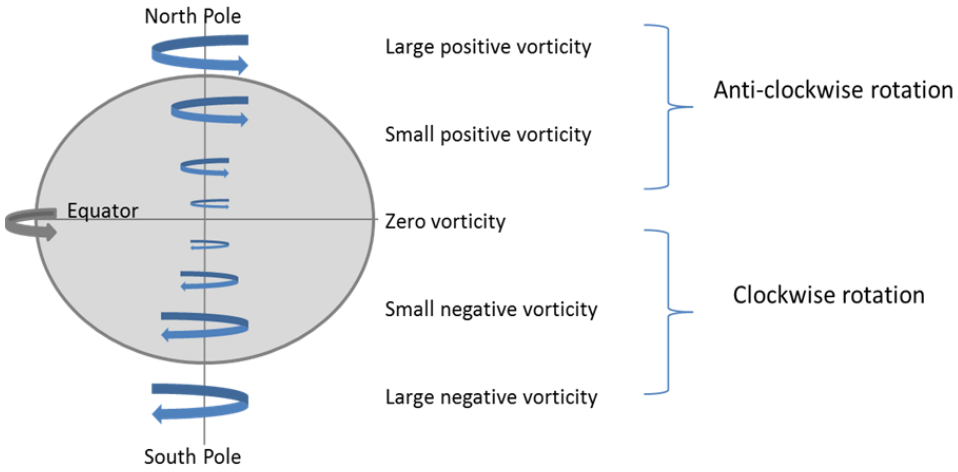

Figure 1.18: The equator to pole gradient of potential vorticity, due to the Earth's rotation (*Colling*, 2004).

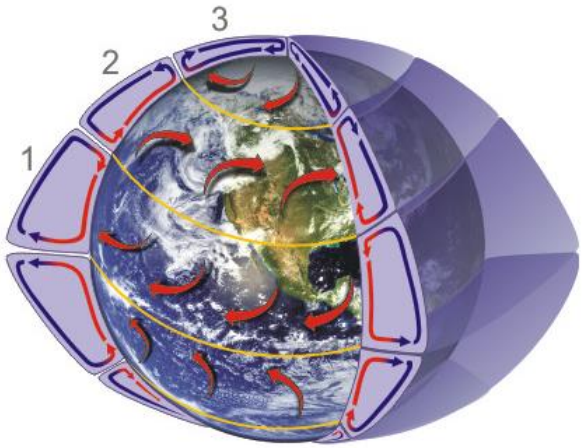

Figure 1.19: Air circulation in the Earth's atmosphere can be divided into three main cells in each hemisphere: (1) the Hadley cell, (2) the Ferrel cell, and (3) the polar cell (*NOAA*, 2011).

1.5.2. The Governing Equations of Atmospheric Motion

In the early twentieth century, Vilhelm Bjerknes compiled a few equations which appeared to govern the time evolution of the atmosphere. These equations could not be solved analytically (*Warner*, 2011) as some of the equations are non-linear and, therefore, are susceptible to chaos (*Gleick*, 1987). A simplified version of these equations is used in GCMs to represent atmospheric dynamics and provide a basic understanding of atmospheric processes.

In this thesis, the governing equations of atmospheric motions are described according to the 'Eulerian' description. This means that the motion of an air parcel is studied from a fixed point in space. An alternative way to express atmospheric motion is via the 'Lagrangian' description, which means that the flow of an air parcel is studied from a point in space which moves with the air parcel itself.

1.5.2.1. The Equation of State

The atmosphere is usually approximated as an ideal gas for simplicity, and modifications need to be made when concerned with effects such as moisture. The ideal gas law states that each air parcel obeys the following relationship:

$$P = \frac{NkT}{V} \tag{1.19}$$

where

P = pressure,
N = number of molecules,
k = Boltzmann's constant,
T = temperature, and
V = volume.

The number of molecules, N, may also be written as $M/(\mu u)$, where M = mass, μ = molecular mass, and u = the unified atomic mass unit (*Lee* and *Ryan*, 2015), so that the ideal gas law may be rewritten as $P = (\rho kT)/(\mu u)$, where ρ = density. Additionally, Boltzmann's constant may be rewritten in terms of the ideal gas constant, R, such that $k = R/N_A$, where N_A is Avogadro's number and

$N_A \times u = 1$ g/mol (*Sánchez-Lavega*, 2011). The ideal gas law may then be written as $P = (\rho RT)/\mu$.

1.5.2.2. The Continuity Equation

Matter is often redistributed throughout the atmosphere, but it cannot be created or destroyed. This imposes a restriction on how the mass of a particular air parcel can be changed; the change of mass inside an air parcel (such as that shown in Figure 1.20) must be equal to the sum of the net mass flows coming from all directions in 3-dimensional space. This law, which is known as the continuity equation, means that a parcel of air can be replaced by air of different density when air flow exists. For example, an air parcel in a divergent flow field experiences a reduction in density.

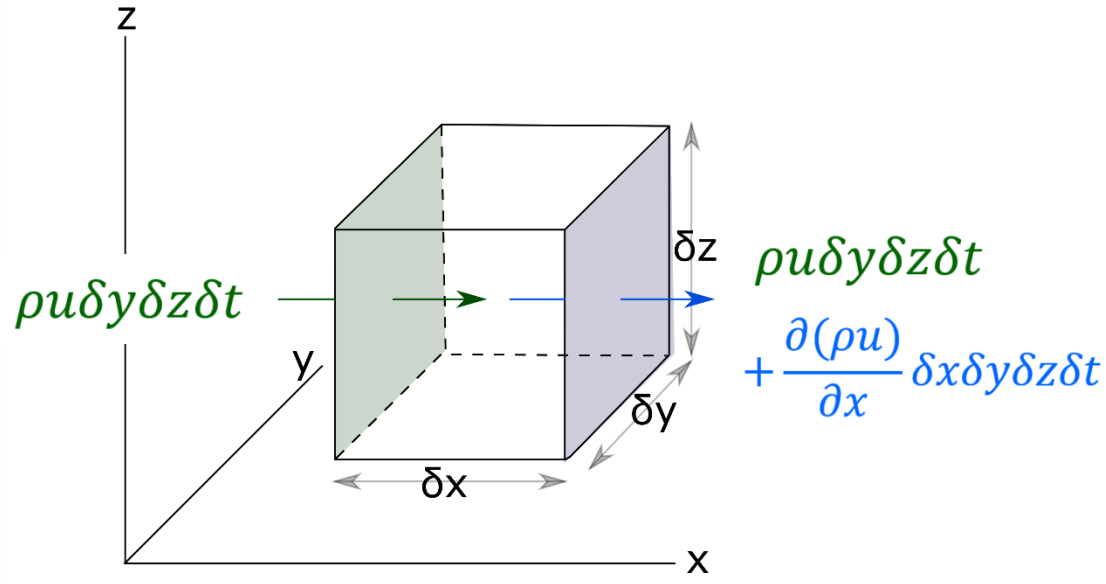

Figure 1.20: Schematic of a fixed (Eulerian) air parcel of volume $\delta x \delta y \delta z$ in 3-dimensional Cartesian coordinate frame, adapted from *Holton* (1992).

In order to understand the continuity equation, the change of mass in the x-direction only is considered. The mass entering the green shaded region in Figure 1.20 over a time δt is simply $\rho(u\delta y\delta z)\delta t$, where ρ is the air parcel density and u is the wind in the x-direction. The mass leaving the opposite face (*i.e.* the blue shaded region) of the air parcel is $\rho(u\delta y\delta z)\delta t + \frac{\partial(\rho u)}{\partial x}\delta x\delta y\delta z\delta t$,

where $\frac{\partial(\rho u)}{\partial x}\delta x$ denotes the change in mass flow over the distance δx in the x-direction. Therefore the change in mass in the x-direction can be written as $-\frac{\partial(\rho u)}{\partial x}\delta x\delta y\delta z\delta t$. In a similar way, the change in mass in the y- and z-directions can be written as $-\frac{\partial(\rho v)}{\partial y}\delta x\delta y\delta z\delta t$ and $-\frac{\partial(\rho w)}{\partial z}\delta x\delta y\delta z\delta t$ respectively, where (u, v, w) is the 3-dimensional wind. Therefore, the net change of mass inside the air parcel can be expressed as $\frac{\partial \rho}{\partial t}\delta x\delta y\delta z\delta t = -\frac{\partial(\rho u)}{\partial x}\delta x\delta y\delta z\delta t - \frac{\partial(\rho v)}{\partial y}\delta x\delta y\delta z\delta t - \frac{\partial(\rho w)}{\partial z}\delta x\delta y\delta z\delta t$ (*e.g. Holton* (1992)). Dividing both sides of this equation by $\delta x\delta y\delta z\delta t$, the continuity equation is obtained in its simplest form as follows:

$$\frac{\partial \rho}{\partial t} = -\frac{\partial(\rho u)}{\partial x} - \frac{\partial(\rho v)}{\partial y} - \frac{\partial(\rho w)}{\partial z}. \qquad 1.20$$

The continuity equation may alternatively be written in its mass divergence form as $\frac{\partial \rho}{\partial t} + \nabla \cdot (\rho U) = 0$ or, using the vector identity $\nabla \cdot (\rho U) \equiv \rho \nabla \cdot U + U \cdot \nabla \rho$, in its velocity divergence form as $\frac{D\rho}{Dt} + \rho \nabla \cdot U = 0$ where $\frac{D\rho}{Dt} = \frac{\partial \rho}{\partial t} + U \cdot \nabla \rho$ (which is the form used, for example, by *Nappo* (2002)).

1.5.2.3. The Navier-Stokes Equation

The Navier-Stokes equation describes the flow of fluids, and can be described as the conservation of momentum equation for fluids. It is based on Newton's 2nd law of motion and basically states that the rate of change of momentum of a fluid parcel will be equal to the sum of the forces acting on that fluid parcel. In its most general form, the Navier-Stokes equation may be written as $\rho\left(\frac{\partial \vec{v}}{\partial t} + \vec{v} \cdot \nabla \vec{v}\right) = -\nabla P + \nabla \cdot \mathrm{T} + \mathrm{F}$ (*Cochrane*, 2016), where the term $\left(\frac{\partial \vec{v}}{\partial t} + \vec{v} \cdot \nabla \vec{v}\right)$ represents the acceleration of the fluid parcel, and the forces on the right of the equation represent the forces which act on the fluid parcel, *i.e.* the pressure gradient, the stress tensor (which takes movements within the fluid parcel into account), and any other external forces (*e.g.* the gravitational force).

The major (fundamental) atmospheric forces are the pressure gradient force, the gravitational force and the internal frictional force (viscosity), and since atmospheric motion is generally referred to using a coordinate system which is rotating with the Earth, the apparent Coriolis and centrifugal forces must also be included (*e.g. Holton* (1992)). If all of these forces are taken into consideration, the apparent acceleration of an air parcel in a rotating frame of reference moving with the Earth is given by the following Navier-Stokes equation:

$$\frac{\mathrm{d}\vec{v}}{\mathrm{dt}} = -\frac{\nabla p}{\rho} + \vec{g} + \vec{a}_{\mathrm{f}} - \left(2\vec{\Omega} \times \vec{v}\right) - \left(\vec{\Omega} \times \left(\vec{\Omega} \times \vec{r}\right)\right), \qquad 1.21$$

where

$-\nabla p$ is the pressure gradient force,
$\vec{g}$ is the acceleration due to gravity,
$\vec{a}_{\mathrm{f}}$ is the frictional acceleration,
$-\left(2\vec{\Omega} \times \vec{v}\right)$ is the Coriolis acceleration,
where $\vec{\Omega}$ is the angular velocity of the Earth, and
$-(\vec{\Omega} \times (\vec{\Omega} \times \vec{r}))$ is the centrifugal acceleration,
where $\vec{r}$ is the displacement from centre of the Earth to centre of the air parcel.

The Navier-Stokes equation may sometimes be further simplified, since the Coriolis force, the centrifugal force and the frictional force are all usually relatively small in comparison to the other terms. In other words, it is often assumed (*e.g. Nappo* (2002)) that the atmosphere is frictionless and irrotational, thus producing the simplified Navier-Stokes equation, $\frac{\mathrm{d}\vec{v}}{\mathrm{dt}} = -\frac{\nabla p}{\rho} + \vec{g}$.

1.5.2.4. The 1st Law of Thermodynamics

One of the fundamental physical principles is that energy cannot be created or destroyed. Two air parcels can exchange energy by work done or by heat transfer from one parcel to the other. The first law of thermodynamics for an air parcel (which is approximated as an ideal gas and accounts for adiabatic and diabatic effects on temperature (*Warner*, 2011)) is given by

$$\rho C_{\mathrm{p}} \frac{\partial T}{\partial t} = k\nabla^2 T - \rho C_{\mathrm{p}} \vec{u} \nabla T + S, \qquad 1.22$$

where

C_p is the specific heat capacity at constant pressure,
k is the thermal conductivity,

$\vec{u}$ is the fluid velocity,

and the major terms are

the total rate of change of energy in the parcel of air, $\rho C_{\mathrm{p}} \frac{\partial T}{\partial t}$,
the rate of change of energy due to conduction, $k\nabla^2 T$,
the rate of change of energy due to convection, $-\rho C_{\mathrm{p}} \vec{u} \nabla T$, and
the rate of change of energy due to radiation, S.

1.5.2.5. Conservation of Water

As shown in Table 1.1, water vapour accounts for <3% of the total mass of the atmosphere. Despite its low abundance, it plays a huge role in atmospheric dynamics because of its physical and radiative properties (*Stevens* and *Bony*, 2013). The water mixing ratio, which is the ratio of water to dry air in an air parcel, is a highly variable quantity, and depends on variables such as latitude, altitude, and season. The relationship between the water mixing ratio, evaporated water, and condensed water (given by *Kalnay* (2003)) is

$$\frac{\mathrm{d}q}{\mathrm{d}t} = E - C, \qquad 1.23$$

where

E = the mass of evaporated water,
C = the mass of condensed water, and
q = the water mixing ratio.

1.5.3. Dynamical Models of the Atmosphere

Using current knowledge of local interactions of air masses, water, energy, and momentum, atmospheric models are used in an attempt to explain the atmosphere's large-scale features, fluctuations, and response to external pressures (*Schmidt*, 2007). Atmospheric models may be categorised into three main groups: simple, intermediate and complex. Simple models include a minimum number of physical processes which can all be described by simple mathematical equations and can be solved analytically. Intermediate models include a small number of (but more than simple models) physical processes. They may require large computational times, and so computers are needed for these models. The benefit of simple and intermediate models is that they

provide a comprehensible view of atmospheric dynamics. They can also be used to interpret or troubleshoot the more complex models. Complex models include the largest possible number of physical processes and so they require very long computational times, but they are the most accurate way of representing the atmosphere and predicting its future behaviour and so are used in GCMs and Numerical Weather Prediction (NWP) models. Any of these models may include dynamical, radiative or chemical processes, which may in turn affect each other via interactions illustrated in Figure 1.21, but the inclusion of such interactions make the model progressively more complex and therefore many interactions are neglected for a simple analysis (*Andrews*, 2005).

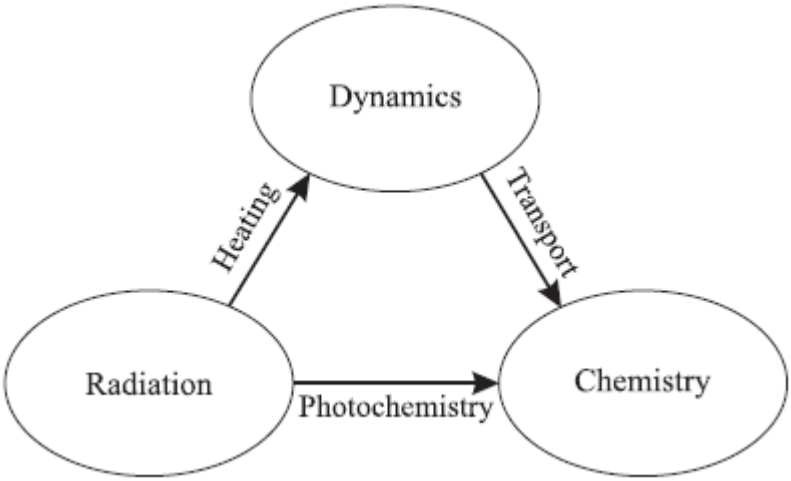

Figure 1.21: Interactions between the three main physical process types which are included in atmospheric models (*Andrews*, 2005).

The basic building blocks for any of these atmospheric model types are the equations (each of which describe a physical, chemical, or biological process in the climate system) in which they use. Some of these equations are more complex/fundamental than others. For example, some of the governing equations of the atmosphere (*i.e.* the continuity equation and the Navier-Stokes equation), which have been described in section 1.5.2, are partial differential equations which involve differentiation in space and time. In order to side-step the difficulties associated with such equations (*i.e.* the equations cannot be handled by a computer since the initial conditions are not known over

continuous temporal or spatial dimensions), they are generally simplified. This may be done using the finite difference method, where the equations are converted to a discrete form, and are only defined for specific times and locations which are separated by non-zero time and spatial steps (*Goosse*, 2015). A general classification scheme for equation types, in order of increasing complexity, is as follows:

1. Equations which can be calculated from fundamental principles, *e.g.* orbital mechanics, conservation of energy, and the ideal gas law.
2. Continuous equations which must be transferred to their discrete counterparts for numerical evaluation, *e.g.* transfer of radiation through the atmosphere and the Navier-Stokes equation of fluid motion.
3. Equations verified only by observation rather than by theory, *e.g.* evaporation as a function of wind speed and humidity.

Complex models are currently in use for a variety of reasons. For example, NWP and climate models are both used to make short/long-term forecasts by integrating the governing equations of the atmosphere over time, using some initial known state and boundary conditions. The initial state may not be known with great accuracy, and this poses a problem in terms of chaotic atmospheric processes whose time evolutions are highly dependent on initial conditions. To combat this problem, an ensemble of forecasts are generally now used, each starting with different initial conditions whose range is determined by the uncertainty on the initial state. The forecast confidence is then determined by the deviation in the ensemble of forecasts from each other. NWP models, in particular, require an extremely accurate representation of the atmosphere in order to accurately predict its condition days to weeks in advance. In order to represent the atmosphere to this level of accuracy, both large- and small-scale dynamical processes must be represented in the models. One issue is that some small-scale processes (such as drag due to small-scale GWs, turbulence, cloud micro-physics processes, *etc.*) occur on a sub-grid scale,

meaning that they occur on scales which are smaller than the spatial resolution of the model (which is visualised in Figure 1.22). They therefore cannot be explicitly represented in the model, and in order to include such processes, they must be parameterised - meaning that empirical or theoretical approximations of small-scale processes must be expressed in terms of some of the larger-scale processes which can be represented in models (*e.g. Andrews* (2005); *Goosse* (2015)).

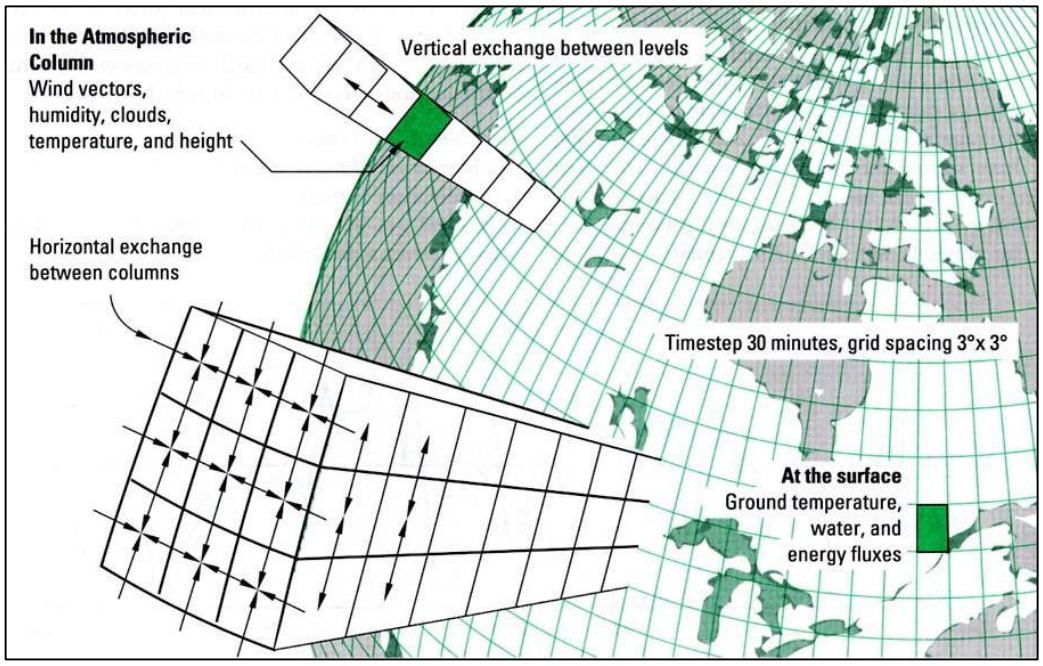

Figure 1.22: An example of grids used to create a global climate model of the atmosphere (*Ball*, 2012).

As there always exists a limited amount of computational resources, different atmospheric models have different goals, and so they apply different parameterisations with unique tunings depending on how complex they need to be. For example, they may be dynamics-only models or chemistry-coupled models, depending on why they are being used (*Alexander et al.*, 2010). Climate models and NWP models also have different requirements. NWP models, as discussed, must include as much detail as possible in order to accurately produce short-term forecasts. Alternatively, climate models focus on the long-term (years to decades) behaviour and change of the atmosphere and

so processes which only contribute to the day-to-day variation of the atmosphere are not of vital importance in such models (*Andrews*, 2005).

Because of a lack of observations and limited computational capabilities, some approximations about atmospheric circulation are often made in atmospheric models. The major approximations include (*i*) geostrophic balance (between two major horizontal forces; the Coriolis force and the pressure force due to large-scale radiative and adiabatic heating/cooling), and (*ii*) hydrostatic balance (between two major vertical forces; the force of gravity and the buoyancy force). These approximations do not accurately represent some observations which have been made. For example, temperature and wind measurements from the polar mesosphere (*Hartquist et al.*, 2009) and stratosphere (*Mitchell et al.*, 2016) are not accounted for in these models.

With the ever increasing numerical capabilities of computers, more components are constantly being added to atmospheric models in order to obtain a more accurate representation of the atmosphere. Since the 1960s, climate models have increased our understanding of the general circulation of the atmosphere and the potential dangers of human interference on the Earth's climate (*Lynch*, 2009).

Atmospheric models are currently being used to discover links between major weather events in various layers of the atmosphere. This is done by replicating major weather events and, in particular, studying how their effects propagate vertically. These links could be useful for the prediction of GPS, radio signal, and aviation disruptions. The Whole Atmosphere Community Climate Model (WACCM) is an example of one such model. WACCM was developed by the National Centre for Atmospheric Research (NCAR) in Colorado. It is a comprehensive numerical model which spans altitudes from the Earth's surface up as high as the thermosphere, unifying modelling in the lower, middle, and upper atmosphere. *Garcia et al.* (2007) provide details on the calculation of the

GW spectrum which is calculated by WACCM (version 3) for non-orographic waves generated in the troposphere at ~500 mbar and oriented in the wind direction at their source. The GW source stress spectrum is specified as a Gaussian in phase speed using the following equation:

$$\tau_s(c) = \tau_b \exp\left[-\left(\frac{c - U_s}{c_w}\right)^2\right]$$

where

τ_s is the GW source stress spectrum,
τ_b represents the seasonal and latitudinal variation of τ_s,
c is the GW phase speed,
U_s is the absolute value of the source wind (Gaussian centre), and
c_w is the Gaussian RMS width.

The GW source spectrum was calculated for each day of the year at the latitude of Davis Station, as shown in Figure 1.23. Later in this thesis, in Chapter 3, this source spectrum will be commented on with respect to actual GW measurements made at Davis Station, but a direct comparison cannot be made as they correspond to different altitudes.

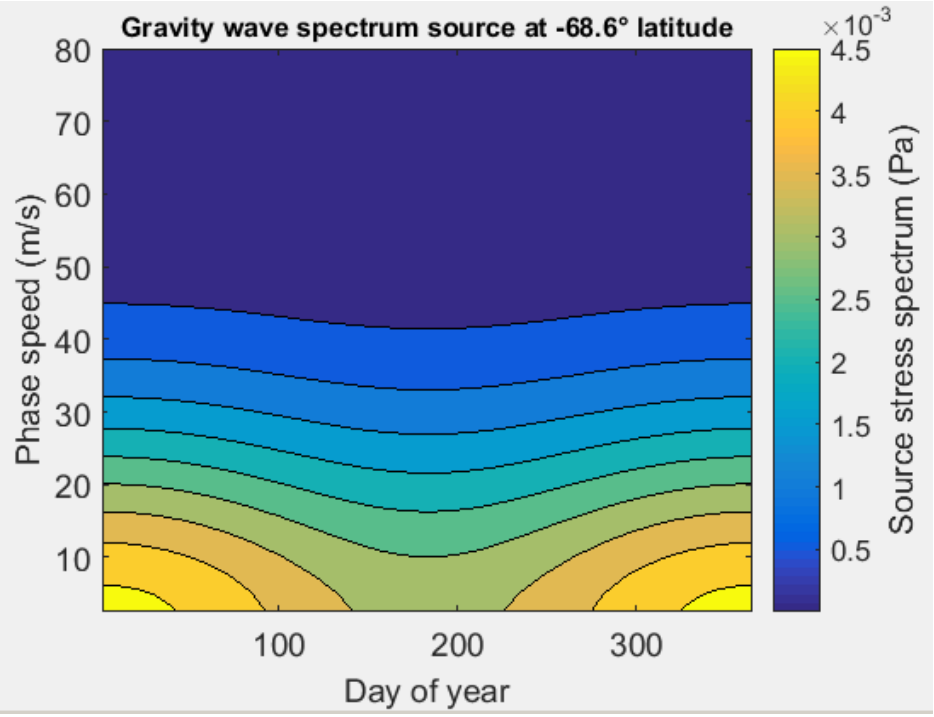

Figure 1.23: WACCM's GW source spectrum parameterisation at Davis Station (68.6° S), calculated using documentation provided by *Garcia et al.* (2007).

1.6. Atmospheric Waves

Atmospheric waves play a vital role in atmospheric dynamics. They are a mechanism by which the atmosphere can propagate disturbances, and are a result of restoring force action on air parcels which have been displaced from their equilibrium positions. These restoring forces may be due to compressibility, gravity, rotation, or electromagnetic effects, and this is what defines the type of atmospheric wave. Examples of atmospheric waves include acoustic waves, gravity waves and planetary waves (*Holton*, 1992). Atmospheric waves can contribute greatly to global circulation in the atmosphere. As mentioned in section 1.1, they can transport energy, momentum and trace constituents through the atmosphere. This is illustrated in Figure 1.24.

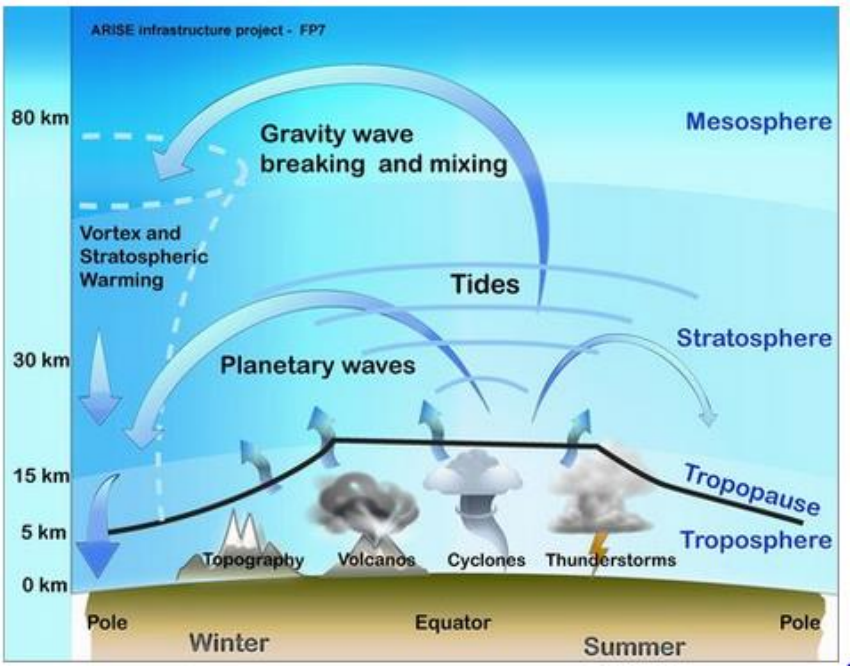

Figure 1.24: Dynamics of the troposphere-stratosphere-mesosphere exchanges including contribution of GWs and planetary waves (*ARISE*, 2015).

The amplitude of atmospheric waves increases with an increase in altitude as, in order to maintain a constant energy flux, they must compensate for the exponential decrease in air density with altitude. This amplification is proportional to $\frac{1}{\sqrt{\rho}}$, where ρ is the density of the air (*e.g. Bittner et al.* (2010);

Nappo (2002)). At a certain altitude, the waves dissipate. In the case of acoustic waves, this dissipation is generally due to viscosity or thermal conductivity, and occurs in the upper atmosphere at ~110−160 km, depending on the exact wave frequency. In the case of gravity waves, energy dissipation is generally due to convective or shear instability, causing the waves to break in the upper atmosphere. Other wave energy dissipation mechanisms may occur before the wave reaches the upper atmosphere due to, for example, wave blocking by strong winds (*Blanc et al.*, 2010).

1.6.1. Planetary Waves

Planetary waves, also known as Rossby waves (named after meteorologist Carl-Gustaf Rossby) are very large-scale ($\lambda_h \approx 4000 - 8000$ km), transverse, low-frequency waves, an example of which is shown in Figure 1.25. The restoring force which drives planetary waves is the conservation of vorticity with altitude when there is a mean gradient of vorticity with latitude (as shown in Figure 1.18), and so they form due to the rotation of a planet (*e.g.* they have been observed in the atmospheres of Earth, Venus and Mars). They are generally stationary, or move very slowly in the westward direction (*Taylor*, 2010). The number of planetary wave cycles around a given latitude circle on the Earth is called the zonal wavenumber (*Wackter*, 1976).

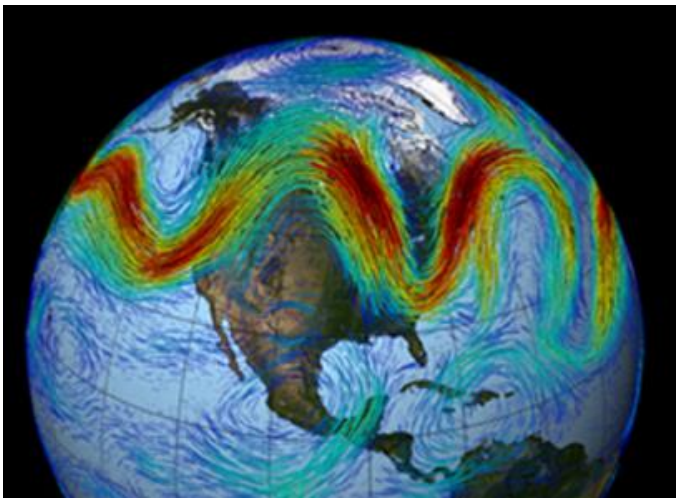

Figure 1.25: Planetary wave structure visible in the polar jet stream – Figure from NASA's Goddard Space Flight Center.

Planetary waves can lead to dramatic deviations of the air flow from its climatological mean in the mid- to high-latitudes. For example, during the darkness of winter, a wind pattern in the stratosphere (at ~60 km (*Evers* and *Haak*, 2010)) called the polar vortex circulates around the pole, preventing warm air from mixing in. This zonal wind forms due to the latitudinal temperature gradient in the middle atmosphere, which arises from solar heating (*Tsuda*, 2014). This wind barrier allows the cold air over the pole to get even colder, and it remains strong right into spring, especially in the southern hemisphere where there is less land mass to break it up than in the northern hemisphere. Planetary waves can disturb this winter-time polar vortex, causing it to break up or change direction. In particular, the propagation and breaking of planetary waves as they travel from the troposphere to the stratosphere can cause a sudden stratospheric warming (SSW). SSWs are rapid increases in polar stratospheric temperature (up to tens of degrees Kelvin in the space of a week (*Blanc et al.*, 2010)), and can occur during winter or spring. SSWs can cause a lasting effect (sometimes lasting more than 2 months after the event (*Blanc et al.*, 2010)) on tropospheric climate.

1.6.2. Acoustic Waves

Acoustic waves (*a.k.a.* sound waves), whose restoring force is the compression force, are high-frequency longitudinal waves that propagate at the speed of sound (*Hecht et al.*, 2007) by the alternating adiabatic compression and expansion of air (*Holton*, 1992). They create small pressure fluctuations in comparison to the background pressure, and these fluctuations can range from hundredths to tens of pascals (*Evers* and *Haak*, 2010). Acoustic waves are ducted in an atmospheric wave guide formed by the different gradients of the atmosphere, and so they can propagate over very large distances (*Blanc et al.*, 2010).

Acoustic waves may be characterised by their infrasound (below the human hearing threshold of ~20 Hz) frequency range. The lower frequency limit,

known as the acoustic cut-off frequency (N_A), of infrasound is determined by the thickness of the atmospheric layer through which it propagates using the formula $N_A = c_s/(2H)$, where c_s is the speed of sound, H is the scale height (described in Appendix B.3), and the unit is rad s^{-1} (*Gossard* and *Hooke*, 1975). The typical value for the acoustic cut-off frequency in the troposphere is ~3.3 mHz (~5 minutes). When the wave frequency becomes too low (below the acoustic cut-off frequency), gravity begins to act on the air which has been displaced by the wave. In this case, when gravity becomes part of the restoring force, the waves become gravity waves, which are transverse waves propagating slower than the speed of sound. The upper cut-off frequency for gravity waves (N) is called the Brunt-Väisälä frequency (described in Appendix B.4) and is typically ~2.9 mHz (~5.7 minutes) in the troposphere, although this depends on atmospheric stability in the region (*Evers* and *Haak*, 2010). The frequency difference between acoustic and gravity waves is illustrated in Figures 1.26 and 1.27. It can also be seen from these two figures that between the acoustic and gravity dominated regimes, waves are evanescent (*a.k.a.* external waves or lamb waves). Evanescent waves lack vertical phase variation, and thus don't freely propagate vertically (*Hecht et al.*, 2007).

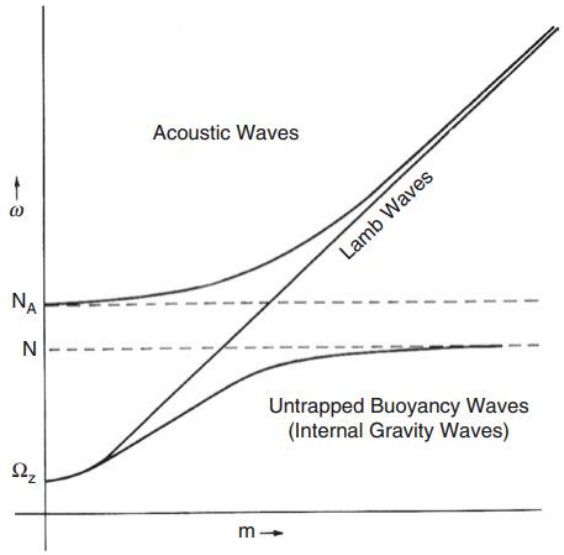

Figure 1.26: Acoustic-Gravity dispersion diagram for waves propagating in the vertical direction (*Gossard* and *Hooke*, 1975).

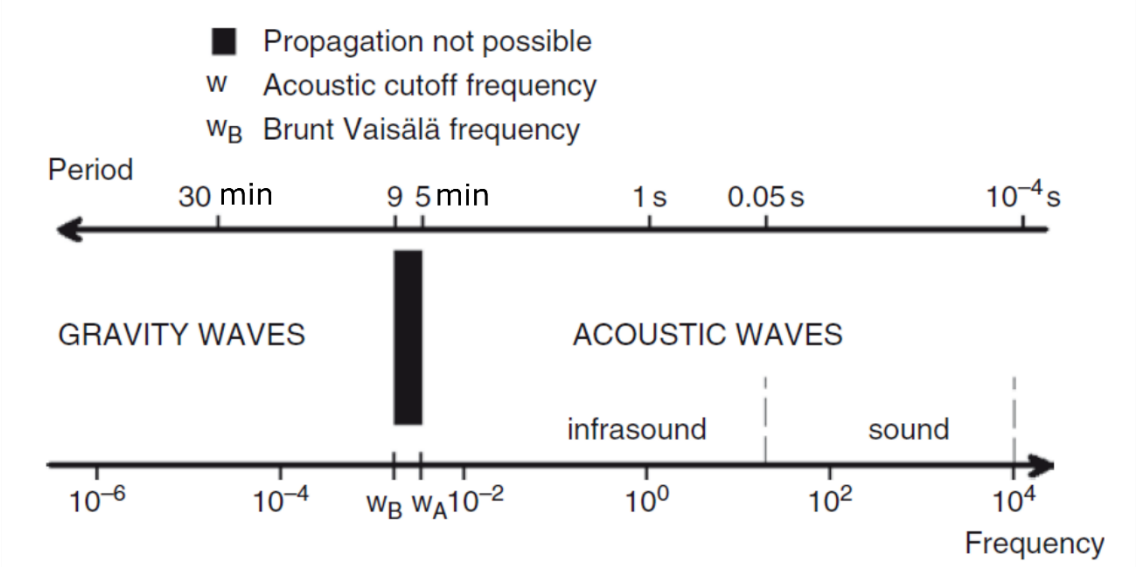

Figure 1.27: The frequency range of gravity waves and acoustic waves. w_B and w_A here denote the Brunt-Väisälä frequency and the acoustic cut-off frequency respectively (*Blanc et al.*, 2010).

The International Monitoring System (IMS) infrasound network detects a large number of infrasound signals every day. The sources of these signals are often unknown, and they may result from a wide range of different natural or anthropogenic events. Examples of natural pseudo-continuous infrasound sources, with typical frequencies <0.5 Hz (*Le Pichon et al.*, 2010), include microbaroms (standing waves generated by storms at the ocean surface), airflow over mountains, aurorae, meteors, calving of icebergs/glaciers, and volcanic eruptions. Some examples of more intense natural events which generate sharp bursts of infrasound activity, generally with frequencies of $0.2-2$ Hz (*Le Pichon et al.*, 2010), include severe convective storms, earthquakes, or larger volcanic eruptions. Some anthropogenic sources of infrasound include rocket launching, supersonic aircraft, and chemical or nuclear explosions (*Campus* and *Christie*, 2010). A surprisingly large temperature impact at high altitudes from infrasound (produced by ocean swells) has been estimated, with 5- and 10-second period infrasound waves inducing heating rates of 30 and 11 K/day (respectively) at altitudes of $110-140$ km (*Blanc et al.*, 2010).

Infrasound data has many practical applications, including: (*i*) validation and extension of atmospheric models (by determining atmospheric structure with potentially unprecedented spatial and temporal resolution using the quasi-continuous natural infrasound sources such as microbaroms (*Le Pichon et al.*, 2010)) which is especially important between 40 and 90 km altitude where there is a particular lack of routine measurements (*Le Pichon et al.*, 2010), (*ii*) geophysical hazard warning systems (by making use of the ducted (high speed and low attenuation) nature of these waves) and (*iii*) global warming monitoring (*Campus* and *Christie*, 2010).

1.6.3. Gravity Waves

Gravity waves (*a.k.a.* buoyancy waves) can be described as oscillations of air parcels lifted by the buoyancy force and restored by the force of gravity. Only stably stratified fluids (whose density increases with depth) are able to support and propagate GW motions. This is because, when the fluid boundary is disturbed, oscillations (which propagate as GWs) occur as gravity tries to restore it to its stable equilibrium state.

GWs may occur between any stable layers of fluids of different density. There are two main types of GWs: surface GWs and internal GWs. Surface GWs oscillate on the surface between two fluid mediums, where the light fluid is overlying the heavy fluid (*e.g.* surface GWs are often seen between water and air, as shown in Figure 1.28). Internal GWs oscillate within a stratified fluid medium, where density decreases with height (*e.g.* internal GWs propagate within the atmosphere, as shown in Figure 1.29).

The Earth's atmosphere is almost always stably stratified, except for the planetary boundary layer (a thin atmospheric layer which is in contact with the Earth's surface – ranging from about 500−3500 m in depth (*McGrath-Spangler* and *Denning*, 2012)). Therefore, it would be reasonable to assume that GWs are ubiquitous in the Earth's atmosphere (*Nappo*, 2002). In particular, a stably

stratified night-time atmosphere is a common occurrence because heat is lost to space by radiation during the night (*Cushman-Roisin*, 2014). This is important to note because the GW observations of the OH* airglow used in this project are all made at night.

Figure 1.28: Surface GWs visible on the boundary between water and air.

Figure 1.29: Internal GWs visible in tropospheric clouds in a stable atmosphere. (left) Photo taken in Maynooth, Co. Kildare on 13th August 2015 by the author. (right) Photo taken in Kilcock, Co. Kildare on 29th March 2015 by Frank Mulligan.

GWs have a particular set of characteristics which define them amongst other atmospheric waves. They are transverse waves whose upper cut-off frequency is the Brunt-Väisälä frequency, which is typically ~ 2.9 mHz (as illustrated in Figure 1.27) and lower cut-off frequency is the Coriolis parameter, f, which is given by $f = 2\Omega_E \sin(\phi_L)$ where $\Omega_E = 7.292 \times 10^{-5}$ rad s^{-1} (*Nappo*, 2002). Since GW periods are generally quite long, the force due to gravity is much stronger than the force due to air pressure differences, and so air pressure differences are usually neglected in the case of gravity waves (as described by the Boussinesq

approximation in Appendix B.5). GWs may propagate in any direction with horizontal spatial scales of tens to thousands of kilometres (where the higher frequency waves generally occur at shorter horizontal scales (*Ploughonven* and *Zhang*, 2014)), vertical spatial scales theoretically ranging anywhere from 0 to ∞ (*Alexander et al.*, 2010), and temporal scales of minutes to hours (*Fritts* and *Alexander*, 2003).

Some examples of gravity wave sources include stably stratified air flowing over an irregular lower boundary (*e.g.* air flow over mountains), convective systems (which dominate the tropics), and geostrophic adjustment occurring due to unbalanced flow near jets, fronts, and wave-wave interactions. GWs caused by convective systems are quite complicated as they can have a full range of speeds, frequencies, and spatial scales and so they can be found at a large horizontal distance away from their source, making it hard to trace them back to their source (*Fritts* and *Alexander*, 2003). GWs caused by orography generally create hot spots of very intense GW activity (*Hoffmann et al.*, 2013), but the integrated contribution of non-orographic sources (such as jets/fronts) is comparable to the integrated contribution of orographic sources, while also representing a different spectrum of waves which force the middle atmosphere in different ways to orographic waves. Several studies have indicated very strong GW activity in the vicinity of jet/front systems (*Ploughonven* and *Zhang*, 2014), and this will be studied in further detail in Chapter 4 for the case of the stratospheric polar-night jet, and in Chapter 5 for cases of mesospheric fronts.

The mechanism by which GWs contribute to atmospheric circulation, structure, and variability is wave energy dissipation. The main atmospheric processes which cause wave dissipation include convective and dynamical instabilities (which are described in Appendix B.4), wave-wave elastic interactions, wave-wind interactions, and radiative damping (*e.g. Lu et al.* (2009); *Takahashi et al.* (2014); *Tsuda* (2014)). The resulting divergence of dissipating wave-associated energy and momentum-flux produces changes in the acceleration and

temperature of the mean flow (*Gossard* and *Hooke*, 1975). In other words, although it is known that differential solar heating is largely responsible for the general circulation of the middle atmosphere, zonal mean momentum dissipation processes cause some deviations from the radiative equilibrium in temperature and wind profiles. During the summer in the middle atmosphere, when planetary waves are weak, it is thought that GW attenuation (above their energy dissipation altitude) with altitude is the main cause of momentum dissipation (*Geller*, 1983). Accurate approximations of this wave momentum-flux in the upper atmosphere are needed. The first ever observation of GW momentum-fluxes in the mesosphere was made by *Vincent* and *Reid* (1983) and, since then, there have been many different methods used to observe GW momentum-fluxes. An attribute that all of these methods have in common is that they measure fluctuations about some mean to show the presence of GWs, then measure the amplitudes of the waves, and finally calculate the momentum-fluxes (*e.g.* using temperature or wind measurements) (*Alexander et al.*, 2010).

Wave breaking, which is a result of wave dissipation, is shown diagrammatically in Figure 1.24. GWs move through the different atmospheric layers before breaking due to either convective or dynamical (shear) instability which has been caused by either growth of the wave amplitude with height or through reduction of the vertical wavelength by Doppler-shifting (*e.g. Tsuda* (2014)). The wave breaking process due to convective instability is now described in more detail. The energy carried by an upward-propagating GW is assumed to be conserved. Therefore, as the GW moves into air which is less dense, its amplitude increases. At a certain altitude, usually in the MLT region, the wave amplitude eventually becomes large enough such that it causes the temperature to decrease more rapidly with height than the surrounding air. This results in convective instability, causing the wave to dissipate by breaking. This instability causes turbulence and mixing of air from different origins. As air from different origins mix, a transfer of energy, momentum, and trace

constituents occurs. This affects the wind and, hence, adiabatic heating and cooling.

GW dissipation depends on the difference between GW speed and local wind speed, as a GW will be absorbed if the wind speed is equal to or greater than the wave speed. In other words, GWs generally become unstable and dissipate at altitudes (*a.k.a.* critical levels) near or below where the intrinsic wave frequency, $\widehat{\omega}$, tends to zero. This is known as critical-level filtering of GWs, and is illustrated in Figure 1.30. Since wind speeds fluctuate depending on season, so does GW filtering and, hence, the amount of GWs reaching the mesosphere will also vary with season. As a result, GWs tend to break in the polar stratosphere in the winter and the polar mesosphere in the summer, causing a much higher GW-induced drag, or wind acceleration, and adiabatic cooling in the summer mesosphere than in the winter mesosphere (*Hartquist et al.*, 2009).

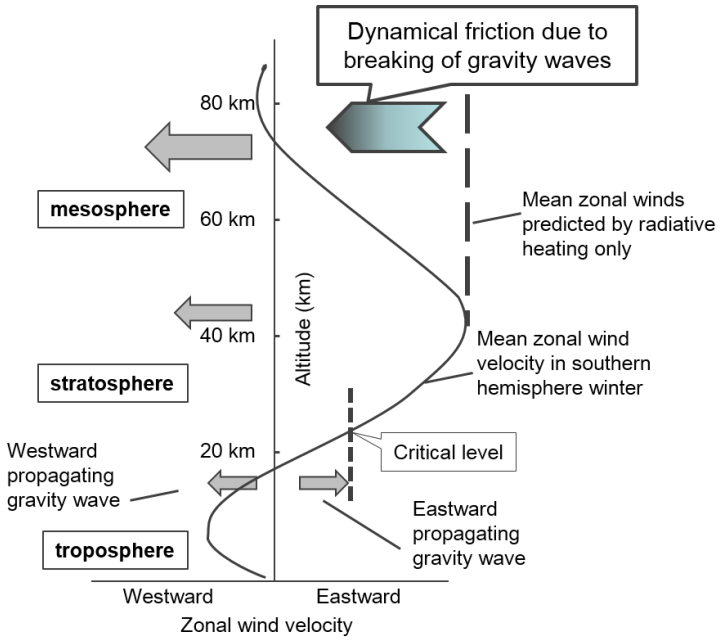

Figure 1.30: Schematic illustrating the interaction between background winds and upward-propagating GWs, in particular via critical-level filtering. This figure is adapted from *Tsuda* (2014) for the southern hemisphere.

Due to wave breaking, GWs play a crucial role in determining the state of the middle atmosphere (*Fritts* and *Alexander*, 2003). In particular, they are a main driving force in the determination of the thermal and wind structures of the

polar mesopause. They drive the atmosphere away from thermal equilibrium by inducing a summer- to winter-pole circulation in the mesopause region (*Blanc et al.*, 2010). This makes them essential elements of global climate models, in which they are currently misrepresented (*Dowdy et al.*, 2007). Therefore, one of the main aims of this project is to provide a better understanding of GW activity near the Antarctic mesopause so that climate modelling studies may benefit from more representative model constraints and, thus, better predictions. Although the main focus here is on GWs in the mesopause region, they can also influence atmospheric structure at even higher altitudes. For example, studies have shown that GWs generated by tropical storms may provide the seed forcing needed to describe equatorial spread-F phenomena in the ionosphere (*Taylor et al.*, 2009).

Large-scale, upward-propagating waves, which are generated by tropical storms, drive a global atmospheric circulation from the equator to the poles. When the waves reach the pole regions, air is pushed downward, which leads to polar vortex fluctuations. GWs deposit their momentum and decelerate zonal winds, causing an uplift of air at the summer pole, leading to (*i*) adiabatic cooling to below the ice nucleation threshold of ∼183 K (*Noel* and *Pitts*, 2012), which creates favourable conditions for the formation of PSCs and destruction of ozone (*Newman et al.*, 2003), (*ii*) a meridional transport from the summer to winter poles, and (*iii*) a downward transport at the winter pole (*Blanc et al.*, 2010).

1.6.4. Instabilities/ Ripples

Ripples are wave-like structures which are thought to be generated above the stratospheric jet at ∼50−70 km due to convective (temperature gradients) or dynamical (wind shear) instabilities (described in Appendix B.4). They are treated separately to GWs in this thesis because of the different physical characteristics which they exhibit. Since ripples result from instabilities, they may have periods lower than the Brunt-Väisälä period. They also usually have a much smaller horizontal wavelength to GWs, with an upper cut-off

wavelength of ~15−17.5 km generally suggested (*Yue et al.* (2010a); *Nakamura et al.* (1999); Peterson and Adams (1983)). In this thesis, GWs are characterised as having $\lambda_h \geq 15$ km and ripples are characterised as having $\lambda_h < 15$ km, in agreement with *Yue et al.* (2010a). It is thought that ripples generally have a persistency of <45 minutes (*Suzuki et al.*, 2011) and cover a small geographic area of less than 5000 km^2 (*Yue et al.*, 2010b), but little is known about their intermittency or period (*Hecht et al.*, 2007).

In the mesopause, large-amplitude diurnal and semi-diurnal tides often produce large wind shears and negative temperature gradients of >|10 ℃/km|. These can create dynamical or convective instabilities, respectively, in the atmosphere. When these instabilities break, they create turbulence causing mixing of atmospheric constituents in the region. Therefore, in order to produce accurate models of the mesopause region, an understanding of the lifetime and evolution of instabilities is important (*Hecht et al.*, 2014).

1.6.5. Tides

A tide is a global-scale wave motion with a period which is a sub-multiple of the solar day. Gravitational tides are caused by the apparent daily motion of the Sun and the planets' satellites. For example, the gravitational attraction between the Earth and the Moon is the primary cause of tides in the Earth's oceans (the Sun also has an effect which is much less dominant since it is at a much greater distance from the Earth). In the atmosphere, gravitational tides are negligible compared to thermal tides, which are caused by the diurnal heating effect of the Sun on pressure, temperature and winds (*Taylor*, 2010). There are, of course, multiple modes of thermal tides due to solar heating variability by season, day, and half-day. Each of these can be observed in pressure and wind fields, and they play a crucial role in atmospheric dynamics as they transfer mass between regions of high and low atmospheric pressure (*Sánchez-Lavega*, 2011).

1.6.6. The Quasi-Biennial Oscillation

Large-scale, long-term oscillations are observed near the equator in the stratospheres (between ~16 and 50 km on Earth) of several planets (*Sánchez-Lavega*, 2011). On Earth, these oscillations occur on three temporal scales: annual, semi-annual and quasi-biennial. The annual cycle involves westward winds in the summer hemisphere and eastward winds in the winter hemisphere. The interaction of the semi-annual oscillation (SAO) with some short-period ($\sim 10-15$ days) Kelvin waves and mixed planetary-gravity waves (periods of $\sim 4-5$ days) produces the quasi-biennial oscillation (QBO), which has a vertical phase propagation of ~1 km/month (*Gossard* and *Hooke*, 1975) downward and a period in the range of $24-30$ months (as illustrated in Figure 1.31) (*Sánchez-Lavega*, 2011).

As mentioned above, the QBO is observed near the equator. However, due to atmospheric waves which propagate from pole to pole, QBO effects modulate the waves and the effects are thus present around the globe. One of its effects is the temporal variation it presents in the blocking (filtering) of GWs as they propagate vertically upward to the mesosphere (*Baldwin et al.*, 2001).

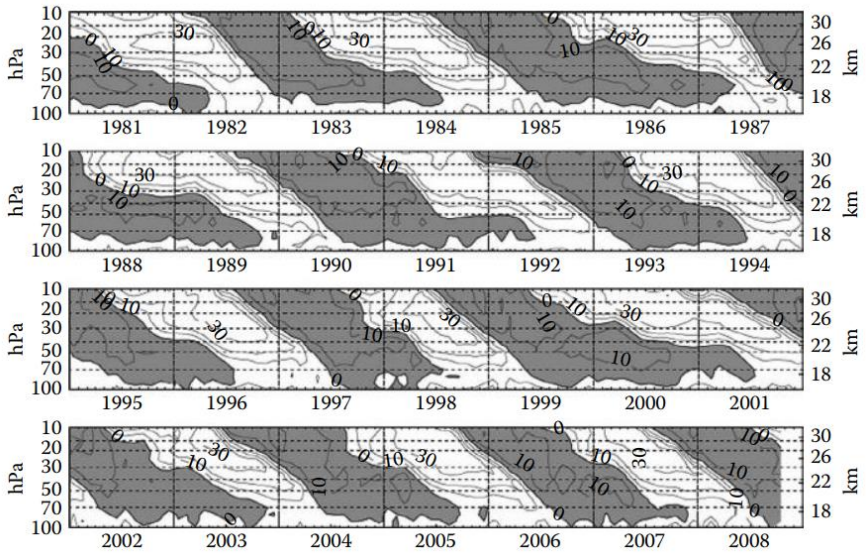

Figure 1.31: A time-height section of the monthly mean zonal winds (in m/s), showing the downward propagation as a result of the QBO. Eastward winds are shaded in grey (*Sánchez-Lavega*, 2011).

1.7. Gravity Waves

1.7.1. Detection of Atmospheric Gravity Waves

There are several methods used to detect GWs and measure their characteristics, some of which will be outlined in this section. All of these methods can be categorised as either remote sensing or *in situ* measurements. Each observation method is sensitive only to GWs of specific periods and scales (*Fritts* and *Alexander*, 2003).

1.7.1.1. Remote Sensing

The technique by which observations of atmospheric properties in a region far removed from the detector are made is known as remote sensing (*Nappo*, 2002). Some examples of atmospheric remote sensing techniques include active measurements such as radar, lidar, and sodar, and passive measurements such as imaging of the airglow from ground and from satellites, cloud observations, and riometer observations of ionospheric absorption.

Radar

Radar (radio detection and ranging) instruments measure the backscatter of pulses of radio waves. Different frequency radars are used to detect different atmospheric properties. They are often used to measure wind speeds and direction and can reach altitudes up to the MLT region due to the radar's lack of absorption by the atmosphere (as shown in Figure 1.32). GW characteristics can then be inferred from the wind perturbations (*e.g. Yasui et al.*, (2016); *Vincent* and *Reid* (1983); Song *et al.* (2016); *Tsuda* (2014)).

Two types of radar are generally used in atmospheric studies: Doppler radar and frequency-modulated continuous-wave (FM-CW) radar. Doppler radars transmit radio pulses using a directional antenna. These radio pulses are scattered if there are changes in refractive index along the beam, *e.g.* due to turbulence, temperature or humidity changes, on scales of half a wavelength of

the radio pulse. The component of the scattered pulse parallel to the antenna direction is received by the antenna, and the time delay between the transmitted and received pulses is used to infer the distance to the scattering region. If the scattering region moves, the received pulse is Doppler shifted and the resulting frequency change can be used to infer the velocity of the scattering region. FM-CW radars are used to detect finer scale inhomogeneities in the atmosphere. This can be done by using two identical antennae placed beside each other, allowing the instrument to transmit and receive signals at the same time. To get range information, the transmitted frequency is linearly modulated between two frequencies over a particular time, and the received signal is Doppler shifted by moving scattering regions, so that when the transmitted and received signals are combined, a beat frequency is generated. The time delay between the transmitted and received signals can be used to calculate the distance to the scattering region (*Nappo*, 2002).

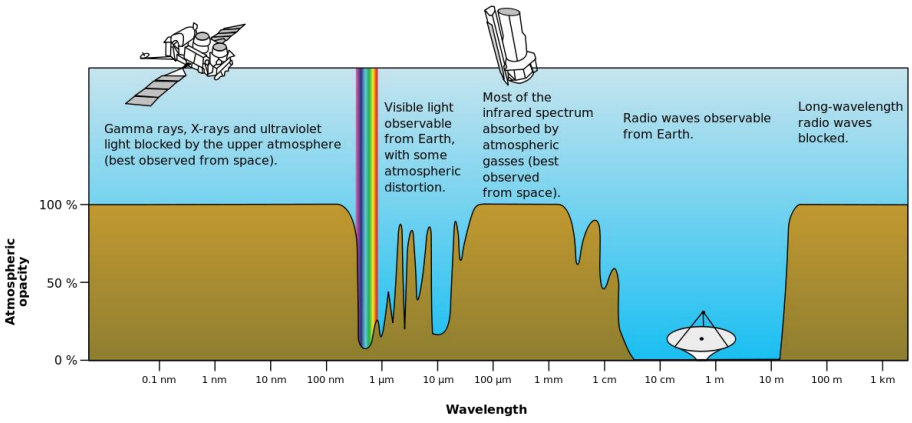

Figure 1.32: A schematic of the atmosphere's opacity to various wavelengths of electromagnetic radiation. Radio waves, corresponding to the wavelength range ~0.015−10 m, are not absorbed by the atmosphere. Image credit: NASA (public domain).

Of tremendous benefit to this project is the presence of an MF (medium-frequency) Doppler radar, which was supplied by Atmospheric Radar Systems and is in operation (since 1993) at Davis Station, providing very high resolution horizontal wind data which is available throughout the year and is evenly sampled in time. The MF radar transmits 1.94 MHz Gaussian pulses of 30 µs

duration through a vertically directed square antenna array, and receives echoes with 2 km vertical resolution using an equilateral triangle of receivers. By measuring the movement of reflected radio waves over these three receivers, meridional and zonal winds between ~60 and 100 km altitude in 2 km steps can then be determined, as shown in Figure 1.33 (*Murphy et al.*, 2007). The wind variances, after removal of tidal harmonic components, have been used in the past to study GW activity in period ranges from 20−120 minutes and 120−480 minutes (*Dowdy et al.*, 2007). Also located at Davis Station is a 33.2 MHz meteor radar instrument, whose 2014−2015 data has been used in the past to infer information about GW momentum-flux in the MLT region (*Love* and *Murphy*, 2016). Finally, a VHF (very high frequency) radar (55 MHz) has been in place at Davis Station since 2002, making short-period waves and turbulence possible to examine. The VHF radar can be used to determine temperatures in the 85-100 km altitude range due to its relation with meteor trail delays. These radar datasets at Davis Station provide very good synergy capabilities with other co-located instruments, and use of the MF radar will be made in this project to obtain more information about the intrinsic properties of GWs over Davis Station.

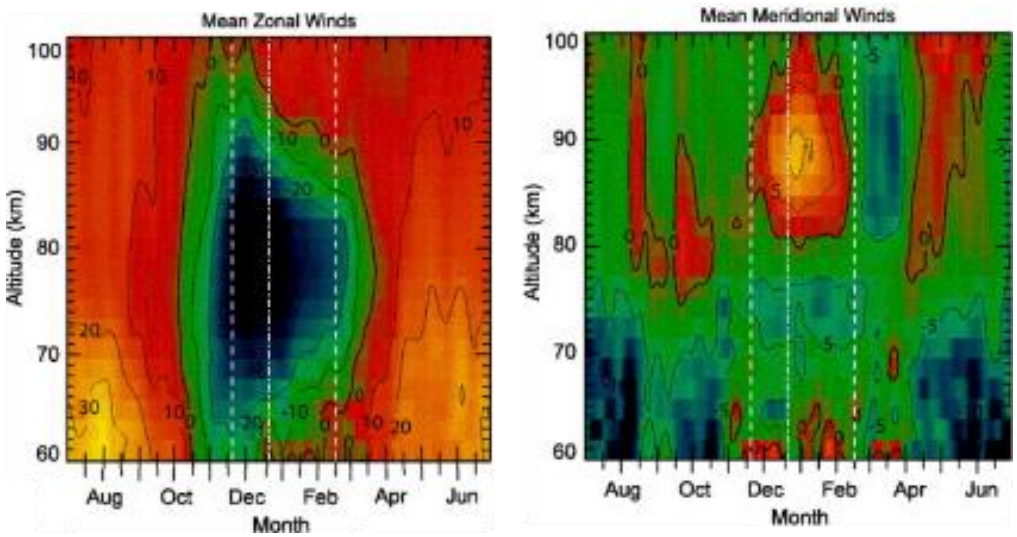

Figure 1.33: Annual average (left) zonal and (right) meridional winds between 60 and 100 km altitude from 1994 to 2004 at Davis Station, determined from medium-frequency radar measurements (*Morris et al.*, 2006).

Lidar

Lidar (light detection and ranging) instruments measure the backscatter of pulses of light. This is the most recent of the remote sensing techniques, with the first reported use of lidar for studying GWs by Collis *et al.* (1968). Lidar instruments are based on the same principle as radar instruments, the difference being that the effects of atmospheric absorption must now be taken into account and the scattering takes place due to molecules and aerosols rather than refractive index variations (*Andrews*, 2005).

Lidars are tuned to a specific frequency to correspond to particular atomic or molecular transitions, so that the height of certain molecular species can be used to infer information about GWs (*e.g. Kogure et al.* (2016); *Friedman* (2003); *Kaifler et al.* (2015)). Some examples of lidars which have been used to study GWs include tropospheric ruby lidars, mesospheric sodium lidars, and tropospheric Raman water vapour lidars (*Nappo*, 2002). Wind or temperature perturbations are usually measured, which are then used to characterise GWs. Among all GW detection techniques, lidars provide the highest temporal resolution over observation periods up to several days and highest vertical resolution over a wide altitude range (*Kaifler et al.*, 2015).

There is a Rayleigh lidar instrument in operation at Davis Station since early 2001. The Rayleigh lidar probes at a wavelength of 532 nm, which is in the green part of the visible spectrum. This lidar is shown in Figure 1.34, and it is used to retrieve densities and temperatures in the ∼30−70 km altitude range. *Alexander et al.* (2011), for example, used these measurements to calculate gravity wave potential energies in the upper stratosphere/lower mesosphere region above Davis Station between 2007 and 2008. There was also a Doppler iron lidar, probing the Doppler-broadened resonance line of iron at 386 nm in operation at Davis between December 2010 and December 2012. This data has been used to measure temperature and vertical wind profiles in the MLT region

($\sim 80-100$ km) and to subsequently calculate gravity wave potential energy density (*Kaifler et al.*, 2015). Both of these Davis Station lidar datasets provide very good synergy capabilities with the co-located instruments, but they have not been made use of in this particular project.

Figure 1.34: A ground-based LIDAR instrument in operation at Davis Station (Photo by Adam Christensen).

Sodar

Sodar (sound detection and ranging) instruments measure the backscatter of pulses of sound. Sodar is the same as radar, except it uses sound pulses instead of radio frequency pulses of energy. This makes sodar more useful for studying GWs in the atmospheric boundary layer, because the interactions in this region are much stronger from sound than from electromagnetic radiation. It is used to detect waves, turbulence, and shear instabilities in the boundary layer (*Nappo*, 2002).

Satellite Observations

Nadir-(observations which are made by looking straight down at a planet) and limb-(observations which are at an angle that just skims the surface of the planet) viewing satellite measurements (illustrated in Figure 1.35) are commonly used to study GWs. Both geometry schemes have their advantages. Limb-viewing satellites observe a much larger portion of the atmosphere, and so the chances of observing sparsely distributed substances are quite high. This

viewing angle also provides better vertical resolution. On the other hand, nadir-viewing satellite observations are less obscured by clouds, and so they are able to reach the lowest parts of the atmosphere. They also provide very good horizontal resolution (in the order of tens of kilometres) (*Andrews*, 2005).

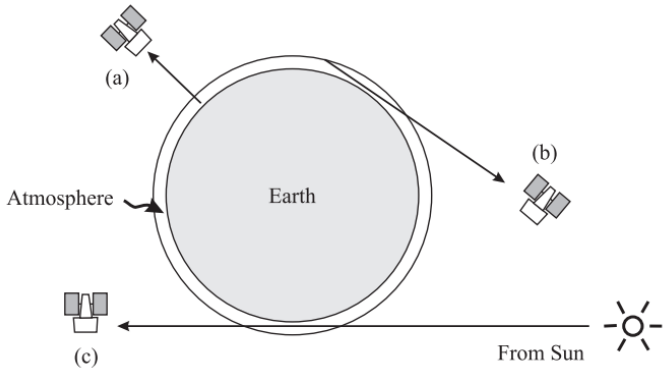

Figure 1.35: The geometry of (a) nadir-viewing, (b) limb-viewing, and (c) limb-viewing solar occultation satellites (*Andrews*, 2005).

Satellite measurements have the advantage of being geographically unlimited. All other methods for GW detection are restricted to specific locations, leading to measurement biases, especially in remote regions such as open oceans. It is only through satellite measurements that the necessary global coverage is provided.

Since 1994, infrared limb-scanning satellites have been used to study temperature perturbations due to GWs. Limb scanning is only sensitive to GWs with vertical wavelengths $>2-5$ km, depending on the instrument, and horizontal wavelengths $>100-200$ km because of the limb scanning geometry of the satellite (*Alexander et al.*, 2010). Infrared satellite images are most useful for the study of mountain waves, *i.e.* stationary gravity waves formed on the lee side of mountains (*Nappo*, 2002).

Some recent GW studies using satellite-measured temperature perturbations include *Wu et al.* (2008) who studied global GW variances using NASA's Aura Microwave Limb Sounder (MLS) data, *Wright et al.* (2011) who compared three instruments (HIRDLS (High Resolution Dynamics Limb Sounder), COSMIC

(Constellation Observing System for Meteorology, Ionosphere and Climate), and SABER (Sounding of the Atmosphere using Broadband Emission Radiometry)) for the study of stratospheric GWs, and *Wright et al.* (2016) who combined co-located satellite measurements (from the nadir-sensing AIRS (Atmospheric Infrared Sounder) and MLS) to observe GWs in 3-D.

Ground-Based Airglow Observations

Ground-based airglow observations can be made using radiometers, spectrometers, interferometers, and temperature mappers, all of which are passive instruments. They measure the column abundance of radiances of a particular wavelength band. They often operate at infrared wavelengths in order to make use of the infrared OH* airglow at ~87 km (described in detail in section 1.4.3) (*e.g. Tarasick* and *Hines* (1990); *Tarasick* and *Shepherd* (1992); *French* (2005); *Hecht* (2005); *Wachter et al.* (2015); *Taylor et al.* (2016b)). They also sometimes operate at other wavelengths to make use of the sodium airglow which emits yellow light at ~92 km (*e.g. Matsuda et al.* (2014); *Espy et al.* (2013)), or the oxygen airglow which emits green light at ~97 km (*e.g. Taylor et al.* (1995); *Medeiros et al.* (2005)). As described in section 1.4.3 in relation to the OH* airglow, GWs (which are usually generated in the lower atmosphere) propagate to higher altitudes, where their amplitudes increase due to the lower air density and the conservation of energy and momentum, and affect the airglow intensity (*e.g. Christensen et al.* (2016)). Therefore, GWs can be detected in the night airglow.

Airglow imaging is a very useful technique for studying the horizontal structure of GWs. Horizontal phase speed, direction, and wavelength can be measured quite accurately using this relatively cost-effective technique (*Matsuda et al.*, 2014). It is often done using all-sky cameras, which use fish-eye lenses. This is a good technique for obtaining an image of a very large portion of the sky. The spatial distortion in the image is then corrected using known stars in the FOV

and the image is projected onto a uniformly-spaced grid (*e.g. Garcia et al.* (1997); *Pugmire et al.* (2014)). If the GWs have very long wavelengths (thousands of kilometres), then they will take up a large portion of the image and will provide enough power and spectral resolution to find their wavelengths using spectral analysis techniques. However, most GWs only take up a small portion of the image. This portion of the image which contains the GWs must then be identified and isolated before the wavelengths can be measured. If done manually, selecting the image portion to analyse adds a level of subjectivity to the analysis which can give inconsistent results and is a time consuming process. It is also biased toward waves exhibiting long wavelength and large amplitudes. Further discussion on analysis techniques of airglow observations will be provided in section 2.5. OH* airglow images can be obtained using different types of detectors. For example, charge couple devices (CCDs) (*e.g. Taylor et al.* (2009)) and indium gallium arsenide (InGaAs) detectors (*e.g. Pugmire et al.* (2014)) are often used.

Pautet et al. (2014) have shown the capabilities of a new infrared digital imaging system, the Advanced Mesospheric Temperature Mapper (AMTM), by creating intensity and temperature maps from the OH*$(3-1)$ emission band. This system provided a spatial resolution of ~0.5 km, a temporal resolution of ~30 minutes, and a FOV of 120°.

Ground-based OH* airglow observation data from Davis Station are used in this project. The instrument, known as UWOSCR (University of Western Ontario Scanning Radiometer), is a near-infrared scanning radiometer, developed by the Space and Atmospheric Research Group at the University of Western Ontario, Canada, and has been operating at Davis Station since 1999. It has a very narrow FOV, corresponding to just ~24 km × 24 km at the airglow layer. This instrument will be discussed in detail in Chapter 2. Since 2012, there has also been an all-sky camera located at Davis Station. A comparison study between

these two datasets was done, and is described in detail in Chapter 3 (section 3.1.3).

One problem with airglow imaging, like most GW detection methods, has been its limited spatial extent, and especially its limitation to ground. A new project has been proposed by *Moffat-Griffin* (2016) which will perform non-stationary airglow imaging using a ship-borne imaging system consisting of three radiometers, each with a FOV of 1°. Using these observations, it will be possible to determine GW characteristics near the mesopause above the oceans in a portion of the GW spectrum which has previously been untouched.

Cloud Observations

Clouds have proved useful for the study of atmospheric dynamics, acting as tracers for wave structures which form or propagate at their level. As shown in Figure 1.2 and Figure 1.29 (in sections 1.2.1 and 1.6.3 respectively), gravity waves can be observed in cloud formations. A visual explanation of how this happens is shown in Figure 1.36. If, in a stable atmosphere, an air parcel is pushed up (*e.g.* by an obstacle such as a mountain) it cools adiabatically (if it exchanges no heat with the surrounding air). It will then sink back down due to its high density compared to the surrounding warm air, overshoots the equilibrium state as a result of inertia and is pushed back up. This oscillation continues, forming a GW. If the air is humid enough, it will condense to form a cloud, then evaporate, condense, *etc.* to form clouds at crests of the wave.

Until recently, cloud observations have only been qualitative, but now mesospheric fronts have been characterised quantitatively using ground-based images of noctilucent clouds (NLCs) along with background temperature measurements from SABER (*Dalin et al.*, 2013). *Pautet et al.* (2011) also developed a technique to analyse NLC images which have been available since 2004 in Stockholm, Sweden.

NLCs occur in the upper mesosphere, between ~80 and 85 km altitude, in a layer ~2–3 km thick. They are most frequently observed between latitudes of ~50 and 60° north and south. They are composed of small ice particles, which form in the summer mesosphere, when temperatures are very low (*Pautet et al.*, 2011).

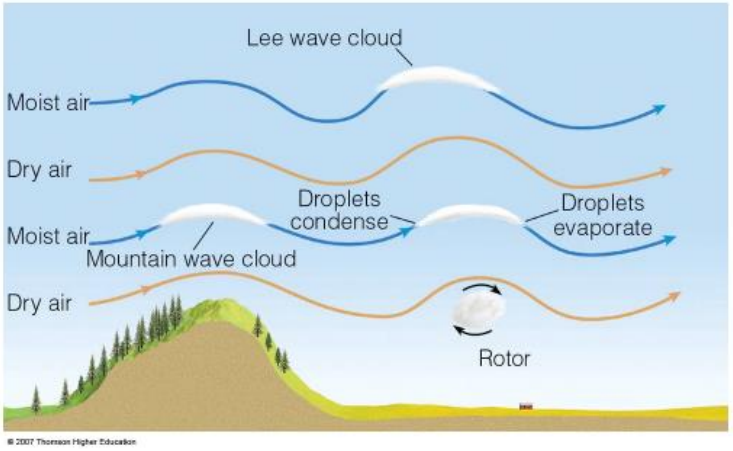

Figure 1.36: A visual explanation of the formation of GW clouds over a mountain (*Stevens*, 2015).

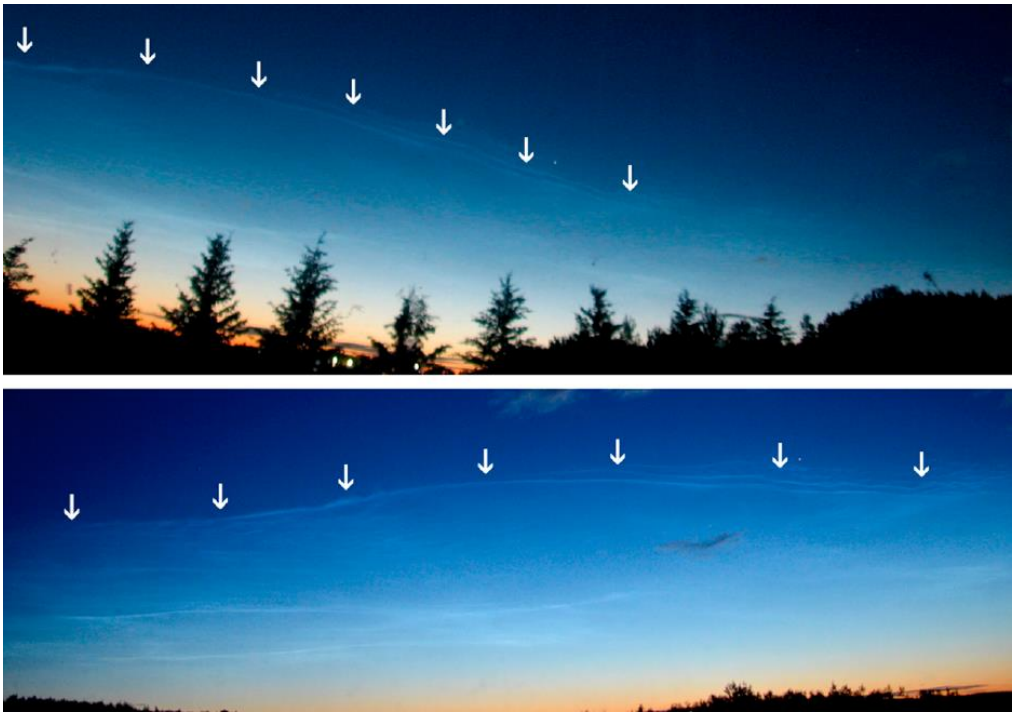

Figure 1.37: A mesospheric front visible in NLCs on 30th June 2012 at two locations separated by 24.6 km near Athabasca University, Canada from two synchronised automated cameras (*Dalin et al.*, 2013).

GW ray-tracing has also recently been done using NLC photographic observations in combination with a 3-D numerical model. In this way, a wave was traced all the way from the NLC observation in the mesosphere back to its tropospheric source (*Dalin et al.*, 2015). Previous studies of NLCs using lidars were also able to trace NLCs back to their source with the help of a 3-D particle transport model. Without a transport model, observational studies have not been able to trace NLCs back to their source because of their high drift speeds of ∼100−300 m/s (*Hartquist et al.*, 2009).

Riometer Observations

A riometer (Relative Ionospheric Opacity Meter) measures the intensity of cosmic radio noise received at the Earth's surface. This is used to infer atmospheric absorption at a peak altitude of ∼90 km, due to their frequencies of ∼28−40 MHz. This absorption layer, which has a thickness of ∼12−20 km, corresponds to the D-region of the ionosphere. The imaging riometer for ionospheric studies (IRIS) beams onto a horizontal plane in the absorption layer using a narrow beam antenna array (*e.g. Moffat-Griffin et al.* (2008); *Mbatha et al.* (2013)).

Imaging riometers were used, for example, by *Mbatha et al.* (2013) at the South African National Antarctic Exhibition, Antarctica and *Moffat-Griffin et al.* (2008) at Halley Station, Antarctica to extract GW parameters from the absorption region. GWs observed have vertical wavelengths greater than the thickness of the absorption layer. The spatial resolution of the imaging riometer (minimum 22 km in these two studies) restricts the spectrum of observable GWs according to their horizontal wavelengths.

1.7.1.2. *In situ* Measurements

In situ measurements are performed by instruments which are in direct contact with the atmospheric region in which they are making measurements. Some

examples of platforms used to make *in situ* measurements include balloons, rocket soundings, and aircraft.

Balloons

There are two types of balloons which are used to study GWs: conventional balloons and super-pressure balloons. Conventional balloons have lifetimes of a few hours to days, whilst super-pressure balloons have lifetimes of up to several months. When a balloon is released, it will naturally drift along constant-buoyancy surfaces, and thus if the position of the balloon is tracked then the air motion can be estimated. In conventional balloons, the volume changes inside the balloon depending on its temperature. This means that its buoyancy changes, and the air motions can't be accurately measured. On the other hand, super-pressure balloons, which were first introduced by *Angell and Pack* (1960), maintain almost constant volume. Therefore, after launch and ascent, they drift on constant-density surfaces, covering wide (intercontinental) geographical areas before bursting (*Nappo*, 2002). As the balloons drift with the wind, their positions may be used to infer horizontal wind and pressure fluctuations associated with GWs (*Geller et al.*, 2013). Another advantage of using super-pressure balloons to study GWs is that, because they move with the background wind, they behave as quasi-Lagrangian tracers. This means that they measure the intrinsic frequency of GWs, an important term which is used in the Navier-Stokes equations to calculate wave properties (*Vincent and Hertzog*, 2014). Nonetheless, conventional balloons are still very useful. They are used to carry radiosondes to the lower stratosphere (up to ~25 km) to obtain high vertical resolution temperature and wind data. This data, together with GW polarization relations and the assumption that wave-energy flux is upward, is used to obtain information on short vertical wavelength GWs below ~25 km altitude (*Alexander et al.*, 2010). The frequency of radiosonde launches is usually limited to about twice per day, however, and so perturbations due to

GWs are usually estimated by subtracting an averaged or smoothed profile from a measured profile *(Fritts and Alexander*, 2003).

Some examples of GW studies in Antarctica using radiosonde data include *Moffat-Griffin et al.* (2011) and *Murphy et al.* (2014). *Moffat-Griffin et al.* (2011) performed an 8-year study of radiosonde data at Rothera Station, which is located in the Antarctic Peninsula, a hotspot for GW activity. Hodographs of individual wave packets were used to infer information about GW horizontal propagation direction and vertical energy propagation direction (*Moffat-Griffin et al.*, 2011). *Murphy et al.* (2014) performed a climatological study on lower stratospheric GWs using radiosonde observations from 2001 to 2012 at Davis Station, Antarctica. They observed, using Stokes parameters, that approximately half of the waves observed in the winter (between early May and mid-October) stratosphere above Davis Station propagate downward, and they attributed the source of GWs in the winter lower stratosphere to an imbalance in the polar vortex (*Murphy et al.*, 2014).

Rocket Soundings

Temperature and wind data from rocket soundings can be used as a rough measure of GW activity from ~20-65 km altitude, and climatologies have been performed on such data (*e.g. Hirota* (1997); *Eckermann et al.* (1995)). *Baker and Stair* (1988) also used rocket soundings to measure the OH* layer's altitude at different locations and times of year. A distinct advantage of rocket soundings is their vertical extent; they can reach much higher altitudes than balloons or aircraft. Even more so than radiosondes, rocket soundings are too infrequent to resolve the relatively short temporal scale of gravity waves and so, in order to estimate GW activity, the background temperature and wind profiles are generally subtracted from the rocket sounding data and the small-scale perturbations are assumed to be caused by GWs. They are very sparse in geographical distribution whilst also being quite expensive to launch, making

them an unappealing option in the current, more advanced state of GW research.

Aircraft

Aircraft measurements have been used as platforms for remote sensing. For example, *Eckermann et al.* (2016) detected mountain waves in the OH* and Na airglow during the DEEPWAVE (deep propagating gravity wave experiment) project. However, they are more often used as platforms for *in situ* measurements, especially over mountains, to study fluctuations in the background atmosphere which are associated with GWs. Changes in the altitude of the aircraft, along with changes in temperature, pressure, and wind, are used to infer the vertical velocities of the waves (*Nappo*, 2002). Information about the horizontal wavelength spectrum of GWs in the stratosphere can be inferred from these measurements (*Fritts and Alexander*, 2003). One example of this is *in-situ* GW measurements made by *Bramberger et al.* (2017), which was also part of the DEEPWAVE project.

Aircraft are particularly useful for mountain wave observations because these waves are stationary (*i.e.* they have zero horizontal phase speed) and so repeated observations of the same wave field is possible (*Nappo*, 2002). Aircraft studies have been carried out to relate GW characteristics in the stratosphere to their sources in the troposphere, such as mountains, but also to other GW sources such as convective and frontal systems (*Fritts and Alexander*, 2003).

Aircraft studies are too limited in duration to provide any climatological GW information, and so their main use is in providing information about GW variability during case studies. Nevertheless, this information is useful for providing boundary conditions to climate models (*Fritts and Alexander*, 2003).

1.7.2. Modelling Gravity Wave Effects

As mentioned earlier, GWs have global effects on the circulation from the lower to upper atmosphere. Yet, observational studies needed to constrain their

forcing in climate models are still insufficient, especially in remote areas such as Antarctica (*Mihalikova et al.*, 2016). GWs are usually much smaller in scale than the grid size of models (*Ortland* and *Alexander*, 2006). Therefore, the required characteristics (*e.g.* distribution of momentum-flux, wavelengths, frequencies, *etc.*) can only be defined with high-resolution observation methods. Parameterisations, with different assumptions and tunings depending on the particular model, are currently used to simulate GW effects in global climate models and weather forecasting applications. These parameterisations are based on global observations of GW characteristics. Unfortunately, since GWs have a small spatial scale and are intermittent in occurrence, their associated parameterisations have not been well-defined in global models which generally have a horizontal spatial resolution of the order of several hundred kilometres (*Kalnay*, 2003). Recently though, global datasets of GW characteristics in the stratosphere have become available with improved resolution and analysis methods. Therefore, sub-grid scale GWs can now be analysed more accurately. Using supercomputers, large-scale wind and temperature profiles can now be simulated without GW parameterisations, meaning that GW effects can be parameterised as functions of space and time. The simulation of GWs depends on the equations used by the model, *e.g.* whether or not hydrostatic balance is assumed, and on the spatial and temporal scales used. This can cause differences in the momentum-flux spectrum, for example, which is calculated at any particular location and time (*Alexander et al.*, 2010).

Linear theory (see Appendix B.1) describes most of what is known about GWs. This involves simplified equations, and so it comes with some limitations. The assumptions are that a gravity wave is expanded into the mean background flow (which is assumed to be horizontally uniform and approximately steady with time), and its perturbation is assumed to be so much smaller than background values that it doesn't affect the background state. Products of the perturbation are also small enough to be neglected, and so this means that

interactions of GWs are neglected. GWs can still undergo interference; they just cannot interact with each other. This is not an accurate assumption of the real atmosphere, and so linear theory only provides a first-order estimate of most GWs. Nevertheless, it is actually very useful as it provides a better understanding of GWs than a complicated non-linear theory would. The linear equations which describe GWs are also much faster to compute than non-linear systems. The wave equation for linear GWs is called the Taylor-Goldstein equation (*Nappo*, 2002), and is shown in Appendix B.1.

GW drag is needed in models to accurately represent winds at altitudes above 15 km because wave amplitude increases exponentially with height. However, many current NWP models don't include the 20−90 km altitude range, which is the altitude range needed for long-range (>1 week) forecasts of tropospheric conditions due to dynamical coupling between the middle and lower atmosphere (*Kim et al.*, 2003).

GWs can be characterised by wave-induced temperature perturbations, $T'(z,t)$, and gravity wave potential energy densities per unit mass, E_p, defined as:

$$E_p = \frac{1}{2}\frac{g^2}{N^2(z,t)}\overline{\left(\frac{T'(z,t)}{T_0(z,t)}\right)^2}, \qquad 1.24$$

where

T_0 = the undisturbed background temperature,
z and t denote altitude and time, respectively, and
overbars indicate temporal averages with regard to the duration of the observation.

(*Kaifler et al.* (2015); *Lu et al.* (2015)).

They can also be characterised by wave-induced velocity perturbations, and gravity wave kinetic energy per unit mass, E_k, defined as:

$$E_k = \frac{1}{2}\left[\,\overline{u'}^2 + \overline{v'}^2 + \overline{w'}^2\,\right], \qquad 1.25$$

where

$\overline{u'}$ is the zonal wind perturbation,
$\overline{v'}$ is the meridional wind perturbation, and
$\overline{w'}$ is the vertical wind perturbation.

$\overline{u'}$, $\overline{v'}$, and $\overline{w'}$ are assumed to be due to the GW, and so they represent the wave amplitude in each spatial direction (*Moffat-Griffin et al.*, 2011).

Wave momentum-flux can be inferred from GW polarisation relations if the intrinsic frequency, $\hat{\omega}$, of a GW is known. Zonal and meridional momentum-fluxes are given in Equations 1.26 and 1.27, respectively (*Ern et al.*, 2017).

$$\overline{u'w'} = \frac{\rho}{2}\frac{g^2}{N^2}\overline{\left(\frac{T'}{T_0}\right)^2}\frac{k}{m} \qquad 1.26$$

$$\overline{v'w'} = \frac{\rho}{2}\frac{g^2}{N^2}\overline{\left(\frac{T'}{T_0}\right)^2}\frac{l}{m} \qquad 1.27$$

where

ρ = density, and
k and l are the zonal and meridional wave numbers.

The direction of E_p, E_k, and momentum-flux is that of the group velocity of the wave, which is given by Equation 1.28 (*Fritts* and *Alexander*, 2003).

$$\begin{aligned}\left(c_{gx}, c_{gy}, c_{gz}\right) &= \left(\frac{\partial\omega}{\partial k}, \frac{\partial\omega}{\partial l}, \frac{\partial\omega}{\partial m}\right) \\ &= (\bar{u}, \bar{v}, 0) + \frac{[k(N^2-\hat{\omega}^2), l(N^2-\hat{\omega}^2), -m(\hat{\omega}^2-f^2)]}{\hat{\omega}(k^2+l^2+m^2+(4H)^{-2})}\end{aligned} \qquad 1.28$$

where

ω is the observed wave frequency,
(k, l, m) are the wavenumbers,
$(\bar{u}, \bar{v}, 0)$ is the background wind,
$\hat{\omega} = \omega - k\bar{u} - l\bar{v}$ is the intrinsic wave frequency,
N is the Brunt-Väisälä frequency,
f is the Coriolis parameter, and
H is the scale height.

Upon examination of Equation 1.28, it may be seen that if $m > 0$, then $c_{gz} < 0$, and if $m < 0$, then $c_{gz} > 0$. This means that an upward-propagating wave transports energy and momentum downward, and downward-propagating waves transport energy and momentum upward.

1.8. Thesis Outline

The primary aim of this thesis is to construct a climatology of gravity waves observed near the mesopause above an Antarctic observation station. In this chapter, the role of atmospheric gravity waves in terms of atmospheric dynamics and models has been introduced. Their effects have been put into

perspective in relation to other major atmospheric motions, and the importance of their measurements on a global scale has been described.

The remainder of this thesis will focus on the analysis of gravity waves and ripples observed above Davis Station, Antarctica during the period 1999-2013. In Chapter 2, the ground-based OH* airglow imager and the techniques used to analyse its data will be described. Chapter 3 will show the analysis software tests which were performed before showing a summary of the GWs and ripples observed during the 15-year period. Ray-tracing, which was used to determine the possible sources of all GWs, is presented in Chapter 4 and the results of this ray-tracing study are discussed in terms of the climatology. Finally, in Chapter 5, some case studies of mesospheric frontal events which were verified by a co-located all-sky camera are examined, and a summary of potential mesospheric fronts for an 11-year period (when no all-sky data was available for verification) is presented. The thesis will close with a summary and discussion of results, conclusions which could be made, and suggestions for future work.

2. INSTRUMENTATION AND ANALYSIS TECHNIQUES

2.1. Introduction

A radiometer instrument with scanning capability, known as UWOSCR (University of Western Ontario Scanning Radiometer), is located at Davis Station, Antarctica (as shown in Figure 2.1). This instrument was designed to scan the overhead sky every minute of darkness (during the austral winter) for infrared light emissions primarily from hydroxyl radicals at ~87 km altitude, and has been doing so since February 1999. In this thesis, the variation of these emissions has been used to examine the passage of gravity waves through the mesopause region above the station. The focus of this chapter will be to detail the UWOSCR instrument, and the techniques that have been used to process its images and extract gravity wave characteristics.

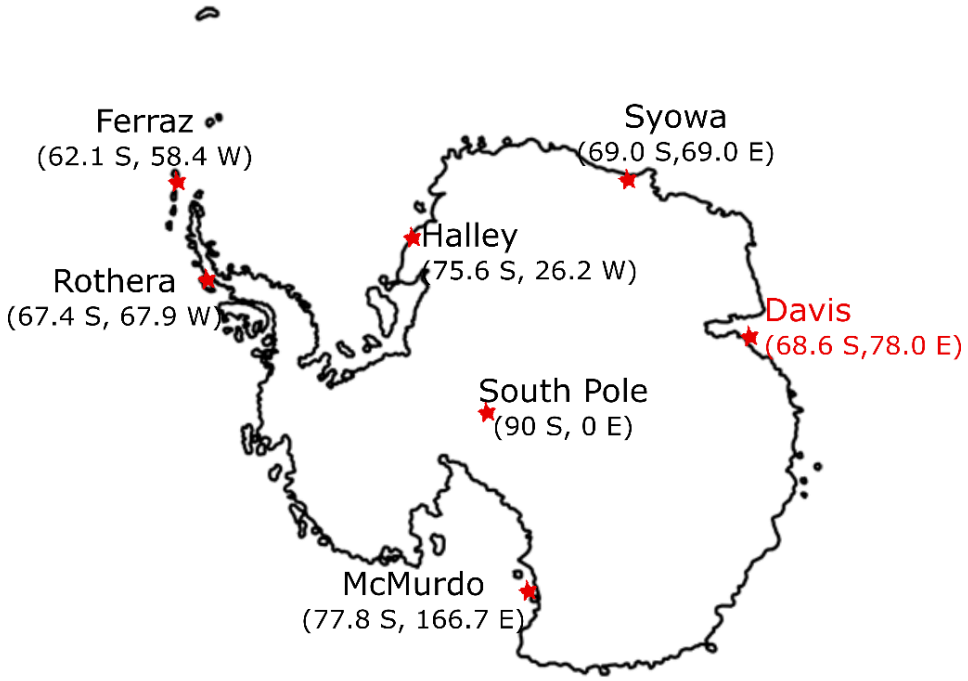

Figure 2.1: Outline map illustrating the co-ordinates of some Antarctic research stations, with Davis Station marked in red. The choice of research stations to place on this map was based on other GW studies of interest in this thesis.

2.2. Instrument Description

UWOSCR is a ground-based instrument which makes airglow observations, and so it falls within the ground-based airglow instrument category described in section 1.7.1.1. As discussed in section 1.7.1.1, this GW detection technique has its advantages and disadvantages compared to the other measurement techniques and, as with all of the measurement techniques, it covers a unique spatial, temporal and spectral range of GWs which cannot be captured by any other technique. In this section, specific details of this ground-based airglow instrument are provided.

As mentioned in section 2.1, the UWOSCR instrument measures infrared light emissions from OH* radicals near the mesopause. In section 1.4.3, it was noted that OH* emissions have wavelengths ranging from $\sim 0.5 - 4$ μm (red and infrared) and are caused by the vibrationally excited radicals in the interaction between ozone and atomic hydrogen (as shown in Equation 1.1). UWOSCR is sensitive to the brightest of these emissions, between ~1.10 and 1.65 μm. It scans a ~24 km × 24 km horizontal portion of this airglow, as depicted in Figure 2.2. With this spectral and spatial range, UWOSCR is ideal for the study of short-period GWs passing through the OH* emission layer directly above the station at which it is placed.

The instrument itself was conceived and developed by Professor Bob Lowe and colleagues of the Space and Atmospheric Research Group at the University of Western Ontario, Canada. It has two modes in which it may operate: zenith mode and scanning mode. When in zenith mode, it remains in a fixed position at the zenith with a FOV of 1°. When in scanning mode, its instantaneous FOV is 1°, as before, but it scans through 16×16 pixels every minute to simulate a wider FOV of $16^\circ \times 16^\circ$ and thus allow for the examination of GW characteristics. The UWOSCR instrument at Davis Station has always been operating in scanning mode, and so it is the only mode that will be discussed in this thesis.

A schematic is shown in Figure 2.2 depicting the mechanism by which the instrument performs a 16×16 pixel raster scan of the night sky. The dwell time on each pixel is ~0.22 seconds so that one full raster scan is completed every ~0.22×256=56.32 seconds, leaving a remaining ~3.68 s in each minute for the instrument to write the data to a file and return to its starting position. Assuming the airglow layer altitude is ~87 km, the horizontal extent associated with the 1° instantaneous FOV is 87×tan(1°)=1.52 km (using the small angle approximation, *i.e.* $\sin(\theta)\approx\tan(\theta)$). Therefore, the horizontal extent associated with a 16°×16° FOV is ~24 km × 24 km.

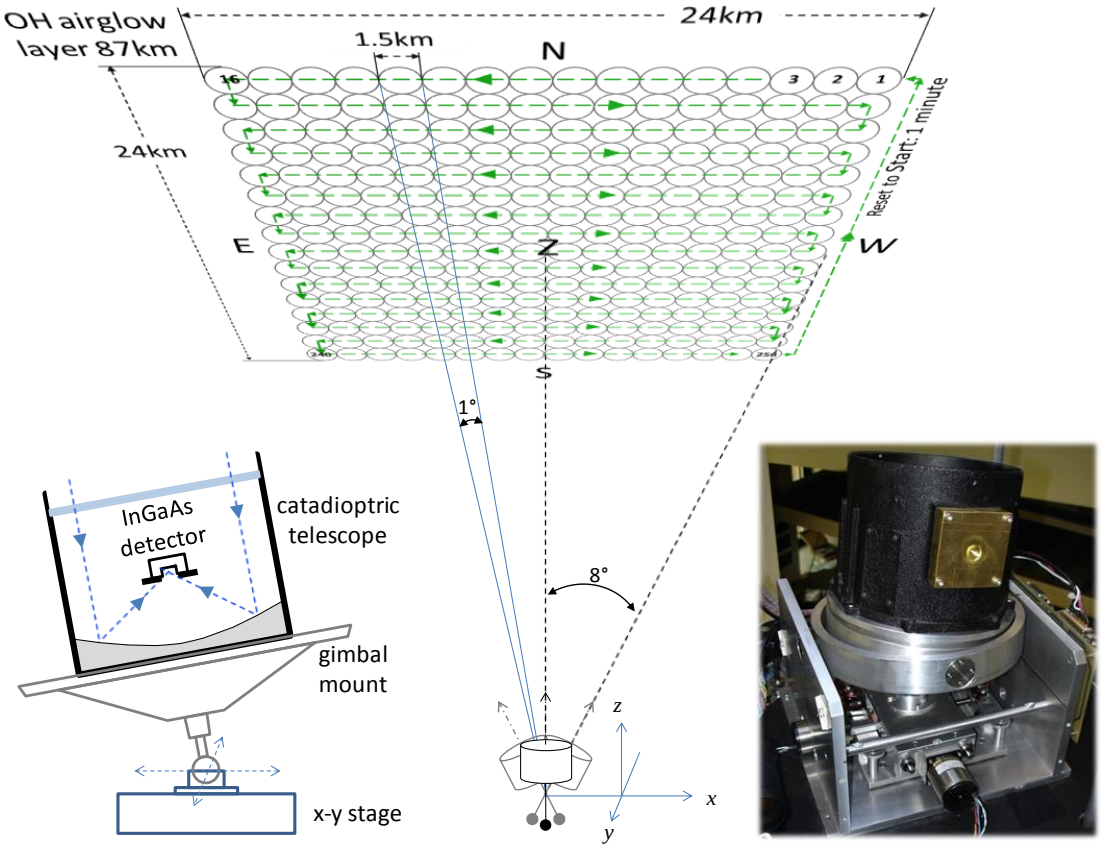

Figure 2.2: (left) A schematic and (right) a photo of UWOSCR, and (centre) a schematic showing the 16×16 point raster scan array and the FOV at the height of the hydroxyl layer. With a ~0.22 second dwell time at each point, the field of 256 points and return to start is completed in 1 minute. This image was composed by John French of the Australian Antarctic Division.

The detector itself is a thermoelectrically cooled (to reduce dark current) InGaAs (indium gallium arsenide) PIN photodiode (p-n photodiode with a wide

intrinsic region) with a silicon window to filter out any light with wavelength ≲1100 nm. It is limited at the low-frequency end to 1650 nm by the photodiode sensitivity (*Stockwell* and *Lowe*, 2001b). UWOSCR can thus make observations of intensity in the spectral range ~1100−1650 nm, where the most prominent hydroxyl emissions are due to vibrational level changes of Δv =2 and Δv =3, as shown in Figure 2.3. Also within this spectral range are two relatively weak O_2 emission lines at 1270 nm and 1580 nm. Since it operates in the infrared band, the detector becomes saturated with sunlight, and therefore the instrument is controlled by an almanac file so that it automatically turns on when the Sun is more than 6° below the horizon. The detector receives light from a catadioptric telescope ($f/\#$ =0.4, 12 cm aperture) which is mounted on a gimbal which is oriented so that the telescope can be moved in the meridional and zonal directions.

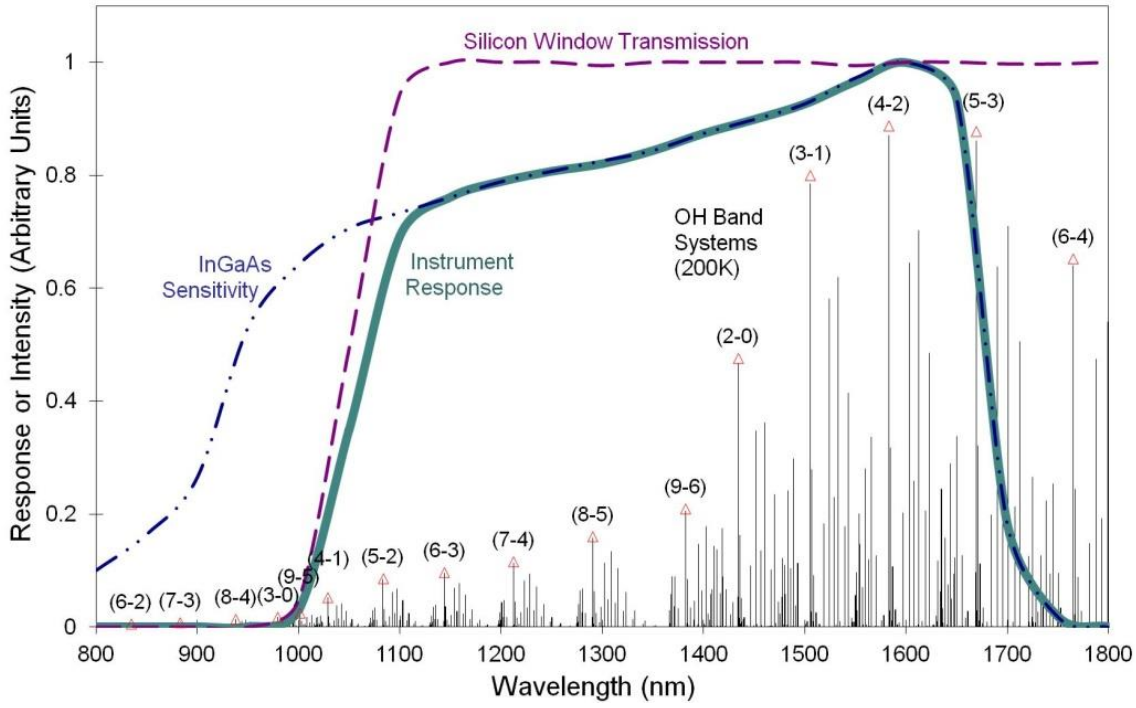

Figure 2.3: The spectral response of UWOSCR. This image was composed by John French of the Australian Antarctic Division.

Instrument uncertainty is periodically estimated by operating the instrument in 'dark night mode', meaning that the entrance aperture to the telescope is fully

covered. UWOSCR's intensity uncertainty measurement can then be approximated by the standard deviation of the dark nights' intensities. From these dark nights, it has been determined that the signal-to-noise ratio on a single pixel is ~50−70 (*Stockwell* and *Lowe*, 2001b).

In this thesis, the modulations in the radiation emitted from the OH* layer were used (as described in section 1.7.1.1 for any ground-based airglow instrument) to infer the characteristics (*e.g.* horizontal phase velocity, horizontal wavelength, and frequency) of GWs passing through the mesopause. These characteristics can be measured manually by examining a series of images in which a GW is visible (as will be described in section 2.5.1). Some other analysis methods which can be used to determine these GW parameters include beamsteering in the slowness domain and wavelet analysis (*Nappo*, 2002). These methods have both been tailored specifically for UWOSCR images at the University of Western Ontario and they will be described in detail in sections 2.5.2 and 2.5.3. In the past (*e.g. Stockwell and Lowe* (2001)), a network of three separate UWOSCR instruments have been in operation at three locations simultaneously. By comparing results from the three instruments, information about the direction of propagation of GWs with a very large spatial extent could be determined. There is only one UWOSCR instrument in operation in Antarctica, and thus this technique was not used in this thesis.

Finally, some of the main advantages and disadvantages of the UWOSCR instrument will be noted, before moving on to a more specific description about the images it produces. UWOSCR has the advantage of being able to detect small-scale GWs with a good spatial and temporal resolution (1.5 km and 1 minute, respectively) in a cost-effective manner. On the other hand, it is limited by its narrow overall FOV (~24 km × 24 km), giving it a distinct disadvantage compared to all-sky OH* cameras when attempting to examine larger-scale GWs. Another disadvantage, which is not specific to UWOSCR as it applies to any ground-based airglow detection method, is that clouds scatter

the light emissions which are coming from the hydroxyl radicals. Thus, on a cloudy night, the OH* airglow which is observed has been scattered in all directions, making it almost impossible to detect waves. To determine which nights have cloud present in the FOV, the presence of stars in the images may be used as they are only visible when the sky is clear. Overall, despite UWOSCR's drawbacks, plenty of useful data is obtained from the instrument since it runs continuously during every minute of darkness. The series of images may be analysed to find the characteristics of waves passing through the FOV.

A brief outline of the analysis of the UWOSCR images is given in Figure 2.4, and will be described in detail in this chapter. The pre-processing step accounts for the scanning nature of the instrument, the processing step calculates the dominant velocity and period in each image of the file (except 16 frames at the beginning and end of the file due to a windowing process which is used), and the post-processing step extracts only image sequences which are deemed to have a wave structure passing through them.

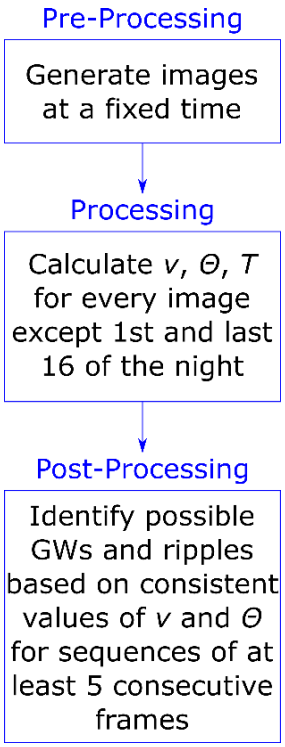

Figure 2.4: General outline of the analysis procedure which will be described in detail in this chapter. v, θ, and T denote dominant speed, direction and period, respectively, in an image.

2.3. Data Acquisition

Each file which is created by UWOSCR in scanning mode is named yyyymmdd.dav - corresponding to the day (dd), month (mm) and year (yyyy) that the file was created - and contains the following information for each image in the file: the day of the month, the detector temperature, the ambient temperature, and 256 intensity values.

The reason for the measurement of ambient and detector temperatures is that, together with the performance of the thermoelectric cooler (TEC), they can be used to determine the DC offset corresponding to the level of dark current. For example, if the ambient temperature is 15℃ and the TEC reduces the temperature at the detector by approximately 35℃, then the detector temperature should be approximately −20℃ and dark current may be estimated from the deviation from this value.

The intensity values recorded are signed 12-bit integers because the analog-to-digital converter used is a 12-bit bidirectional device, and so integers may have values ± 2047. From this range, it is clear that UWOSCR measures relative (not absolute) intensities as they may be negative numbers. The instrument has not been calibrated to measure absolute intensities because it is not necessary for the particular purpose for which UWSOCR was designed and because calibration of intensity is very difficult on an absolute scale - there would be a different calibration factor for each night as the atmosphere is so changeable, and the intensity of a known fixed star would also have to be measured using the same instrument.

2.4. Image Correction

The data must undergo initial formatting to account for the scanning nature of the instrument (shown by the green arrows in Figure 2.2 on page 79). All pixels in a given frame are associated with different timestamps, each ∼0.22 seconds apart. In order to consider these pixels as one image, they must first be

interpolated to a fixed time. This fixed time was chosen to be when the instrument was facing the central pixel in the image, *i.e.* 28.16 seconds after the scan started. If this adjustment of the data was not done, the method for determining wave velocities would be in error. In particular, the direction and speed of fast moving waves could not be determined accurately.

In order to interpolate the intensity of a pixel at any particular point in time, the intensity of that pixel some time before and after that particular time is used to fit intensity as a function of time. The point in time to which each pixel in a frame is interpolated is the time at the start of that image scan plus 28.16 seconds (*i.e.* half way through the scanning time for the image). Since one frame is needed on both sides of a particular frame in order to perform interpolation, the first and last frames of the file must be discounted in the final analysis. The interpolation technique used is shown in the 'AdjustData()' function in Appendix C and a basic summary of it is as follows. A 'multiplier' is used to determine how many time steps into the scan a particular pixel $[i][j]$ is, where i increases toward the left (west) of the image and j increases toward the bottom (south) of the image. The multiplier values (0,1,...,254,255) increase in the direction of the green arrows shown in Figure 2.2. At any particular time, it is assumed that intensity changes linearly between the two surrounding frames, so that the intensity at any particular time is given by Equation 2.1. An illustration of the general idea of the pre-processing step is shown in Figure 2.5.

$$Intrp[i][j] = Initial[i][j] + (56.32 - \Delta t) * \frac{dI}{dt} \qquad 2.1$$

where

$Intrp[i][j]$ is the intensity at the new fixed time (interpolated value),
$Initial[i][j]$ is the intensity at the initial time of the frame,
56.32 seconds is the total scanning time in each minute,
$\Delta t = \frac{multiplier[i][j]}{255} \times 56.32$ seconds, and
$\frac{dI}{dt}$ is the rate of change of intensity between the surrounding frames.

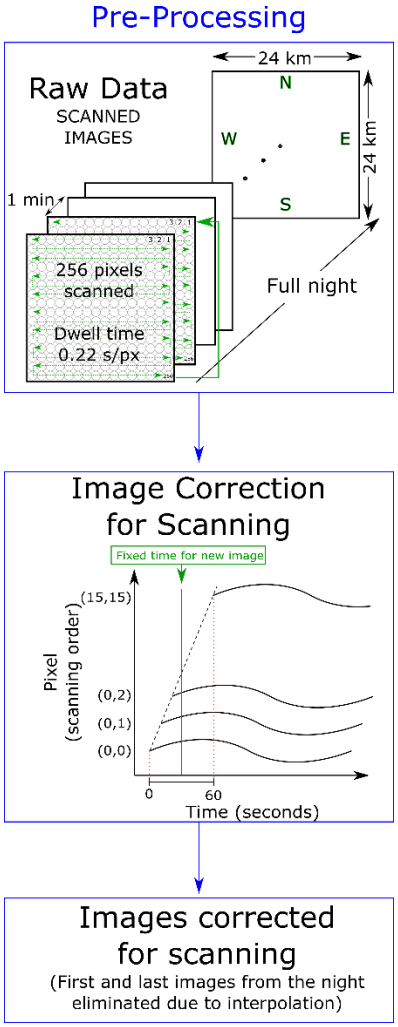

Figure 2.5: An overview of the pre-processing step.

Once the data file has been re-made so that each image corresponds to a fixed time, analysis techniques may be used to determine the characteristics of waves which pass through the FOV. Such analysis techniques for the UWOSCR data are described in section 2.5.

Before the description of the analysis techniques, some final image correction considerations will be discussed briefly. The first point is that stars which are visible within the FOV cause an intensity peak, which usually occupies one pixel in the frame. These may be easily removed and replaced with an average value from the surrounding pixels, and an option is included to do this in some LabVIEW analysis software developed for this project. However, since they occupy only one pixel and are usually very dim compared to the OH* airglow,

they have a negligible effect on the calculation of GW characteristics and so were not considered by the analysis techniques described in section 2.5. The final point on image correction is that there were a number of occasions, generally lasting several minutes, in the UWOSCR dataset when the images 'hopped' up and down (in the north-south direction). Due to its intermittency, and the fact that only a handful of occasions of when it happened have been identified, the Davis Station engineers could not identify the cause of this mechanical error. The data files which exhibited this error were not used in the final analysis, although the post-processing (which will be described in section 2.6) should remove this data anyway.

2.5. Analysis Techniques

As already mentioned, the recorded UWOSCR image sequences can be used to determine a number of characteristics of small-scale GWs. This section begins with a simple manual approximation of these characteristics before discussing two more advanced techniques developed at the University of Western Ontario: the S-Transform method, and the De Serrano and Lowe method.

Of particular interest in this thesis is a method which can deal with extensive amounts of imaging data with no bias caused by the user who is processing the data, as this is important for a reliable characterisation of GWs and could be applied to imaging data at various observation sites. The De Serrano and Lowe method had the least user-intervention of the three methods described here and thus it was the method which was used to analyse the UWOSCR dataset at Davis Station. This software was available in executable format, and documentation on the code was also provided. Using this documentation, a LabVIEW program was developed to perform this technique in order to (*i*) verify the technique performed as expected and (*ii*) allow future users of the De Serrano and Lowe method to change the variables (*e.g.* image size, temporal resolution and spatial resolution) to suit their particular instrument. Figure 2.6 was designed as an overview of all analysis implementations used, and its

content will be referred to throughout this thesis. The results presented in this thesis are all calculated using the executable code (hereafter known as '`UWO_exe`') provided by the University of Western Ontario, as the LabVIEW code had not been finalised and verified before the analysis phase of this work. There are slight variations between the `UWO_exe` and the LabVIEW code, which will be discussed in Chapter 3, and which could not be reconciled due to a lack of documentation related to `UWO_exe`. The results from `UWO_exe` were also not an exact match with the source code (hereafter known as '`UWO_source`') provided by staff at the University of Western Ontario. Efforts were made during this project to reconcile `UWO_exe` with `UWO_source` by varying the window lengths used, but an exact match was not found. `UWO_source` did not include a final version of the period calculation software and this section of the code did not compile. This was less critical since the Fast Fourier Transform (FFT) is well known and understood and so it could be easily implemented in the LabVIEW code.

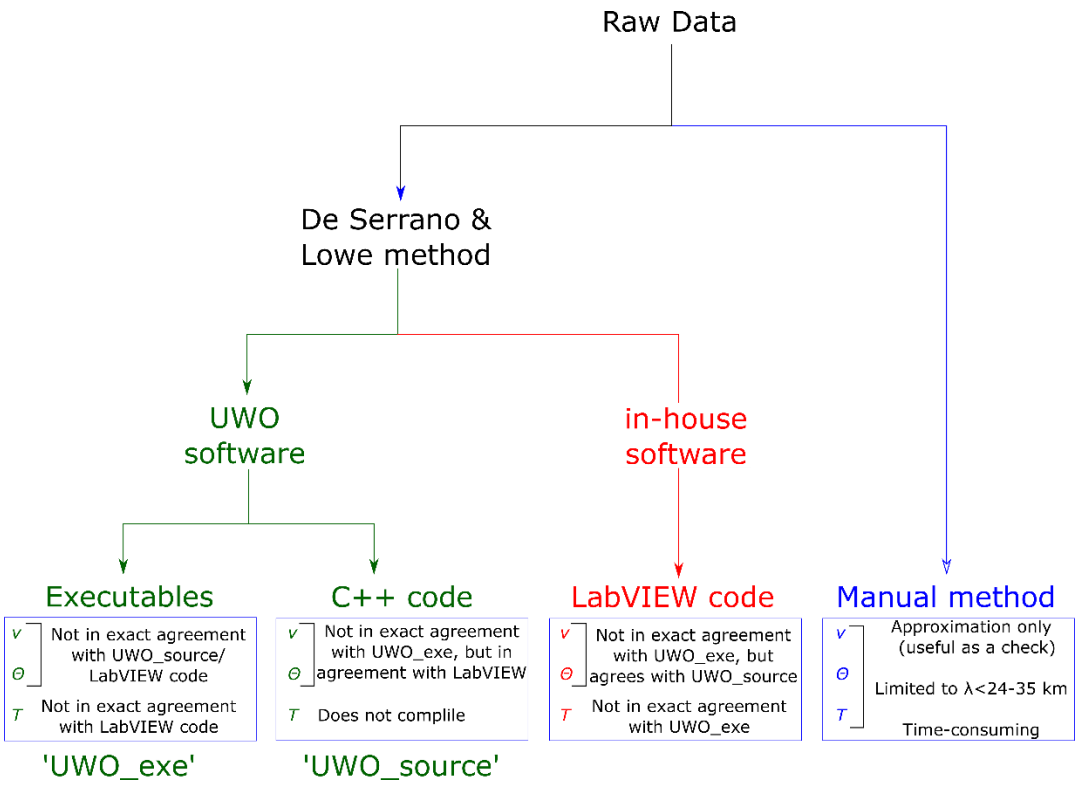

Figure 2.6: A schematic showing the implementation of the analysis procedure.

2.5.1. Manual Approximation

Performing a simple manual analysis on a series of images where a wave crest is visible can prove very useful in obtaining approximate characteristics of a particular GW event. It is also an understandable (and probably the only) way of checking the reliability of automated methods. The only problem with using the manual approximation for a large dataset is that it is very time consuming, whilst also introducing subjectivity, since the user must decide where exactly the crest of a wave lies. It also produces a separate bias, where waves with wavelengths >24−35 km (depending on wave direction) cannot be characterised as two peaks do not fit within the FOV. This will become clearer in the following section, in which the exact meaning of 'manual approximation' is described.

Figure 2.7 shows a gravity wave passing over Davis Station on a particular night. A set of images, corresponding to the duration of the gravity wave, are placed side-by-side along with the timestamp associated with each one.

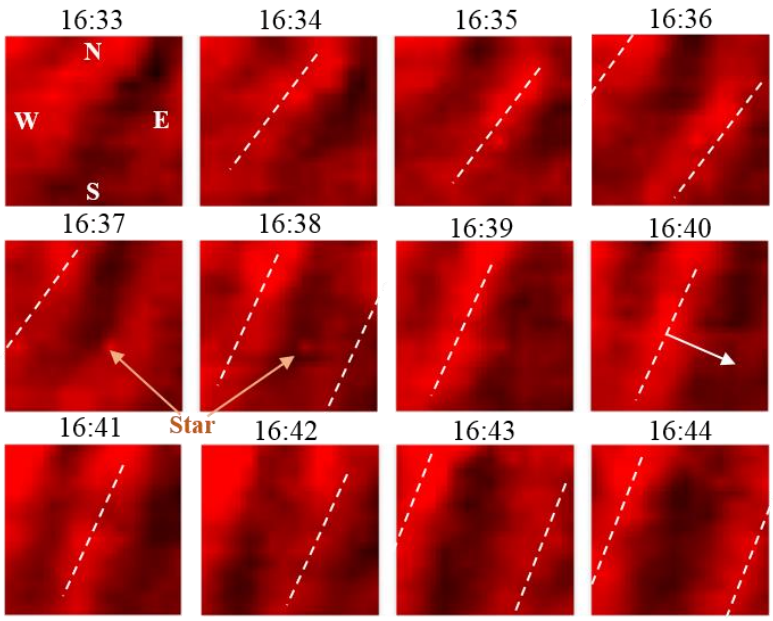

Figure 2.7: A set of UWOSCR images from 16:33−16:44 on 2nd July 2006 at Davis Station, where a GW is passing through the FOV. Dashed white lines are drawn onto the images at the approximate positions of the wave crests as a guide to the eye. The white arrow indicates the propagation direction of the wave, where north is toward the top of the image. A star, which is faintly visible in some images, is highlighted between 16:37 and 16:38 UT.

It is known that each image produced by UWOSCR has a FOV of 16°×16°, which corresponds to ~24 km × 24 km at the airglow layer (at ~87 km altitude), and the time between each image is 1 minute. If a wave moves across the array of pixels with little or no change in frequency, then the arrival times of the disturbance at each pixel (found using the wave crest position at a given time) can be used to calculate wave speed $\left(\frac{\text{distance moved}}{\text{time taken}}\right)$, direction and wavelength (distance between two adjacent wave crests in the same image). This is known as beamsteering in the slowness domain (*Nappo*, 2002), and can be done using a ruler and protractor (*i.e.* the manual method), or it can be done using automated methods (*e.g.* as in section 2.5.3.1).

During this project, manual approximations were performed on a portion of the GWs observed to check the reliability of the automated analysis method used. Some of these comparisons will be shown in Chapter 3.

2.5.2. The S -Transform

The intensity of light emissions may be recorded as a function of time (as seen from Figure 2.7), but it is often informative to view the frequency content of the light emissions in order to analyse each frequency separately. To do this, spectral analysis – which decomposes a waveform into a sum of sinusoids of varying frequencies, phases, and amplitudes – may be used.

The S-transform was developed by *Stockwell et al.* (1996b) at the University of Western Ontario for time- and space-local spectral analysis. Time- and space-local spectral analysis is important as the local changes of a spectrum with time or space can be obscured by the spectrum of the entire time series or spatial extent (*e.g. Mansinha et al.* (1997)). This is particularly relevant for GW studies, since GWs usually persist for only a few minutes and may only partly fill the FOV of the imager.

To perform spectral analysis, one must be able to convert from time, to time-frequency, to frequency, and back to time with no loss of information. Several

methods have been developed in the past which can do this (*e.g.* the Fourier transform). The wavelet transform, the Gabor transform, and the S-transform also do this, while also having an additional advantage of time- and space-localisation. These methods will be discussed in further detail in this section.

2.5.2.1. The Fourier Transform

The Fourier transform is a method of spectral analysis which is used to calculate the total cross-spectrum or power spectrum over the entire time series. It provides a good global view of the spectrum but does not provide information about how the spectrum varies with time (*Nappo*, 2002). Harmonic analysis is a possibility for identifying how the spectrum varies with time, but in that case the frequency must be identified in an earlier step (*e.g.* by Fourier transform).

If a waveform is periodic, it may be represented by the summation of sinusoids which have a discrete number of frequencies. This is called a Fourier series. To calculate the frequency spectrum of a waveform which changes over time, the Fourier transform, $H(f)$, is used as shown in Equation 2.2, where the time series corresponding to the Fourier transform is denoted by $h(t)$.

$$H(f) = \int_{-\infty}^{\infty} h(t) e^{-i2\pi ft} dt \qquad 2.2$$

Then, the time series, $h(t)$, can be recovered from the spectrum using the inverse Fourier transform, as follows:

$$h(t) = \int_{-\infty}^{\infty} H(f) e^{i2\pi ft} df \qquad 2.3$$

(*Mansinha et al.*, 1997).

The Discrete Fourier Transform (DFT) is the equivalent of the continuous Fourier transform shown in Equation 2.2, except it is for signals known only at N points separated by a fixed sample time. The DFT can take a long time to compute if N is large because it will have N^2 complex multiplications and $N(N-1)$ complex additions to calculate (*Brigham*, 1974). However, with the

invention of the FFT algorithm (*Cooley and Tukey*, 1965), computation time for a discrete Fourier transform could be reduced so that it is proportional to $N\log_2 N$ rather than N^2 (as was the case with the DFT). The only problem with the FFT is that the number of data points, N, must be an integer power of 2. The FFT is the most commonly used tool to transform data into the frequency domain. It collapses all of the timing information to provide a total power for each frequency, within the resolution available, *i.e.* (signal duration)$^{-1}$. To focus on responses from a certain frequency range, filters may be used.

As alluded to already, the Fourier Transform does not provide information about how the spectrum varies with time. This lack of time localisation is not suitable for the study of short-period GWs. One solution is to split $h(t)$ into segments before transforming it into the frequency domain. This method is known as the Short Time Fourier Transform (STFT), or the Gabor transform. It must be noted, though, that there is a trade-off between time localisation and the resolution of frequencies; time localisation leads to degradation of the resolution of frequencies in each segment's spectrum (*Mansinha et al.*, 1997).

2.5.2.2. The Wavelet Transform

The wavelet transform, first formally introduced by *Goupillaud et al.* (1984), is a means of time-local spectral analysis. Instead of using cosinusoids, the wavelet transform uses user-defined wavelets, which are small waves localised in time (examples of which are shown in Figure 2.8), as basis functions to represent $h(t)$.

The wavelet may be translated (usually via a windowing process) or stretched/squeezed along the time axis. A translated wavelet locates the time of interest within the signal, whereas a dilated wavelet allows signals of different scales to be analysed.

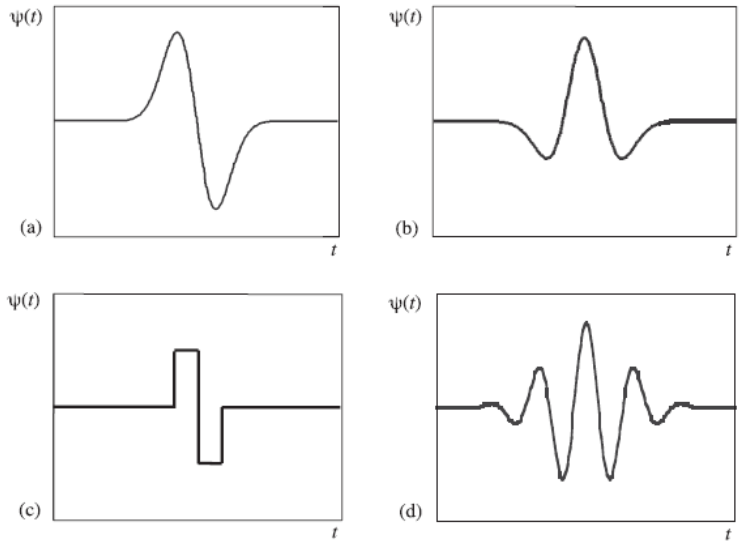

Figure 2.8: Some examples of commonly-used wavelets are (a) Gaussian wavelets, which correspond to the 1st derivative of a Gaussian, (b) Mexican hat wavelets, which correspond to the 2nd derivative of a Gaussian, (c) Haar wavelets, and (d) Morlet wavelets. The chosen wavelet can be dilated (stretched/squeezed) or translated along the time axis. This image was taken from *Addison* (2002).

The wavelet transform, $T(a,b)$, is simply a convolution of the mother wavelet, $\psi(t)$, with the signal, $x(t)$, as follows:

$$T(a,b) = w(a)\int_{-\infty}^{\infty} x(t)\psi^*\left(\frac{t-b}{a}\right)dt \qquad 2.4$$

where

$w(a)$ = the weighting function, which is usually set to $a^{-0.5}$,
a = the dilation parameter, and
b = the translation parameter (*Addison*, 2002).

2.5.2.3. The 1-D S-Transform

The Stockwell transform (*a.k.a.* the S-transform) is based on the wavelet transform, but it uses absolute referencing of the phase information in time.

Stockwell et al. (1996a) express the wavelet transform as $T(a,b) = \int_{-\infty}^{\infty} x(t)\psi(a,t-b)dt$, where the variables have been renamed to agree with Equation 2.4 above. The S-transform is then given by $S(f,b) = e^{i2\pi ft}T(f,b)$ where the mother wavelet is a Gaussian-modulated cosinusoid, defined as $\psi(f,t) = \frac{|f|}{2\pi}e^{-\frac{t^2f^2}{2}}e^{-i2\pi ft}$. Put simply, the dilation

parameter in the wavelet transform has been replaced with the frequency, f. The result is the 1-D S-transform which translates the Gaussian window but not the phase modulation, as shown in Equation 2.5.

$$S(f,b) = \int_{-\infty}^{\infty} \frac{|f|}{\sqrt{2\pi}} e^{-\frac{(b-t)^2 f^2}{2}} x(t) e^{-i2\pi f t} dt \qquad 2.5$$

The S-transform differs from the Gabor transform only by window size. The window size for the Gabor transform is a Gaussian function, whereas the window size for the S-transform is proportional to frequency. This means that the S-transform has better spectral clarity at low frequencies and better temporal clarity at high frequencies (*Mansinha et al.*, 1997).

2.5.2.4. The 2-D S-Transform

Similar to the wavelet transform, the S-transform can also be applied to 2-D signals (*e.g.* images). *Stockwell et al.* (1996a) applied the S-transform to UWOSCR images, as shown in Figure 2.9.

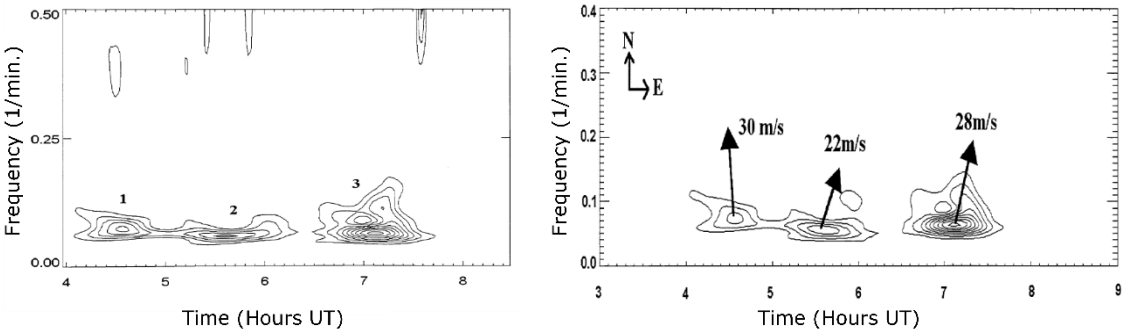

Figure 2.9: (left) An amplitude S-matrix for a particular pixel in a UWOSCR image. (right) An amplitude S-matrix for the same pixel, with phase velocities of individual wave packets calculated (*Stockwell et al.*, 1996a).

For each pixel, an amplitude S-matrix is obtained and wave packets are manually identified. Then, the phase speed of each wave packet can be obtained by using the known distance between pixels and by using time lags calculated using cross spectral analysis (*Stockwell et al.*, 1996a). This method is particularly good at extracting subtle differences in spatial frequencies (*Mansinha et al.*, 1997), and so it can provide good approximations of GW

parameters in UWOSCR images. However, the manual identification of wave packets introduces a level of subjectivity that should be avoided in order to automatically process all UWOSCR data at Davis Station since 1999, and so the technique will not be discussed further in this thesis.

2.5.3. The De Serrano and Lowe Method

This analysis method was developed by Ron De Serrano and Bob Lowe at the University of Western Ontario specifically to analyse UWOSCR images. The method was adopted over a 2-D FFT (*Garcia et al.*, 1997) or 3-D FFT method due to the fact that there were very few pixels in the x- and y- directions (although there were many frames in the time dimension). Performing an FFT in the x- and y- directions (which extends 16 pixels in each direction) would yield only 8 points, making it a poor choice for UWOSCR data. The De Serrano and Lowe method makes maximum use of the data available using a cross-correlation technique. As with a 3-D FFT technique, windowing in space and time is still part of the challenge for the De Serrano and Lowe method as it involves user intervention at some level, but it is minimised in this case.

The final output from the De Serrano and Lowe analysis method is the date and time, the zonal and meridional components of the dominant velocity, and the dominant period and wavelength associated with each frame in a data file. A general outline of this procedure is shown in Figure 2.10.

The software first calculates the dominant zonal and meridional velocity associated with each frame using an analysis method which is known as beamsteering in the slowness domain. This method is outlined, for example, by *Briggs* (1968), and a commented version of the code used by De Serrano and Lowe (called '`vel_dir`') is provided in Appendix C for clarity.

The next part of the analysis involves a pair of programs called '`qvel_dir.cpp`' and '`ron2.cpp`' which determine the dominant period and, hence, wavelength in each frame by calculating the FFT of the time variation of

the weighted centre of 32 successive frames. The final version of this source code was not available, and so is not provided here.

The methods for each of these two stages are described in detail in this section. A schematic is shown in Figure 2.11 to provide a brief outline of the De Serrano and Lowe method.

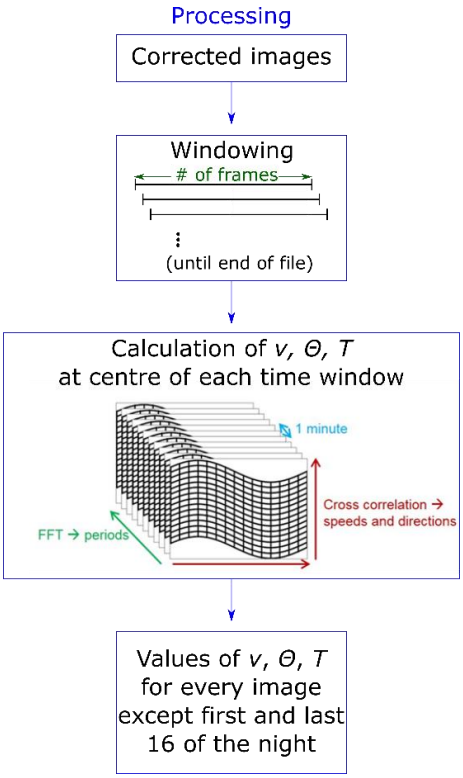

Figure 2.10: Overview of the analysis procedure.

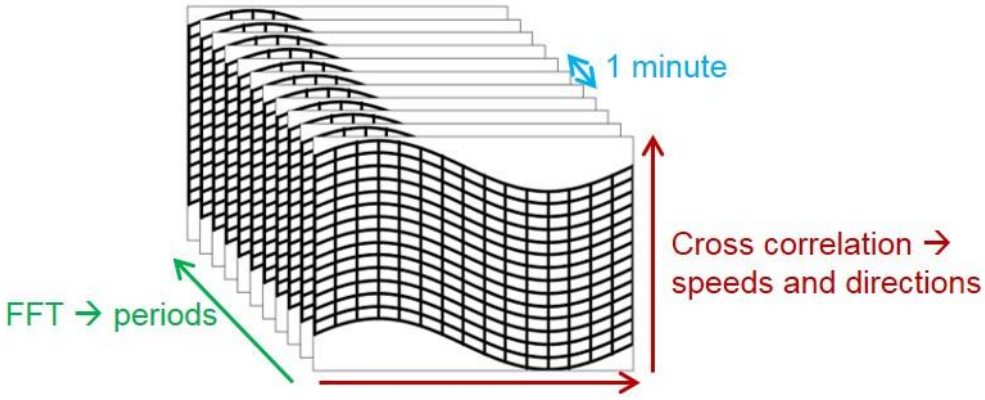

Figure 2.11: A cartoon outlining the De Serrano and Lowe analysis method. It is based on two 1-D correlations between the OH* signal at different points in the image at a range of nearby times, and an FFT of the weighted mean centre to obtain periods.

2.5.3.1. Calculation of Phase Speed and Direction

As mentioned in section 2.5.1, if a wave passes through the FOV with little or no change in frequency and wavenumber, then the arrival time of the wave at different points in the image can be used to determine its direction and speed. *Giers et al.* (1997) outlined a simple method to do this based on observations made at three different locations. In the case of UWOSCR, there are 256 locations (or pixels). Nevertheless, the principle remains the same as that outlined by *Giers et al.* (1997) - it simply needs to be iterated for all pixels in the UWOSCR images.

The basic concept is as follows. Considering a plane wave moving at speed v, as described in Figure 2.12, it can be seen that the wave front passes point A first, then point C, and then point B. Points A, B and C are chosen such that $|AB| = |AC|$. Suppose it takes time t_{AB} for the wave front to move from A to B, and time t_{AC} for the wave front to move from A to C. Then, these times can be written as $t_{AB} = \frac{|AB|\cos\theta}{v}$ and $t_{AC} = \frac{|AC|\sin\theta}{v}$. The meridional velocity $\left(V_m = \frac{|AC|}{t_{AC}}\right)$ can then be re-written as $\frac{v}{\sin\theta}$, the zonal velocity $\left(V_z = \frac{|AB|}{t_{AB}}\right)$ can be re-written as $\frac{v}{\cos\theta}$, and the angle of propagation $\left(\theta = \tan^{-1}\left(\frac{V_m}{V_z}\right)\right)$ can be re-written as $\theta = \tan^{-1}\left(\frac{t_{AB}}{t_{AC}}\right)$. The overall phase speed, v, which is calculated by $v = \frac{|AC|\sin\theta}{t_{AC}} = \frac{|AB|\cos\theta}{t_{AB}}$ can then be re-expressed in terms of meridional and zonal velocity (V_m and V_z respectively). Taking the first half of this expression, and replacing $\sin\theta$ with $\sqrt{1-\cos^2\theta} = \sqrt{1-\left(\frac{vt_{AB}}{|AB|}\right)^2}$ gives the expression $v = \frac{|AC|}{t_{AC}}\sqrt{1-\left(\frac{vt_{AB}}{|AB|}\right)^2}$. Multiplying both sides of this equation by $\frac{|AB|}{t_{AB}}$ and then squaring both sides, one obtains $(v * V_z)^2 = (V_m * V_z)^2 - (v * V_m)^2$ and thus $v = \frac{V_m V_z}{\sqrt{{V_m}^2 + {V_z}^2}}$.

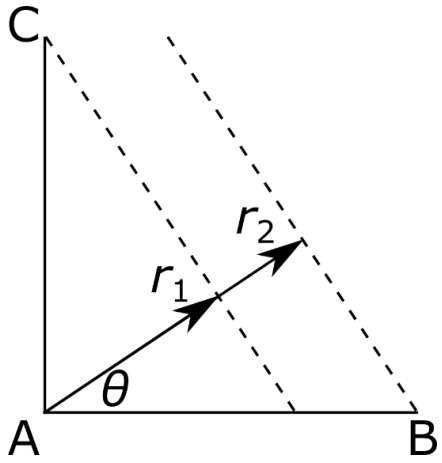

Figure 2.12: Schematic of a plane wave moving with speed v in the direction θ with respect to the line AB. This figure was composed by Frank Mulligan, adapted from *Giers et al.* (1997).

As described in section 2.4, when a UWOSCR image is obtained, all points in the image are interpolated to a fixed time to account for the scanning nature of the instrument. Since the images are then at a fixed time interval (one minute between each image), a cross-correlation analysis such as that performed by *Giers et al.* (1997) can be performed between two pixels A and B, and two pixels A and C, where $|AB|$ and $|AC|$ are in orthogonal directions. By doing this over a series of frames, the time taken for an intensity peak to pass from one pixel to the next can be found (*Briggs*, 1968). Then, using the equations above, the direction of propogation of the wave, θ, can be determined from t_{AB} and t_{AC}. Since the distances $|AB|$ and $|AC|$ are known ($\sim 1.5 \times \sqrt{2}$ km at the airglow layer if they are adjacent pixels, as shown in green in Figure 2.14), the velocity of an intensity peak can then be calculated. As will be described, a large number of pixels can be used for more accurate results.

If there is a monochromatic wave passing through the FOV, it will be seen at different pixels, but at different times. Figure 2.13 shows the time series of three different pixels, and the time lag between them can be measured manually. There are, however, 256 pixels and so the De Serrano and Lowe method was designed to do this automatically.

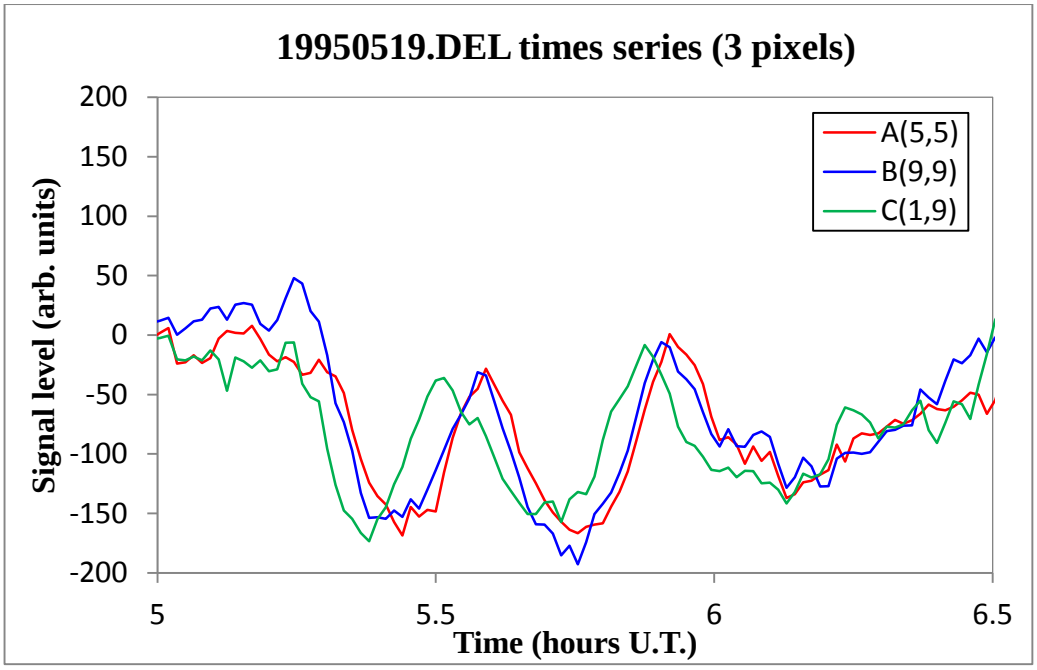

Figure 2.13: Time lag between some sample pixels as a GW passes through the FOV of a UWOSCR instrument at Delaware, Canada. For clarity, only three pixels were chosen for the plot, but there are 256 pixels which could be shown.

This automatic method uses a time window of length 21 frames at pixel A. Within this time window, maximum correlation between A and B, and between A and C are found by sliding values for B and C (corresponding to the central 11 frames of the 21-frame time window) along the 21 values for A. The time where maximum correlation between A and C is found, and the time where maximum correlation between A and B are found are both stored separately, along with the values of their correlations. Then, the velocity in the AB and AC directions are calculated using these time lags which correspond to maximum correlation. The frame to which these velocity values are attributed to is the mid-point of the 21-frame window. Then, the 21-frame window at A moves forward sequentially in overlapping steps (of one frame), and the whole process is repeated at each step until the end of the file is reached. This is done for pixel separations of 1, 2, 3 and 4 (as shown in Figure 2.14) so that whichever pixel separation corresponds to maximum cross correlation is used. This is then repeated for all three-pixel combinations in each image, and the average

velocities v_{AB} and v_{AC} corresponding to maximum correlation within the slider are then associated with that image.

As one may observe from Figure 2.14, the cross correlations aren't actually in the meridional and zonal directions. AB and AC were deliberately rotated by 135° to eliminate false waves that arise from different noise levels in each direction due to a drift in the detector output caused by the east-west character of the scan. Therefore, a correction factor must be applied to the angle of propagation, as demonstrated in Figure 2.15.

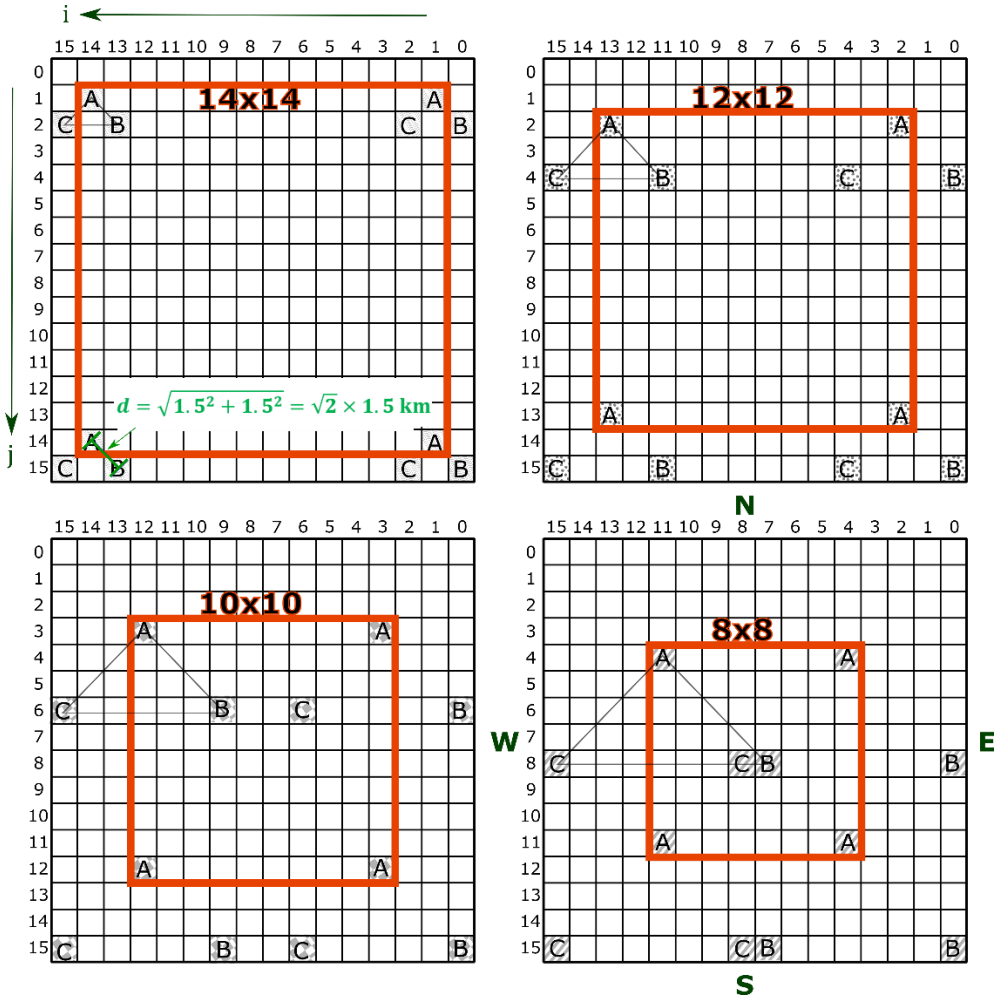

Figure 2.14: A schematic showing the limitation in the number of possible correlations which can be calculated (pixels outlined in red) due to pixel separations of (top left) one, (top right) two, (bottom left) three, and (bottom right) four. The top of each image corresponds to north as shown in the bottom right image. The values of i increase in the westward direction and the values of j increase in the southward direction, in agreement with the scanning order of pixels and with the code shown in Appendix C. The distances AB and AC are calculated as shown in green (pixel separation$\times\sqrt{2}\times$1.5 km).

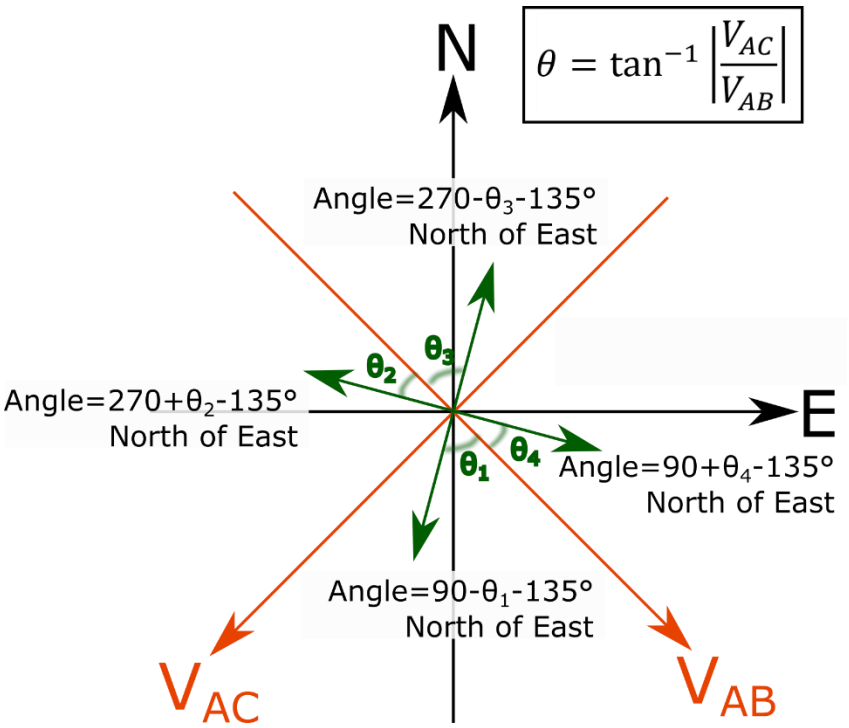

Figure 2.15: Schematic showing the frame of reference of the `vel_dir` program versus a geographic reference frame, and how angle (in degrees north of east) is calculated.

It should be noted here that the window length may be changed by the user using the LabVIEW program, and that this may be useful since using a different window length will optimise the analysis for particular wave speeds. If the window length is changed, so too must the slider length change to ⌈0.5×window length⌉. The choice of the time window length depends on the expected persistence of the waves. It is important to choose a window length long enough to get maximum use out of the data (*i.e.* in order to view the entirety of the wave as it passes through the FOV) and short enough so that the cross-correlation works (*i.e.* the wave is persisting in as many of the images as possible). De Serrano and Lowe chose the window length (based on velocities of large amplitude waves which had been observed) to be 21 images. This is optimised for GW velocities of 26, 32, 39, and 46 m s^{-1} depending on the pixel separation used. The following equation (*Huang*, 1993) shows how these optimal velocities are calculated:

$$\text{Optimal GW velocity (m/s)} = \frac{\text{diagonal FOV (m)}}{\text{\# frames in slider} \times \text{time res (s)}} \qquad 2.6$$

For example, for a pixel separation of 2, then a side length of 16-2(2)=12 pixels can be used, giving a FOV of 12°×12°=18 km × 18 km. Then the optimal GW velocity is given by $\frac{\sqrt{2\times18000^2}}{11\times60}$ ≈39 m/s.

The De Serrano and Lowe method was used by *Huang* (1993) to analyse small-scale GW activity in the OH* airglow using a UWOSCR instrument located at Delaware. Huang measured average errors in velocities for simulated waves with different velocities. It was found that an increase in velocity gave a decrease in measurement reliability, especially when noise was introduced. He also stated that this method with a fixed window length will not give good results in the case of curved wave fronts or varying background wind, for example, and suggested cross-spectral methods for the study of the wave field (*Huang*, 1993).

2.5.3.2. Calculation of Period

The dominant period in each frame is obtained by calculating the FFT of the time variation of the weighted mean centre (x_c, y_c) of a number of successive frames. Again, an appropriate time window length must be chosen. This window length was chosen to be 32 minutes, so that the maximum detectable period was 16 minutes. The minimum detectable period was 2 minutes due to the 1-minute sampling rate. The period calculated was then associated with the time at the centre of the window. Then, the time window slides along the entire night in overlapping steps to calculate the dominant period associated with each frame.

For each time window, the mean value of x_c and y_c associated with those 32 frames is subtracted from x_c and y_c to remove the DC component, and an apodization function is then applied to the new x_c and y_c. A Hanning function is used because it is simple to implement, and because it is a good trade-off between leakage and resolution (*Brigham*, 1988). An FFT of this signal provided a frequency spectrum, from which the dominant frequency could be

determined. This best-fit frequency was obtained by fitting a 3-point quadratic to the maximum frequency, thus artificially improving frequency resolution. The period of the time variation of x_c and y_c is then attributed to a GW, under the assumption that there is only one monochromatic GW passing through the FOV, that it takes up the entire FOV, and that it is the only moving feature in the FOV. The period assigned to a given frame is the period of sequences of either x_c or y_c, whichever has the most power associated with it. The dominant wavelength of the GWs for the given frames is then calculated (wavelength=period×velocity).

Since the source code was not available for the period calculation, the output from `UWO_exe` was compared to a version of the same method which was implemented in LabVIEW in order to verify that both sets of code produced similar results. The part of `UWO_exe` which calculates periods (*i.e.* `q_veldir.exe` and `ron2.exe`) which was provided by Kelly Ward of the UWO, was used to obtain the final results presented in this thesis. The `qvel_dir` code calculated the change in the location of the weighted mean centre of successive frames, and repeated this for all sets of frames within the dataset. The `ron2` code used the variation of the weighted mean centre in the x and y directions to determine the dominant period in each image. It achieved this by calculating the peak of the FFT of the variation of the weighted mean centres for 32 successive frames at a time.

An example of a period calculation on a synthetic wave (using the LabVIEW code) is shown below in Figure 2.16 and Figure 2.17. The synthetic wave has a period of 5 minutes for the duration of 240 minutes and is sampled every minute. It propagates at an angle of 140° north of east at a speed of ~67 m/s.

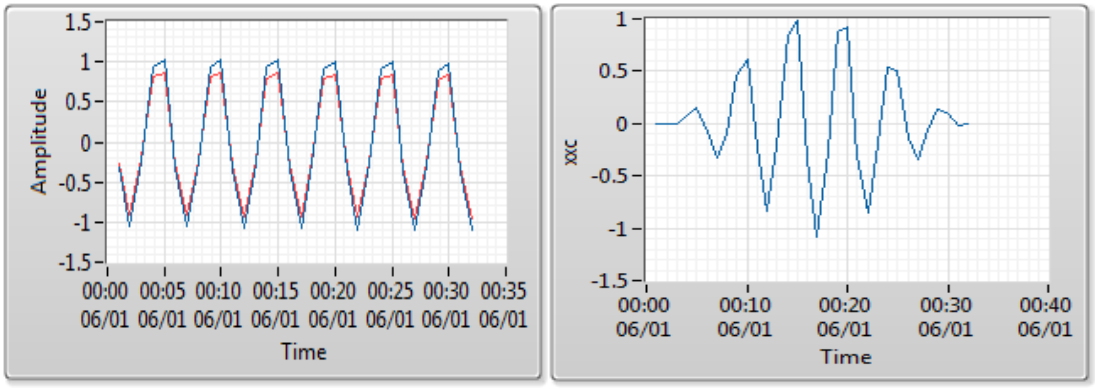

Figure 2.16: Period calculation for the synthetic wave described above. (left) Weighted mean centre of x_c (blue) and y_c (red) for 32 successive frames, with the average values of x_c and y_c already subtracted. (right) A Hanning window applied to x_c for 32 successive frames.

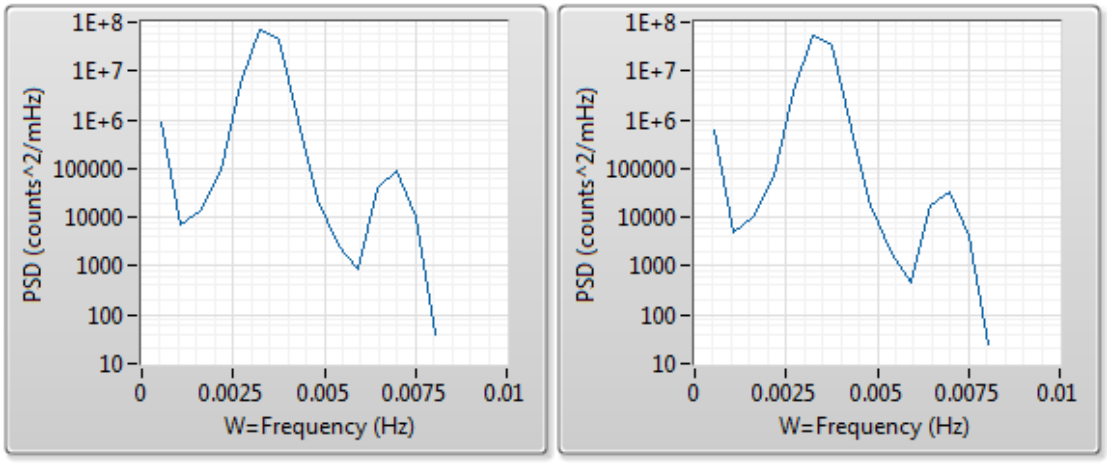

Figure 2.17: Power spectral density for a range of frequencies computed from an FFT of the apodized (left) x_c and (right) y_c for the same synthetic wave.

From Figure 2.16 and Figure 2.17, it can be seen that slightly more of the wave's power was in the x-component, and so the frequency associated with the highest power in x_c is assigned to the central frame in this time window. In this case, the dominant frequency was 3.2×10^{-3} Hz, corresponding to a period of 5.2 minutes. This example shows how well this period calculation method works for synthetic waves whose periods don't change as a function of time. With real waves, the situation is more challenging.

The window length for the FFT is user-defined in the LabVIEW program, and is currently set to 32 frames, to correspond with the De Serrano and Lowe code and to give a maximum detectable period of 16 minutes.

A final summary of the processing step is shown in Figure 2.18, which ultimately results in values for speed, direction and period at the centre of each time window within the file.

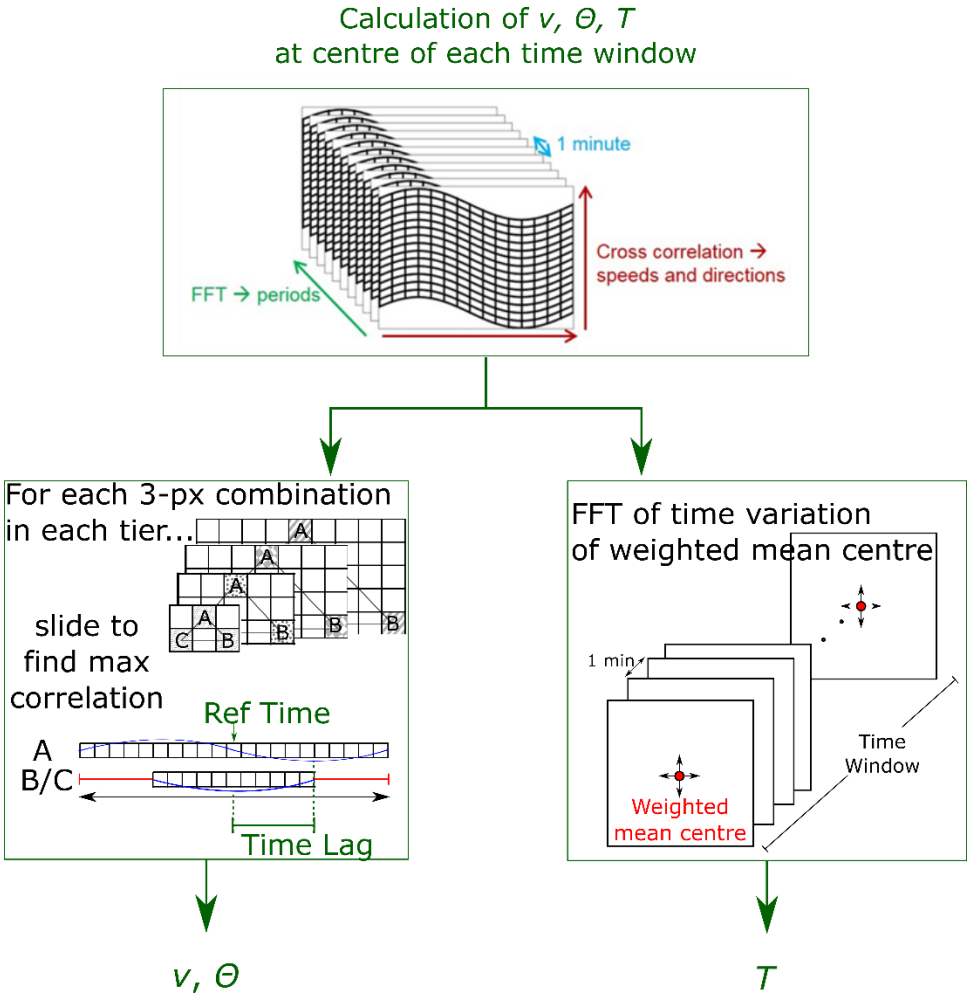

Figure 2.18: Overview of the processing step in the analysis procedure.

2.6. Post-Processing

After applying the De Serrano and Lowe method, the dominant speed, direction, period, and wavelength associated with every image (except 16 images at the start and end due to the window length of 32 frames used for the period calculation) in a given file is now known. Not every image will contain a GW and so two criteria were applied to identify images which contained wave structures. The main assumptions in establishing such criteria are that any physical wave will be present for several minutes and that its characteristics will vary relatively slowly during that period. Figure 2.19 outlines, in a broad sense,

these two criteria whose requirements are based on consistent values of velocity for sequences of at least 5 consecutive frames.

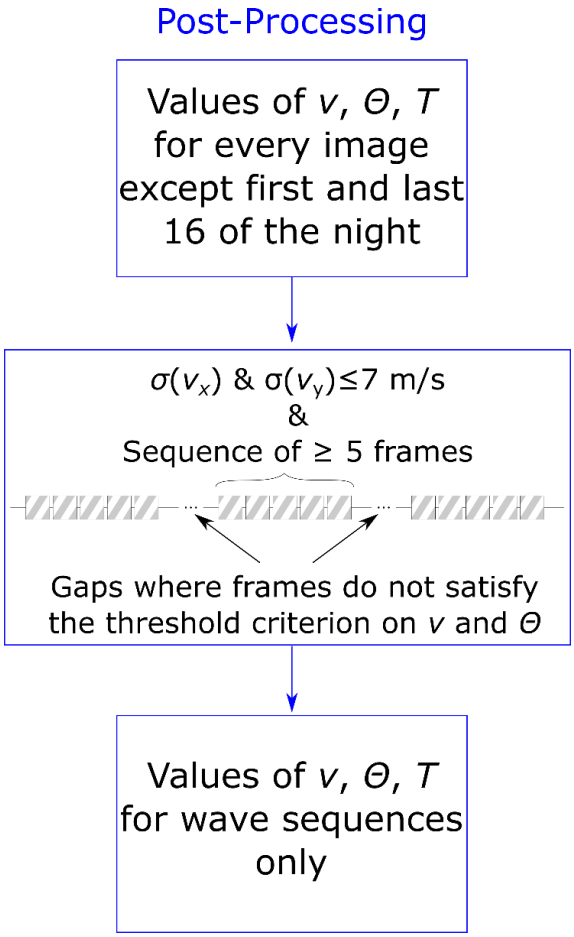

Figure 2.19: A block diagram illustrating the general idea of the post-processing step of the analysis procedure.

The first criterion related to how much the GW velocity should change from frame to frame. The change in velocity was determined by calculating the standard deviation of five consecutive values of the zonal and meridional velocities ($\sigma(v_x)$ and $\sigma(v_y)$) centred on each frame, attributing the result to the mid-point of the five-frame interval. A maximum limit (which will be referred to as 'L' throughout this thesis) was then set for $\sigma(v_x)$ and $\sigma(v_y)$. All frames whose zonal or meridional standard deviation exceeded this limit were excluded from further processing. As it was not known what this limit should be, a trial and error approach was initially taken, and so L was user-defined in the post-processing software which was developed. The choice of L is a compromise

between the risk of rejecting valid measurements and accepting invalid measurements. Limits of 5, 7, 10, 15 and 25 m/s were all considered in the analysis. With the largest limit, it was suspected that some invalid measurements may have been accepted as a larger proportion of waves could not be distinguished manually (as in section 2.5.1). When performing the initial analysis, a limit of 5 m/s was chosen in order to err on the side of caution. Then, following some comments from one of the referees on a paper (*Rourke et al.*, 2017), it was decided to relax this criterion in order to ensure that there were sufficient numbers of GWs to be representative of the seasons. The final analysis was performed with a standard deviation limit of 7 m/s as a result. As will be shown in Chapter 3, the climatological results did not change significantly as the standard deviation limit was varied. When examining case studies later in the thesis (in Chapter 5), this limit was increased to 15 m/s to include some clear events which had been rejected by the 7 m/s criterion. This may indicate that the 7 m/s limit resulted in the rejection of some valid GW events.

The standard deviation limit on the meridional and zonal velocities results in propagation direction variation limits which are not easily defined, since the angle variation depends on the particular values of meridional and zonal velocity. Figure 2.20 shows the variation (over five consecutive frames) in wave propagation direction which is allowed for the 7 m/s standard deviation limit. It shows this for values of meridional and zonal velocity which correspond to a structure velocity of ~20−100 m/s, as this was the general range of GW phase speeds observed in the data. Meridional and zonal speeds of less than ~25 m/s generally did not correspond to structure velocities of 20−100 m/s, and thus they are not shown in the figure. If one considers a typical wave speed of ~60 m/s, produced by meridional and zonal velocities of 90 m/s and 80 m/s respectively, then the change in propagation direction allowed is $\pm 11.7\%$ of $\tan^{-1}\left(\frac{V_m}{V_z}\right) = 48.4^\circ$ north of east, which corresponds to $\pm 5.7^\circ$. This is just a

typical example, but as may be seen in Figure 2.20, this value can change significantly depending on the values of meridional and zonal velocity.

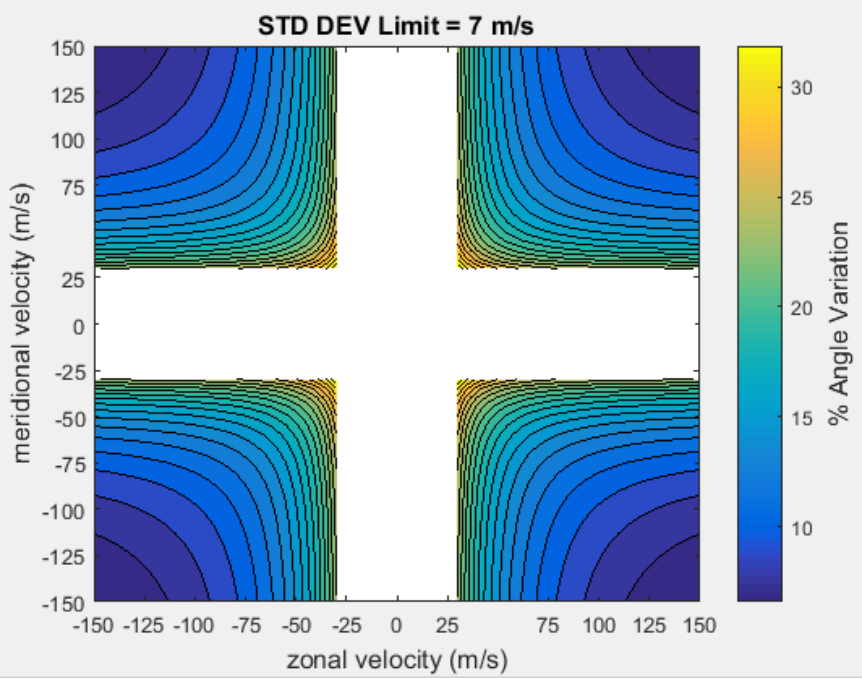

Figure 2.20: Change in angle (in colour) accepted for a range of different meridional and zonal velocities when using the post-processing standard deviation threshold of L=7 m/s. Zonal and meridional velocities with absolute values of ≤25 m/s are not shown as they generally result in a structure velocity which is outside the range 20−100 m/s and thus are not representative of the results presented.

The data remaining after the first criterion was then passed on to the second criterion. The second criterion related to the persistence of the wave. This criterion checked the time difference between two 'consecutive' frames which passed criterion 1, and only if there were five or more actual consecutive frames (*i.e.* without a gap), then these frames were taken as a sequence of a single gravity wave. All gravity wave sequences of this nature in the data were retained, and all other data was eliminated. The minimum number of consecutive frames required was set to five frames. An example of data before and after these post-processing criteria is shown in Figure 2.21, where it can be seen that only sequences of consistent velocities are retained and velocities which deviate substantially from the surrounding frames (such as between ~20:30 and 21:00 UT) are rejected.

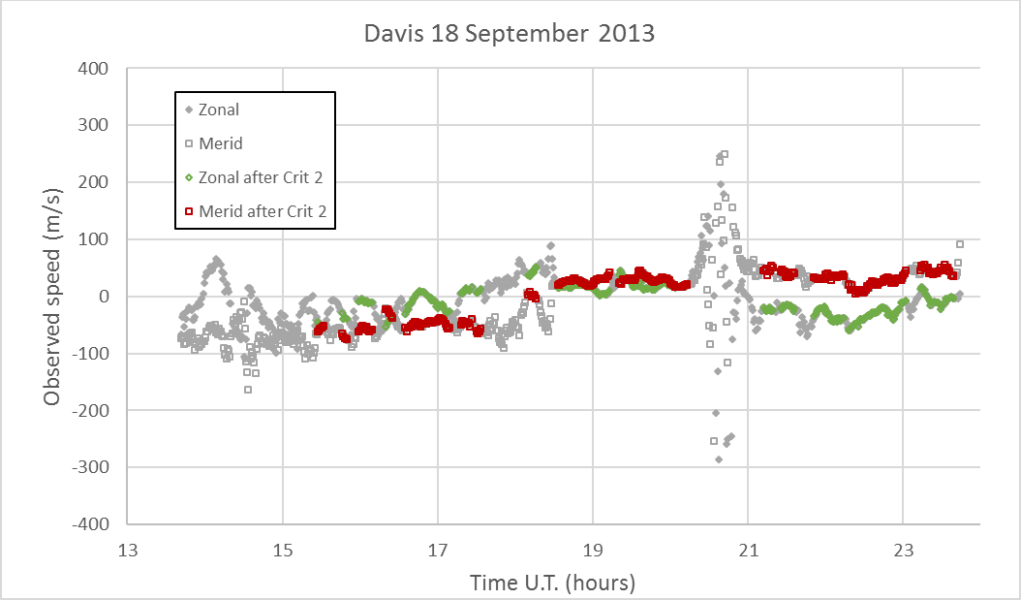

Figure 2.21: Observed zonal and meridional speeds on the night of 18 September 2013 at Davis Station (positive is eastward and northward). The grey points were eliminated when criteria 1 and 2 were applied to this night.

Any remaining sequence which contained less than five frames of ripples (λ_h <15 km) and less than five frames of band-type gravity waves (λ_h ≥15 km) was not analysed as it was assumed that ripples and band-type GWs could not interchange within a single sequence.

This reduced set of data was then used to study gravity waves and ripples over Davis Station between February 1999 and November 2013. The program developed to do all this post-processing has helped in expanding our capabilities in interpreting the data. There is now greater flexibility than before in the time period that may be studied and in the criteria that may be applied when selecting GWs.

This chapter has documented details of the UWOSCR instrument and the analysis methods which will be employed in subsequent chapters. Some of the rather intricate details described here will become clearer as the methods are applied to actual data in Chapter 3.

3. GRAVITY WAVE MEASUREMENTS

Climatologies provide information about long-term variabilities of atmospheric phenomena which can then be used to constrain climate models. Efforts to observe and understand GW climatology is an active area of research, albeit a daunting observational challenge, because global models require GW parameterisations (as described in section 1.7.2). Long-term observations at single sites can provide useful information about the seasonal and interannual variation of GWs (*Fritts and Alexander*, 2003). As such, UWOSCR has been running continuously during the austral winter months at Davis Station since 1999 for this purpose. As mentioned in Chapter 1, when interpreting the results from this instrument for climate model parameterisations, one must consider that, as a single instrument, it is sensitive only to a small portion of a broad spectral range of GWs. Climatologies from other instruments will also be necessary to consider in order to avoid inferring false climatological patterns from a single-instrument dataset.

In this chapter, a climatological study of GWs and ripples observed by UWOSCR during the period 1999-2013 is presented. The De Serrano and Lowe analysis method (`UWO_exe`, as defined in Figure 2.6) was used for this climatology, and the post-processing standard deviation limit (described in section 2.6) which was used was L=7 m/s. The chapter is thus split up into two main sections: (*i*) testing of the De Serrano and Lowe software and (*ii*) climatological results of GWs and ripples obtained from the 15-year dataset at Davis Station.

3.1. Software Testing

The purpose of this section is to quantify the level of uncertainty associated with the analysis method used. Software tests of `UWO_exe` will be shown in sections 3.1.1-3.1.3. In section 3.1.1, synthetic waves of varying amplitude and noise levels are generated and the wave parameters are recovered using the

analysis software. Section 3.1.2 will show results obtained for some real gravity wave events and compare them to manual approximations of the same events. In section 3.1.3, comparisons will be made between results obtained from UWOSCR using `UWO_exe` and results obtained by an independent analysis method from a co-located OH* airglow imager. Finally, some tests of new LabVIEW software (which is based on the De Serrano and Lowe analysis method) will be presented in section 3.1.4.

3.1.1. Results for synthetic waves

Results from four different sets of synthetic waves will be presented in this section. The difference between each set of waves is shown in Table 3.1. There are 15 waves within each set, each of which maintain the same amplitude, noise level, persistence and start time as all other waves within that particular set. All waves within all sets shown have a fixed horizontal wavelength (30 km) and direction of propagation (45° north of east). Each wave within a particular set has a different period. The periods of these waves range from 2−16 minutes in steps of 1 minute. Each of these waves have a designated 240 minutes within their set, and may persist for all or part of this designated time. For example, each of the waves in the 1st and 2nd sets persist for the full 240 minutes, whereas the waves in the 3rd set begin 60 minutes from the start of their designated 240-minute interval and end after 2 full wave cycles have been completed. The noise files, which were applied to the latter three sets of waves, are actual dark night files recorded by a UWOSCR instrument at Maynooth. The amplitude parameter has arbitrary units (with a maximum of 500), but the image sequences shown will provide a general idea of how these values compare with real gravity waves.

Best results will clearly occur when the wave contains no noise signal, when the amplitude of the wave is very high and when the wave persistence is greatest. Clearly, this is not realistic for actual gravity waves, hence why some results are also shown for when noise is added, when the wave amplitude becomes very

low, and when wave persistence is as low as 1-2 wave cycles. For comparison with real waves which will be shown later in this chapter, the sequence of images corresponding to one particular synthetic wave from each of the four cases are shown in Figures 3.1-3.4.

Set	Amplitude (max 500)	Noise	Persistence	Start time (min)	λ (km)	T (min)	θ ($^\circ$ NoE)
1	500	None	240 min	0	30	2-16	45
2	20	DARK0129.MAY	240 min	0	30	2-16	45
3	20	DARK0129.MAY	2 cycles	60	30	2-16	45
4	50	DARK0129.MAY	1 cycle	60	30	2-16	45

Table 3.1: A table showing the characteristics which vary for each set of synthetic waves. There are 15 waves within each set, each of which maintain the same amplitude, noise, persistence and start time for their particular set.

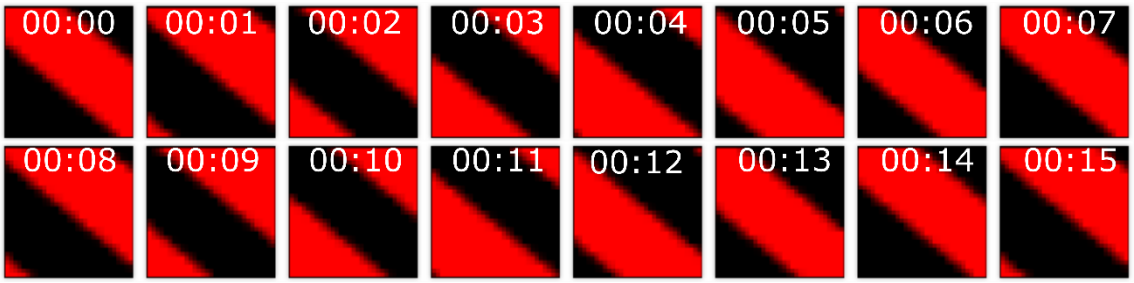

Figure 3.1: A subset of the image sequence for the synthetic wave with period of 7 minutes in set 1. This wave has no noise signal applied, has an amplitude of 500, and persists for 240 minutes. The order of the images are left to right, then top to bottom, and each image is one minute apart.

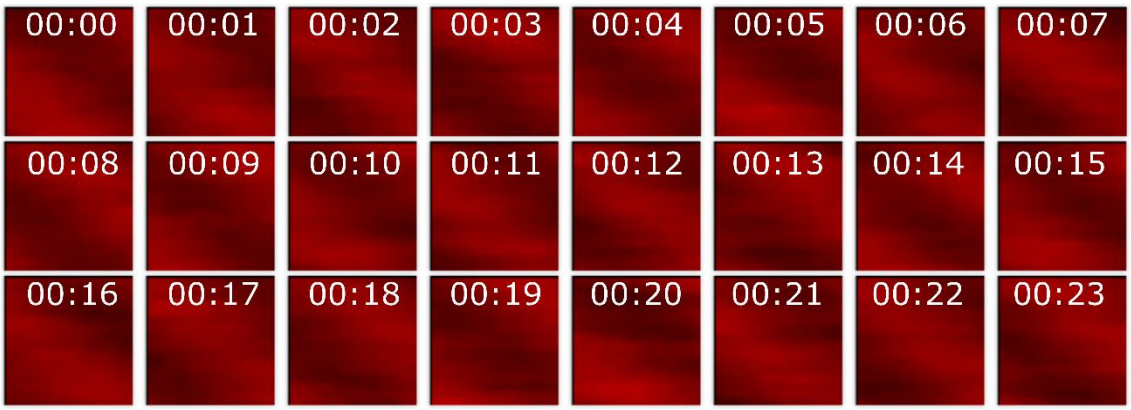

Figure 3.2: A subset of the image sequence for the synthetic wave with period of 5 minutes in set 2. This wave has a noise signal applied, has an amplitude of 20, and persists for 240 minutes.

Figure 3.3: Image sequence for the synthetic wave with period of 12 minutes in set 3. This wave has a noise signal applied, has an amplitude of 20, and persists for two wave cycles. It is visible between 01:04 and 01:28 above.

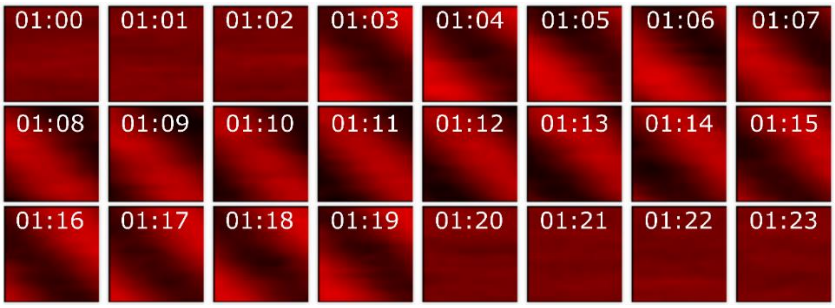

Figure 3.4: Image sequence for the synthetic wave with period of 16 minutes in set 4. This wave has a noise signal applied, has an amplitude of 50, and persists for one wave cycle. It is visible between 01:03 and 01:19 above.

The results before and after the post-processing step for each set of waves will now be shown. Figures 3.5-3.8 show the recovered values for wave period, phase speed and propagation direction for each minute in each set before post-processing. The 'ideal' values shown on these plots are the values which have been synthesised. The first two wave sets are straight-forward in this regard - the ideal values are continuous throughout the full set (as shown in Figure 3.5 and Figure 3.6). In the case of the latter two wave sets, a wave should only be present at particular times during the set and so very large deviations from the characteristics of the synthesised waves can be expected at times when a wave is not present (which is most of the time). This is observed in Figure 3.7 and Figure 3.8.

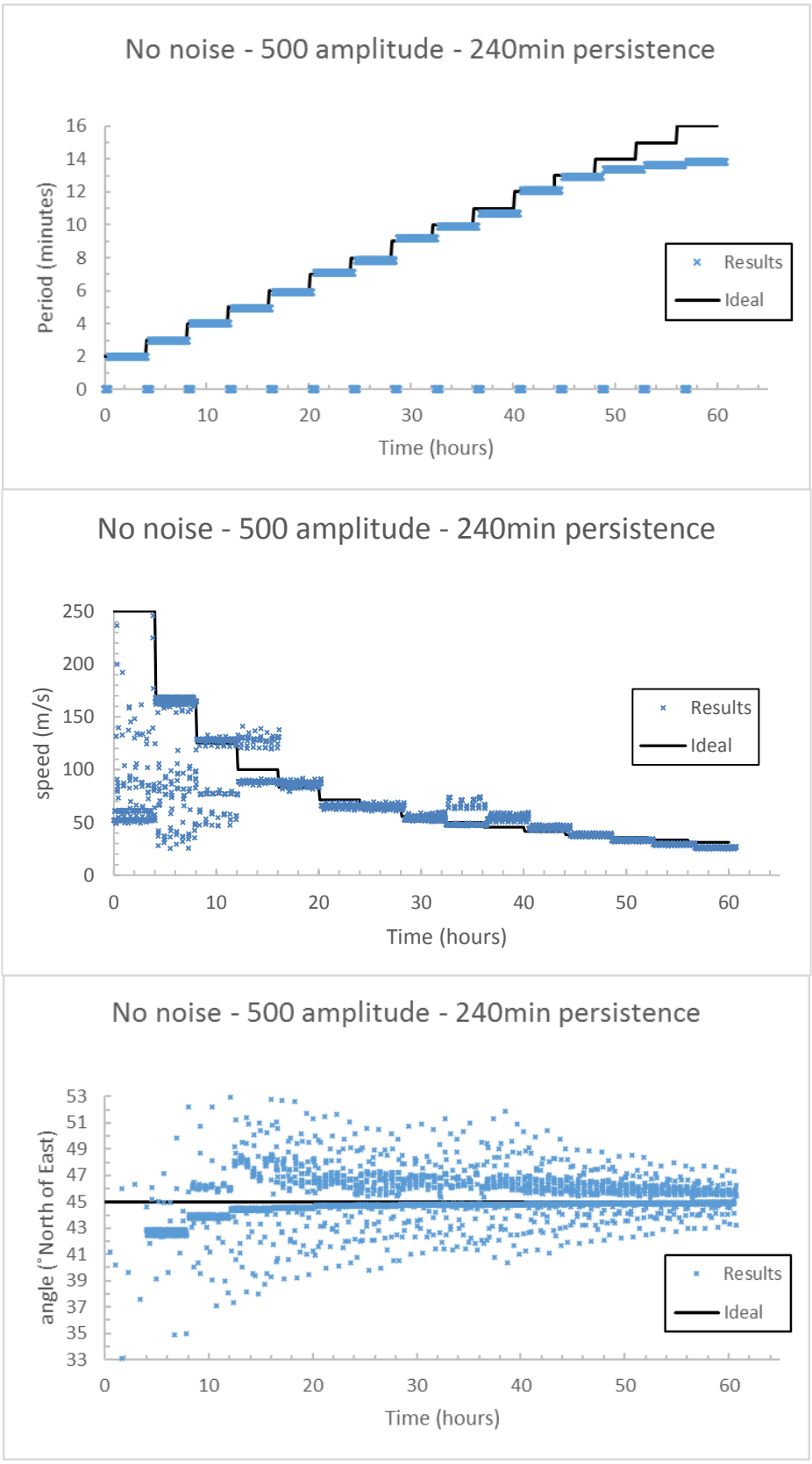

Figure 3.5: Results of synthetic waves in set 1 before post-processing.

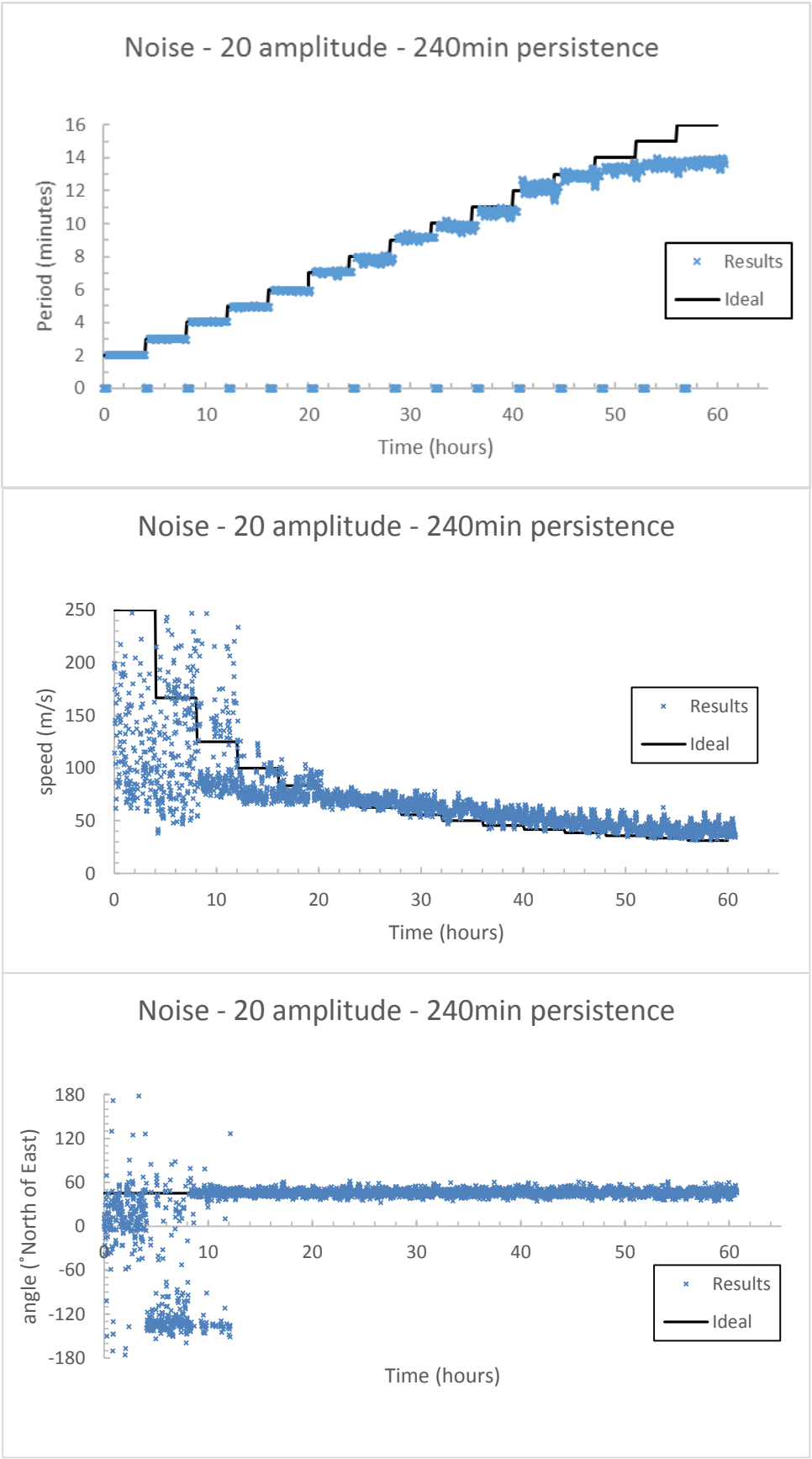

Figure 3.6: Results of synthetic waves in set 2 before post-processing.

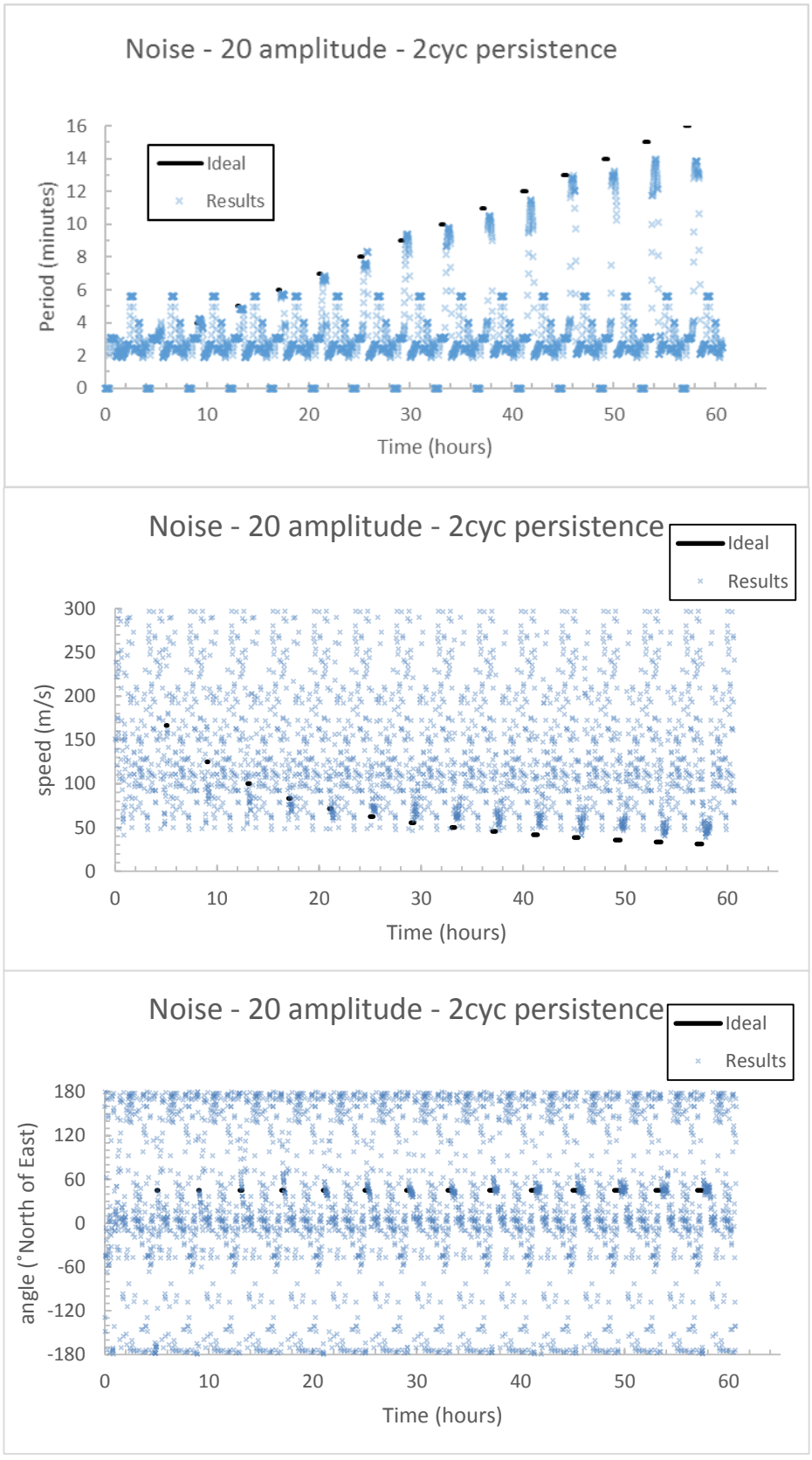

Figure 3.7: Results of synthetic waves in set 3 before post-processing.

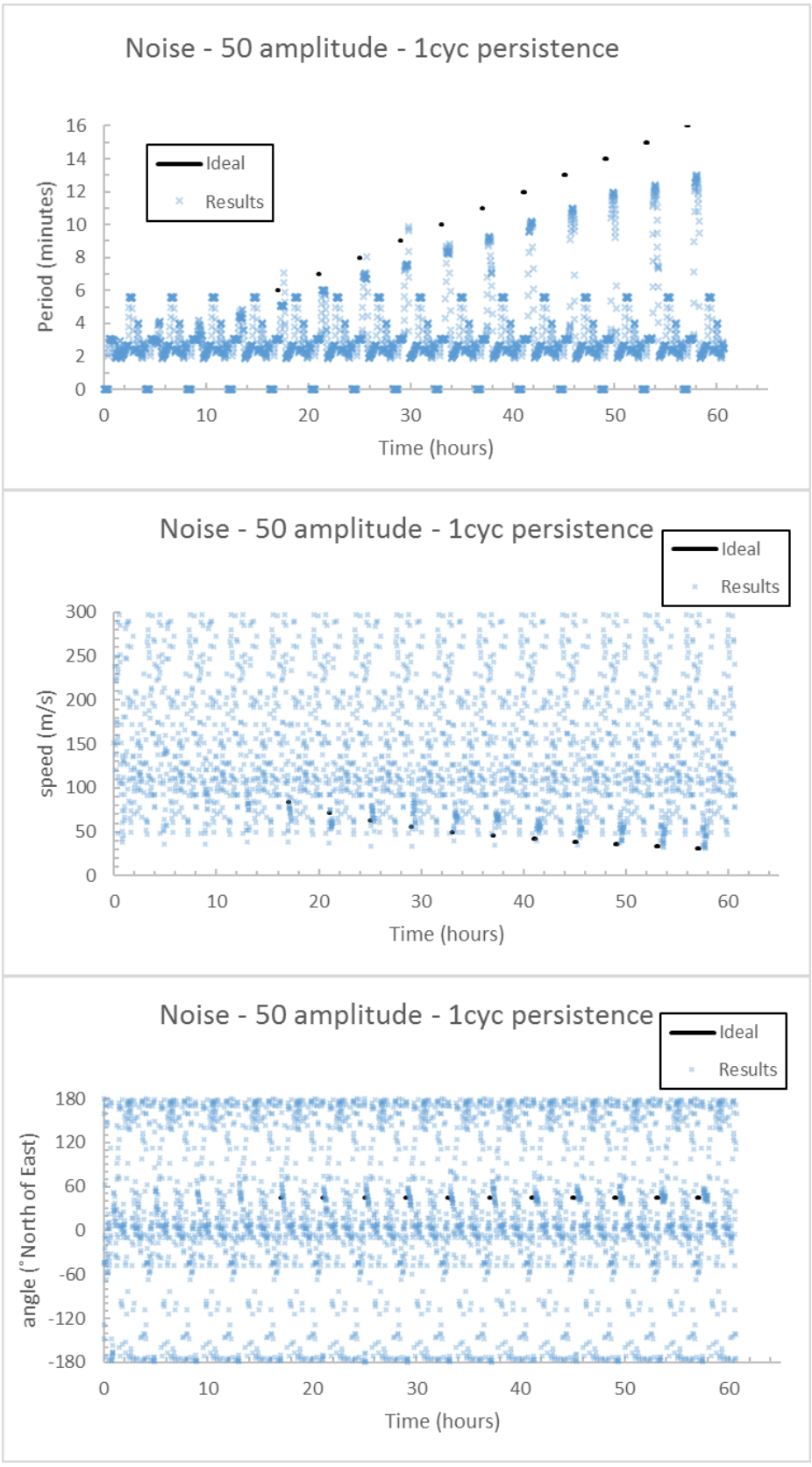

Figure 3.8: Results of synthetic waves in set 4 before post-processing.

The results for each wave in each set which corresponded to the best results for all three wave characteristics (period, speed, and direction) are shown in Figures 3.9-3.12, before the post-processed results for each set are shown in Figures 3.13-3.16. The best-case results (which are reported in Figures 3.9-3.12) were determined by checking the results from each frame, and considering which frame corresponded most closely to the ideal wave parameters at this time. This involved a trade-off between accuracy of velocities versus accuracy of periods, as their optimal values were often associated with different frames. There were one or two outliers from the ideal case in all four sets of results due to this trade-off.

When post-processing is performed on the results, the most uncertain results are generally eliminated. The plots below (Figures 3.13-3.16) show the post-processed results of the four sets of synthetic waves and, as discussed in section 2.6, the standard deviation limit which was used was L=7 m/s.

The post-processed results from set 1 (in Figure 3.13) show that the period of a 2−10 minute wave may be obtained to an accuracy of <10 seconds, the period of an 11−13 minute wave may be obtained with <20 second accuracy, and the period of a 14−16 minute wave may have an uncertainty of up to ~2 minutes. Uncertainties of periods tend to increase with an increase in period, possibly because the weighted mean centre does not move with high enough frequency to be captured accurately by an FFT on a 32-minute window. Speeds generally are accurate to at least ±10 m/s. In the most extreme case (which one would not likely ever observe), the 2-minute period wave (with a speed of 250 m/s) could not be captured correctly within the FOV by the cross-correlation method, leading to spurious values of ~50 m/s. In fact, due to the nature of the cross-correlation method, if the window length (21 frames) is greater than twice the wave period, then there may be ambiguity (of a multiple of period) in the time lag corresponding to maximum correlation, although this is generally not the case for real waves as phase and amplitude vary slightly with time.

Propagation angles were generally within ~2° of the ideal case, but some waves with an uncertainty of ±8° (along with the one spurious case mentioned earlier, where angle was 90° north of east) were also accepted in extreme cases.

With data such as that shown in set 2 (Figure 3.14), waves with low period (2-3 minutes)/high speed (≳120 m/s) may not be characterised accurately. This was again due to the combination of high speed and low period of these waves. These results did not pass the post-processing criteria and thus were rejected. Of those waves which were accepted, they had period uncertainties of <30 seconds for waves with periods up to 10 minutes, <1 minute up to a period of 14 minutes, and up to ~2 minutes for waves synthesised with periods of 15−16 minutes. Wave speed uncertainties had values up to ~30 m/s and were generally over-estimated for waves with period >7 minutes. Propagation angles had uncertainties of ±~10°.

From the 3rd and 4th sets of waves (shown in Figure 3.15 and Figure 3.16), results were accepted for waves with periods >4 minutes, and the wave times were determined correctly by the post-processing software. In the best-case scenario for each of these waves, periods were obtained to within an accuracy of ~20−120 seconds, although this period drifts slowly for each wave, creating a wide spread of possible periods. Best-case wave speeds generally are accurate to within 0−10 m/s, but again these values have a spread of up to ~30 m/s. Propagation angles had uncertainties of <10° for these two sets of waves.

Although not flawless, this method produces reliable values for almost all synthetic waves discussed, and clearly works best for very persistent waves where several full window lengths are uncontaminated by noise. In the case of very bright and persistent waves, uncertainties can be as low as 30 seconds, 5 m/s, and 2° for period, speed and direction respectively. In the case of very low-amplitude and short-duration waves, uncertainties may be as high as 14 minutes, 30 m/s and 10°, depending on the quality of data. However, these are

all theoretical values and so testing of the analysis method using real waves is described in the following section.

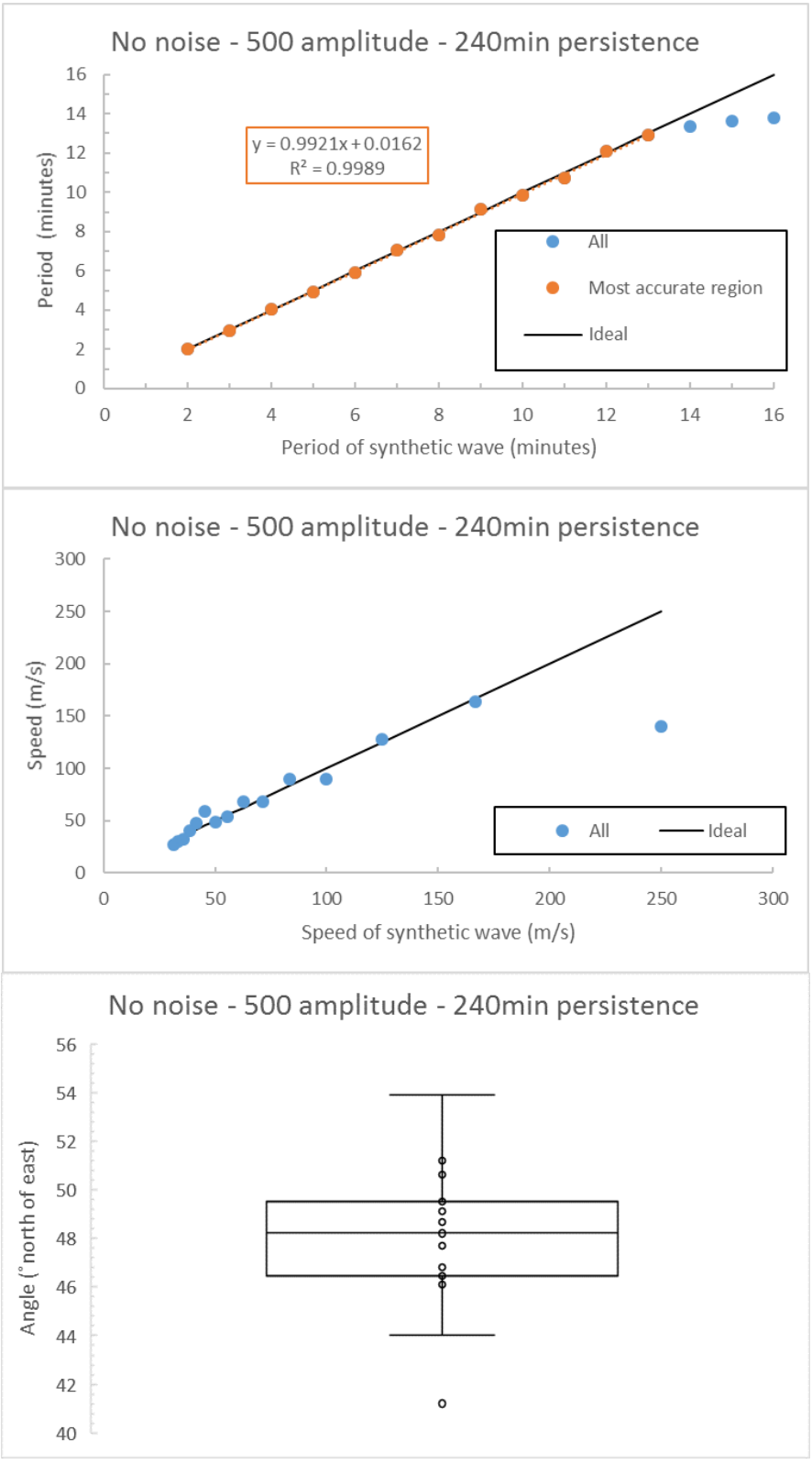

Figure 3.9: Best-case results for the 15 synthetic waves in set 1.

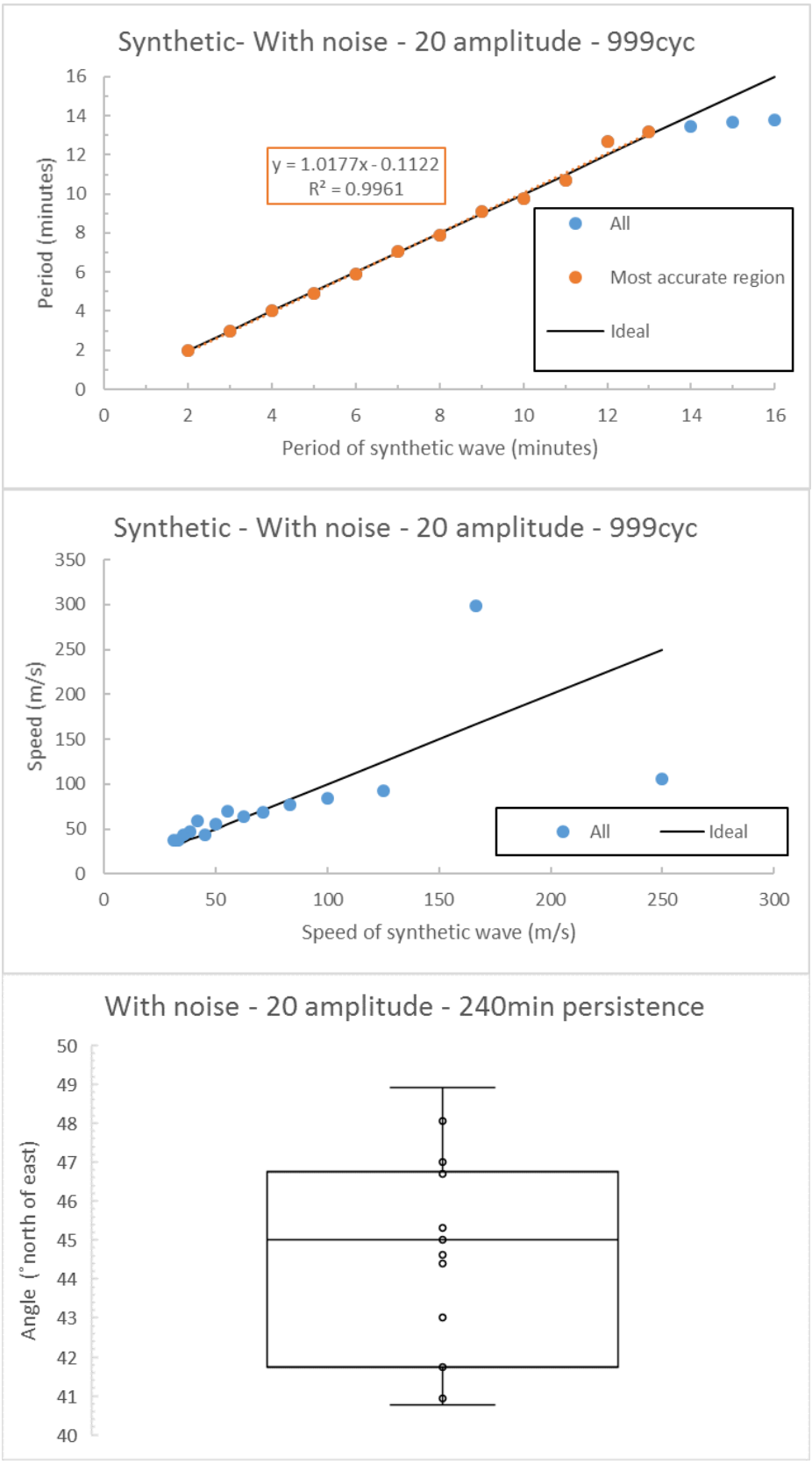

Figure 3.10: Best-case results for the 15 synthetic waves in set 2.

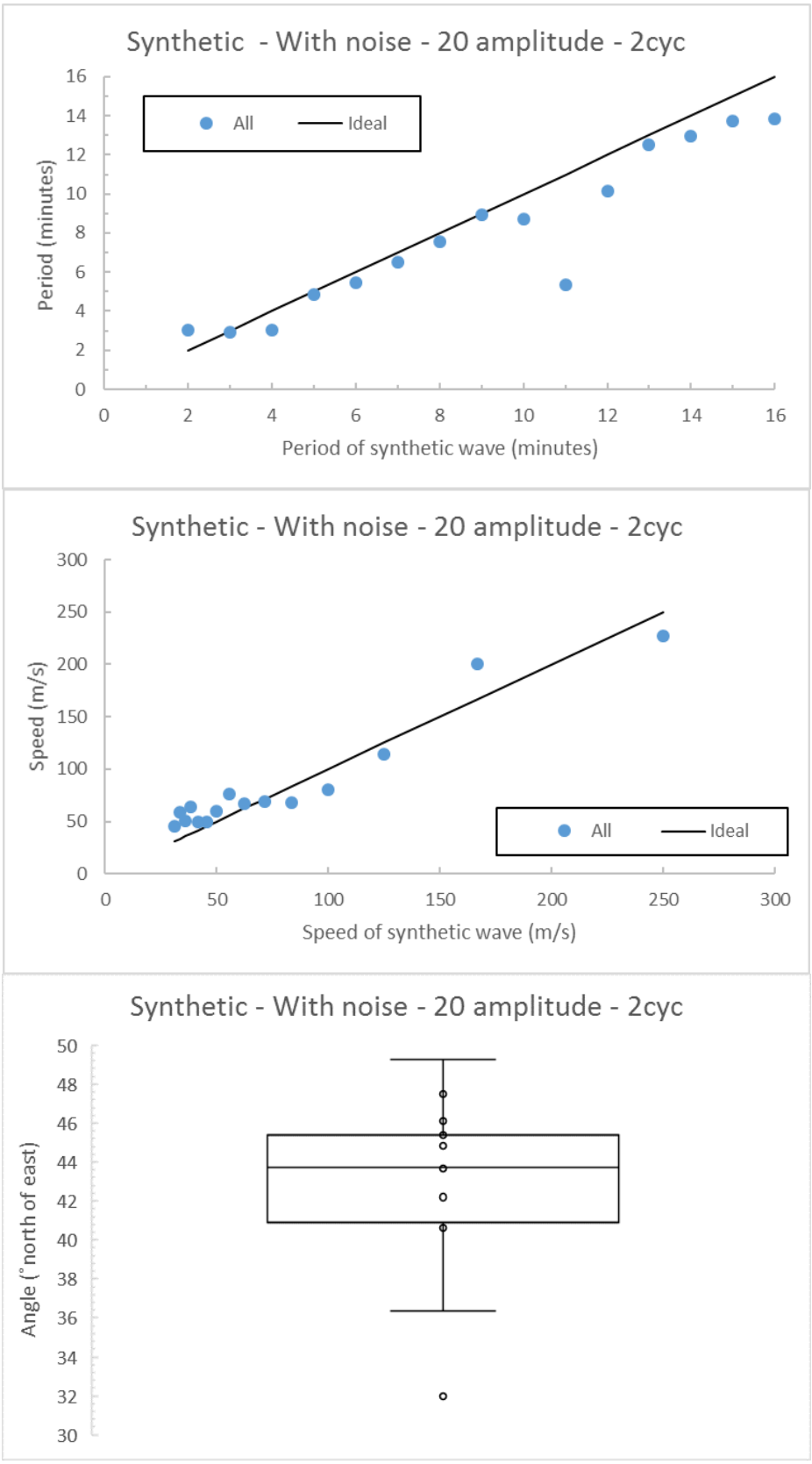

Figure 3.11: Best-case results for the 15 synthetic waves in set 3.

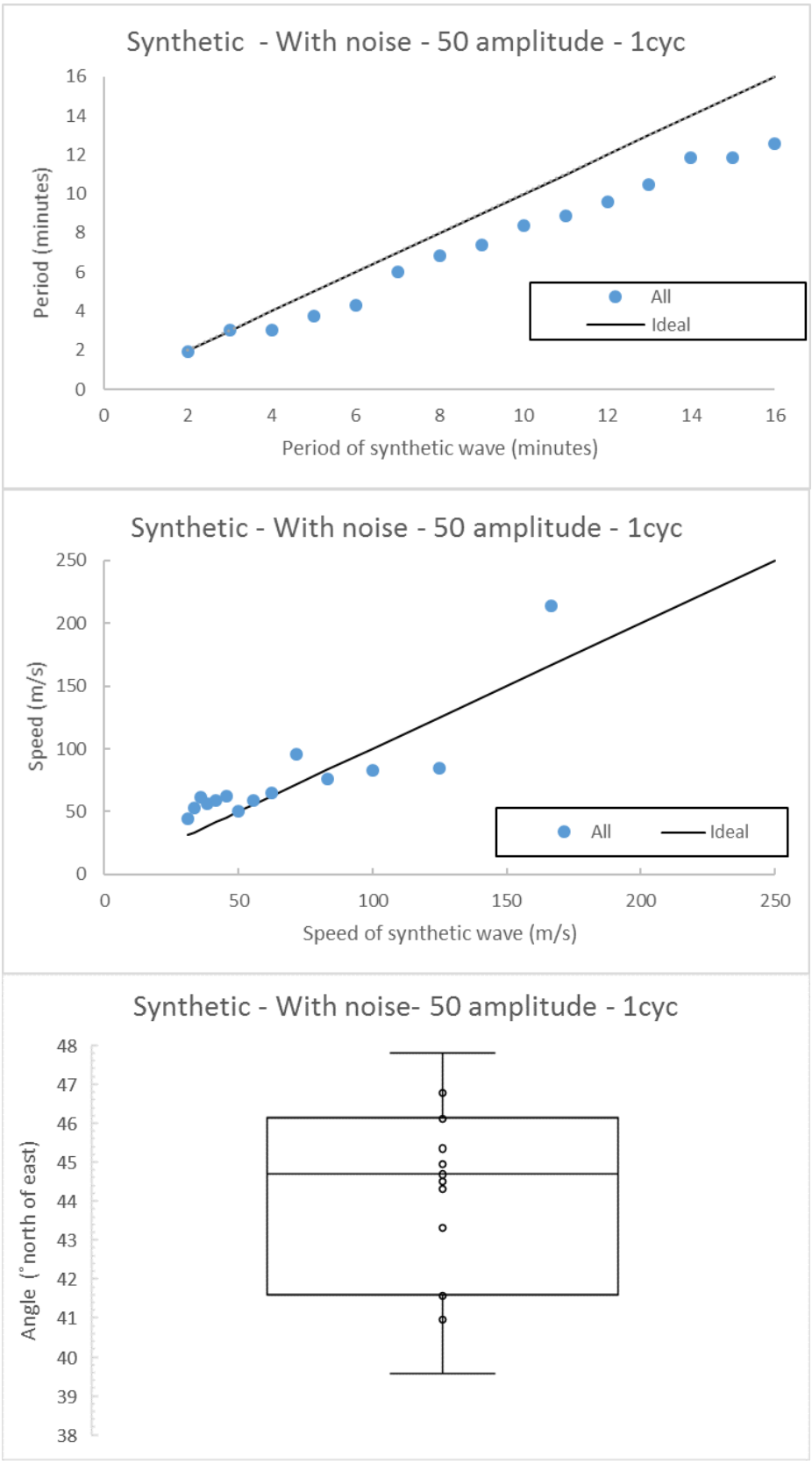

Figure 3.12: Best-case results for the 15 synthetic waves in set 4.

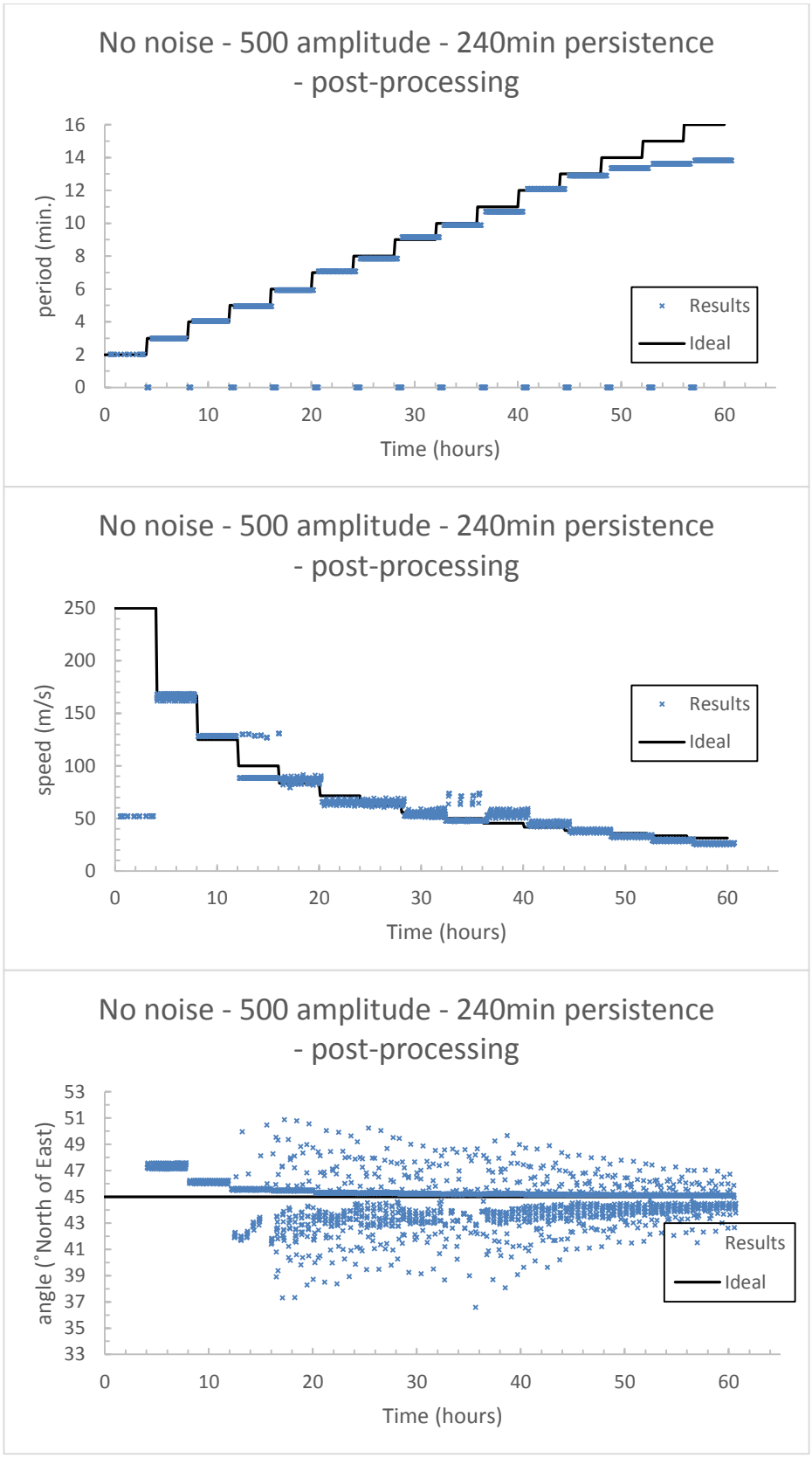

Figure 3.13: Results for set 1 after post-processing.

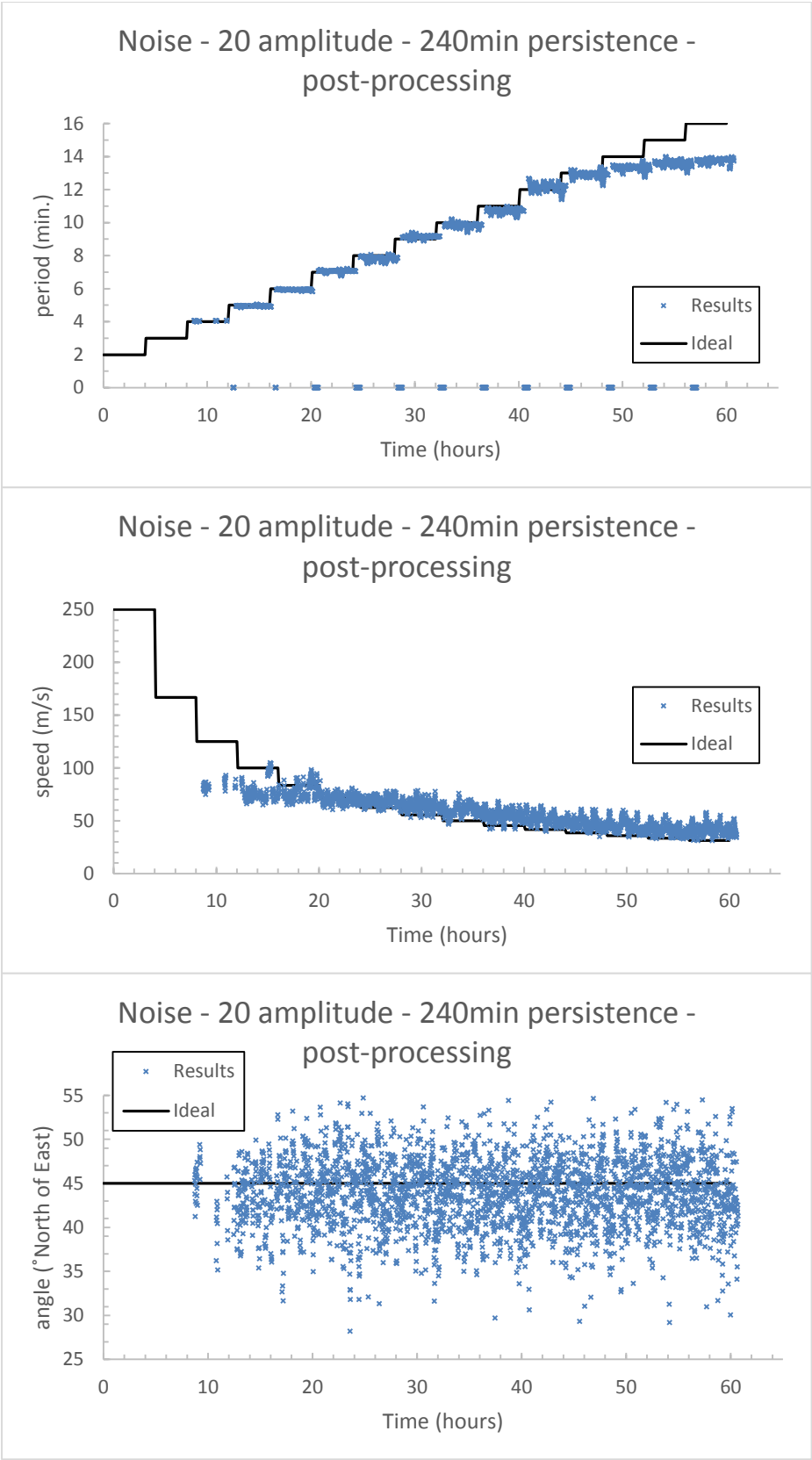

Figure 3.14: Results for set 2 after post-processing.

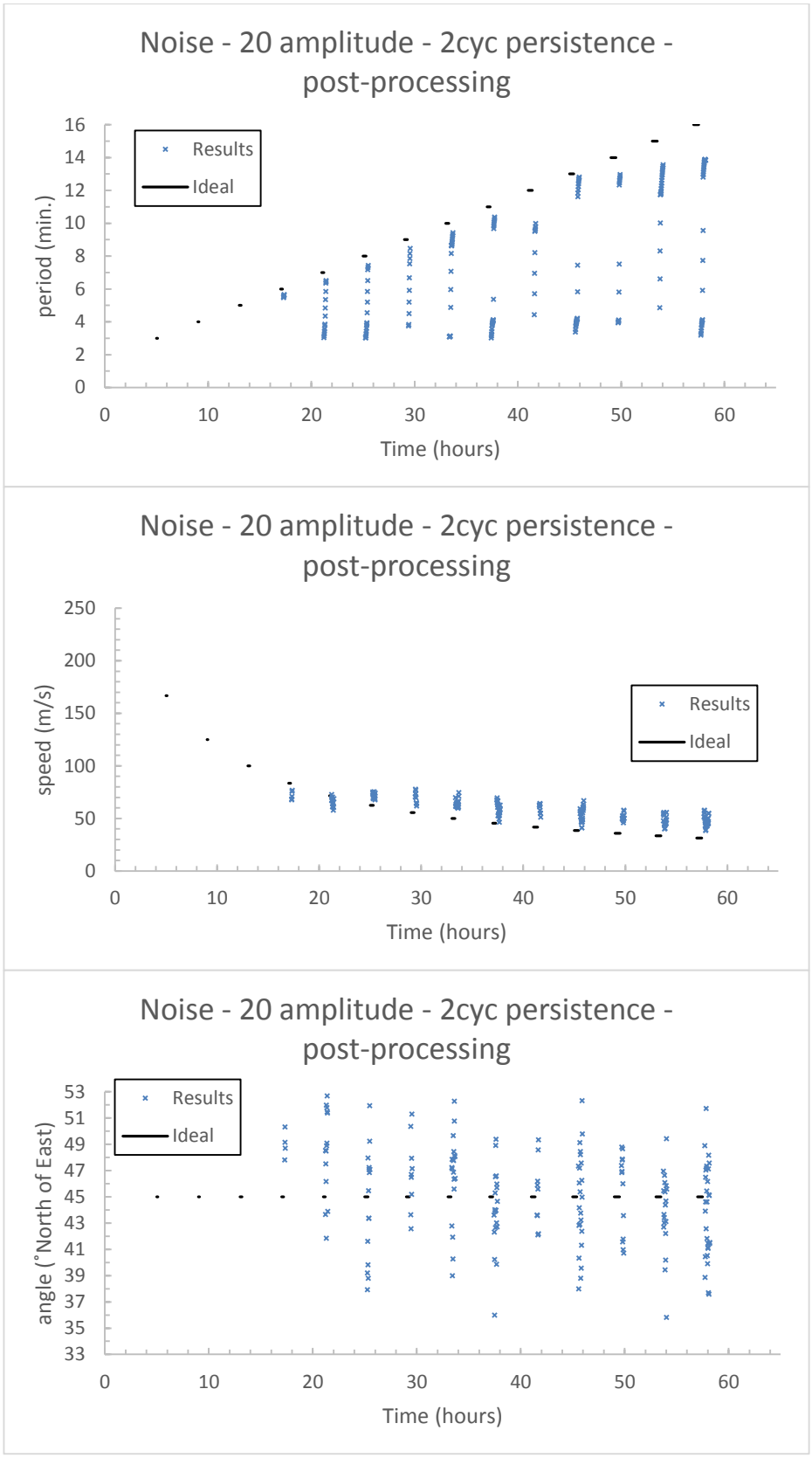

Figure 3.15: Results for set 3 after post-processing.

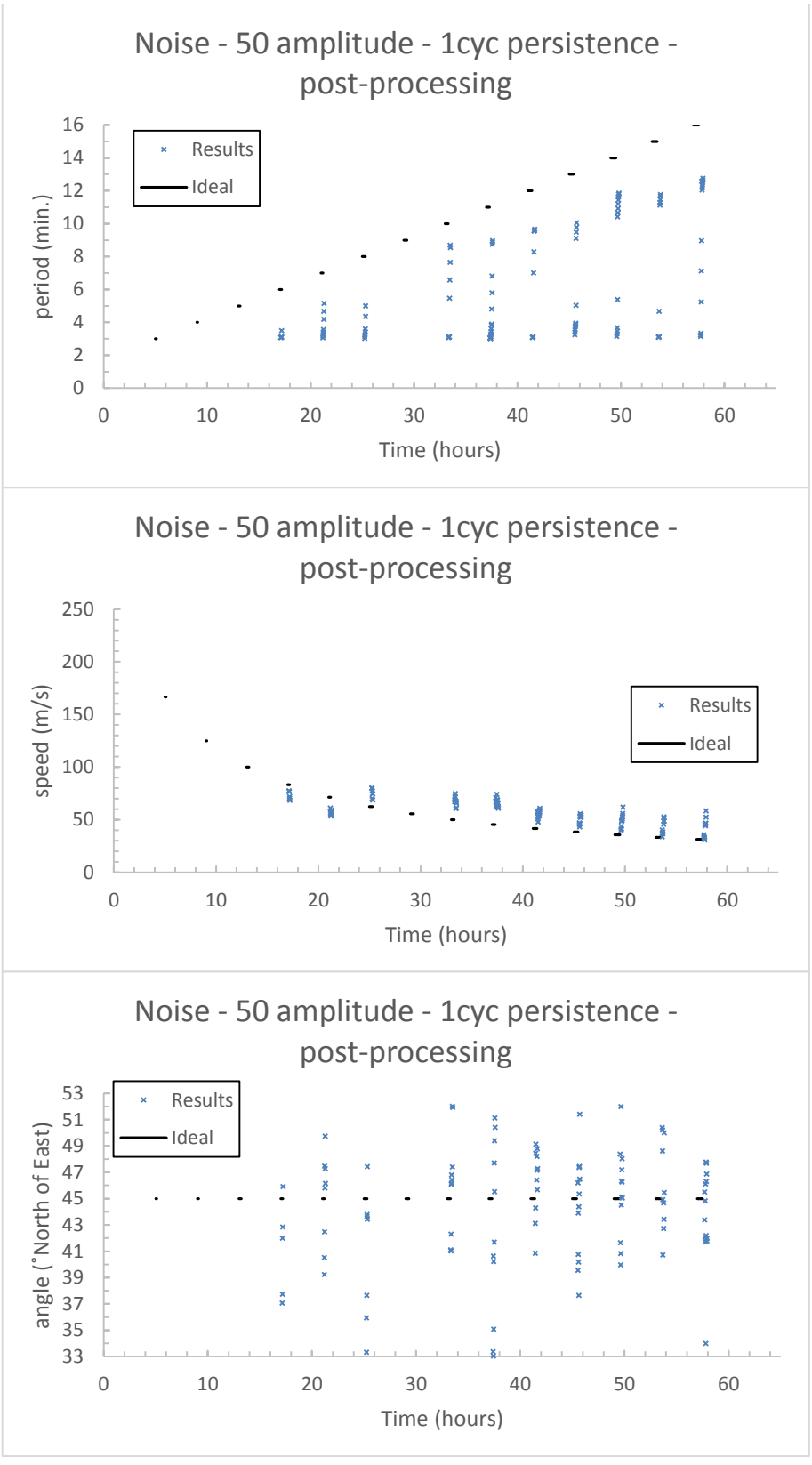

Figure 3.16: Results for set 4 after post-processing which, when compared with corresponding processed results in Figure 3.8, demonstrates the value of post-processing.

3.1.2. Results for real waves checked manually

As a further software test, a manual approximation of waves detected by the automated method between 1999 and 2013 was performed. The post-processing standard deviation limit (described in section 2.6) in this case was set to L=5 m/s to reduce the number of waves (from 1808 waves with L=7 m/s down to 851 waves with L=5 m/s) which needed to be characterised by the time-consuming manual approximation method.

As mentioned in section 2.5.1, the manual analysis method is very useful for obtaining the approximate characteristics of a particular GW event, and can thus be used to check (approximately) the reliability of the automated analysis method for real waves. One must keep in mind that the manual results presented in this section have been biased by *(i)* subjectivity, and *(ii)* FOV limitations. Subjectivity was introduced when deciding where exactly a wave crest lies within the image, and FOV limitations caused waves with wavelengths >24−34 km (depending on wave direction) to be ignored as two peaks did not fit within the FOV. In addition, very faint waves which could be distinguished mathematically could not be distinguished by eye, resulting in a reduction in the number of waves whose characteristics could be approximated. A brief summary of manual wave characteristics for all waves will be presented in this section, along with some individual cases which both agreed and disagreed with the automated analysis. A full appreciation of these results may not be gained until the end of Chapter 4, but in this section the focus is merely on their significance from a software testing point of view.

The `UWO_exe` program, followed by post-processing with L=5 m/s, identified 851 waves during the period 1999-2013. From these 851 waves, 390 were characterised manually. The majority of the remaining 461 waves could not be distinguished clearly by eye, although some others were also eliminated as they could not be characterised in full manually (*e.g.* wavelength could not be determined due to only one peak within the FOV, and direction could not be

determined for waves which appeared stationary within the FOV). For a direct comparison between the two sets of results for these waves, a further 82 waves were eliminated on the basis that `UWO_exe` produced wavelengths for them which was greater than 35 km (the upper wavelength limit which can be identified manually). A summary of the results of the 308 remaining waves from the manual and `UWO_exe` analysis methods is shown in Figure 3.17.

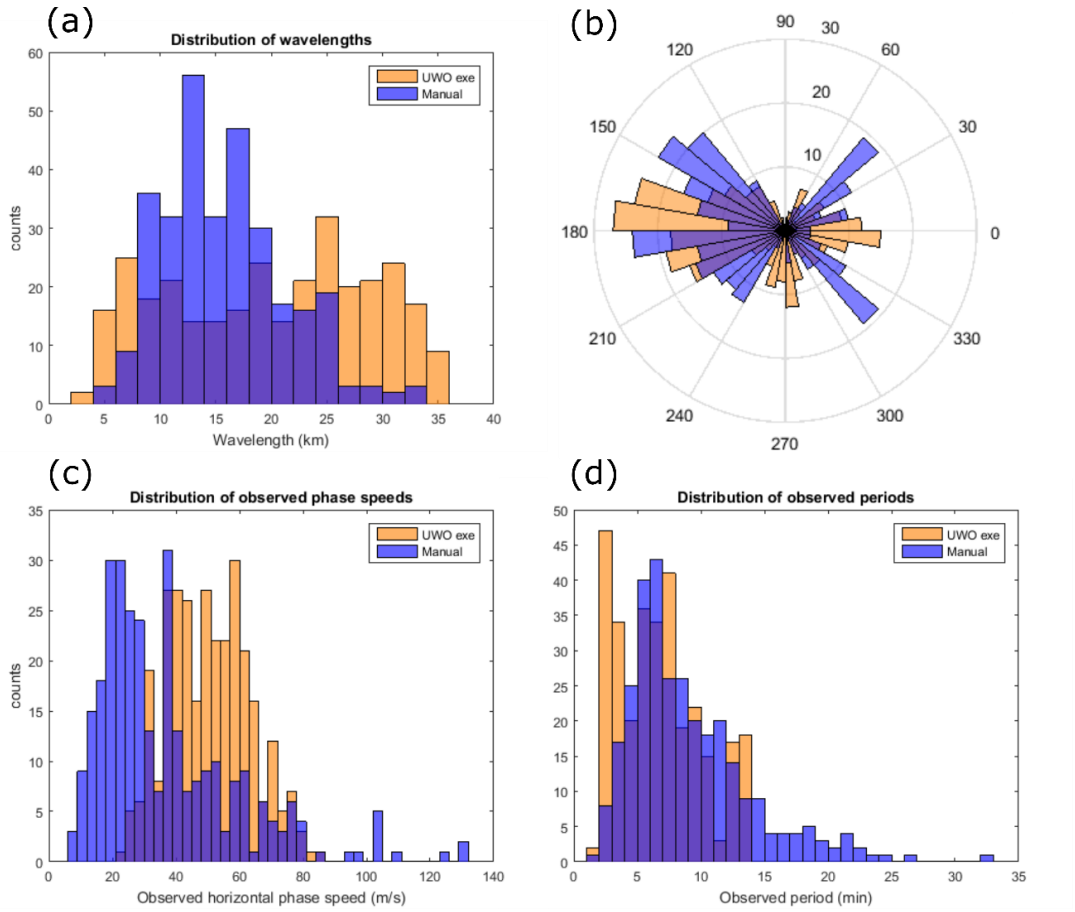

Figure 3.17: Histograms of (a) horizontal wavelength, (b) propagation direction (radial histogram), (c) observed horizontal phase speed and (d) observed period for waves observed between 1999 and 2013. Shown in blue are the waves characterised using the manual approximation, and shown in orange are the waves characterised using `UWO_exe`. Counts are the number of events in a particular bin. The manual results are shown in a transparent blue colour so that the automated results (shown in orange) are not covered up.

Some differences are observed between the manual and `UWO_exe`. It may be seen from Figure 3.17 that the `UWO_exe` analysis generally calculates higher phase speeds and slightly lower periods than that approximated manually. The higher wave speeds were also observed in section 3.1.1 when analysing some

synthetic waves, and so this may be an issue with the analysis method. The tendency toward lower periods was not observed in section 3.1.1. This may in fact be an artefact of the manual calculation, where period, T, is calculated by $T = \frac{\lambda}{v}$ since v is generally calculated as slower using the manual approximation, or it may be due to the approximate nature of the manual method. Otherwise, it may partly be attributed to the fact that the manual method operates on the raw data, not the fixed data (as it was required as an approximation only). In addition, periods greater than 16 minutes could be identified using the manual method, but could not be calculated by `UWO_exe` due to the FFT window length (of 32 frames) chosen.

To conclude this section, the results for the manual and `UWO_exe` results for a few cases are shown to demonstrate the level of agreement (or otherwise) in certain cases. These examples do not include waves which were indistinguishable by eye, since no manual results could be obtained in such cases.

Case 1: Good agreement

Analysis Method	v (m/s)	θ (°N of E)	T (min.)	λ (km)	Time (hrs UT)
Manual	48±7	-140±10	9±1	26±3	22:09
`UWO_exe`	45±10	-157±10	9.5±0.5	26±6	22:09

Table 3.2: Results for a case where there was good agreement between `UWO_exe` and the manual approximation. This case was on 7th July 2013.

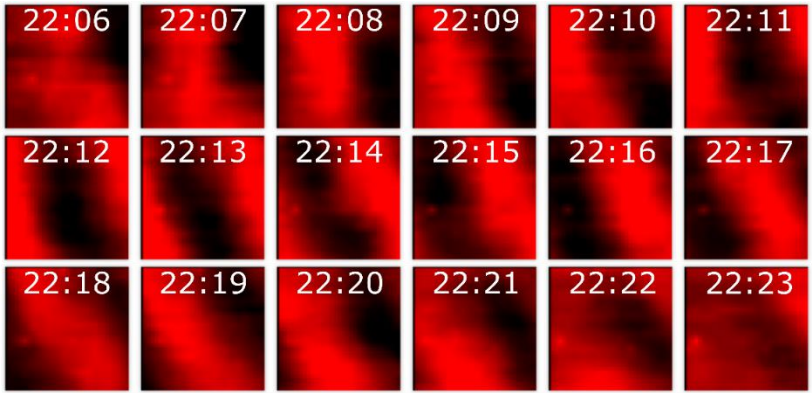

Figure 3.18: Image sequence corresponding to the wave described in Table 3.2 on 7th July 2013.

In this case, very good agreement is found between the manual approximation and the automated software. Phase speeds, periods and propagation directions are within 3 m/s, 17°, and 30 seconds (respectively) of each other. Much of the uncertainty here may come from the subjective nature of the manual analysis, where results are only as accurate as the author's best approximation of the wave crest positions.

Case 2: One peak in FOV

Analysis Method	v (m/s)	θ (°N of E)	T (min.)	λ (km)	Time (hrs UT)
Manual	78±14	38±10	N/A	N/A	14:15
UWO_exe	71±5	33±5	12.8±0.5	55±4.5	14:13

Table 3.3: Results for a case where there was only one peak within the FOV and so period and wavelength could not be estimated using the manual approximation. This case was on 3rd September 2004.

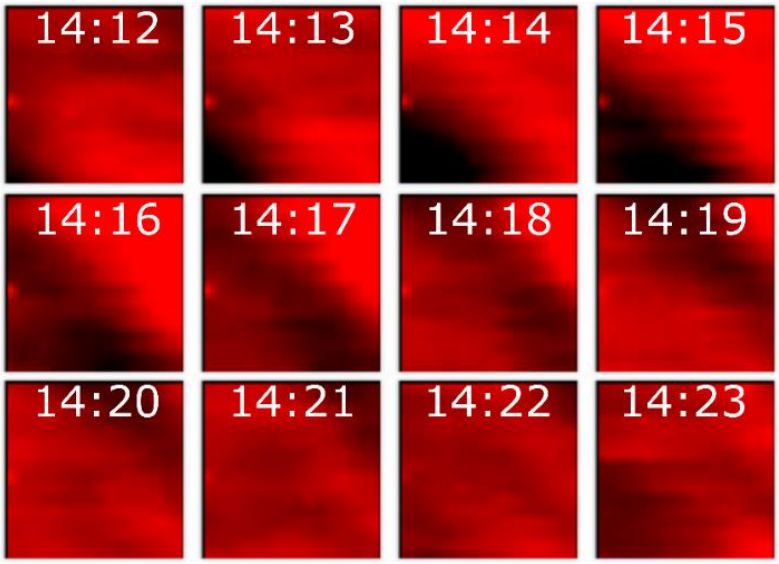

Figure 3.19: Image sequence corresponding to the wave described in Table 3.3 on 3rd September 2004.

In this case, the manual approximation could not be completed. There was only one wave crest within the FOV, and thus the wavelength could not be measured manually. It was possible, however, to compare the velocity results from the two analysis methods. Again, good agreement is observed here with differences of 7 m/s in speed and 5° in propagation direction.

Case 3: Two waves within FOV simultaneously

Analysis Method	v (m/s)	θ (°N of E)	T (min.)	λ (km)	Time (hrs UT)
Manual (1st wave)	37±11	42±10	2.3±0.8	5±1.5	16:07
Manual (2nd wave)	23±5	139±10	N/A	N/A	16:22
UWO_exe	49±10	125±10	12.2±0.5	36±7.5	16:25

Table 3.4: Results for a case where there were two waves within the FOV at the same time. This case was on 10th August 2012.

Figure 3.20: Image sequence showing two waves within the FOV at the same time on 10th August 2012.

In this final case, there were two separate waves within the FOV simultaneously. The automated analysis extracted only one wave at this time, and its characteristics do not match up with either wave. This is a good demonstration of one of the major limitations of the De Serrano and Lowe analysis method. This limitation can be easily understood by considering the method itself. The period calculation is based on the variation of the weighted mean centre of entire images, and so it cannot account for multiple waves, and the velocity calculation, which finds the maximum correlation between different pixels, can only calculate the dominant speed and direction in a given image.

3.1.3. Comparison with results from a co-located OH* imager

The final method which was used to test how robust and accurate the software is was a short comparative study between two OH* airglow imagers located at Davis Station. The two OH* airglow imagers are UWOSCR and a Utah State University (USU) all-sky camera (shown in Figure 3.21). The USU camera was

installed at Davis Station in 2012, and so there are two years of overlap (2012 and 2013) with the UWOSCR data which is analysed in this thesis. Some all-sky data was provided by Mike Taylor and Dominique Pautet from USU, for the purpose of running the De Serrano and Lowe analysis technique on the images. Images from the FOV common to both instruments have been analysed to extract information on the passage of gravity waves over the observing station for a number of test nights during 2012 and 2013. Phase speeds, periods, wavelengths, and predominant propagation directions were compared.

Figure 3.21: The Utah State University all-sky OH* airglow camera which is located at Davis Station since 2012 (*Pugmire et al.*, 2014).

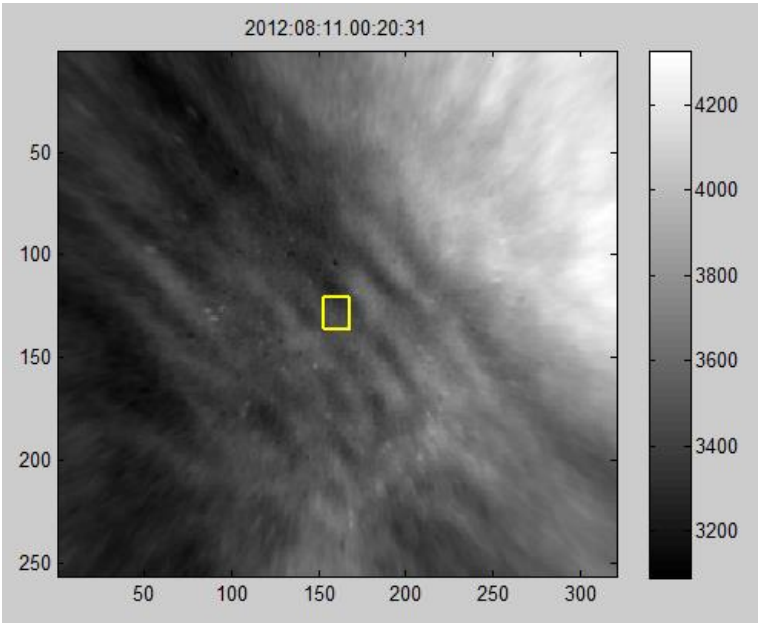

Figure 3.22: A flat-fielded, calibrated, and unwarped all-sky USU image at 00:20:31 UT on 11th August 2012 at Davis, which has been projected onto a 320×256 pixel grid, with each pixel corresponding to 1.5 km of sky at the airglow layer. The top of the image is aligned so that it corresponds to north. The yellow box shows the FOV of UWOSCR, for comparison.

The USU camera has an exposure time of 3 seconds, and it records an image (an example of which is shown in Figure 3.22) every 10 seconds (*Pugmire et al.*, 2014). It has a similar spectral response to UWOSCR as it also uses an InGaAs detector. The spectral response of InGaAs is shown in Figure 2.3, a figure which was made specifically for UWOSCR. The difference between the spectral response of the two imagers is that UWOSCR has an InGaAs detector and a silicon window (leaving it with an overall spectral response of ~1100−1650 nm), whereas the USU camera only has an InGaAs detector (giving it a spectral response of <800−1700 nm). Therefore, as shown in Figure 2.3, the instruments are most sensitive to emissions from the OH*(4−2) and OH*(3−1) bands.

For the purpose of comparison with UWOSCR, the USU images used were projected such that each pixel corresponded to 1.5 km at the airglow layer. In this way, 16×16 pixels centred on the zenith could be extracted from the USU images, to correspond to UWOSCR's FOV of 16×16 pixels, or ~24 km × 24 km. Also to be considered for the comparison was image timing. Interpolated UWOSCR images correspond to the central time of each scan, and there is a new image once every minute. On the other hand, there is a new USU image every 10 seconds. For comparison purposes, every 6th USU image (at the closest possible time to each interpolated UWOSCR image) was extracted for analysis.

A final consideration before comparing the two sets of results was interpolation. Interpolation was used in the UWOSCR analysis to account for the scanning nature of the instrument. It would be incorrect to apply the same interpolation to the USU images, since the all-sky airglow camera is in a fixed position, so that each pixel in a given image corresponds to the timestamp associated with that image. Therefore, when analysing the USU camera images, `UWO_exe` which incorporated the UWOSCR image correction technique could not be used. Instead, the LabVIEW software (based on the De Serrano and Lowe method) was used to calculate velocities and to create the input files necessary for `UWO_exe`'s period calculation code, `qveldir.exe` and `ron2.exe`. This

LabVIEW software was simply modified so that the user can choose whether to interpolate images or not and, whenever analysing USU images, it was set so that it didn't perform any interpolation.

The comparisons, related to the USU all-sky camera, which were made are as follows:

1. Manual comparisons between some UWOSCR images and the corresponding central portion of the USU images were performed to ensure both imagers were observing the same thing and to ensure the automated analysis was performing correctly.
2. The central portion of the USU images were analysed using the De Serrano and Lowe method to produce the dominant velocity and period in each frame. Two criteria (as outlined in section 2.6) were then applied to these results to decide which images contained a gravity wave. The De Serrano and Lowe method was compared with the USU analysis method for these USU image sequences.

The test nights for which the above comparisons were performed were: 03/04 April 2012, 23/24 June 2012, 10/11 August 2012, 28/29 May 2013, and 26/27 June 2013. These nights were chosen because there were GWs clearly visible in the UWOSCR and USU images, and the De Serrano and Lowe analysis software produced some results which corresponded to the same time as these GW events.

In relation to the second point above, the USU analysis results were sent by Dominique Pautet from USU and so the author was not involved in performing this analysis technique. These results provide a good overall test of the analysis method. For clarity, the USU analysis method will now be described briefly.

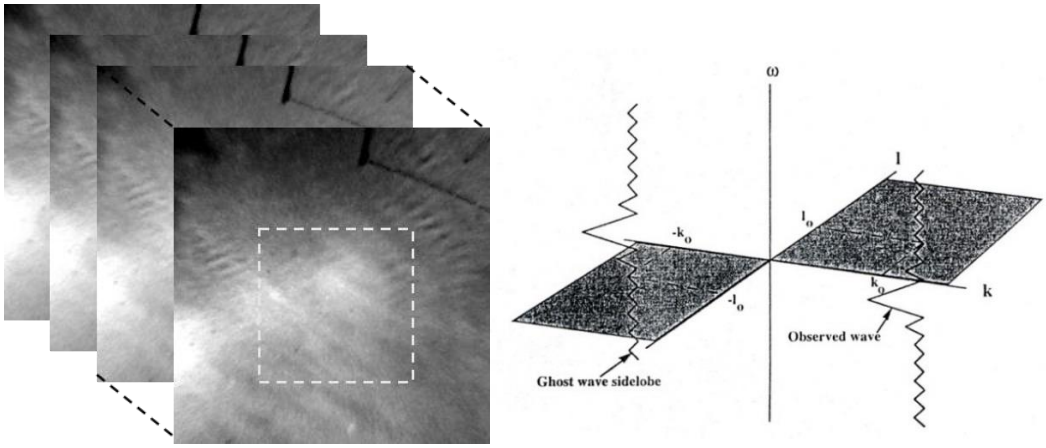

Figure 3.23: (left) A selection of the region of interest in a sequence of flat-fielded, calibrated, and unwarped images (*Pautet*, 2016). (right) Determination of the k, l spectrum (*Coble et al.*, 1998).

As shown in Figure 3.23, the region of interest in a sequence of flat-fielded, calibrated, and unwarped images is selected to perform a 3-D FFT on. The k, l spectrum is obtained by first calculating the k, l, w spectrum, and then integrating over just the negative frequencies. Due to the finite time extent of the images, 'ghost wave' side lobes of positive frequency wave components leak into the negative frequency domain, leading to ambiguities in wave direction. Ghost wave side lobes are minimized by temporal pre-whitening and windowing and by proper choice of the upper integration limit (instead of integrating over all negative frequencies) (*Coble et al.*, 1998). This leads to an unambiguous k, l spectrum, an example of which is shown in Figure 3.24.

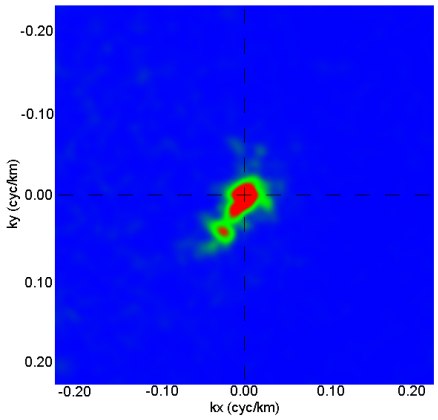

Figure 3.24: An unambiguous k, l spectrum, processed with eight images. From this spectrum the mean direction was calculated to be 211° east of north, and the mean horizontal wavelength was calculated (using the horizontal wavenumbers k and l) to be 21.9 km (*Pautet*, 2016).

3.1.3.1. Manual comparison between UWOSCR and USU images

Figures 3.25-3.29 show manual comparisons between UWOSCR and USU images for particular GW events. On the left of these images are actual UWOSCR sequences whereas on the right, the central 16×16 pixels of every 6th USU image is seen. Dashed lines are drawn onto the images in the approximate locations of the wave crests as a guide to the eye. Using the manual approximation method outlined in section 2.5.1, approximate values for phase speed, v, propagation direction, θ, period, T, and wavelength, λ_h, were calculated for each image sequence.

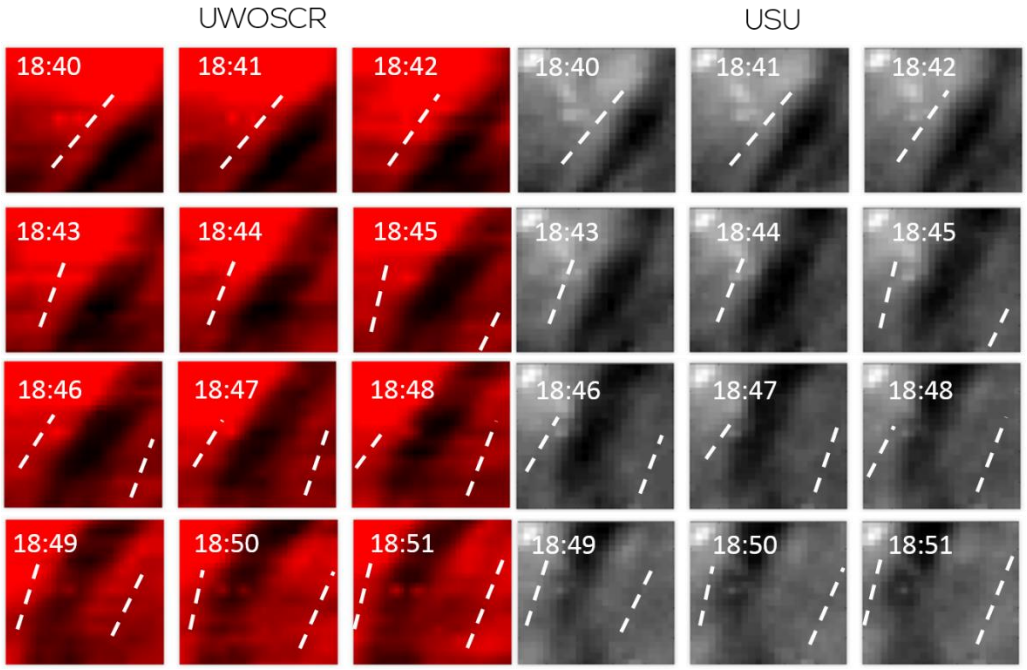

Figure 3.25: Manual comparison of (left) UWOSCR and (right) USU images for a particular GW event on 3 April 2012.

From Figure 3.25, very good agreement is observed between both imagers. In fact, both sequences of images appear identical in both timing and intensity patterns, leading to identical manual approximation results for both. The approximate wave parameters calculated were $v = 20$ m/s, $T = 14.3$ minutes, $\lambda_h = 17.2$ km, and $\theta = -60°$ east of north. It would be expected that an automated analysis of both sets of images shown here should lead to identical results.

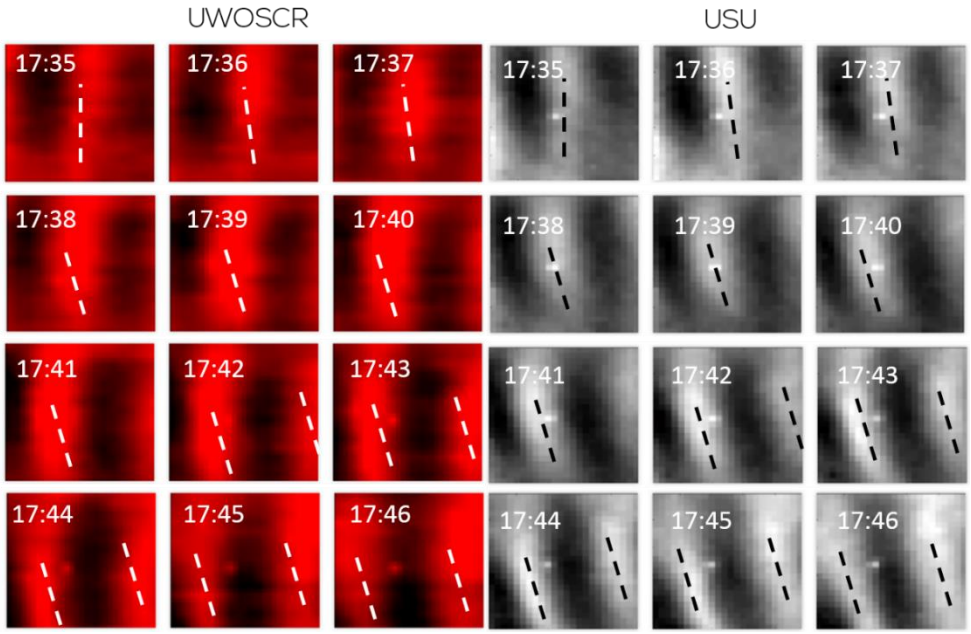

Figure 3.26: Manual comparison of (left) UWOSCR and (right) USU images for a particular GW event on 23 June 2012.

Again, from Figure 3.26, images from both instruments appear identical. Approximate values for wave parameters in this case were v =14.1 m/s, T =16.3 minutes, λ_h =13.8 km, and $\theta = -105^\circ$ east of north.

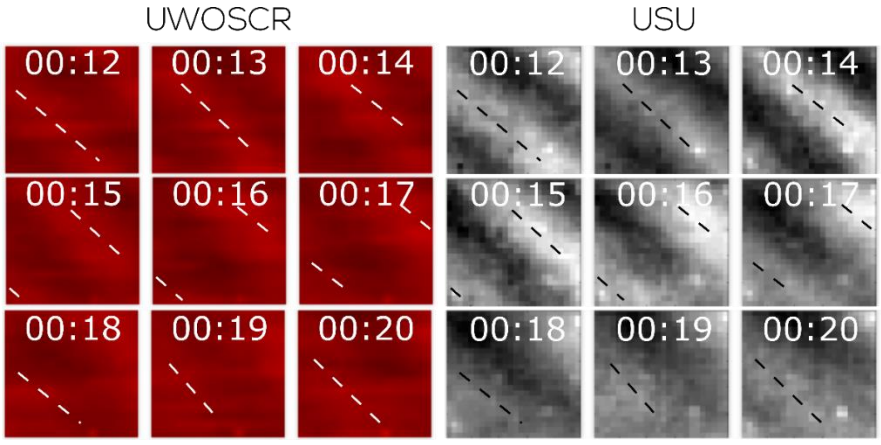

Figure 3.27: Manual comparison of (left) UWOSCR and (right) USU images for a particular GW event on 11 August 2012.

From Figure 3.27, it may be seen that the wave crest positions for both imagers are the same. Approximate values for wave parameters were v =50.8 m/s, T =6 minutes, λ_h =18.3 km, and θ =45° east of north.

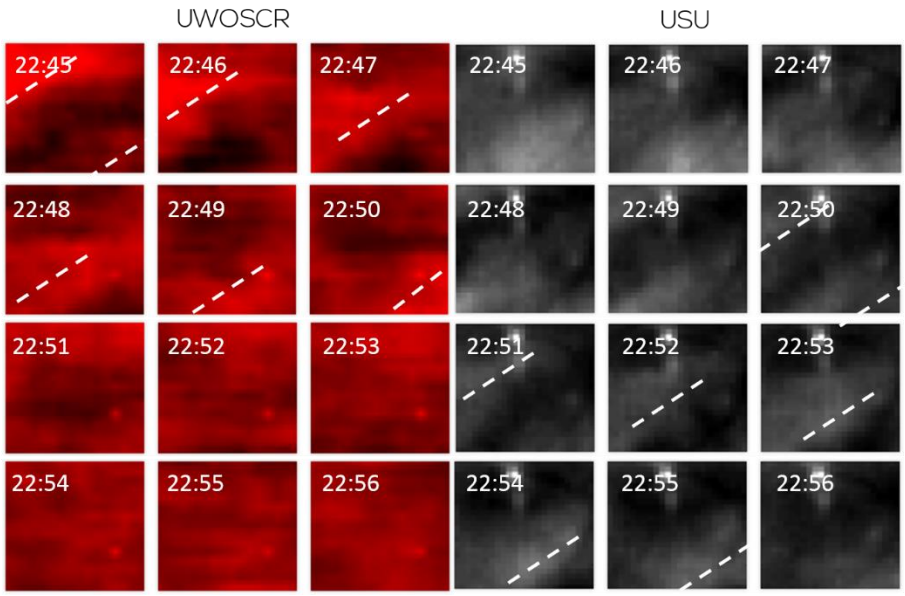

Figure 3.28: Manual comparison of (left) UWOSCR and (right) USU images for a particular GW event on 28 May 2013.

From Figure 3.28, approximate values for wave parameters were v =56.8 m/s, T =18.2 minutes, λ_h =28 km, and θ =147° east of north. Unfortunately, in this case, the instruments were not synchronised, resulting in a time difference of ~5 minutes. Following discussion with Dominique Pautet (who provided the USU images), it was concluded that the clock of one or other instrument had deviated from the actual time on this particular night.

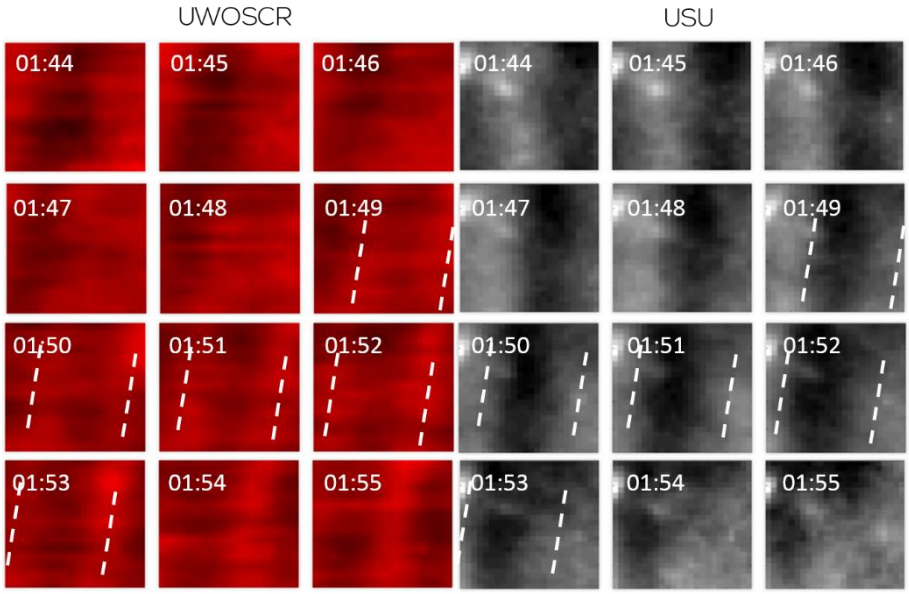

Figure 3.29: Manual comparison of (left) UWOSCR and (right) USU images for a particular GW event on 27 June 2013.

From Figure 3.29, good agreement between the two sets of images is observed, and approximate values for wave parameters were v =28.3 m/s, T =9.1 minutes, λ_h =15.4 km, and $\theta = -80°$ east of north.

From the manual comparisons, it was found that both instruments appear to detect the same OH* fluctuations (as expected), although sometimes to different degrees of intensity. Both instruments observe the same portion (both spatially and spectrally) of the OH* airglow layer. This is a reassuring result for UWOSCR's instrumentation. It follows that the results from the De Serrano and Lowe method on both sets of images should match. This will now be tested for the same cases as above.

3.1.3.2. Software Tests of the De Serrano and Lowe Method

This subsection will show some comparisons between the De Serrano and Lowe method, the manual approximation, and the USU analysis method for the same set of gravity waves as shown in the previous subsection. Ideally, all of these analysis methods should agree.

Figures 3.30-3.35 show comparisons between results calculated using the De Serrano and Lowe method (*a.k.a.* the 'UWOSCR analysis method' in these images), the manual approximation method, and the USU analysis method. Results from the USU analysis method for these test events were provided by Dominique Pautet. The solid black line in these figures indicates the $y = x$ line. All points should lie on this line if the methods agree with each other.

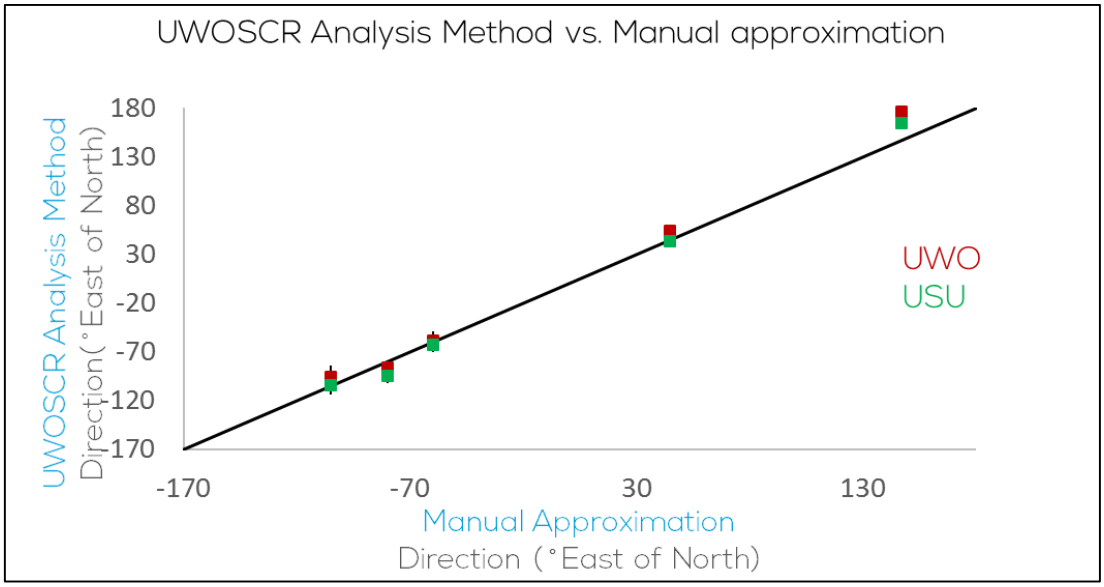

Figure 3.30: A comparison between the propagation directions calculated using the UWOSCR analysis method and those calculated using the manual approximation method for both UWOSCR and USU images during all of the test events.

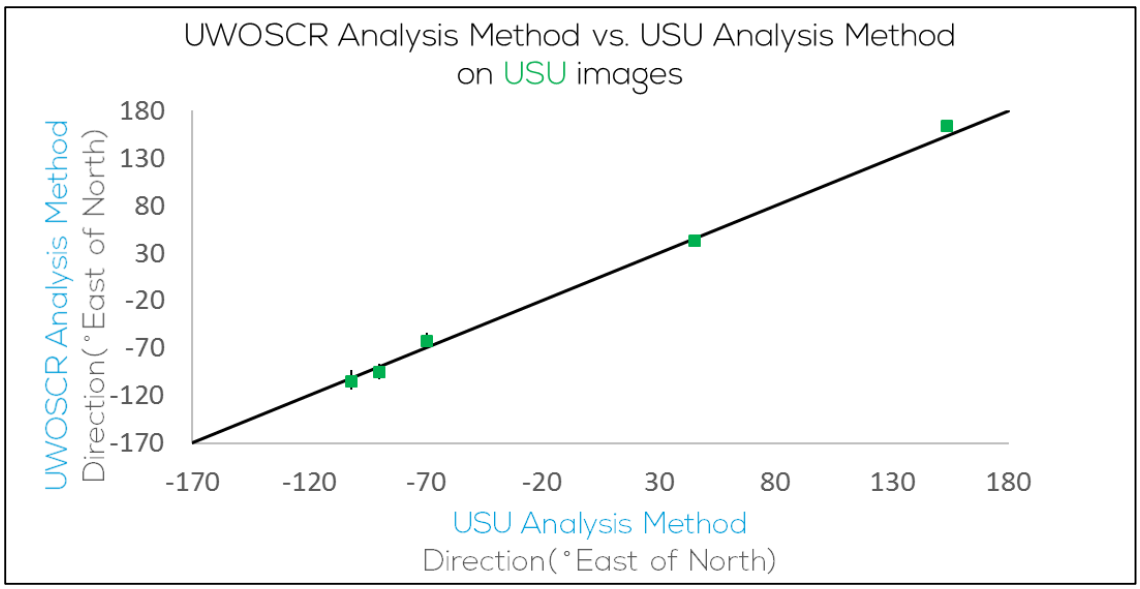

Figure 3.31: A comparison between the directions calculated using the UWOSCR analysis method and those calculated using the USU analysis method for USU images during all of the test events.

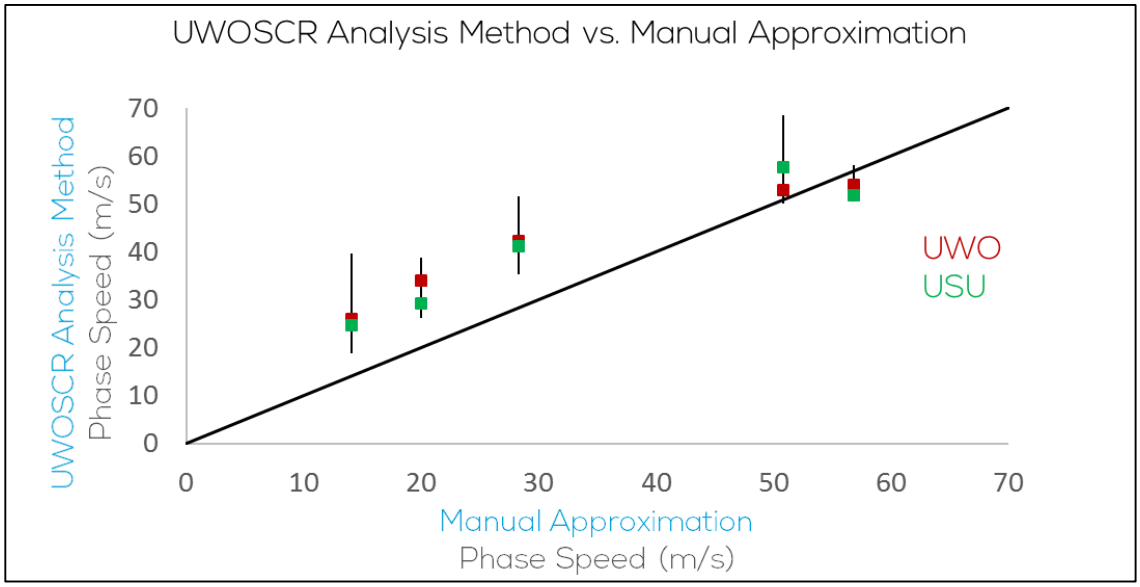

Figure 3.32: A comparison between the phase speeds calculated using the UWOSCR analysis method and those calculated using the manual approximation method for both UWOSCR and USU images during all of the test events.

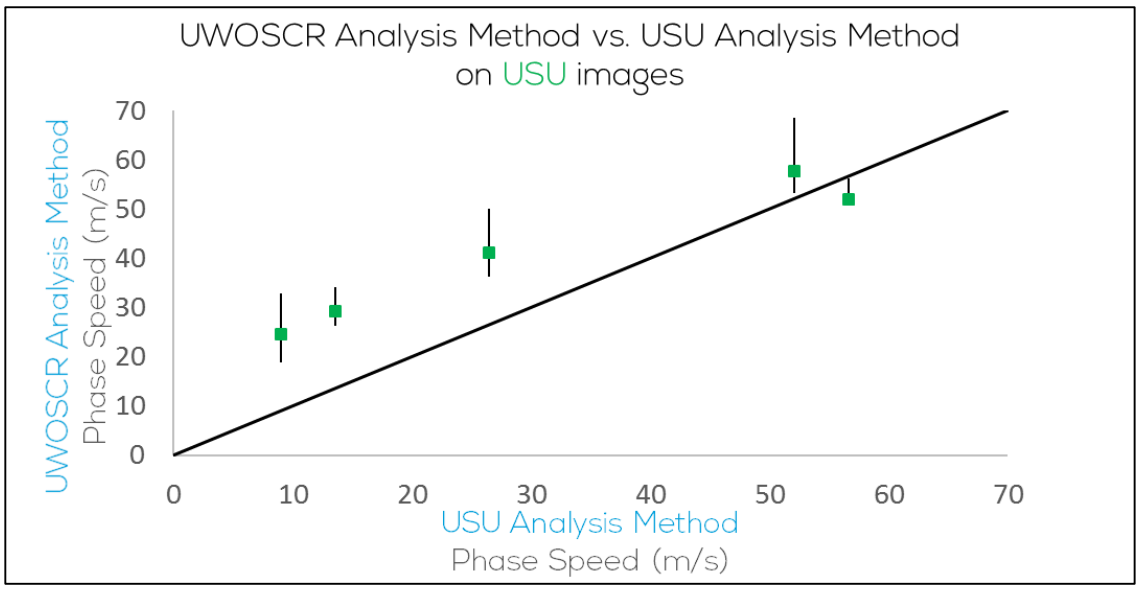

Figure 3.33: A comparison between the phase speeds calculated using the UWOSCR analysis method and those calculated using the USU analysis method for USU images during all of the test events.

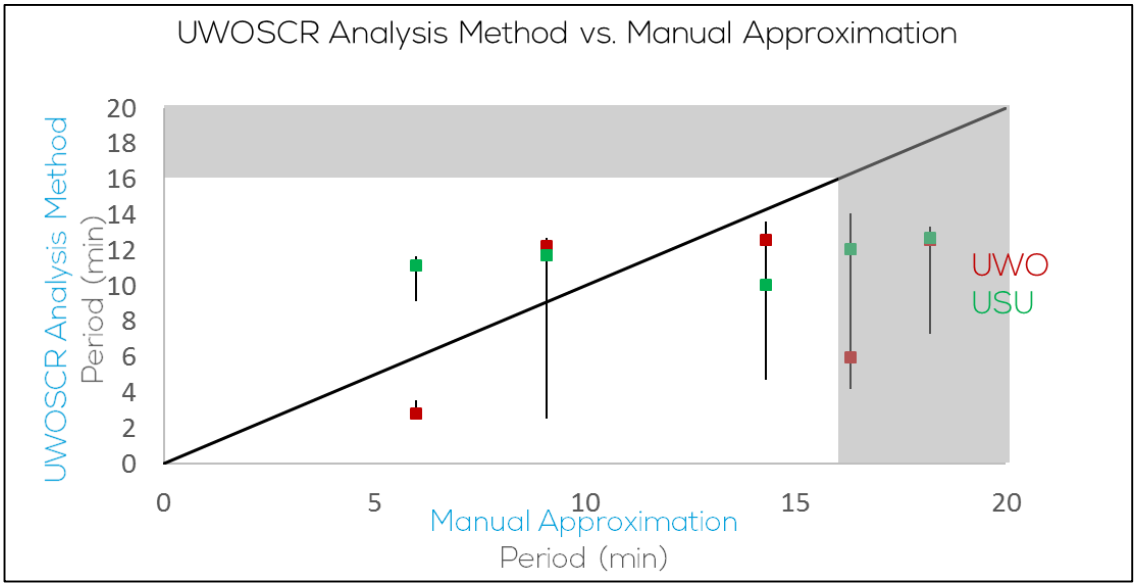

Figure 3.34: A comparison between the periods calculated using the UWOSCR analysis method and those calculated using the manual approximation method for both UWOSCR and USU images during all of the test events. The shaded region indicates where the period has exceeded 16 minutes, and hence the De Serrano and Lowe method cannot determine periods in this range.

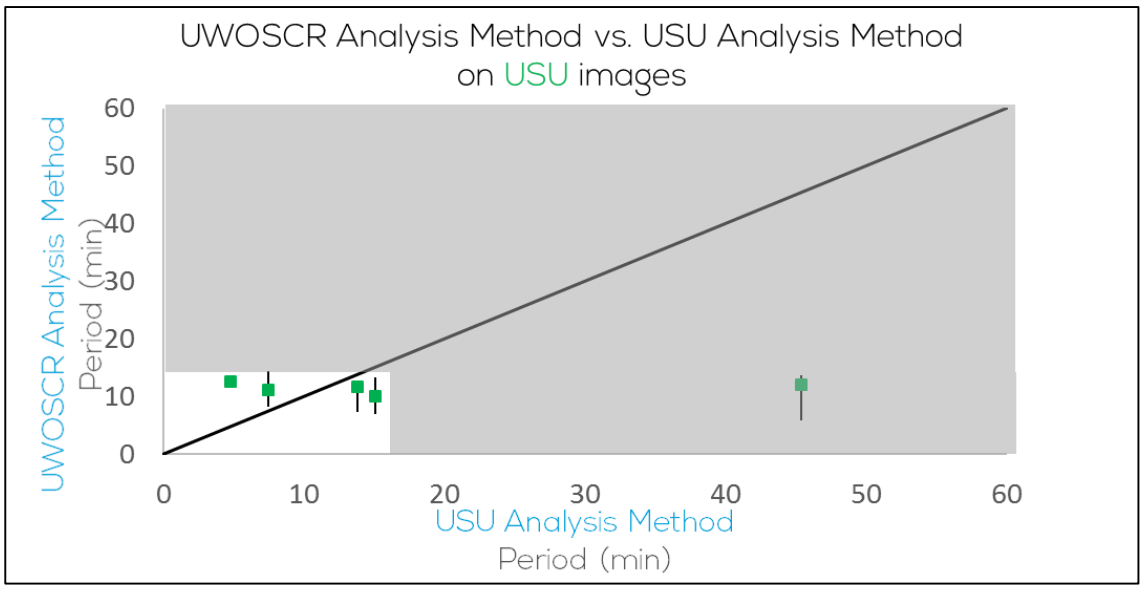

Figure 3.35: A comparison between the periods calculated using the UWOSCR analysis method and those calculated using the USU analysis method for USU images during all of the test events. The shaded region indicates where the period has exceeded 16 minutes, and hence the De Serrano and Lowe method cannot determine periods in this range.

Overall, this short comparative study has proved useful for software testing, and it has provided some insight into the accuracy and robustness of the De Serrano and Lowe method. It has also provided some reassurance that the GW propagation directions calculated by the software are correct, but it has

uncovered some underlying problems with the phase speed and period calculations. Wavelengths are simply a result of the phase speed and period and so need not be shown.

It must be concluded from this comparative study that, in the future, the De Serrano and Lowe method needs further refinement, and this is currently being investigated. The offset in phase speeds seen in Figure 3.32 and Figure 3.33 needs to be corrected. Since this offset is seen especially for lower phase speeds, this may be a problem with the window length choice. Possible reasons for the large uncertainties in period may be that the weighted centre method puts too much confidence in one number, or that the window length for the FFT needs to be varied. A possible replacement for the weighted centre method is a combination of 256 FFTs, the M-transform method (*Matsuda et al.*, 2014) or something similar to the S-transform. The M-transform (available as IDL code), which was designed to perform phase velocity spectral analysis on all-sky images, is currently being investigated for use on the UWOSCR images. The LabVIEW software does allow for a variation in window length for both the cross-correlation and the FFT parts of the analysis, but a method in which the window length adapts to a particular wave has not yet been established, and seems like the next logical step in terms of software improvement.

3.1.4. Initial LabVIEW program tests

In this section, some results obtained from `UWO_exe` are compared with the corresponding results obtained from the LabVIEW program (which is based on the same method). Results from synthetic waves are shown first in Figure 3.36 and Figure 3.37, followed by a couple of individual cases in Error! Reference source not found.. Finally, this section will end with a list of some extensions to the De Serrano and Lowe method which have been implemented using LabVIEW.

Synthetic results for waves with periods of less than 6 minutes were not shown because, although the LabVIEW software calculates their periods accurate to within a few seconds, it does not provide a good estimate of wave velocity for these particular waves. This LabVIEW velocity calculation software, which agrees with the C++ code shown in Appendix C, does not agree exactly with `UWO_exe`. `UWO_exe` calculates low-period velocities more accurately for reasons which are currently not known, and which will need to be investigated further in the future.

Periods calculated using the LabVIEW program are possible at values of FFT window length divided by an integer such that periods of 32 minutes, 16 minutes, 10.7 minutes, 8 minutes, 6.4 minutes, 5.3 minutes, 4.6 minutes, 4 minutes, *etc.* are possible. In `UWO_exe`, the peak of the frequency spectrum was found so that periods could be estimated at 1-minute intervals. This has not yet been done with the LabVIEW software, and so large period steps are observed for waves with longer periods.

Table 3.2 and Table 3.3, which compared `UWO_exe` with manual results for some individual cases, may now be extended as follows in Error! Reference source not found.. Good agreement is found between all three sets of results, especially for the wave observed on 7th July 2013.

Analysis Method	v (m/s)	θ (°N of E)	T (min.)	λ (km)	Date (dd/mm/yy)	Time (hours UT)
Manual	48±7	-140±10	9±1	26±3	07/07/13	22:09
`UWO_exe`	45±10	-157±10	9.5±0.5	26±6	07/07/13	22:09
LabVIEW	43±11	-158±33	10.7±5	27±5	07/07/13	22:09
Manual	78±14	38±10	N/A	N/A	03/09/04	14:15
`UWO_exe`	71±5	33±5	12.8±0.5	55±4.5	03/09/04	14:13
LabVIEW	68±5	55.5±2	16±0.5	63±3	03/09/04	14:13

Table 3.5: An extended version of Table 3.2 and Table 3.3, now including LabVIEW results.

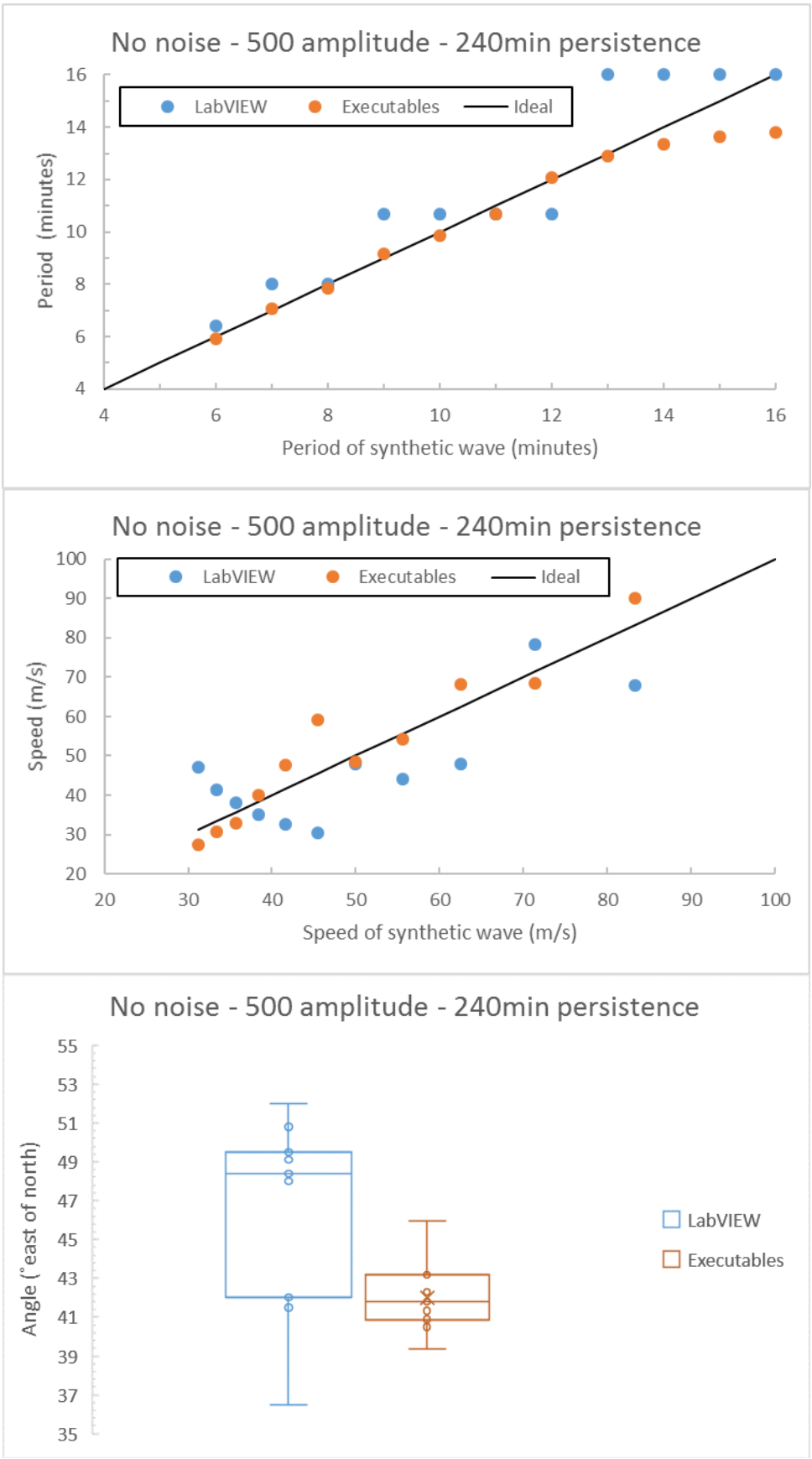

Figure 3.36: Results for synthetic waves in set 1 in section 3.1.1 with periods between 6 and 16 minutes.

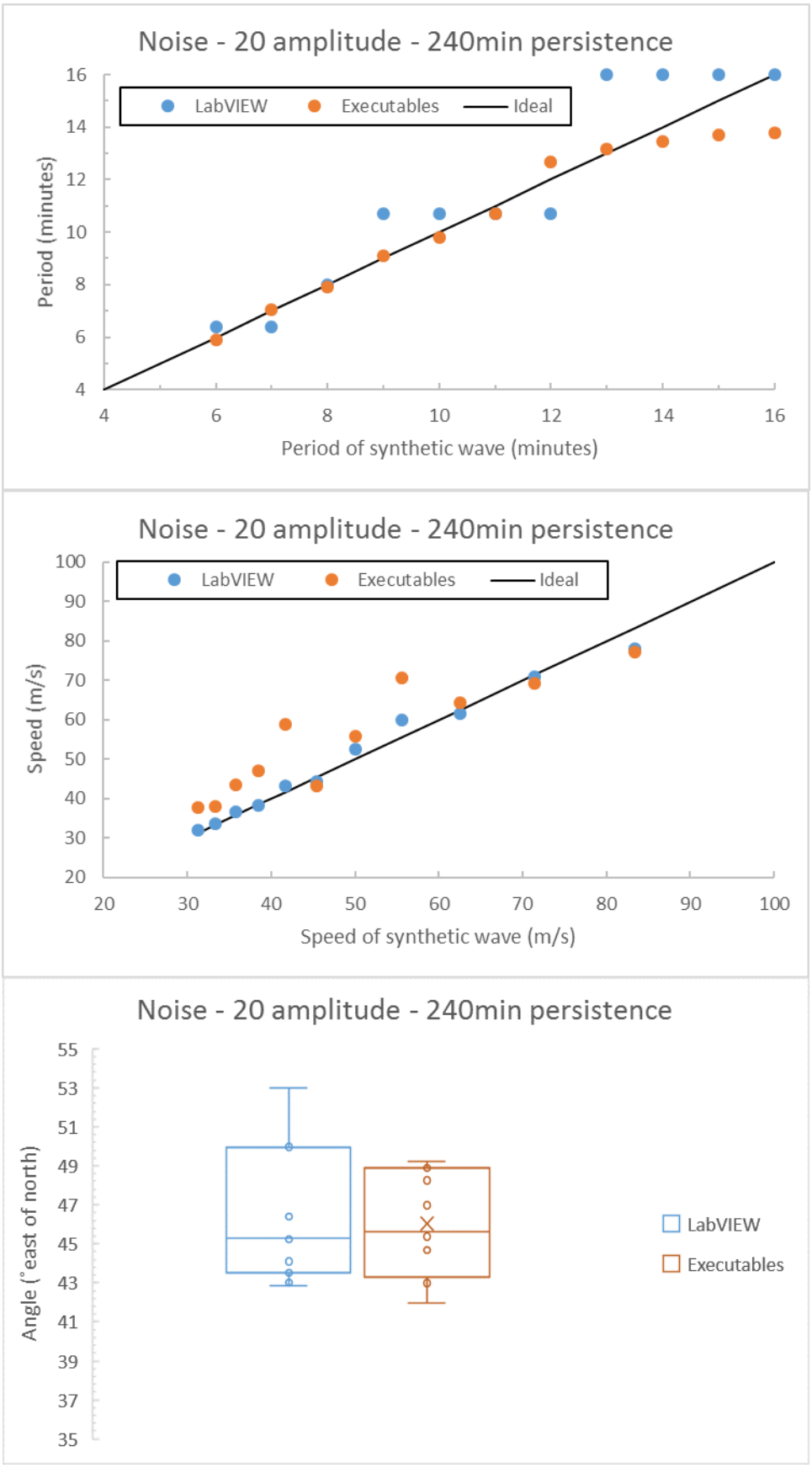

Figure 3.37: Best results for synthetic waves in set 2 in section 3.1.1 with periods between 6 and 16 minutes.

3.1.4.1. Extensions to the De Serrano and Lowe analysis method

The LabVIEW program is designed to perform the De Serrano and Lowe analysis method followed by post-processing to reject any times where no GWs are present. This program can be used exactly as required for UWOSCR, but it is also adaptable to sequences of images from other instruments as follows:

1. Images with any time spacing may be analysed, as long as the time spacing between each image is constant.
2. Interpolation is optional so that images which have been taken from a non-scanning instrument may be analysed.
3. The size of the image may be changed along with the distance between pixels at the airglow layer.

In addition to its instrument adaptability, the program has several other new user-defined options as follows:

1. The window length for both the cross-correlation and FFT sections of the analysis may be varied.
2. Stars can be removed from images if desired. This works by replacing each pixel in an image by the average of four of its surrounding pixels (above, below, to the left, and to the right).
3. The post-processing limits for standard deviation of velocity and for minimum GW persistence may be varied.
4. There is an option to perform the FFT analysis using a number of different window lengths and to then only accept periods that are consistent using each window length.

3.2. Climatological Results of Gravity Waves and Ripples during the period 1999-2013

The 15-year climatology of GWs and ripples presented here is split into a number of subsections. The distributions of different wave characteristics are first examined, before comparing them with results at other Antarctic stations,

studying their variation with time, and finally testing the effect of the variation of the post-processing velocity standard deviation threshold (L).

Before presenting the climatological results, it is important, for the purpose of compilation of statistics (*e.g.* for climate models) to consider what is meant by one GW observation count (*Love* and *Murphy*, 2016). Traditionally in GW studies (*e.g. Nielsen et al.* (2009); *Bageston et al.* (2009); *Matsuda et al.* (2014)), one GW observation count means any single wave event, which may persist for any length of time. The results presented in this thesis are in line with this traditional method, unless otherwise specified. Another method for counting, which was used while performing preliminary work on this chapter, was counting each minute for which a wave is detected as one count. These results are not shown as they produce almost identical trends to those shown here. This particular method has some advantages when comparing with climate models, but cannot be easily used as input to the ray-tracing program (which will be discussed in Chapter 4). Finally, in some cases in this chapter, count will be normalised to observing time in a particular month, year or hour, but it will be explicitly stated whenever this is the case.

3.2.1. GW distributions for the entire observational period

Distributions of GW propagation directions, phase speeds, periods and wavelengths are presented in this section. Since the UWOSCR instrument is sensitive to very small-scale structures, a climatology of ripples could also be performed in order to partially address some questions related to ripples outlined in section 1.6.4 (*i.e.* their persistency, intermittency and period).

In this section, wave characteristics are presented in both their ground-based (observed) and intrinsic forms. Intrinsic wave characteristics were determined using coincident background wind measurements at 86 km altitude which were available from a medium-frequency (MF) radar located at Davis Station. These wind observations (which are documented by *Murphy* and *Vincent* (2000)) were

hourly-averaged and were available at 10-minute intervals such that the wind at the closest possible time to each wave observation could be used. The conversion itself is given by $c_i = c_{obs} - u_h$, where c_i is the intrinsic phase speed, c_{obs} is the observed phase speed, and u_h is the background wind speed in the direction of phase propagation (*Nielsen et al.*, 2009). Intrinsic period, τ_i, may then be calculated as $\tau_i = \frac{\lambda_h}{c_i}$ (*Lu et al.*, 2009).

Propagation directions are shown in Figure 3.38 in both their observed and intrinsic forms, and the seasonal variation of observed propagation directions is shown Figure 3.39. From Figure 3.38 (left), one may see that observed GWs at Davis Station usually travel directly southward, eastward or westward. The majority of ripples travel westward, with a substantial amount also travelling southward. It is also interesting to note from Figure 3.38 (right) that the pronounced Cartesian directions do not exist to the same extent for the intrinsic form of GW and ripple propagation directions. Nevertheless, the distinct lack of northward propagating waves exists for both the observed and intrinsic forms. From Figure 3.39, it can be seen that most GWs occur toward the beginning and end of the (epoch) winter season, with peak activity during April, May and August. It may also be seen that most ripples occur between February and June with very few ripples observed in the latter half of the year. The reason for this is currently unknown.

All other distributions of wave characteristics which have been determined are shown in Figure 3.41. Plot (a) in this figure illustrates that two quite distinct distributions for horizontal wavelength were observed – one for GWs ($\lambda_h \geq 15$ km) and one for ripples ($\lambda_h < 15$ km). From this histogram, it may be seen that peak horizontal wavelength for GWs was ~24−26 km whereas peak wavelength for ripples was ~8−10 km. Plot (b) shows the distribution of persistence, and was cut-off at 70 minutes for clarity, as very few waves exceeded this value. The majority of waves persisted for ~6−8 minutes. Plots (c) and (e) show

observed and intrinsic phase speeds, respectively. It was found that observed phase speeds of GWs (∼50−80 m/s) are generally slightly faster than observed ripple phase speeds (∼40−60 m/s). It was also noted that the distribution of intrinsic phase speeds for GWs and ripples were very similar, and were both non-zero meaning that they both would propagate independently of background wind. Ripples were, however, partially advected by the background wind since their observed and intrinsic distributions were shifted significantly (by ∼10−20 m/s) with respect to each other. Plots (d) and (f) show observed and intrinsic periods, respectively. It may be clearly seen here that observed ripple period is generally ∼2−3 minutes (reminiscent of remnant turbulent structures) and the observed GW period is greater than the Brunt-Väisälä period (∼5 minutes).

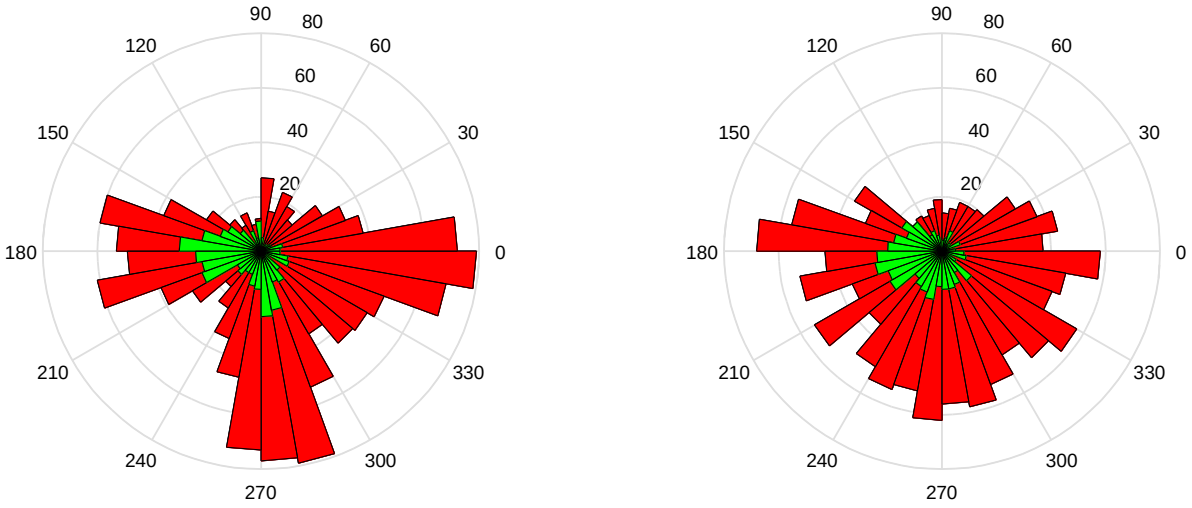

Figure 3.38: Radial histograms of (left) observed and (right) intrinsic GW propagation directions during the period 1999-2013 at Davis Station. Ripples (λ_h <15 km) are shown in green and band-type GWs (λ_h ≥15 km) are shown in red. This figure was published by *Rourke et al.* (2017).

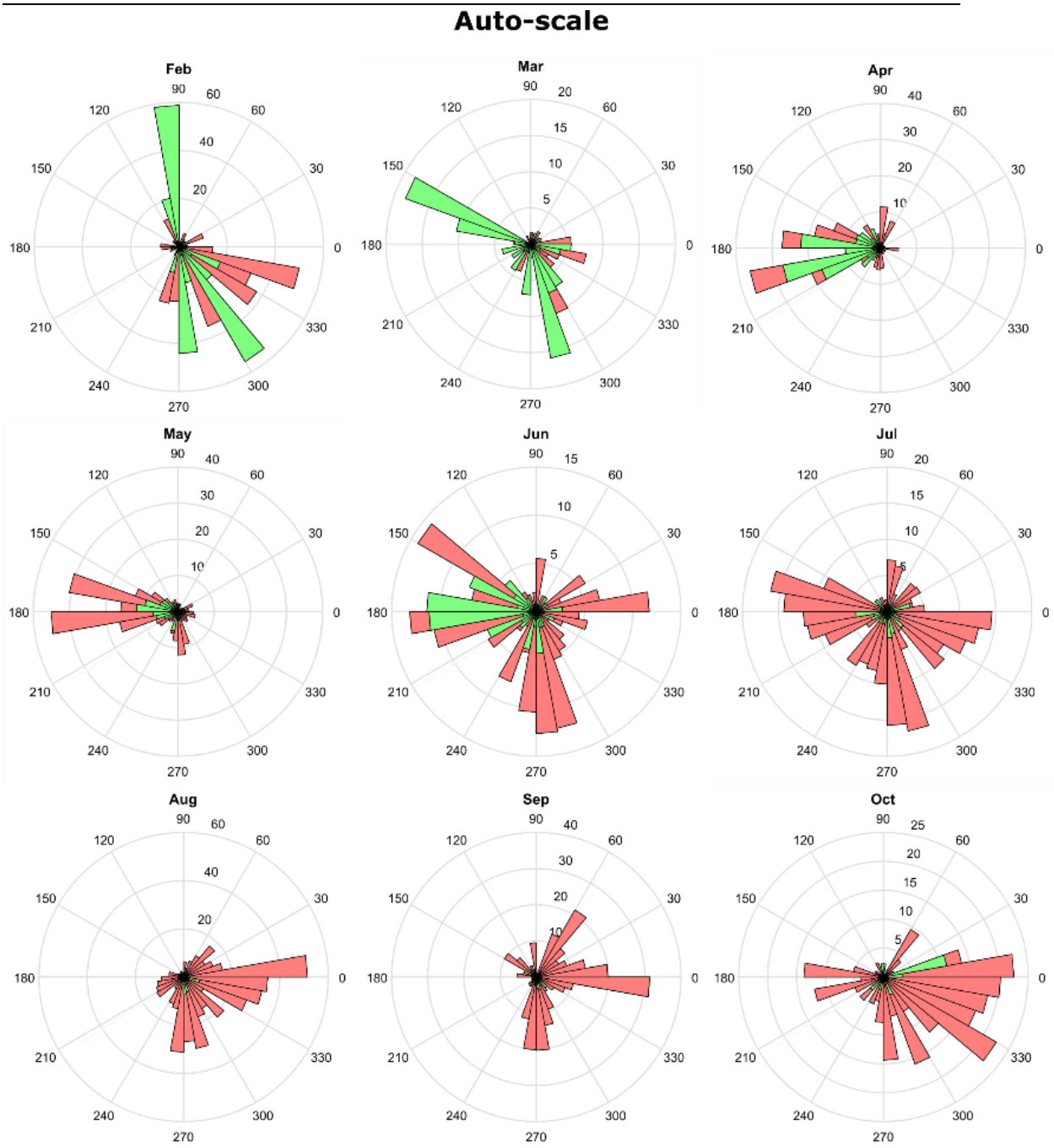

Figure 3.39: Distribution of observed GW (red) and ripple (green) propagation directions, organised by month. Counts are given as the time in which wave events were detected as a percentage of the total observing time in that particular month, scaled up by a factor of 500. Distributions are presented with an autoscaled radial axis. To give a sense of these numbers, the total number of minutes for which waves were detected in August (all years) was 3584. A version of this figure was published by *Rourke et al.* (2017).

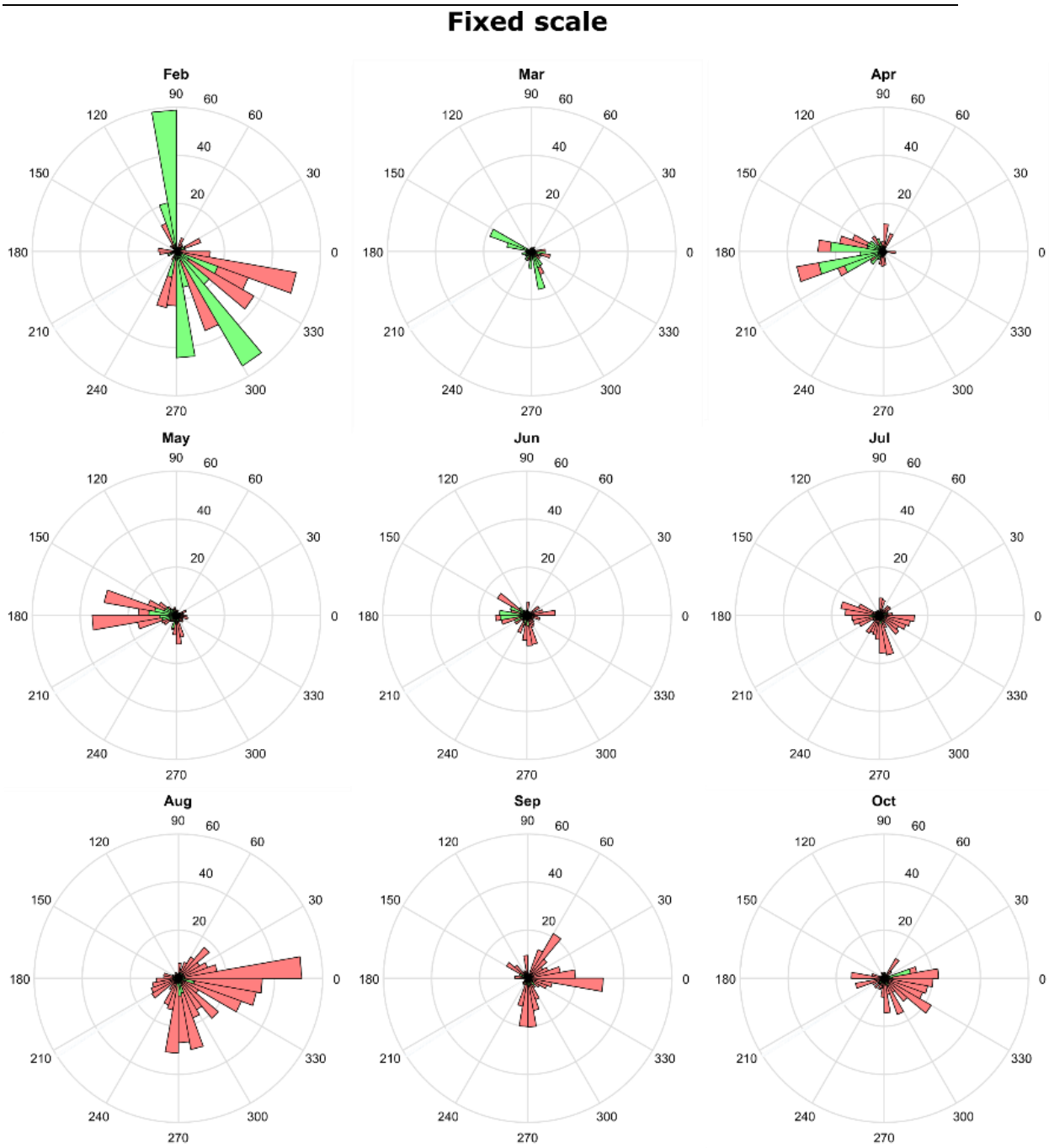

Figure 3.40: As in Figure 3.39, but with a fixed maximum count of 60% on the radial axis.

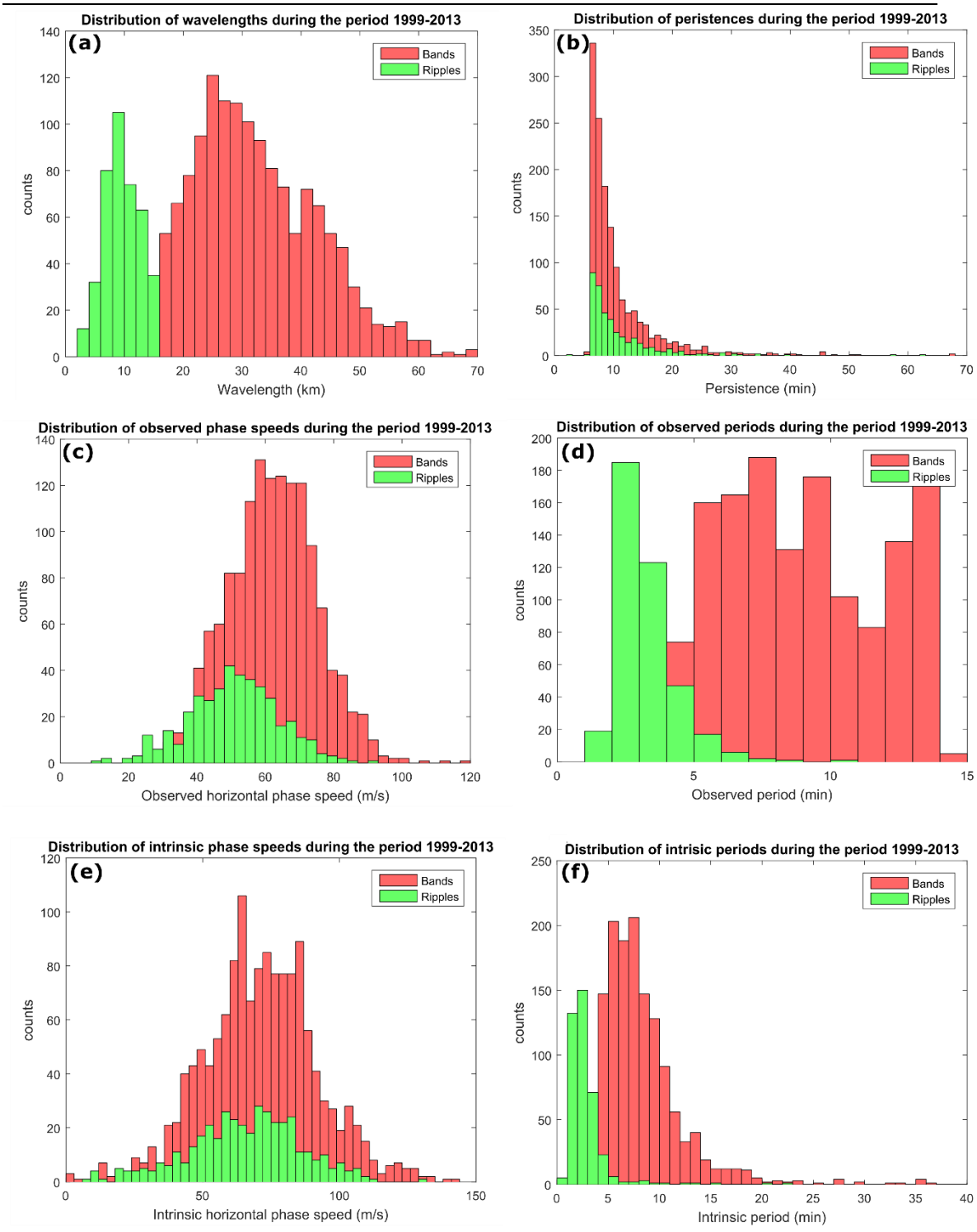

Figure 3.41: Histograms of (a) horizontal wavelength, (b) persistence, (c) observed horizontal phase speeds, (d) observed periods, (e) intrinsic horizontal phase speeds, and (f) intrinsic periods for all GWs and ripples observed between 1999 and 2013. This figure was published by *Rourke et al.* (2017).

3.2.2. Comparisons with other Antarctic observations

Some comparisons between the climatological results at Davis Station were made with other Antarctic Stations during specific time periods. Comparisons were made (in Figures 3.42-3.43) with results from two Antarctic stations: the British station, Halley and the Brazilian station, Commandante Ferraz (see map in Figure 2.1 for their exact locations). These comparisons demonstrate that UWOSCR observations are in general agreement with observations at other locations, whilst also demonstrating the variability of wave activity around the Antarctic continent using different measurement techniques.

It may be seen from Figures 3.42-3.43 that UWOSCR is much more sensitive to ripples than the Halley results observed by *Nielsen et al.* (2009) and the Commandante Ferraz results observed by *Bageston et al.* (2009), and hence the extension to lower wavelengths and periods for the Davis results. The period comparisons shown in the bottom of both of these figures demonstrate the limitations resulting from the chosen FFT window length, as the period observations at Davis Station cannot be extended beyond 16 minutes. Finally, although the peaks between datasets vary, the general range of wave characteristics observed are similar and it is reassuring that relatively consistent results are observed near the mesopause at different Antarctic stations.

A more general comparison of wave characteristics between various locations is shown in Figure 3.44. All sets of results are in general agreement. Additionally, a trend of $\lambda_h\,(\mathrm{km}) \approx 2.5T\,(\mathrm{min.})^{1.05}$ which was observed for GWs observed in Brazil (*Taylor et al.*, 2009) appears to hold true for various locations, including Davis Station, where the same trend is now extended to even shorter periods.

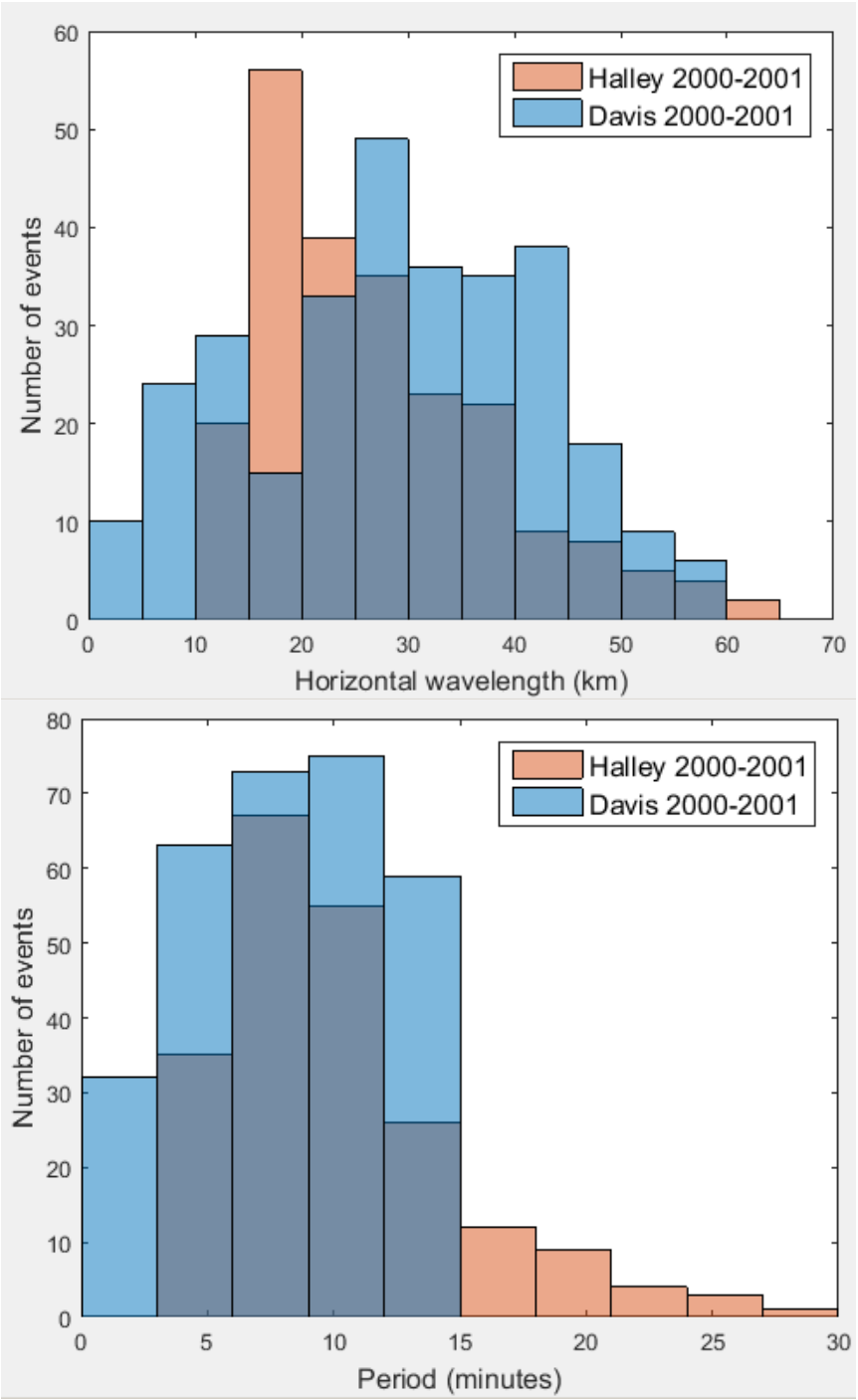

Figure 3.42: Histograms of (top) horizontal wavelength and (bottom) period during the period 2000/2001 at (blue) Davis Station from UWOSCR and (red) Halley Station from an all-sky airglow imager (*Nielsen et al.*, 2009).

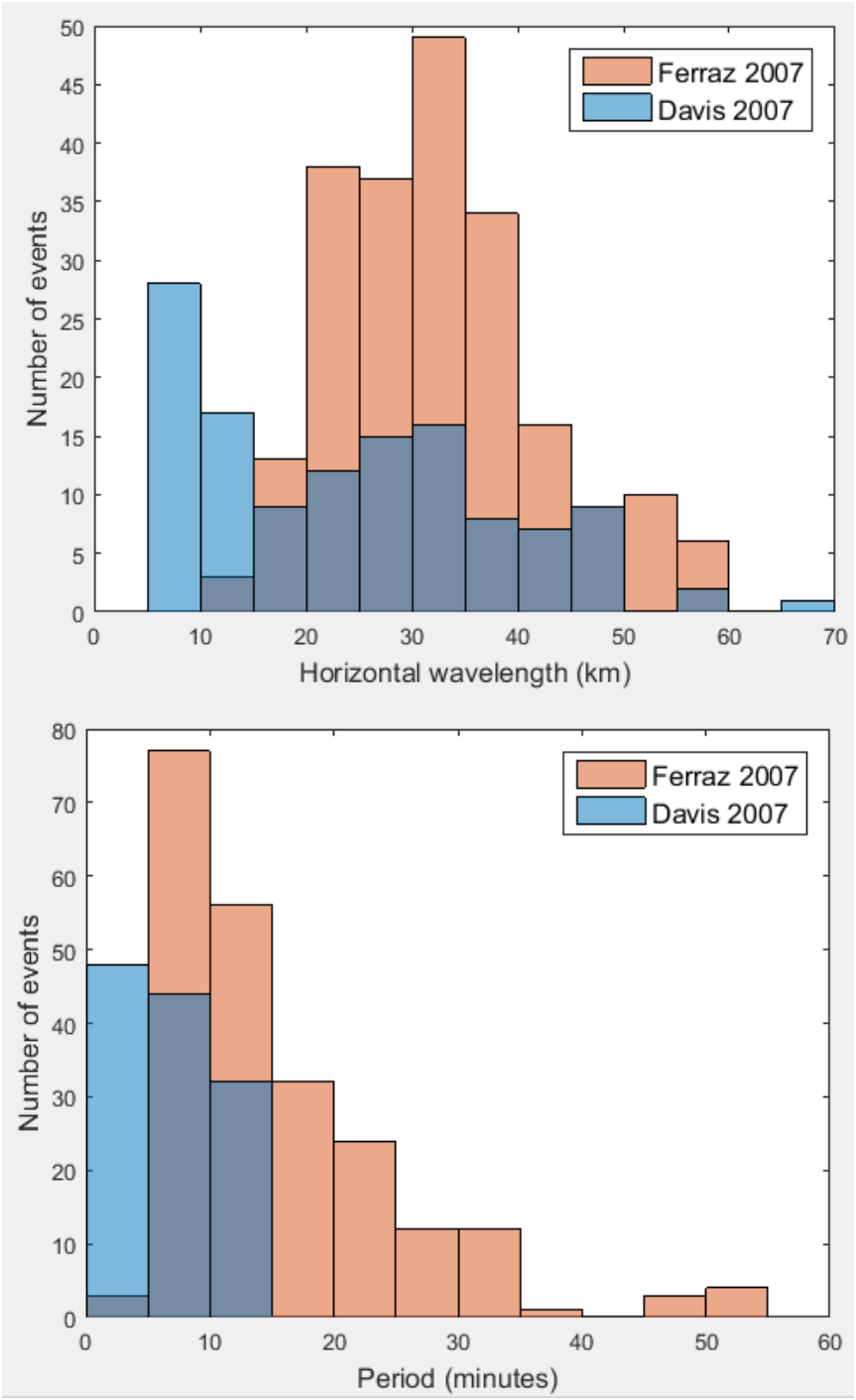

Figure 3.43: Histograms of (top) horizontal wavelength and (bottom) observed period during 2007 at (blue) Davis Station from UWOSCR and (red) Commandante Ferraz Station from an all-sky airglow imager (*Bageston et al.*, 2009).

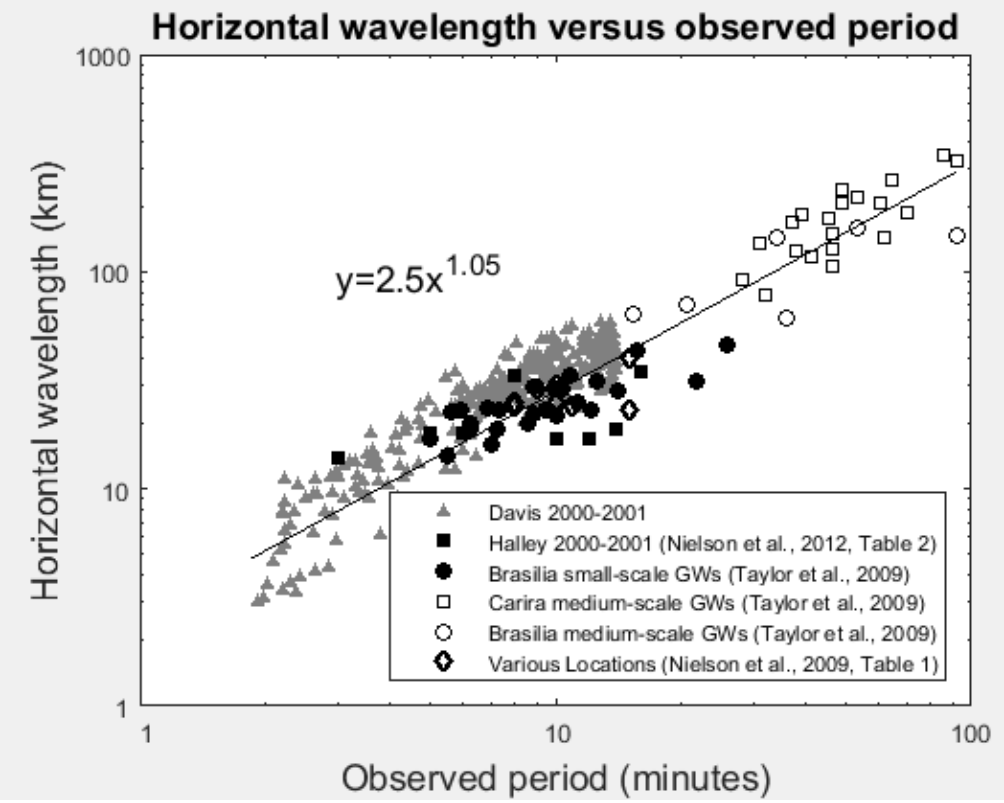

Figure 3.44: Comparison of the relationship between horizontal wavelength and observed period of a subset (2000-2001) of Davis data with Brazil data, Halley data, and other data adapted from *Taylor et al.* (2009, Figure 8), *Nielsen et al.* (2012, Table 2), and *Nielsen et al.* (2009, Table 1), respectively. This figure was published by *Rourke et al.* (2017).

3.2.3. Time series of GW trends and characteristics

In this section, the variation of GW characteristics with time is investigated. Figures 3.45-3.49 show the variation of observed phase speed, period, horizontal wavelength, wave persistence and propagation direction, respectively, by year (from 1999-2013). The interquartile range for speed, period, wavelength and persistence is shown for each year. Each of the parameters are compared to corresponding results from Halley Station during the period 2000-2001 (except wave persistence and propagation direction as these could not be retrieved from *Nielsen et al.* (2009)) and good agreement is found in each case. Very little variation in wave characteristics is observed inter-annually, and so there does not appear to be an obvious inter-annual trend among the Davis results.

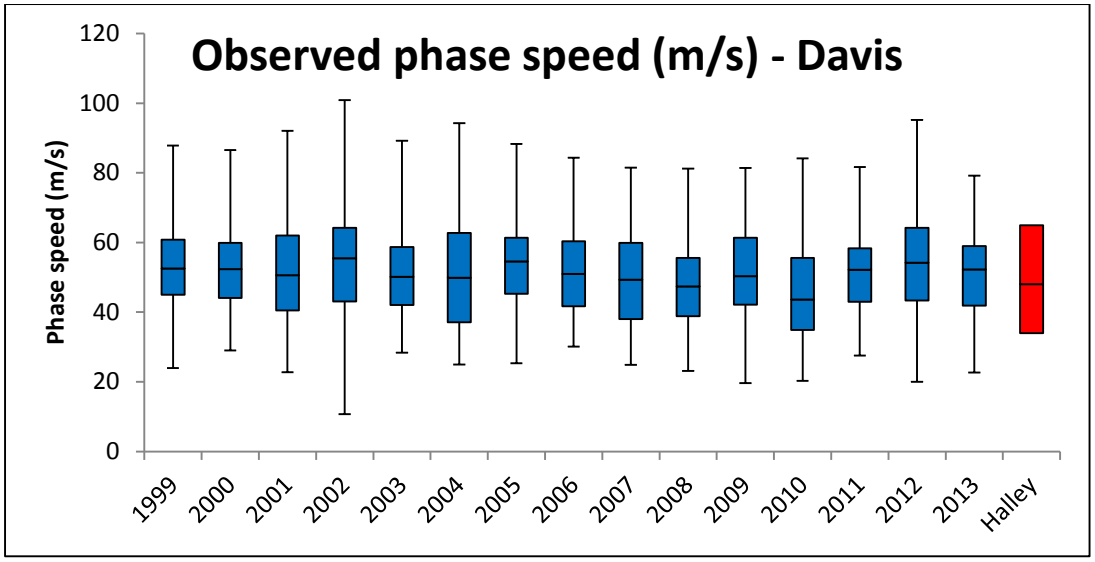

Figure 3.45: The observed phase speed for all GWs observed at Davis during the period 1999-2013. In red, the observed phase speed for GWs during the period 2000/2001 at Halley Station, Antarctica is shown.

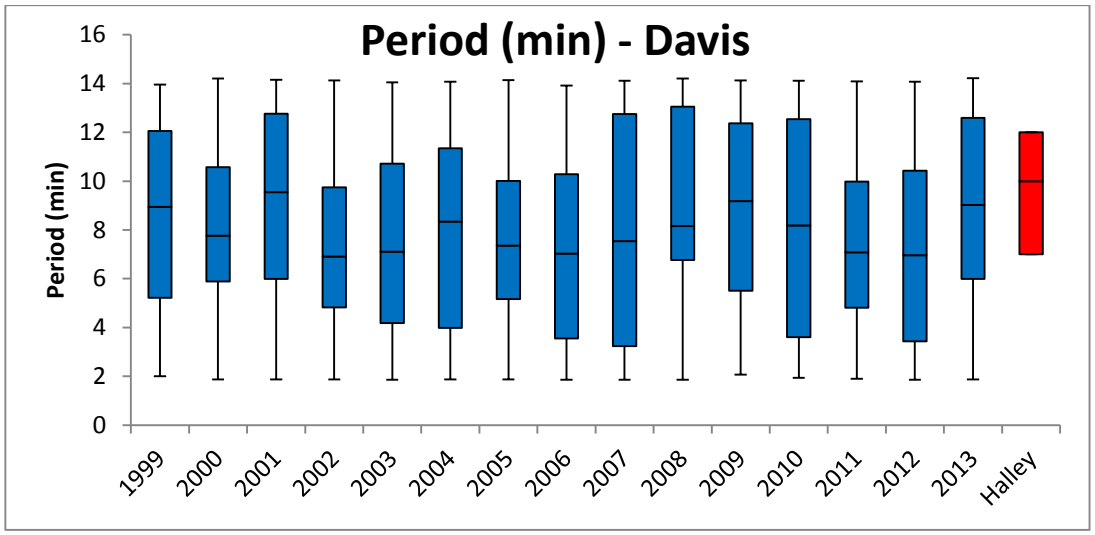

Figure 3.46: The observed period for all GWs observed at Davis during the period 1999-2013. In red, the observed period for GWs at Halley during the period 2000/2001 is shown.

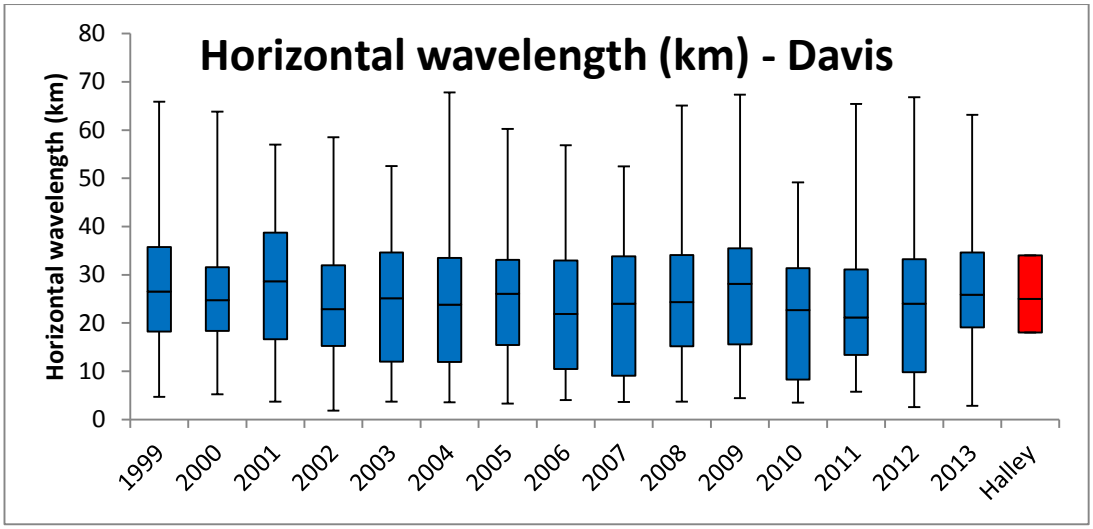

Figure 3.47: The observed horizontal wavelength for all GWs observed at Davis during the period 1999-2013. In red, the observed horizontal wavelength for GWs at Halley during the period 2000/2001 is shown.

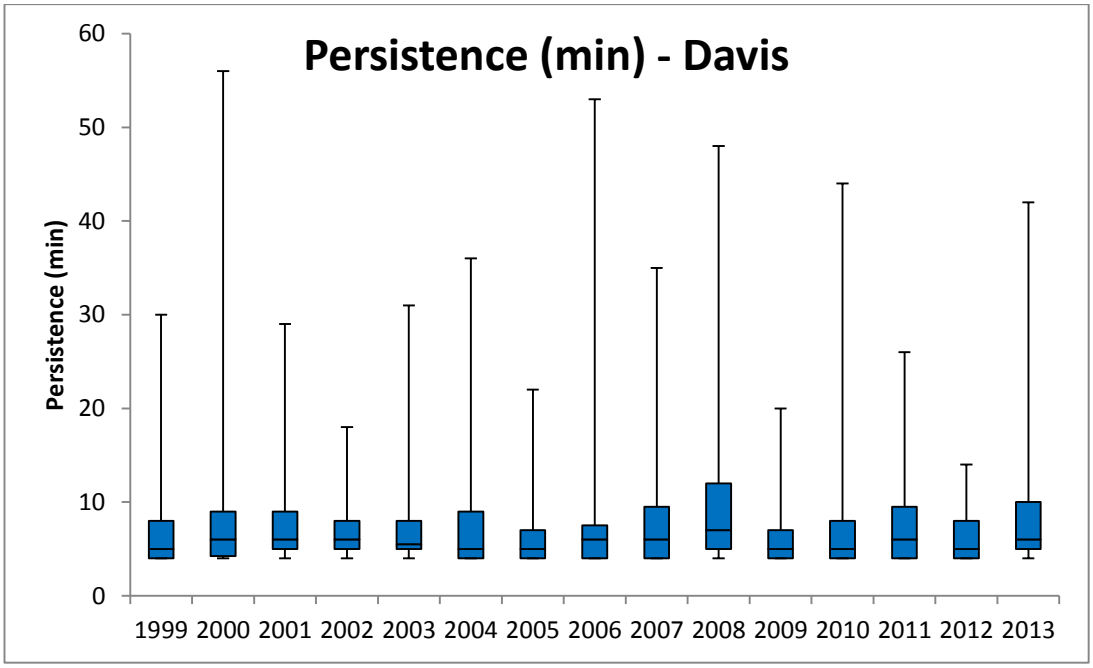

Figure 3.48: The persistence of GWs observed at Davis during the period 1999-2013.

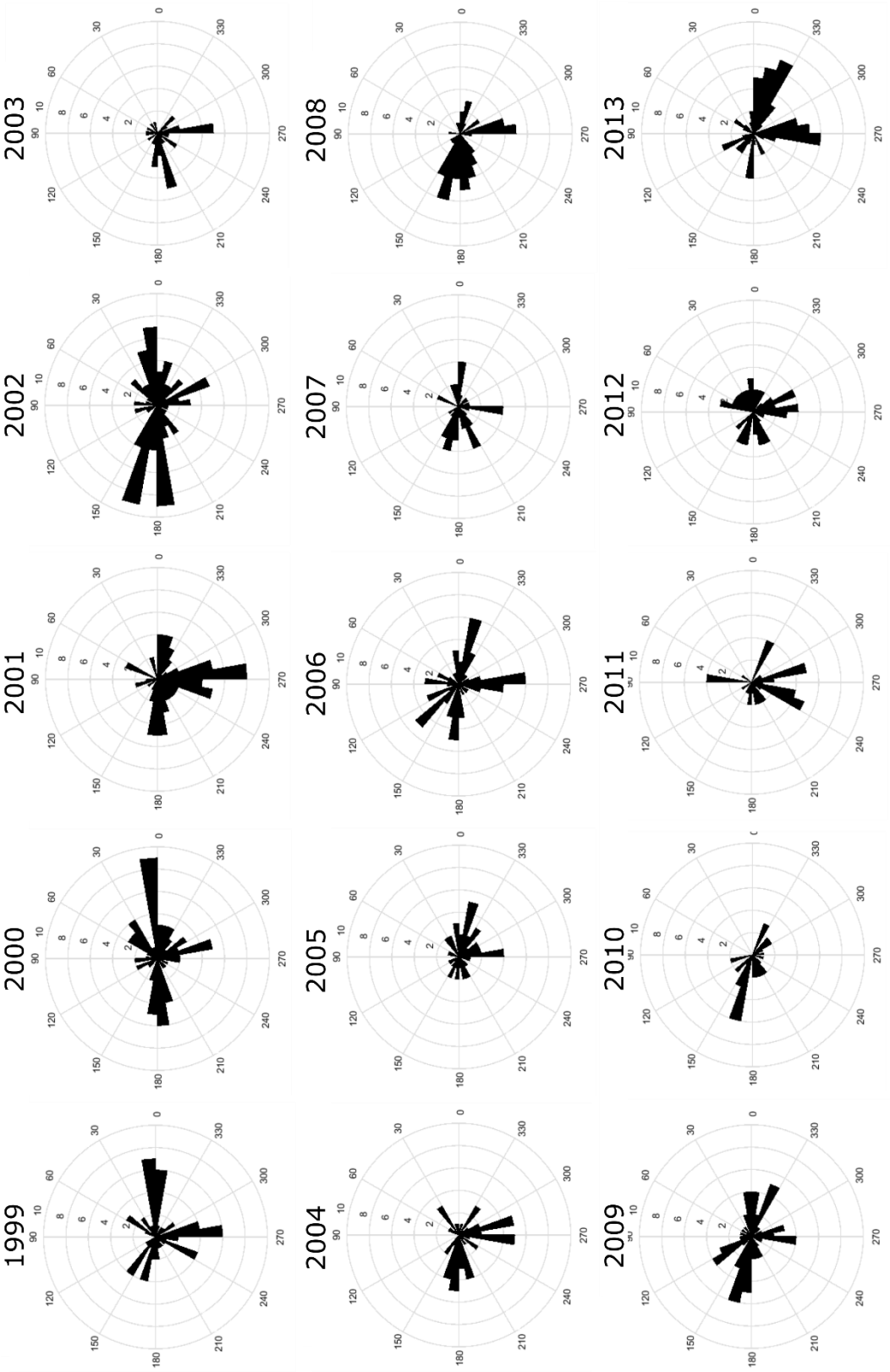

Figure 3.49: The observed propagation directions for all GWs observed at Davis during the period 1999-2013.

The variation of wave activity observed at Davis is summarised in Figure 3.50. The actual wave count for each time period is shown in blue, whereas the counts shown in black have been normalised by the observing time in a particular year, month or hour of the day, in order to remove false trends due to observing time.

Finally, the GW observations were compared to the WACCM (Whole Atmosphere Community Climate Model) GW source spectrum (*Garcia et al.*, 2007) parameterisation for Davis Station, shown in Figure 1.23 on page 45. WACCM's spectrum (corresponding to non-orographic sources in the troposphere) shows a clear seasonal variation in wave velocity, with lower GW phase speeds during mid-winter. This trend is not observed in the UWOSCR (mesopause) results, where wave speed generally remains between ~30 and 80 m/s all year round. Although these phase speeds cannot be directly compared due to the altitude difference, this may be a demonstration of the well-known (*e.g. Choi* and *Chun* (2013)*; Garcia et al.* (2017)) discrepancy between current global climate model GW parameterisations and reality. *Garcia et al.* (2017) have made some progress on the modification of the WACCM orographic source function (not yet implemented), but the non-orographic source spectrum (shown in Figure 1.23) may still require further improvements (*e.g. Ern et al.* (2017)). The climatological results presented in this thesis may form part of the observational requirement for such improvements.

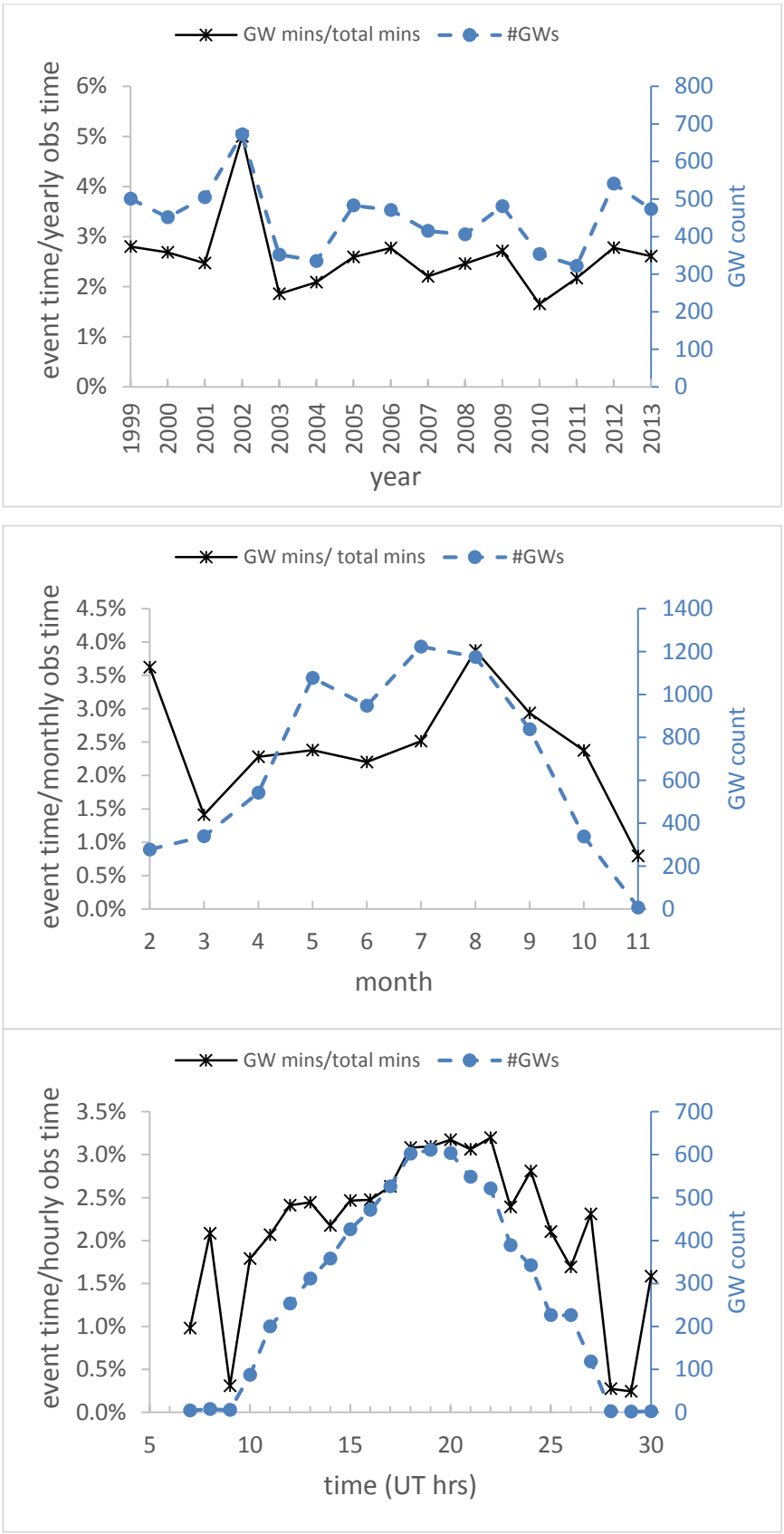

Figure 3.50: Gravity wave event time by month, year, and hour. Counts in black are normalised by (top) yearly, (middle) monthly, or (bottom) hourly observing time. Counts is blue are the number of actual wave events.

3.2.4. Variation of the post-processing standard deviation limit

The effect of the variation of the standard deviation limit set out in the post-processing criteria is now examined by presenting the climatological results for limits of L=5 m/s, 10 m/s and 15 m/s. Results using the 7 m/s limit are already presented above. As observed below in Figures 3.51-3.54, there is no major effect on the general trends, but there is a difference in the number of waves accepted using each limit.

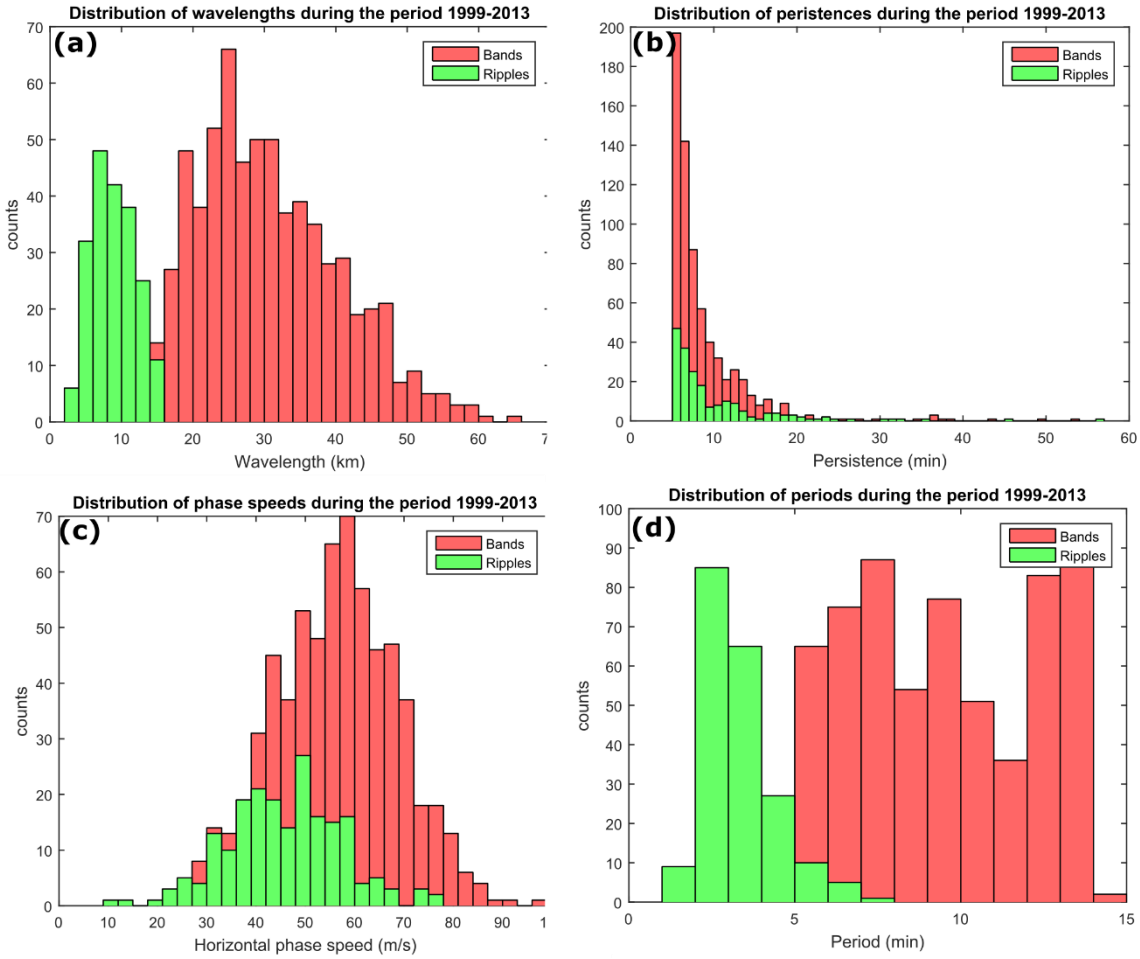

Figure 3.51: Histograms of (a) horizontal wavelength, (b) persistence, (c) observed horizontal phase speeds, and (d) observed periods for all GWs and ripples observed between 1999 and 2013 using the L=5 m/s post-processing limit.

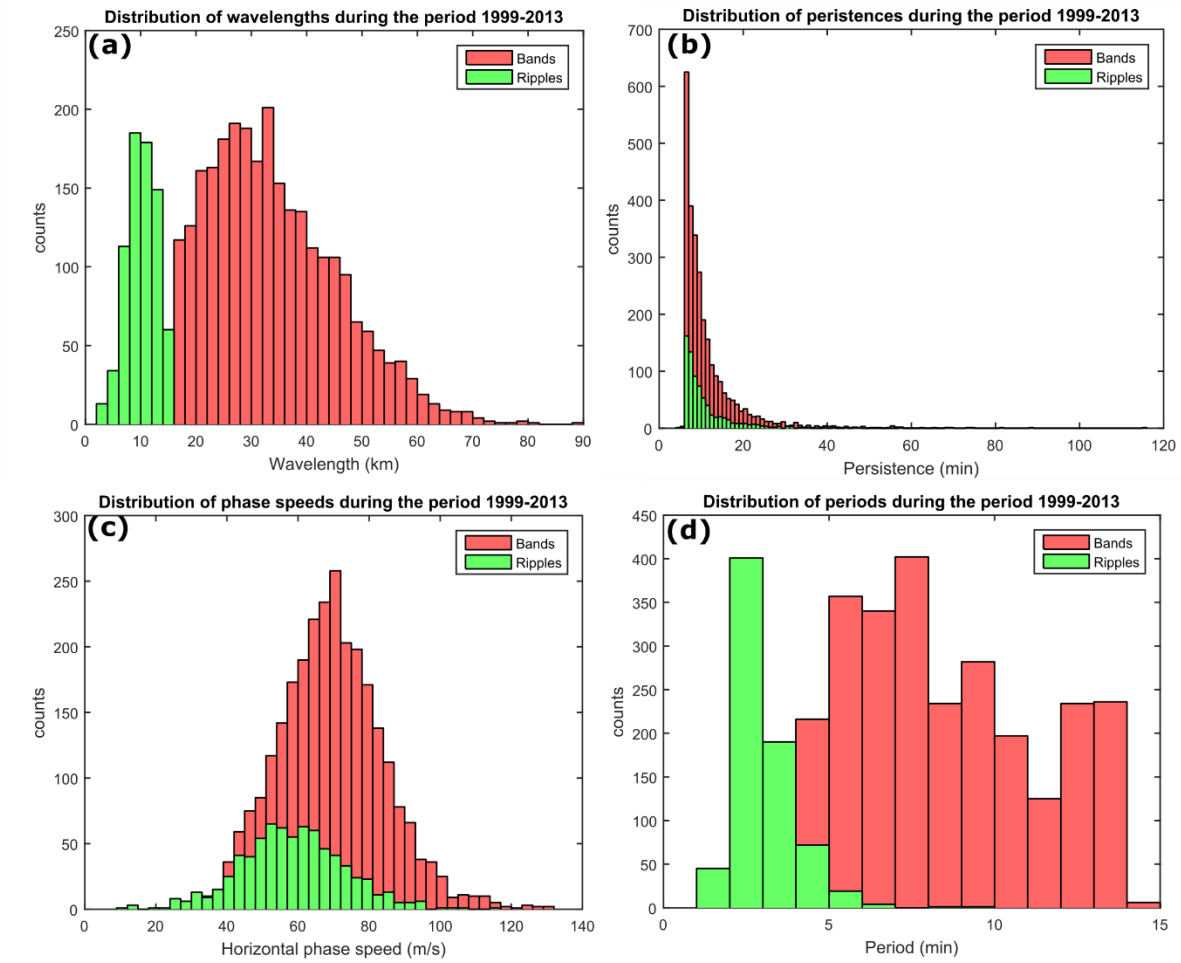

Figure 3.52: Histograms of (a) horizontal wavelength, (b) persistence, (c) observed horizontal phase speeds, and (d) observed periods for all GWs and ripples observed between 1999 and 2013 using the L=10 m/s post-processing limit.

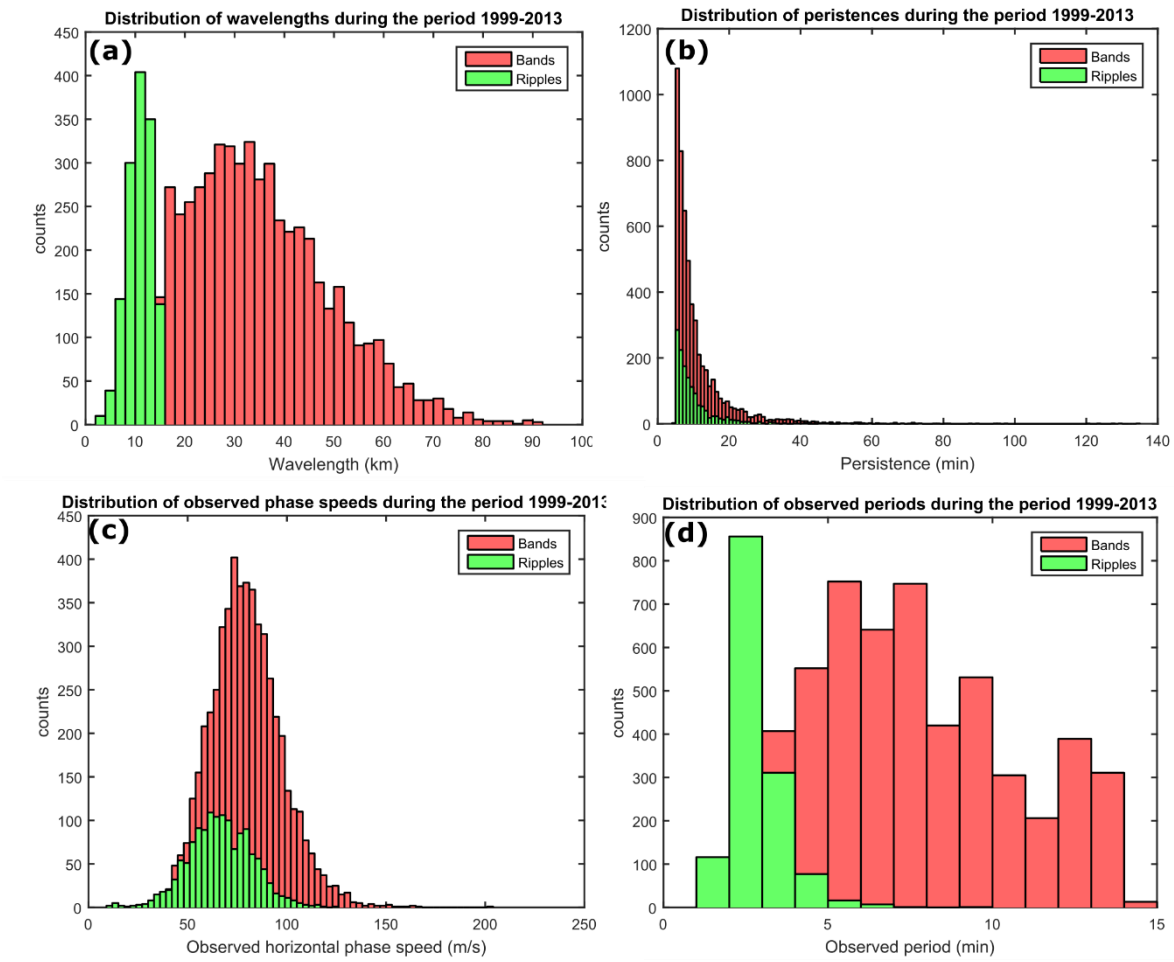

Figure 3.53: Histograms of (a) horizontal wavelength, (b) persistence, (c) observed horizontal phase speeds, and (d) observed periods for all GWs and ripples observed between 1999 and 2013 using the L=15 m/s post-processing limit.

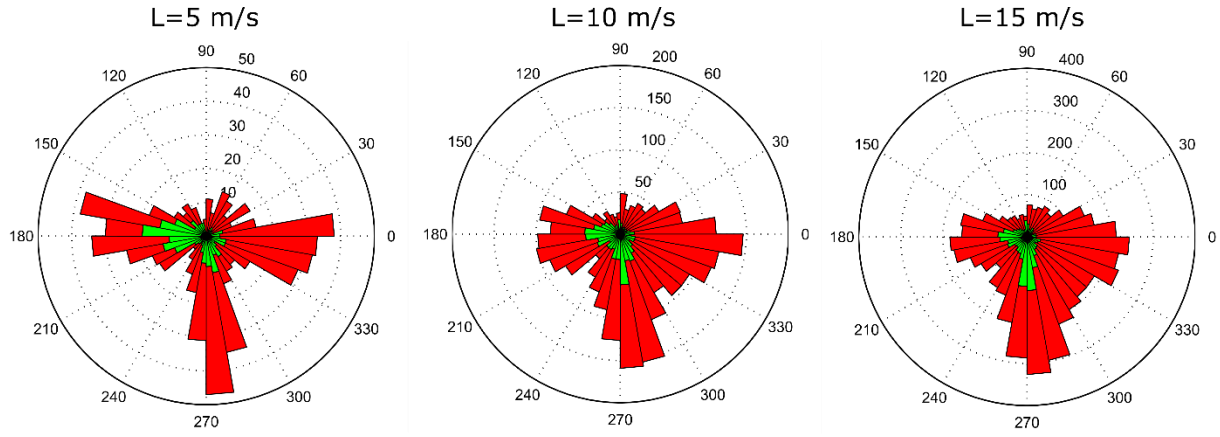

Figure 3.54: Radial histograms of observed GW (red) and ripple (green) propagation directions during the period 1999-2013 using the (left) L=5 m/s, (centre) L=10 m/s and (right) L=15 m/s post-processing limits.

3.3. Conclusions and Future Work

In this chapter, detections of GWs and ripples using the UWOSCR instrument were presented. It would be useful to consider these climatological results (15 years in extent) when determining GW parameteristations for global climate models. In doing this, it would also be critical to include other GW measurements in the models, as UWOSCR (as with any individual instrument) has its own particular observational filter to a very broad range of GWs which actually exist in the atmosphere. UWOSCR, by its nature, observes only a small portion of these waves. Figures Error! Reference source not found.-3.57 illustrate the challenge of measuring GWs in general, and how a synergy of different measurement techniques, including both local and global observations, are needed in order to capture their full spectral, spatial and temporal range (*Alexander et al.*, 2010). These figures also identify the unique observational filter of UWOSCR, and how its measurements fit into the overall set of GW observations.

Error! Reference source not found. and Figure 3.56 show the observational filters for several instruments which have been considered by *Wright et al.* (2016b), and now include (in black) the observational filter for UWOSCR. This is not a comprehensive overview of all GW instruments and, in fact, it is only comprised of satellite observations (from AIRS, COSMIC, HIRDLS, MLS Aura, SAAMER and SABER – all described in *Wright et al.* (2016b)) and radiosonde observations. For a more comprehensive study of spectral, spatial and temporal overlap regions, other observational filters such as those from MF radar and lidar observations, would need to be included. Shaded grey regions in Figure 3.56 indicate spectral regions which are not covered by any of the instruments, and these regions have been reduced by the UWOSCR dataset.

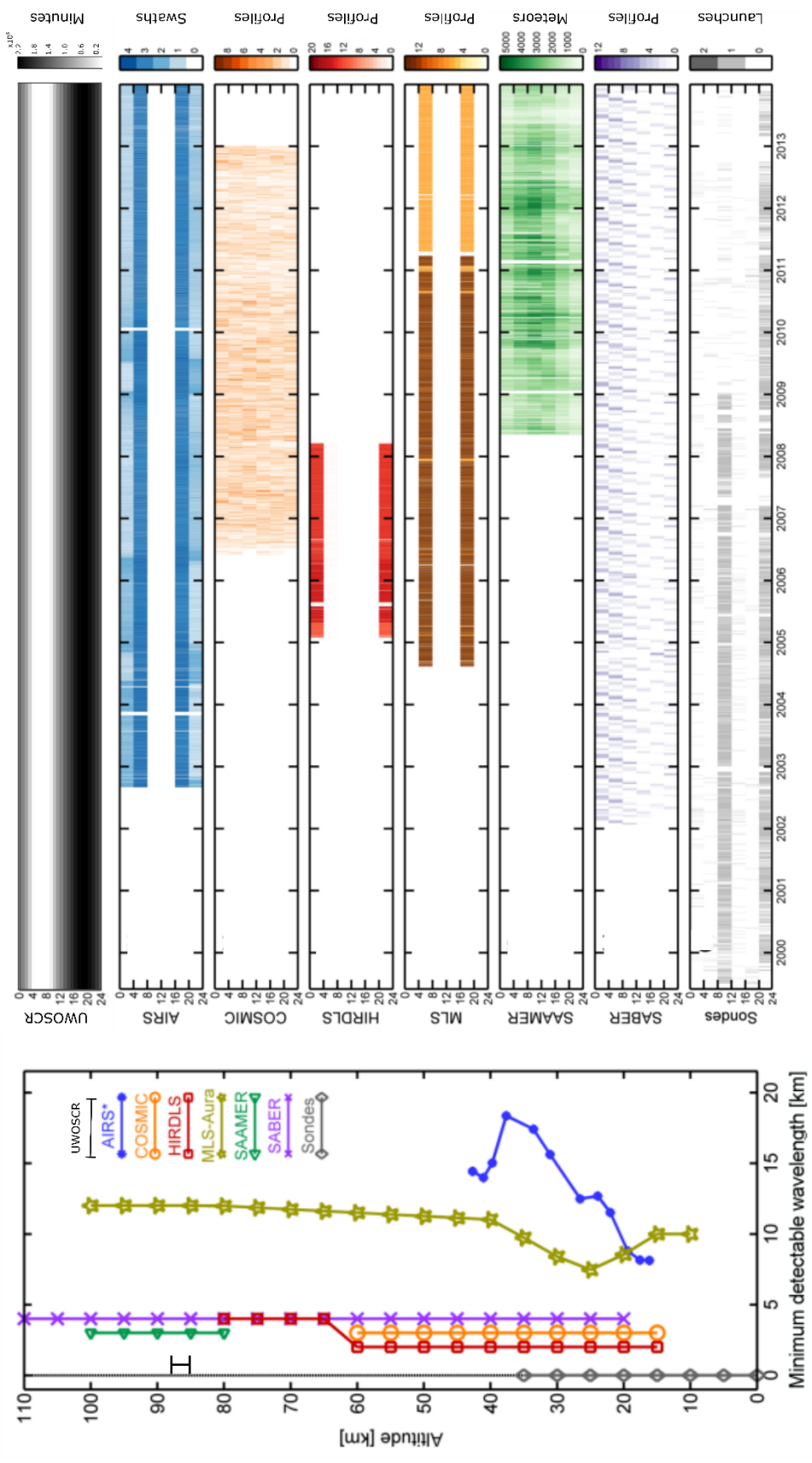

Figure 3.55: Altitudinal and temporal coverage of UWOSCR with respect to a multi-instrument network of GW instruments. This figure was published by *Wright et al.* (2016b, Figure 6) and was adapted to show (in black) (left) the altitude range of UWOSCR observations, and (top right) the total observation time during the years 1999-2013 by hour.

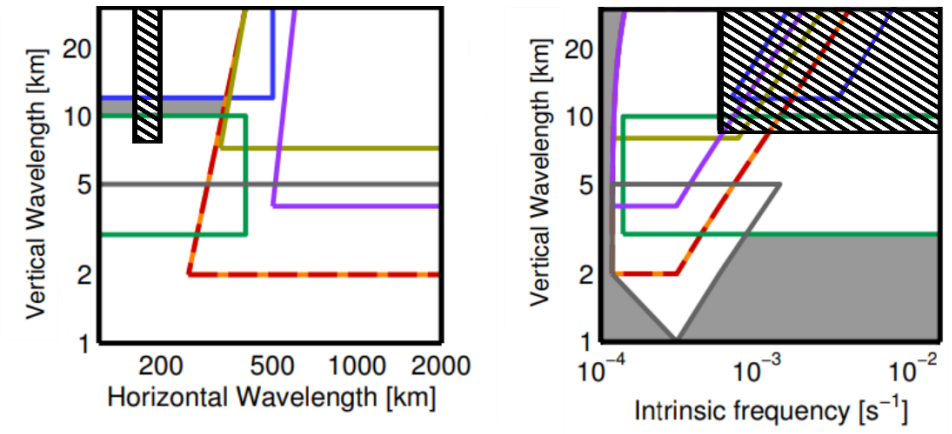

Figure 3.56: Spectral coverage of UWOSCR with respect to a multi-instrument network of GW instruments. This figure was published by *Wright et al.* (2016b, Figure 9) and was adapted to show (in black, hatched boxes) the range of vertical wavelengths available from the UWOSCR observations along with (left) the horizontal wavelength range, and (right) the intrinsic frequency range. Regions shaded in grey are still not observed by this range of instruments.

Figure 3.57 is a more general outline of the horizontal extent and the time scale of the structures which can be characterised using the De Serrano and Lowe analysis method. It places the wave measurements made in this chapter into perspective as they are compared to a full atmospheric observational window.

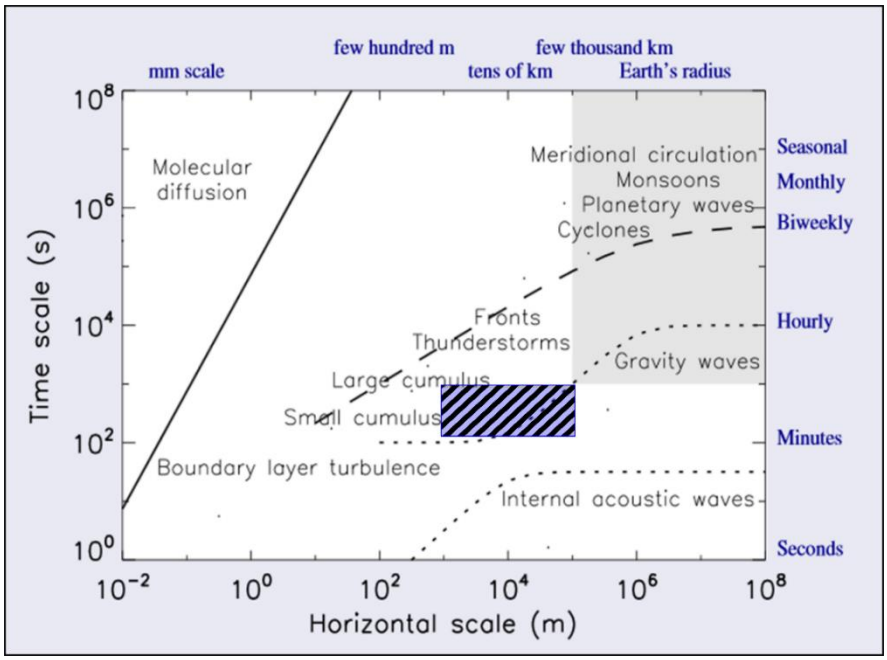

Figure 3.57: A schematic published by *Thurburn* (2011) outlining the spatial and temporal scales of different atmospheric structures and processes. The grey shaded region corresponds to what can generally be resolved by global climate models. This is a modified version of Figure 1.17 in which a hatched region has been overlaid on the plot to indicate the range of horizontal wavelengths and periods observable using the UWOSCR analysis method.

3.3.1. Software

The software used attempts to extract the parameters of the GWs present near the mesopause. In ideal cases (*i.e.* very large amplitude waves, well within the limit of detection), the software works well. As the signal-to-noise ratio decreases, the accuracy of the recovered GW parameters also decreases until it reaches a level where values cannot be relied upon.

A quantitative examination of the accuracy of `UWO_exe`, along with a new LabVIEW version of the same analysis method, has been performed. These sets of software produce realistic values for wave characteristics under perfect conditions, but it still requires improvements. In particular, it was found that phase velocities are generally over-estimated in the case of longer period waves and that the accuracy of the period calculation is highly dependent on no other wave structures existing within the FOV during the FFT time window. Although window lengths were chosen based on the characteristics of some high-amplitude waves which were observed by UWOSCR, there are particular biases associated with these choices. Wave-adaptive window lengths are the next step in software improvement. This would eliminate ambiguities in time lags associated with maximum correlation, and would allow a new spectrum of waves (*i.e.* a different range of speeds and periods) to be examined.

The LabVIEW software has introduced some new possibilities for instrument and analysis adaptability, but is not yet in a suitable state for distribution to others who might be interested in using it. In its current form, it can only produce accurate velocity results for waves with periods greater than 5 minutes. Along with perfecting the analysis technique, it will also be helpful to future users if this code is translated into a free and more accessible (and more easily documentable) programming language (*e.g.* Python).

3.3.2. Climatology

Wave characteristics, calculated using the De Serrano and Lowe software, have been used to develop a climatology of GWs and ripples above Davis Station over a 15-year period. The accuracy of these results is reflected in section 3.1, where it was found that the presented wave speeds (especially for slow-moving waves) may be slightly higher than reality. Some spurious period values may be included in the dataset, but it is assumed that for the most part only one wave will pass through UWOSCR's FOV within a 32-minute period and so, with such a large dataset, the number of spurious period values should be too low to affect climatological trends.

The main findings of the climatology are:

1. Two distinct distributions (one for GWs and one for ripples) of horizontal wavelength were observed, as shown in Figure 3.41(a). Both of these distributions obeyed the relation $\lambda_h(\text{km}) \approx 2.5T(\text{min.})^{1.05}$, which was first shown to fit GW data by *Taylor et al.* (2009). It was found that this trend is consistent with several previous studies (as shown in Figure 3.44), and it has now been extended using the UWOSCR data to include ripples.
2. An unusual distribution of propagation directions over Davis Station was observed, as shown in Figure 3.39. There was a difference in the observed directional distribution of GWs and ripples, and so they were again considered separately. A clear preference for southward, eastward and westward propagating waves (in their distinct Cartesian directions) was observed, but with few ripples propagating eastward. There was a distinct lack of northward propagating waves, a result that is generally consistent with previous high-latitude studies (*e.g. Matsuda et al.* (2014); *Nielsen et al.* (2009); *Suzuki et al.* (2009)). Intrinsic propagation directions also showed a lack of northward propagating waves, but they were more evenly distributed in all southward directions (*i.e.* there were

no gaps in the southeast or southwest directions). A full discussion on observed propagation directions is given in *Rourke et al.* (2017), where ray-tracing results are used to help attribute the pronounced propagation directions to a seasonal-dependent GW source variability. Critical level filtering was rejected as a possibility for directionality based on the ray-tracing results. This is in agreement with a recent paper by *Matsuda et al.* (2017).

3. GW and ripple activity showed some variation over season, year, and time of day which was unrelated to observing time, as shown in Figure 3.50. Months when a large amount of wave activity was observed relative to observing time in that month were February and August, whereas peak wave activity observed was in April, May and August. These results are in general agreement with *Dowdy et al.* (2007) who studied the seasonal variation of GWs with periods ranging from 20-120 minutes above Davis Station during the period 1994-2005 using MF radar observations. They found peak activity during the winter months with two smaller peaks in March and August. The number of waves observed each year varied between approximately 50 and 100 events, except for 2002 when >160 events were observed. Interestingly, this was the only year during the observation period when there was a major southern hemisphere sudden stratospheric warming (SSW) and so there may be a link between the increase in GW activity and the SSW. Finally, there appeared to be a slight increase in waves observed close to local midnight, for which no explanation is currently known.

4. RAY-TRACING

4.1. Introduction

As GWs propagate, they are refracted due to wind shear and temperature gradients in their vicinity. This refraction can significantly change waves' ray paths and, ultimately, the location in which they break (*e.g. Wright et al.* (2017)). Ray-tracing is a technique used to track the trajectories of individual waves, both spatially and temporally, as they propagate through the atmosphere. It can be performed in two directions. Forward ray-tracing tracks the waves from their origin through the atmosphere, whereas reverse ray-tracing traces the waves back to their source region from a particular point at which they were observed. In order to perform either type of ray-tracing, information about the horizontal structure of the background atmosphere at a number of altitude steps, as well as some initial wave parameters, is required.

In this chapter, reverse ray-tracing, which was performed in order to identify the approximate geographical and altitudinal origin of the GWs observed by UWOSCR over Davis Station, is described. Reverse ray-tracing was implemented using MATLAB software (provided in Appendix D) based on earlier work by *Jones* (1969), *Lighthill* (1978), and *Marks and Eckermann* (1995), and tested using results from *Pramitha et al.* (2014). This technique, along with the basic ray-tracing equations, will be described in sections 4.2 and 4.3. Section 4.4 details some software testing of the MATLAB program, before presenting the results for Davis Station in section 4.5. The significance of these results will be discussed in section 4.6 before making some concluding remarks in section 4.7.

4.2. Ray-tracing Equations

The ray-tracing equations shown below are linearized equations in Cartesian co-ordinates, and are taken from *Marks and Eckermann* (1995). They are valid in

a compressible atmosphere under the WKB and Boussinesq approximations (which are described in Appendices B.5 and B.7 respectively) and where acoustic waves are excluded by neglecting the perturbations of pressure terms in the thermodynamic equation (Equation 1.22). It is also assumed that the background wind and wave parameters do not vary locally with time $\left(\frac{\partial}{\partial t} = 0\right)$.

The wave position ray-tracing equations are expressed in Equation 4.1, with the wavenumber ray-tracing equations expressed in Equation 4.2. These expressions describe how the wave position and wave characteristics vary during a time-step, dt.

$$\frac{d\vec{x}}{dt} = \frac{\partial \omega}{\partial \vec{k}} = c_g(\vec{k}) \tag{4.1}$$

$$\frac{d\vec{k}}{dt} = -\frac{\partial \omega}{\partial \vec{x}} \tag{4.2}$$

where

$\vec{x} = (x, y, z)$ is the position vector of the wave,
ω is the ground-based (Eulerian) wave frequency,
$\vec{k} = (k, l, m)$ is the wavenumber vector, and
$c_g(\vec{k})$ is the Eulerian group velocity.

The ray-tracing equations are separated into their three spatial directions in Equations 4.3-4.8. These equations are used to determine the new wave parameters at each altitude step during the reverse ray-tracing process. They are derived from the Taylor-Goldstein equation which is described in Appendix B.1.

$$\frac{dx}{dt} = U + \frac{k(N^2 - \hat{\omega}^2)}{\hat{\omega}\Delta} \tag{4.3}$$

$$\frac{dy}{dt} = V + \frac{l(N^2 - \hat{\omega}^2)}{\hat{\omega}\Delta} \tag{4.4}$$

$$\frac{dz}{dt} = \frac{-m(\hat{\omega}^2 - f^2)}{\hat{\omega}\Delta} \tag{4.5}$$

$$\frac{dk}{dt} = -k\frac{\partial U}{\partial x} - l\frac{\partial V}{\partial x} - \frac{1}{2\hat{\omega}\Delta}\left[\frac{\partial N^2}{\partial x}(k^2+l^2) - \frac{\partial \alpha^2}{\partial x}(\hat{\omega}^2 - f^2)\right] \quad 4.6$$

$$\frac{dl}{dt} = -k\frac{\partial U}{\partial y} - l\frac{\partial V}{\partial y} - \frac{1}{2\hat{\omega}\Delta}\left[\frac{\partial N^2}{\partial y}(k^2+l^2) - \frac{\partial \alpha^2}{\partial y}(\hat{\omega}^2 - f^2)\right] - \frac{f}{\hat{\omega}\Delta}\frac{\partial f}{\partial y}(m^2+\alpha^2) \quad 4.7$$

$$\frac{dm}{dt} = -k\frac{\partial U}{\partial z} - l\frac{\partial V}{\partial z} - \frac{1}{2\hat{\omega}\Delta}\left[\frac{\partial N^2}{\partial z}(k^2+l^2) - \frac{\partial \alpha^2}{\partial z}(\hat{\omega}^2 - f^2)\right] \quad 4.8$$

where

U and V are the winds in the zonal and meridional directions,
N is the Brunt-Väisälä frequency,
$\hat{\omega} = \omega - kU - lV$ is the intrinsic wave frequency,
$\alpha = \frac{1}{2H}$, where H is the density scale height,
$\Delta = k^2 + l^2 + m^2 + \alpha^2$, and
$f = 2\Omega_{\mathrm{E}} \sin(\phi_{\mathrm{L}})$ is the Coriolis parameter,
where
Ω_{E} is the rotation rate of the Earth, and
ϕ_{L} is the latitude of the wave.

It can be seen from these equations that a great detail of information about the background atmosphere (*e.g.* the background horizontal wind, the background temperature, and the initial wave parameters) is required in order to calculate the change in wave parameters over time.

4.3. Method

The approach to ray-tracing taken in this thesis is based on the ray-tracing equations described in section 4.2. After processing the UWOSCR images as described in Chapter 2, each wave observation had a horizontal wavelength, λ_h, observed phase speed, c_{obs}, observed propagation direction, ϕ_{obs}, observed period, T_{obs}, and hence observed angular frequency, $\omega = \frac{2\pi}{T_{obs}}$, associated with it (as illustrated in summary form in Chapter 3). The intrinsic phase speed, c_i, was then calculated using coincident background wind speed, u_{h}, in the direction of the wave using $c_i = c_{obs} - u_{\mathrm{h}}$ (*Nielsen et al.*, 2009). Corresponding

intrinsic propagation direction, ϕ_i, and period, T_i, were calculated using the zonal and meridional intrinsic phase speed and the horizontal wavelength (which is not affected by the background winds (*Lu et al.*, 2009)). Coincident background wind data at the observation altitude was obtained from hourly-averaged MF radar wind data (described in section 1.7.1.1) available at 10-minute intervals above Davis Station. It is these intrinsic wave parameters which form the input for the MATLAB ray-tracing program.

Figure 4.1 shows an atmospheric latitude-longitude-altitude 'cube' of zonal wind (U), meridional wind (V), and temperature (T) data. At the top of this 'cube', at ~87 km altitude, the initial wave parameters (shown in red) are known.

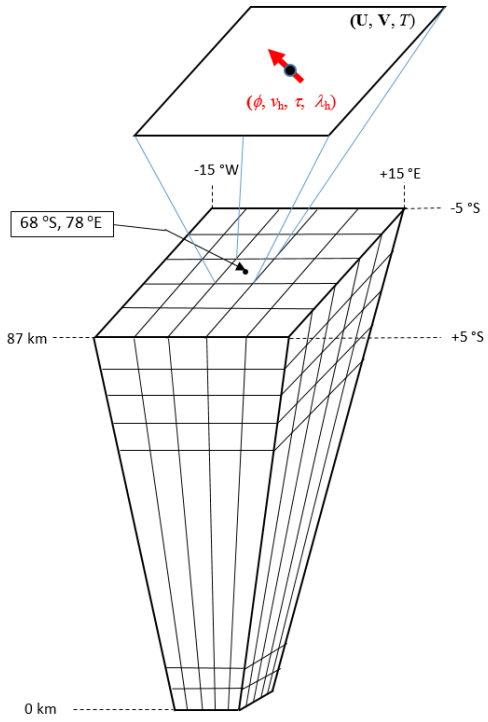

Figure 4.1: Schematic illustrating the parameters required in order to perform ray-tracing. This figure was produced by Frank Mulligan.

As seen from Figure 4.1, background wind and temperature measurements at a number of altitude steps near Davis Station are needed in order to execute the ray-tracing program. Ideally, detailed knowledge of these parameters within a geographical radius of approximately 500 km would be available for this purpose. However, such data is not available and, instead (as done in other

studies such as *Wrasse et al.* (2006) and *Pramitha et al.* (2014)), climatological wind and temperature models are used as the best available substitute. Due to the use of these climatological values, interpretation of the ray-tracing results obtained using this data must be tempered with the knowledge that the actual wind and temperature may be significantly different to the climatological values used, and so the results will not be condition-specific. A longitude-latitude-height 'cube' (*Eckermann* and *Marks*, 1997) of background climatological wind (obtained from the Horizontal Wind Model (HWM-07) which will be described briefly in the following paragraph) and temperature (obtained from the MSIS-E-90 model which will also be described below) data was created for each day of the year. The horizontal extent of this 'cube' was 10° in latitude and 30° in longitude (corresponding to ~1000 km^2 at the surface), and its vertical extent was 0-100 km in altitude. The grid-spacing was 1° in latitude, 3° in longitude, and 1 km in altitude. A cubic spline was applied in all three dimensions to the wind and temperature data so that they varied smoothly to satisfy the WKB approximation used in the ray-tracing equations (*Eckermann* and *Marks*, 1997). The vertical step size of the splined data was 100 m, while the horizontal step size was 0.001° in both longitude and latitude (corresponding to ~40.6 m and ~11 m respectively).

Since the results obtained depend largely on the background atmosphere used, the MSIS-E-90 and HWM-07 climatological models are now described briefly. MSIS-E-90 (*Hedin*, 1991) is the 1990 US Navy empirical model of neutral temperatures and densities in the atmosphere from the ground to the exosphere (indicated by the E in MSIS-E-90). MSIS stands for Mass Spectrometer and Incoherent Scatter Radar, as these were the two data sources used for earlier versions of the model. MSIS-E-90 data is available online for any year since 1958 at any time and location (*McGuire*, 2016). HWM-07 is the 2007 version of the Horizontal Wind Model, an empirical model which represents over 50 years of data from satellites, rockets, and ground-based instruments. This model is

accessed via MATLAB's Aerospace Toolbox package. It is a function of latitude, longitude, altitude, day of year, and time of day (*Drob et al.*, 2008). Values from these models were produced for the Davis Station region and are shown in Figures 4.2-4.4 to provide a general idea of atmospheric winds and temperatures during a climatological year at Davis. The only MSIS-E-90 temperature data shown is between days 32 and 334 of the year, as no summer-time observations are used in this project.

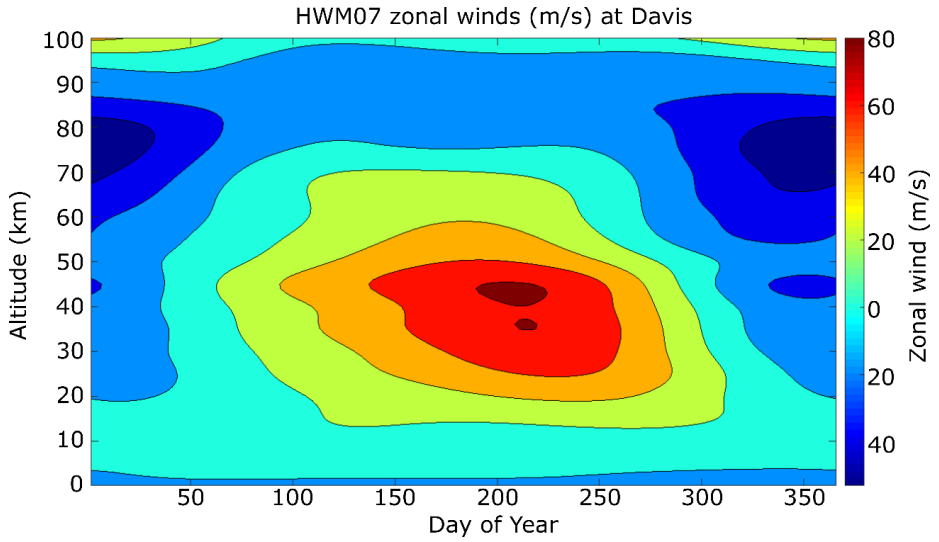

Figure 4.2: Contour plot showing the climatological background zonal wind (in m/s) over Davis Station from the HWM-07 model. This plot shows geographically-averaged values for all latitudes and longitudes within the data 'cube'.

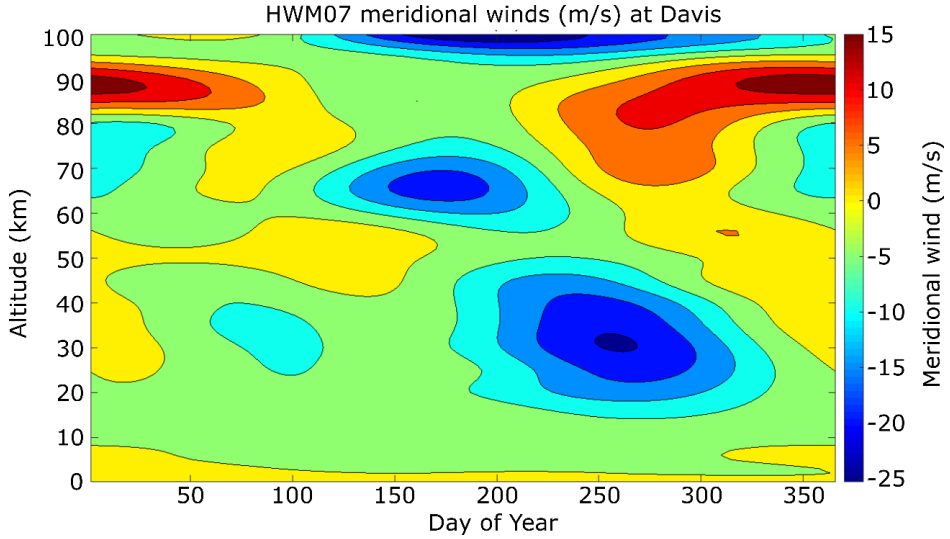

Figure 4.3: Contour plot showing the climatological background meridional wind (in m/s) over Davis Station from the HWM-07 model. This plot shows geographically-averaged values for all latitudes and longitudes within the data 'cube'.

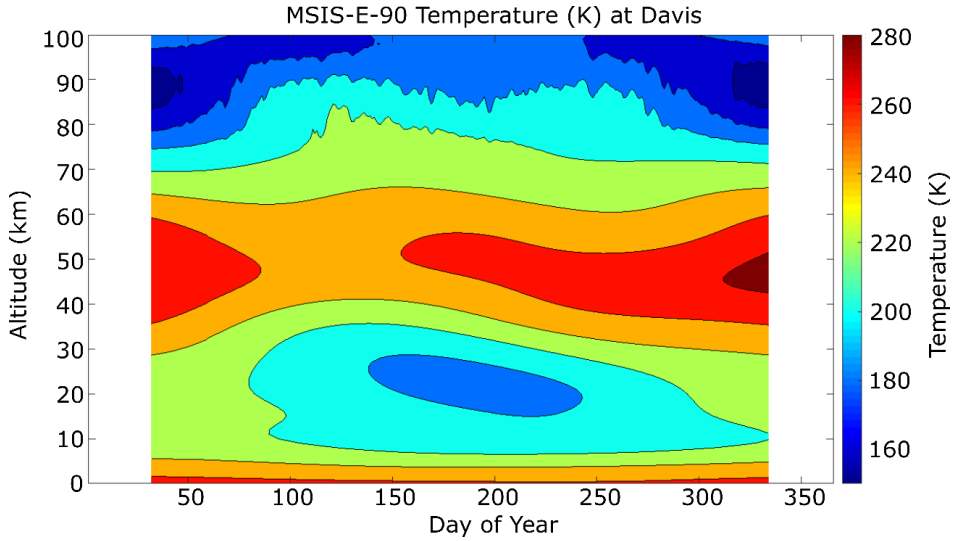

Figure 4.4: Contour plot showing the climatological background temperature (in K) over Davis Station from the MSIS-E-90 model. This plot shows geographically-averaged values for all latitudes and longitudes within the data 'cube'.

The smoothed temperature data was used to calculate a corresponding 'cube' of N^2 and α^2 values, as required by Equations 4.3-4.8. The Brunt-Väisälä frequency squared (N^2) is obtained from Equation B.4 in Appendix B.4 which states that $N^2 = \left(\frac{g}{T}\right)\left(dT/dz + \frac{g}{c_p}\right)$, where $\frac{g}{c_p} \approx 9.5\times10^{-3}$ K m^{-1} is the adiabatic lapse rate. Acceleration due to gravity, g, is determined by $g(z) = g_0\left(\frac{R_E}{R_E+z}\right)^2$, where g_0 =9.8 m s^{-2} is the acceleration due to gravity at the Earth's surface, $R_E \approx 6371$ km is the radius of the Earth, and z is the altitude which g corresponds to. At z =87 km altitude, for example, g ≈9.5 m s^{-2}. The scale height, which is subsequently used to calculate α, is calculated from $H = \frac{RT}{g\mu}$, as described in Appendix B.3, where the molecular mass is given by μ =29 g mol^{-1} and the universal gas constant is given by R =8.314×10^3 J kg^{-1} K^{-1}.

The remaining parameters required by the ray-tracing equations are now described. In order to resolve a wave with a very fast vertical group velocity, c_{gz}, (say 25 m/s) moving to the next vertical step (100 m away), a sufficiently small initial time-step size, dt, must be chosen for the ray-tracing. Based on this, an initial time-step size of 4 s was chosen. After the first vertical

step down, the new actual vertical group velocity $\left(c_{gz} = -\frac{dz}{dt}\right)$ was used to calculate the new time-step ($dt = \left|\frac{100}{c_{gz}}\right|$ seconds) at each vertical step (*Marks* and *Eckermann*, 1995). The wavenumber vector, $\vec{k}$, was obtained using the horizontal wavelength ($\vec{k} = \frac{2\pi}{\lambda_h}$). In particular, $k = \vec{k}\cos(\phi_i)$ and $l = \vec{k}\sin(\phi_i)$. The vertical wavenumber, m, was obtained using the dispersion relation (Equation B.9). The Coriolis parameter, f, is given by $f = 2\Omega_E \sin(\phi_L)$, where $\Omega_E = 7.292\times10^{-5}$ rad s^{-1}.

Knowing the initial intrinsic wave parameters, the observing location (altitude, latitude, and longitude), the 'cube' of horizontal wind, Brunt-Väisälä frequency, and scale height, the Coriolis parameter at each latitude, and the time-step at each vertical level, the ray-tracing equations (Equations 4.3-4.8) are integrated for each wave event in order to trace them back to their region of origin.

The ray-tracing of any particular wave ends under any of the following conditions:

1. The WKB approximation no longer holds, which happens when the WKB parameter $\delta = \frac{1}{m^2}\left|\frac{\partial m}{\partial z}\right| \approx \left|\frac{1}{c_g m^2}\frac{dm}{dt}\right| \geq 1$ (as stated in Appendix B.7).
2. The wave cannot propagate vertically, *i.e.* $m^2 < 0$.
3. The wave is approaching a critical layer, *i.e.* $\hat{\omega} < 0$ or $\hat{\omega} \to 0$.
4. The vertical wavelength becomes smaller than 1 km and close to a critical level, *i.e.* $m^2 > 1\times10^{-6}$ m^{-2}.

In practice, for reverse ray-tracing, condition 4 always occurred before condition 3 was reached.

The MATLAB software was tested using (*i*) results obtained using Crispin Marks' and Stephen Eckermann's Gravity-wave Regional Or Global Ray Tracer (GROGRAT) code, which is described in *Marks and Eckermann* (1995) and

Eckermann and Marks (1997), and (*ii*) results from Gadanki and Hyderabad, India, obtained by *Pramitha et al.* (2014), who also employed the same reverse ray-tracing method as *Marks and Eckermann* (1995). It was then used to trace all wave events detected by UWOSCR (whose characteristics were obtained using the De Serrano and Lowe analysis method described in Chapter 2) back to their approximate source regions in order to provide a better understanding of the observations.

4.4. Software Testing

In this section, two separate software tests of the MATLAB ray-tracing code are presented. Firstly, GROGRAT is applied to some example GW data from Davis Station to study the differences/similarities between the GROGRAT and MATLAB code. Then, using 14 wave events observed in India, a comparison is done between the ray-tracing results reported by *Pramitha et al.* (2014), the results obtained using GROGRAT, and the results obtained using the MATLAB ray-tracing software.

4.4.1. Comparison with GROGRAT code

GROGRAT is a well-recognised ray-tracing program developed by C.J. Marks and S.D. Eckermann in the early 1990's based on the previous work of *Lighthill* (1978) and *Jones* (1969) and subsequently used to perform both forward- and reverse- ray-tracing of gravity waves in several studies (*e.g. Preusse et al.* (2009); *Ern et al.* (2009a); *Gerrard et al.* (2004); *Yamashita et al.* (2013)). Using a copy of this code, reverse ray-tracing was applied to a random selection of GWs which have been observed at Davis Station using UWOSCR. In order to do this, background atmospheric data (wind and temperature) as well as initial GW parameters must be supplied to the program. To match the MATLAB software, the same 'cube' of background climatological data from HWM-07 and MSIS-E-90 models was used, with an extent of $\pm 5^{\circ}$ latitude and $\pm 15^{\circ}$ latitude from Davis Station, and $0-100$ km in altitude. Since radiative and turbulent damping is not included in the MATLAB ray-tracing software

due to lack of wave amplitude information in the UWOSCR dataset, saturation and damping were excluded from the GROGRAT code. A time-step of -0.001 hours (minus for reverse ray-tracing) was also chosen to match the MATLAB software.

Some (51) wave events observed using UWOSCR at Davis Station were chosen at random to compare the ray-tracing results from the MATLAB and GROGRAT software. A summary of the results is shown in Table 4.1. Reasonable agreement between both sets of software was established, but some differences remained. For example, it was found that, for 13 events, the MATLAB software estimated the source at ~ 10 km altitude while the GROGRAT code estimated the altitude source region of these same events to be between ~12 and 27 km. Based on this, it appears the tropospheric cut-off for the GROGRAT code is somewhat higher. In addition, for 19 wave events, it was found that MATLAB and GROGRAT agreed (to within $\pm 0.4^{\circ}$ longitude, $\pm 0.3^{\circ}$ latitude, and ± 0.7 km) at some earlier time-step, but that GROGRAT continued ray-tracing beyond a MATLAB terminating condition (usually the WKB parameter becoming >1 or m^2 becoming $>10^{-6}$ m^{-2}). This difference partly arose due to the termination condition for the WKB parameter being > 2.0 in the GROGRAT software and > 1.0 in the MATLAB software. Excluding these two differences, all other estimated wave sources agreed to within $\pm$ 2.2° longitude and $\pm$ 0.4° latitude. The source altitude difference between the two sets of code was usually within $\pm$ 5 km of each other, but was outside this range (up to ~ 12 km difference) for five additional events and differed by 73 km for one event.

Event No.	Observed Wave Parameters				Source [MATLAB code]			Source [GROGRAT code]			Absolute Difference			Relevant GROGRAT Step			Abs. dfference at this step		
	φ (°N of E)	λ_h (km)	T (min)	v (m/s)	Long (°)	Lat (°)	Alt (km)	Long (°)	Lat (°)	Alt (km)	Long (°)	Lat (°)	Alt (km)	Long (°)	Lat (°)	Alt (km)	Long (°)	Lat (°)	Alt (km)
1	74.9	39.5	14.0	47.1	70.4	-70.1	9.9	72.6	-69.8	21.2	2.2	0.3	11.3						
2	-103.1	44.6	10.1	73.3	76.6	-67.3	10.0	76.5	-67.5	20.6	0.1	0.2	10.6						
3	55.4	29.7	7.3	68.4	71.3	-69.2	10.0	72.3	-69.2	17.9	1.0	0.0	7.9						
4	-101.6	56.7	12.1	78.0	76.4	-66.9	10.0	76.4	-67.2	20.2	0.0	0.3	10.2						
5	-106.7	52.1	11.7	74.2	76.9	-67.1	10.0	76.8	-67.4	20.3	0.1	0.3	10.3						
6	-39.4	36.8	10.1	60.6	75.3	-68.0	39.0	62.7	-65.7	27.9	12.6	2.3	11.1	74.9	-68.0	39.0	0.4	0.0	0.0
7	20.5	32.8	10.5	52.0	74.8	-68.8	40.4	62.9	-68.0	22.5	11.9	0.8	17.9	74.6	-68.8	40.7	0.2	0.0	0.3
8	-21.0	27.4	9.7	47.0	76.5	-68.5	46.1	78.0	-68.6	46.1	1.5	0.1	0.0						
9	-5.2	45.5	17.0	44.7	75.0	-68.5	47.0	61.3	-67.3	41.4	13.7	1.2	5.6	75.0	-68.6	47.3	0.0	0.1	0.3
10	-17.2	45.4	8.6	88.3	77.9	-68.6	83.1	78.0	-68.6	85.8	0.1	0.0	2.7						
11	17.4	35.2	12.7	46.2	70.7	-68.7	9.9	71.2	-68.7	12.3	0.5	0.0	2.4						
12	-96.9	41.7	14.5	48.0	78.0	-66.6	9.9	78.3	-66.8	16.4	0.3	0.2	6.5						
13	174.0	53.5	11.0	81.0	82.4	-68.8	10.0	78.0	-68.6	83.0	4.4	0.2	73.0						
14	-106.3	44.8	19.4	38.4	79.4	-66.0	10.0	79.9	-66.3	18.0	0.5	0.3	8.0						
15	-104.6	35.2	9.5	103.4	77.1	-67.4	9.9	77.0	-67.6	21.7	0.1	0.2	11.8						
16	-138.8	41.7	20.8	30.7	79.4	-67.3	10.0	78.6	-67.5	27.3	0.8	0.2	17.3						
17	-177.7	53.5	18.6	43.1	80.2	-68.4	49.5	79.8	-68.4	28.8	0.4	0.0	20.7	80.0	-68.5	49.3	0.2	0.1	0.2
18	-132.9	41.7	8.0	62.0	78.4	-68.4	66.6	78.3	-68.4	62.1	0.1	0.0	4.5	78.3	-68.4	66.7	0.1	0.0	0.1
19	-143.2	41.7	8.0	65.2	78.5	-68.5	70.7	78.4	-68.5	67.0	0.1	0.0	3.7	78.4	-68.5	70.6	0.1	0.0	0.1
20	-147.5	53.5	8.6	96.2	78.5	-68.5	70.8	78.5	-68.4	63.6	0.0	0.1	7.2	78.5	-68.5	71.0	0.0	0.0	0.2
21	-146.9	41.7	8.0	67.3	78.5	-68.5	70.9	78.4	-68.5	66.9	0.1	0.0	4.0	78.4	-68.5	71.0	0.1	0.0	0.1
22	-158.5	53.5	6.7	63.3	78.4	-68.5	73.7	78.3	-68.6	72.6	0.1	0.1	1.1						
23	-151.2	44.8	5.6	63.9	78.2	-68.5	78.7	78.0	-68.6	87.0	0.2	0.1	8.3						
24	-126.1	35.1	18.2	32.1	78.0	-67.1	10.0	77.2	-67.3	24.8	0.8	0.2	14.8						
25	167.7	47.2	13.5	58.1	79.2	-68.6	60.7	79.1	-68.7	49.1	0.1	0.1	11.6	79.1	-68.6	60.4	0.1	0.0	0.3
26	173.9	37.7	10.4	60.2	78.8	-68.6	70.2	78.7	-68.6	63.9	0.1	0.0	6.3	78.7	-68.6	70.9	0.1	0.0	0.7

Table 4.1: Example GWs at Davis whose sources are estimated both by the MATLAB software and by GROGRAT. This table is continued on the following page.

Event No.	Observed Wave Parameters				Source [MATLAB code]			Source [GROGRAT code]			Absolute Difference			Relevant GROGRAT Step			Abs. dfference at this step		
	φ (°N of E)	λ_h (km)	T (min)	v (m/s)	Long (°)	Lat (°)	Alt (km)	Long (°)	Lat (°)	Alt (km)	Long (°)	Lat (°)	Alt (km)	Long (°)	Lat (°)	Alt (km)	Long (°)	Lat (°)	Alt (km)
27	169.8	23.8	10.8	36.8	79.1	-68.6	70.2	78.9	-68.6	68.9	0.2	0.0	1.3						
28	-169.2	40.8	8.8	77.1	78.6	-68.5	70.8	78.5	-68.6	69.7	0.1	0.1	1.1						
29	144.6	31.2	8.1	64.3	78.4	-68.7	71.6	78.4	-68.7	72.1	0.0	0.0	0.5						
30	-166.5	32.4	7.3	74.3	78.5	-68.5	71.7	78.4	-68.6	71.3	0.1	0.1	0.4						
31	-102.8	16.4	5.9	46.6	78.2	-68.5	75.4	78.0	-68.6	87.0	0.2	0.1	11.6						
32	151.9	20.4	7.0	48.8	78.4	-68.5	75.4	78.3	-68.6	73.9	0.1	0.1	1.5						
33	-103.7	27.8	6.5	71.3	78.1	-68.5	76.8	78.0	-68.6	86.0	0.1	0.1	9.2						
34	-140.8	27.8	5.7	81.0	78.0	-68.6	83.8	78.0	-68.6	87.0	0.0	0.0	3.2						
35	54.4	33.1	18.1	30.5	74.1	-70.2	9.9	75.0	-69.9	20.3	0.9	0.3	10.4						
36	-62.8	45.0	10.5	71.1	76.6	-67.5	10.0	76.8	-67.5	16.1	0.2	0.0	6.1						
37	-2.5	30.6	35.3	14.4	77.0	-68.5	57.3	62.4	-67.2	41.8	14.6	1.3	15.5	77.1	-68.6	56.9	0.1	0.1	0.4
38	-46.5	42.5	10.8	65.4	77.9	-68.5	73.4	78.0	-68.6	79.5	0.1	0.1	6.1						
39	-71.6	37.4	8.9	70.2	78.1	-68.4	73.4	78.0	-68.6	85.7	0.1	0.2	12.3						
40	-24.6	26.2	11.5	37.8	77.9	-68.6	81.0	78.0	-68.6	85.3	0.1	0.0	4.3						
41	97.6	23.0	6.6	58.3	78.1	-68.7	81.8	78.1	-68.7	83.0	0.0	0.0	1.2						
42	-58.9	41.8	11.4	61.2	77.9	-68.5	82.6	76.5	-67.5	15.3	1.4	1.0	67.3	78.0	-68.6	82.8	0.1	0.1	0.2
43	-151.1	46.2	12.4	62.0	80.0	-68.5	10.0	79.6	-68.1	23.8	0.4	0.4	13.8						
44	-127.8	35.2	9.4	62.3	78.4	-68.2	44.4	78.4	-68.0	22.5	0.0	0.2	21.9	78.4	-68.3	44.6	0.0	0.1	0.2
45	-144.1	46.7	10.2	76.4	78.9	-68.3	44.5	79.2	-68.1	22.3	0.3	0.2	22.2	78.9	-68.3	44.8	0.0	0.0	0.3
46	-134.5	47.9	9.8	81.1	78.7	-68.3	49.1	78.8	-68.0	22.0	0.1	0.3	27.1	78.7	-68.3	49.8	0.0	0.0	0.7
47	-140.3	34.8	9.3	62.1	78.7	-68.3	50.0	78.7	-68.2	22.7	0.0	0.1	27.3	78.7	-68.4	50.4	0.0	0.1	0.4
48	-137.8	33.6	9.2	60.8	78.6	-68.3	50.2	78.6	-68.1	22.6	0.0	0.2	27.6	78.6	-68.4	50.3	0.0	0.1	0.1
49	-141.4	33.8	9.0	62.5	78.5	-68.2	72.1	78.5	-68.2	23.0	0.0	0.0	49.1	78.5	-68.5	72.6	0.0	0.3	0.5
50	-132.6	56.8	9.6	98.7	78.4	-68.4	72.7	79.0	-68.0	21.1	0.6	0.4	51.6	78.4	-68.5	72.8	0.0	0.1	0.1
51	-149.5	45.5	8.2	92.8	78.4	-68.5	73.4	78.4	-68.5	73.4	0.0	0.0	0.0						

Table 4.1 continued.

4.4.2. Comparison with code by Pramitha *et al.* (2014)

Observed wave parameters (taken from *Pramitha et al.* (2014), Table 1) from 14 wave events observed in atomic oxygen airglow emissions (~97 km altitude) over Gadanki, India (13.5 ° N, 79.2 ° E) on 17th and 19th March 2012 (labelled G1-G5) and Hyderabad, India (17.5 ° N, 78.5 ° E) on 8th March 2010 (labelled H1-H9) are shown in Table 4.2. In order to test the in-house reverse ray-tracing MATLAB software, both the MATLAB and the GROGRAT software are applied to these waves. In Table 4.2, the MATLAB results are compared with both GROGRAT and the results obtained by *Pramitha et al.* (2014).

Based on the five Gadanki wave events, it was found that the source longitude and latitude of both sets of code (Pramitha's code and the MATLAB code) were within $\pm 0.7°$ and $\pm 1.2°$ of each other, respectively. The source altitude for both sets of code was within ± 4 km of each other for three events, but was >30 km for the G2 and G5 events. In general, for this limited dataset, it appears that there is reasonable agreement between the two sets of results. Differences do not appear to have arisen due to the absence of radiative and turbulent damping in the MATLAB software, as GROGRAT agrees with the MATLAB code even when these options are turned on in the GROGRAT software. It is more probable that differences are due to the different atmospheric background data (U, V, and T) used at Gadanki by *Pramitha et al.* (2014) (where the 'Gadanki model' was used in place of the HWM-07 and MSIS-E-90 combination).

A better comparison between the three sets of software can be made with the Hyderabad GW data, where the same background atmosphere (*i.e.* a HWM-07 and MSIS-E-90 combination) is used in all three sets of ray-tracing code. As shown in Table 4.2, there are much greater differences between the three sets of results for four of nine of these waves (H1, H4, H7, and H8). All three source altitudes don't agree for any of these nine waves but the disparity between the waves terminating at ~12−13 km altitude according to MATLAB and *Pramitha*

et al. (2014) (H2, H3, H6, and H9) and GROGRAT's estimation of the same altitudes may be due to a higher lower-boundary in the GROGRAT software. Apart from H1, H4, H7, and H8, all three sets of software agree on the source longitude and latitude to a precision of $\pm 1.3^{\circ}$ and $\pm 0.2^{\circ}$ respectively.

Event	Date	Observed wave parameters				Source [MATLAB code]			Source [*Pramitha et al.*, 2014]			Source [GROGRAT code]			Absolute difference from MATLAB results					
															Pramitha			GROGRAT		
		φ (°N of E)	λ_h (km)	T (min)	v (m/s)	Long (°)	Lat (°)	Alt (km)	Long (°)	Lat (°)	Alt (km)	Long (°)	Lat (°)	Alt (km)	Long (°)	Lat (°)	Alt (km)	Long (°)	Lat (°)	Alt (km)
G1	17/03/12	102	85	18	78	79.5	10.6	14.1	79.9	10.8	13.0	79.5	11.2	26.8	0.4	0.2	1.1	0.0	0.6	12.7
G2	17/03/12	98	34	9	63	79.2	13.5	96.9	79.4	12.3	17.0	79.2	13.5	97.0	0.2	1.2	79.9	0.0	0.0	0.1
G3	17/03/12	132	12	6	33	79.2	13.5	97.0	79.2	13.4	96.9	79.2	13.5	97.0	0.0	0.1	0.1	0.0	0.0	0.0
G4	19/03/12	62	134	12	186	79.2	13.5	96.9	79.1	13.2	92.9	79.2	13.5	97.0	0.1	0.3	4.0	0.0	0.0	0.1
G5	19/03/12	142	16	8	33	79.2	13.5	97.0	79.9	12.7	66.9	79.2	13.5	97.0	0.7	0.8	30.1	0.0	0.0	0.0
H1	8/3/10	11	39	16	41	78.3	17.6	94.8	70.2	15.8	10.5	73.3	15.9	61.1	8.1	1.8	84.3	5.0	1.7	33.7
H2	8/3/10	16	57	16	59	74.6	16.4	12.8	75.3	16.4	13.5	75.3	16.5	29.5	0.7	0.0	0.7	0.7	0.1	16.7
H3	8/3/10	21	74	16	77	75.3	16.3	13.3	75.9	16.3	14.5	75.9	16.5	29.0	0.6	0.0	1.2	0.6	0.2	15.7
H4	8/3/10	11	39	20	32.5	78.4	17.6	96.1	76.3	17.1	67.6	73.4	13.1	91.2	2.1	0.5	28.5	5.0	4.5	4.9
H5	8/3/10	16	57	20	48	72.2	15.7	12.2	72.7	15.7	12.5	73.5	15.8	53.7	0.5	0.0	0.3	1.3	0.1	41.5
H6	8/3/10	21	74	20	61.7	74.0	15.8	12.9	74.7	15.8	13.5	74.6	16.0	28.3	0.7	0.0	0.6	0.6	0.2	15.4
H7	8/3/10	11	39	23	28	78.5	17.5	97.0	75.8	16.9	68.5	73.4	18.6	93.5	2.7	0.6	28.5	5.1	1.1	3.5
H8	8/3/10	16	57	23	41	78.1	17.7	94.0	68.3	14.8	11.5	73.5	15.5	62.6	9.8	2.9	82.5	4.6	2.2	31.4
H9	8/3/10	21	74	23	54	72.6	15.3	12.6	73.4	15.4	13.5	73.5	15.5	29.6	0.8	0.1	0.9	0.9	0.2	17.0

Table 4.2: Observed wave parameters and estimated source region of 14 wave events observed at Gadanki and Hyderabad, India. Sources are estimated using GROGRAT and MATLAB, and compared with results by Pramitha et al. (2014, Table 1).

4.5. Climatological Results

In this section, the calculated wave origins of observed band-type GWs at Davis Station during the period 1999−2013 is presented. Ray-tracing is not performed on the observed ripples because some of them may be the result of turbulence and instabilities (*Hecht et al.*, 2014) and therefore they could invalidate the ray-tracing statistics of GWs. The input wave parameters, in this case, have been post-processed with the L=7 m/s criterion (as described in section 2.6). This results in approximately 120 events per winter season (an increase of approximately 64 events per winter season when compared to the L=5 m/s criterion), which is comparable to the number reported by *Nielsen et al.* (2009) and *Matsuda et al.* (2014).

Figure 4.5 (a-c) shows the altitude of wave origin as a function of (a) intrinsic period, (b) horizontal wavelength, and (c) the percentage of waves (compared to the total number of observed band-type wave events, *i.e.* 1407) at each altitude. From Figure 4.5 (c), four distinct altitude regions of most frequent GW origin can be identified. A large proportion (45%) of observed band-type waves could not be ray-traced significantly below the altitude of detection (~87 km) because they satisfied condition 2 ($m^2 < 0$) for ray-tracing termination. This may imply that a large proportion of ducted waves are trapped near the airglow layer. This is in agreement with very recent (preliminary) results which indicate that a large proportion of GWs detected at Davis Station are ducted compared to at other Antarctic locations (*Pautet*, 2018). The three other most frequent altitude regions that waves were traced back to were ≤10 km (15% of total number of observed band-type waves, *i.e.* 204 waves), 70−80 km (15% of total number of observed band-type waves, *i.e.* 208 waves), and 45 − 55 km (9.5% of total number of observed band-type waves, *i.e.* 134 waves). The geographical end points along with the seasonal and directional distribution of these three groups are further investigated later, in Figure 4.7 and Figure 4.8 respectively. The termination condition for the majority of the waves traced to 45−55 km was

condition 4 ($m^2 > 1 \times 10^{-6}$ m^{-2}, *i.e.* $\lambda_h < 1$ km). This group tended to have intrinsic periods in the range 9−13 minutes and horizontal wavelengths in the range 34−36 km. The 70−80 km group tended to have shorter intrinsic periods in the range $7-9$ minutes and shorter horizontal wavelengths in the range 25−38 km. Figure 4.5 (d) shows a typical winter-time altitude profile from the climatological wind and temperature data, and is a subset of the data shown in Figures 4.2-4.4.

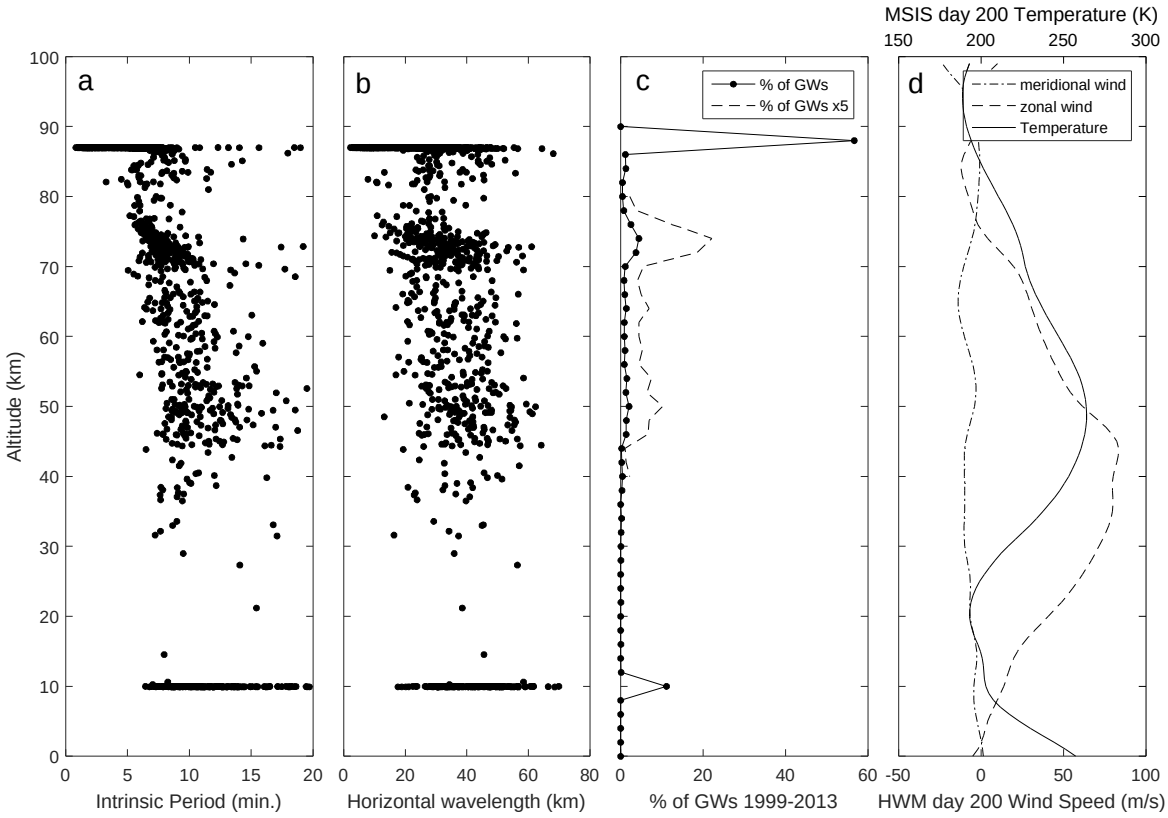

Figure 4.5: Termination altitude of traced GWs as a function of (a) intrinsic period, (b) horizontal wavelength, (c) percentage of traced GWs, and (d) typical wintertime (day of year = 200) wind and temperature profiles at Davis Station, obtained from HWM-07 and MSIS-E-90 models respectively (*Rourke et al.*, 2017).

In Figure 4.6, the inter-annual variation of the group of waves which originated in the troposphere compared to the number of waves observed near the mesopause is examined. The percentage of the total number of waves in a given year traced to the troposphere varied between 9 and 19%, with a mean of 15%. This may be compared with other ray-tracing studies such as *Kim et al.* (2010),

Bageston et al. (2011a), *Gerrard et al.* (2004), *Wrasse et al.* (2006a), and *Wrasse et al.* (2006b) who found that 23%, 7%, 23%, 24-60%, and 15% (respectively) of waves observed were traceable to the troposphere. The waves traceable to the troposphere at Davis Station tended to have directions which were predominantly southward, horizontal wavelengths which were greater than approximately 20 km, and intrinsic periods which were greater than approximately 6.5 minutes. Waves generated in the troposphere near Davis Station may, for example, be terrain-generated (*e.g. Nappo* (2002)), storm-generated (*e.g. Chou et al.* (2016); *Garcia et al.* (2017)), or the result of interactions of planetary waves with the background wind field (*e.g. Mehta et al.* (2017)).

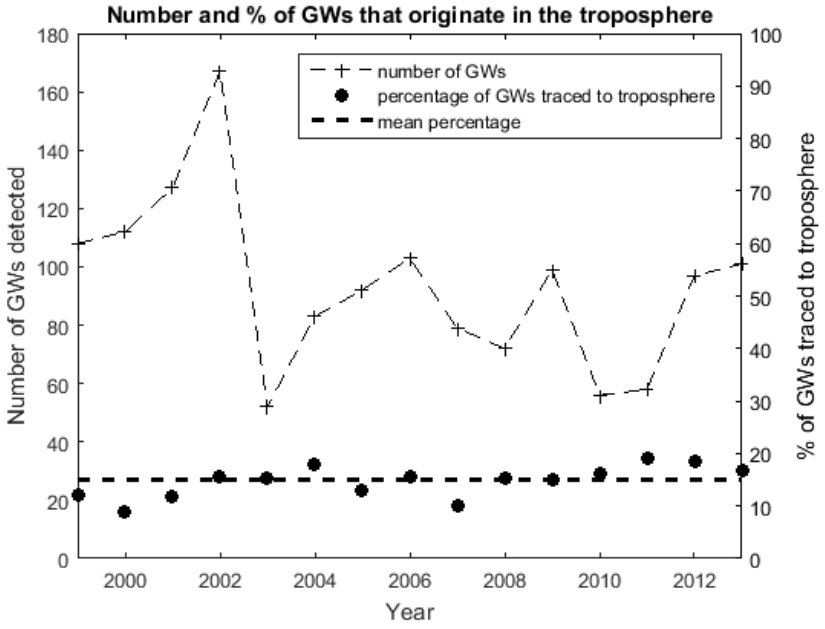

Figure 4.6: Number of waves detected by year (+) and percentage of those waves traced to the troposphere (•). The dashed black horizontal line indicates the mean percentage of waves traced to the troposphere over all years (*Rourke et al.*, 2017).

In Figures 4.7-4.8, the three groups of waves which have been traced back to the different altitude regions (namely ≤ 10 km, $45-55$ km, and $70-80$ km) are examined in further detail. Figure 4.7 shows the geographical end-points of the waves in each of these three groups, with the majority of waves originating within approximately 300 km of the observing station. Figure 4.8 shows the

distribution of observed propagation directions as well as the seasonal variation of the waves in each of the three altitude groups. The counts in this figure are normalised by monthly observing time. The tropospheric group (lower panels) have a very pronounced southward observed propagation direction with a large peak during August-October and minor peaks in February and May. The 45−55 km group (middle panels) have a maximum in the early austral spring period (September) with a smaller peak in late autumn (April). The September group have observed propagation directions which are predominantly eastward, whereas the April/May group have observed propagation directions which are predominantly westward. The 70−80 km group (upper panels) show a strong mid-winter maximum and are generally directed westward. The results from these two figures will be discussed in further detail in section 4.6.

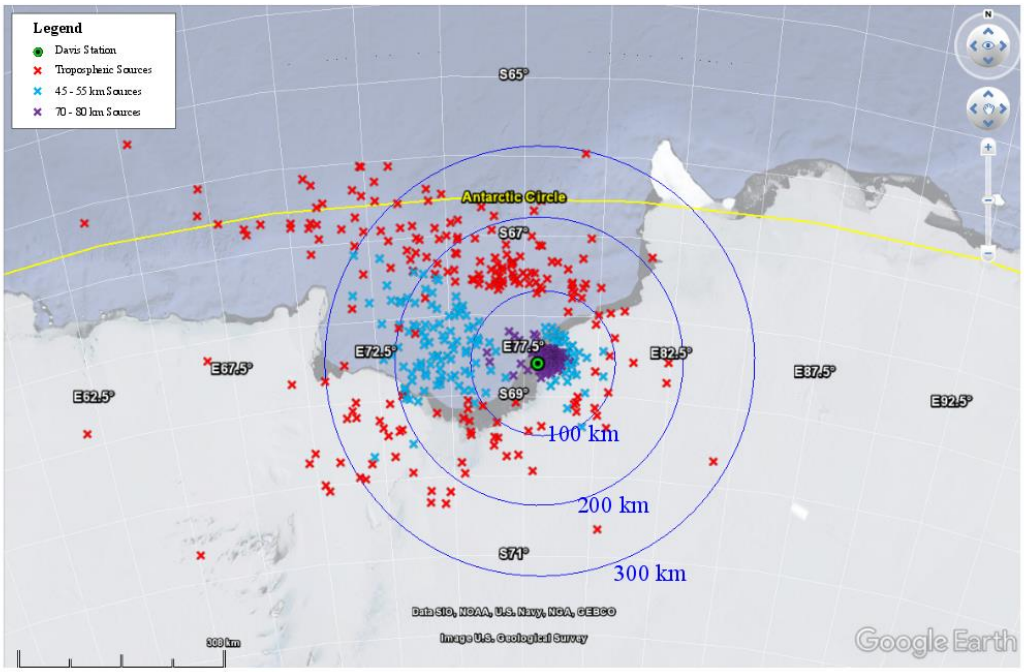

Figure 4.7: Geographical distribution of the endpoints of GWs with termination points reverse ray-traced to the troposphere (red), the 45−55 km altitude region (blue), and the 70−80 km altitude region (purple) (*Rourke et al.*, 2017).

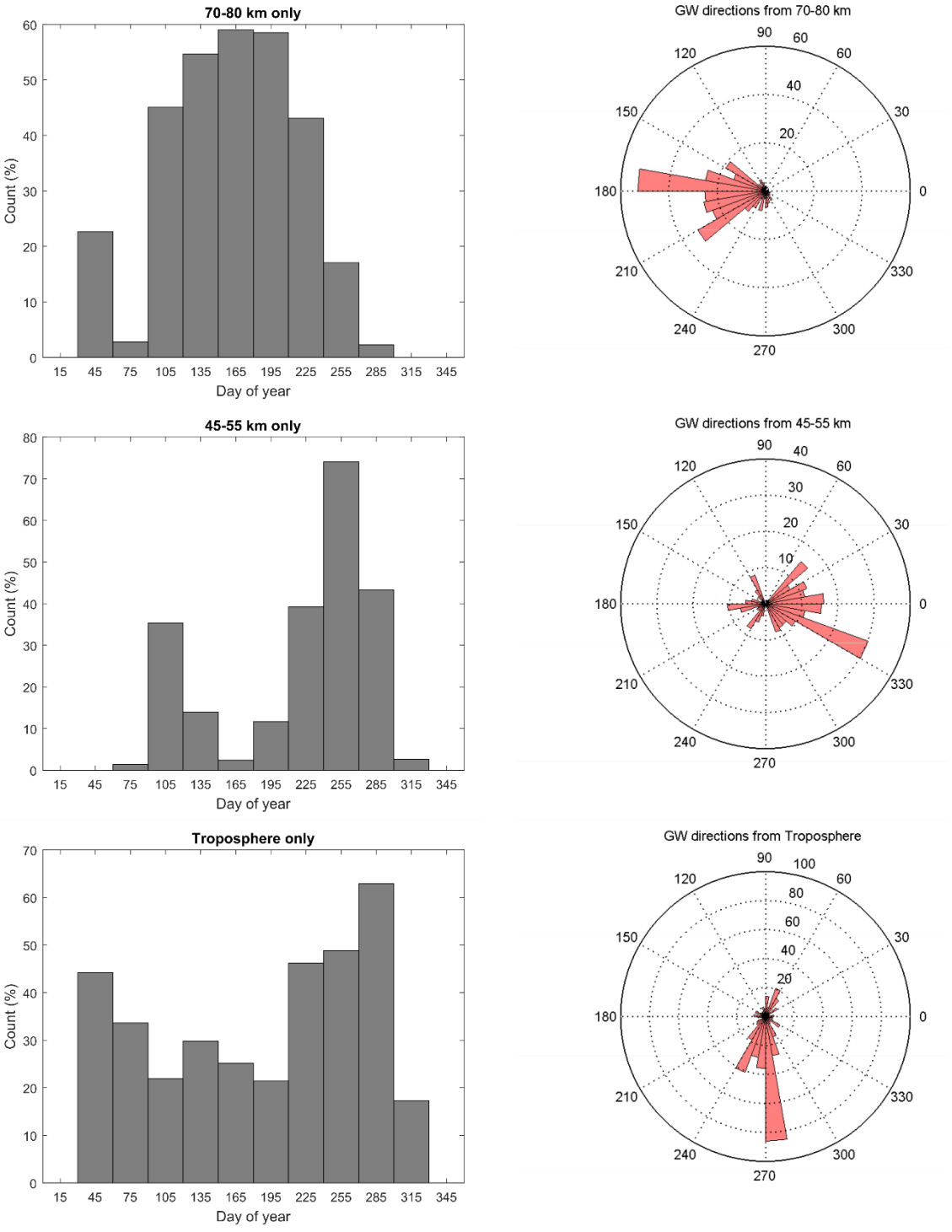

Figure 4.8: Seasonal and directional distribution of the GWs for three populations selected according to the altitude that the reverse ray-tracing terminated. The groups terminated in the troposphere (lower two panels), at an altitude range of 45−55 km (middle panels), and at an altitude range of 70−80 km (upper panels). Counts are given as the time in which wave events were detected as a percentage of the total observing time in that particular month, scaled up by a factor of 500 (*Rourke et al.*, 2017).

4.6. Discussion

Through reverse ray-tracing 15 years of GW observations over Davis Station, four distinct groups of waves have been identified, classified by their termination altitudes, as follows: those (45% of waves observed) which could not be substantially traced beyond their observation altitude (~87 km), those (15% of waves observed) which originated in the 70−80 km altitude range, those (9.5% of waves observed) which originated in the 45−55 km altitude range, and those (15% of waves observed) which originated in the troposphere, at altitudes ≤10 km. These groups, which were identified in Figure 4.5(c), have been shown separately in Figure 4.7 and Figure 4.8.

Figure 4.8 shows a distinct zonal and meridional anisotropy of the observed propagation directions which is dependent on the source altitude. The majority of the eastward propagating waves observed belong to the 45−55 km source region, the westward propagating waves belong to the 70−80 km (and partly the 45-55 km) source region, and the southward propagating waves belong to the tropospheric source region. Since the eastward propagating waves do not tend to have tropospheric sources, critical level filtering of waves (propagating upward from the troposphere and being blocked by the polar stratospheric jet) is not responsible for the zonal anisotropy in the observed propagation directions. In fact, it appears more likely that the zonal anisotropy is produced by an imbalance in the polar jet, as was found to be the case in previous studies (*e.g. Suzuki et al.* (2013); *Tateno and Sato* (2008)) and suggested by other studies (*e.g. Alexander et al.* (2011); *Sato et al.* (2009)). This is further supported by the seasonal variation of the zonal anisotropy, where there is a strong westward lobe in autumn (corresponding to the formation of the polar vortex) and a strong eastward lobe in spring (corresponding to the break-down of the polar vortex). In addition, the waves originating at 45−55 km (the altitude of the polar jet) have two large seasonal peaks in April (autumn) and

September (spring) propagating predominantly westward and eastward respectively.

The geographical sources of the observed waves are shown in Figure 4.7, and are again characterised into groups based on their source altitude. Most of the observed waves originated within approximately 300 km of the station. It was found that one region dense in GW sources was in the troposphere, approximately 100−200 km north-west of the station. A possible explanation for these waves could be the interaction of planetary waves with the background tropospheric winds, as was the case for short-period mesospheric GWs observed at South Pole Station (*Mehta et al.*, 2017). This has not yet been investigated for the GWs observed at Davis Station.

The most likely explanation for the group of waves traced to the 45-55 km region (in the vicinity of the very strong polar jet) appears to be GW generation due to instabilities in the polar jet (*e.g. Mehta et al.* (2017); *Alexander et al.* (2011); *Tateno* and *Sato* (2008)), since most of these waves were generated either directly to the east or west of the station, were propagating either eastward or westward at the observation altitude, and occurred during the formation and break-down of the polar vortex. The large majority of the waves generated between 70 and 80 km altitude had local origins directly to the east of the station and tended to be propagating westward at the altitude of detection, but the mechanism by which they were generated is currently unknown.

4.7. Conclusions and Future Work

A simple reverse ray-tracing program, based on the equations outlined in section 4.2, was developed using MATLAB software and tested using GROGRAT and results from *Pramitha et al.* (2014). This software was used to determine both the altitudinal and geographical origin of GWs observed at Davis Station during the period 1999-2013. Based on the results, four main groups of GW sources

have been identified in the vicinity of the station, and the characteristics and properties of the waves associated with each these groups have been examined.

Those waves which could not be ray-traced significantly below their observing altitude are tentatively suggested as evanescent waves or waves ducted from other locations. This means that they may have sources at very large horizontal distances from Davis Station, which cannot be quantified through the ray-tracing technique used. The group which originated between 70 and 80 km altitude were locally generated to the east of the station in mid-winter. The group which originated near the polar vortex (45−55 km) were generated to the east and west of the station and corresponded to the timing of the break-down and formation of the polar vortex respectively. Finally, the group which propagated all the way up from the troposphere had a pronounced concentration of wave sources ∼100−200 km north-west of the station, and were propagating predominantly southward at the observation altitude. The percentage of this latter group of waves (∼15% of the total number of observed GWs) is quite low in comparison with previous published reports and suggests that the majority of the GWs observed are generated above the polar jet, *i.e.* there is not a huge transfer from the troposphere to the mesopause region at Davis Station compared to other places on the planet. This is not unexpected since the terrain in the vicinity of Davis Station is not such as to produce GWs, even though there is a strong prevailing wind at the station.

Future work here includes further investigation on the interaction of planetary waves with background wind, and tropospheric sources in general. Additionally, an improvement of the background atmospheric field (U , V , and T) from climatological to re-analysis data may produce more condition-specific results, which would be especially important when dealing with individual case studies.

5. MESOSPHERIC FRONTS

5.1. Introduction

Up until this point, the UWOSCR data as a whole has been examined in order to produce a climatology of gravity waves and ripples over the station. Now, in this chapter, case studies of five ducted frontal events are presented which have been found within the dataset. In addition to these five case studies, up to 278 potential (unverified) frontal events are surveyed and five of these events are examined in detail. Although frontal events were briefly introduced in section 1.6.3, this chapter begins with detail specific to mesospheric fronts.

The two most common examples of fronts are known as walls and bores. A mesospheric bore can be described as a well-defined, large-scale, high-amplitude leading edge of a structural feature which may be observed in airglow emission (*e.g.* broadband OH* or OI (557.7 nm)) as a sudden (step-like) enhancement or depletion. It may be followed by one or more trailing wave-like oscillations which are phase-locked to the leading front and significantly smaller in amplitude (*e.g. Taylor et al.* (1995)*; Bageston et al.* (2011); *Brown et al.* (2004); *Dewan* and *Picard* (2001); *Medeiros et al.* (2005)). Walls are fronts which are well-defined on both the leading edge and the trailing edge (*Brown et al.*, 2004), and may also be followed by trailing oscillations (*Swenson* and *Espy*, 1995). An example of a 'spectacular' bore event, observed in both the OH* and OI airglow emission layers, is shown in Figure 5.1.

In order for the travelling disturbances of fronts to be maintained at large spatial scales in the airglow emission, they must be trapped (or 'ducted') in the vertical direction (*e.g. Walterscheid et al.* (2012); *Dewan* and *Picard* (1998)) in a region of enhanced stability. This means that, since they propagate horizontally only, the vertical momentum and energy fluxes of fronts should, ideally, be zero. In reality, very few disturbances are ideally ducted, and so

they have small vertical momentum and energy fluxes that alternate up/down as the wave packet "bounces" between reflective boundaries (*e.g. Snively et al.* (2013); *Friedman* (1966)).

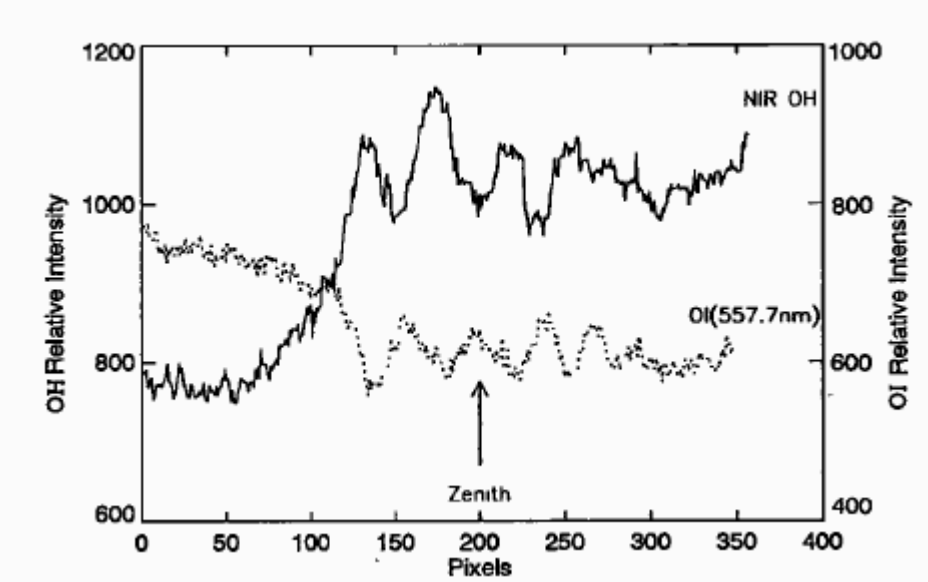

Figure 5.1: A sharp intensity increase (decrease), followed by wave-like oscillations, observed in the OH* (OI) airglow emission as a spectacular bore event passes through the emission layers. The image shows the relative intensity scan across the camera field normal to the wave crests. The wavelength corresponds to approximately 19 km (*Taylor et al.*, 1995).

It is useful to think of ducted waves in terms of optics where, if the refractive index of a medium is changed, a light beam propagating through this change will be partially reflected. In the atmosphere, a similar situation occurs with GWs when the vertical wavenumber changes. An abrupt change in Brunt-Väisälä frequency or background wind speed at a particular altitude can cause an abrupt change in the local vertical wavenumber, and can consequently cause GWs to be reflected. If the distance between two of such reflecting levels is a multiple of the GW's vertical wavelength, then the reflected and incident waves can constructively interfere, causing wave resonance. This is called a ducted wave, where the ducting layer acts as a waveguide (*Nappo*, 2002). Therefore, one way to find out whether a wave is ducted is to calculate the vertical wavenumber, m, of the wave for a range of altitudes, as one can then determine whether that wave can exist at different altitudes under the particular

background conditions. If m^2 is greater than zero, the wave can exist and propagate freely at that point and if m^2 is less than zero it cannot. This means that, within the duct, $m^2 > 0$ but, both above and below the duct, $m^2 < 0$, as shown in Figure 5.2.

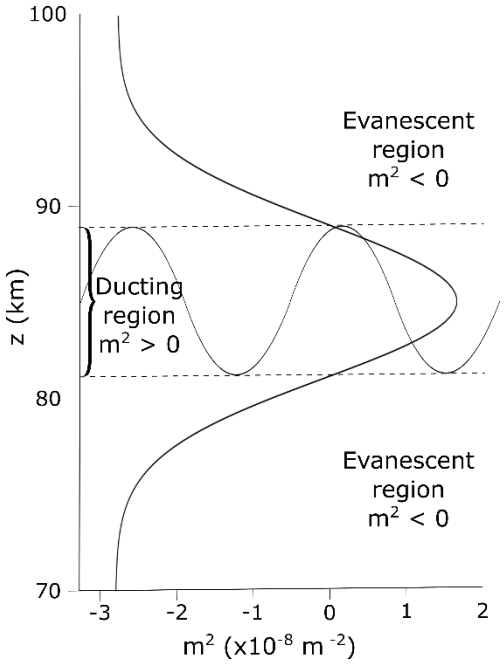

Figure 5.2: Schematic showing a ducted wave.

The vertical wavenumber squared, m^2, can be calculated from the Taylor-Goldstein equation, the wave equation for GWs, which is given by Equation B.1 in Appendix B.1. A solution to the Taylor-Goldstein equation is given by the dispersion relation in Equation 5.1. This solution assumes that the background wind and Brunt-Väisälä frequency vary slowly over a wave cycle in the vertical direction (*i.e.* the WKB approximation, as described in Appendix B.7) and so the shear term can be ignored.

$$m^2 = \frac{N^2}{(c-\bar{u}_k)^2} - \frac{\bar{u}_k{}''}{\bar{u}_k - c} - k^2 - \frac{1}{4H^2} \qquad 5.1$$

(*e.g. Bageston et al.* (2011); *Nappo* (2002); *Fritts* and *Yuan* (1989)).

Fritts and *Yuan* (1989) stated that the term depending on curvature of mean velocity profile $\left(\frac{\bar{u}_k''}{\bar{u}_k - c}\right)$ is so small in most cases of interest that m^2 depends

primarily on the other terms, and so the dispersion relation is often written as $m^2 = \frac{N^2}{(c-\bar{u}_k)^2} - k^2 - \frac{1}{4H^2}$ (*e.g. Pautet et al.* (2018); *Walterscheid et al.* (2012)).

As mentioned already, if $m^2 < 0$ waves are external/evanescent (no vertical propagation). This happens if:

- $(\bar{u}_k - c)$ is large, meaning that the wind is opposed to the GW propagation direction,
- k^2 is large, meaning that horizontal wavelength is small,
- $\frac{1}{4H^2}$ is large, meaning that scale height is small and hence static stability is low.

Within the duct, conditions will be opposite ($m^2 > 0$, meaning that the wave is internal) so that the wave can propagate vertically within the duct (*Walterscheid et al.*, 2012).

Background temperature and wind have a huge effect on the calculation of m^2 via the terms N^2 and $\bar{u}_k$ respectively. A duct which is created by a temperature inversion, *i.e.* a discontinuity in the temperature lapse rate, is called a thermal duct, whereas a duct which is created by wind in the direction of wave propagation is called a Doppler duct. Although these distinctions provide information about the cause of the duct, *Fritts* and *Yuan* (1989) noted that there is no reason to distinguish between a thermal, Doppler, or mixed duct (except that a thermal duct can support a wave travelling in any direction whereas a Doppler duct is sensitive to the wave propagation direction) because vertical propagation of the wave depends only on m and its variations. Thermal ducts appear to be the more dominant of the two ducting mechanisms in the mesosphere (*e.g. Pautet et al.* (2018)) as they are longer-lived (persisting up to several days) and they can extend over very large regions.

A temperature inversion in the mesosphere is known as a Mesospheric Inversion Layer (MIL). It is defined as a layer of increasing temperature in the mesosphere. These layers can be approximately 2-10 km in depth, and can have a local temperature maximum which exceeds the background mean temperature by more than $20-50$ K. MILs are frequent and often persistent, but their characteristics exhibit an annual variation. In particular, MILs at high- to mid-latitudes have a maxima in winter (*Fritts et al.*, 2017a). The relationship between MILs, GWs and turbulence has not yet been resolved, and so it is unknown whether GWs and turbulence cause, or are caused by, MILs (*Fritts et al.*, 2017c).

Although ducting (due to, for example, temperature or wind inversions) is a common phenomenon in the lower atmosphere (*Dewan* and *Picard*, 2001) and at low- to mid-latitudes (*e.g. Taylor et al.* (1995); *Walterscheid et al.* (2012) and references therein), very little evidence exists for well-defined thermal or Doppler (*i.e.* due to wind) ducts between 80 and 100 km at high latitudes. For example, just 5% of observed waves at Halley Station, Antarctica during the period 2000-2001 were found to be Doppler ducted due to relatively weak wind flow within the MLT at high latitudes (*Snively et al.*, 2013). Since local ducting is a physical requirement for bores to exist (*Dewan* and *Picard*, 1998), these frontal events are very rarely observed in the MLT at high latitudes (*e.g. Bageston et al.* (2011); *Pautet et al.* (2018)). In view of the paucity of such events and the substantial length of the Davis dataset, it was considered worthwhile to examine the data for evidence of ducted mesospheric fronts. The following sections detail this investigation.

5.2. Method

In order to calculate m^2 using Equation 5.1, background conditions (wind and temperature) at the approximate time and location of each wave observed by UWOSCR were used.

The winds used in this chapter (to create the m^2 profiles) are hourly-averaged values of meridional and zonal winds available at 10 second intervals from a co-located MF radar (described in section 1.7.1.1). At times, wind data is rejected if it does not pass the data quality check performed by the Australian Antarctic Division, and so there is missing wind data at those times (usually at particular altitudes only). When this occurs, twice as many $\bar{u}_k''$ values (and consequently m^2 values) can not be calculated. Any missing m^2 values on the plots shown in section 5.3 are as a result of this missing wind data.

Background temperature profiles were retrieved from SABER satellite data. SABER (Sounding of the Atmosphere using Broadband Radiometry) is one of four instruments on-board NASA's TIMED (Thermosphere Ionosphere Mesosphere Energetics Dynamics) satellite, which was launched in December 2001 and is still in operation. SABER performs global measurements of the atmosphere using a 10-channel broadband limb-scanning infrared (1.27−17 μm) radiometer, providing (amongst other variables) vertical profiles of temperature and OH* volume emission rate (VER). The selection criteria applied to the temperature profiles were that they must be within 15° longitude and 5° latitude (*i.e.* within less than ~883.5 km) of Davis Station. These selection criteria were chosen based on temperature profile distances used in other frontal event studies (*e.g. Bageston et al.* (2011); *Giongo et al.* (2018)). If there were multiple of such profiles for a particular wave event, then the one at the closest possible time to the time of the wave observation was used. Unfortunately, none of the SABER profiles during the months February, June, or October, or during the year 2013 fell within the selection criteria. This is due to the yaw manoeuvre cycle (which occurs once every 60 days) of the TIMED satellite, and is well-illustrated in Figure 8 of *Baker et al.* (2007). In addition, SABER data is only available from the year 2002 onwards.

In the case of missing SABER data, temperature data (available from 2004 onward) from the MLS (Microwave Limb Sounder) instrument on-board

NASA's Aura satellite was used. The MLS instrument measures oxygen thermal emission, which can then be used to determine temperature between approximately 9 and 90 km altitude. Since the upper boundary of this dataset is close to the mesopause region, the data is smoothed in this region and so it is not ideal for our purposes. However, after going through all of the February, June, October, and 2013 data, there were only 10 events which had a sudden large increase/decrease in intensity, which were clearly visible in the UWOSCR images, and which were detected as a wave using the 15 m/s post-processing standard deviation limit (described in section 2.6). From these ten waves, only seven had corresponding wind data and, and using the MLS temperature data, none of the remaining seven waves had an m^2 duct.

Using a table of m^2 versus altitude (from 70−100 km) for each wave, it could be determined which waves were trapped in a vertical duct. By examining the temperature and wind profiles, it could also be determined whether the duct was created due to temperature or wind conditions. This is illustrated in Figure 5.3 for clarity.

To summarise the possible methods of detection of mesospheric fronts, *Dewan* and *Picard* (2001) compiled a list of eight requirements for their identification. These requirements are:

1. The front must separate light and dark regions in the airglow emission.
2. Undular bores must be followed by waves which are phase-locked to the leading front. However, there may be no trailing waves behind non-undular bores.
3. The bore must be ducted vertically by a wind and/or temperature inversion.
4. Complementary features may be observed in different airglow layers.
5. Bore velocity and wavelength should obey $U^2 = g' \frac{h_1(h_1+h_0)}{2h_0}$ and $kh_1 = 3\sqrt{\frac{h_1-h_0}{2h_0}}$, where U is the phase velocity of the bore, g' is the

buoyant acceleration due to gravity, h_1 is the depth of the duct, $h_1 - h_0$ is the depth (amplitude) of the bore, and k is the wavenumber of the bore's trailing oscillations (if they exist).

6. Change in temperature across the front should be approximately equal to $(h_1 - h_0) \times 10$ K km^{-1}.
7. The number of trailing waves associated with an undular bore should increase gradually over time.
8. The presence of bores may be linked with the presence of strong GW sources.

For the detection of mesospheric fronts presented in this thesis, requirements 1 and 3 were used (similar to, *e.g.*, *Carvalho et al.* (2017)). Points 2, 7, and 8 were not associated with all mesospheric frontal events and so were not used as requirements. The remaining requirements were simply not possible to check given the data available. For requirement number 4, this was because there was no complementary airglow emission data available at Davis Station, while requirement numbers 5 and 6 could not be validated due to the lack of wave amplitude information. This is because UWOSCR measures intensity in arbitrary units, and so the absolute amplitude of the fronts could not be calculated.

In relation to requirement 6, it was possible to check if there was a temperature change associated with the front by using co-located Czerny-Turner spectrometer data (details of which are provided in, *e.g.*, *French* and *Mulligan* (2010)), but as described above, it was not possible to quantify the temperature change with respect to the amplitude of the front. The Czerny-Turner spectrometer measures OH* temperatures, and its data is available for the full period 2002-2012 (*i.e.* the period during which SABER data is also available). Unfortunately, at the time of writing this thesis, only data for the years 2008-2012 (along with two case study nights in 2005 and 2006) had been transferred

to the author and hence these are the only years which were checked to date for large temperature changes.

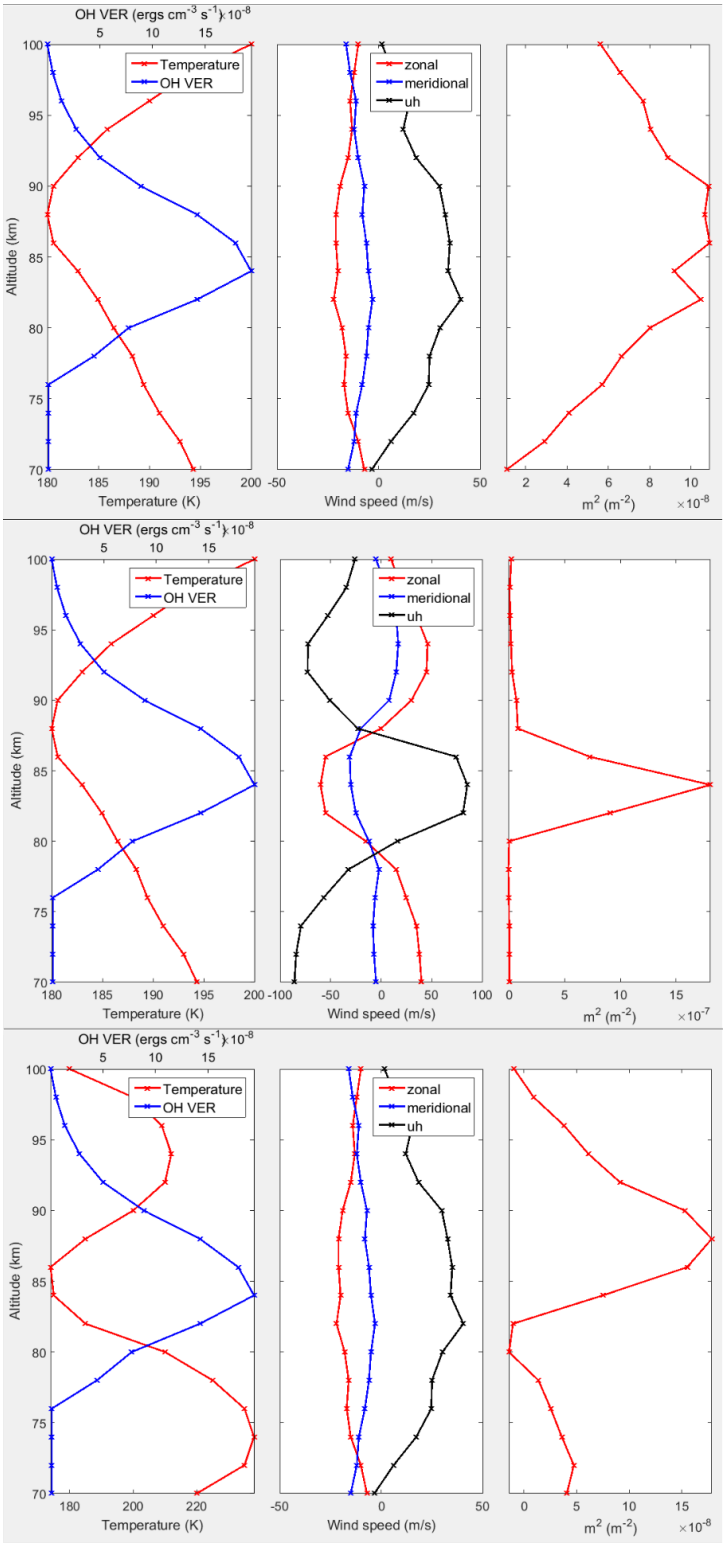

Figure 5.3: A schematic showing the difference between (top) no duct (freely propagating wave), (middle) a Doppler duct (in the ~80−88 km altitude range), and (bottom) a thermal duct (in the ~82−98 km altitude range) for a wave propagating north-westward (120° north of east) at a speed of 100 m/s with a wavelength of 35 km.

A final requirement for mesospheric fronts is that they must have large spatial scales (*e.g. Brown et al.* (2004)). This poses a problem for UWOSCR, whose FOV is too narrow to tell if a particular ducted bright/dark 'wave' was a front. Therefore, images from a co-located all-sky OH* airglow camera, operated by Utah State University (USU) since 2012, were used to confirm the presence of several fronts during 2012 (when both SABER and USU data were available). In all other cases, it could not be verified whether a front was really present.

5.3. Results

The results for this chapter are split into two main sections. Section 5.3.1 deals with some case studies of mesospheric fronts in 2012 which have been verified by the USU all-sky camera. Section 5.3.2 provides a summary of all waves which have reached a specific threshold in intensity change and which are ducted. It has not been possible to verify if the waves reported in section 5.3.2 are mesospheric fronts due to the small FOV of UWOSCR and lack of complementary all-sky data during the period 1999-2011. There is a possibility that some of these fronts may be, in later work, verified by an all-sky auroral imager system (which is sensitive to both the aurora and to the OI 557.7 nm emission centred at approximately 97 km altitude) which was in operation at Davis Station during the period 2002-2011. This will only be possible for fronts which are trapped in a duct which incorporates the peak emission of both the OH* and OI airglow layers. Five of the potential (unverified) frontal events are also examined in section 5.3.2 to the same level of detail as the five verified events, as they appeared to be particularly good candidates for fronts. The confidence in two of five of these potential events was subsequently improved upon inspection of the Czerny-Turner spectrometer data.

5.3.1. Verified Frontal Events during 2012

Table 5.1 shows the wave characteristics and ray-tracing results for five waves observed using UWOSCR which could be compared to fronts observed by the USU all-sky camera located at Davis Station. These wave characteristics were

calculated using the analysis method ('`UWO_exe`') described in Chapter 2. When performing post-processing on these waves, the limit on standard deviation of five consecutive values of the zonal and meridional velocities (described in section 2.6) was increased to L=15 m/s. This was because waves 2−4, shown below in Table 5.1, were not detected for their full duration when the limit was set to L=7 m/s. This appeared to be due to a slow change in wave crest direction for the second wave, some overlapping features within the FOV for the third wave, and two structures (ripples and a front) simultaneously with the FOV for the fourth wave. The first wave shown was not detected at all with the limit set to 7 m/s, but was detected in full when it was set to 9 m/s. This may imply that our previously chosen standard deviation limit of 7 m/s is too strict, causing some real waves to be omitted from the results (as discussed in section 2.6).

Date	**UT (hours)**	**θ (°N of E)**	**C_o (m/s)**	**T (min.)**	**λ_h (km)**	**Persistence (min.)**	**Source longitude (°E)**	**Source latitude (°N)**	**Source altitude (km)**
14/07/12	0.503	58.3	85	12.5	63	12	77.7	-68.74	72.8
14/07/12	2.693	354	62	8.5	32	15	78.0	-68.58	86.9
09/08/12	1.053	14	68	6.3	26	9	78.0	-68.58	87.0
10/08/12	16.408	125	49	12.2	36	7	78.4	-68.70	72.4
11/08/12	0.028	32	65	2.8	11	21	78.0	-68.57	87.0

Table 5.1: Wave characteristics of five frontal events which were observed by both UWOSCR and the Utah State University all-sky camera.

It can be seen from Table 5.1 that the first two waves constitute a 'double bore event', a phenomenon which has been previously observed in the mesosphere by *Smith et al.* (2017) for example. One of these (the second one) will be shown in this chapter, along with the 4th event shown in Table 5.1. The remaining case studies from Table 5.1 are included in Appendix E.1 for completeness.

Case 2 from Table 5.1 -

A bright bore detected between 02:42 and 02:56 UT on 14-Jul-2012:

Figure 5.4 and Figure 5.5 display a series of images showing the second detected front (part two of the double bore event), whose characteristics are shown in

Table 5.1, between 02:42 and 02:56 UT on 14th July 2012. This front was detected by the USU camera from approximately 02:00-02:54 UT (as shown in Figure 5.5) but didn't reach UWOSCR's FOV until approximately 02:44 UT (as shown in Figure 5.4), at which point it had grown quite faint. Although it may be difficult to distinguish from Figure 5.5, some faint ripples can be seen in the dark region before the leading front, similar to those observed in the first part of this double bore event (shown in Appendix E.1). There is also a trailing wave-like oscillation phase-locked to the front in this case.

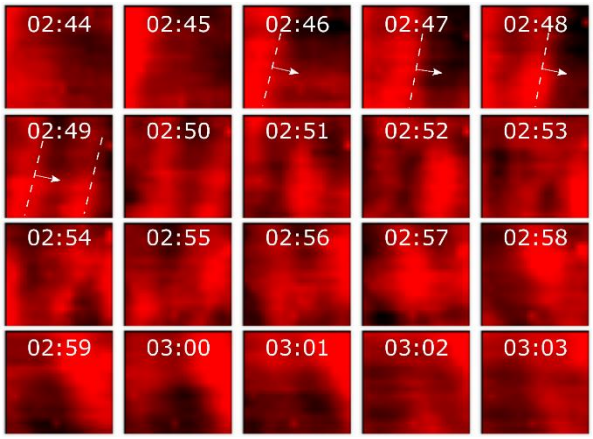

Figure 5.4: Sequence of UWOSCR images from 02:44-03:03 UT on 14th July 2012. White dashed lines have been added to some wave crests, along with an arrow indicating propagation direction, as a guide to the eye.

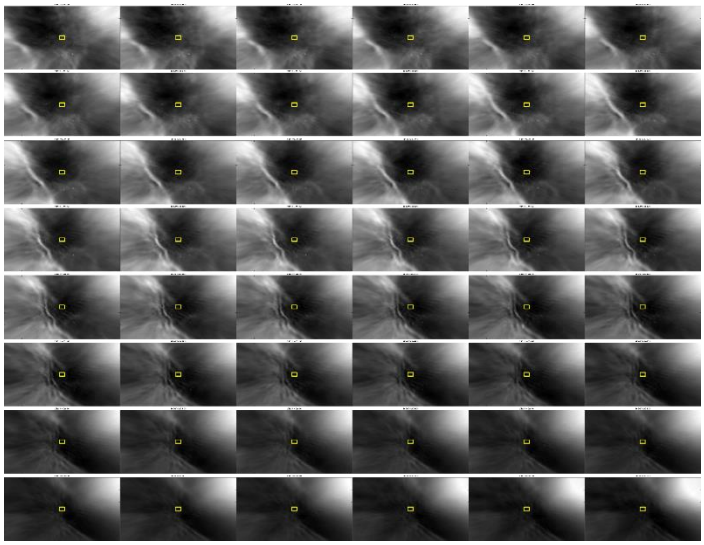

Figure 5.5: A series of images recorded by the USU camera between 02:07 and 02:54 UT on 14th July 2012. Images are arranged in chronological order from left to right and top to bottom. Each image corresponds to 480 km × 384 km at ~87 km altitude. The yellow boxes in each image corresponds to UWOSCR's FOV.

Manual analysis (*i.e.* with a ruler and protractor) of this front (using the UWOSCR images) gives an observed propagation direction of $\theta \approx 346^\circ \pm 10^\circ$ north of east, an observed phase speed of $v \approx 73 \pm 4$ m/s, and a horizontal wavelength (of the trailing wavelets) of $\lambda_h \approx 13 \pm 3$ km. This is in good agreement with the parameters calculated using the analysis method (shown in Table 5.1), except for the λ_h value, which may have been calculated incorrectly by the automated analysis due to the large intensity difference between the bright front and its trailing wavelets. With a shorter λ_h and higher v (to match the results from the manual analysis), the period of this front would be much shorter ($T \approx 3 \pm 1$ minutes).

The calculation of the m^2 profile at the closest possible time to the frontal event was performed as described in section 5.2 and the result is shown in Figure 5.6. Thermal inversions at altitudes of approximately 78 km and 92 km caused m^2 to become negative, thus creating reflective boundaries at these two levels. Between these two levels, there existed a deep (~14 km) thermal duct where the observed front could freely propagate. Within the ducting region, the wind was travelling very fast in the same direction as the wave (and no Doppler duct was present) and so this favoured GW propagation.

The intrinsic period of this particular front was 7.2 ± 1 minutes. Based on theoretical considerations, *Snively et al.* (2013) proposed that a thermal duct is likely when the intrinsic period is less than 7 minutes and that reflection at the base of the thermosphere is possible when the intrinsic period is between 7 and 10 minutes, especially if the horizontal wavelength is greater than 30 km. This boundary is shown in Figure 5.7, which is taken directly from *Snively et al.* (2013). The intrinsic period of this front is just on the border proposed by *Snively et al.* (2013) and, as shown in Figure 5.6 (left), a thermal duct is observed at the base of the thermosphere, in agreement with their proposal.

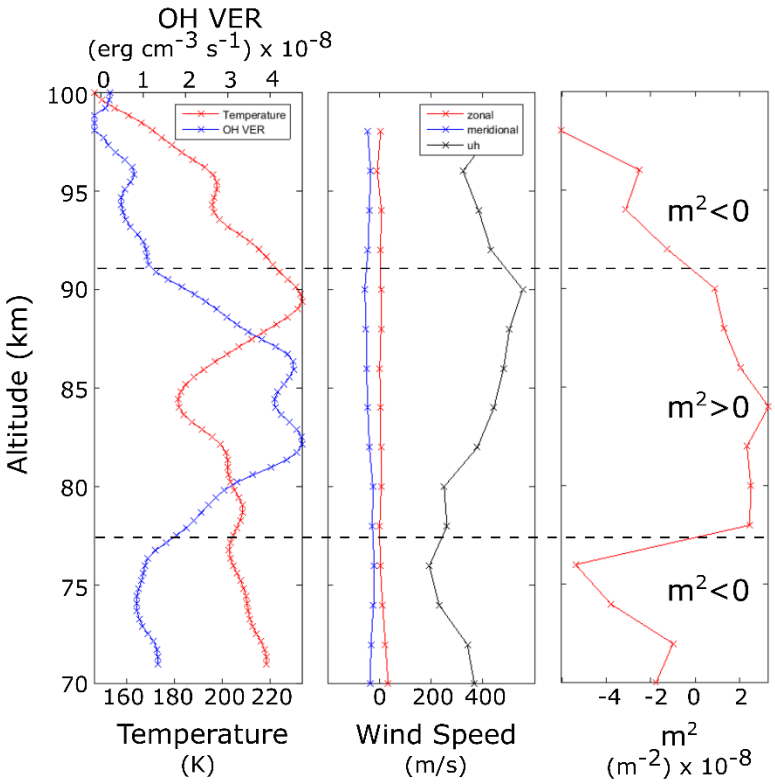

Figure 5.6: (left) Temperature profile (red) and OH* Volume Emission Rate (VER) profile (blue) calculated from an available SABER profile which was measured 2.7 hours after the frontal event and which corresponded to a region which was ~276 km north-west of Davis Station, (centre) hourly-averaged profiles of zonal wind (red), meridional wind (blue), and wind in the direction of the wave, u_h, (black) measured using the co-located MF radar, and (right) the vertical wavenumber squared (m^2) profile corresponding to the temperature and wind measurements. Dashed lines indicate where GWs can no longer propagate due to their m^2 value.

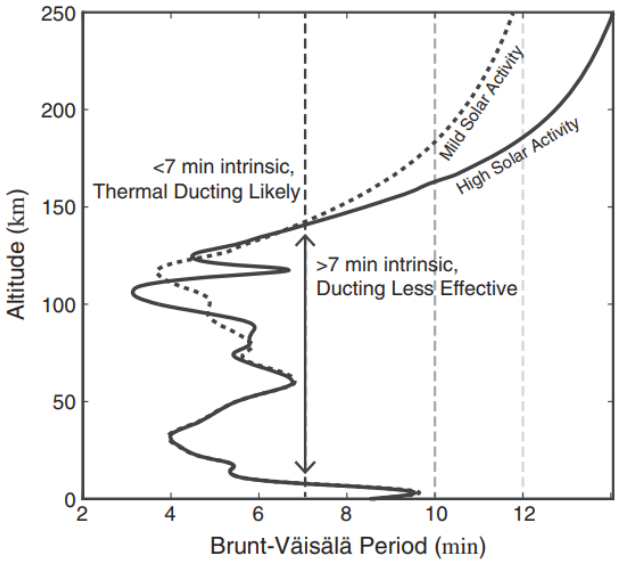

Figure 5.7: Emperical model buoyancy profiles, showing different regimes of propagation, approximated by divisions in intrinsic period (*Snively et al.*, 2013).

This front could not be ray-traced significantly below the mesopause region; the ray-tracing was terminated at 86.9 km altitude where it was estimated that intrinsic frequency ω = 0.0164 rad/s, the WKB parameter, δ = 2.71, m^2 = 8.92×10^{-9} rad^2/m^2, Richardson's number, R_i = 70.03, and N^2 = 3.82×10^{-4} rad^2/s^2. Thus, the condition for which the wave couldn't freely propagate further was that $\delta > 1$, meaning that shears in background wind flow were no longer negligible compared to shears generated by the wave. The interpretation of these ray-tracing results must be tempered with the knowledge that they were calculated using climatological background values for wind and temperature. Although they were very useful for a climatological study, they may not be accurate for a particular case study, as background conditions may vary significantly from the climatological conditions at a particular time. From the calculated m^2 profile at the closest possible time and location to the wave (shown in Figure 5.6 (right)), it can be seen that vertical propagation is possible down to approximately 78 km, where m^2 becomes less than zero. Therefore, it is likely that the front was observed in the OH* emission at its peak altitude (between ~82 and 86 km, where emission was greater than 4×10^{-8} ergs cm^{-3} s^{-1}), and that it was trapped vertically between approximately 78 and 92 km.

Finally, the Czerny-Turner spectrometer data plot for this night is shown in Figure 5.8. This plot (along with all Czerny-Turner spectrometer plots shown in this thesis) was generated by John French of the Australian Antarctic Division. From Figure 5.8, some complementary results are observed, including a large OH* temperature increase of ~ 40 K, OH* intensity increase of ~300−400 counts/second, a very high signal-to-noise ratio, and a clear sky. All of these measurements are consistent with the passage of a mesospheric front and they support the interpretation of the OH* airglow images.

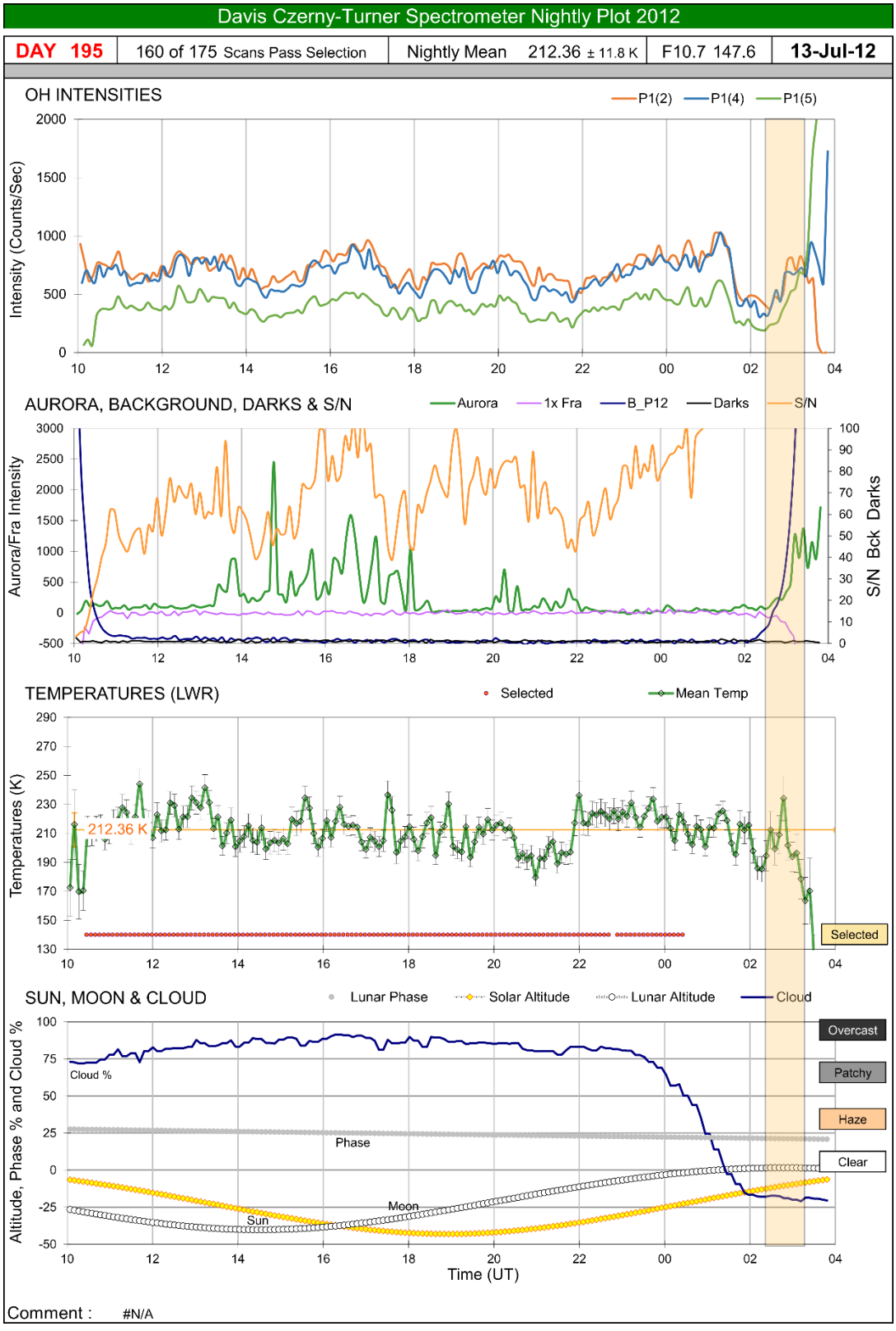

Figure 5.8: Czerny-Turner spectrometer data for the night of 13$^{\text{th}}$–14$^{\text{th}}$ July 2012. Time series of (top) rotationally-excited OH* intensities, (second from top) aurora, background signal, and signal-to-noise ratio, (second from bottom) OH* temperature, (bottom) cloud, moon and sun level, is shown, with highlighted times corresponding to the approximate time of the front.

Case 4 from Table 5.1 -

A dark bore detected between 16:24 and 16:30 UT on 10-Aug-2012:

Figure 5.9 displays a series of images between 16:03 and 16:38 UT on 10th August 2012, showing a very prominent front. This front was detected by the USU camera (shown in Figure 5.10) from approximately 16:00 UT but didn't reach UWOSCR's FOV until approximately 16:20 UT.

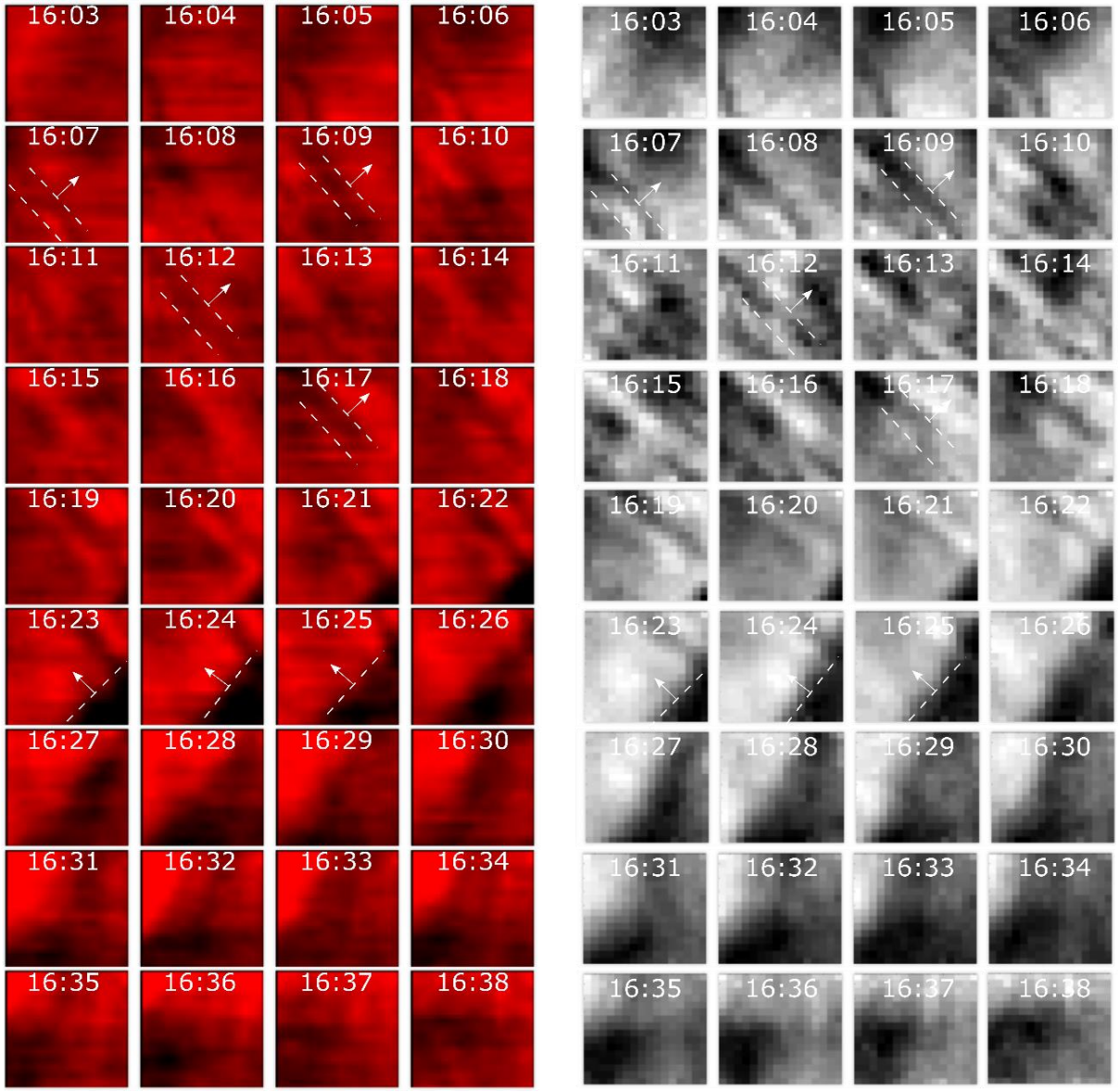

Figure 5.9: Sequence of (left) UWOSCR and (right) central portion of USU images from 16:03-16:38 UT on 10th August 2012, with ripples visible between 16:06 and 16:24 UT and a dark front moving across the FOV between 16:20 and 16:35 UT whose propagation direction is approximately perpendicular to the earlier ripples.

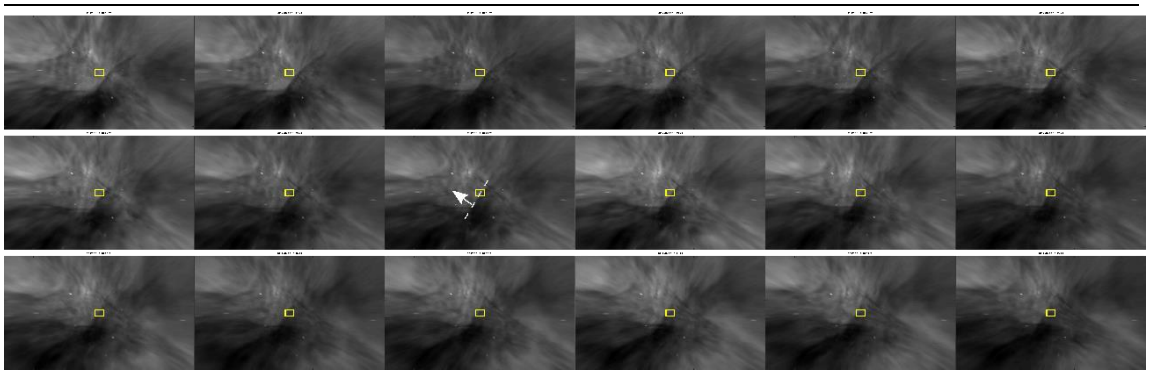

Figure 5.10: An enlarged view of a subset (between 16:16 and 16:33 UT) of the series of all-sky images recorded by the USU camera on 10th August 2012.

It can be seen from the sequences of images (in Figure 5.9) that the ripples between approximately 16:12 and 16:24 UT travel in a north-eastward direction, approximately perpendicular to the dark front. Although their origin is unknown, these types of small-scale structures, which propagate perpendicularly to the more widely spaced bands, have been often observed in the UWOSCR images and have also been reported in the past (*e.g. Garcia et al.* (1997); *Swenson* and *Mende* (1994); *Carvalho et al.* (2017); *Fritts et al.* (1993) and references therein). They are thought to be linked to convective instabilities (*e.g. Li et al.* (2017)).

Manual analysis of this front gives an observed propagation direction of $\theta \approx 139^{\circ} \pm 4^{\circ}$ north of east, an observed phase speed of $v \approx 23 \pm 3$ m/s. As there were no trailing wavelets associated with this front, the horizontal wavelength could not be calculated manually. The values produced by the automated analysis method for phase speed and propagation direction for this front may have been affected to some degree by the two wave-like structures (the ripples and the dark front) which were present in the FOV at the same time.

Figure 5.11 displays some UWOSCR intensity data near the time of the front using plots which are known as keograms. Keograms display intensity on a plot of longitude (*a.k.a.* an 'E-W keogram') or latitude (*a.k.a.* a 'N-S keogram') as a function of time. For the UWOSCR images, the central row of the image is

kept constant for the E-W keogram and the central column of the image is kept constant for the N-S keogram. Keograms are generally used to identify and measure the properties of large-scale waves that persist over a long period of time (*Taylor et al.*, 2009). It is essentially a quick way of searching a long series of images for GWs. From the two keograms in Figure 5.11, it is confirmed (between approximately 16.4 and 16.6 UT on 10$^{\text{th}}$ August 2012) that the front moves in a predominantly north-westward direction. This is in general agreement with the value produced by the analysis (125° north of east), shown in Table 5.1. The ripples which were observed before the front may also be seen in the keograms, travelling in an approximately perpendicular direction (north-eastward) to the dark front.

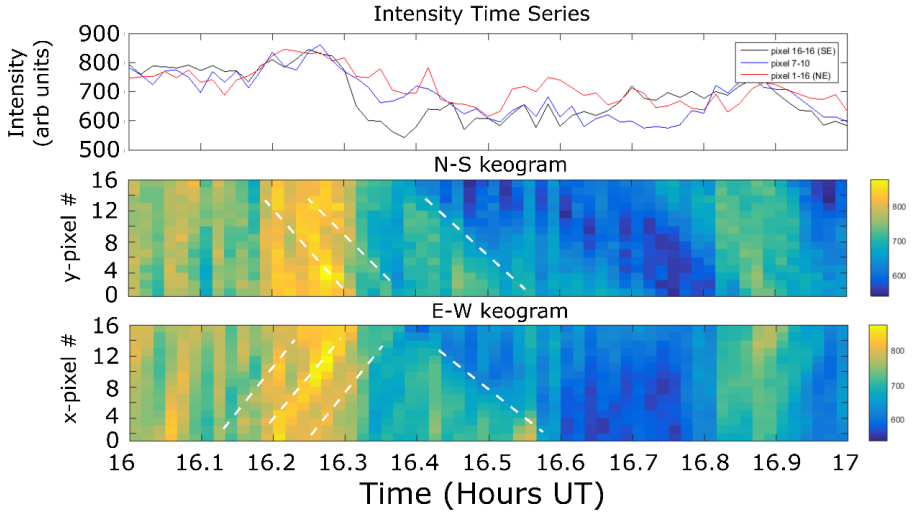

Figure 5.11: (top) Plot of the OH* intensity as a function of time at a number of different pixels (labelled X-Y where X is the no. of pixels down from the top of the image and Y is the no. of pixels across from the left of the image) in the UWOSCR image series between 16 and 17 UT on 10$^{\text{th}}$ August 2012, showing the the oscillation of the ripples and the subsequent rapid decrease in intensity (~40% in 5 minutes at a particular pixel) due to the dark front, (middle) keogram of the central column (north-south direction, where pixel 0 corresponds to north) of the UWOSCR images, and (bottom) keogram of the central row (east-west direction, where pixel 0 corresponds to west) of the UWOSCR images, where the colour corresponds to recorded intensity (in arbitrary units). The dashed lines indicate the front as a guide to the eye.

The resulting m^2 profile for this bore is shown in Figure 5.12. A thermal inversion at an altitude of approximately 98 km caused m^2 to become negative, thus creating a reflective boundary at this level. Throughout the altitude range

shown ($70-100$ km), winds are opposing the front's propagation direction, meaning that reflection should be at its most effective (*e.g. Snively et al.* (2013)). However, this Doppler inversion (which is also shown in Figure 5.13) did not cause m^2 to become negative, as it was possibly comparatively too weak to do so. Below approximately 76 km, there was not enough wind information to calculate m^2 and so a lower reflective boundary could not be determined.

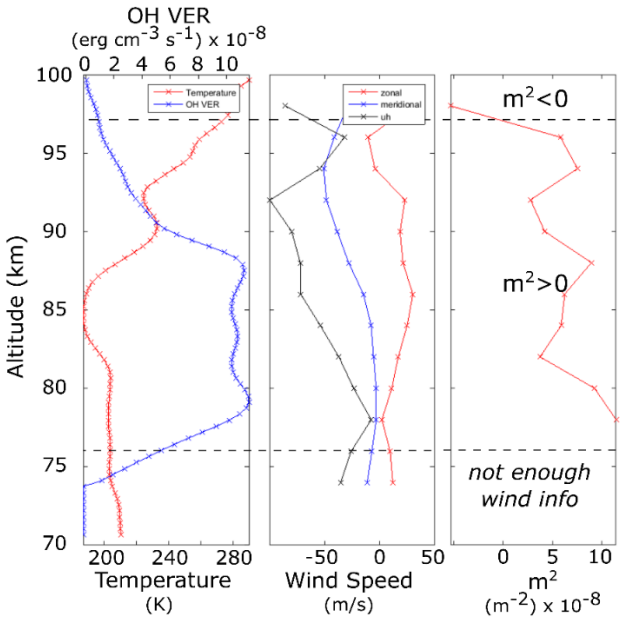

Figure 5.12: As in Figure 5.6, but now corresponding to case 4 of the verified fronts. The SABER profile used here was measured 48 minutes after the frontal event and corresponded to a region which was ~708 km south-west of Davis Station.

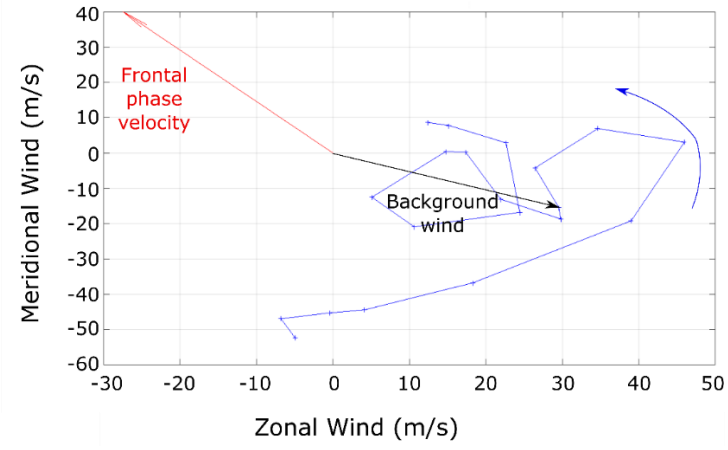

Figure 5.13: Hodograph indicating the phase velocity of the front (red) and the background wind at 86 km altitude at the time of observation of the front (black). Blue crosses indicate the background wind measurements (at 86 km altitude) in half-hour intervals before and after the frontal event. The blue arrow indicates the general change in background wind over time.

The intrinsic period of this particular front (7.5 ± 1 minutes) is just on the border proposed by *Snively et al.* (2013) between where thermal ducting is likely and where reflection at the base of the thermosphere is possible. In this case, both of these are true as reflection at the base of the thermosphere was created by a temperature inversion.

This front was ray-traced down to 72.4 km. At this altitude, intrinsic frequency ω = 0.0151 rad/s, δ = 1.03, m^2 = 1.40×10^{-8} rad^2/m^2, R_i = 38.9, and N^2 = 3.72×10^{-4} rad^2/s^2, and so the condition for which the wave couldn't propagate further at this altitude was that $\delta > 1$. At 72 km, though, there was no wind information available and so m^2 was not calculated at this altitude. From the calculated m^2 profile at the closest possible time and location to the wave, it can be seen that vertical propagation is possible up to approximately 98 km, where m^2 becomes less than zero. Therefore, the front appears to be trapped in a very large vertical duct from approximately 72 km up to approximately 98 km, between where there was a very wide range (~15 km) of very strong OH* emission ($>10^{-7}$ ergs cm^{-3} s^{-1}).

Czerny-Turner spectrometer data corresponding to the time of this front (shown in Figure 5.14) provided some complementary results, including an OH* temperature increase of ~20 K, a high signal-to-noise ratio, and a clear sky. From Figure 5.14, it may be seen that there was some auroral activity at this time, which reduces data confidence. Yet, this front was verified by the all-sky camera and it can be seen that the auroral peak was not visible within the FOV (in Figure 5.10 for example). It may be possible to conclude from this evidence that Figure 5.14 shows a false aurora detection - it could be a complementary peak in the OI (557.7 nm) emission at ~97 km. This seems especially likely since the front was ducted between ~72 and 98 km, which includes the emission peaks of both the OI and OH* airglow layers.

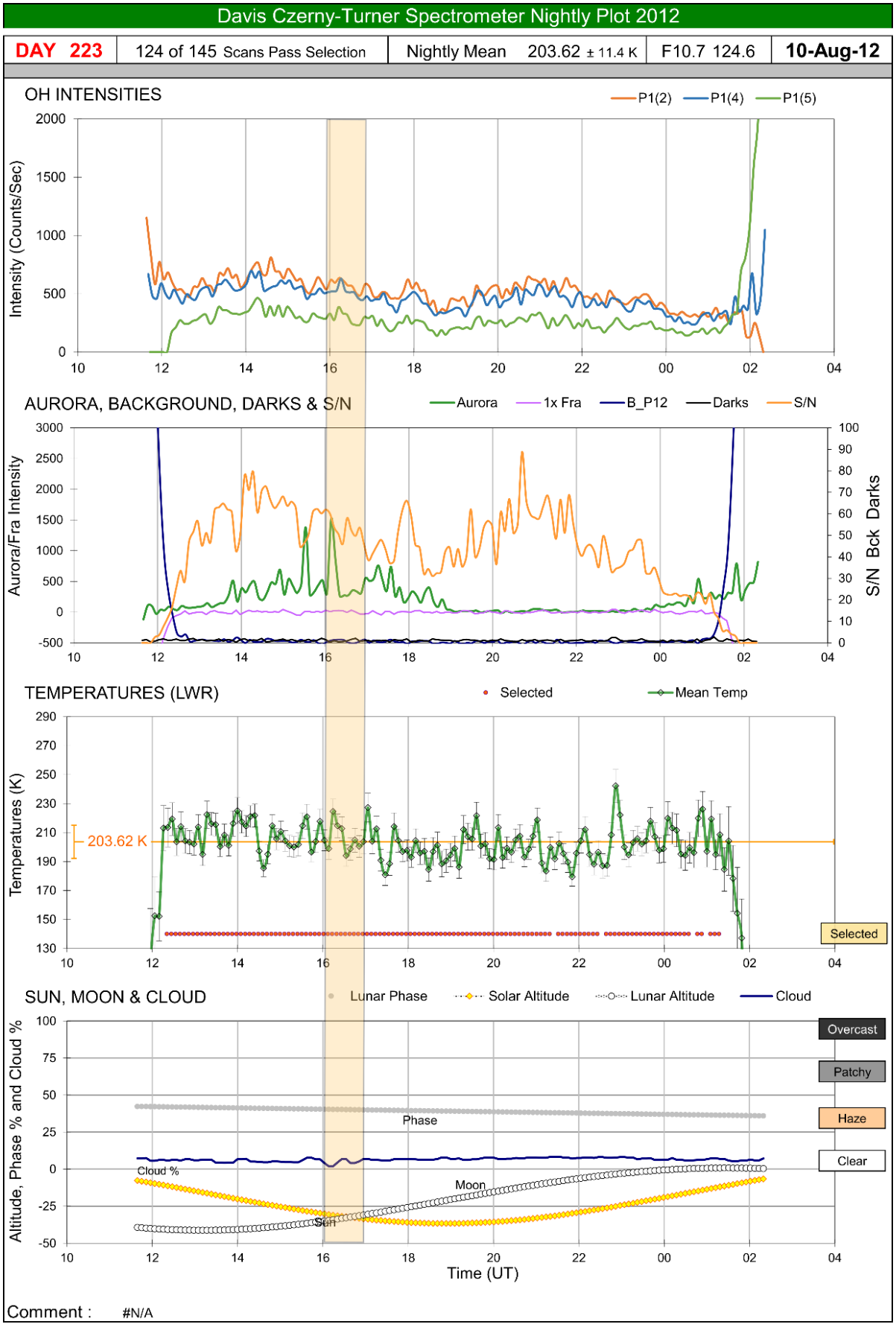

Figure 5.14: As in Figure 5.8 but for the night of 10th–11th August 2012.

5.3.2. Potential Frontal Events between 2002 and 2012

In this section, a survey of 278 potential frontal events observed during an 11-year period (2002−2012) is presented. Although these events have not been verified by all-sky data, they possess some of the attributes associated with fronts, thus they are referred to here as 'potential' frontal events. The majority of these events were observed in a ducting region anywhere between 70 and 100 km, and they were also associated with a sharp increase/decrease in intensity of the OH* emission.

Starting with the UWOSCR dataset between 1999 and 2013, it was immediately reduced to the years 2002-2012, based on the availability of temperature data which was satisfactory for the calculation of m^2 profiles. At this point, there were 4831 remaining waves (using the post-processing standard deviation limit of $L = 15$ m/s) to check for potential fronts. However, based on lack of availability of adequate temperature data (due to the TIMED satellite yaw cycle) during certain months (namely February, June, October, and November), this dataset was reduced by ~25% to 3635 waves. For each individual wave, two criteria were checked:

1. whether there was a large and sudden increase/decrease in brightness, and

2. whether the wave was ducted by temperature and/or wind inversions.

Criterion 1 was checked using keograms. Whenever a sudden large increase or decrease appeared in the keograms, then that wave was passed on to the next stage for further investigation. Future work here, involving an automated criterion for a minimum intensity change in a maximum time, will be important to reduce the subjective nature of this check. Nevertheless, the initial work presented here will be useful when developing the new automated system, as it will help determine a reasonable fixed setting for the minimum intensity change and maximum time in which that change occurs. If the event passed the first

criterion, it was passed on to criterion 2, where the vertical wavenumber squared profile for each wave between 70 and 100 km was calculated as described in section 5.2. The event was accepted as a potential front if it was trapped in a duct, or if it could possibly be trapped in a duct and it was not possible to tell due to lack of data below 70 km or if some wind data was missing. The number of potential events observed using this method during the period $2002-2012$ was 278. This provides an indicator of how prevalent mesospheric fronts are within the dataset, and it corresponds to 7.6% of the eligible 3635 wave events observed during the 11-year period (which excludes the austral summer period). For comparison, *Pautet et al.* (2018) observed 86 events during 4 austral winters at South Pole Station, which is a similar rate (~22 events/year) to our potential rate observed (~25 events/year).

First, in section 5.3.2.1, details related to five individual case studies which appeared to be particularly strong candidates for frontal events are presented, followed by a survey of all potential fronts in section 5.3.2.2. Interpretation of these results must be tempered with the knowledge that they may not all be actual frontal events due to the narrow FOV of UWOSCR and the slightly subjective nature of their selection. However, since a large number of events are being summarised, some trends presented may be characteristic of frontal events at Davis Station.

5.3.2.1. Case Studies of Potential Frontal Events

Table 5.2 shows the wave characteristics and ray-tracing results for five potential frontal events observed using UWOSCR. As in the previous section, these wave characteristics were calculated using the `UWO_exe` analysis method described in Chapter 2 and the post-processing limit on standard deviation of five consecutive values of the zonal and meridional velocities was set to L=15 m/s. From Table 5.2, it can be seen that the second and third waves constitute a double bore event. In this section, case studies 1 and 4 will be shown, but again the remaining case studies are included in Appendix E.2 for completeness.

Date	UT (hours)	θ (°N of E)	C_o (m/s)	T (min.)	λ_h (km)	Persistence (min.)	Source longitude (°E)	Source latitude (°N)	Source altitude (km)
16/09/05	23.16	183	73	6.2	27	7	77.97	-68.58	87
10/07/06	21.16	198	85	7.4	38	6	77.97	-68.58	86.97
10/07/06	21.58	164	92	8.4	47	5	77.97	-68.58	87
07/07/08	0.00	183	52	13.6	43	24	78.56	-68.50	71.35
13/08/11	16.695	172	44	9.4	25	14	77.97	-68.58	87

Table 5.2: Wave characteristics of five potential frontal events which were observed by UWOSCR.

Case 1 from Table 5.2 -

A potential bright wall detected between 23:10 and 23:16 UT on 16-Sept-2005:

Figure 5.15 displays a series of images showing the first potential (unverified) front whose characteristics are shown in Table 5.2, between 23:10 and 23:16 UT on 16th September 2005. No wave-like structures are phase-locked to the front in this case, and it has well-defined edges on both the leading edge and the trailing edge, making it a likely candidate for a wall event.

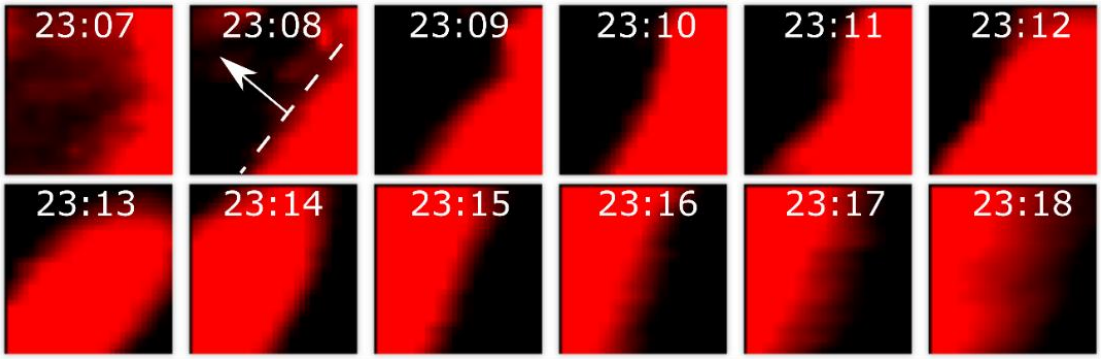

Figure 5.15: A series of images recorded by UWOSCR between 23:07 and 23:18 UT on 16th September 2005. The dashed line indicates the leading front and the arrow indicates the direction of propagation.

From the two keograms in Figure 5.16, it is confirmed (between approximately 23:00 and 23:18 UT on 16th September 2005) that the front and its trailing waves move in a predominantly westward direction. This is in agreement with the value produced by the analysis (183° north of east), shown in Table 5.2.

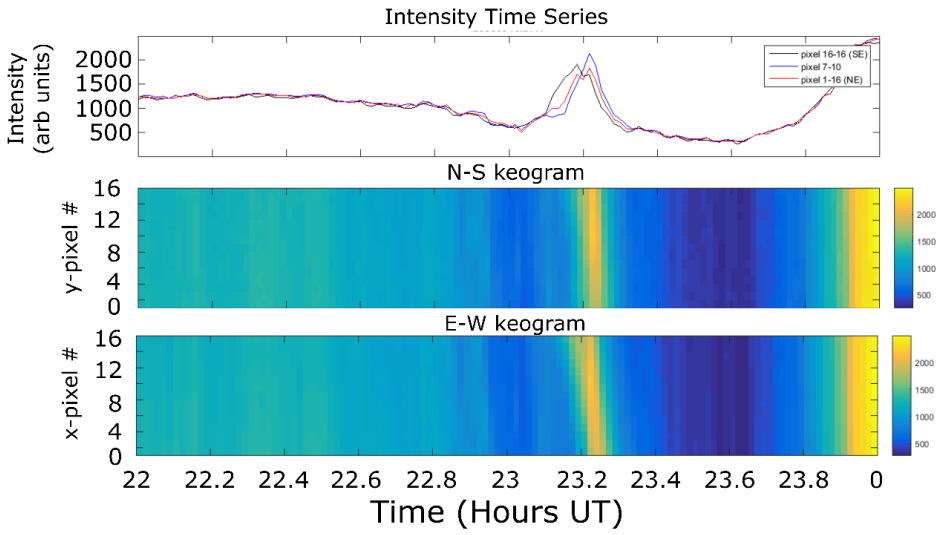

Figure 5.16: As in Figure 5.11 but between 22:00 UT on 16th September 2005 and 00:00 UT on 17th September 2005.

Manual analysis of this front gives an observed propagation direction of $\theta \approx 143^{\circ} \pm 12^{\circ}$ north of east and an observed phase speed of $v \approx 49 \pm 3$ m/s. The horizontal wavelength could not be calculated as there were no trailing waves locked to the front. The value calculated manually for phase velocity is ~24 m/s slower than and $\sim 28^{\circ}$ out of agreement with that calculated by the automated method. The cross-correlation method may have struggled with the very wide wave crest in this particular case.

The resulting m^2 profile for this potential front is shown in Figure 5.17. Thermal inversions at altitudes of approximately 72 km and 86 km cause m^2 to become negative, thus creating reflective boundaries at these levels. This ducting region is relatively weak as the winds are strongly opposing (by ~200−500 m/s) the wave direction throughout the duct.

This front could not be ray-traced significantly below the mesopause region; the ray-tracing was terminated at 87 km altitude where it was estimated that intrinsic frequency $\omega = 0.0184$ rad/s, $\delta = 4.25$, $m^2 = -6.11 \times 10^{-9}$ rad^2/m^2, $R_i = 53.54$, and $N^2 = 3.43 \times 10^{-4}$ rad^2/s^2. Thus, the conditions for which the wave couldn't freely propagate further was that $\delta > 1$ and $m^2 < 0$, meaning that

shears in background wind flow were no longer negligible compared to shears generated by the wave thereby preventing the wave from propagating vertically. Therefore, it seems that the front was observed in the OH* emission at its peak altitude (between ~84 and 86 km, where emission was greater than 2×10^{-7} ergs cm^{-3} s^{-1}) which was below 87 km (the assumed observation point for the ray-tracing analysis) and that it was trapped vertically between approximately 72 and 86 km. This would explain why propagation conditions were not favourable at 87 km altitude, as this was just above the upper reflective boundary of the duct.

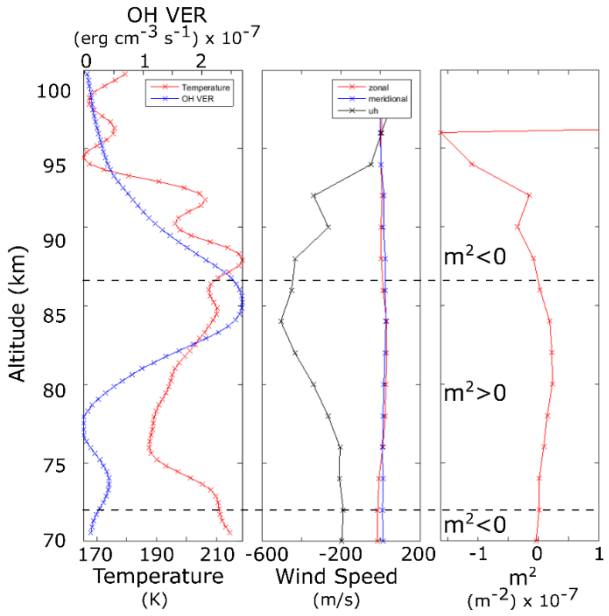

Figure 5.17: As in Figure 5.6, but now corresponding to case 1 of the potential frontal events. The SABER profile used here was measured 5.77 hours after the potential frontal event and corresponded to a region which was ~535 km south-west of Davis Station.

Confidence in this particular potential front was diminished upon inspection of the Czerny-Turner spectrometer data (shown in Figure 5.18), as a very low signal-to-noise ratio (along with high cloud and auroral signals) was observed at the event time and throughout the entire night. This is thus one example of an event which had been marked as a potential front but, due to low data quality demonstrated by the Czerny-Turner spectrometer plots, is now marked as an unlikely potential front.

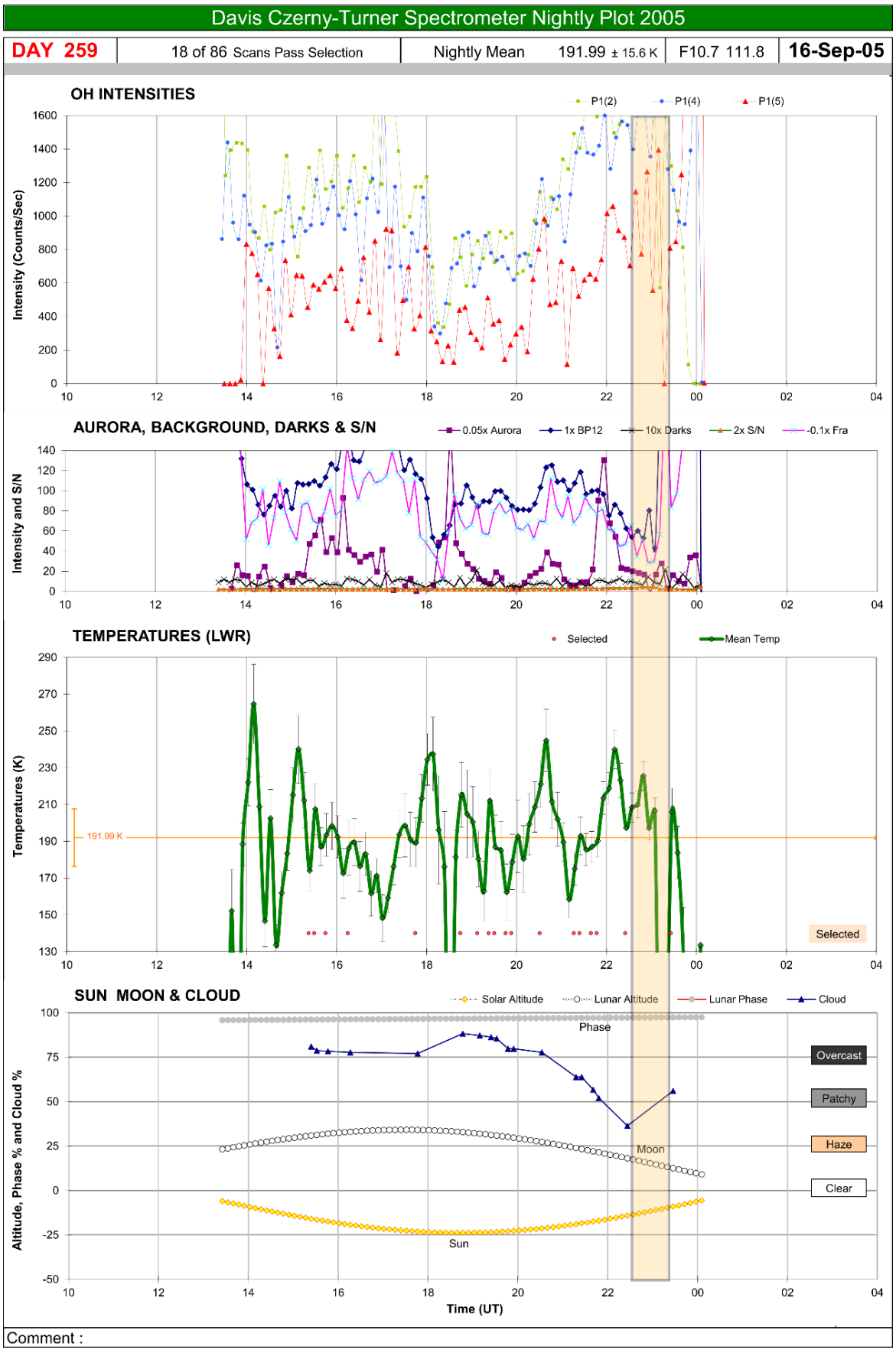

Figure 5.18: As in Figure 5.8 but for the night of 16th–17th September 2005.

Case 4 from Table 5.2 -

A potential bright front detected between 00:00 and 00:23 UT on 7-Jul-2008:

Figure 5.19 displays a series of images showing the fourth potential (unverified) front whose characteristics are shown in Table 5.2, between 00:00 and 00:23 UT on 7th July 2008. There is a trailing wave-like oscillation locked behind the front in this case. In addition, a bright but unducted GW event was observed just before the observation of the potential front, and is included in the image series in Figure 5.19.

Figure 5.19: A series of images recorded by UWOSCR between 22:45 UT on 6th July 2008 and 00:34 UT on 7th July 2008. Dashed lines indicate phase fronts and arrows indicate propagation directions. An unducted GW can be clearly seen between approximately 22:45 and 23:06 UT, followed by a potential front and one trailing oscillation between approximately 00:08 and 00:30 UT.

From the two keograms in Figure 5.20, it is confirmed (between approximately 00:00 and 00:30 UT on 7th July 2008) that the front moves in a predominantly westward direction. This is in general agreement with the value produced by the analysis (183° north of east), shown in Table 5.2. Bright waves may also be seen in the keograms between approximately 22:30 and 23:30 UT, also moving in a predominantly westward direction.

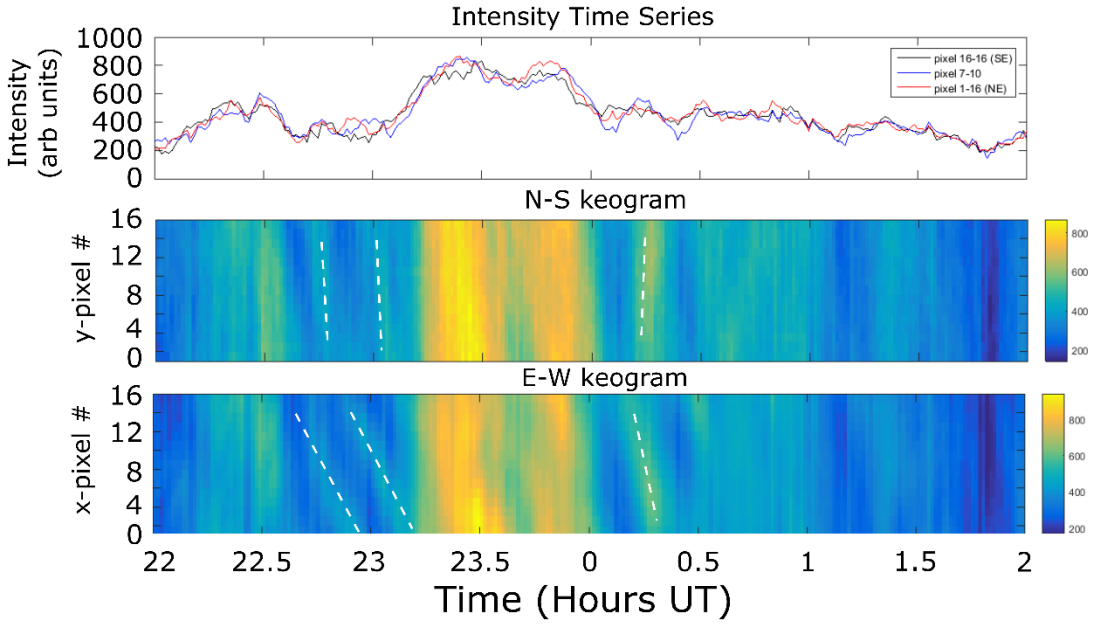

Figure 5.20: As in Figure 5.11 but between 22:00 UT on 6th July 2008 and 02:00 UT on 7th July 2008.

Manual analysis of this front gives an observed propagation direction of $\theta \approx 190° \pm 10°$ north of east, an observed phase speed of $v \approx 26 \pm 3$ m/s, and a horizontal wavelength (between the leading front and trailing oscillation) of $\lambda_h \approx 24 \pm 7$ km. Although the value for the propagation direction matches that produced by the automated analysis method, the manual approximation of speed and wavelength are both low by comparison. This could be due to the intensity difference between the leading front and its trailing wave, or the width of the wave crests within the FOV being quite large (thus causing the correlation between a variety of different pixel combinations to be the same and

so not distinguishing between the left and right sides of the crest, which corresponds to at least a 7 km difference).

The resulting m^2 profile for this potential frontal event is shown in Figure 5.21. Thermal inversions at altitudes of approximately 80 km and 84 km cause m^2 to become negative, thus creating reflective boundaries at these levels. Throughout this altitude region, winds are strongly opposing the propagation direction of the wave, and thus they reduce the value of m^2 significantly.

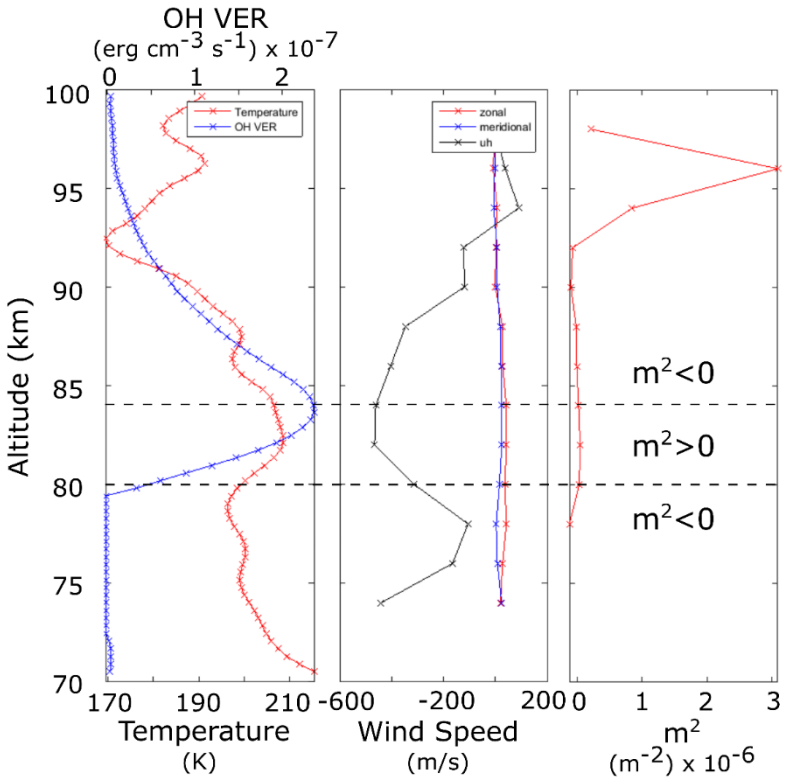

Figure 5.21: As in Figure 5.6, but now corresponding to case 4 of the potential frontal events. The SABER profile used here was measured 147.25 hours before the potential frontal event and corresponded to a region which was ~542 km north-west of Davis Station.

The ray-tracing for this event was terminated at 71.35 km altitude where it was estimated that intrinsic frequency ω = 0.0141 rad/s, δ = 1.06, m^2 =1.30×10^{-8} rad^2/m^2, R_i =17.24 and N^2 = 3.67×10^{-4} rad^2/s^2. Thus, the condition for which the wave couldn't freely propagate further was that $\delta > 1$, meaning that shears in background wind flow were no longer negligible compared to shears generated by the wave. In this case, the ray-tracing results suggest that vertical

propagation is possible between 71 and 87 km altitude. Using non-climatological values for wind and temperature it becomes evident that vertical propagation is only possible between 80 and 84 km. Therefore, the event observation must have been slightly lower than the peak OH* emission altitude (~84 km where emission was greater than 2×10^{-7} ergs cm^{-3} s^{-1}) where it was ducted between approximately 80 and 84 km by two thermal inversions.

Czerny-Turner spectrometer data corresponding to the time of this front (shown in Figures 5.22 and 5.23) provided some complementary results, including wave-like OH* temperature oscillations with peak-to-peak amplitudes of ~20 K, OH* intensity increases of up to ~600 counts/second, a very high signal-to-noise ratio, and a clear sky.

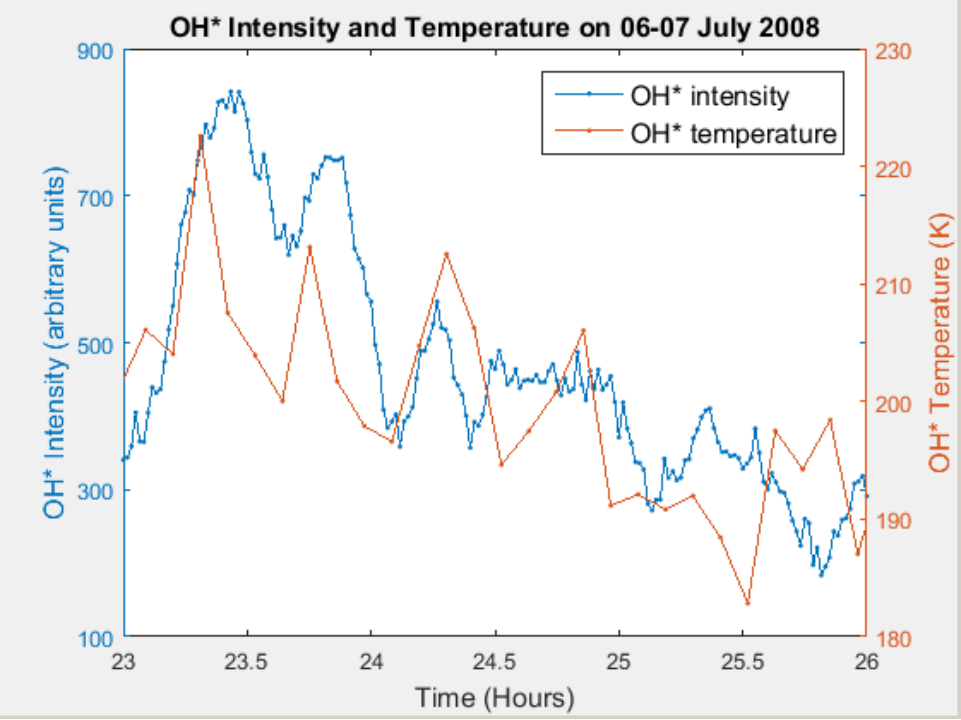

Figure 5.22: Time series of mean OH* intensity in the UWOSCR images (in blue) and corresponding time series of mean OH* temperature from the Czerny-Turner spectrometer data (in orange) at the time corresponding to the mesospheric frontal event.

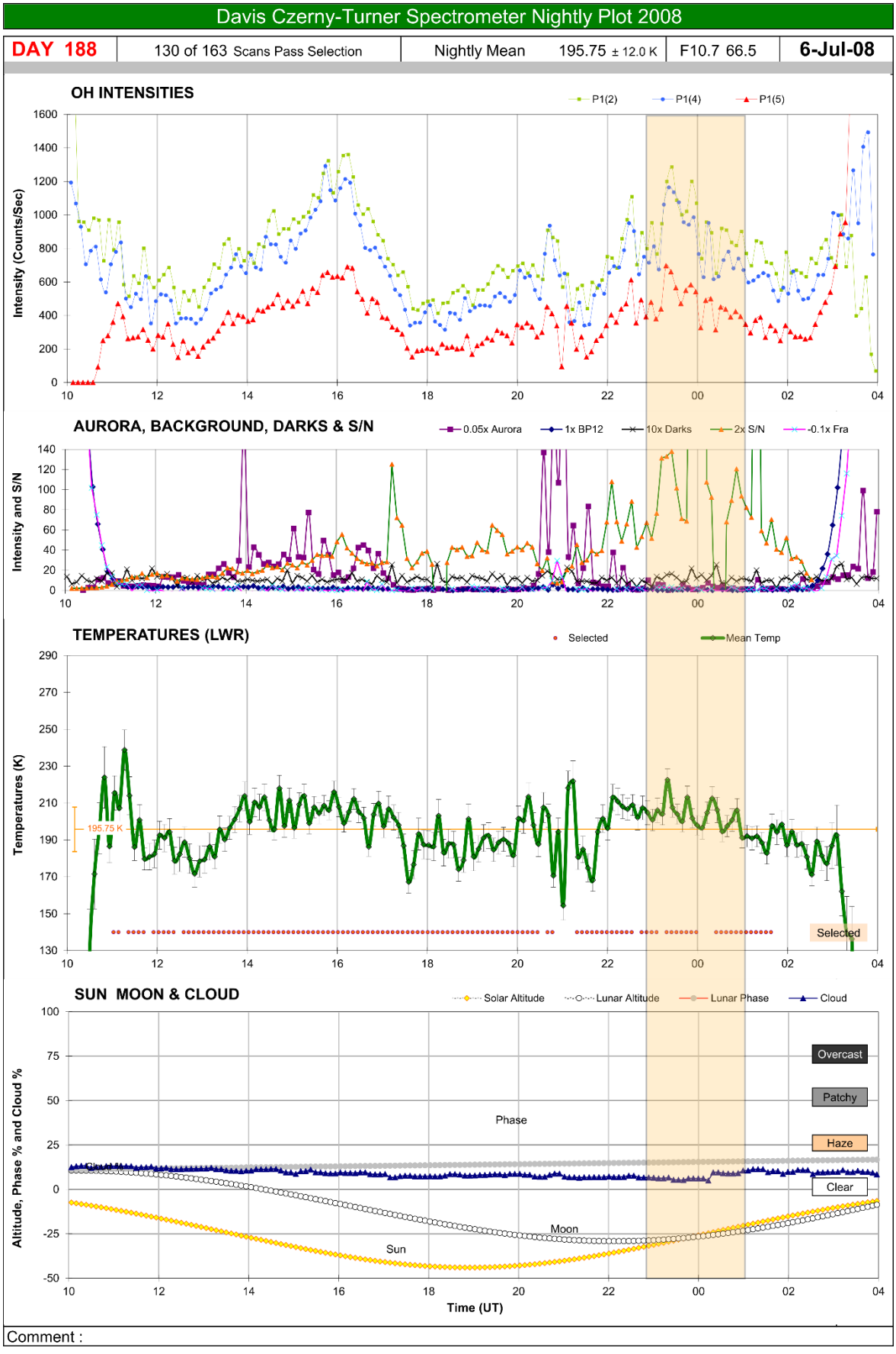

Figure 5.23: As in Figure 5.8 but for the night of 6$^{\text{th}}$–7$^{\text{th}}$ July 2008.

5.3.2.2. Survey of 278 Potential Frontal Events

Figure 5.24 shows the distribution of some general characteristics (*i.e.* persistence of the event within the FOV, wavelength, observed and intrinsic period, and observed and intrinsic phase speed) of the 278 potential frontal events. These characteristics do not vary substantially from band-type GWs in general (as can be seen when compared with Figure 7 of *Rourke et al.* (2017), which is included in Appendix A). Radial histograms of observed and intrinsic propagation directions are shown in Figure 5.25, and in this particular figure they are compared to the corresponding plots for all observed waves using a post-processing standard deviation limit of L=15 m/s for a direct comparison. From this figure, it is observed that the potential frontal events travel predominantly eastward and westward. The seasonal variation of these propagation directions are shown in Figure 5.26, where it is observed that the waves propagate predominantly westward in May, both eastward and westward in July, and predominantly eastward in August. The reason for this seasonal variation in propagation directions has not yet been determined, but it may be due to a seasonal variation in the ducting mechanisms (*i.e.* wind and/or temperature). The polar vortex is strong (~50 m/s in May and ~80 m/s in July and August based on NCEP/NCAR reanalysis data at 10 mbar) during these particular months, but it doesn't change direction, and so it doesn't seem to be the major factor in this seasonal-dependent anisotropy in propagation directions. In addition, since the primary ducting mechanism for the case studies was thermal ducting and not Doppler ducting, it seems more likely that the seasonal variability is caused by a variation in the temperature structure over the station. One interpretation is that this temperature structure variability is related to the change in planetary wave activity at Davis Station. Previous studies have shown that a maximum in planetary wave activity on the Eastern Antarctic Continent occurs in July (*Irving* and *Simmonds*, 2015) and planetary wave activity over Davis Station, in particular, occurs in June/July (*Reisin et al.*, 2014) as shown in Figure 5.28. This increase in PW activity may

actually cause an increase in the number of MILs during these months, which in turn could increase the number of observed frontal events in the MLT.

Event times of the potential frontal events (compared to the event time of all wave events) are examined in Figure 5.27. In order to normalise the data based on observing time, the count (y-axis) is given by the number of minutes that a particular event is observed as a percentage of the total observing time in that particular epoch year, month or hour. The same counting scale is also used in Figure 5.28 and Figure 5.29.

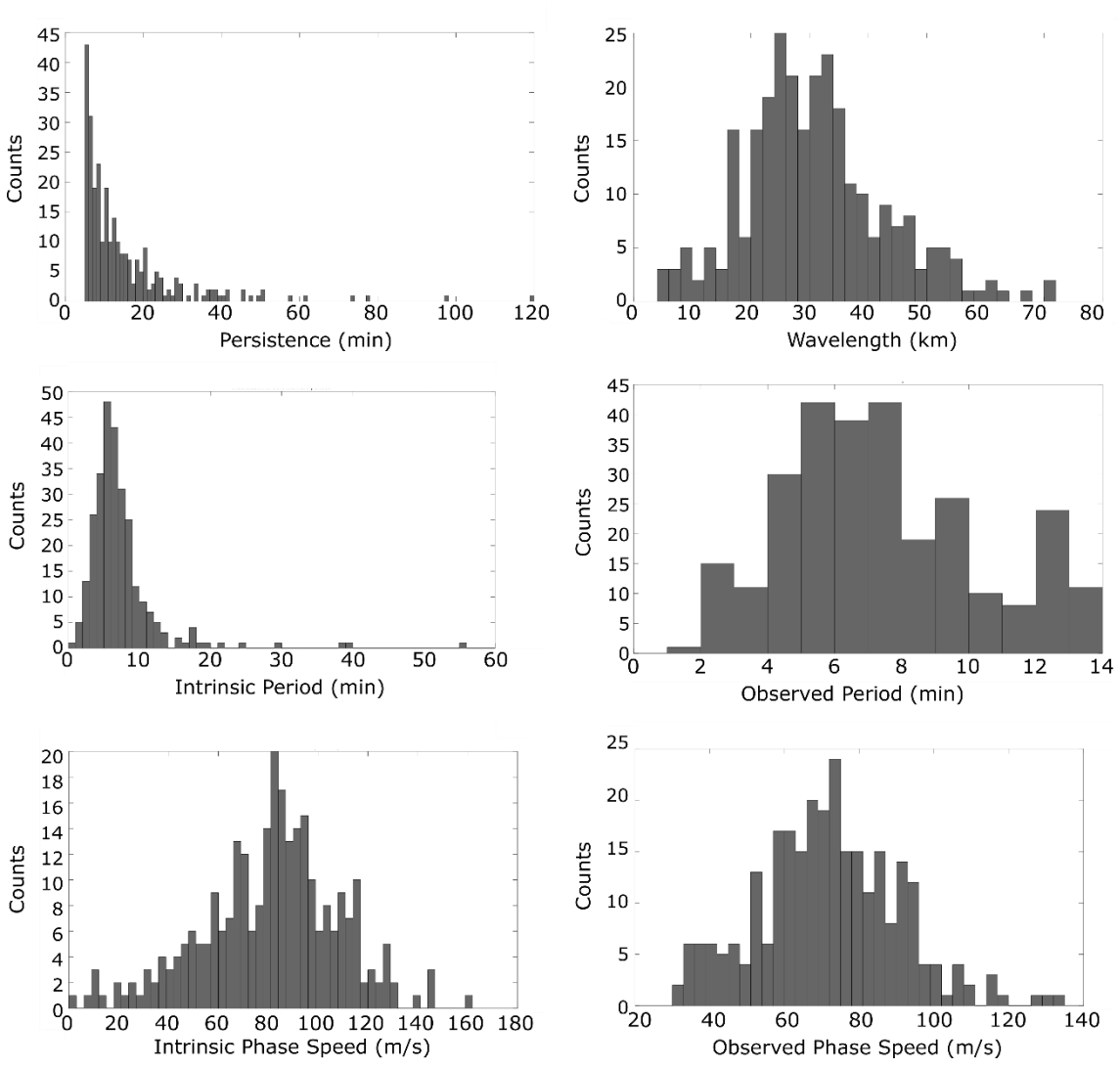

Figure 5.24: Histograms showing the distribution of (top left) persistence, (top right) wavelength, (middle left) intrinsic period, (middle right) observed period, (bottom left) intrisic phase speed, and (bottom right) observed phase speed of the potential frontal events. Counts in this case indicate the number of individual events.

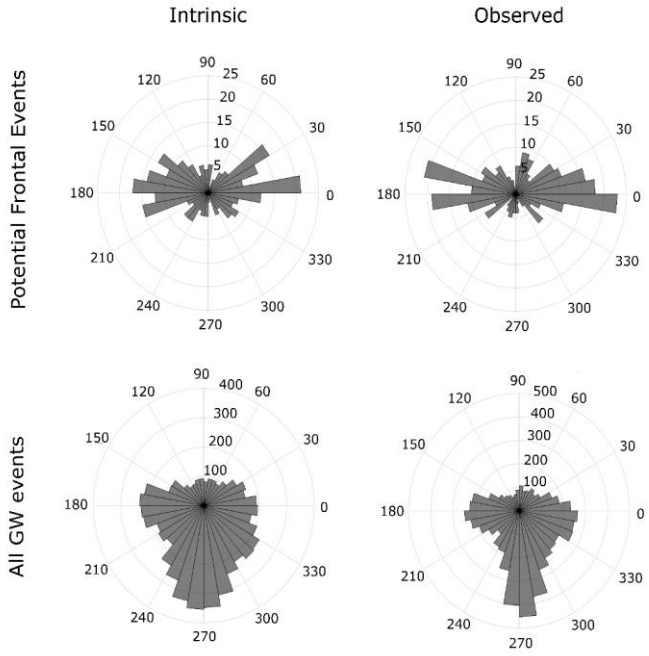

Figure 5.25: Radial histograms showing the distribution of observed propagation directions of (top) the potential frontal events and (bottom) all wave events during the period 2002-2012. Both intrinsic (left) and observed (right) directions are shown. Counts indicate the number of individual events.

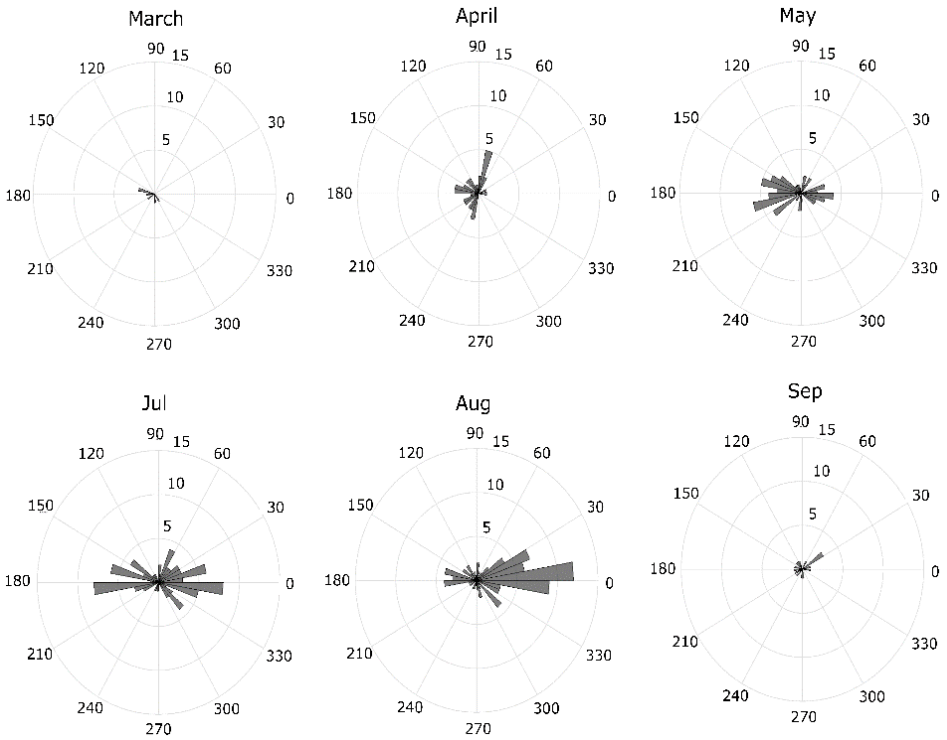

Figure 5.26: Radial histograms showing the distribution of observed propagation directions of the potential frontal events during particular months. Counts indicate the number of individual events.

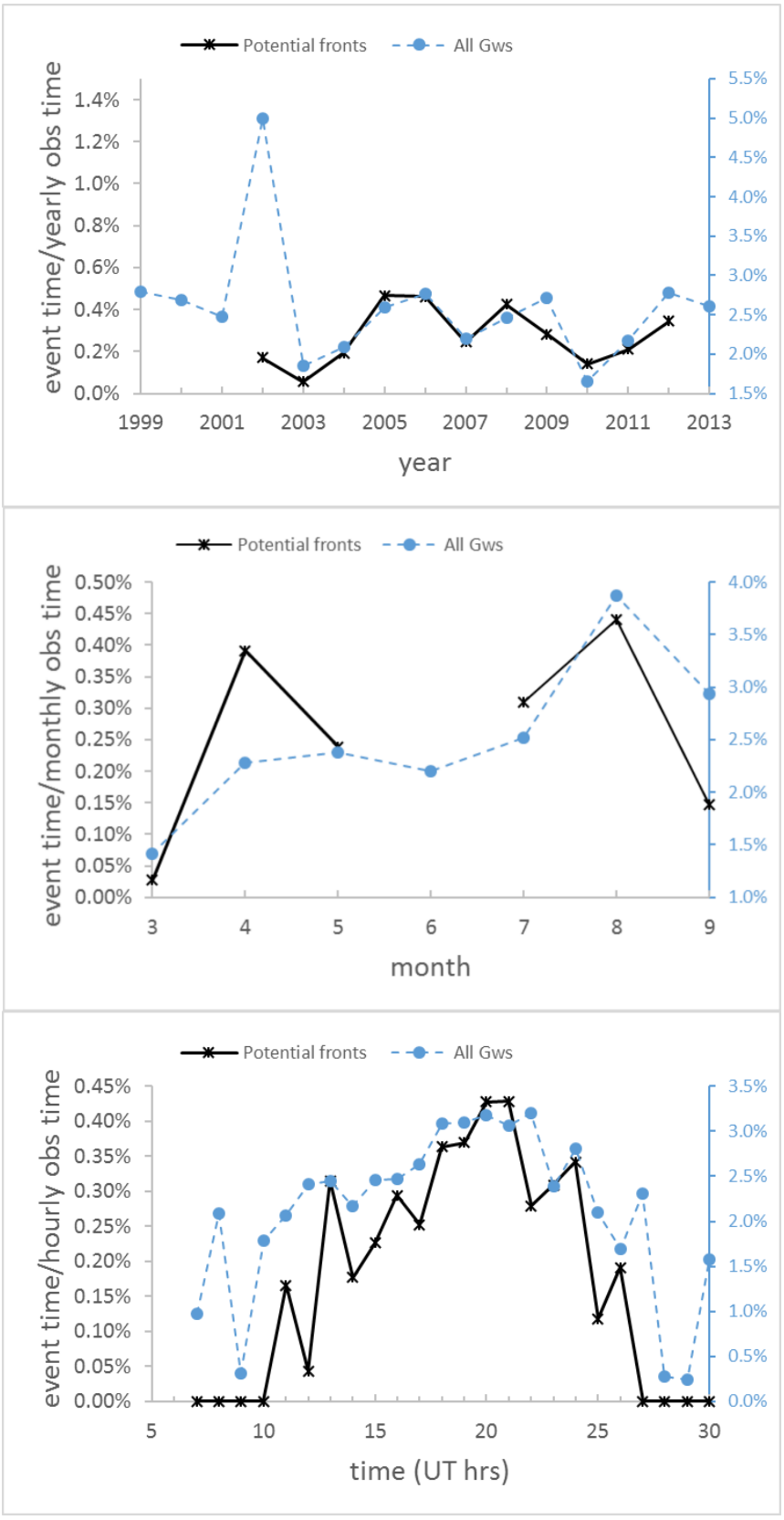

Figure 5.27: Event time of the 278 potential frontal events normalised by observing time during each (top) year, (centre) month, and (bottom) hour of day.

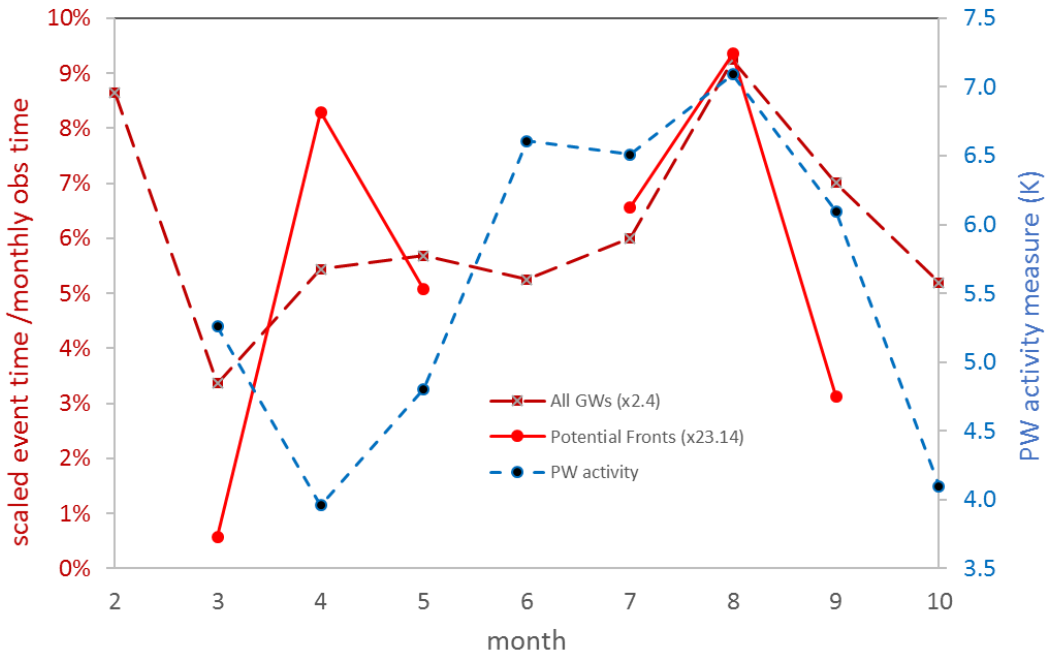

Figure 5.28: Scaled event time of (bright red) the 278 potential frontal events (as shown in Figure 5.27) and (dark red) all GW events as a function of month, plotted along with (blue) a climatological measure of planetary wave activity at Davis Station adapted from Figure 3 of *Reisin et al.* (2014).

Figure 5.29 shows a summary of the seasonal-, directional-, and source region-dependent aspects of the potential frontal events. It can be seen that the scaling for each source region is different. This is because the majority of these events (69%) could not be ray-traced below 80 km. The source regions of the remaining events were 70−80 km (14%), 30−70 km (12%) and <10 km (5%). This suggests that only 17% of the potential frontal events observed do not appear to have ducts in the 70−100 km region, and thus must have a very deep duct (extending from their source region to the mesopause region) if they are in fact real mesospheric fronts. As observed previously, these events propagate predominantly eastward and westward and it is now observed that the majority of eastward propagating waves correspond to the latter half of the year (July-September) and were ducted above 80 km whereas the majority of westward propagating waves correspond to the earlier part of the year (March-May). Of the few events which had tropospheric origin, these events have one major peak (in August) when they propagate in a variety of directions.

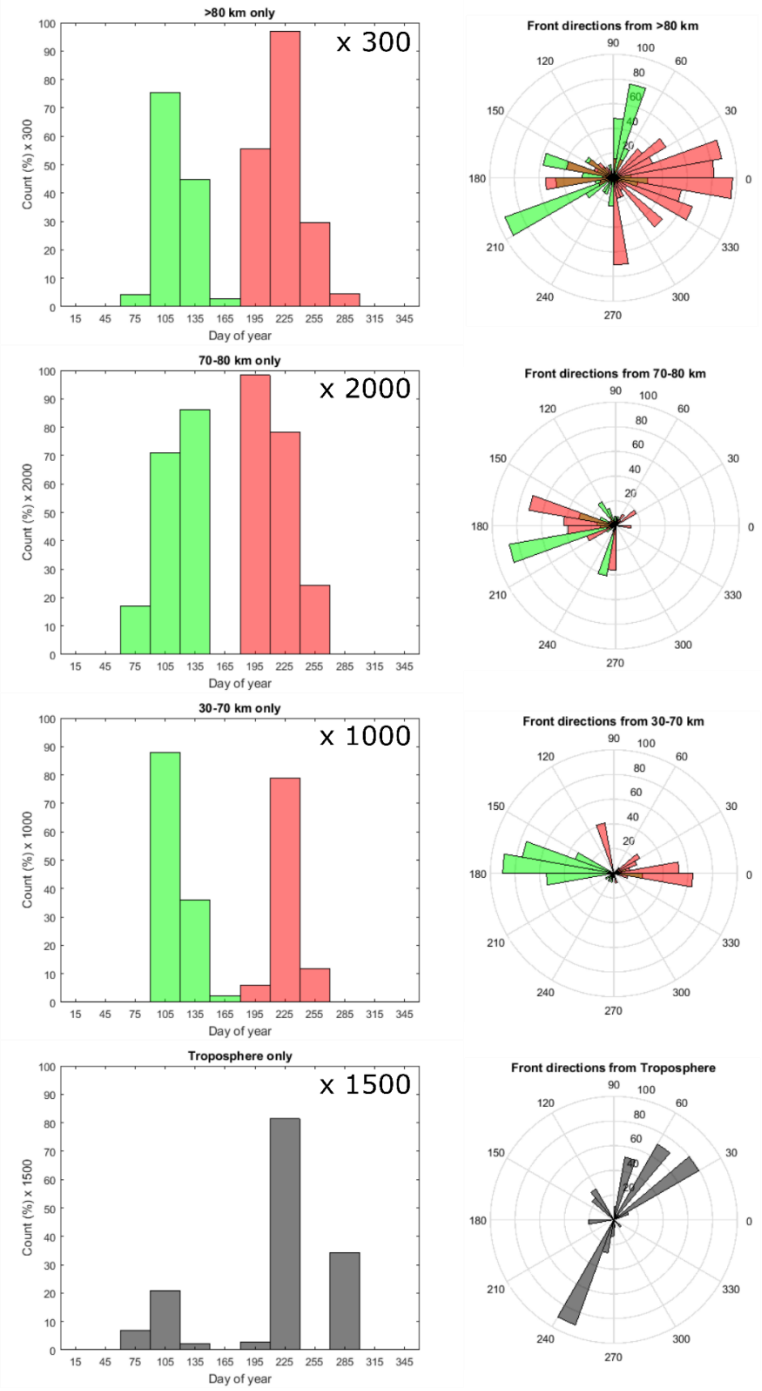

Figure 5.29: Seasonal and directional distribution of potential fronts for four populations selected according to the altitude that ray-tracing terminated. The groups terminated in the troposphere (bottom row), in the altitude range 30−70 km (second from bottom), in the altitude range 70−80 km (second from top), and above 80 km (top). Counts for all plots are given as the time in which wave events were detected as a percentage of the total observing time for the epoch month that they corresponded to, scaled up (for clarity) by a factor of 300, 2000, 1000 or 1500 depending on the altitude region. Colours (red and green) are used to show the seasonal-dependent propagation direction of the waves, where relevant.

Czerny-Turner spectrometer plots for the period 2008−2012 were inspected as a confidence test for the (116) potential frontal events which occurred during this period. Large temperature changes under clear sky and high signal-to-noise ratio conditions were observed for 67 (~58%) of these 116 events. Confidence in this 58% of potential frontal events is thus greatly increased, while confidence in the remaining 42% is dented to some extent. Although 67 events are not enough to provide a reliable summary, distributions of the characteristics of these events are shown separately in Figures 5.30-5.31 due to the increased confidence level in them.

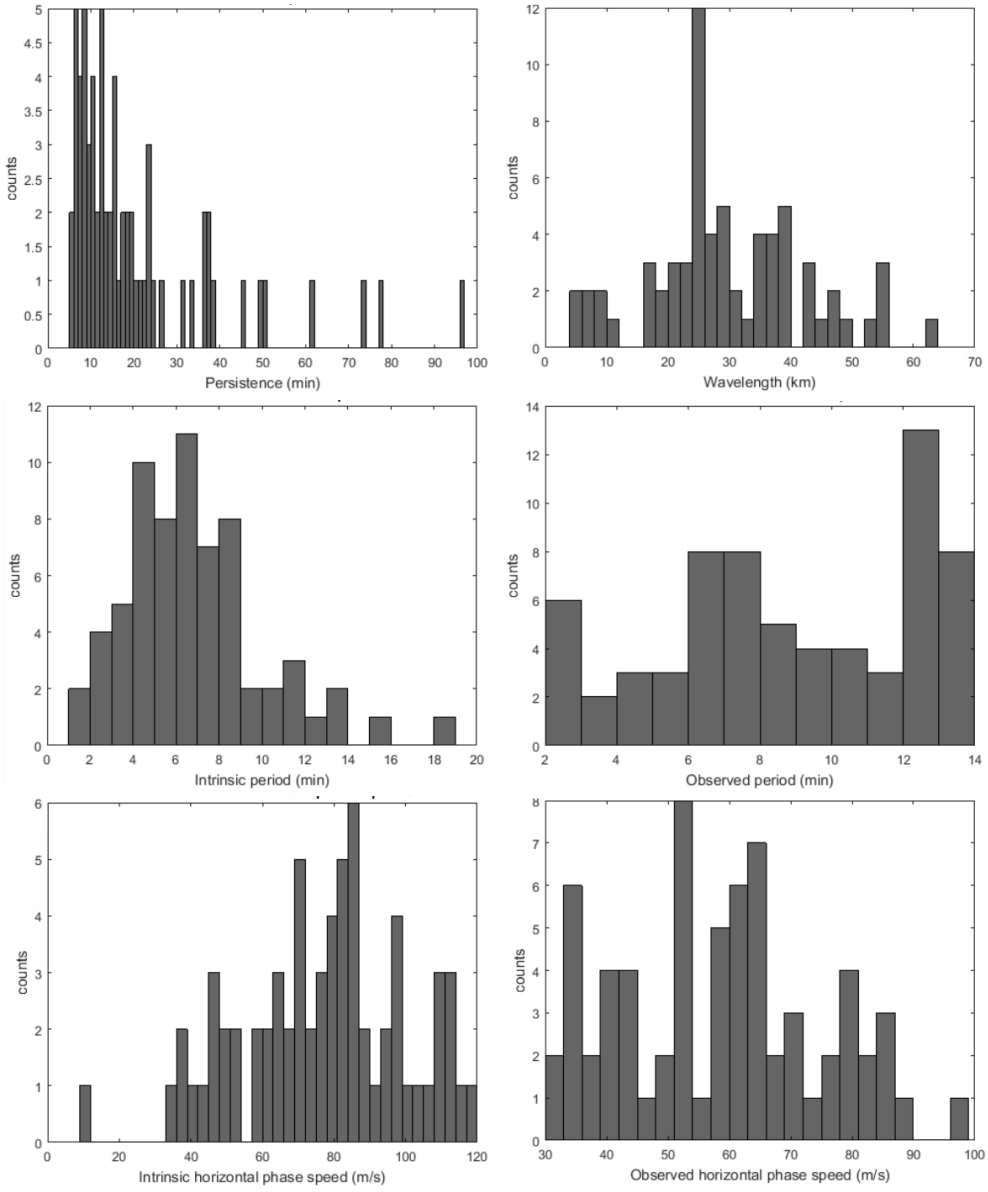

Figure 5.30: As in Figure 5.24, but only for the 67 events discussed above.

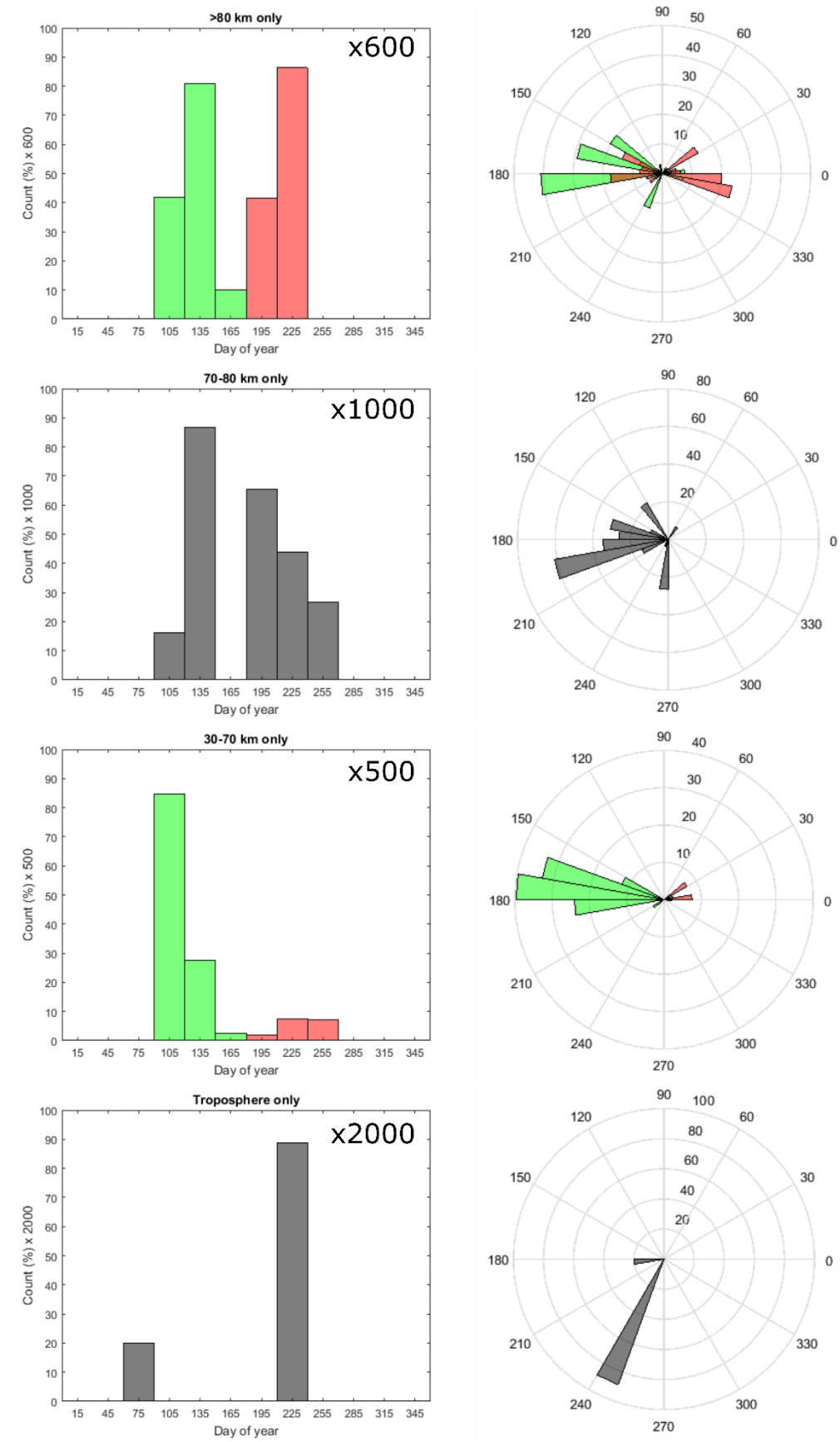

Figure 5.31: As in Figure 5.29, but only for the 67 events discussed above. Different scaling factors are used for each altitude group, as shown.

Figure 5.32: As in Figure 5.27, but only for the 67 potential frontal events discussed above.

5.4. Conclusions and Future Work

In this chapter, five verified frontal events from 2012 were examined, along with up to 278 potential frontal events during the years 2002−2012. Since the FOV of UWOSCR was too small to verify mesospheric fronts independently, there was a reliance on all-sky images recorded simultaneously to confirm their presence on a larger scale. Fortunately, there was some time overlap in the 1999−2013 UWOSCR dataset with Utah State University's co-located all-sky OH* imager, which has been recording images since 2012. Therefore, some frontal event observations made by USU were used to confirm the presence of potential frontal events in the UWOSCR data. Five of the all-sky frontal event observations occurred simultaneously with UWOSCR events which had been characterised as potential frontal events, and these events have been examined in detail in section 5.3.1. In section 5.3.2, a survey of the remaining potential frontal events was then performed to extract any general trend related to mesospheric frontal events over Davis Station, and five of these potential fronts were examined in detail. It is hoped that, in the future, images from an auroral imager system may be used, as it was in operation at Davis Station during the period 2002−2011, but only its 2011 data (which was checked but contained no complementary data) was available during the time of writing this thesis. This auroral imager was sensitive to the OI green line (557.7 nm) emission which is centred at approximately 97 km (as well as aurora at much higher altitudes), and thus it may contain complementary observations for some of the potential frontal events if the fronts are propagating in a ducting region which encompasses both the OH* and OI emission peaks. This seems like a plausible option since bores have previously been observed with co-located OI and OH* detectors both showing the same effect, but opposite in depletion/enhancement (*e.g. Taylor et al.* (1995); *Medeiros et al.* (2005)). Further Czerny-Turner complementary OH* temperature data also needs to be examined during the period 2002−2007 in order to gain a better estimate of the number of likely

potential frontal events during the full 11-year period, and their characteristics. In addition, it would be useful to obtain all data from the USU imager during 2012 in order to cross-check all potential fronts observed by UWOSCR in 2012, rather than just the five case studies examined here. It would also be worthwhile to obtain more logs or data from the entire USU dataset (*i.e.* from 2012−2017) and compare them with the updated UWOSCR dataset so that, if any trends in frontal activity then become apparent, it will be easier to narrow down where to look in the 1999−2011 UWOSCR dataset (when no all-sky OH* images were available). Putting this future work aside for now, the remainder of this section focusses on some conclusions based on the work already completed.

Based on the summary of 278 potential frontal events, the following trends were observed:

1. Distributions of event persistence, phase speed, wavelength and period do not vary substantially from those of band-type GWs within the UWOSCR dataset.
2. Propagation directions were predominantly eastward and westward, with the majority of eastward propagating waves occuring during the latter half of the year (July-September) and being ducted above 80 km, and the majority of westward propagating waves occuring during the earlier part of the year (March-May). The most likely propagation direction of a potential front at the observing altitude (~87 km) also depended on the altitude region from which its source originated, as shown in Figure 5.29. The lack of southward propagating waves (when compared to the result for all band-type GWs as in Figure 5.25) may be attributed to the comparative lack of events whose source was traced to the troposphere ($\sim 5\%$ of all potential fronts, compared to $\sim 15\%$ of all GW events observed by UWOSCR) because the majority of GW events that

originated in the troposphere were observed by UWOSCR to be propagating southward (as shown in Figure 4.8 on page 190).

3. The distribution of event time for potential fronts did not vary substantially from event time of all GWs, as can be seen in Figure 5.27. When normalised to monthly observing time, there was a peak in potential frontal activity in April and August. When normalised to yearly observing time, there were peaks in 2005, 2006, and 2008. Although there was a substantial increase in the number of GWs observed in 2002, there were relatively few potential frontal events observed during that year. Finally, when normalised to hourly observing time, it was found that the majority of potential fronts occurred between 13 and 24 UT, which is very similar to the trend observed for all GW events.
4. The number of potential fronts observed ($\sim$25 events/year) compares well with a recent mesospheric frontal event study by *Pautet et al.* (2018) who observed an average of $\sim$22 events/year at South Pole Station.

From this study of verified and unverified fronts detected by UWOSCR, a number of double bore events were observed, two of which were examined as case studies. Double bore events have been observed previously in the mesosphere (*e.g. Smith et al.* (2017); *Brown et al.* (2004)) and in both cases they were attributed partly to an increase in synoptic GW activity due to tropospheric cold fronts which coincided with their occurrence. This may also be the case at Davis Station where, generally, there is a large, sudden temperature difference over the coastal region (as shown in Figure 5.33). Otherwise, it may be possible to attribute an unusual number of observed fronts in a short period of time to a persistent MIL over the station, as MILs can often last for several days extending over large regions (*Pautet et al.*, 2018). As mentioned earlier in the chapter, persistent MILs during the months of July and August may be a result of increased planetary wave activity during this time.

For example, Damian Murphy (of the Australian Antarctic Division) and Mike Taylor (of Utah State University) have done some work (not yet published) on fronts above Davis Station since 2012. They observe many of these events during particular months of the year, and found that there is often a stationary planetary wave-1 structure at around $80-90$ km that creates a constant background temperature region. They believe this may be acting as a duct. It doesn't occur at other longitudes because of the wave-1 structure. *Irving* and *Simmonds* (2015), on the other hand, found that wave-3 structures were more often associated with months of strong tropospheric planetary wave activity in the southern hemisphere. From these studies, it appears that planetary wave 1 or 3 structures may be related to persistent MILs above Davis Station. From the results presented here, it also seems that thermal inversions appear to be the primary ducting mechanism for observed events. However, a link between planetary wave activity and the occurrence of fronts is not well-supported by the results shown in Figure 5.28.

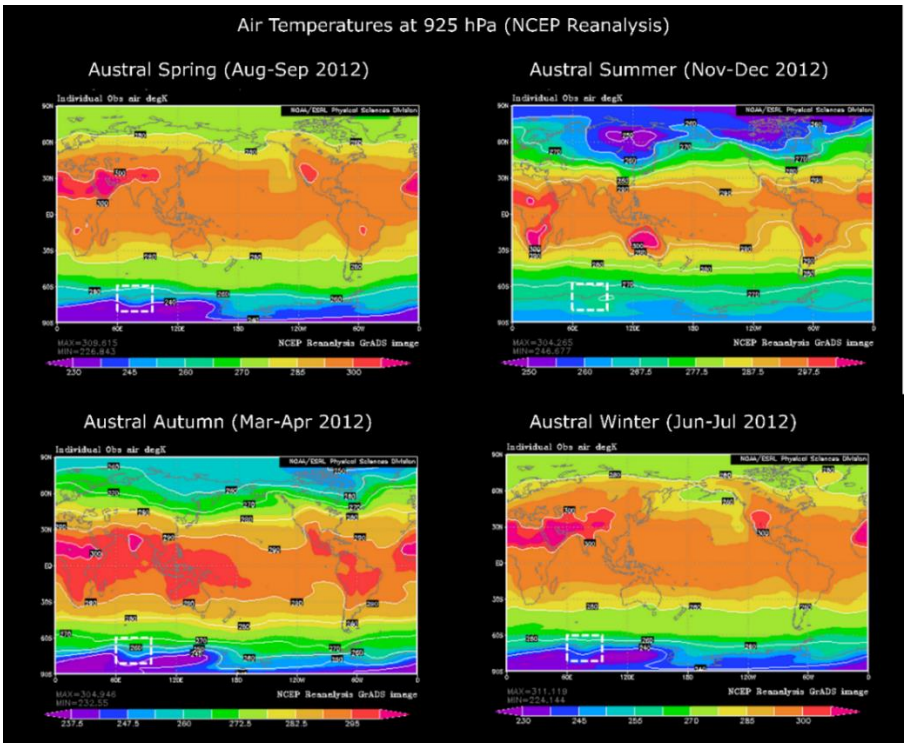

Figure 5.33: NCEP reanalysis air temperature data (values in Kelvin) close to surface level (925 mbar) during different seasons in 2012. The dashed white box outlines the region surrounding Davis Station.

Finally, despite having made observations of potential frontal events which would not be possible by any other instrument during the period of study, it must be concluded that, in order to detect mesospheric fronts, an all-sky OH* camera appears to be far superior to a UWOSCR-type instrument. Nonetheless, a UWOSCR-type instrument may be useful for complementary measurement of their characteristics.

6. SUMMARY AND CONCLUSIONS

6.1. Placement of Work in the Field

The Antarctic continent and the Southern Ocean are key parts of the Earth's climate system. The continent stores most of the Earth's freshwater, generates large amounts of sea ice, and is surrounded by circumpolar currents of air and water. Antarctic conditions influence the pattern of ocean circulation (known as the thermohaline circulation) which transports heat from the tropics toward the poles and increases the ability of the oceans to absorb carbon dioxide from the atmosphere. As such, all of the world's major industrialised nations have established scientific bases on Antarctica under the guidance of the Scientific Committee on Antarctic Research (SCAR) which is an inter-disciplinary committee of the International Science Council (ISC). Due to research performed at such stations, the understanding of Antarctic climate processes and their connection to the global climate system has advanced in the past 10-20 years. The roles of sea ice, surface ice, melting, reflection of sunlight by ice and clouds, anthropogenic changes to the ozone layer, global warming, and circumpolar circulations of sea water and wind are all better understood now than they were a few decades ago. Nevertheless, many aspects of the role of Antarctica in the Earth's climate system remain unresolved. Gravity waves are one such subject. These waves, which are ever-present in the air above us, are known to have a strong connection with the variability of the atmosphere and are often linked with extreme events such as sudden stratospheric warmings (*e.g. Limpasuvan et al.* (2012)), and the spring-time depletion of stratospheric ozone over Antarctica (*e.g. Carslaw et al.* (1998)).

Ground-based gravity wave observations from Antarctica are a particularly important complement to satellite observations over the region. Satellites with high polar orbits provide the global coverage needed for numerical weather prediction, but they do not allow continuous monitoring at one location. The

logistical challenges associated with obtaining ground-based measurements mean that they are rather rare and their rarity, along with their increased accuracy compared to satellite-based measurements, increase their value. In order to combine the efforts of individual scientific groups operating ground-based instruments in Antarctica, a SCAR action group known as ANGWIN (ANtarctic Gravity Wave Instrument Network) was established in 2011.

The work presented in this thesis forms part of a much wider network of gravity wave measurements. This includes ANGWIN (as shown in Figure 6.1) but also includes other international efforts made by groups such as ARISE (Atmospheric dynamics Research InfraStructure in Europe) and WCRP (World Climate Research Programme). Projects under such groups are providing new and valuable contributions to the production of more accurate and realistic climate models, which are key to more accurate weather prediction (both in the Earth's atmosphere as well as in space) and long-term climate change simulations. The improvement of such climate models is a huge global challenge which involves making a large number of local observations around the globe and subsequently assimilating them into climate models.

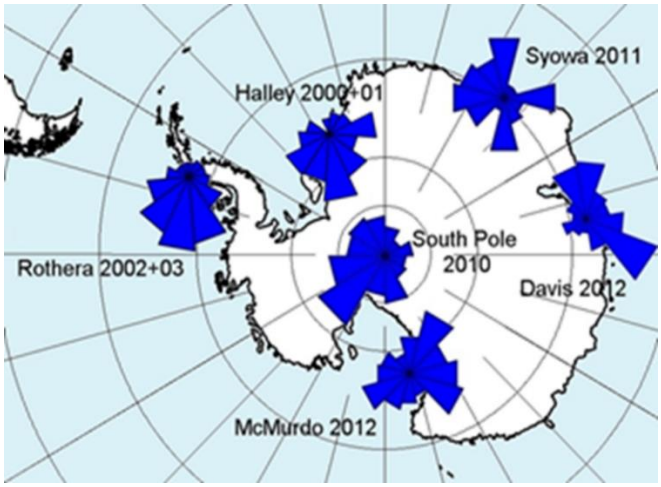

Figure 6.1: Contribution of ANGWIN research stations to the propagation directions of small-scale GWs in the Antarctic MLT (*Taylor et al.*, 2016a).

The work presented here specifically contributes to an improved understanding of atmospheric dynamics in the MLT region, where the importance of GWs is

well-known, but poorly constrained by observations. Some unresolved areas of research in this field include the characterisation of the influence of mountain waves on the MLT, the determination of gravity wave source regions, the study of the interaction of GWs with planetary waves, spontaneous emission of GWs from jets/fronts, and the disparity between observations and models. Although much more projects of this nature will be required in order to answer all questions about the role of GWs in climate models, this work has closed a significant gap in knowledge of long-term characteristics of short-wavelength gravity waves and ripples (along with their source regions), particularly over Davis Station, Antarctica. Figure 6.1 illustrates the importance of making measurements at this location in order to complete the basic coverage of GWs over Antarctica. It is hoped that these findings will eventually be incorporated into climate models (such as WACCM) by international collaborators who form the GW drag parameterisation project team, and who are actively developing the representation of GWs in global climate models. The complexity of the challenge posed means that the work of a thesis such as this can only address a limited subset of outstanding questions. The main findings in this regard are set out in section 6.2 below.

6.2. Overview and Findings

This thesis has focussed on the extraction of gravity wave parameters from a large dataset (15 years) of OH* airglow images corresponding to the mesopause region (~ 87 km altitude) above Davis Station, Antarctica. The main instrument used for this study was a scanning radiometer known as UWOSCR, which is sensitive to the brightest of the OH* infrared emissions and which was designed with a narrow field of view in order to observe small-scale gravity waves and ripples. Although this narrow field of view was a major limiting factor during the work on mesospheric fronts in Chapter 5, it did allow for a climatological study of small-scale GWs and ripples whose spectral, spatial and temporal range had not been covered by any other instrument at Davis Station

during the period 1999−2011 (before the introduction of Utah State University's all-sky OH* camera in 2012).

In Chapter 1, an introduction to gravity waves, in the context of the major role they play in atmospheric dynamics, was presented. The parameterisation of small-scale gravity waves was also described, due to the importance of their inclusion in global climate models. Following on from this motivation, the focus of the remainder of this thesis was on the characterisation of these wave features in the Antarctic mesopause region – a region which is, at present, particularly misrepresented in climate models.

Chapter 2 described the unique characteristics of the UWOSCR instrument in detail. Its design led to the development of a particular set of analysis methods, which were developed by Bob Lowe and colleagues at the University of Western Ontario, and these methods were documented in this chapter, with particular emphasis on the De Serrano and Lowe method which was chosen for use in this project due to its lack of subjectivity.

The De Serrano and Lowe analysis method was applied to the Davis Station UWOSCR data in Chapter 3. From the software testing part of this chapter, it was concluded that, although the method works well for a certain range of waves and under perfect conditions, some improvements could be made to expand the capabilities of this method. Initial work on the expansion of this method was done via a LabVIEW program which allows for the variation of window lengths, image size, temporal resolution, and image type (scanned or still image). The results from this chapter were used to construct a climatology of gravity waves and ripples between 1999 and 2013. This provides a valuable summary of gravity wave and ripple statistics within a particular spectral range (2−16 minutes) near the mesopause above Davis Station. The main results from the climatology presented in this chapter (and also published in *Rourke et al.* (2017)) were that (*i*) both gravity waves and ripples obeyed the relation

λ_h (km) $\approx 2.5\,T$ (min.)$^{1.05}$, an empirical relation which is in agreement with previous studies (*Taylor et al.*, 2009) but is now extended to include ripples (at shorter periods and wavelengths), and (*ii*) gravity waves and ripples exhibited an unusual distribution in observed propagation directions, with a near-complete absence of northward-propagating waves. The timing of the eastward/westward propagating waves corresponded with the annual formation/break-up of the polar vortex and appears to be a likely source for these waves.

The approximate source regions of observed gravity waves between 1999 and 2013 were calculated in Chapter 4 using a reverse ray-tracing method developed by *Marks and Eckermann* (1995). This allowed for the identification of four distinct groups of gravity wave sources, each with a distinct geographical origin and predominant observed propagation direction. These source groups were:

1. Those waves which couldn't be ray-traced significantly below their observing altitude (45% of GWs observed), primarily due to the termination condition $m^2 < 0$, which means that these waves couldn't propagate vertically. This suggests that there may be a large proportion of trapped/ducted waves near the mesopause over the station, which may have travelled very large horizontal distances before their observation.
2. A group of waves (15% of all GWs observed) which couldn't be ray-traced below 70−80 km altitude. The primary reason for the ray-tracing termination of this group was that the WKB parameter became larger than 1, and so the WKB approximation (which was an underlying assumption for the ray-tracing equations) was no longer valid.
3. The group (9.5% of all GWs observed) which originated in the 45−55 km altitude range. The ray-tracing was terminated at this altitude range primarily because the waves were approaching a critical level ($m^2 > 10^{-6}$ m^{-2}), which may correspond to the polar vortex. The timing of this group of waves corresponds to the formation and break-up of the polar

vortex. Secondary wave generation due to instabilities created by these strong winds is a likely source for this group of waves.

4. The waves which were ray-traced all the way down to the troposphere (15% of all GWs observed). The majority of these waves were generated between ~ 100 and 200 km north-west of the station and were propagating southward over Davis Station. These waves, which were observed relatively consistently throughout the seasons and years, may be storm-generated or may be due to the interaction of planetary waves with the background wind field.

Chapter 5 details an investigation of mesospheric fronts (large-scale, horizontally-propagating features associated with an intense OH* brightness change). The level of frontal activity near the mesopause above Davis Station was investigated using a combination of instruments at Davis Station, including UWOSCR (for measurement of OH* intensity variations), the medium-frequency radar (for wind profile measurements), the Czerny-Turner spectrometer (for OH* temperature measurements), and the OH* all-sky camera (for OH* intensity variations over a wider field of view), along with SABER temperature profiles close to the station (available between 2002 and 2012). The large spatial extent of these fronts could only be verified by the all-sky camera, which was not installed at the station until 2012, leading to a large number of unverified events between 2002 and 2011. Confidence in a subset of all 278 potential frontal events was tested using measured OH* temperature data, and it was found that confidence in ~58% of this subset was improved. A survey of all 278 (~25 events/year) potential frontal events found that wave characteristics (persistence, speed, wavelength and period) did not vary substantially from all GWs observed, but that propagation directions were predominantly eastward and westward only. The lack of southward propagating waves (compared to all GWs) may be attributed to the reduction in the proportion of fronts which could be ray-traced to the troposphere (~5%

of all potential frontal events, compared to ~15% of all GWs). Event time of the potential fronts showed a similar trend to all GWs, except that during 2002, when there was a large increase in GW activity, there was not a corresponding increase in potential frontal activity.

6.3. Future Work

The research presented in this thesis highlights the possibility of further work on the topic in terms of the analysis procedure, the climatological results, and the mesospheric frontal event investigation.

The De Serrano and Lowe analysis procedure used in this thesis has been very useful for an objective overview of gravity wave and ripple statistics over the 15-year period. However, it does not come without its limitations. The major limitations of this procedure stem from the window lengths chosen for both the velocity and period calculation. The waves which may be captured by this procedure are limited to $2-16$ minute periods and are optimised for speeds of $26-46$ m/s. Additionally, the procedure only works for when one wave is passing through the field of view during the chosen window length, which is not always an accurate assumption. In an effort to improve the capabilities of this method, some initial program variations have been made, as described above. More major program modifications may be required in order to increase the range of GWs which can be analysed accurately, especially if there is more than one wave within the field of view during a particular window length. In particular, the weighted-mean-centre method may place too much emphasis on one value within each image and so it may be more appropriate to perform 256 FFTs on each window and then extract the most dominant period. Finally, the tendency of the analysis method toward higher wave speeds than manually approximated requires further investigation, but may be solved upon variation of the 21-minute window length to better suit waves of different speeds. In this regard, a wave-adaptive window length would be desirable, although it may not be possible without user-intervention.

The climatology may be updated by almost four years of new data (2014-2018), and it would be appropriate to do so in order to verify that new GW parameter distributions remain consistent with the 15 years of data analysed. The ray-tracing results from this climatology also need to be investigated in further detail. The approximate geographical source region for observed upward-propagating waves has been established, but the actual source mechanism is not known for three out of four of these source regions. The 45−55 km group of GWs appear to be generated by the polar vortex, but supporting evidence for the tropospheric and mesospheric sources has not yet been found.

In terms of the mesospheric fronts, UWOSCR has demonstrated some capabilities of frontal event identification when used in conjunction with other instruments. These other instruments have not yet been exploited to their full capabilities. Confidence in the 2002−2007 potential frontal events has yet to be quantified using Czerny-Turner spectrometer data. Additionally, more all-sky aurora images need to be obtained (for the period 2002−2010), as they may include some complementary OI (557.7 nm) emission data. This instrument did not provide any complementary data for the 2011 potential frontal events, but this may be because ducts were not positioned in such a way as to include the brightest parts of both the OH* and OI airglow emissions during these events.

In addition to the above, other instruments are located at Davis Station (*e.g.* lidar, balloons, and the Fabry-Perot spectrometer) which have not been used in this project. These instruments may provide data which could be used in conjunction with the UWOSCR data to determine the maximum amount of information possible about particular GW events.

In the wider context, it is known that GW parameterisation in current global climate models (*e.g.* WACCM) do not reflect reality. The climatological results presented in this thesis may form part of the observational requirement for improvements of such parameterisations, just as terrain-generated GW

observations in the past have helped improve GCM representation of the Antarctic cold pole bias (*Garcia et al.*, 2017).

APPENDIX A. RESEARCH PAPER

A Climatological Study of Short-Period Gravity Waves and Ripples at Davis Station, Antarctica (68°S,78°E), During the (Austral Winter February-October) Period 1999-2013.

Rourke, S., Mulligan, F.J., French, W.J.R. and Murphy, D.J.

Published in *Journal of Geophysical Research: Atmospheres*, 122(21), 11388-11404, doi: 10.1002/2017JD026998, 2017.

Part of a Special Section:
Atmospheric Gravity Wave Science in the Polar Regions and First Results from ANGWIN

AGU PUBLICATIONS

JGR

Journal of Geophysical Research: Atmospheres

RESEARCH ARTICLE
10.1002/2017JD026998

Special Section:
Atmospheric Gravity Wave Science in the Polar Regions and First Results from ANGWIN

A Climatological Study of Short-Period Gravity Waves and Ripples at Davis Station, Antarctica (68°S, 78°E), During the (Austral Winter February–October) Period 1999–2013

S. Rourke[1], F. J. Mulligan[1], W. J. R. French[2], and D. J. Murphy[2]

[1]Department of Experimental Physics, National University of Ireland, Maynooth, Maynooth, Ireland, [2]Australian Antarctic Division, Kingston, Tasmania, Australia

Key Points:
- Gravity waves and ripples have been observed in winter mesopause OH* emissions at Davis Station, Antarctica, from 1999 to 2013
- Intrinsic wave propagation directions exhibited meridional anisotropy as well as seasonal and altitude-dependent zonal anisotropy
- Reverse ray tracing was used to identify the altitudinal and geographical origin of the observed waves

Correspondence to:
S. Rourke,
sharon.rourke@mu.ie

Citation:
Rourke, S., Mulligan, F. J., French, W. J. R., & Murphy, D. J. (2017). A climatological study of short-period gravity waves and ripples at Davis Station, Antarctica (68°S, 78°E), during the (austral winter February–October) period 1999–2013. *Journal of Geophysical Research: Atmospheres*, *122*. https://doi.org/10.1002/2017JD026998

Received 24 APR 2017
Accepted 9 OCT 2017
Accepted article online 14 OCT 2017

Abstract A scanning radiometer deployed at Davis Station, Antarctica (68°S, 78°E), has been recording infrared (1.10–1.65 μm) images of a small region (24 km × 24 km) of the zenith night sky once per minute each austral winter night since February 1999. These images have been processed to extract information on the passage of gravity waves (GWs) (horizontal wavelength, $\lambda_h > 15$ km) and ripples ($\lambda_h \leq 15$ km) over the observing station. Phase speeds, periods, horizontal wavelengths, and predominant propagation directions have been deduced. Observed speeds were found to be highly correlated with horizontal wavelengths as has been reported in previous studies. Reverse ray tracing of the detected GWs only enabled us to identify four distinct groups. On average, only 15% of waves detected can be traced back to the troposphere, and a large proportion (~45%) were not successfully reverse traced substantially below the airglow layer. Two smaller groups were found to reach a termination condition for reverse ray tracing at altitudes near 50 km and 75 km. Of those that reached the termination altitude in the troposphere (10 km), most of the end points fell within a radius of 300 km of the station, with a very pronounced concentration of wave initiation to the northwest of the observing point. The predominant direction of propagation was southward, and they were observed throughout the year. Recent reports suggest the interaction of planetary waves with the background wind field as a potential source for these waves.

1. Introduction

Gravity waves (GWs) have become a subject of intense study in recent years because quantifying their influence is essential for simulations of climate change scenarios (Hamilton, 1997). Global circulation models (GCMs) employed for such simulations must include some form of parameterization scheme (Garcia et al., 2007) to represent the vertical transfer of the atmosphere's momentum and energy due to GWs since individual GWs are generally too small to be resolved by the global model grids. These parameterizations require detailed knowledge of GW characteristics such as wavelengths, phase speeds, and periods on a global scale (Alexander & Barnet, 2007). This knowledge must come from a combined set of measurements from different observation methods because, although global GW observations are available from satellites and balloons, each observation method is sensitive to only a portion of the GW spectrum and a portion of the atmosphere (Wright et al., 2016). Since GWs are intermittent in space and time, local observations are currently more accurate than global observations, with local values of momentum flux often more than an order of magnitude larger than averaged fluxes (Alexander et al., 2010). Current GCM parameterizations are not sufficient. It is already known (Choi & Chun, 2013) that GCMs do not accurately represent the intense stratospheric GW activity that occurs in the Southern Hemisphere winter. In this region, there is a known GW hot spot due to the Antarctic Peninsula and the Transantarctic Mountains (Hoffmann et al., 2013). Missing stratospheric GW drag in this region (at ~60°S) in GCMs is believed to be responsible for the so-called "cold pole problem." This is where the modeled southern polar vortex is too cold by 5–10 K, persists too long into spring, is too strong by ~10 m/s, and is located too far poleward, leading to poor predictions of ozone hole dissipation timing (Choi & Chun, 2013; McLandress et al., 2012).

Knowledge of GW activity at higher altitudes is also important. It has been long since known (Vincent & Reid, 1983) that GWs are a key driver of meridional circulation in the mesosphere from the summer to winter pole. In this paper, we study mesopause GW/ripple activity using a data set recorded from 1999 to 2013. The results

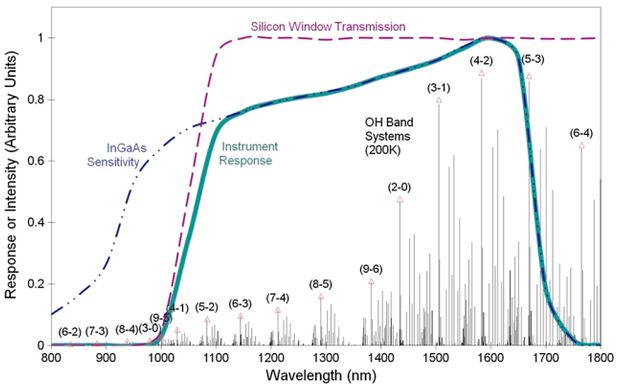

Figure 1. The emission spectrum of hydroxyl night airglow in the region of interest with typical InGaAs detector sensitivity and silicon window transmission which yield the instrument response.

of this study contribute to an international collaborative observational effort known as ANGWIN (Antarctic Gravity Wave Instrument Network) (Matsuda et al., 2017).

The Antarctic mesosphere and lower thermosphere (MLT) is recognized as one of the least understood regions of the atmosphere, and only recently has this region been investigated with a variety of different instruments (Dowdy et al., 2007). Ground-based optical studies of short-period GWs at high latitudes are particularly sparse because observation conditions are less than ideal, especially during the summer months when airglow observations cannot be made (Pautet et al., 2011). Studies on upward propagating GWs through the MLT, in the polar regions specifically, are also required for a better understanding of magnetosphere-thermosphere-ionosphere coupling, lower thermosphere dynamics, and ionospheric variabilities (Takahashi et al., 2014).

Methods of measuring GW parameters currently in use include remote sensing of temperature and wind profiles from satellites (Krebsbach & Preusse, 2007; Preusse et al., 2009), radiosondes (Leena et al., 2012; Moffat-Griffin et al., 2011; Reeder et al., 1999), rocket soundings (Goldberg et al., 2004; Rapp et al., 2001), lidar (Gardner & Voelz, 1987; Werner et al., 2007; Yang et al., 2008), radar (Hibbins et al., 2007; Vincent et al., 2010), and ground-based airglow observations (Bageston et al., 2009; Hecht et al., 2007; Nakamura et al., 1999; Nielsen et al., 2009). Part of the challenge is that GW phenomena occur over a very broad spectral range with periods ranging from minutes to several hours and spatial scales from tens to thousands of kilometers. Each observation technique tends to be sensitive only to some portion of that spectrum (Fritts & Alexander, 2003; Gardner & Taylor, 1998).

Monitoring the effects of the passage of these GWs on naturally occurring atmospheric emissions has proven to be quite an effective method of measuring their parameters (Bageston et al., 2009; Hecht et al., 2007; Nakamura et al., 1999; Nielsen et al., 2009; Yue et al., 2010). Perhaps one of the most intuitively satisfying methods is the recent class of CCD imagers currently applied to this problem (Nakamura et al., 1999; Taylor et al., 1995). In these cases, the entrance optics is frequently a fish eye lens to image almost the entire sky or a very substantial portion of it.

Hydroxyl airglow is used as a GW tracer in this study. The hydrogen-ozone reaction, $H + O_3 \rightarrow OH^*(v \leq 9) + O_2$ is the primary production mechanism for rovibrationally excited hydroxyl in the upper atmosphere (Bates & Nicolet, 1950). Production of O_3 (via $O + O_2 + M$) and loss processes through reaction with atomic oxygen and collisional quenching with O_2 and N_2 confine OH* to a layer ~8 km thick and centered near 87 km altitude. Vibration-rotation transitions from the excited radical result in an extensive band emission spectrum ranging from ~500 nm through the near infrared region to ~4 μm, with total emission intensity ~ 5 MR (Krassovsky et al., 1962). Figure 1 shows part of this emission spectrum, with the sequence of brightest ($\Delta v = 2$ and $\Delta v = 3$) bands between 1.4 and 1.7 μm. This spectral range is covered by the instrument described in section 2.

The hydroxyl layer emission rate will respond to the propagation of GWs/ripples through the layer, both as a result of density perturbations (changing the concentration of reacting species) and temperature perturbations (changing the reaction rates) induced by the wave. Time lag and altitude differences between these mechanisms complicate the emission response, but these processes have been extensively modeled (Liu & Swenson, 2003; Makhlouf et al., 1998; Swenson & Gardner, 1998; Walterscheid et al., 1987), and generally the relative intensity perturbations are larger (by factor of ~ 8–10) than the temperature perturbations. This property is known as the Krassovsky ratio $\frac{\Delta I}{\bar{I}} = \eta\left(\frac{\Delta T}{\bar{T}}\right)$, where $\eta > 8$ for longer period waves (Krassovsky, 1972). Swenson and Gardner (1998) found that OH* volume emission rate fluctuations were largest on the bottomside of the layer (~ 3 km below the OH* peak). This was subsequently verified by satellite observations by Nikoukar et al. (2007). On the bottomside of the layer, effects due to the redistribution of atomic oxygen dominate, while fluctuations in rotational temperature are largest near the peak, thereby introducing a phase difference (greatest for short vertical wavelengths) between intensity and temperature variations. Some "filtering" of the GW spectrum (Alexander, 1998; Wright et al., 2016) is inherent in observing wave effects integrated over the OH* layer profile. A response will only be observed if the vertical wavelength

of the GW is larger than the thickness of the layer and the period of oscillation is greater than the timescale for transport of the reacting species. As a general guide, vertical wavelengths shorter than 10 km and periods less than 10–25 min (about the chemical lifetime of O_3) (Makhlouf et al., 1998) have an attenuated response in the OH* airglow. This includes all but the shortest period GWs as the Brunt-Väisälä buoyancy period is ~ 5 min at the mesopause.

This report focuses on the analysis of a time series of "images" of the horizontal structure in OH* nightglow recorded by UWOSCR (University of Western Ontario SCanning Radiometer) in order to derive parameters of internal GWs/ripples, namely, horizontal phase velocity (v_h), direction (ϕ), wave period (T), and horizontal wavelength (λ_h). After a brief description of the instrument characteristics in section 2, the analysis method is described in section 3. Section 4 shows results obtained at Davis Station during the period 1999–2013. GW sources at Davis Station are investigated in section 5 by performing reverse ray tracing on mesopause observations. Section 6 discusses possible explanations for the asymmetry observed in the direction of GW propagation and potential sources of the GWs detected above the observing station.

2. Instrumentation

The results reported here were obtained from data (French & Mulligan, 2017) recorded by a scanning radiometer, known as UWOSCR, during the period 1999–2013. This instrument has an instantaneous field of view (FOV) of 1° and scans through a small portion of the sky (24 km×24 km) and, therefore, is most sensitive to small-scale, short-period GWs/ripples. It is one of the University of Western Ontario's near-infrared scanning radiometers, which are ground-based instruments that have been used at various locations to measure GW parameters using the hydroxyl night airglow since the early 1990s (Stockwell & Lowe, 2001a, 2001b). UWOSCR consists of a 12 cm aperture catadioptric telescope ($f/\# = 0.4$) coupled to an *x-y* stage, driven by stepper motors under computer control. The detector is a thermoelectrically cooled, large area planar (positive-intrinsic-negative) InGaAs photodiode which, in conjunction with the transmission cutoff of the silicon entrance window, provides a spectral response in the range 1,100 to 1,650 nm (Figure 1). This region contains some of the brightest vibration-rotation bands of OH*, primarily the (2-0), (3-1), (4-2), and (5-3) bands in the $\Delta v = 2$ sequence and the (7-4), (8-5), and (9-6) bands in the $\Delta v = 3$ sequence.

The instantaneous FOV of the telescope (1°) corresponds to a 1.5 km diameter "footprint" at the height of the airglow layer. The observing sequence drives the telescope in a raster scan of a square, 16 × 16 points in 1° increments with a dwell time per point of ~ 0.22 s, such that the 256 "pixels" in the grid are sampled in ~ 56 s. The telescope is then returned to the start position, and the sequence is repeated once per minute. The result is a 16 × 16 pixel "image" sequence with 1 min resolution, corresponding to a 24 ×24 km grid at the height of the airglow layer and centered at the zenith. Figure 2 illustrates the relationship between UWOSCR operation and the emission layer.

With the low noise and dark current of the detector, the signal-to-noise ratio of each pixel is typically ~ 100. Control software automatically starts and stops the sequence acquisition in all weather conditions between civil twilights (Sun $>6°$ below horizon) each night. Orientation of the grid is determined by theodolite measurement of the *x-y* stage and by reference to stars that are clearly visible in the OH* images recorded by UWOSCR and normally occupy one pixel. Figure 3 shows an example of a sequence of 12 images (frames) from UWOSCR.

With such a small FOV, UWOSCR is most sensitive to small-scale, short-period GWs. It was believed that these waves carried momentum more efficiently and changed the velocity of the mean flow more effectively than large-scale GWs, suggesting that they were the main contributors to vertical transfer of horizontal momentum in the atmosphere (Fritts et al., 2014; Matsuda et al., 2014; Tsuda, 2014). However, a recent report by Sato et al. (2017) found that longer-period (~1 h to 1 day) waves are responsible for a larger contribution of momentum flux than short-period (~8 min to 1 h) waves in the Antarctic summer MLT. The restriction to short-period GWs in UWOSCR does have its disadvantages. For example, long-period waves are known to be less susceptible to critical-level wind filtering as they are much faster and can, therefore, propagate to higher altitudes. This makes long-period waves better suited for ray tracing studies to identify possible GW source regions (Taylor et al., 2009).

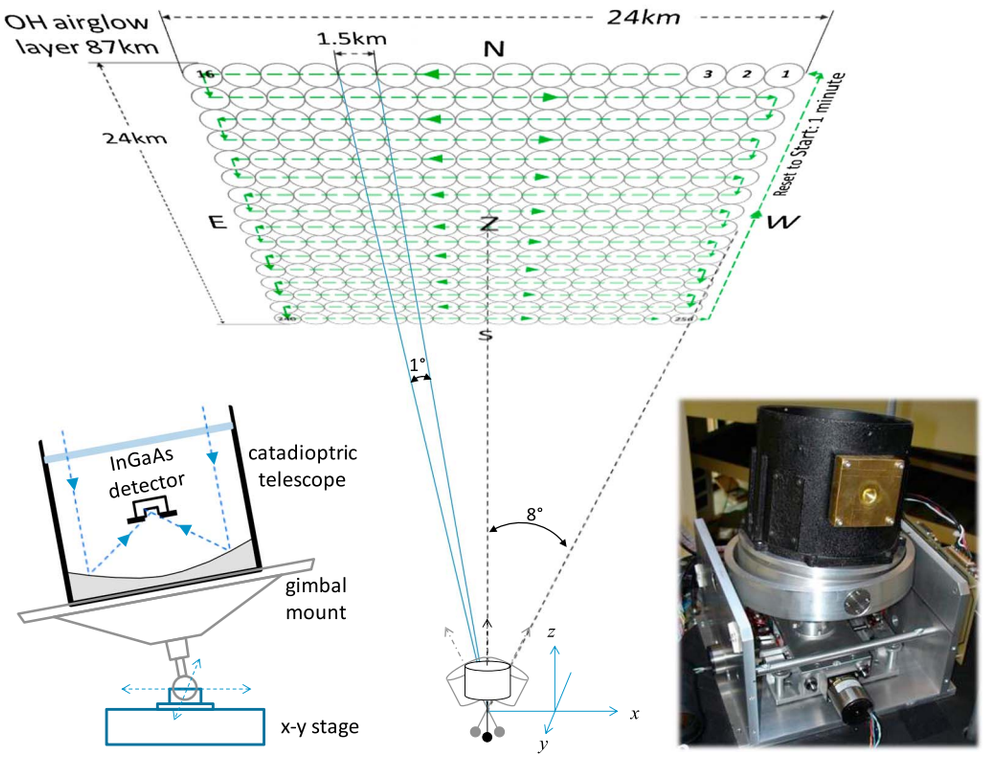

Figure 2. A schematic (left inset) of the UWOSCR instrument (right inset) and FOV at the height of the hydroxyl layer, showing the 16 × 16 point raster scan array. With a 0.22 s dwell time at each point, the field of 256 points and return to start is completed in 1 min.

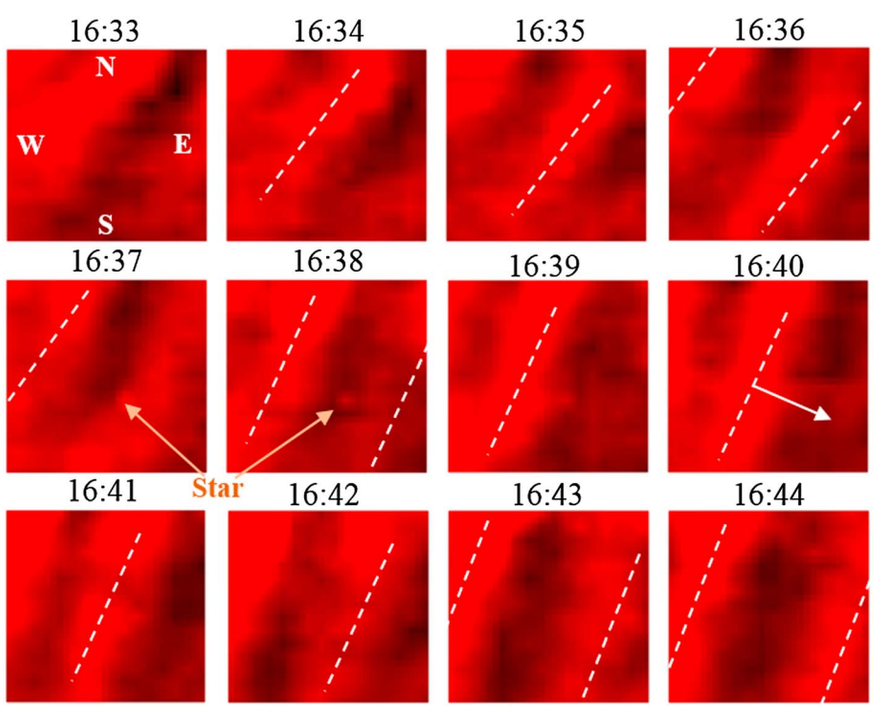

Figure 3. A sequence of 12 frames from UWOSCR on 2 July 2006 at Davis Station. The sequence shows the progression of wavefronts across the FOV (peaks indicated by dashed lines as a guide to the eye). A star is faintly visible between 16:34 and 16:39 UT.

3. Image Sequence Analysis

This section describes how the recorded image sequences are processed to determine characteristics of apparent GWs/ripples that pass through the FOV. There are quite a few techniques in use (Briggs, 1968; Coble et al., 1998; Garcia et al., 1997; Stockwell & Lowe, 2001a) that can do this. One of the main advantages of the method employed here is that it is independent of the user.

3.1. Determination of Wave Period

The period, T, of the dominant wave for a given image is determined from the fast Fourier transform (FFT) of the time variation of the weighted mean center (x_c, y_c) of 32 successive images centered on the frame in question. Weighted mean center coordinates are calculated as

$$x_c = \sum_{i=1}^{16} i\left(\sum_{j=1}^{16} s(i,j)\right) / \sum_{i=1}^{16}\left(\sum_{j=1}^{16} s(i,j)\right) \text{and } y_c = \sum_{j=1}^{16} j\left(\sum_{i=1}^{16} s(i,j)\right) / \sum_{j=1}^{16}\left(\sum_{i=1}^{16} s(i,j)\right)$$

where $s(i,j)$ represents the signal in a pixel with coordinates (i,j).

With a sampling rate of 1 min and a maximum window length of 32 frames, the range of wave periods detectable is 2–16 min. FFTs of sequences of both x_c and y_c are calculated separately, each providing wave amplitudes at 16 equal frequency intervals in the range from 0 to the Nyquist frequency (0.0625 min^{-1}). The peak of the frequency spectrum (maximum plus one point on either side) is fitted with a quadratic to obtain the best fit frequency. The frequency assigned to a given image is the one with the largest power. The observed period of the wave is determined from this frequency ($T = 1/f$) and can take any value in the range 2 to 16 min. As such, orographic waves are not detected by this analysis.

This method suffers from the disadvantage that it can only identify the dominant period present in the data. A series of images that contain two distinct waves with different speeds and directions will give a result that may not be a true representation of either wave.

3.2. Determination of Wave Direction and Speed

The method used to determine GW phase velocity is based on the concept of "lag analysis" or "beamsteering in the slowness domain," which is that if a wave moves across an array of sensors with little change in frequency or wave number, then the arrival times of the disturbance at each sensor can be used to calculate the wave characteristics (Briggs, 1968; Giers et al., 1997; Nappo, 2002). Two one-dimensional correlations in orthogonal directions in the image are used to determine zonal and meridional velocity components.

Cross-correlation analysis of intensity between any two pixels provides the time needed for an intensity peak to pass from one pixel to the next. The measured time lag between two pixels consists of two parts: the actual time lag between the two time series and the time lag offset between the two pixels due to the raster scan. Applying this procedure in two orthogonal directions gives the time delay for these two directions from which we can determine the direction and the phase speed (Giers et al., 1997; Nappo, 2002). Knowing the pixel separation at the nominal altitude of the OH* layer (~87 km; von Savigny et al., 2012, and references therein) to be approximately 1,500 m (angular separation of 1°), the phase speed and direction of propagation of an intensity peak can be found for the orientation of the two pixels used. Since the image contains 256 pixels, calculations are done on all possible pixel combinations at 1, 2, 3, and 4 pixel separations.

When applying the cross-correlation method to obtain the time lags, a window length must be chosen for the cross correlation. This choice depends on the persistence and the period of the waves that we hope to measure. If our choice of window length is considerably shorter than the persistence of the wave, we are not making maximum use of the available data, whereas if our window choice is longer than the persistence of the wave, our cross-correlation calculation may no longer be valid. Guided by estimates of large-amplitude waves observed in the data, the window length was set to 21 frames.

Intrinsic speed, c_i, is calculated from observed speed, c_{obs}, and coincident background wind speed in the direction of the wave, u_{h}, as $c_i = c_{\text{obs}} - u_{\text{h}}$ (Nielsen et al., 2009). Background wind was obtained from hourly averaged MF radar wind data available at 10 min intervals at an altitude of 86 km above Davis Station (Murphy & Vincent, 2000).

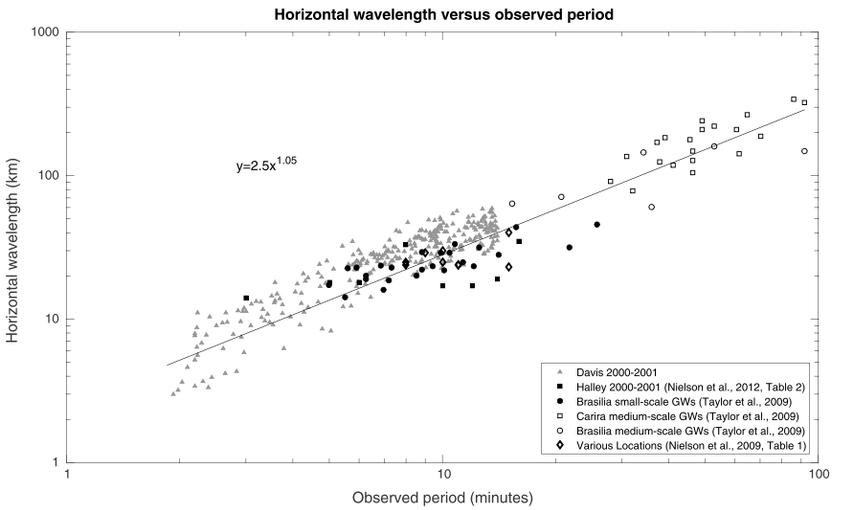

Figure 4. Comparison of the relationship between horizontal wavelength and observed period for a subset (for clarity on the plot) of Davis data with Brazil data, Halley data, and other data adapted from Taylor et al. (2009, Figure 8), Nielsen et al. (2012, Table 2), and Nielsen et al. (2009, Table 1), respectively.

The horizontal wavelength, λ_h, is calculated from $\lambda_h = c_{obs}T_{obs}$ (Lu et al., 2009), where T_{obs} is the observed period. The horizontal wavelength was also determined from the spatial lag analysis of image sequences as a check for consistency in the parameters derived.

3.3. Application of Selection Criteria

The method outlined above yields values of horizontal velocity, direction, period, and horizontal wavelength for each image recorded with the exception of 16 images at the start and end of the night. Values of these four parameters are produced by the analysis for each image, even when the UWOSCR telescope is recording detector noise only. It was necessary, therefore, to establish a robust method to eliminate false wave detections while retaining valid measurements.

The main assumption in establishing such a method is that any physical wave will be present for several minutes and that its characteristics will vary relatively slowly during that period. The assumption was implemented by applying two criteria to the variation of the velocity assigned to each image as follows. The median of the velocity was determined using a sliding five-point window centered on each image. Criterion 1 required that the velocity for a particular image be within ±7 m/s of the median. The choice of a five-point window and 7 m/s was a compromise between failing to eliminate poor data versus the risk of rejecting valid measurements. A second criterion was imposed such that results were only retained for images that satisfied criterion 1 for at least five consecutive minutes. Once again the value of five consecutive images was a compromise similar to that described earlier in this paragraph. On nights that were known to be cloudy, a few images survived the application of criterion 1, but no images survived both 1 and 2.

The sequence shown in Figure 3, of a GW passing through the FOV on 2 July 2006 between around 16:33 UT and 16:44 UT was processed as described above. The resulting wave parameters were as follows: ϕ = (−24±3)° north of east, v_h= (41 ± 8) m/s, T = (7 ± 1) min, and λ_h = (18 ± 5) km.

4. Results

In the results presented, waves are counted such that one count corresponds to one observed wave of any duration. Figure 4 shows the results obtained from UWOSCR overlaid on results obtained from Brazil by Taylor et al. (2009); from Halley Station, Antarctica, by Nielsen et al. (2012); and from various other locations as summarized by Nielsen et al. (2009). It can be seen that all sets of results are in agreement and that the trend $\lambda_h(\text{km}) \approx 2.5(T(\text{min}))^{1.05}$ continues for even shorter periods than observed at Brazil and Halley.

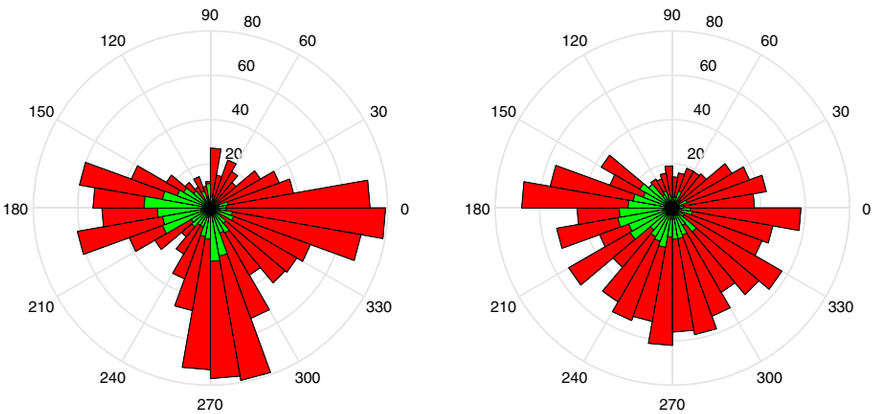

Figure 5. Histogram of (left) observed and (right) intrinsic propagation directions of bands (red) and ripples (green) above Davis Station from 1999 to 2013, where 90°=north.

From Figure 5(left), it can be seen that the observed GWs propagated in distinct directions, with the majority of band-type waves propagating poleward, westward, and eastward and the majority of ripples propagating westward and poleward. From Figure 5(right), it can be seen that there is a meridional anisotropy in intrinsic propagation directions, with very few waves propagating equatorward. However, there is no anisotropy in the zonal direction in the case of intrinsic values. A seasonal variation was also observed, where the majority of observed waves occurred in the winter months, in particular, April, May, and August, as shown in Figure 6 (bottom), and very few ripples were observed from July to October, as shown in Figure 6(top).

Figure 7 summarizes the result of our image analysis in the form of histogram plots of the observed and intrinsic wave characteristics during the period 1999–2013. Figure 7a shows that there are two distinct distributions for horizontal wavelengths, one for ripples (where typically λ_h ≈8–10 km) and one for bands (where typically λ_h≈24–26 km). From Figure 7b it can be seen that waves typically persist for ~6–8 min, but, in rare cases, waves persist for up to ~20–70 min. Figure 7c shows a more symmetric distribution of observed phase speeds with ripples usually propagating at observed horizontal phase speeds of ~40–60 m/s and bands usually propagating with speeds of ~50–80 m/s. From Figure 7d, it can be seen that the observed period of ripples is usually between 2 and 3 min (reminiscent of remnant turbulent structures; Hecht et al., 2014) and the observed period of bands appear to have two maxima at ~7 min and ~13 min, although the latter may partially be an artifact of the analysis as there is an artificial upper boundary at 16 min. Figures 7e and 7f show the corresponding intrinsic values to Figures 7c and 7d, respectively. It is noted that the intrinsic speed of ripples is not calculated to be 0 (Figure 7e) suggesting that their position changes independently of the background wind.

5. Ray Tracing

In an effort to understand our observations, we performed reverse ray tracing of the GWs observed above Davis Station using the approach described by Marks and Eckermann (1995) and implemented by Wrasse et al. (2006) and Tateno and Sato (2008) and more recently in Pramitha et al. (2015). Although the intrinsic speed of the ripples is not calculated to be 0 (Figure 7e), they have been excluded from the ray tracing because some of these may result from turbulence and instabilities (e.g., Hecht et al., 2014). In such cases, their inclusion in the ray tracing could invalidate the resultant statistics. Ideally, detailed knowledge of the wind and temperature fields within a radius of about 500 km above the observing station would be available for the reverse ray tracing. Such data are rare, with the result that climatological models of wind and temperature are usually employed as the best available substitute. The background wind used here for reverse ray tracing was obtained from the Horizontal Wind Model (HWM-07) (Drob et al., 2008), while the temperature data were taken from the MSIS-E-90 model (Hedin, 1991). A "cube" of wind and temperature data (Eckermann & Marks, 1997) 10° in latitude, 30° in longitude, and in the altitude range 0–100 km was created centered on Davis Station for each day of the year. The grid spacing within the segment was 1° latitude, 3° longitude, and 1 km in the vertical direction. Cubic spline interpolations were used in all

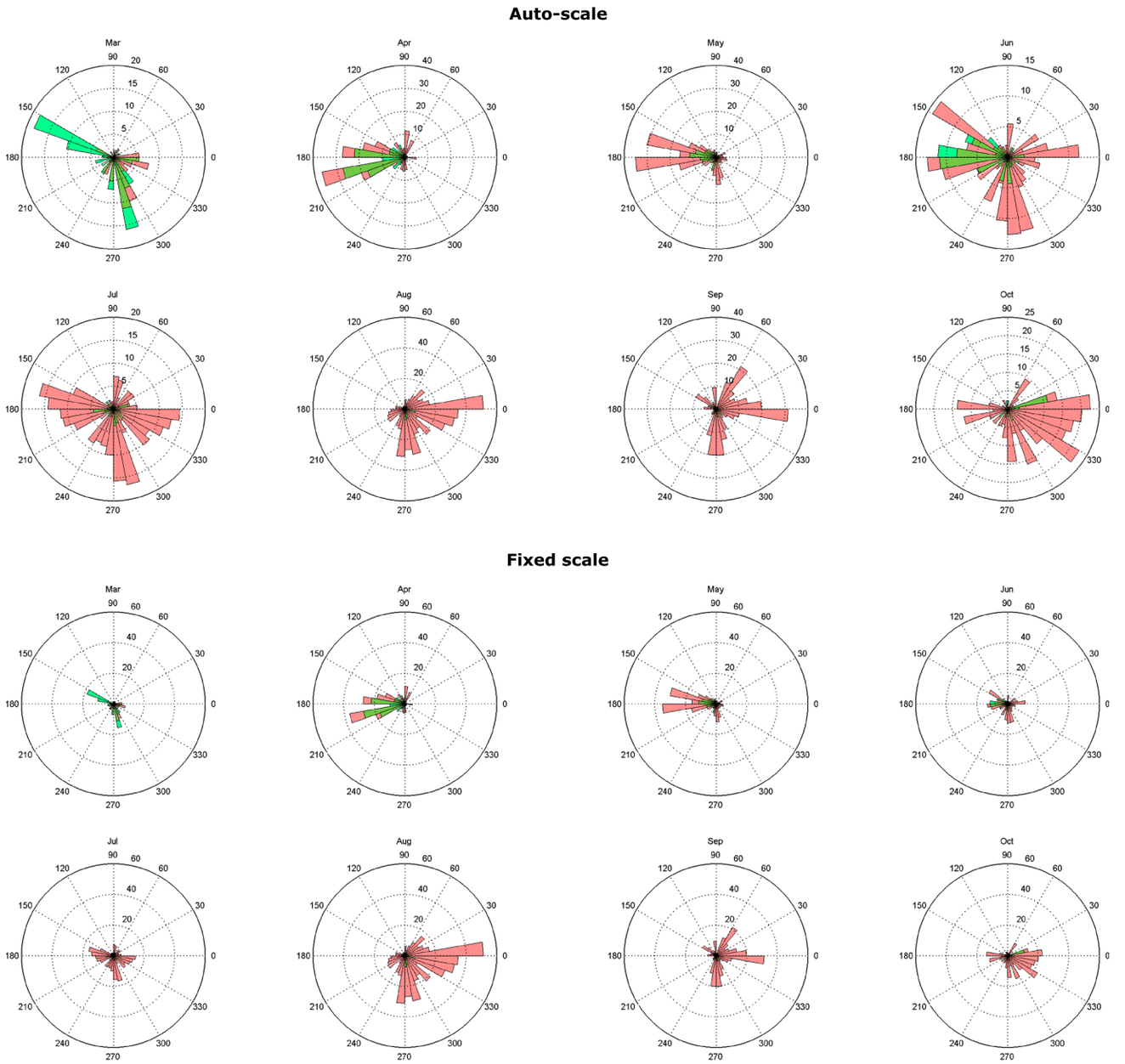

Figure 6. Distribution of observed GW (red) and ripple (green) propagation directions, organized by month. Counts are given as the time in which wave events were detected as a percentage of the total observing time in that particular month, scaled up by a factor of 500. Distributions are presented with both (top) an autoscaled and (bottom) a fixed radial axis, with maximum percentage = 60%. The total number of minutes during which waves were detected in August (all years) was 3,584.

three dimensions to ensure that the spatial derivatives of the background atmospheric parameters varied smoothly to satisfy the WKB (Wentzel-Krammers-Brillouin) approximation used in deriving the ray tracing equations (Eckermann & Marks, 1997). Interpretation of the ray tracing results below must be tempered with the knowledge that the actual wind and temperature field may differ significantly from the climatological values used.

Each GW detected by the UWOSCR instrument was specified by an intrinsic wave phase speed, intrinsic propagation direction, horizontal wavelength, and intrinsic period at the mean altitude of the OH* emission layer (~87 km). Intrinsic parameters were obtained using the locally measured radar winds at the hour of observation. The wave was then reverse ray traced until it reached the troposphere termination altitude

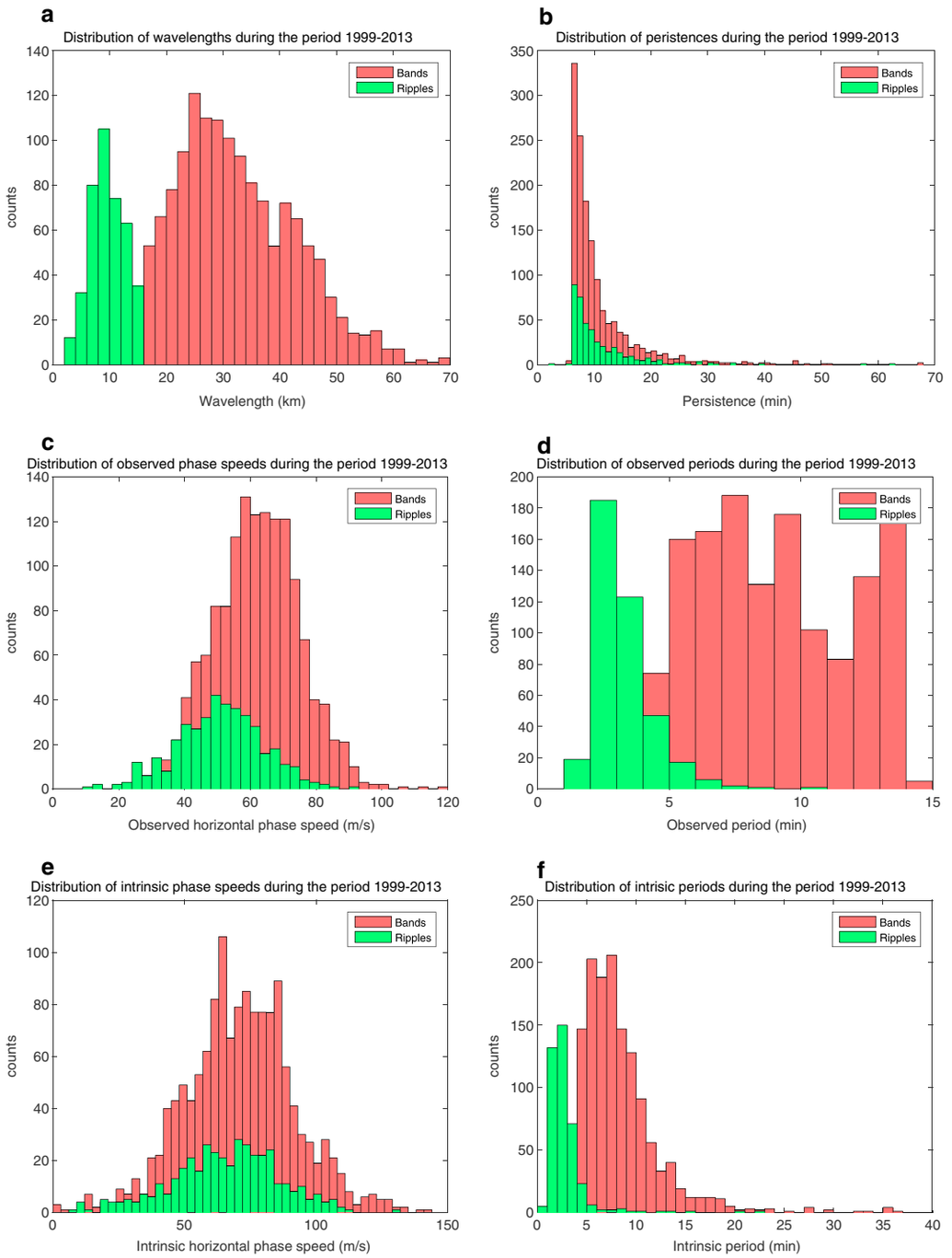

Figure 7. Histograms of (a) horizontal wavelengths, (b) persistence, (c) observed horizontal phase speeds, (d) observed periods, (e) intrinsic horizontal phase speeds, and (f) intrinsic periods for all GWs observed during the period 1999–2013.

(10 km) or until the conditions for wave propagation were no longer valid. Following Wrasse et al. (2006) and Pramitha et al. (2015), the four conditions applied when wave propagation is no longer valid were (1) the WKB approximation used to derive the ray tracing equations no longer holds; (2) the vertical wave number squared, $m^2 < 0$, which means that the wave cannot propagate vertically; (3) the intrinsic frequency $\hat{\omega} < 0$ or close to 0 meaning that the wave is approaching a critical layer; and (4) $m^2 > 1 \times 10^{-6}$ (cycles^2/m^2), which means that the vertical wavelength becomes smaller than 1 km and close to a critical level. In

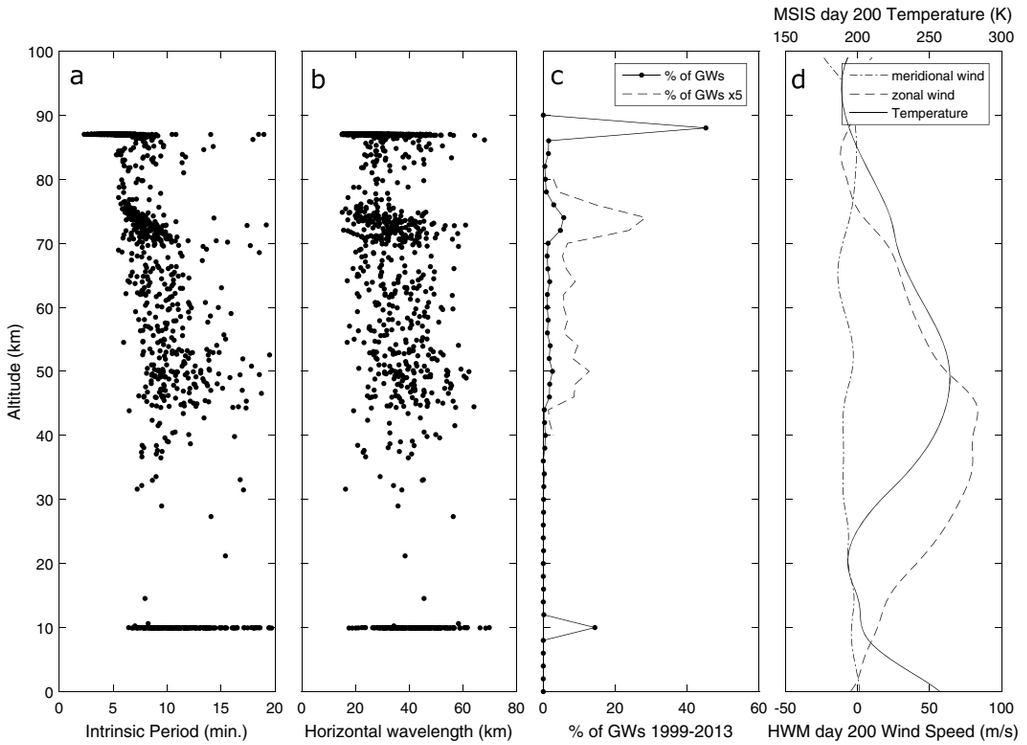

Figure 8. Termination altitude of traced GWs as a function of (a) period, (b) horizontal wavelength, and (c) number of traced GWs. (d) Typical wintertime (day of year = 200) wind and temperature profiles at Davis Station, obtained from HWM-07 and MSIS-E-90 models, respectively.

practice, condition (4) always occurred before condition (3) was reached. A total of 1,407 individual waves over the period 1999 to 2013 were reverse ray traced using this method. Typical uncertainties in the reverse ray tracing results arising from uncertainties in the wave parameter measurements are approximately 1° longitude, 0.25° latitude, and 5 km altitude, although the uncertainty on altitude is very dependent on the terminating point.

A summary of the results of the reverse ray tracing is illustrated in Figure 8c, which shows the percentage of waves that reached a given altitude before a termination condition occurred. On average, ~15% of the GWs detected at the altitude of the OH* layer near the mesopause reached the troposphere termination at 10 km. This is consistent with reports from Wrasse et al. (2006) and Kim et al. (2010) who found that 15% (at Cachoeira Paulista, Brazil) and 23% (at Mount Bohyun, Korea) respectively of waves were traceable to the troposphere, while more than 70% were of mesospheric origin. A large proportion (45%) of the waves ray traced reached the termination condition at, or only slightly below, the altitude of detection (~87 km) because $m^2 < 0$, which means that the atmospheric conditions were unfavorable for vertical wave propagation. This may imply a large proportion of ducted waves that are trapped near the airglow layer.

The altitude profile of the traced waves shows two small but well-defined peaks, one near 50 km and the other at 74 km. The peak near 50 km appears to correspond to the middle atmospheric jet. The termination condition for the majority of those in the peak near 50 km was $m^2 > 1 \times 10^{-6}(\text{cycles}^2/\text{m}^2)$, which means that the vertical wavelength was smaller than 1 km and close to a critical level. The group of waves with termination points between 70 and 80 km tend to have intrinsic periods in the range 7–9 min and horizontal wavelengths in the range 26–38 km (see Figure 8), whereas the group of waves with termination points between 45 and 55 km tend to have longer intrinsic periods (9–13 min) and horizontal wavelengths (34–46 km).

Figure 9 shows the percentage of waves that reach the troposphere for each year. The GWs that reach the troposphere in the reverse ray tracing are characterized by having (1) directions that are predominantly southward, (2) λ_h generally between ~35 and 48 km, and (3) intrinsic periods $>$ ~6.5 min. In contrast, the waves for which the reverse ray tracing terminates near the detection altitude (~87 km) have intrinsic

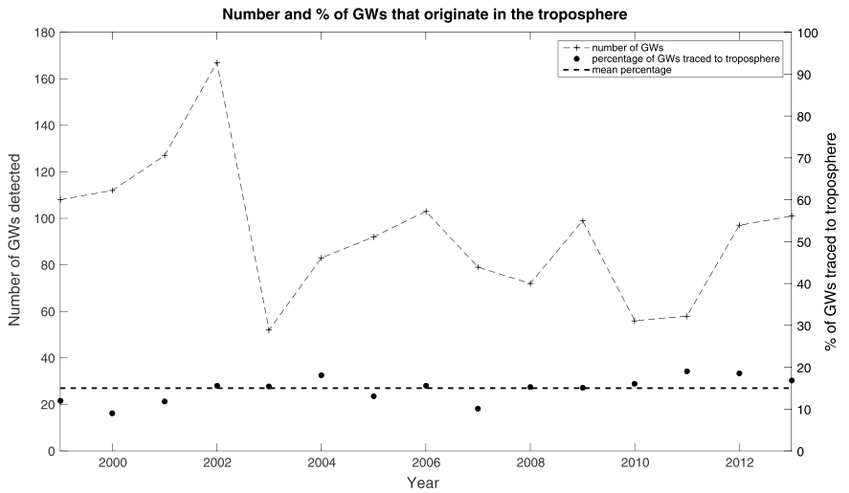

Figure 9. Number of waves detected by year (crosses) and percentage of those waves traced to troposphere (dots). The dashed black horizontal line is the mean percent of waves traced to the troposphere over all years.

periods generally between ~4.5 and 6.5 min and horizontal wavelengths that are generally between 20 and 30 km.

The geographic location of the wave end points that reached the termination altitude (10 km) in the troposphere (204 waves), the 45–55 km region (134 waves), and the 70–80 km region (208 waves) are shown in Figure 10 with the majority of the points falling within a radius of 300 km of the station. These results are discussed in section 6.

Figure 11 shows histograms of the seasonal variation and direction of propagation of the three groups of waves identified by the vertical profile in the reverse ray tracing. The tropospheric group (Figure 11, bottom

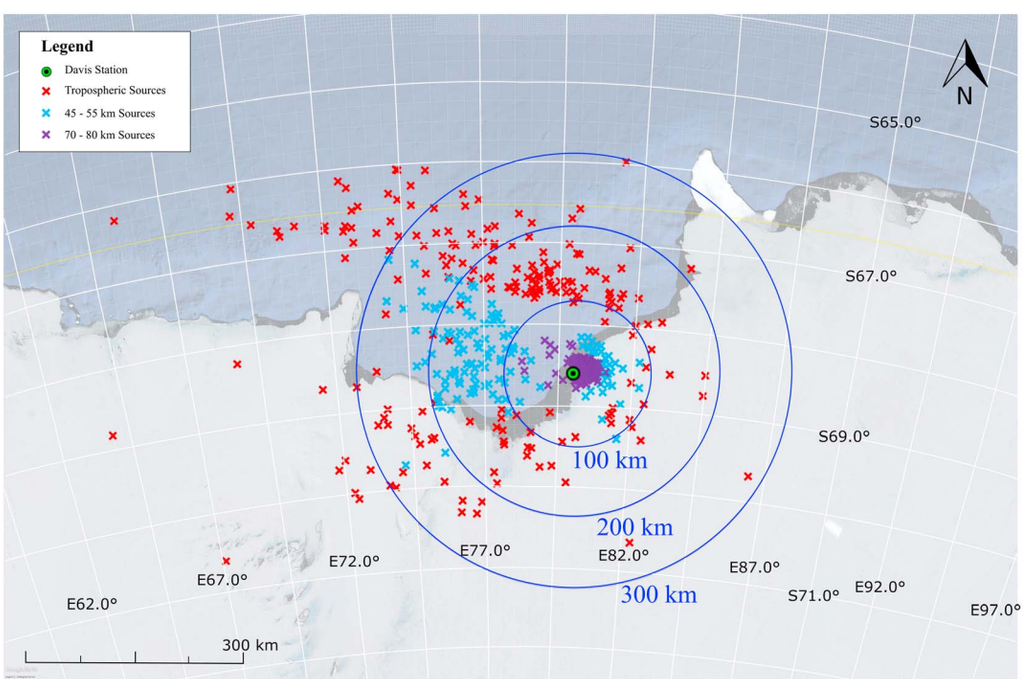

Figure 10. Geographic distribution of the end points of GWs with termination points reverse ray traced to the troposphere (red), the 45–55 km altitude region (blue), and the 70–80 km altitude region (purple).

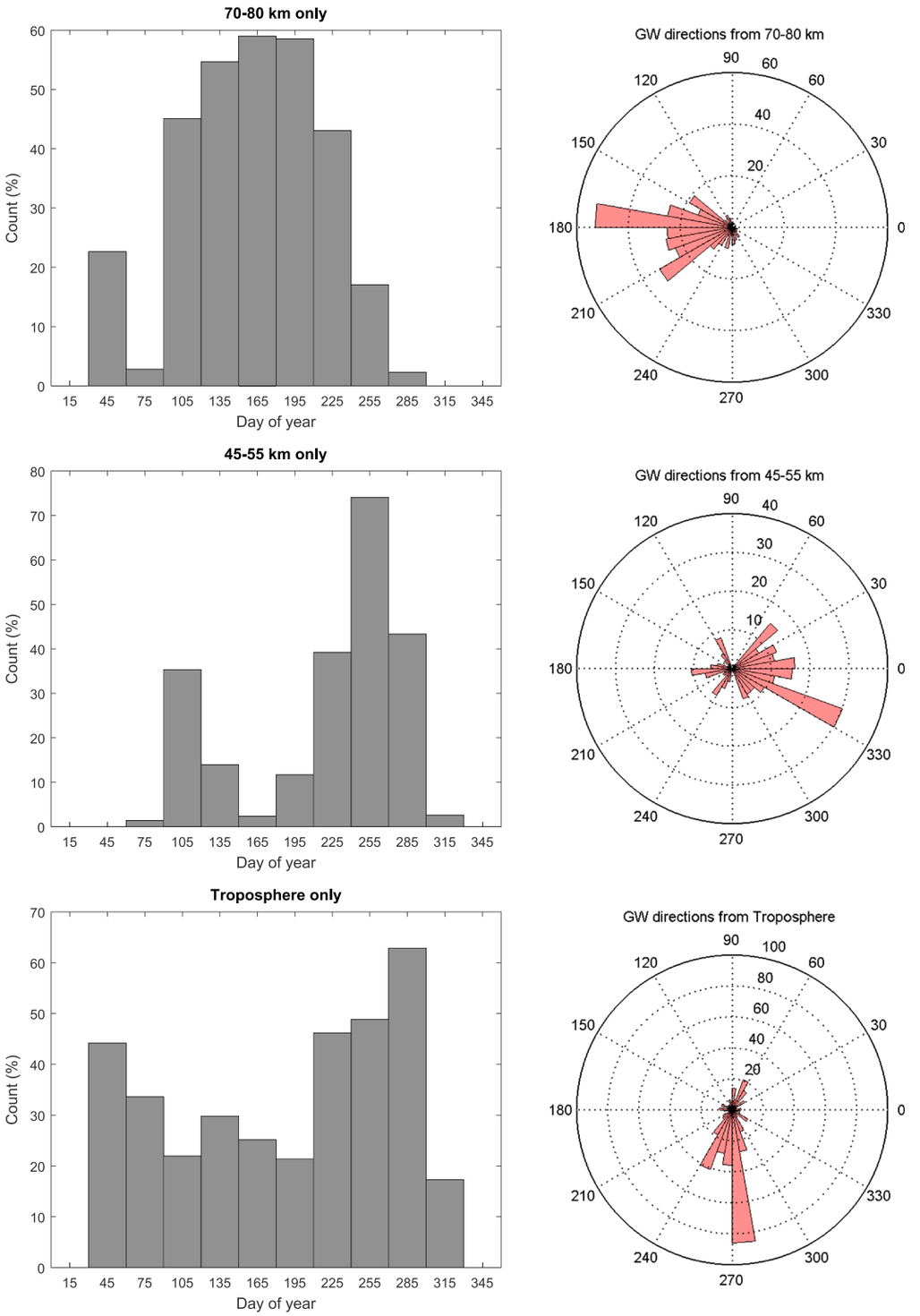

Figure 11. Seasonal and directional distribution of the GWs for three populations selected according to the altitude that the reverse ray tracing terminated. The groups terminated (bottom row) in the troposphere, (middle row) at an altitude range 45–55 km, and (top row) at an altitude range 70–80 km. Counts are given as the time in which wave events were detected as a percentage of the total observing time in that particular month, scaled up by a factor of 500.

row) have a very pronounced southward direction of propagation, with a large peak during August–October and minor peaks in February and in May.

The group with ray traced end points at 45–55 km (Figure 11, middle row) have a maximum in the early austral spring period (September) with a smaller peak in late autumn (April). The September group propagate predominantly eastward, whereas the April group tend to be westward propagating. The group that terminate ray tracing in the 70–80 km altitude region (Figure 11, top row) show a strong midwinter maximum and are generally directed westward. The quite different directions of the three groups and the seasonal difference in their occurrence is discussed in greater detail in section 6.

6. Discussion

Ground-based airglow observations made during February–October over 15 years at Davis Station are used to construct a climatology of the horizontal characteristics of GWs and ripples near the mesopause. The main findings are

1. Two distinct distributions of horizontal wavelength were observed (as shown in Figure 7), both obeying the relation $\lambda_h(\text{km}) \approx 2.5T(\text{min.})^{1.05}$. This trend is consistent with previous results (Nielsen et al., 2009, 2012; Taylor et al., 2009), as shown in Figure 4, but is now extended to include shorter horizontal wavelengths.
2. An unusual distribution of propagation directions over Davis Station was observed, as shown in Figure 5. There was a difference in the observed directional distribution of GWs and ripples, and so they were considered separately. A clear preference for poleward, eastward, and westward propagating GWs was observed but with few ripples propagating eastward. There was also a lack of equatorward waves, a result that is generally consistent with previous high-latitude studies (Matsuda et al., 2014; Nielsen et al., 2009; Suzuki et al., 2009). When the intrinsic directions of the GWs and ripples were determined (by taking account of the background wind from the coincident MF radar wind measurements), the "gaps" in the non-Cartesian directions disappeared as shown in Figure 5(right). Propagation directions will be discussed in further detail below.
3. Ray tracing enabled us to identify four distinct groups among the full set of GWs, each group classified by their termination altitudes as follows: waves that reached a termination condition at ~87 km altitude (~45% of total number of observed waves), those that terminate between 70 and 80 km (~15% of total number of observed waves), those that terminate between 45 and 55 km altitude (~9.5% of total number of observed waves), and finally those that terminate in the troposphere (~15% of total number of observed waves). These groups can be seen in Figures 8a–8c.
4. The timing of GW/ripple activity during the period March–October can be seen in Figure 6 (bottom). The majority of waves observed were in the winter months, with peaks in April, May, and August. This is in good agreement with Dowdy et al. (2007), who studied the seasonal variation of GWs with periods ranging from 20 to 120 min above Davis Station between 1994 and 2005 using MF radar. They found a peak of GW activity during the winter months, with two smaller peaks in March and August.

We consider two possible explanations for the seasonal variability and prominent distribution of GW propagation directions observed: source variability and vertical critical-level filtering, which has been extended to include turning level reflection (Tomikawa, 2015), in the stratospheric mean wind. We first consider vertical critical-level filtering (linking the springtime breakdown of the polar vortex to mesospheric GWs). During the winter, a very strong eastward circulation develops in the polar stratosphere, usually reaching wind speeds of more than ~80 m/s (HWM-07). This jet can block eastward propagating waves (Matsuda et al., 2014; Tomikawa, 2015; Tsuda, 2014), except those whose phase speeds are larger than the eastward wind speed, from moving upward past the stratosphere, while westward propagating waves can move freely upward.

Since ripples have shorter wavelengths than GWs as shown in Figure 7a, they are considerably more susceptible to both critical-level filtering and particularly to turning level reflection, because their periods become shorter than the Brunt-Väisälä period in the large vertical shear as explained by Tomikawa (2015). This could explain why ripples would be almost all filtered out, and, as a result, there would be many fewer ripples than GWs observed in the winter mesopause (as is the case above Davis). When the polar vortex breaks down in springtime, the zonal wind reverses, facilitating eastward propagating GWs while blocking westward

propagating GWs (Kaifler et al., 2015). This is consistent with our climatological observations shown in Figure 6 where there is a strong westward lobe in May and a strong eastward lobe in August. It is also in agreement with Alexander et al. (2011), who studied GWs in the upper stratosphere and lower mesosphere (USLM) region above Davis Station during the winters of 2007–2008 and found that GWs dissipate above ~40 km, where the zonal wind speed is at its maximum. However, based on our ray tracing results, the eastward propagating waves observed do not have tropospheric sources—they belong to the 45–55 km source region (as shown in Figure 11, right column), which is above the polar jet. Based on this, we reject critical-level filtering as an explanation for the distinct seasonal dependent zonal anisotropy in our observed GW directions.

The second explanation that we consider for the distinct seasonal dependent zonal anisotropy in GW directions observed is GW sources around Davis Station and their variability. Initial qualitative assessments about GW source regions can be obtained from Figure 5. First, the lack of waves propagating northward above Davis Station and the absence of a significant meridional wind bias (Figure 8d) suggests that the region poleward of Davis Station is a weak GW source. In particular, the prominent GW propagation directions indicate that possible candidate sources of observed GWs are to the north (over the Davis Sea or Indian Ocean), to the west (toward the Amery Ice Shelf), or to the east (toward the Vestfold Hills and the West Ice Shelf). Based on our ray tracing results, four main altitude source regions have been identified. The group that could not be ray traced significantly below the observing altitude generally have periods of ~4.5–6.5 min and horizontal wavelengths of ~20–30 km, and they have a broad spread of propagation directions but with a notable absence of northward headings. Each of the other three groups exhibited a particular propagation direction preference, as shown in Figure 11(right column).

The geographic location of the wave end points that reached each of these altitude regions is shown in Figure 10. It was found that almost all the waves that were traced to between 70 and 80 km (208 waves) occurred in midwinter (June and July), were locally generated to the east of the station, and were propagating westward at the detection altitude. Most of the waves that were traced to just above the stratospheric jet, between 45 and 55 km (134 waves), were generated either to the east or west of the station and were propagating either eastward or westward at the detection altitude. Most of these waves occurred in May and August, which corresponds to the timing of the formation and breakdown of the polar vortex. The waves that were traced all the way down to the troposphere (204 waves) have intrinsic periods greater than 6.5 min, horizontal wavelengths greater than 20 km, and propagation directions predominantly southward; show a very pronounced concentration of wave initiation to the northwest at approximately 100–300 km from the observing point; and occurred consistently throughout all seasons. One possibility for the origin of these waves is the interaction of planetary waves with the background wind fields, as discussed recently by Mehta et al. (2017) for the case of short-period mesospheric GWs detected at the South Pole. A detailed investigation of this hypothesis for the waves reported here is beyond the scope of this work.

In terms of tropospheric sources, Alexander and Murphy (2015) reported that GW production in the lower troposphere above Davis Station was at its most active when large-scale low-pressure systems produced southwestward wind flow that enhanced katabatic winds over the station. The principal source of these GWs was believed to be airflow over an ice ridge line approximately 60 km northeast of Davis, oriented at ~90° with respect to the wind. However, these GWs (orographic in origin) were not expected to reach the middle atmosphere because of low-level (midtroposphere) critical filtering (Alexander & Murphy, 2015). This latter point is supported by our ray tracing results in which virtually no waves reached the troposphere in this geographical region.

Alexander et al. (2011) suggested that GW variability in the USLM above Davis Station may be due to a large source variability or in situ GW generation by the polar vortex, and they ruled out Doppler shifting by background winds in the region. The seasonal variation and propagation direction of the GWs with end points in this region (45–55 km) based on our ray tracing results is consistent with their generation by the polar vortex. This is also in agreement with Sato et al. (2009, Figure 3), who identified Antarctic regions that have a high GW momentum flux in the winter lower stratosphere. From their map, it can be seen that Davis has a momentum flux with an absolute value of 2–4 mPa, most likely indicating either a topographical source in the region or spontaneous GW emission from the strong eastward jets and fronts (Sato et al., 2009).

7. Conclusions

In this paper, we process and analyze ground-based OH* airglow images from Davis Station dating from 1999 to 2013 (excluding summer months) to extract information about the horizontal structure of GWs ($\lambda_h >$ 15 km) and ripples ($\lambda_h \leq 15$ km) at ~87 km altitude. A climatology of phase speeds, horizontal wavelengths, periods, and propagation directions is presented.

Horizontal wavelengths and periods were found to be highly correlated, such that $\lambda_h(\text{km}) \approx 2.5T(\text{min})^{1.05}$, as has been found in previous studies. Source altitude and seasonal dependent predominant propagation directions were observed. Most waves were observed to occur during April, May, and August, which approximately corresponds to the beginning and end of the polar vortex. The predominant wave directions over the station is southward, eastward, and westward for GWs and southward and westward for ripples. We suggest that source variability may be a contributing factor in why we observe these pronounced directions, but further investigation is required to determine the exact cause.

Acknowledgments

The UWOSCR instrument was conceived and developed by R. P. Lowe formerly of the University of Western Ontario. R. P. Lowe died during the preparation of this manuscript, and his passing is a great loss to the authors as well as to the many collaborators over the course of a lifetime in science. The authors would like to thank the staff at Davis Station, Antarctica, for operating and maintaining the instrument over many years. Valuable exchanges with Mike Taylor and Dominique Pautet of Utah State University as well as R. G. Stockwell of GATS, Inc., Boulder, Colorado, on analysis of the data are gratefully acknowledged. We also thank David Turnbull, Ron De Serrano, and Kelly Ward of the University of Western Ontario, Canada, for the use of their analysis software. We are grateful to three anonymous reviewers for their valuable comments. S. R. acknowledges Maynooth University for personal support through a John and Pat Hume Scholarship. The Davis UWOSCR data used in this manuscript are archived in the Australian Antarctic Data Center at data.aad.gov.au. This work is supported by the Australian Antarctic Science program under projects 674,4025 and 4157.

References

Alexander, M. J. (1998). Interpretations of observed climatological patterns in stratospheric gravity wave variance. *Journal of Geophysical Research*, *103*(D8), 8627–8640. https://doi.org/10.1029/97JD03325

Alexander, M. J., & Barnet, C. (2007). Using satellite observations to constrain parameterizations of gravity wave effects for global models. *Journal of the Atmospheric Sciences*, *64*(5), 1652–1665. https://doi.org/10.1175/JAS3897.1

Alexander, M. J., Geller, M., McLandress, C., Polavarapu, S., Preusse, P., Sassi, F., … Watanabe, S. (2010). Recent developments in gravity-wave effects in climate models and the global distribution of gravity-wave momentum flux from observations and models. *Quarterly Journal of the Royal Meteorological Society*, *136*(650), 1103–1124. https://doi.org/10.1002/qj.637

Alexander, S. P., Klekociuk, A. R., & Murphy, D. J. (2011). Rayleigh lidar observations of gravity wave activity in the winter upper stratosphere and lower mesosphere above Davis, Antarctica (69°S, 78°E). *Journal of Geophysical Research*, *116*, D13109. https://doi.org/10.1029/2010JD015164

Alexander, S. P., & Murphy, D. (2015). The seasonal cycle of lower-tropospheric gravity wave activity at Davis, Antarctica (69°S, 78°E). *Journal of the Atmospheric Sciences*, *72*(3), 1010–1021. https://doi.org/10.1175/JAS-D-14-0171.1

Bageston, J. V., Wrasse, C. M., Gobbi, D., Takahashi, H., & Souza, P. B. (2009). Observation of mesospheric gravity waves at Commandante Ferraz Antarctic Station (62°S). *Annales de Geophysique*, *27*(6), 2593–2598. https://doi.org/10.5194/angeo-27-2593-2009

Bates, D. R., & Nicolet, M. (1950). The photochemistry of atmospheric water vapor. *Journal of Geophysical Research*, *55*(3), 301–327. https://doi.org/10.1029/JZ055i003p00301

Briggs, B. H. (1968). On the analysis of moving patterns in geophysics—I. Correlation analysis. *Journal of Atmospheric and Terrestrial Physics*, *30*(10), 1789–1794. https://doi.org/10.1016/0021-9169(68)90098-6

Choi, H. J., & Chun, H. Y. (2013). Effects of convective gravity wave drag in the Southern Hemisphere winter stratosphere. *Journal of the Atmospheric Sciences*, *70*(7), 2120–2136. https://doi.org/10.1175/JAS-D-12-0238.1

Coble, M., Papen, G. C., & Gardner, C. S. (1998). Computing two-dimensional unambiguous horizontal wavenumber spectra from OH airglow images. *IEEE Transactions on Geoscience and Remote Sensing*, *36*(2), 368–382. https://doi.org/10.1109/36.662723

Dowdy, A. J., Vincent, R. A., Tsutsumi, M., Igarashi, K., Murayama, Y., Singer, W., & Murphy, D. J. (2007). Polar mesosphere and lower thermosphere dynamics: 1. Mean wind and gravity wave climatologies. *Journal of Geophysical Research*, *112*, D17104. https://doi.org/10.1029/2006JD008126

Drob, D. P., Emmert, J. T., Crowley, G., Picone, J. M., Shepherd, G. G., Skinner, W., … Vincent, R. A. (2008). An empirical model of the Earth's horizontal wind fields: HWM07. *Journal of Geophysical Research*, *113*, A12304. https://doi.org/10.1029/2008JA013668

Eckermann, S. D., & Marks, C. J. (1997). GROGRAT: A new model of the global propagation and dissipation of atmospheric gravity waves. *Advances in Space Research*, *20*(6), 1253–1256. https://doi.org/10.1016/S0273-1177(97)00780-1

French, W. J. R., & Mulligan, F. J. (2017). Scanning radiometer observations of hydroxyl airglow over Davis, Antarctica, 1999–2016, Aust. Antarct. Data Cent. - CAASM Metadata, https://doi.org/10.4225/15/59114b64b057f. Retrieved from https://data.aad.gov.au/metadata/records/AAS_4157_Davis_UWOSCR_1999-2016

Fritts, D. C., & Alexander, M. J. (2003). Gravity wave dynamics and effects in the middle atmosphere. *Reviews of Geophysics*, *41*(1), 1003. https://doi.org/10.1029/2001RG000106

Fritts, D. C., Pautet, P. D., Bossert, K., Taylor, M. J., Williams, B. P., Iimura, H., … Stober, G. (2014). Quantifying gravity wave momentum fluxes with mesosphere temperature mappers and correlative instrumentation. *Journal of Geophysical Research: Atmospheres*, *119*, 13,583–13,603. https://doi.org/10.1002/2014JD022150

Garcia, F. J., Taylor, M. J., & Kelley, M. C. (1997). Two-dimensional spectral analysis of mesospheric airglow image data. *Applied Optics*, *36*(29), 7374–7385. https://doi.org/10.1364/AO.36.007374

Garcia, R. R., Marsh, D. R., Kinnison, D. E., Boville, B. A., & Sassi, F. (2007). Simulation of secular trends in the middle atmosphere, 1950–2003. *Journal of Geophysical Research*, *112*, D09301. https://doi.org/10.1029/2006JD007485

Gardner, C. S., & Taylor, M. J. (1998). Observational limits for lidar, radar, and airglow imager measurements of gravity wave parameters. *Journal of Geophysical Research*, *103*(D6), 6427–6437. https://doi.org/10.1029/97JD03378

Gardner, C. S., & Voelz, D. G. (1987). Lidar studies of the nighttime sodium layer over Urbana, Illinois: 2. Gravity waves. *Journal of Geophysical Research*, *92*(A5), 4673–4974. https://doi.org/10.1029/JA092iA05p04673

Giers, D. H., Sahai, Y., Cogger, L. L., & Ryan, E. H. (1997). Occurrence characteristics of mesospheric gravity waves at 51°N. *Journal of Atmospheric and Solar - Terrestrial Physics*, *59*(10), 1197–1203. https://doi.org/10.1016/S1364-6826(96)00117-4

Goldberg, R. A., Fritts, D. C., Williams, B. P., Lűbken, F.-J., Rapp, M., Singer, W., … Krueger, D. A. (2004). The MaCWAVE/MIDAS rocket and ground-based measurements of polar summer dynamics: Overview and mean state structure. *Geophysical Research Letters*, *31*, L24S02. https://doi.org/10.1029/2004GL019411

Hamilton, K. (Ed.) (1997). *Gravity wave processes: Their parameterization in global climate models*, *NATO ASI Series: Global Environmental Change* (Vol. 50). Berlin: Springer. https://doi.org/10.1007/978-3-642-60654-0

Hecht, J. H., Liu, A. Z., Walterscheid, R. L., Franke, S. J., Rudy, R. J., Taylor, M. J., & Pautet, P. D. (2007). Characteristics of short-period wavelike features near 87 km altitude from airglow and lidar observations over Maui. *Journal of Geophysical Research*, *112*, D16101. https://doi.org/10.1029/2006JD008148

Hecht, J. H., Wan, K., Gelinas, L. J., Fritts, D. C., Walterscheid, R. L., Rudy, R. J., … Swenson, G. R. (2014). The life cycle of instability features measured from the Andes Lidar Observatory over Cerro Pachon on 24 March 2012. *Journal of Geophysical Research: Atmospheres*, *119*, 8872–8898. https://doi.org/10.1002/2014JD021726

Hedin, A. E. (1991). Extension of the MSIS thermosphere model into the middle and lower atmosphere. *Journal of Geophysical Research*, *96*(A2), 1159–1172. https://doi.org/10.1029/90JA02125

Hibbins, R. E., Espy, P. J., Jarvis, M. J., Riggin, D. M., & Fritts, D. C. (2007). A climatology of tides and gravity wave variance in the MLT above Rothera, Antarctica obtained by MF radar. *Journal of Atmospheric and Solar - Terrestrial Physics*, *69*(4-5), 578–588. https://doi.org/10.1016/j.jastp.2006.10.009

Hoffmann, L., Xue, X., & Alexander, M. J. (2013). A global view of stratospheric gravity wave hotspots located with Atmospheric Infrared Sounder observations. *Journal of Geophysical Research: Atmospheres*, *118*, 416–434. https://doi.org/10.1029/2012JD018658

Kaifler, B., Lübken, F.-J., Höffner, J., Morris, R. J., & Viehl, T. P. (2015). Lidar observations of gravity wave activity in the middle atmosphere over Davis (69°S, 78°E), Antarctica. *Journal of Geophysical Research: Atmospheres*, *120*, 4506–4521. https://doi.org/10.1002/2014JD022879

Kim, Y. H., Lee, C. S., Chung, J. K., Kim, J. H., & Chun, H. Y. (2010). Seasonal variations of mesospheric gravity waves observed with an airglow all-sky camera at Mt. Bohyun, Korea (36°N). *The Journal of Astronomy Space Science*, *27*(3), 181–188. https://doi.org/10.5140/JASS.2010.27.3.181

Krassovsky, V. I. (1972). Infrasonic variations of OH emission in the upper atmosphere. *Annales de Geophysique*, *77*(4), 254–259.

Krassovsky, V. I., Shefov, N. N., & Yarin, V. I. (1962). Atlas of the airglow spectrum 3000–12400 Å. *Planetary and Space Science*, *9*(12), 883–915. https://doi.org/10.1016/0032-0633(62)90008-9

Krebsbach, M., & Preusse, P. (2007). Spectral analysis of gravity wave activity in SABER temperature data. *Geophysical Research Letters*, *34*, L03814. https://doi.org/10.1029/2006GL028040

Leena, P. P., Venkat Ratnam, M., Krishna Murthy, B. V., & Vijaya Bhaskara Rao, S. (2012). Detection of high frequency gravity waves using high resolution radiosonde observations. *Journal of Atmospheric and Solar - Terrestrial Physics*, *77*, 254–259. https://doi.org/10.1016/j.jastp.2012.01.003

Liu, A. Z., & Swenson, G. R. (2003). A modeling study of O_2 and OH airglow perturbations induced by atmospheric gravity waves. *Journal of Geophysical Research*, *108*(D4), 4148. https://doi.org/10.1029/2002JD002474

Lu, X., Liu, A. Z., Swenson, G. R., Li, T., Leblanc, T., & Mcdermid, I. S. (2009). Gravity wave propagation and dissipation from the stratosphere to the lower thermosphere. *Journal of Geophysical Research*, *114*, D11101. https://doi.org/10.1029/2008JD010112

Makhlouf, U. B., Picard, R. H., Winick, J. R., & Tuan, T. F. (1998). A model for the response of the atomic oxygen 557.7 nm and the OH Meinel airglow to atmospheric gravity waves in a realistic atmosphere. *Journal of Geophysical Research*, *103*(D6), 6261–6269. https://doi.org/10.1029/97JD03082

Marks, C. J., & Eckermann, S. D. (1995). A three-dimensional non-hydrostatic ray-tracing model for gravity waves: Formulation and preliminary results for the middle atmosphere. *Journal of the Atmospheric Sciences*, *52*(11), 1959–1984. https://doi.org/10.1175/1520-0469(1995)052%3C1959:ATDNRT%3E2.0.CO;2

Matsuda, T. S., Nakamura, T., Ejiri, M. K., Tsutsumi, M., & Shiokawa, K. (2014). New statistical analysis of the horizontal phase velocity distribution of gravity waves observed by airglow imaging. *Journal of Geophysical Research: Atmospheres*, *119*, 9707–9718. https://doi.org/10.1002/2014JD021543

Matsuda, T. S., Nakamura, T., Ejiri, M. K., Tsutsumi, M., Tomikawa, Y., Taylor, M. J., … Moffat-Griffin, T. (2017). Characteristics of mesospheric gravity waves over Antarctica observed by ANGWIN (Antarctic gravity wave instrument network) imagers using 3-D spectral analyses. *Journal of Geophysical Research: Atmospheres*, *122*, 8969–8981. https://doi.org/10.1002/2016JD026217

McLandress, C., Shepherd, T. G., Polavarapu, S., & Beagley, S. R. (2012). Is missing orographic gravity wave drag near 60°S the cause of the stratospheric zonal wind biases in chemistry–climate models? *Journal of the Atmospheric Sciences*, *69*(3), 802–818. https://doi.org/10.1175/JAS-D-11-0159.1

Mehta, D., Gerrard, A. J., Ebihara, Y., Weatherwax, A. T., & Lanzerotti, L. J. (2017). Short-period mesospheric gravity waves and their sources at the South Pole. *Atmospheric Chemistry and Physics*, *17*(2), 911–919. https://doi.org/10.5194/acp-17-911-2017

Moffat-Griffin, T., Hibbins, R. E., Jarvis, M. J., & Colwell, S. R. (2011). Seasonal variations of gravity wave activity in the lower stratosphere over an Antarctic Peninsula station. *Journal of Geophysical Research*, *116*, D14111. https://doi.org/10.1029/2010JD015349

Murphy, D. J., & Vincent, R. A. (2000). Amplitude enhancements in Antarctic MF radar echoes. *Journal of Geophysical Research*, *105*(D21), 26,683–26,693. https://doi.org/10.1029/2000JD900510

Nakamura, T., Higashikawa, A., Tsuda, T., & Matsushita, Y. (1999). Seasonal variations of gravity wave structures in OH airglow with a CCD imager at Shigaraki. *Earth, Planets and Space*, *51*(7-8), 897–906. https://doi.org/10.1186/BF03353248

Nappo, C. J. (2002). *An introduction to atmospheric gravity waves*. San Diego, CA: Academic Press.

Nielsen, K., Taylor, M. J., Hibbins, R. E., & Jarvis, M. J. (2009). Climatology of short-period mesospheric gravity waves over Halley, Antarctica (76°S, 27°W). *Journal of Atmospheric and Solar - Terrestrial Physics*, *71*(8-9), 991–1000. https://doi.org/10.1016/j.jastp.2009.04.005

Nielsen, K., Taylor, M. J., Hibbins, R. E., Jarvis, M. J., & Russell, J. M. (2012). On the nature of short-period mesospheric gravity wave propagation over Halley, Antarctica. *Journal of Geophysical Research*, *117*, D05124. https://doi.org/10.1029/2011JD016261

Nikoukar, R., Swenson, G. R., Liu, A. Z., & Kamalabadi, F. (2007). On the variability of mesospheric OH emission profiles. *Journal of Geophysical Research*, *112*, D19109. https://doi.org/10.1029/2007JD008601

Pautet, P. D., Stegman, J., Wrasse, C. M., Nielsen, K., Takahashi, H., Taylor, M. J., … Eckermann, S. D. (2011). Analysis of gravity waves structures visible in noctilucent cloud images. *Journal of Atmospheric and Solar - Terrestrial Physics*, *73*(14-15), 2082–2090. https://doi.org/10.1016/j.jastp.2010.06.001

Pramitha, M., Venkat Ratnam, M., Taori, A., Krishna Murthy, B. V., Pallamraju, D., & Vijaya Bhaskar Rao, S. (2015). Evidence for tropospheric wind shear excitation of high-phase-speed gravity waves reaching the mesosphere using the ray-tracing technique. *Atmospheric Chemistry and Physics*, *15*(5), 2709–2721. https://doi.org/10.5194/acp-15-2709-2015

Preusse, P., Eckermann, S. D., Ern, M., Oberheide, J., Picard, R. H., Roble, R. G., … Mlynczak, M. G. (2009). Global ray tracing simulations of the SABER gravity wave climatology. *Journal of Geophysical Research*, *114*, D08126. https://doi.org/10.1029/2008JD011214

Rapp, M., Gumbel, J., & Lübken, F.-J. (2001). Absolute density measurements in the middle atmosphere. *Annales de Geophysique*, *19*(5), 571–580. https://doi.org/10.5194/angeo-19-571-2001

Reeder, M. J., Adams, N., & Lane, T. P. (1999). Radiosonde observations of partially trapped lee waves over Tasmania, Australia. *Journal of Geophysical Research*, *104*(D14), 16,719–16,727. https://doi.org/10.1029/1999JD900038

Sato, K., Kohma, M., Tsutsumi, M., & Sato, T. (2017). Frequency spectra and vertical profiles of wind fluctuations in the summer Antarctic mesosphere revealed by MST radar observations. *Journal of Geophysical Research: Atmospheres*, *122*, 3–19. https://doi.org/10.1002/2016JD025834

Sato, K., Watanabe, S., Kawatani, Y., Tomikawa, Y., Miyazaki, K., & Takahashi, M. (2009). On the origins of mesospheric gravity waves. *Geophysical Research Letters*, *36*, L19801. https://doi.org/10.1029/2009GL039908

Stockwell, R. G., & Lowe, R. P. (2001a). Airglow imaging of gravity waves: 1. Results from a small network of OH nightglow scanning imagers. *Journal of Geophysical Research*, *106*(D15), 17,185–17,203. https://doi.org/10.1029/2001JD900035

Stockwell, R. G., & Lowe, R. P. (2001b). Airglow imaging of gravity waves 2. Critical layer filtering. *Journal of Geophysical Research*, *106*(D15), 17,205–17,220. https://doi.org/10.1029/2001JD900036

Suzuki, S., Shiokawa, K., Hosokawa, K., Nakamura, K., & Hocking, W. K. (2009). Statistical characteristics of polar cap mesospheric gravity waves observed by an all-sky airglow imager at Resolute Bay, Canada. *Journal of Geophysical Research*, *114*, A01311. https://doi.org/10.1029/2008JA013652

Swenson, G. R., & Gardner, C. S. (1998). Analytical models for the responses of the mesospheric OH* and Na layers to atmospheric gravity waves. *Journal of Geophysical Research*, *103*(D6), 6271–6294. https://doi.org/10.1029/97JD02985

Takahashi, T., Nozawa, S., Tsutsumi, M., Hall, C., Suzuki, S., Tsuda, T. T., … Fujii, R. (2014). A case study of gravity wave dissipation in the polar MLT region using sodium LIDAR and radar data. *Annales de Geophysique*, *32*(10), 1195–1205. https://doi.org/10.5194/angeo-32-1195-2014

Tateno, S., & Sato, K. (2008). A study of inertia-gravity waves in the middle stratosphere based on intensive radiosonde observations. *Journal of the Meteorological Society of Japan*, *86*(5), 719–732. https://doi.org/10.2151/jmsj.86.719

Taylor, M. J., Bishop, M. B., & Taylor, V. (1995). All-sky measurements of short period waves imaged in the OI(557.7 nm), Na(589.2 nm) and near infrared OH and O_2(0,1) nightglow emissions during the ALOHA-93 campaign. *Geophysical Research Letters*, *22*(20), 2833–2836. https://doi.org/10.1029/95GL02946

Taylor, M. J., Pautet, P. D., Medeiros, A. F., Buriti, R. A., Fechine, J., Fritts, D. C., … São Sabbas, F. T. (2009). Characteristics of mesospheric gravity waves near the magnetic equator, Brazil, during the SpreadFEx campaign. *Annales de Geophysique*, *27*(2), 461–472. https://doi.org/10.5194/angeo-27-461-2009

Tomikawa, Y. (2015). Gravity wave transmission diagram. *Annales de Geophysique*, *33*(12), 1479–1484. https://doi.org/10.5194/angeo-33-1479-2015

Tsuda, T. (2014). Characteristics of atmospheric gravity waves observed using the MU (middle and upper atmosphere) radar and GPS (Global Positioning System) radio occultation. *Proceedings of the Japan Academy. Series B*, *90*(1), 12–27. https://doi.org/10.2183/pjab.90.12

Vincent, R. A., Kovalam, S., Reid, I. M., & Younger, J. P. (2010). Gravity wave flux retrievals using meteor radars. *Geophysical Research Letters*, *37*, L14802. https://doi.org/10.1029/2010GL044086

Vincent, R. A., & Reid, I. M. (1983). HF Doppler measurements of mesospheric gravity wave momentum fluxes. *Journal of the Atmospheric Sciences*, *40*(5), 1321–1333. https://doi.org/10.1175/1520-0469(1983)040%3C1321:HDMOMG%3E2.0.CO;2

von Savigny, C., McDade, I. C., Eichmann, K. U., & Burrows, J. P. (2012). On the dependence of the OH* Meinel emission altitude on vibrational level: SCIAMACHY observations and model simulations. *Atmospheric Chemistry and Physics*, *12*(18), 8813–8828. https://doi.org/10.5194/acp-12-8813-2012

Walterscheid, R. L., Schubert, G., & Straus, J. M. (1987). A dynamical-chemical model of wave-driven fluctuations in the OH nightglow. *Journal of Geophysical Research*, *92*(A2), 1241–1254. https://doi.org/10.1029/JA092iA02p01241

Werner, R., Stebel, K., Hansen, G. H., Blum, U., Hoppe, U.-P., Gausa, M., & Fricke, K.-H. (2007). Application of wavelet transformation to determine wavelengths and phase velocities of gravity waves observed by lidar measurements. *Journal of Atmospheric and Solar - Terrestrial Physics*, *69*(17-18), 2249–2256. https://doi.org/10.1016/j.jastp.2007.05.013

Wrasse, C. M., Nakamura, T., Tsuda, T., Takahashi, H., Medeiros, A. F., Taylor, M. J., … Admiranto, A. G. (2006). Reverse ray tracing of the mesospheric gravity waves observed at 23°S (Brazil) and 7°S (Indonesia) in airglow imagers. *Journal of Atmospheric and Solar - Terrestrial Physics*, *68*(2), 163–181. https://doi.org/10.1016/j.jastp.2005.10.012

Wright, C. J., Hindley, N. P., Moss, A. C., & Mitchell, N. J. (2016). Multi-instrument gravity-wave measurements over Tierra del Fuego and the Drake Passage—Part 1: Potential energies and vertical wavelengths from AIRS, COSMIC, HIRDLS, MLS-Aura, SAAMER, SABER and radiosondes. *Atmospheric Measurement Techniques*, *9*(3), 877–908. https://doi.org/10.5194/amt-9-877-2016

Yang, G., Clemesha, B., Batista, P., & Simonich, D. (2008). Improvement in the technique to extract gravity wave parameters from lidar data. *Journal of Geophysical Research*, *113*, D19111. https://doi.org/10.1029/2007JD009454

Yue, J., Nakamura, T., She, C. Y., Weber, M., Lyons, W., & Li, T. (2010). Seasonal and local time variability of ripples from airglow imager observations in US and Japan. *Annales de Geophysique*, *28*(7), 1401–1408. https://doi.org/10.5194/angeo-28-1401-2010

APPENDIX B. FURTHER BACKGROUND

B.1. Linear Theory

Linear theory provides a comprehensible and computable description of GWs. The basis of linear theory for GWs is that a variable (*e.g.* temperature or wind) is expanded into a steady or slowly varying background state and has a small perturbation due to the GW which doesn't affect the background state. Although linear theory comes with some limitations, it provides an understandable picture of GW processes (*Nappo*, 2002).

The Taylor-Goldstein equation (given in Equation B.1) is the wave equation for linear GWs. It is derived by linearizing the governing equations (namely conservation of momentum, mass, and thermal energy) under the Boussinesq approximation (which eliminates acoustic waves). It is assumed that there is no Earth rotation, which means that it is not applicable for GWs with periods greater than a few hours (*Godin*, 2015), and that the atmosphere is frictionless. It is this equation which governs the stability of the air flow when small perturbations (such as GWs) are present in the atmosphere. *Nappo* (2002) provides a detailed derivation of the Taylor-Goldstein equation, which is not provided here.

$$\frac{d^2\widehat{w}}{dz^2} + \left[\frac{N^2}{(\mathrm{c}-\bar{u}_k)^2} + \frac{\bar{u}_k{}''}{(\mathrm{c}-\bar{u}_k)} - \frac{\bar{u}_k{}'}{(\mathrm{c}-\bar{u}_k)\mathrm{H}} - k^2 - \frac{1}{4H^2}\right]\widehat{w} = 0 \qquad \text{B.1}$$

where the major terms are

$\widehat{w} = w_1 \cdot \exp(-i(kx-\omega t)) \cdot \exp\left({}^{-z}/_{2H}\right)$ represents the vertical wind,
$\frac{N^2}{(c-\bar{u}_k)^2}$ is the buoyancy term,
$\frac{\bar{u}_k{}''}{c-\bar{u}_k}$ is the curvature term,
$\frac{\bar{u}_k{}'}{(c-\bar{u}_k)\mathrm{H}}$ is the shear term,
k^2 is the non-hydrostatic term,
the term in square brackets is m^2, the vertical wavenumber squared,

and other individual variables are

$N^2 = \frac{g}{T}\left(\frac{dT}{dz} + \Gamma\right)$ is the Brunt-Väisälä frequency squared,
k is the horizontal wave number,
c is the observed phase speed of the wave,
$H = \frac{RT}{g}$ is the scale height,
$\bar{u}_k$ is the wind speed in the direction of the wave, and

$\bar{u}_k'$ and $\bar{u}_k''$ are the first and second derivatives of $\bar{u}_k$ with altitude.

B.2. Hydrostatic Equilibrium

A hydrostatic atmosphere is one in which there is a balance between the downward weight of the atmosphere and the upward pressure force. If an air parcel with unit cross-section, height dz, and density ρ is considered, then the weight of that air parcel is given by $g\rho dz$ and the difference between the pressure P at the bottom and top of the air parcel is given by dP, as shown in Figure B.1.

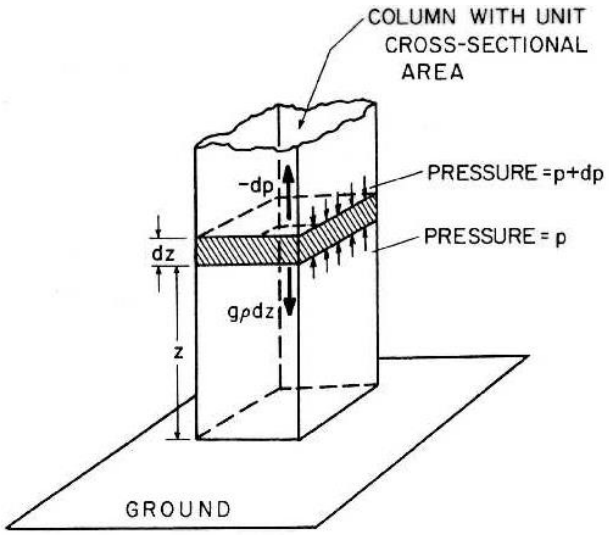

Figure B.1: Hydrostatic balance – the balance of vertical forces in an atmosphere (*Lamb*, 2000).

Then, $-dP = g\rho dz$. In the limit of small dz, this becomes the hydrostatic equation:

$$\frac{dP}{dz} = -g\rho \qquad \text{B.2}$$

B.3. Scale Height

Scale height, H, is a parameter which describes how something fades away with increasing distance. In the case of the atmosphere, it describes how air density decreases with increasing altitude. More specifically, the scale height is the vertical distance over which atmospheric density and pressure decrease by a factor of $\frac{1}{e}$ compared to the ground surface values. An overview of the derivation of the scale height of an isothermal hydrostatic atmosphere is shown

below, but more detailed derivations are provided, for example, by *Nappo* (2002) and *Lee and Ryan* (2015).

Using the ideal gas law (described in section 1.5.2) in the hydrostatic equation (Equation B.2), one obtains $\frac{dP}{dz} = -\frac{gP\mu}{RT}$. Rearranging this equation, and integrating over z, one then obtains $\int_0^z \frac{1}{P} dP = \int_0^z -\frac{g\mu}{RT} dz$. This gives $\ln\left(\frac{P(z)}{P(0)}\right) = \int_0^z -\frac{g(z)\mu(z)}{RT(z)} dz = \int_0^z -\frac{1}{H(z)} dz$, where the scale height is

$$H(z) = \frac{RT(z)}{g(z)\mu(z)}. \qquad \text{B.3}$$

Solving for pressure, one obtains

$$P(z) = P(0) \exp\left(-\int_0^z \frac{dz}{H(z)}\right).$$

Similarly, for density,

$$\rho(z) = \rho(0) \exp\left(-\int_0^z \frac{dz}{H^*(z)}\right),$$

where $H^*(z) = \frac{RT(z)}{g(z)\mu(z)} + \frac{dz}{dT(z)} T(z)$, or $H^*(z) = H(z)$ for an isothermal atmosphere (*e.g. Nappo* (2002); *Lee and Ryan* (2015)).

For the Earth's atmosphere, the average temperature is approximately 288 K and the average molecular mass, μ, is approximately $(0.21)(32) + (0.78)(28) + (0.01)(40) = 29$ g due to its major components at low altitudes (oxygen, nitrogen, and argon). At low altitudes, the acceleration due to gravity is approximately 9.81 m s^{-2}. These values give the following approximation for scale height at low altitudes:

$$H = \frac{(8.31 \text{ J mol}^{-1} \text{ K}^{-1})(288 \text{ K})}{(0.029 \text{ kg mol}^{-1})(9.81 \text{ m s}^{-2})} \approx 8.4 \text{ km}.$$

B.4. Brunt-Väisälä Frequency

The Brunt-Väisälä frequency is the upper boundary for GW frequency, as it describes whether the background atmosphere is stable or not (indicating

whether vertical GW propagation is possible or not). An expression for this frequency can be derived by considering the temperature stability in the atmosphere.

One way of determining the vertical stability of the atmosphere is through the adiabatic lapse rate. Figure B.2 shows a schematic of the rate of change of temperature with altitude for a particular background atmosphere (curved line) and for a particular air parcel in that atmosphere (straight line) between point A and point B. Both the air parcel and the background atmosphere have the same initial temperature at point A. Then, between point A and B, the air parcel is warmer than its surrounding air, and thus it rises up adiabatically with a slope $\frac{dT}{dz} = -\frac{g}{c_p} = \Gamma_d$, where Γ_d is the adiabatic lapse rate for dry air. When the air parcel reaches point B, the background temperature starts to become warmer than the air parcel, and thus the atmosphere does not favour vertical propagation above this point. From this, it can be seen that when the rate of change of atmospheric temperature, $\frac{dT}{dz}$, becomes less than Γ_d, then vertical propagation of an air parcel is possible.

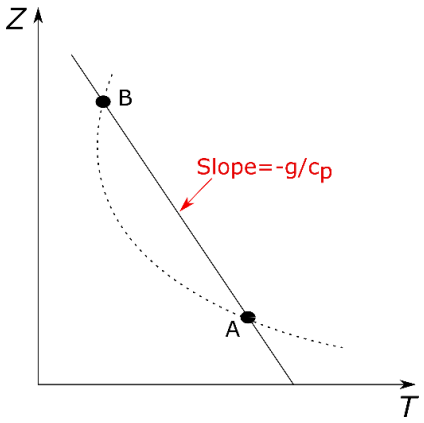

Figure B.2: Schematic showing a background temperature profile (dotted) and an adiabatic profile (solid line) representing the vertical motion of an air parcel, adapted from *Sánchez-Lavega* (2011).

Archimedes' principle may also be used to determine atmospheric vertical stability. That is, the fact that the upward buoyant force, F_B, on an air parcel is equal to the weight, W, of that air parcel can be used. As discussed above,

the air parcel is buoyant when the background temperature, T, is less than the air parcel temperature, T', such that $T < T'$. This means that $\rho > \rho'$, from the equation of state for an ideal gas shown in Section 1.5.2 $\left(P = \frac{\rho RT}{\mu} \right)$. For an air parcel with volume V, the buoyant force on that parcel may be written as $F_B = mg = (\rho - \rho')Vg$. The weight of the air parcel, if displaced by a small vertical distance z', may be written as $W = \rho' V \frac{d^2 z'}{dt^2}$. Therefore, using Archimedes' principle $(\rho - \rho')Vg = \rho' V \frac{d^2 z'}{dt^2}$, this can be simplified as $\frac{d^2 z'}{dt^2} = \frac{g\rho}{\rho'} - g = g\left(\frac{T'}{T} - 1\right)$. If the initial temperature at point A in Figure B.2 is taken to be T_0, the lapse rate of the atmosphere is taken to be $\Gamma = \frac{dT}{dz}$, and the dry adiabatic lapse rate is taken to be $\Gamma_d = -\frac{g}{c_p}$ (which is ~10 K km^{-1} in the 85–90 km altitude range), then one can write $T = T_0 - \Gamma z'$ and $T' = T_0 - \Gamma_d z'$. Then, $\frac{d^2 z'}{dt^2} = g\left(\frac{T_0 - \Gamma_d z'}{T_0 - \Gamma z'} - 1\right) = g\left(\frac{\Gamma - \Gamma_d}{T_0 - \Gamma z'}\right) z' = \frac{g}{T}(\Gamma - \Gamma_d) z'$. The term $\sqrt{\frac{g}{T}(\Gamma - \Gamma_d)}$ is known as the Brunt-Väisälä frequency, N, which is the frequency of oscillation of the air parcel (*Sánchez-Lavega*, 2011). This can be rewritten as

$$N^2 = \frac{g}{T}\left(\frac{dT}{dz} + \frac{g}{c_p}\right). \qquad \text{B.4}$$

The term in brackets in Equation B.4 is known as the thermal static stability. As already discussed, vertical propagation of a parcel is possible whenever $\frac{dT}{dz} < -\frac{g}{c_p}$, and therefore vertical propagation is only possible when $N^2 > 0$. If $N^2 = 0$, then the air parcel is not oscillating, and if $N^2 < 0$ then N is imaginary, meaning that the atmospheric lapse rate exceeds the adiabatic lapse rate, leading to a convective instability (*e.g. Cushman-Roisin* (2014); *Hecht et al.* (2007)).

Equation B.4 can be rewritten in terms of potential temperature (which is defined in Equation B.5) as shown in Equation B.6, because potential temperature remains constant for the air parcel which is rising adiabatically.

$$\theta = T\left(\frac{p_0}{p}\right)^{R/c_p} \qquad \text{B.5}$$

$$N^2 = \frac{g}{\theta}\frac{d\theta}{dz} \qquad \text{B.6}$$

There are two types of instability: convective and dynamical. As has been determined, convective instability occurs when $N^2 < 0$. Dynamical instability, which often leads to Kelvin-Helmholtz billows, can be quantified using another term, the Richardson number. The Richardson number, R_i, is given by Equation B.7. If $0 \leq R_i \leq 0.25$, dynamical instability is likely to occur, and if $R_i < 0$ (*i.e.* $N^2 < 0$), convective instability is likely to occur (*Hecht et al.*, 2007).

$$R_i = \frac{N^2}{\left(\frac{dU}{dz}\right)^2} \qquad \text{B.7}$$

where

$\frac{dU}{dz}$ = horizontal wind shear.

B.5. The Boussinesq Approximation

Under particular conditions, the governing equations of atmospheric motion can be simplified according to what is known as the Boussinesq approximation.

The conditions for when this approximation may be used are *(i)* that the vertical scale of the mean motions (in our case this means the vertical wavelength of the GW, λ_z) must be much less than the scale height, $H = \frac{RT}{g}$, of the atmosphere, and *(ii)* that the perturbations due to these motions are much less than the background values (*Spiegel* and *Veronis*, 1960).

The approximation can be summarised as follows:

1. Fluctuations in density resulting from pressure effects are negligible compared to those resulting from thermal effects.

2. Density fluctuations, in the equations of rate of change of momentum (Equation 1.21) and mass (Equation 1.20), are negligible unless they are

coupled to the gravitational acceleration in the buoyancy force (*Spiegel* and *Veronis*, 1960).

The effect of using the Boussinesq approximation is that the atmosphere becomes incompressible, since fluctuations in density due to pressure effects are negligible, and thus acoustic waves are eliminated.

Some reasoning for this approximation is provided by *Nappo* (2002) by considering the rate of change of momentum equation, *i.e.* $\frac{\mathrm{d}\vec{v}}{\mathrm{dt}} = -\frac{\nabla p}{\rho} + \vec{g}$ and making the substitutions $\rho = \rho_0 + \rho_1$ and $p = p_0 + p_1$, where a subscript of 0 indicates the mean/background value and a subscript of 1 indicates the small perturbation due to a GW. Then, the rate of change of momentum equation becomes $\left(1 + \frac{\rho_1}{\rho_0}\right)\frac{\mathrm{d}\vec{v}}{\mathrm{dt}} = -\frac{\nabla p_0}{\rho_0} + \vec{g} - \frac{\nabla p_1}{\rho_0} + \frac{\rho_1}{\rho_0}\vec{g}$. Assuming the background state is in hydrostatic equilibrium ($\frac{dp}{dz} = -\rho\vec{g}$), then $-\frac{\nabla p_0}{\rho_0} = \vec{g}$. Then, the rate of change of momentum equation becomes: $\left(1 + \frac{\rho_1}{\rho_0}\right)\frac{\mathrm{d}\vec{v}}{\mathrm{dt}} = -\frac{\nabla p_1}{\rho_0} + \frac{\rho_1}{\rho_0}\vec{g}$, where $\frac{\mathrm{d}\vec{v}}{\mathrm{dt}}$ is the inertial term and $\vec{g}$ is the buoyancy term. Since the Boussinesq approximation requires GW perturbations to be much less than background values, and $\lambda_z \ll H$, it follows that $\left|\frac{\rho_1}{\rho_0}\right| \ll 1$ for an isothermal atmosphere. This means that the rate of change of momentum equation can be approximated as $\frac{\mathrm{d}\vec{v}}{\mathrm{dt}} = -\frac{\nabla p_1}{\rho_0} + \frac{\rho_1}{\rho_0}\vec{g}$ when using the Boussinesq approximation. In other words, as stated in point 2 above, the fluctuations in density are negligible unless they are coupled to the buoyancy term (*e.g. Sánchez-Lavega* (2011)). The conservation of mass and thermodynamic equations become $\nabla \cdot \vec{v} = 0$ and $\frac{\partial \rho}{\partial t} + U \cdot \nabla \rho = 0$ because the speed of sound term in the thermodynamic equation, $C_s = \frac{c_p}{c_v}\frac{p}{\rho}$, tends to infinity when $p \gg \rho$ (*Nappo*, 2002).

The squared Brunt-Väisälä frequency is sometimes written in its Boussinesq approximation form (*e.g. Cushman-Roisin* (2014)) as:

$$N^2 = -\frac{g}{\rho_0}\frac{\partial \rho_0}{\partial z}. \qquad \text{B.8}$$

B.6. The Dispersion Relation

The various sinusoidal components of waves in a given wave packet are dispersed to different locations if different wavelengths have different phase speeds, and this dispersion between the phase speed and wavelength is related via the dispersion relation (*Holton*, 1992). It is one of the most important elements of linear wave theory as it relates the angular frequency of a wave to the wave structure and the physical characteristics of the atmosphere (*Nappo*, 2002). The dispersion relation shown here is a solution to the Taylor-Goldstein equation (Equation B.1) when background wind speed is ignored. With compressibility effects neglected to eliminate acoustic waves, the dispersion relation is given by Equation B.9 (*Alexander et al.*, 2010).

$$\widehat{\omega}^2 = \frac{N^2(k^2 + l^2) + f^2(m^2 + \alpha^2)}{k^2 + l^2 + m^2 + \alpha^2} \qquad \text{B.9}$$

where

$\widehat{\omega} = \omega - k\bar{u} - l\bar{v}$ = the intrinsic wave frequency,
f = the Coriolis parameter,
N = the Brunt-Väisälä frequency,
H =the scale height,
$\alpha = (2H)^{-1}$,
k =the zonal wave number,
l =the meridional wave number, and
m =the vertical wave number.

The upper cut-off intrinsic frequency, $\widehat{\omega}_c$, is found by re-arranging the dispersion relation (Equation B.9) with $m = 0$, so that $\widehat{\omega}_c = N^2 - \frac{\alpha^2(N^2 - f^2)}{k^2 + l^2 + \alpha^2}$ and $f^2 < \widehat{\omega}^2 < {\widehat{\omega}_c}^2 \leq N^2$.

B.7. The WKB Approximation

The WKB (Wentzel-Kramers-Brillouin), *a.k.a.* the WKBJ (Wentzel-Kramers-Brillouin-Jeffereys) or LG (Liouville-Green), approximation assumes that wind and Brunt-Väisälä frequency vary slowly over a wave cycle in the vertical. Thus, it is only valid when shears in the background flow can be ignored in

comparison with shears generated by the waves themselves. It is not valid for high-frequency waves, when intrinsic frequency, $\widehat{\omega}$, becomes close to the upper cut-off frequency, $\widehat{\omega}_c = \frac{c}{2H}$ (*Song et al.*, 2014), and the vertical wavenumber becomes very small ($m \to 0$).

In general, when a wave produces variations in the background flow (in the horizontal and in time), the resulting equation may have the form of a second-order linear differential equation, $\frac{d^2w}{dz^2} + m^2 w = 0$, where w is the vertical background wind and m is the vertical wave number. If m is constant, then the solution to this equation would be $w = Ae^{\pm imz}$. In practice, though, m must be considered as a function of z. If $\frac{dm}{dz}$ is small enough, then, locally, the solution is similar to above. A better approximation (the WKB approximation) was found for small $\frac{dm}{dz}$ which will now be described in more detail.

In the WKB method, new co-ordinates, ϕ and W, were introduced such that $\phi = \int m dz$ and $W = \sqrt{m}\, w$. The resulting equation has the form $\frac{d^2W}{d\phi^2} + (1+\delta)W = 0$, where the WKB parameter, $\delta = \frac{1}{m^2}\left|\frac{\partial m}{\partial z}\right| \approx \left|\frac{1}{c_g m^2}\frac{dm}{dt}\right|$. If $\delta \ll 1$, then an approximate solution would be $W = e^{\pm i\phi}$. In this case, the vertical scale (m^{-1}) of the wave is much less than the scale on which m varies (*Gill*, 1982).

The WKB approximation deals with some boundary issues when modelling GW propagation whenever there is significant spatial variation in temperature and wind structure compared to the GW wavelength (*Gossard and Hooke*, 1975). It provides an approximate solution (given in Equation B.10) to the Taylor-Goldstein equation (*Nappo*, 2002).

$$\widehat{w}(z) = \frac{\widehat{w}_0}{\sqrt{m}} \exp\left(\pm \int_0^z m dz\right) \qquad \text{B.10}$$

where

$\widehat{w}_0$ = constant, and

$m^2(z) = \left[\frac{N^2}{(c-u_0)^2} + \frac{u_0''}{(c-u_0)} - \frac{u_0'}{(c-u_0)H} - k^2 - \frac{1}{4H^2}\right]$.

Equation B.10 is also a solution of Equation B.11, which approaches the Taylor-Goldstein equation when $d \ll 1$.

$$\frac{d^2\widehat{w}}{dz^2} + m^2(z)(1+d)\widehat{w} = 0 \qquad \text{B.11}$$

where

$$d = \frac{1}{2m^3}\frac{d^2m}{dz^2} - \frac{3}{4m^4}\left(\frac{dm}{dz}\right)^2.$$

From this, it can be seen that the WKB solution does not allow $m = 0$, a condition which represents wave reflection, because then $d \to \infty$ (*Nappo*, 2002).

APPENDIX C. DE SERRANO AND LOWE C++ CODE

The following program (`vel_dir.cpp`) was used to calculate the meridional and zonal velocities in each frame of a UWOSCR file. The executable version of this code was also provided by Kelly Ward of the University of Western Ontario.

```
1.  // VEL_DIR
2.  // Code written in the University of Western Ontario (UWO)
3.  // Re-written by F. Mulligan from documented sheets of paper at UWO
4.  // Used and commented by S. Rourke @ NUI Maynooth in 2016
5.
6.  // The purpose of this program is to calculate the meridional and zonal velocity
7.  // of wave structures passing through UWOSCR's FOV using a technique known as
8.  // beam-steering in the slowness domain, outlined by Giers et al., 1997.
9.  // Each pixel in each image must first be interpolated to a fixed time
10. // before performing 1-dimensional cross correlations in the meridional and
11. // zonal directions to get the time lag of the wave pattern between two image
12. // points. Meridional and zonal velocities are then determined using the known
13. // distance between pixels and the time lag corresponding to max correlation.
14.
15.
16. // Pre-processor directives
17. #include <iostream.h>
18. #include <stdio.h>
19. #include <string.h>
20. #include <conio.h>
21. #include <math.h>
22. #include <stdlib.h>
23.
24.
25. // Declaration of global variables
26. int sliderLength = 11; //slider length = 11 frames
27. int windowLength = 21; //window length = 21 frames
28. int pixelNum = 16; //16x16 pixels in an image
29. char temp[3]="00";
30. char clock[8];
31. char inputfile[60]="20121004.dav";
32. char outputfile[60]="data.prn";
33. FILE* fpoint1=NULL;
34. FILE* fpoint2=NULL;
35. int frame[11][3];
36. int corframe[21][3];
37. int skyvalue [16][16];
38. int I,J,i,j,FileType=1;
39. int LoopC, LoopB, LoopCP, LoopBP;
40. double CountAC, CountAB;
41. double Temp;
42. double A1C, A2C, A1B, A2B, OldCorrelation,MaxCorAB,MaxCorAC;
43. double diff=90,OldTimeDiffAB,OldTimeDiffAC;
44. double Startime, Velocity,WriteVelocity,WriteAngle,VelocityAC, VelocityAB;
45. float ambient, detector;
46. double readtime[21], frametime, angle;
47. double correlation[21][3], sumdiff[21][3], sumsquare[21][3];
48. double hour, minute, second;
49. double corsum0,corsum2, framesum2, framesum0, corframesum;
50. double B,C,LargestB,LargestC;
51. int loop, counter, loop2 , marker, Location0;
```

```
52. double Array[21][16][16];
53. double Wavelength,TimeDiffAC, TimeDiffAB, CorrelationAB, CorrelationAC;
54. double std,mean;
55.
56.
57. // Function declarations
58. void CalcAngle();     //calculates the angle of wave propagation
59. void CleanOut();      //clears old correlation and time lag values
60. void ToFile();        //Used to write info for each frame to a file
61. void Tier(int value); //calculates the max correlation in each direction for
62.                       //different pixel distances, 'value'
63. void AdjustData();    //to account for the scanning nature of the instrument by
64.                       //interpolating images to a fixed time
65. double Getime();      //reads the time from the datafile and formats to decimal
66.
67.
68. int main(int argc, char *argv[], char *env[])
69. {
70.     FileType = 1;  //FileType=1 when data contains ambient and detector temps
71.     Location0 = 0; //Location0=1 when analysing Delaware UWOSCR images
72.                    //as this instrument was NOT oriented so that top of image
73.                    //corresponded to north.
74.
75.     if (fpoint1=fopen(inputfile,"rb"))
76.     {
77.         cout << inputfile << " open" << endl;
78.     }
79.     else
80.     {
81.         cout << " ERROR on 1";
82.         getch();
83.         exit(0);
84.     }
85.
86.     Startime=Getime();
87.     fread(skyvalue,2,256,fpoint1); //reads 1st frame from input file
88.
89.     //Remakes data file to account for scanning nature of instument
90.     AdjustData();
91.     inputfile[0]='d'; //vel_dir will produce files called 'dYYYMMDD.dav'
92.                       //eg if inputfile=20121004.DAV, output is d0121004.DAV
93.     if (fpoint1=fopen("data.prn","rt"))
94.     {
95.         cout << inputfile << " open" << endl;
96.     }
97.     else
98.     {
99.         cout << " ERROR on 2";
100.    }
101.    if (fpoint2=fopen(inputfile,"wt"))
102.    {
103.        cout << outputfile << " open" << endl;
104.    }
105.    else
106.    {
107.        cout << " ERROR on 3";
108.    }
109.
110.    //Gets intensities for 1st window length of 21 frames
111.    for(loop=0;loop<windowLength;loop++)
112.    {
113.        fscanf(fpoint1,"%lf ",&readtime[loop]); //Reads times for this window
114.        for(i=0; i<pixelNum; i++)
115.        {
116.            for(j=0; j<pixelNum; j++)
117.            {
```

```
118.                fscanf(fpoint1,"%lf ",&Array[loop][i][j]); //Gets intensity
119.                                                           //at each pixel
120.            }
121.        }
122.    }
123.
124.    //Gets intensities for each window
125.    while (!feof(fpoint1))
126.    {
127.        //Advance to next frame
128.        for(loop=0; loop<windowLength; loop++)
129.        {
130.            readtime[loop]=readtime[loop+1];
131.            for(i=0; i<pixelNum; i++)
132.            {
133.                for(j=0; j<pixelNum; j++)
134.                {
135.                    Array[loop][i][j]=Array[loop+1][i][j];
136.                }
137.            }
138.        }
139.
140.        //Holds the frame time for first 21 frames
141.        fscanf(fpoint1,"%lf ",&readtime[21]);
142.        for(i=0;i<pixelNum;i++)
143.        {
144.            for(j=0;j<pixelNum;j++)
145.            {
146.                fscanf(fpoint1,"%lf ",&Array[21][i][j]);
147.            }
148.        }
149.        // Tier 1 ------------------------------------------------------------
150.        CleanOut(); //Clears correlation and time lag to prepare for Tier
151.        Tier(1);    //Value = 1 means distance is 1 pixel
152.        if(TimeDiffAC)
153.        {
154.            //Gets time lag and corresponding correlation between the
155.            //pixels A and C which correlate the most
156.            TimeDiffAC = TimeDiffAC / CountAC;
157.            CorrelationAC = CorrelationAC / 196; //no. pixels checked as we must
158.                                                 //neglect the outer rim of
159.                                                 //pixels after Tier 1
160.                                                 //=> 14x14 pixels left
161.        }
162.        else
163.        {
164.            TimeDiffAC=0;
165.        }
166.        if(TimeDiffAB)
167.        {
168.            TimeDiffAB = TimeDiffAB / CountAB;
169.            CorrelationAB = CorrelationAB / 196;
170.        }
171.        else
172.        {
173.            TimeDiffAB=0;
174.        }
175.
176.        if(TimeDiffAC || TimeDiffAB)
177.        {
178.            Velocity=sqrt((TimeDiffAC*TimeDiffAC) + (TimeDiffAB*TimeDiffAB));
179.            Velocity=1500*1.4142/(Velocity*3600); //meters/sec
180.                                                  //1500*1.4142 = diagonal pixel
181.                                                  //distance in metres for Tier1
182.        }
183.        else
```

```
184.        {
185.            Velocity=0;
186.        }
187.        CalcAngle(); //calculates the angle of wave propagation
188.        VelocityAB = sin( (angle)/57.3 )*Velocity; //57.3=180/pi
189.        VelocityAC = cos( (angle)/57.3 )*Velocity;
190.
191.        //Check if this tier value was the best so far
192.        //and if it was then this is the one too keep for now
193.        //AB and AC directions are treated separately and so may have different
194.        //tier values by the end
195.        if(CorrelationAB >MaxCorAB)
196.        {
197.            MaxCorAB = CorrelationAB;
198.            OldTimeDiffAB = TimeDiffAB;
199.        }
200.        if( CorrelationAC > MaxCorAC )
201.        {
202.            MaxCorAC = CorrelationAC;
203.            OldTimeDiffAC = TimeDiffAC;
204.        }
205.        //This was the first tier so the above two if statements were irrelevant
206.        //in this case!
207.        MaxCorAB = CorrelationAB;
208.        MaxCorAC = CorrelationAC;
209.        OldTimeDiffAC = TimeDiffAC;
210.        OldTimeDiffAB = TimeDiffAB;
211.
212.        //print out values to the screen to have a record of what's happening
213.        printf("%4.4f %3.2f %3.2f %2.4f %2.4f %2.3f %2.3f %2.2f %2.2f %2.2f\n",
214.               readtime[10], CountAB, CountAC, TimeDiffAB, TimeDiffAC,
215.               CorrelationAB, CorrelationAC, angle, VelocityAB, VelocityAC );
216.
217.        // Tier 2 ------------------------------------------------------------
218.        // This is a very similar code block to that for Tier 1
219.        CleanOut(); //Clears correlation and time lag to prepare for a new tier
220.        Tier(2);    //value = 2 => distance between points being correlated with
221.                    //each other is 2 pixels
222.
223.        if( fabs(TimeDiffAC) > 0 )
224.        {
225.            TimeDiffAC = TimeDiffAC / CountAC;
226.            Temp =  CorrelationAC /144; //no. pixels checked as we must neglect
227.                                        //the outer two rims of pixels after
228.                                        //Tier 2 => 12x12 pixels left
229.            CorrelationAC = Temp;
230.        }
231.        else
232.        {
233.            TimeDiffAC=0;
234.        }
235.
236.        if( fabs(TimeDiffAB)>0 )
237.        {
238.            TimeDiffAB = TimeDiffAB / CountAB;
239.            Temp = CorrelationAB / 144;
240.            CorrelationAB = Temp;
241.        }
242.        else
243.        {
244.            TimeDiffAB=0;
245.        }
246.
247.        if(TimeDiffAC || TimeDiffAB)
248.        {
249.            Velocity=sqrt(( TimeDiffAC*TimeDiffAC ) + ( TimeDiffAB*TimeDiffAB));
```

```
250.            Velocity=2*1500*1.4142/(Velocity*3600);// meters/sec
251.                                                   //2*1500*1.4142 is diagonal
252.                                                   //distance between 2 pixels
253.                                                   //in metres (Tier2=>2 pixels)
254.        }
255.        else
256.        {
257.            Velocity=0;
258.        }
259.
260.        CalcAngle();
261.        VelocityAB = sin( (angle)/57.3 )*Velocity;
262.        VelocityAC = cos( (angle)/57.3 )*Velocity;
263.
264.        if(CorrelationAB >MaxCorAB)
265.        {
266.            MaxCorAB=CorrelationAB;
267.            OldTimeDiffAB=TimeDiffAB/2; //time lag per pixel (2 pixels)
268.        }
269.
270.        if(CorrelationAC >MaxCorAC)
271.        {
272.            MaxCorAC=CorrelationAC;
273.            OldTimeDiffAC=TimeDiffAC/2;
274.        }
275.
276.        printf("%4.4f %3.2f %3.2f %2.4f %2.4f %2.3f %2.3f %2.2f %2.2f %2.2f\n",
277.              readtime[10],CountAB,CountAC,TimeDiffAB,TimeDiffAC,CorrelationAB,
278.              CorrelationAC,angle,VelocityAB, VelocityAC);
279.
280.        // Tier 3 ---------------------------------------------------------------
281.        // This is a very similar code block to that for Tiers 1 and 2
282.        CleanOut();
283.        Tier(3);
284.        if(TimeDiffAC)
285.        {
286.            TimeDiffAC = TimeDiffAC/CountAC;
287.            CorrelationAC = CorrelationAC/100; //10x10 pixels left
288.        }
289.        else
290.        {
291.            TimeDiffAC=0;
292.        }
293.        if(TimeDiffAB)
294.        {
295.            TimeDiffAB = TimeDiffAB/CountAB;
296.            CorrelationAB = CorrelationAB/100;
297.        }
298.        else
299.        {
300.            TimeDiffAB=0;
301.        }
302.
303.        if(TimeDiffAC || TimeDiffAB)
304.        {
305.            Velocity=sqrt(( TimeDiffAC*TimeDiffAC) + (TimeDiffAB*TimeDiffAB ));
306.            Velocity=3*1500*1.4142/(Velocity*3600); // meters/sec
307.                                                    // 3 pixel diagonal distance
308.        }
309.        else
310.        {
311.            Velocity=0;
312.        }
313.
314.        CalcAngle();
315.        VelocityAB = sin( (angle)/57.3 )*Velocity;
```

```
316.        VelocityAC = cos( (angle)/57.3 )*Velocity;
317.
318.        if(CorrelationAB >MaxCorAB)
319.        {
320.            MaxCorAB=CorrelationAB;
321.            OldTimeDiffAB=TimeDiffAB/3; //time lag per pixel (3 pixels)
322.        }
323.        if(CorrelationAC >MaxCorAC)
324.        {
325.            MaxCorAC=CorrelationAC;
326.            OldTimeDiffAC=TimeDiffAC/3;
327.        }
328.
329.        printf("%4.4f %3.2f %3.2f %2.4f %2.4f %2.3f %2.3f %2.2f %2.2f %2.2f \n",
330.               readtime[10],CountAB,CountAC,TimeDiffAB,TimeDiffAC,CorrelationAB,
331.               CorrelationAC,angle,VelocityAB, VelocityAC);
332.
333.        // Tier 4 ---------------------------------------------------------------
334.        // This is a very similar code block to that for Tiers 1, 2 and 3
335.        CleanOut();
336.        Tier(4);
337.        if(TimeDiffAC)
338.        {
339.            TimeDiffAC=TimeDiffAC/CountAC;
340.            CorrelationAC =  CorrelationAC/64; //8x8 pixels left
341.        }
342.        else
343.        {
344.           TimeDiffAC=0;
345.        }
346.        if(TimeDiffAB)
347.        {
348.            TimeDiffAB=TimeDiffAB/CountAB;
349.            CorrelationAB = CorrelationAB/64;
350.        }
351.        else
352.        {
353.            TimeDiffAB=0;
354.        }
355.
356.        if(TimeDiffAC || TimeDiffAB)
357.        {
358.            Velocity=sqrt((TimeDiffAC*TimeDiffAC)  +  (TimeDiffAB*TimeDiffAB ));
359.            Velocity=4*1500*1.4142/(Velocity*3600); // meters/sec
360.                                                    // 4 pixel diagonal distance
361.        }
362.        else
363.        {
364.            Velocity=0;
365.        }
366.
367.        CalcAngle();
368.        VelocityAB=sin( (angle)/57.3 )*Velocity;
369.        VelocityAC=cos( (angle)/57.3 )*Velocity;
370.
371.        if(CorrelationAB >MaxCorAB)
372.        {
373.            MaxCorAB=CorrelationAB;
374.            OldTimeDiffAB=TimeDiffAB/4; // time lag per pixel
375.        }
376.        if(CorrelationAC >MaxCorAC)
377.        {
378.            MaxCorAC=CorrelationAC;
379.            OldTimeDiffAC=TimeDiffAC/4;
380.        }
381.
```

```
382.        printf("%4.4f %3.2f %3.2f %2.4f %2.4f %2.3f %2.3f %2.2f %2.2f %2.2f\n",
383.               readtime[10], CountAB, CountAC, TimeDiffAB, TimeDiffAC,
384.               CorrelationAB, CorrelationAC, angle, VelocityAB, VelocityAC );
385.        //End of tiers as running out of pixels to correlate with each other
386.
387.        // calculate final velocity and direction ------------------------------

388.        // Use time lags which correspond to maximum correlation
389.        TimeDiffAC=OldTimeDiffAC;
390.        TimeDiffAB=OldTimeDiffAB;
391.        CorrelationAC=MaxCorAC;
392.        CorrelationAB=MaxCorAB;
393.
394.        if(TimeDiffAC || TimeDiffAB)
395.        {
396.            Velocity=sqrt((TimeDiffAC*TimeDiffAC) + (TimeDiffAB*TimeDiffAB));
397.            Velocity=1500*1.4142/(Velocity*3600); // meters/sec
398.            //Had calculated TimeDiff per pixel previously so now can just use
399.            //one pixel in the velocity calculation
400.        }
401.        else
402.        {
403.            Velocity=0;
404.        }
405.        CalcAngle(); //Rotates co-ordinate system so that it is in x-y dir
406.                     //and calculates propagation angle in degrees north of east
407.        VelocityAB = sin( (angle)/57.3 )*Velocity; //meridional speed
408.        VelocityAC = cos( (angle)/57.3 )*Velocity; //zonal speed
409.
410.        //Print out velocities corresponding to best correlation in every
411.        //image, in both the AB and AC directions
412.        printf("%4.4f %3.2f %3.2f %2.4f %2.4f %2.3f %2.3f %2.2f %2.2f %2.2f\n",
413.               readtime[10], CountAB, CountAC, TimeDiffAB, TimeDiffAC,
414.               CorrelationAB, CorrelationAC, angle, VelocityAB, VelocityAC );
415.
416.        CalcAngle();
417.        cout << angle << "  " << Velocity;
418.        cout << endl << endl;
419.        ToFile();
420.        CleanOut();
421.    }
422.
423.    fclose(fpoint1);
424.    fclose(fpoint2);
425.    cout << "done ";
426.    return(1);
427.} //end of main
428.
429.//--------------------------------------------------------------------------
430.void CalcAngle()
431.//Rotates co-ordinate system so that it is in x-y dir
432.//and calculates propagation angle in degrees north of east
433.{
434.    if( (TimeDiffAB != 0) && (TimeDiffAC != 0) )
435.    {
436.        angle = atan( TimeDiffAC/TimeDiffAB )*57.3;
437.    }
438.
439.    // Wave propagating between 45 and 135 degrees north of east
440.    if( ( TimeDiffAB<0 ) && ( TimeDiffAC<0 ) )
441.    {
442.        angle=270-angle;
443.    }
444.    // Wave propagating between -45 and 45 degrees north of east
445.    else if ( ( TimeDiffAB>0 ) && ( TimeDiffAC<0 ) )
446.    {
```

```
447.          angle=90-angle;
448.      }
449.      // Wave propagating between 225 and 315 degrees north of east
450.      else if ( ( TimeDiffAB>0 ) && ( TimeDiffAC>0 ) )
451.      {
452.          angle=90-angle;
453.      }
454.      // Wave propagating between 135 and 225 degrees north of east
455.      else if ( ( TimeDiffAB<0 ) && ( TimeDiffAC >0 ) ) //Quad 4
456.      {
457.          angle=270-angle;
458.      }
459.      // Wave not propagating in any direction
460.      if(angle<0) angle=0;
461.
462.      angle = angle-135; // adjusts for non x-y direction of AB and AC
463.                         // so that angle calculated is in degrees north of east
464.
465.      if(Location0) angle = angle+90; //If analyzing Delaware data then angles
466.                                      //are shifted and so numbers in comments
467.                                      //above also need to be shifted
468.
469.      //Want to output a positive number
470.      if(angle<0) angle = angle+360;
471.      if(angle>360) angle = angle-360;
472.}
473.//---------------------------------------------------------------------------
474.double Getime()
475.// reads the time from the datafile and formats to decimal
476.{
477.     // read the clock for this image
478.     fread(&clock, sizeof(clock), 1, fpoint1);
479.
480.     // if it is a normal image, it should have ambient and detector temperature
481.     if(FileType)
482.     {
483.         fread(&ambient, sizeof(ambient), 1, fpoint1);
484.         fread(&detector, sizeof(detector), 1, fpoint1);
485.     }
486.
487.     // get hour, minute and second
488.     strncpy(temp,&clock[2],2);  hour = atof(temp);
489.     strncpy(temp,&clock[4],2);  minute = atof(temp);
490.     strncpy(temp,&clock[6],2);  second = atof(temp);
491.
492.     if( (hour+(minute/60)+(second/3600) ) < Startime)
493.     // have passed midnight, so add 24 hours to the time
494.     {
495.         return 24+hour+(minute/60)+(second/3600);
496.     }
497.     else
498.     {
499.         return hour+(minute/60)+(second/3600);
500.     }
501.}
502.//---------------------------------------------------------------------------
503.void Tier(int value) //calculates the max correlation between A and B and
504.                      //between A and C for different pixel distances, 'value'
505.                      //during a time window of 21 frames
506.{
507.     CountAB=0; CountAC=0;
508.
509.     //All possible pixel combinations (for a pixel distance of 'value')
510.     //are checked. The value determines the limits for the number of pixel
511.     //combinations which can be checked.
512.
```

```
513.    //E.g. if pixel distance = 1, then A can not exist in the outer rim
514.    //(1 pixel) of the image (as this is where the values of B and C will lie)
515.    //and so A can exist only between I,J=1-14 in this case.
516.
517.
518.    //I increases as the pixel moves westward in the image
519.    for(I=value; I<pixelNum-value; I++)
520.    {
521.        //J increases as the pixel moves southward in the image
522.        for(J=value; J<pixelNum-value; J++)
523.        {
524.            //All images in the chosen window length are loaded
525.            for(loop=0;loop<windowLength;loop++)
526.            {
527.                // location A - load the full window length no. of frames
528.                corframe[loop][1]=Array[loop][I][J]; // A
529.
530.                // locations B and C - load a slider length no. of frames (11)
531.                // B and C slide along the full window length (21) at A to find
532.                // a time of max correlation between A and B and between A and C
533.                if (loop>4 && loop<16) //The sliders are in the centre of
534.                                       //the window length
535.                {
536.                     frame[loop-5][0]=Array[loop][I-value][J+value]; // B
537.                     frame[loop-5][2]=Array[loop][I+value][J+value]; // C
538.                }
539.            }
540.            marker=0;
541.
542.            //11 slider positions along the 21 frames so we loop 11 times
543.            for(loop=0; loop<(windowLength-sliderLength+1); loop++)
544.            {
545.                // calculate means for a particular pixel over slider time
546.                for(loop2=0; loop2<sliderLength; loop2++)
547.                {
548.                    corframesum = corframesum + corframe[loop+marker][1]; //A
549.                    framesum2 += frame[loop2][2];                         //C
550.                    framesum0 += frame[loop2][0];                         //B
551.                    marker++;
552.                }
553.                corframesum /= 11; //mean A
554.                framesum2 /= 11;   //mean C
555.                framesum0 /= 11;   //mean B
556.                marker=0;
557.
558.                // calculate sum and difference of squares
559.                // for a particular pixel over slider time
560.                for(loop2=0; loop2<sliderLength; loop2++)
561.                {
562.                    // 2 cross-correlations between A&B and A&C
563.                    // sum of (A-meanA)(B-meanB)
564.                    sumdiff[loop][0] += (corframe[loop+marker][1] - corframesum)
565.                                        *(frame[loop2][0] - framesum0);
566.                    // sum of (A-meanA)(C-meanC)
567.                    sumdiff[loop][2] += (corframe[loop+marker][1] - corframesum)
568.                                                *(frame[loop2][2] - framesum2);
569.
570.                    // Auto-correlation at A
571.                    // sum of square of (A-meanA)
572.                    sumsquare[loop][1]+= (corframe[loop+marker][1]-corframesum)
573.                                        *(corframe[loop+marker][1]-corframesum);
574.
575.                    // Auto-correlations at B and C
576.                    // sum of square of (B-meanB)
577.                    sumsquare[loop][0] += (frame[loop2][0] - framesum0)
578.                                          *(frame[loop2][0] - framesum0);
```

```
579.                    // sum of square of (C-meanC)
580.                    sumsquare[loop][2] += (frame[loop2][2] - framesum2)
581.                                          *(frame[loop2][2] - framesum2);
582.                    marker++;
583.                }
584.
585.                // do not allow sumofsquares to equal 0 - no division by 0
586.                if(!sumsquare[loop][2]) sumsquare[loop][2]=.00001l;
587.                if(!sumsquare[loop][0]) sumsquare[loop][0]=.00001l;
588.                if(!sumsquare[loop][1]) sumsquare[loop][1]=.000001;
589.
590.                // Correlation for each slider time at B and C
591.                // final correlations for AB
592.                correlation[loop][0] = sumdiff[loop][0] /
593.                                       (  sqrt(sumsquare[loop][0])*
594.                                          sqrt(sumsquare[loop][1])  );
595.                // final correlations for AC
596.                correlation[loop][2] = sumdiff[loop][2] /
597.                                       (  sqrt(sumsquare[loop][2])
598.                                          * sqrt(sumsquare[loop][1]) );
599.
600.                // Re-initialise variables
601.                // before moving on to next slider position
602.                corframesum=0;
603.                framesum2=0;
604.                framesum0=0;
605.                sumdiff[loop][0] =0;
606.                sumdiff[loop][2] =0;
607.                sumsquare[loop][1] =0;
608.                sumsquare[loop][0] =0;
609.                sumsquare[loop][2] =0;
610.                marker=0;
611.            }
612.
613.            // Subroutine for finding highest correlation-----------------------
614.            // The largest correlation of the 11 is in LargestB/LargestC
615.            // The time of largest correlation is in B and C
616.            // The time lag between locations is readtime[1O]-B & readtime[lO]-C
617.            B=0; LargestB=-100;
618.            C=0; LargestC=-100;
619.            loop=0;
620.
621.            //minus two values on either end because
622.            //we will be getting a 3-pt parabolic fit
623.            for(loop=2;loop<sliderLength-2;loop++)
624.            {
625.                if( correlation[loop][0] > LargestB) //B
626.                {
627.                    LargestB = correlation[loop][0];
628.                    B = readtime[loop+5]; //get time at centre of that slider
629.                    LoopB = loop;
630.                }
631.                if(correlation[loop][2] > LargestC) //C
632.                {
633.                    LargestC = correlation[loop][2];
634.                    C = readtime[loop+5];
635.                    LoopC=loop;
636.                }
637.            }
638.
639.            // 3 point parabolic fit around peak value to get better peak
640.            // first derivative = 0
641.
642.            diff=.01564; //(0.22*256)/3600 = image scan time in hours
643.
644.            if(correlation[LoopC][2] > correlation[LoopC-1][2] &&
```

```
645.                correlation[LoopC][2] > correlation [LoopC+1][2])
646.            //if largest correlation for C really is a peak then a 3-point
647.            //parabola is fitted around it to find approximate a time when
648.            //the correlation between A and C is slightly better
649.            {
650.                CountAC=CountAC+1;
651.                A1C =((-1)*correlation[LoopC-1][2]+correlation[LoopC+1][2])/2;
652.                A2C = 1.5*(correlation[LoopC-1][2]+correlation[LoopC+1][2])
653.                        - (correlation[LoopC-1][2] + correlation[LoopC][2]
654.                        +  correlation[LoopC+1][2]);
655.
656.                if(A2C)  C = C+ ((-1*A1C)/A2C)*diff;
657.                TimeDiffAC=TimeDiffAC+(C-readtime[10]);
658.                CorrelationAC = CorrelationAC + LargestC;
659.            }
660.
661.            // The same 3-point fit is done for the B value
662.            if(correlation[LoopB][0] > correlation[LoopB-1][0]&&
663.               correlation[LoopB][0] > correlation[LoopB+1][0] )
664.            {
665.                CountAB = CountAB+1;
666.                A1B = ((-1)*correlation[LoopB-1][0]+correlation [LoopB+1][0])/2;
667.                A2B = 1.5*(correlation [LoopB-1][0] + correlation[LoopB+1][0])
668.                        - (correlation[LoopB-1][0] + correlation[LoopB][0]
669.                         + correlation[LoopB+1][0] );
670.
671.                if (A2B) B = B+((-1*A1B)/A2B )*diff;
672.
673.                TimeDiffAB = TimeDiffAB + (B-readtime[10]);
674.                CorrelationAB = CorrelationAB + LargestB;
675.            }
676.
677.        }//end of I
678.    }//end of J
679.}//end of Tier
680.
681.//-------------------------------------------------------------------------------
682.void ToFile()
683.//Writes the meridional and zonal velocities for the centre frame of current
684.//window to a file, along with their corresponding max correlation values, and
685.//the standard deviation of intensities in that image
686.{
687.    mean=0;
688.    std=0;
689.
690.    // average intensity in the central image of the window
691.    for(i=0; i<pixelNum; i++)
692.    {
693.        for(j=0; j<pixelNum; j++)
694.        {
695.            mean += Array[10][i][j];//10 is at the centre of the 21 frame window
696.        }
697.    }
698.    mean=mean/256;
699.
700.    // standard deviation of same intensities
701.    for(i=0;i<pixelNum;i++)
702.    {
703.        for(j=0;j<pixelNum;j++)
704.        {
705.            std += fabs(Array[10][i][j]-mean);
706.        }
707.    }
708.    std /= 256;
709.
710.    fprintf(fpoint2,"%f  %f  %f  %f  %f  %f\n", readtime[10],VelocityAB,
```

```
            VelocityAC,CorrelationAB,CorrelationAC, std);
}
//------------------------------------------------------------------------------
void CleanOut()
//Initialises variables which are changed in Tier
{
    TimeDiffAC=0;
    TimeDiffAB=0;
    CorrelationAC=0;
    CorrelationAB=0;

    for(loop=0;loop<11;loop++)
    {
        correlation[loop][0] = 0;
        correlation[loop][1] = 0;
        correlation[loop][2] = 0;
    }
}
//---------------------------------------------------------------------
void AdjustData()
//Adjusts the data to account for the scanning nature of the instrument
//This involves determining the order in which pixels were scanned and then
//interpolating the intensities in each image to a fixed time (the time at
//the centre of the scan)
{
     long double deltaT, rateofchange=0, multiplier[16][16];
     double Writetime;
     int firstframe[16][16];
     int secondframe[16][16];
     int thirdframe[16][16];
     double finalframe[16][16];
     double time1, time2, time3;

     if (fpoint2=fopen("data.prn","wt"))
     {
         cout << "data.prn" << " open" << endl;
     }

     // multiplier determines how many pixels into the scan we are
     // for each co-ordinate [i][j] in the image.
     // i increases in the westward direction
     // j increases in the southward direction
     multiplier[0][0]=0;
     multiplier[1][0]=1;
     multiplier[2][0]=2;
     multiplier[3][0]=3;
     multiplier[4][0]=4;
     multiplier[5][0]=5;
     multiplier[6][0]=6;
     multiplier[7][0]=7;
     multiplier[8][0]=8;
     multiplier[9][0]=9;
     multiplier[10][0]=10;
     multiplier[11][0]=11;
     multiplier[12][0]=12;
     multiplier[13][0]=13;
     multiplier[14][0]=14;
     multiplier[15][0]=15;

     multiplier[0][1]=31;
     multiplier[1][1]=30;
     multiplier[2][1]=29;
     multiplier[3][1]=28;
     multiplier[4][1]=27;
     multiplier[5][1]=26;
     multiplier[6][1]=25;
```

```
777.      multiplier[7][1]=24;
778.      multiplier[8][1]=23;
779.      multiplier[9][1]=22;
780.      multiplier[10][1]=21;
781.      multiplier[11][1]=20;
782.      multiplier[12][1]=19;
783.      multiplier[13][1]=18;
784.      multiplier[14][1]=17;
785.      multiplier[15][1]=16;
786.
787.      multiplier[0][2]=32;
788.      multiplier[1][2]=33;
789.      multiplier[2][2]=34;
790.      multiplier[3][2]=35;
791.      multiplier[4][2]=36;
792.      multiplier[5][2]=37;
793.      multiplier[6][2]=38;
794.      multiplier[7][2]=39;
795.      multiplier[8][2]=40;
796.      multiplier[9][2]=41;
797.      multiplier[10][2]=42;
798.      multiplier[11][2]=43;
799.      multiplier[12][2]=44;
800.      multiplier[13][2]=45;
801.      multiplier[14][2]=46;
802.      multiplier[15][2]=47;
803.
804.      multiplier[0][3]=63;
805.      multiplier[1][3]=62;
806.      multiplier[2][3]=61;
807.      multiplier[3][3]=60;
808.      multiplier[4][3]=59;
809.      multiplier[5][3]=58;
810.      multiplier[6][3]=57;
811.      multiplier[7][3]=56;
812.      multiplier[8][3]=55;
813.      multiplier[9][3]=54;
814.      multiplier[10][3]=53;
815.      multiplier[11][3]=52;
816.      multiplier[12][3]=51;
817.      multiplier[13][3]=50;
818.      multiplier[14][3]=49;
819.      multiplier[15][3]=48;
820.
821.      multiplier[0][4]=64;
822.      multiplier[1][4]=65;
823.      multiplier[2][4]=66;
824.      multiplier[3][4]=67;
825.      multiplier[4][4]=68;
826.      multiplier[5][4]=69;
827.      multiplier[6][4]=70;
828.      multiplier[7][4]=71;
829.      multiplier[8][4]=72;
830.      multiplier[9][4]=73;
831.      multiplier[10][4]=74;
832.      multiplier[11][4]=75;
833.      multiplier[12][4]=76;
834.      multiplier[13][4]=77;
835.      multiplier[14][4]=78;
836.      multiplier[15][4]=79;
837.
838.      multiplier[0][5]=95;
839.      multiplier[1][5]=94;
840.      multiplier[2][5]=93;
841.      multiplier[3][5]=92;
842.      multiplier[4][5]=91;
```

```
843.     multiplier[5][5]=90;
844.     multiplier[6][5]=89;
845.     multiplier[7][5]=88;
846.     multiplier[8][5]=87;
847.     multiplier[9][5]=86;
848.     multiplier[10][5]=85;
849.     multiplier[11][5]=84;
850.     multiplier[12][5]=83;
851.     multiplier[13][5]=82;
852.     multiplier[14][5]=81;
853.     multiplier[15][5]=80;
854.
855.     multiplier[0][6]=96;
856.     multiplier[1][6]=97;
857.     multiplier[2][6]=98;
858.     multiplier[3][6]=99;
859.     multiplier[4][6]=100;
860.     multiplier[5][6]=101;
861.     multiplier[6][6]=102;
862.     multiplier[7][6]=103;
863.     multiplier[8][6]=104;
864.     multiplier[9][6]=105;
865.     multiplier[10][6]=106;
866.     multiplier[11][6]=107;
867.     multiplier[12][6]=108;
868.     multiplier[13][6]=109;
869.     multiplier[14][6]=110;
870.     multiplier[15][6]=111;
871.
872.     multiplier[0][7]=127;
873.     multiplier[1][7]=126;
874.     multiplier[2][7]=125;
875.     multiplier[3][7]=124;
876.     multiplier[4][7]=123;
877.     multiplier[5][7]=122;
878.     multiplier[6][7]=121;
879.     multiplier[7][7]=120;
880.     multiplier[8][7]=119;
881.     multiplier[9][7]=118;
882.     multiplier[10][7]=117;
883.     multiplier[11][7]=116;
884.     multiplier[12][7]=115;
885.     multiplier[13][7]=114;
886.     multiplier[14][7]=113;
887.     multiplier[15][7]=112;
888.
889.     multiplier[0][8]=128;
890.     multiplier[1][8]=129;
891.     multiplier[2][8]=130;
892.     multiplier[3][8]=131;
893.     multiplier[4][8]=132;
894.     multiplier[5][8]=133;
895.     multiplier[6][8]=134;
896.     multiplier[7][8]=135;
897.     multiplier[8][8]=136;
898.     multiplier[9][8]=137;
899.     multiplier[10][8]=138;
900.     multiplier[11][8]=139;
901.     multiplier[12][8]=140;
902.     multiplier[13][8]=141;
903.     multiplier[14][8]=142;
904.     multiplier[15][8]=143;
905.
906.     multiplier[0][9]=159;
907.     multiplier[1][9]=158;
908.     multiplier[2][9]=157;
```

```
909.      multiplier[3][9]=156;
910.      multiplier[4][9]=155;
911.      multiplier[5][9]=154;
912.      multiplier[6][9]=153;
913.      multiplier[7][9]=152;
914.      multiplier[8][9]=151;
915.      multiplier[9][9]=150;
916.      multiplier[10][9]=149;
917.      multiplier[11][9]=148;
918.      multiplier[12][9]=147;
919.      multiplier[13][9]=146;
920.      multiplier[14][9]=145;
921.      multiplier[15][9]=144;
922.
923.      multiplier[0][10]=160;
924.      multiplier[1][10]=161;
925.      multiplier[2][10]=162;
926.      multiplier[3][10]=163;
927.      multiplier[4][10]=164;
928.      multiplier[5][10]=165;
929.      multiplier[6][10]=166;
930.      multiplier[7][10]=167;
931.      multiplier[8][10]=168;
932.      multiplier[9][10]=169;
933.      multiplier[10][10]=170;
934.      multiplier[11][10]=171;
935.      multiplier[12][10]=172;
936.      multiplier[13][10]=173;
937.      multiplier[14][10]=174;
938.      multiplier[15][10]=175;
939.
940.      multiplier[0][11]=191;
941.      multiplier[1][11]=190;
942.      multiplier[2][11]=189;
943.      multiplier[3][11]=188;
944.      multiplier[4][11]=187;
945.      multiplier[5][11]=186;
946.      multiplier[6][11]=185;
947.      multiplier[7][11]=184;
948.      multiplier[8][11]=183;
949.      multiplier[9][11]=182;
950.      multiplier[10][11]=181;
951.      multiplier[11][11]=180;
952.      multiplier[12][11]=179;
953.      multiplier[13][11]=178;
954.      multiplier[14][11]=177;
955.      multiplier[15][11]=176;
956.
957.      multiplier[0][12]=192;
958.      multiplier[1][12]=193;
959.      multiplier[2][12]=194;
960.      multiplier[3][12]=195;
961.      multiplier[4][12]=196;
962.      multiplier[5][12]=197;
963.      multiplier[6][12]=198;
964.      multiplier[7][12]=199;
965.      multiplier[8][12]=200;
966.      multiplier[9][12]=201;
967.      multiplier[10][12]=202;
968.      multiplier[11][12]=203;
969.      multiplier[12][12]=204;
970.      multiplier[13][12]=205;
971.      multiplier[14][12]=206;
972.      multiplier[15][12]=207;
973.
974.      multiplier[0][13]=223;
```

```
975.     multiplier[1][13]=222;
976.     multiplier[2][13]=221;
977.     multiplier[3][13]=220;
978.     multiplier[4][13]=219;
979.     multiplier[5][13]=218;
980.     multiplier[6][13]=217;
981.     multiplier[7][13]=216;
982.     multiplier[8][13]=215;
983.     multiplier[9][13]=214;
984.     multiplier[10][13]=213;
985.     multiplier[11][13]=212;
986.     multiplier[12][13]=211;
987.     multiplier[13][13]=210;
988.     multiplier[14][13]=209;
989.     multiplier[15][13]=208;
990.
991.     multiplier[0][14]=224;
992.     multiplier[1][14]=225;
993.     multiplier[2][14]=226;
994.     multiplier[3][14]=227;
995.     multiplier[4][14]=228;
996.     multiplier[5][14]=229;
997.     multiplier[6][14]=230;
998.     multiplier[7][14]=231;
999.     multiplier[8][14]=232;
1000.            multiplier[9][14]=233;
1001.            multiplier[10][14]=234;
1002.            multiplier[11][14]=235;
1003.            multiplier[12][14]=236;
1004.            multiplier[13][14]=237;
1005.            multiplier[14][14]=238;
1006.            multiplier[15][14]=239;
1007.
1008.            multiplier[0][15]=255;
1009.            multiplier[1][15]=254;
1010.            multiplier[2][15]=253;
1011.            multiplier[3][15]=252;
1012.            multiplier[4][15]=251;
1013.            multiplier[5][15]=250;
1014.            multiplier[6][15]=249;
1015.            multiplier[7][15]=248;
1016.            multiplier[8][15]=247;
1017.            multiplier[9][15]=246;
1018.            multiplier[10][15]=245;
1019.            multiplier[11][15]=244;
1020.            multiplier[12][15]=243;
1021.            multiplier[13][15]=242;
1022.            multiplier[14][15]=241;
1023.            multiplier[15][15]=240;
1024.
1025.            counter=0;
1026.
1027.            deltaT=0.01564; //(0.22*256)/3600 = image scan time in hours
1028.            time1=Getime();
1029.            fread(firstframe,2,256,fpoint1);
1030.            time2=Getime();
1031.            fread(secondframe,2,256, fpoint1);
1032.            time3=Getime();
1033.            fread(thirdframe,2,256,fpoint1);
1034.            Writetime=time1-deltaT; //initialise WriteTime
1035.
1036.            if( time1 > time2 ) // If time2 is exactly on midnight
1037.            {
1038.                time1=Getime();
1039.                fread(firstframe,2,256,fpoint1);
1040.                time2=Getime();
```

```
1041.                 fread(secondframe,2,256,fpoint1);
1042.                 time3=Getime();
1043.                 fread(thirdframe,2,256,fpoint1);
1044.                 Writetime=time1-deltaT;
1045.             }
1046.
1047.             cout << "Interpolating data file to new datafile!!!" ;
1048.             while (!feof(fpoint1))
1049.             {
1050.                 //Step forward to the next frame
1051.                 Writetime = Writetime + deltaT; //Writetime will be the time at the
1052.                                                 //end of scanning time between 2 frames
1053.
1054.                 //Always check if we've reached midnight
1055.                 if(Writetime<Startime) Writetime = Writetime+24;
1056.
1057.                 if(time1 < Writetime) // an interpolation is needed in this case
1058.                 {
1059.                     fprintf(fpoint2,"%f ",Writetime);
1060.
1061.                     //Interpolate image to a fixed time pixel by pixel
1062.                     //The fixed time will be half way through the scanning time
1063.                     for(i=0; i<pixelNum; i++)
1064.                     {
1065.                         for(j=0; j<pixelNum; j++)
1066.                         {
1067.                             if( Writetime > time1 + (multiplier[i][j]/255)*deltaT
1068.                                 && Writetime < time2 + (multiplier[i][j]/255)*deltaT)
1069.                             {
1070.                                 //rate of change of intensity with time
1071.                                 rateofchange=(secondframe[i][j]-firstframe[i][j])/
1072.                                              (time2-time1);
1073.                                 //new intensity
1074.                                 finalframe[i][j]=firstframe[i][j]+
1075.                                                  ((Writetime-time1-(multiplier[i][j]/
1076.                                                  255)*deltaT) * rateofchange);
1077.                             }
1078.                             else if (Writetime > time2+(multiplier[i][j]/255)* deltaT
1079.                                      && Writetime < time3+(multiplier[i][j]/255)*
1080.                                      deltaT)
1081.                             {
1082.                                 rateofchange=(thirdframe[i][j]-secondframe[i][j])/
1083.                                              (time3-time2);
1084.
1085.                                 finalframe[i][j] = secondframe[i][j]+
1086.                                                  ((Writetime-time2-(multiplier[i][j]/
1087.                                                     255)*deltaT)*rateofchange);
1088.                             }
1089.                             else
1090.                             {
1091.                                 cout << "Missing Frame using median"
1092.                                      << time1+(multiplier[i][j]/255)*deltaT
1093.                                      << " "<< time2+(multiplier[i][j]/255)*deltaT
1094.                                      << " "<< time3+(multiplier[i][j]/255)*deltaT
1095.                                      << " " << Writetime <<  endl;
1096.
1097.                                 finalframe[i][j]=secondframe[i][j];
1098.                             }
1099.
1100.                             fprintf(fpoint2, "%f ", finalframe[i][j]) ;
1101.                         }//end of j
1102.                     }//end of i
1103.
1104.                     fprintf(fpoint2,"\n");
```

```
1105.                 }
1106.                 if (time3 < Writetime + deltaT) // a time shift forward is needed here
                      
1107.                 {
1108.                     for(i=0; i<pixelNum; i++)
1109.                     {
1110.                         for(j=0;j<pixelNum;j++)
1111.                         {
1112.                             firstframe[i][j]=secondframe[i][j];
1113.                             secondframe[i][j]=thirdframe[i][j];
1114.                         }
1115.                     }
1116.                     time1=time2;
1117.                     time2=time3;
1118.                     time3=Getime();
1119.                     fread(thirdframe,2,256, fpoint1);
1120.                 }
1121.             }
1122.             fclose(fpoint2);
1123.             fclose(fpoint1);
1124.         }
```

APPENDIX D. IN-HOUSE REVERSE RAY-TRACING SOFTWARE

The following MATLAB code, written by Frank Mulligan, was based on the method outlined by *Marks and Eckermann* (1995) and was tested using results from *Pramitha et al.* (2014).

```
% GW Ray tracing: 'ray_tracing_GWs_v5.m'
% Author: Frank Mulligan
% Date: 10 March 2017

% Modified prog: ray_tracing_GWs_v4 to make this one
% Signifcant change is in line 311 : xt = xt + dx_deg; -->xt = xt - dx_deg;
% This was based largely on results from Hyderabad to get the longitudes
% correct.

% Modified prog: ray_tracing_GWs_v3 to make this one
% changing from Gadanki to Davis.  Quite a few tings to be aware of
% Davis has negative latitudes.  Longitude steps are in 3 degrees at 68 S
% to get similar distances from station in lat and lon

% Attempt based on paper by Pramitha et al (2014) Atm. Phys. Chem.
% Event G1 night of 17 March 2012
% Gadanki Station geographic coordinates 13.5 N, 79.2 E, altitude was taken
% as 97 km (O1S emission)
% Final location of this event was determined to be 10.8 N, 79.9 E, 13 km.

% ------------------------------------------------------------------------
clear all;

% Read in the file with GWs from Sharon
% Incorporate the day number into the code to get temperature and wind
fname = ['C:\Users\srourke\Documents\MATLAB\'...
         '18Feb20131725UT raytracing input.xlsx'];
year = 2013;% for year = 1999 : 2013  % use for loop for multiple years

sheet = num2str(year);
ndata = xlsread(fname, sheet);
v_m_s = ndata(:,1);                 % speed in m/s
phi_deg = ndata(:,2);               % direction N of E (E = 0) in degrees
T_min = ndata(:,3);                 % period in minutes
lam_km = ndata(:,4);                % wavelength in km
dayno = ndata(:,5);                 % day of year
clear ndata

% Pre-allocate the space for final values to speed up the program
long_f = zeros(1,length(dayno))';   % Longitude
lat_f = zeros(1,length(dayno))';    % Latitude
alt_f = zeros(1,length(dayno))';    % Altitude
wir_f = zeros(1,length(dayno))';    % Intrinsic frequency
WKB_f = zeros(1,length(dayno))';    % Wentzel-Krammers-Brillouin approx.
m2_f = zeros(1,length(dayno))';     % Vertical_wavenumber ^2
NN_f = zeros(1,length(dayno))';     % Brunt_vaisala_frequency ^2
Ri_f = zeros(1,length(dayno))';     % Richardson number

% For each GW observation, get cube of temp and wind data at that time
for dd = 1 : length(dayno)    % use for loop for multiple events
    day_of_year = dayno(dd);
    % =====================================================================
    % Get wind and temperature values
```

```
54.
55.     xl = (63:3:93);                 % range of longitudes
56.                                     % need to adjust deglong2m for 3 deg
57.     yl = (-63:-1:-73);              % range of latitudes
58.     zl = (0:1:100);                 % range of altitudes
59.
60.     sx = length(xl);
61.     sy = length(yl);
62.     sz = length(zl);
63.
64.     % Pre-allocate the space to speed up the program
65.     U = zeros(sx,sy,sz,'double');   % zonal wind
66.     V = zeros(sx,sy,sz,'double');   % merid wind
67.     T = zeros(sx,sy,sz,'double');   % temperature
68.     N2 = zeros(sx,sy,sz,'double');  % BV_frequency ^2
69.     A2 = zeros(sx,sy,sz,'double');  % alpha ^2
70.
71.     % ========= Get cube of wind values for GW observation days ===========
72.
73.     dir_name = ['C:\Users\srourke\Documents\MATLAB\hwm\Data\'...
74.                 'Davis_+-15deglong_+-5deglat\'];
75.     wind_files = dir(strcat(dir_name,'*Day',num2str(dayno(dd)),'.txt'));
76.     n_frames = size(wind_files);    % get the number of daynnn.txt files
77.                                     % should be sx*sy files for each day
78.
79.     x = 0; y = 0;
80.     for i = 1 : n_frames(1)
81.         filename = strcat(dir_name,wind_files(i).name);
82.         A = load(filename);         % Store merid and zonal winds
83.                                     % from this file in A
84.
85.         % Latitude dimension
86.         if (mod(i,sy)==0)
87.                 y = sy;
88.         else    y = mod(i,sy);
89.         end
90.
91.         % longitude dimension
92.         x = 1+((i-y)/sy);
93.
94.         U(x,y,:) = A(:,2);          % column 2 is U
95.         V(x,y,:) = A(:,1);          % column 1 is V
96.     end
97.
98.     % Clear variables that are no longer needed
99.     clear dir_name wind_files n_frames filename A x y i;
100.
101.    % === Get cube of T, N^2 and alpha^2 values for GW observation days ===
102.
103.    dir_name = ['C:\Users\srourke\Documents\Sharon\Data\'...
104.                'T-cube_Davis_MSIS-E-90\'];
105.    temp_files = dir(strcat(dir_name,'T-cube_Davis*day_',...
106.                        num2str(dayno(dd),'%03.0f'),'.txt'));
107.    n_frames = size(temp_files);    % get the number of day=nnn files
108.
109.    x = 0; y = 0;
110.    for i = 1 : n_frames(1)         % sx*sy files
111.        filename = strcat(dir_name,temp_files(i).name);
112.        [A] = importdata(filename);
113.
114.        % Latitude dimension
115.        if (mod(i,sy)==0)
116.                y = sy;
117.        else    y = mod(i,sy);
118.        end
119.
```

```
        % longitude dimension
        x = 1+((i-y)/sy);

        T(x,y,:)=A.data(2:sz+1,2);  % column 2 is T
                                    % A.data had one extra row at start
                                    % was A.data(:,2)
    end

    % Pre-allocate the memory for N2 and A2
    N2 = zeros(sx,sy,sz,'double');  % BV_frequency ^2
    A2 = zeros(sx,sy,sz,'double');  % alpha ^2

    % Generate N^2 and alpha^2

    % constants needed
    g0 = 9.8;                       % m/(s^2)
    Re = 6371;                      % Radius of Earth in km
    Gama_dry = 9.5e-3;              % in K/m;
    R = 8.314e3;                    % Universal gas constant J/(kg.K)
    m_bar = 29;                     % average mass number
    hz = 0.1;                       % 0.1 km = 100 m vertical step size

    for x = 1 : sx                                  % longitude
        for y = 1:sy                                % latitude
            for z = 1:sz                            % altitude
                g = 9.8 *(Re/(Re+z))^2;             % g is a function of z
                zsp = [z - hz, z, z+hz];            % 3 z-values
                Tzz = spline(zl,T(x,y,:),zsp);      % 3 T(z)-values
                dTdz = (Tzz(3)-Tzz(1))/(2*hz*1000); % K/km --> K/m
                                                    % x by 1000
                N2(x, y, z) = ((g/Tzz(2))*(dTdz + Gama_dry)); % BV_freq
                H = (R*Tzz(2))/(m_bar * g);         % Scale height
                A2(x, y, z) = 1./(4.*H.*H);         % alpha-squared.
            end
        end
    end

    % Clear variables that are no longer needed
    clear dir_name temp_files n_frames filename A x y;

    % ========================================================================
    % Wave parameters
    phi     = phi_deg(dd);
    lam_h   = lam_km(dd);
    T_obs   = T_min(dd);
    c       = v_m_s(dd);

    lam_h = lam_h * 1000;           % horizontal wavelength km --> m
    kh    = 1/lam_h;                % horizontal wave vector (1/m)
    T_obs = T_obs*60 ;              % Observed period min --> sec
    w     = 1/T_obs;                % ground based (eulerian) freq (Hz)

    lat = -68.58; lon = 77.97;      % Davis Station, Antarctica coordinates
    alt = 87;                       % OH altitude in km
    xt = lon; yt = lat; zt = alt;   % initial coordinates

    % Start ray-tracing here
    % See Marks & Eckermann (1995) and Pramitha et al. (2014)

    dt = 4.0;                       % initial time step in seconds
                                    % say Cgz = 25 m/s (vert group vel)
                                    % then dt = 100m/(25m/s) = 4 s

    % Step size in z, x and y
    hz = 0.1;                       % km
    hx = 1e-3;                      % degrees longitude
```

```
186.    hy = 1e-3;                      % degrees latitude
187.
188.    % Initial wave values
189.    k0 = kh*cosd(phi);              % initial zonal wavenumber
190.    l0 = kh*sind(phi);              % initial merid wavenumber
191.
192.    j = 0;                          % number of steps
193.    total_time = 0.0;
194.
195.    % Initial values of terminating conditions
196.    m2 = 0.99e-6;                   % Vertical_wavenumber ^2
197.    WKB = 0;                        % Wentzel-Krammers-Brillouin approx
198.    wir = 1;                        % Intrinsic frequency
199.
200.    % Conditions for termination outlined in e.g, Marks and Eckermann, 1995
201.    % Also stop if imaginary location or troposphere is reached
202.    while((m2 > 0) && (wir > 0) && (WKB < 1.0) && (m2 < 1e-6) &&...
203.          (imag(xt) == 0) && (imag(yt) == 0) && (imag(zt) == 0) &&...
204.          (zt > 10))
205.
206.        j = j+1;                                % dummy index
207.
208.        % conversion of 1 degree lat. and 1 deg long. to meters
209.        deglat2m = 119.949*1000;                % 1 deg lat
210.            % deglon2m must be inside loop as it depends on latitude (yt)
211.            % deglat2m just kept here to keep the two together
212.        deglon2m = 6371*1000*acos(sind(yt)*sind(yt)+...
213.                   cosd(yt)*cosd(yt)*cosd(1));
214.        deglon2m = 3*deglon2m;                  % adjust for 3 degree steps
215.
216.        zsp = [zt-hz, zt, zt+hz];               % 3 z-values h in km
217.        xsp = [xt-hx, xt, xt+hx];               % 3 x-values in degrees
218.        ysp = [yt-hy, yt, yt+hy];               % 3 y-values in degrees
219.
220.        k2 = k0*k0;
221.        l2 = l0*l0;
222.        Omega = 7.2921e-5/acos(0.0);
223.        f = 2*Omega*sind(yt);                   % Coriolis term
224.        fh = 2*Omega*sind(yt+hy);               % Higher limit
225.        fl = 2*Omega*sind(yt-hy);               % Lower limit
226.        dfdy = (fh-fl)/(2*hy*deglat2m);         % Change in f with latitude
227.                                                % /deg lat --> /m
228.        f2 = f*f;                               % (Coriolis term) ^2
229.
230.        % Find the nearest long, lat and alt
231.        dummy = abs(xl-xt);
232.        minx = min(dummy);                      % smallest diff in long
233.        ix = max(find(dummy == min(dummy)));    % index of nearest long
234.        dummy = abs(yl-yt);
235.        miny = min(dummy);                      % smallest diff in lat
236.        iy = max(find(dummy == min(dummy)));    % index of nearest latitude
237.        dummy = abs(zl-zt);
238.        minz = min(dummy);                      % smallest diff in altitude
239.        iz = max(find(dummy == min(dummy)));    % index of nearest altitude
240.
241.        % Get terms needed for ray-tracing equations
242.
243.        UUz = spline(zl,U(ix,iy,:),zsp);        % 3 U(z)-values
244.        dUdz = (UUz(3)-UUz(1))/(2*hz*1000);     % (m/s)/km --> (m/s)/m
245.        UUx = spline(xl,U(:,iy,iz),xsp);        % 3 U(x)-values
246.        dUdx = (UUx(3)-UUx(1))/(2*hx*deglon2m); % (m/s)/deg --> (m/s)/m
247.        UUy = spline(yl,U(ix,:,iz),ysp);        % 3 U(y)-values
248.        dUdy = (UUy(3)-UUy(1))/(2*hy*deglat2m); % (m/s)/deg --> (m/s)/m
249.        UU = UUz(2);                            % U-value at xt,yt,zt
250.
251.        VVz = spline(zl,V(ix,iy,:),zsp);        % 3 V(z)-values
```

```
252.        dVdz = (VVz(3)-VVz(1))/(2*hz*1000);     % (m/s)/km --> (m/s)/m
253.        VVx = spline(xl,V(:,iy,iz),xsp);        % 3 V(x)-values
254.        dVdx = (VVx(3)-VVx(1))/(2*hx*deglon2m); % (m/s)/deg --> (m/s)/m
255.        VVy = spline(yl,V(ix,:,iz),ysp);        % 3 V(y)-values
256.        dVdy = (VVy(3)-VVy(1))/(2*hy*deglat2m); % (m/s)/deg --> (m/s)/m
257.        VV = VVz(2);                            % V-value at xt,yt,zt
258.
259.        NNz = spline(zl,N2(ix,iy,:),zsp);       % 3 N^2(z)-values
260.        dN2dz = (NNz(3)-NNz(1))/(2*hz*1000);    % /(s*s*km) --> /(s*s*m)
261.        NNx = spline(xl,N2(:,iy,iz),xsp);       % 3 N^2(x)-values
262.        dN2dx = (NNx(3)-NNx(1))/(2*hx*deglon2m);% /(s*s*deg) --> /(s*s*m)
263.        NNy = spline(yl,N2(ix,:,iz),ysp);       % 3 N^2(y)-values
264.        dN2dy = (NNy(3)-NNy(1))/(2*hy*deglat2m);% /(s*s*deg) --> /(s*s*m)
265.        NN = NNz(2);                            % N^2-value at xt,yt,zt
266.
267.        Ri(j) = NN/(dUdz*dUdz+dVdz*dVdz);       % Richardson number
268.
269.        AAz = spline(zl,A2(ix,iy,:),zsp);       % 3 alpha^2(z)-values
270.        dA2dz = (AAz(3)-AAz(1))/(2*hz*1000);    % /(m*m*km) --> /(m*m*m)
271.        AAx = spline(xl,A2(:,iy,iz),xsp);       % 3 alpha^2(x)-values
272.        dA2dx = (AAx(3)-AAx(1))/(2*hx*deglon2m);% /(m*m*deg) --> /(m*m*m)
273.        AAy = spline(yl,A2(ix,:,iz),ysp);       % 3 alpha^2(y)-values
274.        dA2dy = (AAy(3)-AAy(1))/(2*hy*deglat2m);% /(m*m*deg) --> /(m*m*m)
275.        AA = AAz(2);                            % alpha^2-value at xt,yt,zt
276.
277.        wir = w - k0*UU - l0*VV;                % intrinsic wave frequency
278.        wir2 = wir*wir;
279.        m2 = (((k2 + l2)*(NN-wir2))/(wir2-f2))- AA; % dispersion relation
280.        m = sqrt(m2);                           % vertical wavenumber
281.        Delta = k2 + l2 + m2 + AA;
282.        Term = (NN-wir2)/(wir*Delta);
283.        dx = (UU + (k0*Term))*dt;
284.        dy = (VV + (l0*Term))*dt;
285.        dz = -((m*(wir2-f2))/(wir*Delta))*dt;
286.        dk = (-k0*dUdx-l0*dVdx-(1/(2*wir*Delta))*...
287.             (dN2dx*(k2+l2)-dA2dx*(wir2-f2)))*dt;
288.        dl = (-k0*dUdy-l0*dVdy-(1/(2*wir*Delta))*...
289.             (dN2dy*(k2+l2)-dA2dy*(wir2-f2))-...
290.             ((f/(wir*Delta))*dfdy*(m2+AA)))*dt;
291.        dm = (-k0*dUdz-l0*dVdz-(1/(2*wir*Delta))*...
292.             (dN2dz*(k2+l2)-dA2dz*(wir2-f2)))*dt;
293.
294.        k0 = k0 + dk;                           % New zonal wavenumber
295.        l0 = l0 + dl;                           % New merid wavenumber
296.        if j == 1                               % Don't step forward as we
297.            m0 = m;                             % didn't use m0 yet
298.        end
299.        m0 = m0 + dm;                           % New vertical wavenumber
300.
301.        % Convert longitude dx(m) --> degrees
302.        dx_deg = ((((cos((dx/(6371*1000))))-(sind(yt)*sind(yt)))/...
303.                  (cosd(yt)*cosd(yt)));
304.        % get the sign correct
305.        if (dx < 0)
306.            sign = -1;
307.        else
308.            sign = 1;
309.        end
310.        dx_deg = sign * acosd(dx_deg);
311.        xt = xt - dx_deg;                       % New longitude
312.        xlon(j) = xt;
313.
314.        % Convert lat(m) --> degrees
315.        yt = yt  - (dy/(111.1949*1000));        % New latitude
316.        % yt = yt  + (dy/(111.1949*1000));      % kept giving wrong answers
317.                                                % had to change + to -
```

```
318.        ylat(j) = yt;
319.
320.        % Convert alt(m) --> km
321.        zt = zt + (dz/1000);                    % New altitude
322.        zalt(j) = zt;
323.
324.        WKB = abs((1/((dz/dt)*m2))*(dm/dt));    % WKB parameter
325.        Cgx(j) = dx/dt;                         % Zonal group velocity
326.        Cgy(j) = dy/dt;                         % Merid group velocity
327.        Cgz(j) = -dz/dt;                        % Vertical group velocity
328.
329.        total_time = total_time + dt;
330.
331.        dt = abs(100/(dz/dt));                  % new time step=(100 m)/Cgz
332.    end
333.
334.    % Store values at termination point
335.    long_f(dd)      = xlon(j);
336.    lat_f(dd)       = ylat(j);
337.    alt_f(dd)       = zalt(j);
338.    wir_f(dd)       = wir;
339.    WKB_f(dd)       = WKB;
340.    m2_f(dd)        = m2;
341.    Ri_f(dd)        = Ri(j);
342.    NN_f(dd)        = NN;
343.    day_of_year     = dayno(dd);
344.
345.end
346.
347.% Write initial parameters along with their termination points to a file
348.M = [phi_deg, v_m_s, T_min, lam_km, dayno, long_f, lat_f, alt_f,...
349.     wir_f, WKB_f, m2_f, Ri_f, NN_f];
350.xlswrite([['C:\Users\srourke\Documents\MATLAB\'...
351.         '18Feb20131725UT raytracing output.xlsx'], M, sheet);
352.% end
```

APPENDIX E. FURTHER CASE STUDIES OF MESOSPHERIC FRONTS

This appendix provides details on the remaining case studies from Table 5.1 (in Appendix E.1) and Table 5.2 (in Appendix E.2) which were not discussed in the main text of Chapter 5.

E.1. Verified Fronts

Case 1 from Table 5.1 –

A bright wall detected between 00:30 and 00:41 UT on 14-Jul-2012:

Figure E.1 and Figure E.2 display a series of images showing the first detected front (part one of the double bore event), whose characteristics are shown in Table 5.1 on page 204, between 00:30 and 00:41 UT on 14th July 2012. This front was detected by the USU camera from approximately 00:00 UT (as shown in Figure E.1) but didn't reach UWOSCR's FOV until approximately 00:26 UT (as shown in Figure E.2). In both sets of images, some ripples may be seen just before the leading edge of the front passes by.

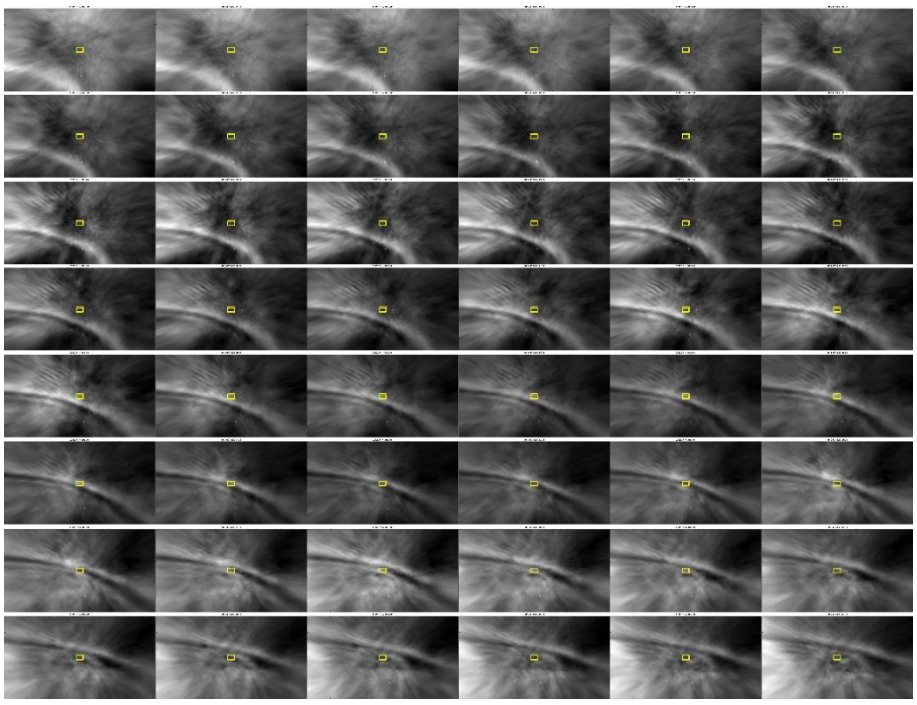

Figure E.1: A series of images recorded by the USU camera between 00:00 and 00:47 UT on 14th July 2012.

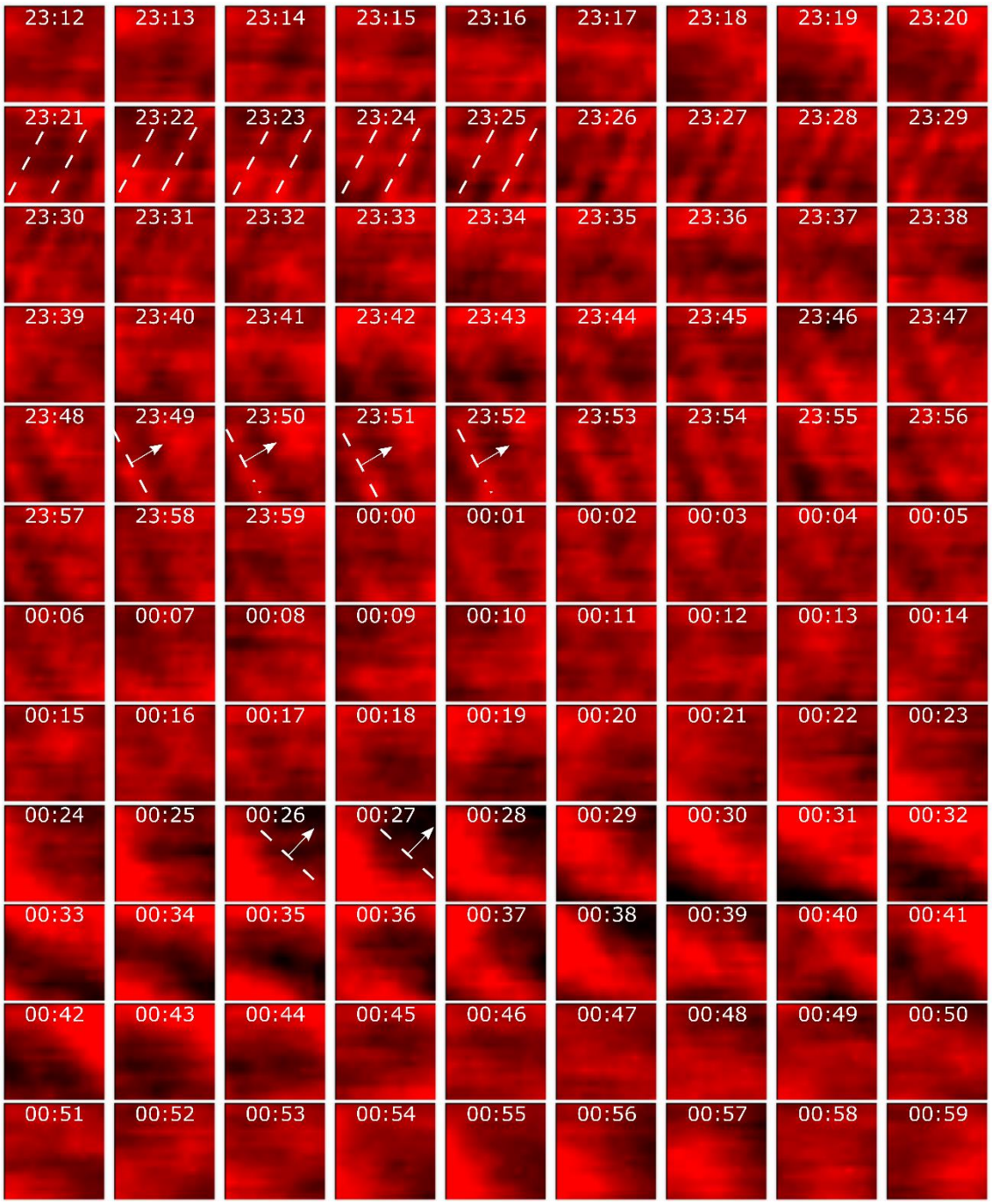

Figure E.2: A series of images recorded by UWOSCR between 23:12 UT on 13th July 2012 and 00:59 UT on 14th July 2012. Dashed lines indicate phase fronts and arrows indicate the direction of propagation, if any.

From the two keograms in Figure E.3, it is confirmed (between approximately 00:24 and 00:33 UT on 14th July 2012) that the front was travelling in a predominantly north-eastward direction. This is in general agreement with the value produced by the analysis (58.3° north of east), shown in Table 5.1 on page 204. The ripples (both the stationary ones between approximately 23:18 and

23:30 UT and the north-eastward propagating ones between approximately 23:45 and 23:57 UT) which were present before the leading front passed through the FOV are also visible on the keograms in Figure E.3.

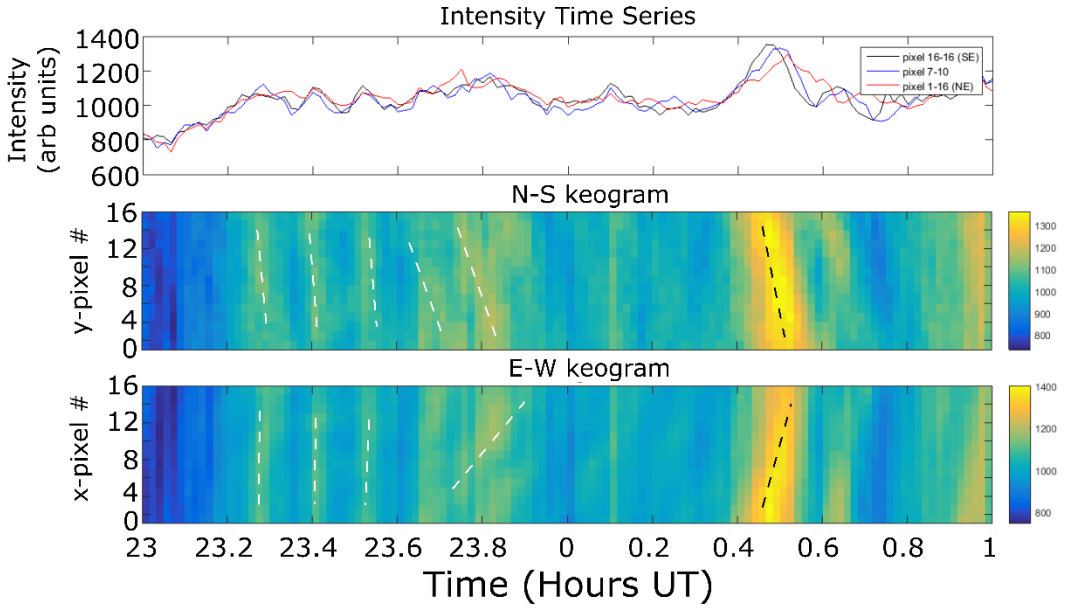

Figure E.3: As in Figure 5.11 but between 23:00 UT on 13th July 2012 and 01:00 UT on 14th July 2012.

Manual analysis of this front gives an observed propagation direction of $\theta \approx 46^\circ \pm 10^\circ$ north of east, an observed phase speed of $v \approx 69 \pm 8$ m/s, and a horizontal wavelength (between the front and its trailing wave) of $\lambda_h \approx 46 \pm 10$ km (calculated from a period of $T \approx 11 \pm 2$ minutes, as the two crests weren't both fully in the FOV at the same time). These are all in fairly good agreement with the parameters calculated using the analysis method (shown in Table 5.1 on page 204).

The resulting m^2 profile for this potential front is shown in Figure E.4. A thermal inversion at an altitude of approximately 94 km causes m^2 to become negative, thus creating a reflective boundary at this level. In addition, there is a weak Doppler duct between approximately 76 and 95 km, which does not cause m^2 to become negative. These weak opposing winds at the time and altitude of the wave are also shown in Figure E.5. Despite these thermal and

Doppler inversions, a lower reflective boundary was not calculated for this particular front. In fact, it was determined that m^2 becomes very large ($>10^{-6}$ m^{-2}) at approximately 70 km, meaning that the wave should be absorbed at this level as the vertical wavelength becomes less than 1 km. Evidently, the wave did not get absorbed, as it continued to propagate horizontally through the FOV. This demonstrates a limitation/short-coming in the calculation of the duct. This could be due to the time and/or spatial separation (4.1 hours and 543 km, respectively) between the temperature profile used and the event time and location. Otherwise, it could demonstrate that the WKB approximation is not valid at this time due to an abrupt change in wind at approximately 74 km altitude, meaning that the solution shown in Equation 5.1 is no longer valid.

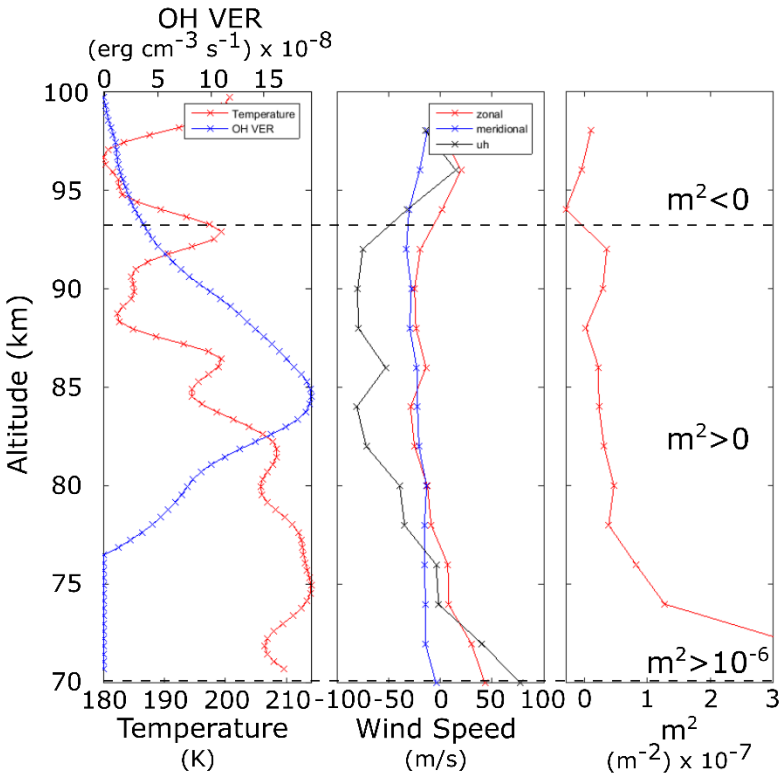

Figure E.4: As in Figure 5.6, but now corresponding to case 1 of the verified frontal events. The SABER profile used here was measured 4.1 hours before the frontal event and corresponded to a region which was ~543 km north-west of Davis Station.

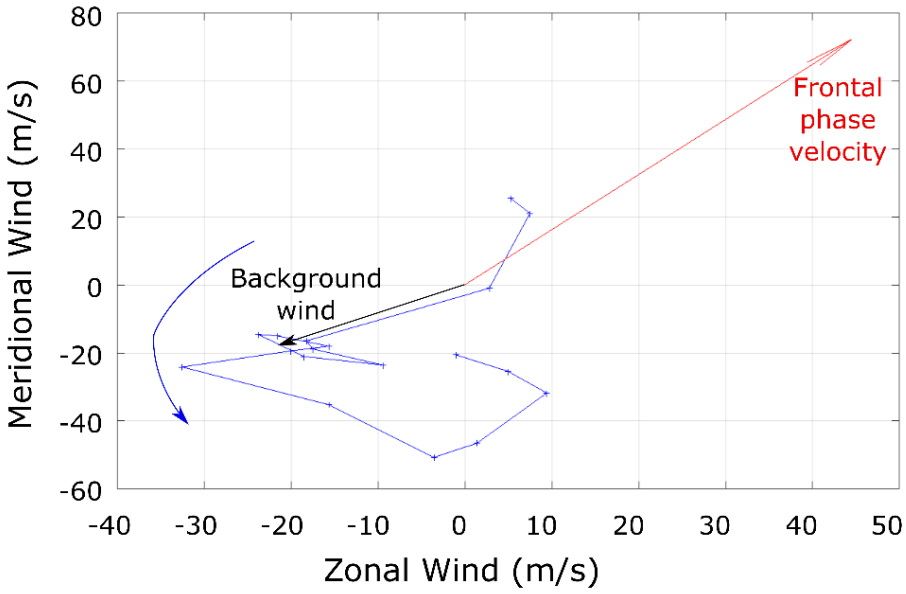

Figure E.5: As in Figure 5.13, but now corresponding to case 1 of the verified frontal events.

The intrinsic period of this particular front was 9.5±1 minutes (between 7 and 10 minutes) with a horizontal wavelength much larger than 30 km and, as shown in Figure E.4 (left), a thermal duct is observed at the base of the thermosphere, in agreement with the proposal by *Snively et al.* (2013).

The ray-tracing for this front was terminated at 72.8 km altitude where it was estimated that intrinsic frequency ω = 0.0115 rad/s, δ = 1.04, m^2 = 1.05×10^{-8} rad^2/m^2, R_i = 19.84, and N^2 = 3.46×10^{-4} rad^2/s^2. Thus, the condition for which the wave couldn't freely propagate further was that $\delta > 1$, meaning that shears in background wind flow were no longer negligible compared to shears generated by the wave. Therefore, it seems that the front was observed in the OH* emission at its peak altitude (between ~84 and 86 km, where emission was greater than 15×10^{-8} ergs cm^{-3} s^{-1}), and that it was trapped vertically somewhere between approximately 70 and 94 km. From these results, it seems that the lower reflective boundary could not be calculated correctly as Equation 5.1 is invalid when the WKB approximation is violated.

Finally, the Czerny-Turner spectrometer data plot for this night is shown in Figure E.6. From Figure E.6, small (~20 K peak-to-peak) wave-like oscillations

in temperature may be seen at the same time as the front passed over the station. Additional supporting data at this time (shown in Figure E.6) included a small peak in OH* intensities, a very high signal-to-noise ratio, and a reduction in cloud cover.

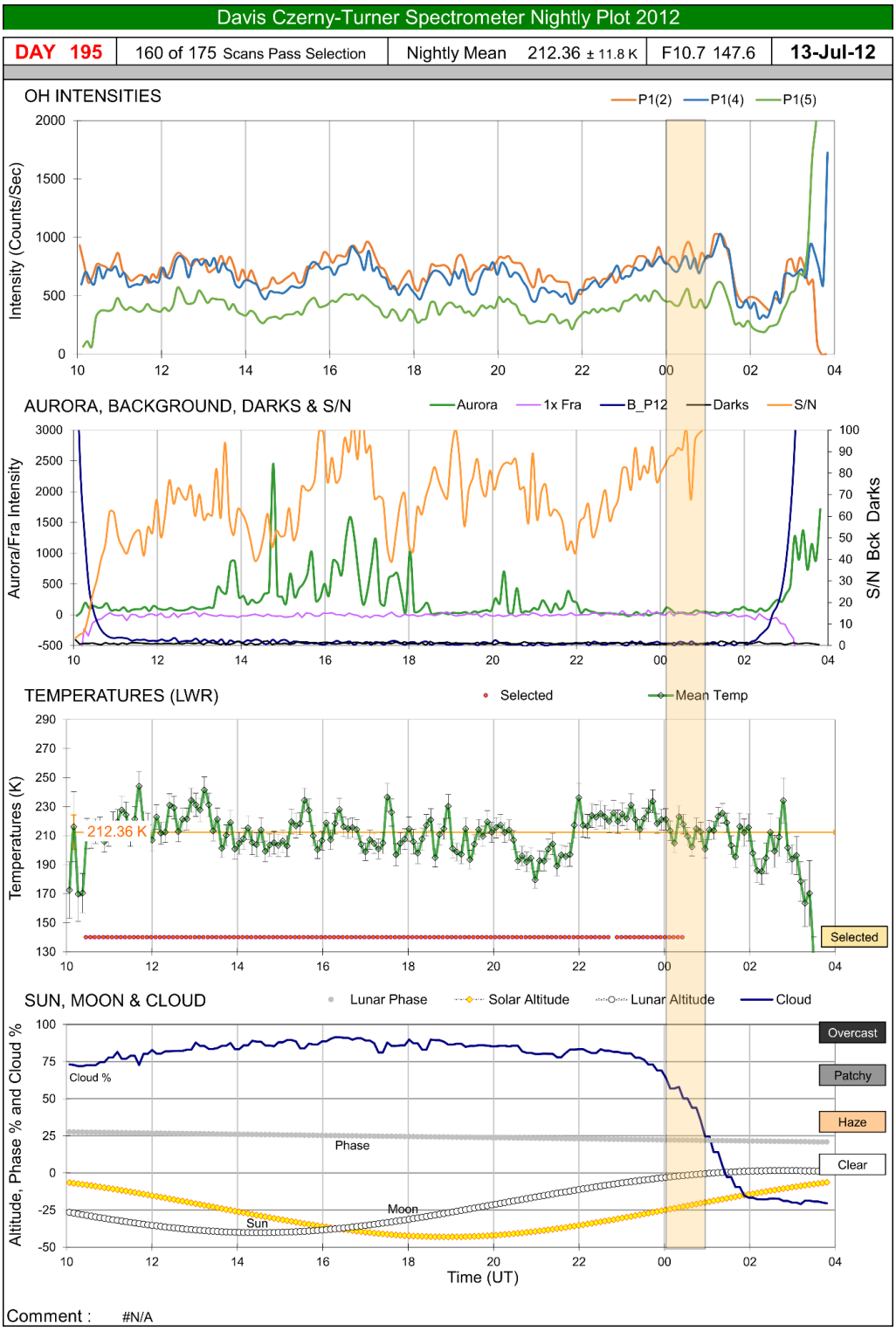

Figure E.6: As in Figure 5.8 but for the night of 13th–14th July 2012.

Case 3 from Table 5.1 –

A dark front detected between 01:03 and 01:11 UT on 09-Aug-2012:

Figure E.7 and Figure E.8 display a series of images showing the third detected front, whose characteristics are shown in Table 5.1 (page 204), between 01:03 and 01:11 UT on 9th August 2012. This front was detected by the USU camera from approximately 00:36 to 01:35 UT (part of which is shown in Figure E.8) but didn't reach UWOSCR's FOV until approximately 01:00 UT (as shown in Figure E.7). Although this front is quite clear in the USU images, it is not so clear in the UWOSCR images, and so the keograms for this front are not shown here. There are several trailing wave-like oscillations phase-locked to the front in this case, and these can be clearly seen in the USU images.

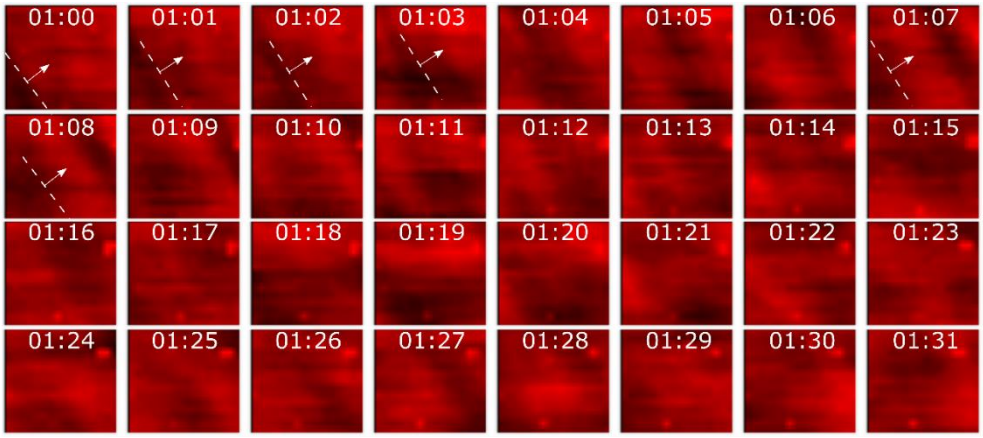

Figure E.7: Sequence of UWOSCR images from 01:00-01:31 UT on 9th August 2012.

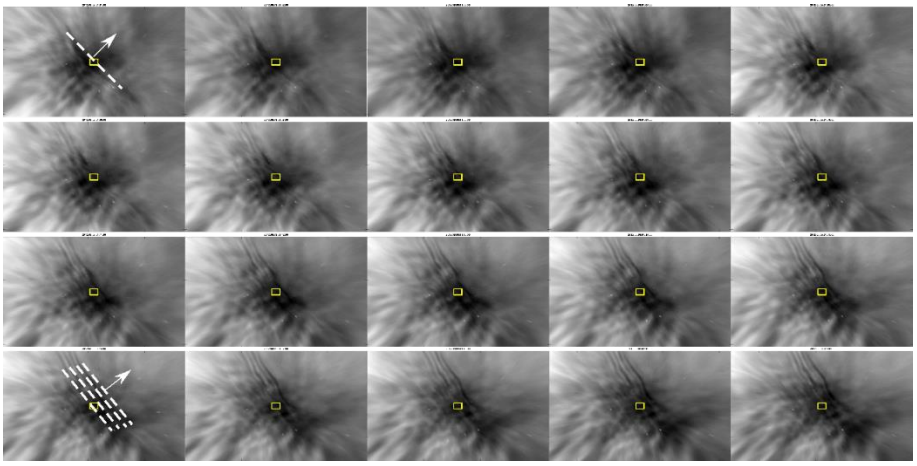

Figure E.8: A series of images recorded by the USU camera between 01:01 and 01:20 UT on 9th August 2012.

Manual analysis of this front gives an observed propagation direction of $\theta \approx 34^\circ \pm 3^\circ$ north of east, an observed phase speed of $v \approx 44 \pm 13$ m/s, and a horizontal wavelength (of the trailing wavelets) of $\lambda_h \approx 14.5 \pm 1.5$ km. These parameters are all slightly different to those calculated using the automated analysis method (whose values are shown in Table 5.1 on page 204).

The resulting m^2 profile for this frontal event is shown in Figure E.9. Thermal inversions at altitudes of approximately 80 km and 98 km caused m^2 to become negative, thus creating a reflective boundary at these two levels. Between these two levels, there existed a deep (~18 km) thermal duct where the observed front could freely propagate. Within the ducting region, there was a weak Doppler inversion at approximately $92 - 94$ km which may have made propagation conditions less favourable (lower m^2 value).

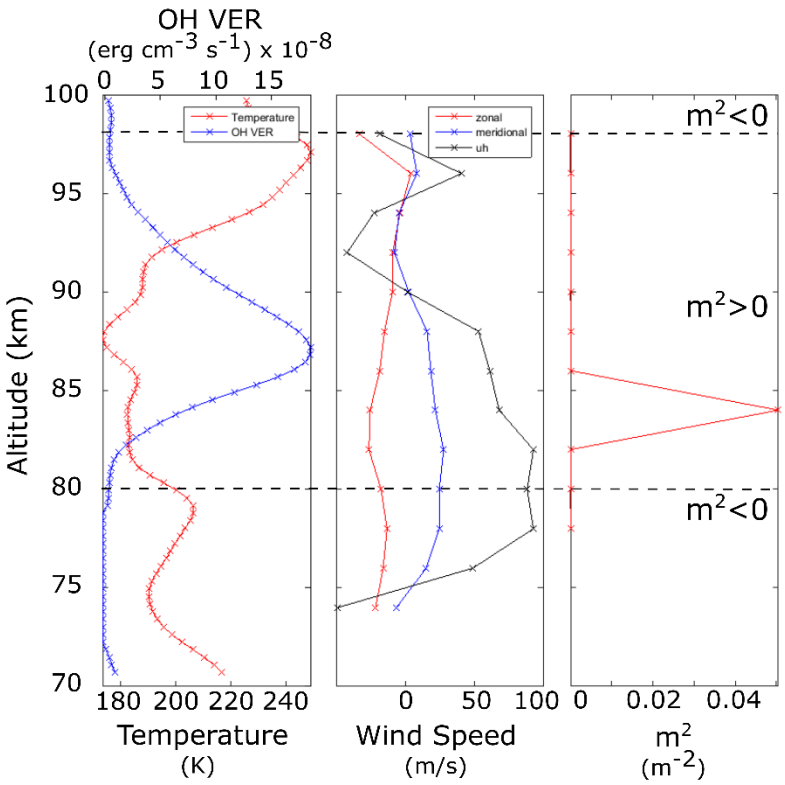

Figure E.9: As in Figure 5.6, but now corresponding to case 3 of the verified fronts. The SABER profile used here was measured 12 minutes before the frontal event and corresponded to a region which was ~789 km north-west of Davis Station.

The intrinsic period of this particular front (5.1 ± 1 minutes) is within the category proposed by *Snively et al.* (2013) where thermal ducting is likely. This categorization is supported by the thermal duct shown in Figure E.9 (left).

This front could not be ray-traced significantly below the mesopause region; the ray-tracing was terminated at 87 km altitude where it was estimated that intrinsic frequency ω = 0.0232 rad/s, δ = 0.23, $m^2 = -2.64\times10^{-8}$ rad^2/m^2, R_i = 49.6, and $N^2 = 3.61\times10^{-4}$ rad^2/s^2. Thus, the condition for which the wave couldn't propagate further at this altitude was that $m^2 < 0$. However, from the calculated m^2 profile at the closest possible time and location to the wave (*i.e.* from the non-climatological data shown in Figure E.9), it can be seen that vertical propagation is possible between 80 and 98 km, where m^2 is greater than zero. Therefore, it seems that the front was observed in the OH* emission near its peak altitude (~87 km, where emission was ~18×10^{-8} ergs cm^{-3} s^{-1}), and that it was trapped vertically between approximately 80 and 98 km.

Czerny-Turner spectrometer data corresponding to the time of this front (shown in Figure E.10) provided some supporting evidence that this was a mesospheric front, including a wave-like OH* temperature oscillation with peak-to-peak amplitude of ~40 K, a small OH* intensity oscillation, a high signal-to-noise ratio, and a clear sky.

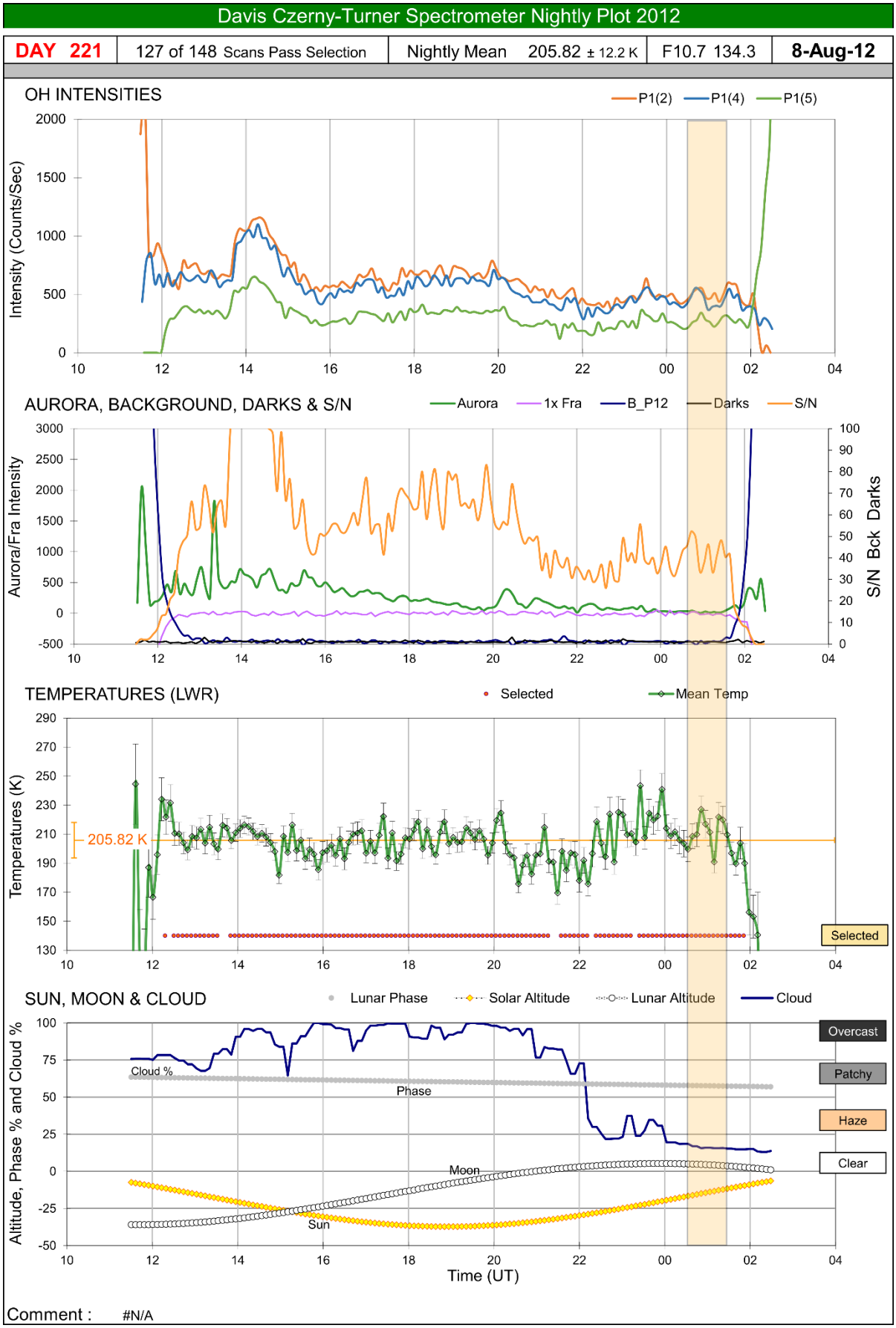

Figure E.10: As in Figure 5.8 but for the night of 8th–9th August 2012.

Case 5 from Table 5.1 –

A dark bore detected between 00:02 and 00:22 UT on 11-Aug-2012:

Figure E.11 and Figure E.12 display a series of images showing the fifth detected frontal event, whose characteristics are shown in Table 5.1 on page 204, between 00:02 and 00:22 UT on 11th August 2012. This front was detected by the USU camera from approximately 23:32 UT, reaching UWOSCR's FOV at approximately 00:00 UT. In the USU images, some ripples may be seen just before the leading edge of the front passes by, again travelling in a perpendicular direction with respect to the front. Some wave-like structures are also phase-locked behind the front, as is often characteristic of an undular bore event.

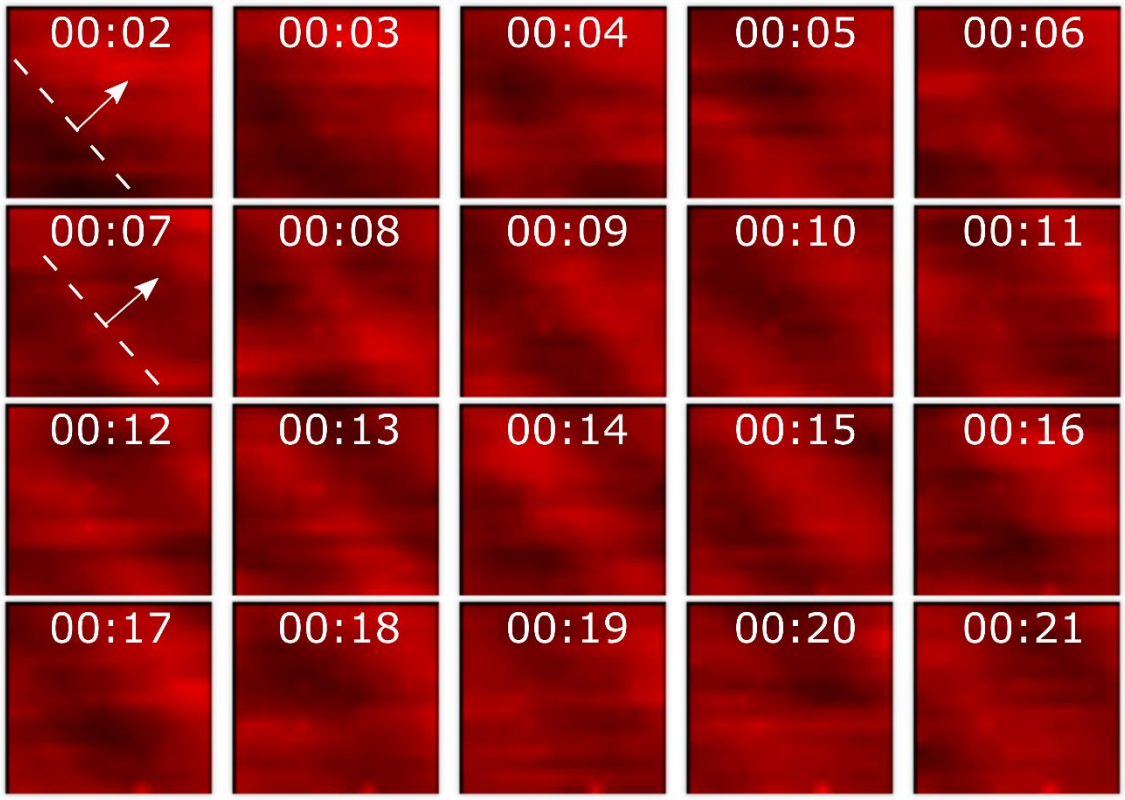

Figure E.11: Sequence of UWOSCR images from 00:02-00:21 UT on 11th August 2012.

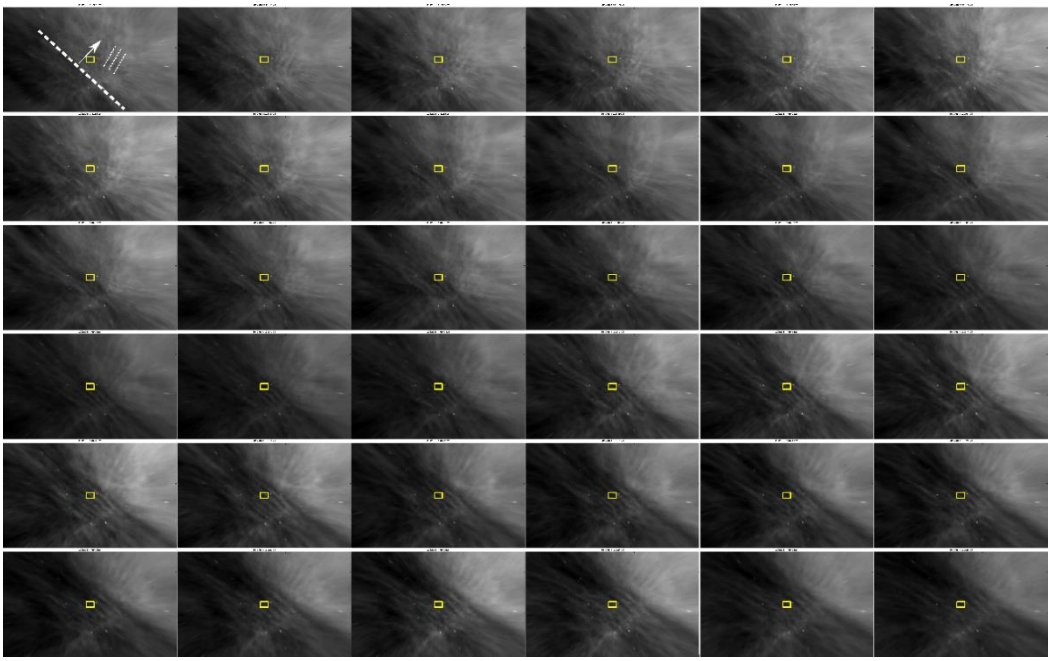

Figure E.12: A series of images recorded by the USU camera between 23:50 on 10th August 2012 and 00:26 UT on 11th August 2012.

From the two keograms in Figure E.13, it is confirmed (between approximately 00:00 and 00:24 UT on 11th August 2012) that the front and its trailing wave-like oscillations move in a predominantly north-eastward direction.

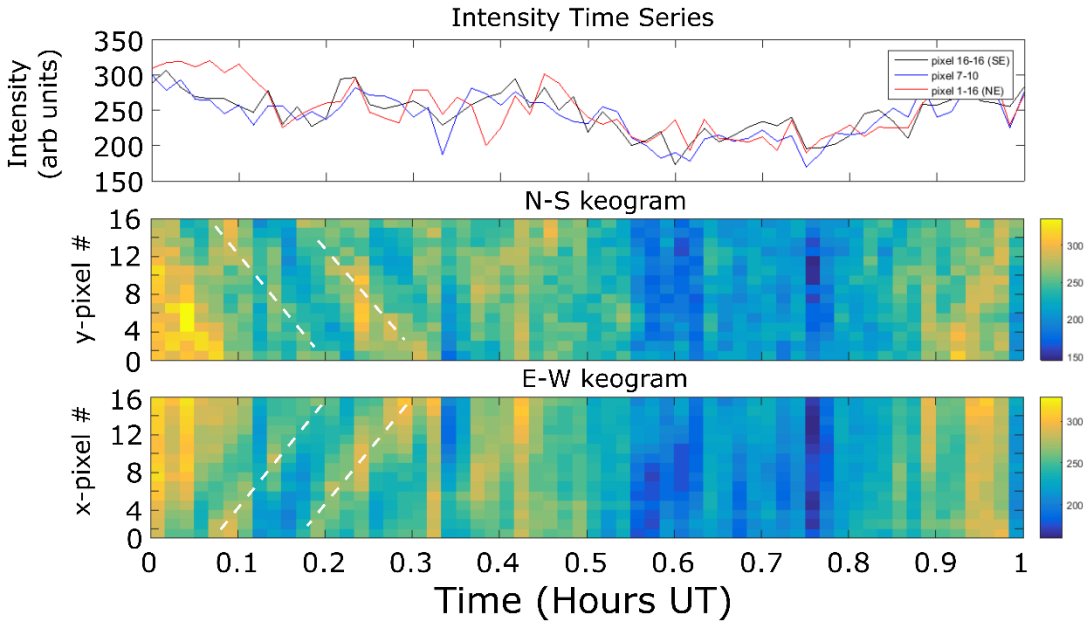

Figure E.13: As in Figure 5.11 but between 00:00 and 01:00 UT on 11th August 2012 (displayed as 24−25 UT).

Manual analysis of this front gives an observed propagation direction of $\theta \approx 40^\circ \pm 5^\circ$ north of east, an observed phase speed of $v \approx 54 \pm 4$ m/s, and a horizontal wavelength (of the trailing wavelets) of $\lambda_h \approx 20 \pm 5$ km. This is in fairly good agreement with the parameters calculated using the analysis method (shown in Table 5.1 on page 204). Again, the differences in this case could be related to the intensity difference between the leading front and its trailing waves.

The resulting m^2 profile for this bore event is shown in Figure E.14. Thermal inversions at altitudes of approximately 80 km and 98 km caused m^2 to become negative, thus creating reflective boundaries at these levels. Within this deep (~18 km) thermal duct, the wind is travelling in the same direction as the front from ~80–85 km, where m^2 is at its largest, and it is travelling in the opposite direction to the front between ~85 and 98 km (also shown in Figure E.15), thus weakening the ducting region but not quite causing m^2 to become negative.

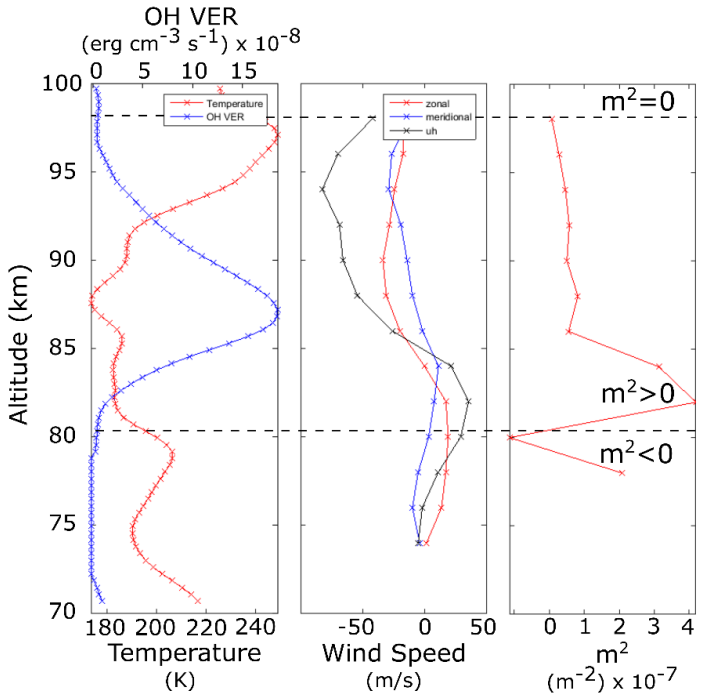

Figure E.14: As in Figure 5.6, but now corresponding to case 5 of the verified fronts. The SABER profile used here was measured 49.5 minutes before the frontal event and corresponded to a region which was ~789 km north-west of Davis Station.

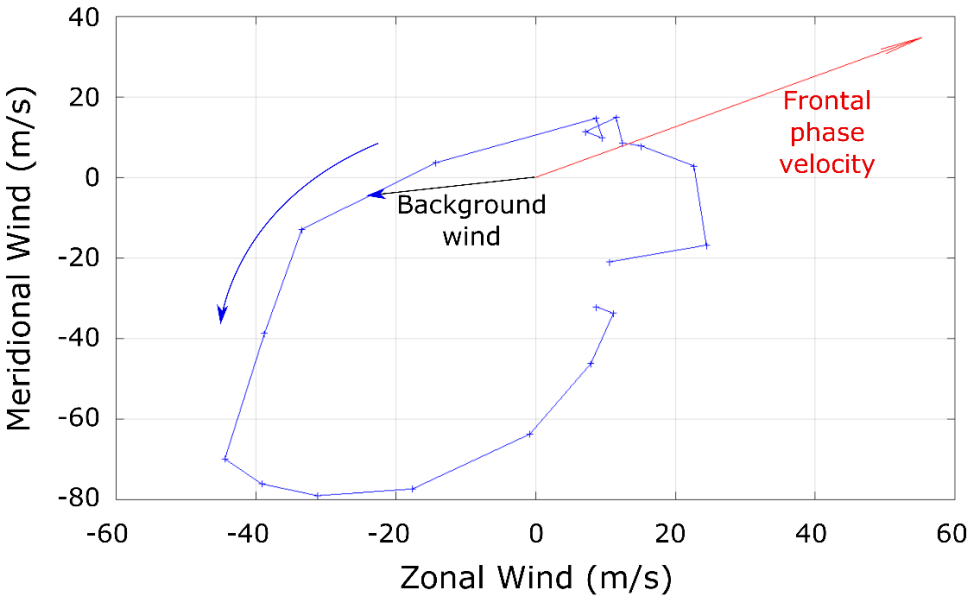

Figure E.15: As in Figure 5.13, but now corresponding to case 5 of the verified frontal events.

The intrinsic period of this particular front (2.2 ± 1 minutes) is within the category proposed by *Snively et al.* (2013) where thermal ducting is likely. This categorization is supported by Figure E.14 (left) where thermal ducting can be seen.

This front could not be ray-traced significantly below the mesopause region; the ray-tracing was terminated at 87 km altitude where it was estimated that intrinsic frequency $\omega = 0.053$ rad/s, $\delta = 0.004$, $m^2 = -2.92\times10^{-7}$ rad^2/m^2, $R_i = 48.9$, and $N^2 = 3.59\times10^{-4}$ rad^2/s^2, and so the condition for which the wave couldn't propagate further at this altitude was that m^2 was less than zero. However, from the calculated m^2 profile at the closest possible time and location to the wave (*i.e.* the non-climatological data), it can be seen that vertical propagation is possible between 80 and 98 km, where m^2 is greater than zero. Therefore, it seems more likely that the front was observed in the OH* emission at its peak altitude (~87 km, where emission was approximately 18×10^{-8} ergs cm^{-3} s^{-1}), and that it was trapped vertically between approximately 80 and 98 km.

Czerny-Turner spectrometer data corresponding to the time of this front (shown in Figure E.16) provided some complementary results, including an OH* temperature change of ~20 K, a fairly large signal-to-noise ratio, and a clear sky.

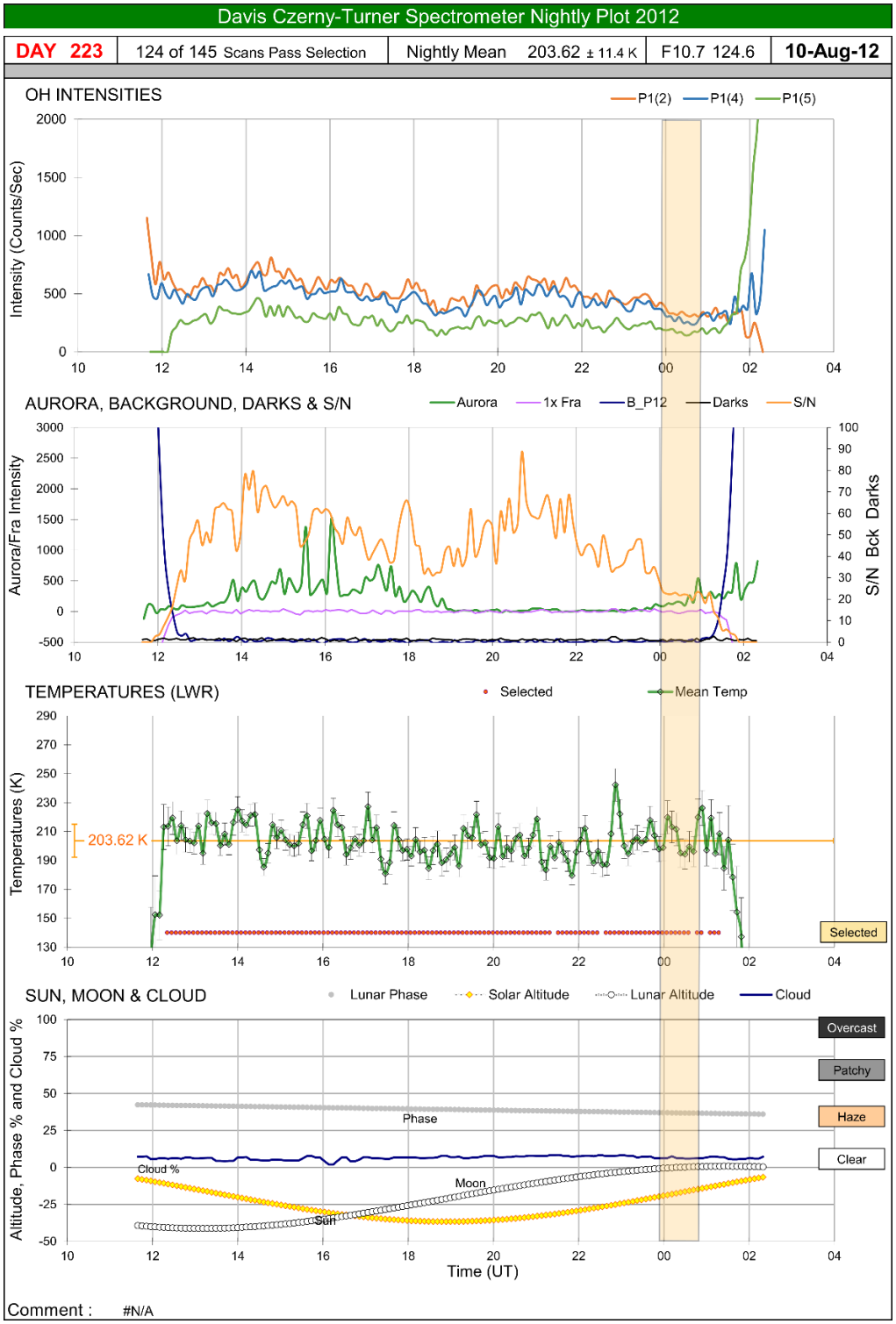

Figure E.16: As in Figure 5.8 but for the night of 10th–11th August 2012.

E.2. Unverified Fronts

Case 2 from Table 5.2 -

A potential dark front detected between 21:10 and 21:15 UT on 10-Jul-2006:

Figure E.17 displays a series of images showing the second potential front, which was part one of a potential double bore event and whose characteristics are shown in Table 5.2 on page 218, between 21:10 and 21:15 UT on 10th July 2006. No wave-like structures were phase-locked to the front in this case.

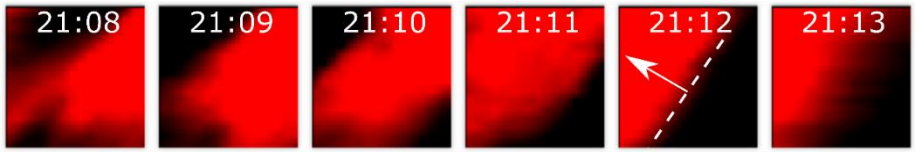

Figure E.17: A series of images recorded by UWOSCR between 21:00 and 21:13 UT on 10th July 2006. The dashed line indicates the front and the arrow indicates the direction of propagation.

From the two keograms in Figure E.18, it is confirmed (between approximately 21:05 and 21:20 UT on 10th July 2006) that the front moves in a predominantly north-westward direction. This is in general agreement with the value produced by the analysis (198° north of east), shown in Table 5.2 on page 218.

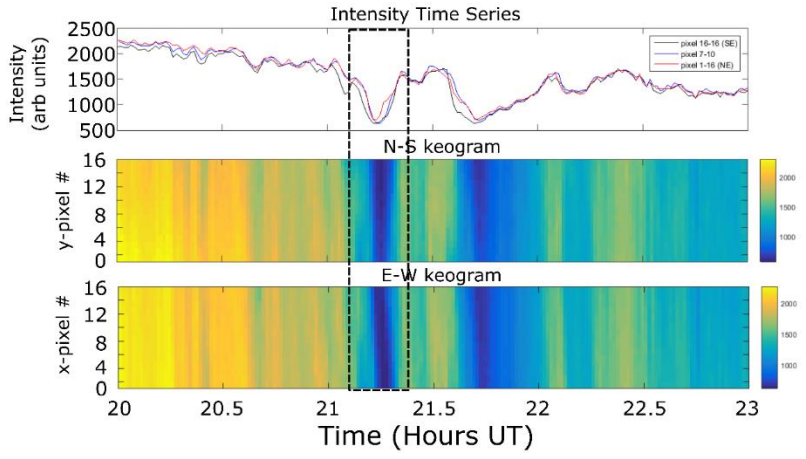

Figure E.18: As in Figure 5.11 but between 20:00 and 23:00 UT on 10th July 2006. The black box indicates the time of the potential frontal event.

Manual analysis of this front gives an observed propagation direction of $\theta \approx 134^{\circ} \pm 12^{\circ}$ north of east and an observed phase speed of $v \approx 132 \pm 7$ m/s. The

horizontal wavelength could not be calculated as there were no trailing waves locked to the front. The value calculated manually for phase velocity is ~47 m/s faster than and ~ 52° out of agreement with that calculated by the automated method. Again, the cross-correlation method may have struggled with the very wide wave crest in this particular case.

The resulting m^2 profile for this potential front is shown in Figure E.19. Thermal inversions at altitudes of approximately 81 km, 88 km, 92 km and 96 km cause m^2 to become negative, thus creating reflective boundaries at these levels. The thermal duct in which this event is more likely trapped is in the range 81−88 km, as the OH* emission is centred much lower than usual (with a peak at approximately 80 km altitude) at this time. Throughout this altitude region, winds are opposed to the propagation direction of the wave. However, between 81 and 88 km, these winds are at their weakest and thus they do not cause m^2 to become negative.

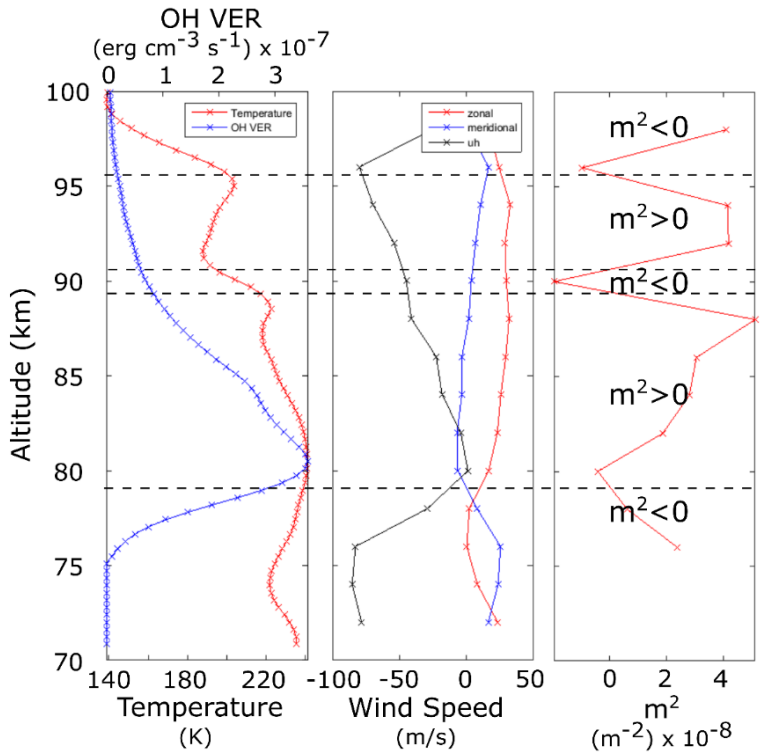

Figure E.19: As in Figure 5.6, but now corresponding to case 2 of the unverified fronts. The SABER profile used here was measured 95.1 hours before the potential frontal event and corresponded to a region which was ~775 km south-west of Davis Station.

This front could not be ray-traced significantly below the mesopause region; the ray-tracing was terminated at 86.97 km altitude where it was estimated that intrinsic frequency ω = 0.0172 rad/s, δ = 1.49, m^2 =2.93×10^{-10} rad^2/m^2, R_i =76.05 and N^2 = 3.81×10^{-4} rad^2/s^2. Thus, the condition for which the wave couldn't freely propagate further was that $\delta > 1$, meaning that shears in background wind flow were no longer negligible compared to shears generated by the wave, and so m^2 could not be calculated using the Taylor-Goldstein equation. Therefore, it seems that the front was observed in the OH* emission just above its peak altitude (~80 km, where emission was greater than 3×10^{-7} ergs cm^{-3} s^{-1}) and that it was trapped vertically between approximately 81 and 88 km due to a thermal duct.

Confidence in this potential front was severely reduced upon inspection of the Czerny-Turner spectrometer data (shown in Figure E.20), as a very low signal-to-noise ratio (along with high background noise and auroral signals) was observed at the event time and throughout the entire night. This is thus an example of an event which had been marked as a potential front but, due to low data quality demonstrated by the Czerny-Turner spectrometer plots, is now marked as an unlikely front.

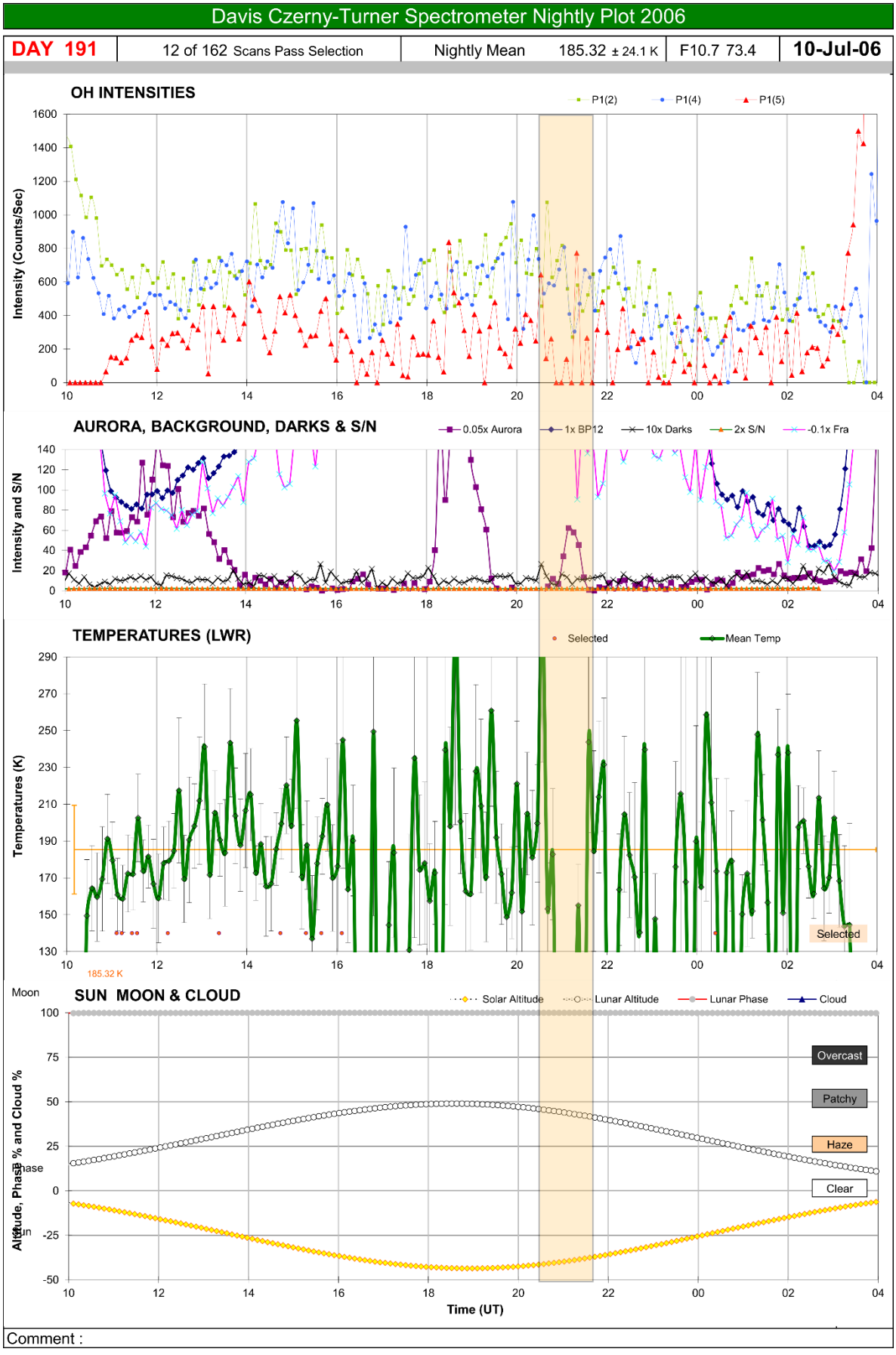

Figure E.20: As in Figure 5.8 but for the night of 10$^{\text{th}}$–11$^{\text{th}}$ July 2006.

Case 3 from Table 5.2 –

A potential dark front detected between 21:34 and 21:38 UT on 10-Jul-2006:

Figure E.21 displays a series of images showing the third potential front, which was part two of a potential double bore event and whose characteristics are shown in Table 5.2 on page 218, between 21:34 and 21:38 UT on 10th July 2006. Again, no wave-like structures were phase-locked to the front in this case.

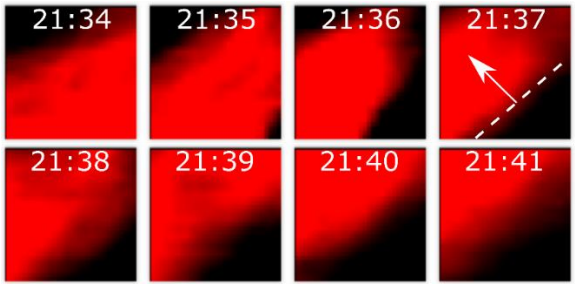

Figure E.21: A series of images recorded by UWOSCR between 21:34 and 21:41 UT on 10th July 2006. The dashed line indicates the front and the arrow indicates the direction of propagation.

From the two keograms in Figure E.22, it is confirmed (between approximately 21:30 and 21:40 UT on 10th July 2006) that there is a sharp decrease in intensity. However, it is not clear from the keogram in what direction the front is propagating as it was very short-lived within the FOV.

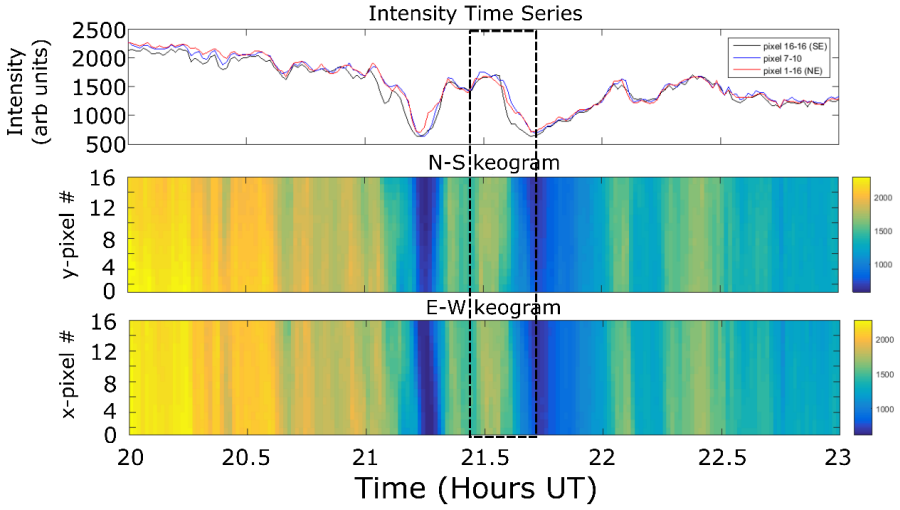

Figure E.22: As in Figure 5.11 but between 20:00 and 23:00 UT on 10th July 2006. The black box indicates the time of the potential frontal event.

Manual analysis of this front gives an observed propagation direction of $\theta \approx 133^{\circ} \pm 13^{\circ}$ north of east and an observed phase speed of $v \approx 38 \pm 3$ m/s. The horizontal wavelength could not be calculated as there were no trailing waves locked to the front. The value calculated manually for phase velocity is ~54 m/s slower than and ~ 18° out of agreement with that calculated by the automated method. Again, the cross-correlation method may have struggled with the very wide wave crest in this particular case.

The resulting m^2 profile for this potential front is shown in Figure E.23. Thermal inversions at altitudes of approximately 90 km and 94 km cause m^2 to become negative, thus creating reflective boundaries at these levels. Throughout this altitude region, winds are either weakly opposed to or weakly aligned with the propagation direction of the wave, and thus do not strongly affect the duct.

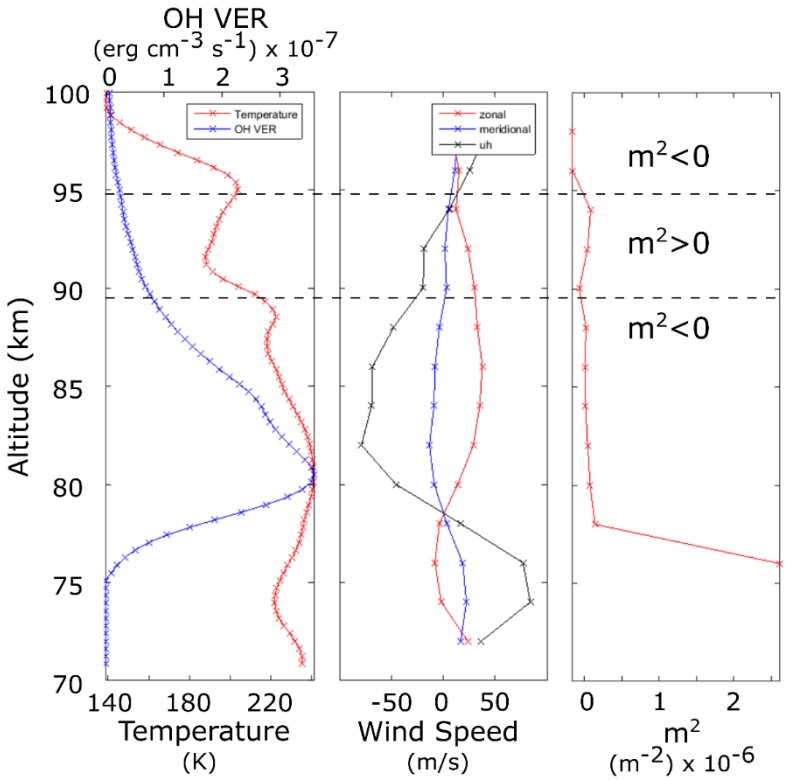

Figure E.23: As in Figure 5.6, but now corresponding to case 3 of the unverified fronts. The SABER profile used here was measured 95.5 hours before the potential frontal event and corresponded to a region which was ~775 km south-west of Davis Station.

This front could not be ray-traced significantly below the mesopause region; the ray-tracing was terminated at 87 km altitude where it was estimated that intrinsic frequency ω = 0.0165 rad/s, δ = 17.18, m^2 =-2.51×10^{-10} rad^2/m^2, R_i =76.05 and N^2 = 3.81×10^{-4} rad^2/s^2. Thus, the conditions for which the wave couldn't freely propagate further was that $\delta > 1$ and that $m^2 < 0$, meaning that shears in background wind flow were no longer negligible compared to shears generated by the wave and that the wave could not propagate vertically. Therefore, it seems that the front was not observed at 87 km altitude, but slightly higher at approximately 90−95 km altitude (where it was ducted by thermal inversions). This would explain the lower intensity observed, as the peak OH* emission at this time was much lower (~80 km), and within the ducting region it was emitting less than 1×10^{-7} ergs cm^{-3} s^{-1}.

Confidence in this potential front was severely reduced upon inspection of the Czerny-Turner spectrometer data (shown in Figure E.20), as a very low signal-to-noise ratio (along with high background noise and auroral signals) was observed at the event time and throughout the entire night. This is thus an example of an event which had been marked as a potential front but, due to low data quality demonstrated by the Czerny-Turner spectrometer plots, is now marked as an unlikely front.

Case 5 from Table 5.2 –

A potential dark front detected between 16:42 and 16:55 UT on 13-Aug-2011:

Figure E.24 displays a series of images showing the fifth potential (unverified) front whose characteristics are shown in Table 5.2 on page 218, between 16:42 and 16:55 UT on 13th August 2011. There is a trailing wave-like oscillation locked behind the front in this case.

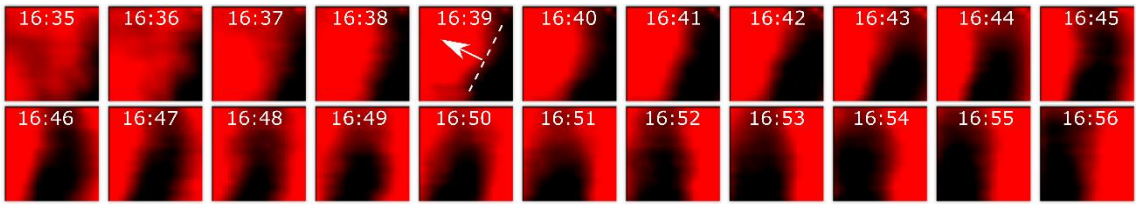

Figure E.24: A series of images recorded by UWOSCR between 16:35 and 16:56 UT on 13th August 2011. The dashed line indicates the leading front and the arrow indicates the direction of propagation.

From the two keograms in Figure E.25, it is confirmed (between approximately 16:30-17:00 UT on 13th August 2011) that the front moves in a predominantly north-westward direction. This is in general agreement with the value produced by the analysis (172° north of east), shown in Table 5.2 on page 218.

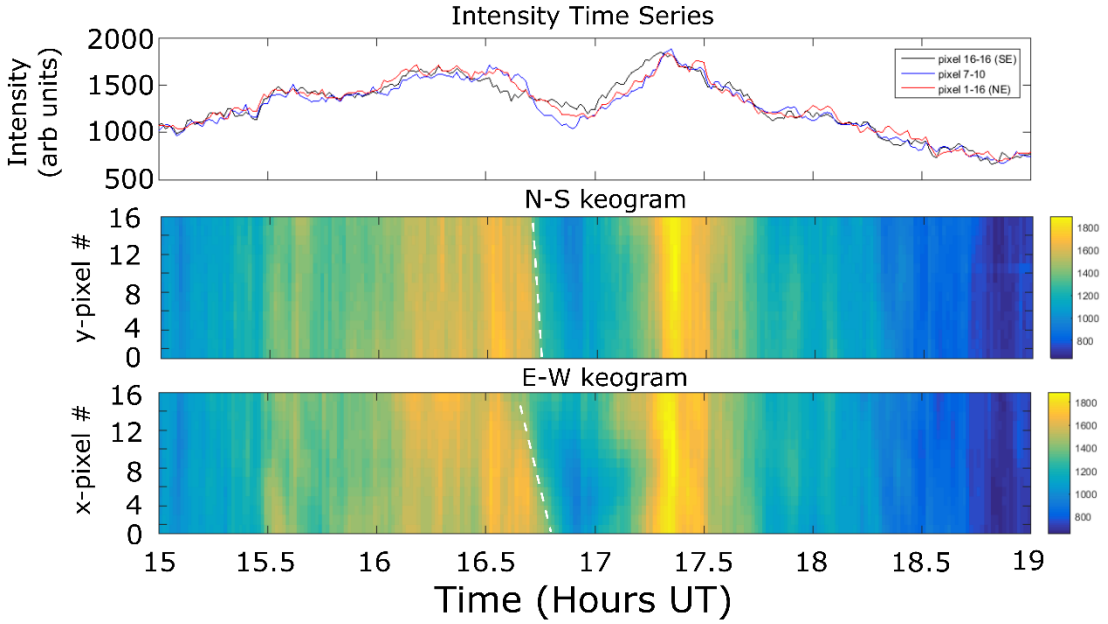

Figure E.25: As in Figure 5.11 but between 15:00 and 19:00 UT on 13th August 2011.

Manual analysis of this front gives an observed propagation direction of $\theta \approx 165° \pm 15°$ north of east and an observed phase speed of $v \approx 18 \pm 2$ m/s. The horizontal wavelength could not be determined in this case as two dark points on the wave are not visible. Again the value for propagation direction agrees with the automated method, but the manually calculated value for speed is ~26 m/s slower than that produced by the automated method, and again may be

due to a fault in the cross-correlation method due to the thickness of the bright crests.

The resulting m^2 profile for this potential front is shown in Figure E.26. Thermal inversions at altitudes of approximately 82 km and 90 km cause m^2 to become negative, thus creating reflective boundaries at these levels. Throughout this altitude region, winds are opposing the propagation direction of the wave (also shown in Figure E.27 for 86 km only), and thus this reduces the value of m^2.

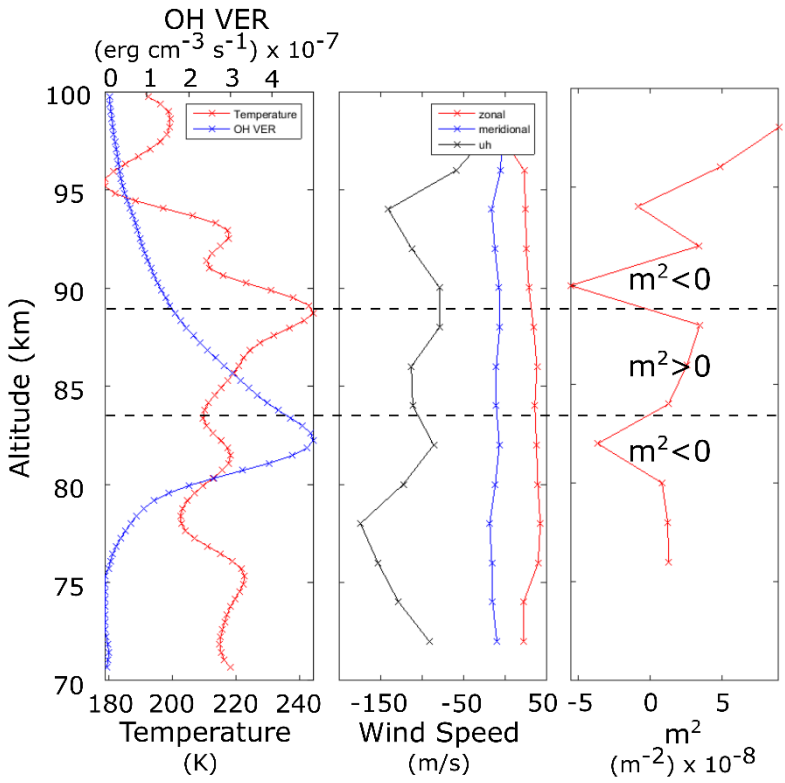

Figure E.26: As in Figure 5.6, but now corresponding to case 5 of the unverified fronts. The SABER profile used here was measured 1.99 hours after the potential frontal event and corresponded to a region which was ~493 km north-west of Davis Station.

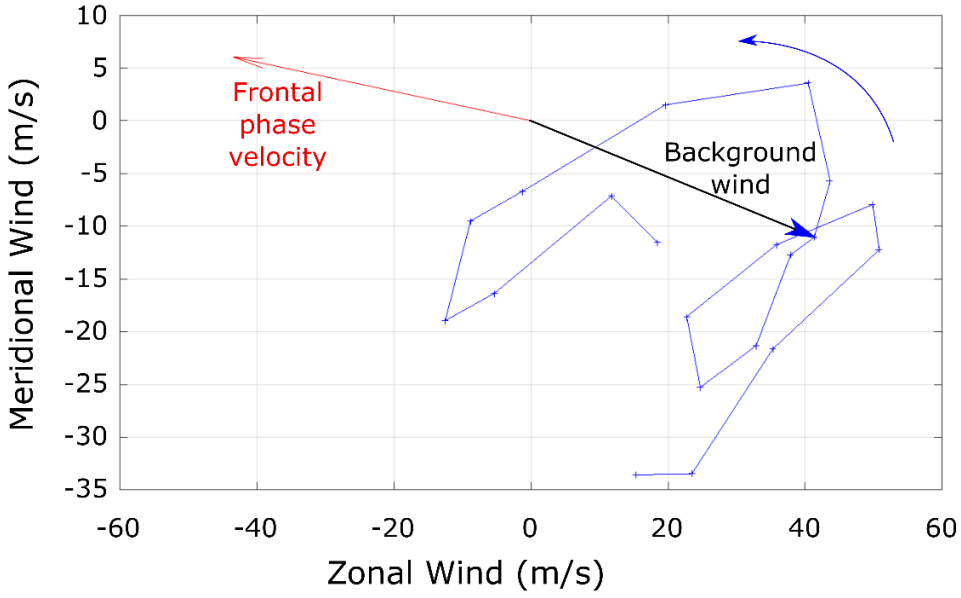

Figure E.27: As in Figure 5.13, but now corresponding to case 5 of the potential frontal events.

The ray-tracing for this event was terminated at 87 km altitude where it was estimated that intrinsic frequency ω = 0.0185 rad/s, δ = 13.73, m^2 =-3.26×10^{-9} rad^2/m^2, R_i =48.68 and N^2 = 3.59×10^{-4} rad^2/s^2. Thus, the conditions for which the wave couldn't freely propagate further was that $\delta > 1$ and that $m^2 < 0$, meaning that shears in background wind flow were no longer negligible compared to shears generated by the wave and that the wave could not propagate vertically. However, using non-climatological values for wind and temperature it becomes evident that vertical propagation is possible between approximately 82 and 88 km. Therefore, the ray-tracing results do not appear to be accurate in this particular case and the event observation must have been slightly higher than the peak OH* emission altitude (which was ~82 km with a peak emission of greater than $\sim5\times10^{-7}$ ergs cm^{-3} s^{-1}).

Czerny-Turner spectrometer data corresponding to the time of this front (shown in Figure E.28) provided some complementary results, including an OH* temperature decrease of ~ 20 K, an OH* intensity increase of ~ 500 counts/second, a high signal-to-noise ratio, and a clear sky.

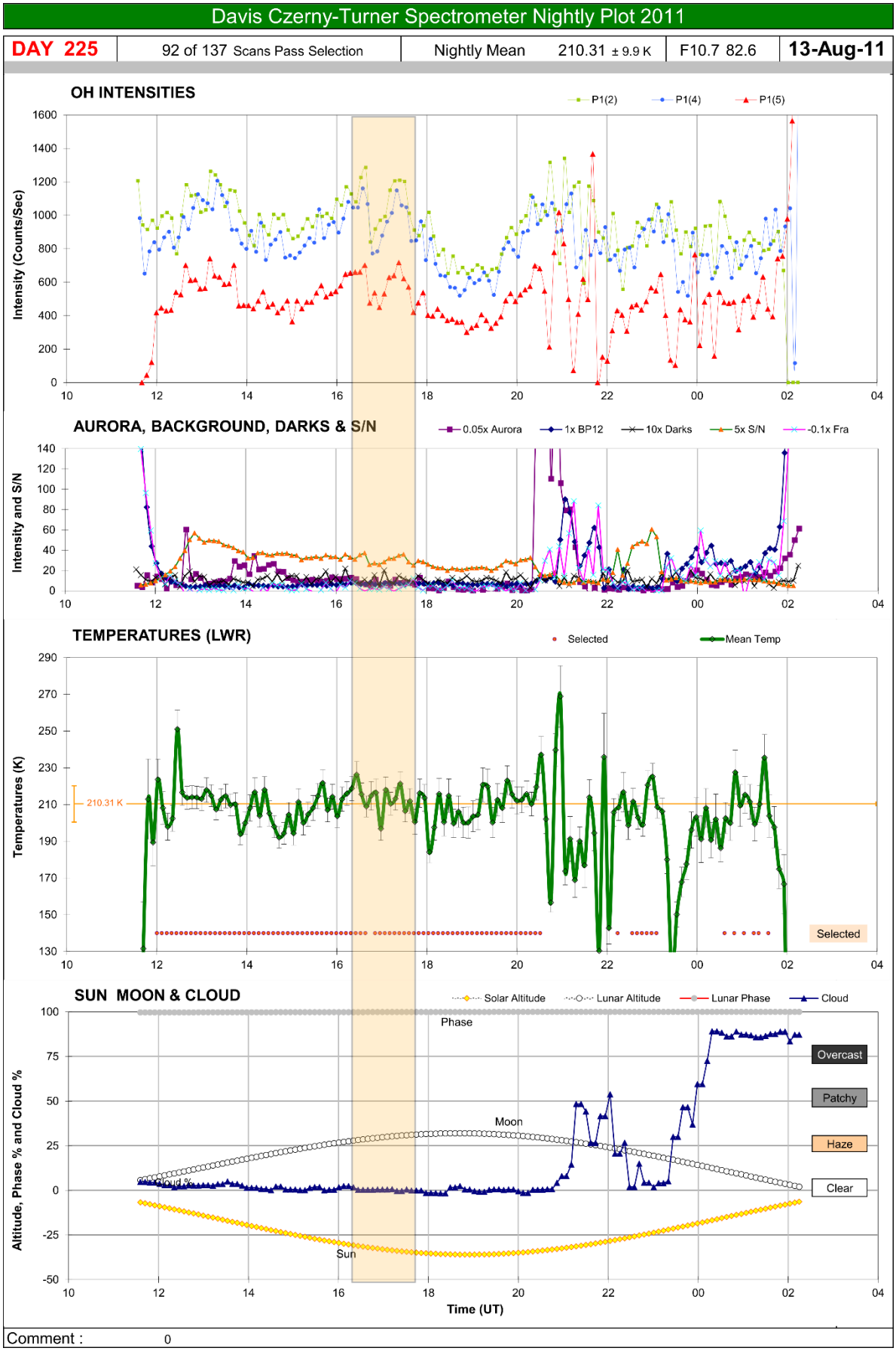

Figure E.28: As in Figure 5.8 but for the night of 13th–14th August 2011.

REFERENCES

Addison, P.S. (2002). The Illustrated Wavelet Transform Handbook - Introduction Theory and Applications in Science, Engineering, Medicine and Finance. Institute of Physics, Bristol.

Akasofu, S.I., and S. Chapman. (1961). The ring current, geomagnetic disturbance, and the Van Allen radiation belts. Journal of Geophysical Research, 66, 1321–1350, doi: 10.1029/JZ066i005p01321.

Alexander, M.J., M.A. Geller, C. McLandress, S. Polavarapu, P. Preusse, F. Sassi, K. Sato, S.D. Eckermann, M. Ern, A. Hertzog, Y. Kawatani, M. Pulido, T.A. Shaw, M. Sigmond, R.A. Vincent, and S. Watanabe. (2010). Recent developments in gravity-wave effects in climate models and the global distribution of gravity-wave momentum flux from observations and models. Quarterly Journal of the Royal Meteorological Society, 136, 1103–1124, doi: 10.1002/qj.637.

Alexander, S.P., A.R. Klekociuk, A.J. McDonald, and M.C. Pitts. (2013). Quantifying the role of orographic gravity waves on polar stratospheric cloud occurrence in the Antarctic and the Arctic. Journal of Geophysical Research: Atmospheres, 118, 11,493-11,507, doi: 10.1002/2013JD020122.

Alexander, S.P., A.R. Klekociuk, and D.J. Murphy. (2011). Rayleigh lidar observations of gravity wave activity in the winter upper stratosphere and lower mesosphere above Davis, Antarctica (69°S, 78°E). Journal of Geophysical Research, 116, doi: 10.1029/2010JD015164.

Van Allen, J.A. (1959). The geomagnetically trapped corpuscular radiation. Journal of Geophysical Research, 64, 1683–1689, doi: 10.1029/JZ064i011p01683.

Van Allen, J.A., and L.A. Frank. (1959). Radiation Around the Earth to a Radial Distance of 107,400 km. Nature, 183, 430–434, doi: 10.1038/183430a0.

Andrews, D.G. (2005). An Introduction to Atmospheric Physics. Third edition. Cambridge University Press, New York.

Angell, J.K., and D.H. Pack. (1960). Analysis of some preliminary low-level constant volume balloon (tetroon) flights. Monthly Weather Review, 88, 235–248.

ARISE. (2015). Atmospheric dynamics. http://arise-project.eu/images/illustration-waves3.jpg.

Bageston, J.V., C.M. Wrasse, P.P. Batista, D. Gobbi, R. Hibbins, and D.C. Fritts. (2011a). Investigation of Gravity Wave Sources in the Antarctic Penninsula by Using the Reverse Ray Tracing Technique, XXV IUGG General Assembly. Melbourne.

Bageston, J.V., C.M. Wrasse, P.P. Batista, R.E. Hibbins, D.C. Fritts, D. Gobbi, and V.F. Andrioli. (2011b). Observation of a mesospheric front in a thermal-doppler duct over King George Island, Antarctica. Atmospheric Chemistry and Physics, 11, 12137–12147, doi: 10.5194/acp-11-12137-2011.

Bageston, J.V., C.M. Wrasse, D. Gobbi, H. Takahashi, and P.B. Souza. (2009). Observation of mesospheric gravity waves at Commandante Ferraz Antarctic Station (62 °S). Annales Geophysicae, 27, 2593–2598, doi: 10.5194/angeo-27-2593-2009.

Baker, D.J., and A.T. Stair. (1988). Rocket measurements of the altitude distributions of the hydroxyl airglow. Physica Scripta, 37, 611–622, doi: 10.1088/0031-8949/37/4/021.

Baker, D.J., B.K. Thurgood, W.K. Harrison, M.G. Mlynczak, and J.M. Russell. (2007). Equatorial enhancement of the nighttime OH mesospheric infrared airglow. Physica Scripta, 75, 615–619, doi: 10.1088/0031-8949/75/5/004.

Baldwin, M.P., L.J. Gray, T.J. Dunkerton, K. Hamilton, P.H. Haynes, W.J. Randel, J.R. Holton, M.J. Alexander, I. Hirota, T. Horinouchi, D.B.A. Jones, J.S. Kinnersley, C. Marquardt, K. Sato, and M. Takahashi. (2001). The quasi-biennial oscillation. Reviews of Geophysics, 39, 179–229, doi: 10.1029/1999RG000073.

Ball, T. (2012). Static climate models in a virtually unknown dynamic atmosphere. http://drtimball.com/wp-content/uploads/2012/07/Atmospheric-Column.jpg.

Bittner, M., K. Höppner, C. Pilger, and C. Schmidt. (2010). Mesopause temperature perturbations caused by infrasonic waves as a potential indicator for the detection of tsunamis and other geo-hazards. Natural Hazards and Earth System Sciences, 10, 1431–1442, doi: 10.5194/nhess-10-1431-2010.

Bjerknes, V. (1904). Das Problem der Wettervorhersage, betrachtet vom Stanpunkt der Mechanik und der Physik. Meteor. Zeits, 21, 1–7.

Blanc, E., A. Le Pichon, L. Ceranna, T. Farges, J. Marty, and P. Herry. (2010). Global Scale Monitoring of Acoustic and Gravity Waves for the Study of the Atmospheric Dynamics. Pages 647–664 in A. Le Pichon, E. Blanc, and A. Hauchecorne, editors, Infrasound Monitoring for Atmospheric Studies. Springer, New York.

Bramberger, M., A. Dörnbrack, K. Bossert, B. Ehard, D.C. Fritts, B. Kaifler, C. Mallaun, A. Orr, P.D. Pautet, M. Rapp, M.J. Taylor, S. Vosper, B.P.

Williams, and B. Witschas. (2017). Does Strong Tropospheric Forcing Cause Large-Amplitude Mesospheric Gravity Waves? A DEEPWAVE Case Study. Journal of Geophysical Research: Atmospheres, 122, doi: 10.1002/2017JD027371.

Brasseur, G.P., and S. Solomon. (1986). Aeronomy of the Middle Atmosphere. Second edition. D. Reidel Publishing Company, Dordrecht, Holland.

Briggs, B.H. (1968). On the analysis of moving patterns in geophysics—I. Correlation analysis.

Brigham, E. O. (1974). The Fast Fourier Transform. Prentice-Hall, New Jersey.

Brigham, E. O. (1988). The Fast Fourier Transform and its Applications. Prentice-Hall, New Jersey.

Brown, L.B., A.J. Gerrard, J.W. Meriwether, and J.J. Makela. (2004). All-sky imaging observations of mesospheric fronts in OI 557.7 nm and broadband OH airglow emissions: Analysis of frontal structure, atmospheric background conditions, and potential sourcing mechanisms. Journal of Geophysical Research, 109, D19104, doi: 10.1029/2003JD004223.

Campus, P., and D.R. Christie. (2010). Worldwide Observations of Infrasonic Waves. Pages 185–234 in A. Le Pichon, E. Blanc, and A. Hauchecorne, editors, Infrasound Monitoring for Atmospheric Studies. Springer, New York.

Carslaw, K.S., M. Wirth, A. Tsias, B.P. Luo, A. Dörnbrack, M. Leutbecher, H. Volkert, W. Renger, J.T. Bacmeister, E. Reimer, and T. Peter. (1998). Increased stratospheric ozone depletion due to mountain-induced atmospheric waves. Nature, 391, 675–678, doi: 10.1038/35589.

Carvalho, A.J.A., I. Paulino, A.F. Medeiros, L.M. Lima, R.A. Buriti, A.R. Paulino, C.M. Wrasse, and H. Takahashi. (2017). Case study of convective instability observed in airglow images over the Northeast of Brazil. Journal of Atmospheric and Solar-Terrestrial Physics, 154, 33–42, doi: 10.1016/j.jastp.2016.12.003.

Charney, J.G. (1951). Dynamical forecasting by numerical process. Pages 470–482 in T.F. Malone, editor. Compendium of meteorology. American Meteorological Society, Boston.

Choi, H.J., and H.Y. Chun. (2013). Effects of Convective Gravity Wave Drag in the Southern Hemisphere Winter Stratosphere. Journal of the Atmospheric Sciences, 70, 2120–2136, doi: 10.1175/JAS-D-12-0238.1.

Chou, C.C., J. Dai, C.L. Kuo, and T.Y. Huang. (2016). Simultaneous observations of storm-generated sprite and gravity wave over Bangladesh. Journal of Geophysical Research: Space Physics, 121, 9222–9233, doi: 10.1002/2016JA022554.

Christensen, L.L., S. Noll, and P. Horálek. (2016). Light Phenomena over the ESO Observatories I: Airglow. The ESO Messenger, 163, 40–42.

Clancy, R.T., B.J. Sandor, A. García-Muñoz, F. Lefèvre, M.D. Smith, M.J. Wolff, F. Montmessin, S.L. Murchie, and H. Nair. (2013). First detection of Mars atmospheric hydroxyl: CRISM Near-IR measurement versus LMD GCM simulation of OH Meinel band emission in the Mars polar winter atmosphere. Icarus, 226, 272–281, doi: 10.1016/j.icarus.2013.05.035.

Claro, M. (2016). Rainbow Bands of Airglow in Gravity Waves above Pico Island Were seen from NOAA/NASA Satellite in Space. http://www.miguelclaro.com/wp/?portfolio=rainbow-bands-of-airglow-in-gravity-waves-above-pico-island.

Coble, M., G.C. Papen, and C.S. Gardner. (1998). Computing two-dimensional unambiguous horizontal wavenumber spectra from OH airglow images. IEEE Transactions on Geoscience and Remote Sensing, 36, 368–382, doi: 10.1109/36.662723.

Cochrane, R. (2016). The Secret Life of Equations. Octopus Publishing Group, London.

Cole, G.H.A., and M.M. Woolfson. (2002). The Atmosphere of the Earth. Page 293–306. Planetary Science: The Science of Planets Around Stars. Institute of Physics, London.

Colling, A. (2004). Ocean Circulation. Second edition. The Open University, Oxford.

Collis, R.T.H., F.G. Fernald, J.E. Alder, R.T. H. Collis, F.G. Fernald, and J.E. Alder. (1968). Lidar Observations of Sierra-Wave Conditions. Journal of Applied Meteorology, 7, 227–233, doi: 10.1175/1520-0450(1968)007<0227:LOOSWC>2.0.CO;2.

Cooley, J.W., and J.W. Tukey. (1965). An algorithm for the machine calculation of complex fourier series. Mathematics of computation, 19, 297–301, doi: 10.2307/2003354.

Cowley, L. (2016). Airglow. http://www.atoptics.co.uk/highsky/airglow1.htm.

Cushman-Roisin, B. (2014). Environmental Fluid Mechanics. John Wiley & Sons, Ltd., New York.

Dalin, P., M. Connors, I. Schofield, A. Dubietis, N. Pertsev, V. Perminov, M. Zalcik, A. Zadorozhny, T. McEwan, I. McEachran, J. Grønne, O. Hansen, H. Andersen, S. Frandsen, D. Melnikov, V. Romejko, and I. Grigoryeva. (2013). First common volume ground-based and space

measurements of the mesospheric front in noctilucent clouds. Geophysical Research Letters, 40, 6399–6404, doi: 10.1002/2013GL058553.

Dalin, P., S. Kirkwood, A. Moström, K. Stebel, P. Hoffmann, and W. Singer. (2004). A case study of gravity waves in noctilucent clouds. Annales Geophysicae, 22, 1875–1884.

Dalin, P., A. Pogoreltsev, N. Pertsev, V. Perminov, N. Shevchuk, A. Dubietis, M. Zalcik, S. Kulikov, A. Zadorozhny, D. Kudabayeva, A. Solodovnik, G. Salakhutdinov, and I. Grigoryeva. (2015). Evidence of the formation of noctilucent clouds due to propagation of an isolated gravity wave caused by a tropospheric occluded front. Geophysical Research Letters, 42, 2037–2046, doi: 10.1002/2014GL062776.

Dewan, E.M., and R.H. Picard. (1998). Mesospheric bores. Journal of Geophysical Research: Atmospheres, 103, 6295–6305, doi: 10.1029/97JD02498.

Dewan, E. M., and R. H. Picard. (2001). On the origin of mesospheric bores. Journal of Geophysical Research: Atmospheres, 106, 2921–2927, doi: 10.1029/2000JD900697.

Dowdy, A.J., R.A. Vincent, M. Tsutsumi, K. Igarashi, Y. Murayama, W. Singer, and D.J. Murphy. (2007). Polar mesosphere and lower thermosphere dynamics: 1. Mean wind and gravity wave climatologies. Journal of Geophysical Research, 112, D17104, doi: 10.1029/2006JD008126.

Drob, D.P., J.T. Emmert, G. Crowley, J.M. Picone, G.G. Shepherd, W. Skinner, P. Hays, R.J. Niciejewski, M. Larsen, C.Y. She, J.W. Meriwether, G. Hernandez, M.J. Jarvis, D.P. Sipler, C.A. Tepley, M.S. O'Brien, J.R. Bowman, Q. Wu, Y. Murayama, S. Kawamura, I.M. Reid, and R.A. Vincent. (2008). An empirical model of the Earth's horizontal

wind fields: HWM07. Journal of Geophysical Research: Space Physics, 113, doi: 10.1029/2008JA013668.

Eckermann, S.D., D. Broutman, J. Ma, J.D. Doyle, P.D. Pautet, M.J. Taylor, K. Bossert, B.P. Williams, D.C. Fritts, R.B. Smith, S.D. Eckermann, D. Broutman, J. Ma, J.D. Doyle, P.D. Pautet, M.J. Taylor, K. Bossert, B.P. Williams, D.C. Fritts, and R.B. Smith. (2016). Dynamics of Orographic Gravity Waves Observed in the Mesosphere Over the Auckland Islands During the Deep Propagating Gravity Wave Experiment (DEEPWAVE). Journal of the Atmospheric Sciences, JAS-D-16-0059.1, doi: 10.1175/JAS-D-16-0059.1.

Eckermann, S.D., I. Hirota, and W.K. Hocking. (1995). Gravity wave and equatorial wave morphology of the stratosphere derived from long-term rocket soundings. Quarterly Journal of the Royal Meteorological Society, 121, 149–186, doi: 10.1002/qj.49712152108.

Eckermann, S.D., and C.J. Marks. (1997). GROGRAT: A new model of the global propagation and dissipation of atmospheric gravity waves. Advances in Space Research, 20, 1253–1256, doi: 10.1016/S0273-1177(97)00780-1.

Ern, M., H.K. Cho, P. Preusse, and S.D. Eckermann. (2009a). Properties of the average distribution of equatorial Kelvin waves investigated with the GROGRAT ray tracer. Atmospheric Chemistry and Physics, 9, 7973–7995, doi: 10.5194/acp-9-7973-2009.

Ern, M., C. Lehmann, M. Kaufmann, and M. Riese. (2009b). Spectral wave analysis at the mesopause from SCIAMACHY airglow data compared to SABER temperature spectra. Annales Geophysicae, 27, 407–416, doi: 10.5194/angeo-27-407-2009.

Ern, M., L. Hoffmann, and P. Preusse. (2017). Directional gravity wave momentum fluxes in the stratosphere derived from high-resolution AIRS temperature data. Geophysical Research Letters, 44, 475–485, doi: 10.1002/2016GL072007.

Espy, P., T. Demissie, M. Hatlen, R. Hibbins, R. de Witt, G. Swenson, and F. Vargas. (2013). A multiple instrument study to differentiate primary versus secondary gravity wave generation in the mesosphere. Page 8712. Geophysical Research Abstracts. EGU General Assembly, Vienna.

Evers, L.G., and H.W. Haak. (2010). The Characteristics of Infrasound, its Propagation and Some Early History. Pages 3–28 in A. Le Pichon, E. Blanc, and A. Hauchecorne, editors, Infrasound Monitoring for Atmospheric Studies. Springer, New York.

Fleming, J.R. (2016). Inventing Atmospheric Science: Bjerknes, Rossby, Wexler, and the Foundations of Modern Meteorology. MIT Press, Cambridge, Massachussetts.

French, W.J.R. (2005). Anomalous winter hydroxyl temperatures at 69°S during 2002 in a multiyear context. Geophysical Research Letters, 32, L12818, doi: 10.1029/2004GL022287.

French, W.J.R., and F.J. Mulligan. (2010). Stability of temperatures from TIMED/SABER v1.07 (2002–2009) and Aura/MLS v2.2 (2004–2009) compared with OH(6-2) temperatures observed at Davis Station, Antarctica. Atmospheric Chemistry and Physics, 10, 11439–11446, doi: 10.5194/acp-10-11439-2010.

Friedman, J.P. (1966). Propagation of internal gravity waves in a thermally stratified atmosphere. Journal of Geophysical Research, 71, 1033–1054, doi: 10.1029/JZ071i004p01033.

Friedman, J.S. (2003). Tropical mesopause climatology over the Arecibo Observatory. Geophysical Research Letters, 30, doi: 10.1029/2003GL016966.

Fritts, D.C., and M.J. Alexander. (2003). Gravity wave dynamics and effects in the middle atmosphere. Reviews of Geophysics, 41, 1003, doi: 10.1029/2001RG000106.

Fritts, D.C., J.R. Isler, G.E. Thomas, and Ø. Andreassen. (1993). Wave breaking signatures in noctilucent clouds. Geophysical Research Letters, 20, 2039–2042, doi: 10.1029/93GL01982.

Fritts, D.C., B. Laughman, L. Wang, T.S. Lund, and R.L. Collins. (2017a). Gravity Wave Dynamics in a Mesospheric Inversion Layer: 1. Reflection, Trapping, and Instability Dynamics. Journal of Geophysical Research: Atmospheres, doi: 10.1002/2017JD027440.

Fritts, D.C., P.D. Pautet, K. Bossert, M.J. Taylor, B.P. Williams, H. Iimura, T. Yuan, N.J. Mitchell, and G. Stober. (2014). Quantifying gravity wave momentum fluxes with Mesosphere Temperature Mappers and correlative instrumentation. Journal of Geophysical Research: Atmospheres, 119, 13583–13603, doi: 10.1002/2014JD022150.

Fritts, D.C., L. Wang, G. Baumgarten, A.D. Miller, M.A. Geller, G. Jones, M. Limon, D. Chapman, J. Didier, C.B. Kjellstrand, D. Araujo, S. Hillbrand, A. Korotkov, G. Tucker, and J. Vinokurov. (2017b). High-Resolution Observations and Modeling of Turbulence Sources, Structures, and Intensities in the Upper Mesosphere. Journal of Atmospheric and Solar-Terrestrial Physics, doi: http://dx.doi.org/10.1016/j.jastp.2016.11.006.

Fritts, D.C., L. Wang, B. Laughman, T.S. Lund, and R.L. Collins. (2017c). Gravity Wave Dynamics in a Mesospheric Inversion Layer: 2.

Instabilities, Turbulence, Fluxes, and Mixing. Journal of Geophysical Research: Atmospheres, doi: 10.1002/2017JD027442.

Fritts, D.C., and L. Yuan. (1989). An analysis of gravity wave ducting in the atmosphere: Eckart's resonances in thermal and Doppler ducts. Journal of Geophysical Research, 94, 18455, doi: 10.1029/JD094iD15p18455.

Garcia, F.J., M.J. Taylor, and M.C. Kelley. (1997). Two-dimensional spectral analysis of mesospheric airglow image data. Applied optics, 36, 7374–7385, doi: 10.1364/AO.36.007374.

Garcia, R.R., D.R. Marsh, D.E. Kinnison, B.A. Boville, and F. Sassi. (2007). Simulation of secular trends in the middle atmosphere, 1950–2003. Journal of Geophysical Research, 112, D09301, doi: 10.1029/2006JD007485.

Garcia, R.R., A.K. Smith, D.E. Kinnison, Á. de la Cámara, D.J. Murphy (2017). Modification of the Gravity Wave Parameterization in the Whole Atmosphere Community Climate Model: Motivation and Results. Journal of the Atmospheric Sciences, 74, 275–291, doi: 10.1175/JAS-D-16-0104.1.

Geller, M.A. (1983). Dynamics of the middle atmosphere (Tutorial lecture). Space Science Reviews, 34, 359–375.

Geller, M.A., M.J. Alexander, P.T. Love, J. Bacmeister, M. Ern, A. Hertzog, E. Manzini, P. Preusse, K. Sato, A.A. Scaife, T. Zhou (2013). A Comparison between Gravity Wave Momentum Fluxes in Observations and Climate Models. Journal of Climate, 26, 6383–6405, doi: 10.1175/JCLI-D-12-00545.1.

Gerrard, A.J., T.J. Kane, S.D. Eckermann, and J.P. Thayer. (2004). Gravity waves and mesospheric clouds in the summer middle atmosphere: A comparison of lidar measurements and ray modeling of gravity waves

over Sondrestrom, Greenland. Journal of Geophysical Research, 109, D10103, doi: 10.1029/2002JD002783.

Giers, D.H., Y. Sahai, L.L. Cogger, and E.H. Ryan. (1997). Occurrence characteristics of mesospheric gravity waves at 51° N. Journal of Atmospheric and Solar-Terrestrial Physics, 59, 1197–1203.

Gill, A. (1982). Atmosphere-Ocean Dynamics. Academic Press, San Diego.

Giongo, G.A., J.V. Bageston, P.P. Batista, C.M. Wrasse, G.D. Bittencourt, I. Paulino, N.M. Paes Leme, D.C. Fritts, D. Janches, W. Hocking, and N.J. Schuch. (2018). Mesospheric front observations by the OH airglow imager carried out at Ferraz Station on King George Island, Antarctic Peninsula, in 2011. Annales Geophysicae, 36, 253–264, doi: 10.5194/angeo-36-253-2018.

Gleick, J. (1987). Chaos: Making a new science. Viking Press, New York.

Godin, O.A. (2015). Wentzel–Kramers–Brillouin approximation for atmospheric waves. Journal of Fluid Mechanics, 777, 260–290, doi: 10.1017/jfm.2015.367.

Goldie, A.H.R. (1925). Waves at an approximately horizontal surface of discontinuity in the atmosphere. Quarterly Journal of the Royal Meteorological Society, 51, 239–246, doi: 10.1002/qj.49705121506.

Goosse, H. (2015). Introduction to climate dynamics and climate modelling. Cambridge University Press, New York.

Gossard, E.E., and W.H. Hooke. (1975). Waves in the Atmosphere: Atmospheric Infrasound and Gravity Waves - their Generation and Propagation. Elsevier Scientific Publishing Company, Amsterdam.

Goupillaud, P., A. Grossmann, and J. Morlet. (1984). Cycle-octave and related transforms in seismic signal analysis. Geoexploration, 23, 85–102, doi: 10.1016/0016-7142(84)90025-5.

Gruzdev, A.N., and G.P. Brasseur. (2005). Long-term changes in the mesosphere calculated by a two-dimensional model. Journal of Geophysical Research, 110, D03304, doi: 10.1029/2003JD004410.

Grygalashvyly, M., G.R. Sonnemann, F.J. Lübken, P. Hartogh, and U. Berger. (2014). Hydroxyl layer: Mean state and trends at midlatitudes. Journal of Geophysical Research: Atmospheres, 119, 12,391-12,419, doi: 10.1002/2014JD022094.

Hartquist, T., O. Havnes, and M. Kassa. (2009). Exploring polar mesospheric summer echoes. Astronomy & Geophysics, 50, 1.08-1.14, doi: 10.1111/j.1468-4004.2009.50108.x.

Hecht, J. H. (2005). Maui Mesosphere and Lower Thermosphere (Maui MALT) observations of the evolution of Kelvin-Helmholtz billows formed near 86 km altitude. Journal of Geophysical Research, 110, D09S10, doi: 10.1029/2003JD003908.

Hecht, J.H., A.Z. Liu, R.L. Walterscheid, S.J. Franke, R.J. Rudy, M.J. Taylor, and P.D. Pautet. (2007). Characteristics of short-period wavelike features near 87 km altitude from airglow and lidar observations over Maui. Journal of Geophysical Research, 112, D16101, doi: 10.1029/2006JD008148.

Hecht, J.H., K. Wan, L.J. Gelinas, D.C. Fritts, R.L. Walterscheid, R.J. Rudy, A.Z. Liu, S.J. Franke, F.A. Vargas, P.D. Pautet, M.J. Taylor, and G.R. Swenson. (2014). The life cycle of instability features measured from the Andes Lidar Observatory over Cerro Pachon on 24 March 2012. Journal

of Geophysical Research: Atmospheres, 119, 8872–8898, doi: 10.1002/2014JD021726.

Hedin, A.E. (1991). Extension of the MSIS Thermosphere Model into the middle and lower atmosphere. Journal of Geophysical Research: Space Physics, 96, 1159–1172, doi: 10.1029/90JA02125.

von Helmholtz, H.L.F. (1868). Über diskontinuierliche Flüssigkeitsbewegungen (On discontinuous liquid motion). Berliner Monatsberichte Konigl Preuss. Akad. Wiss. Berlin, 23, 215–228.

Hirota, I. (1997). Some problems relating to the observed characteristics of gravity waves in the middle atmosphere. Pages 404–406 in K. Hamilton, editor. Gravity wave processes: their parameterization in global climate models, NATO ASI Series 50. First edition. Springer-Verlag, Berlin, Heidelberg.

Hobbs, P.V. (2000). Introduction to Atmospheric Chemistry. Cambridge University Press, New York.

Hoffmann, L., X. Xue, and M.J. Alexander. (2013). A global view of stratospheric gravity wave hotspots located with Atmospheric Infrared Sounder observations. Journal of Geophysical Research: Atmospheres, 118, 416–434, doi: 10.1029/2012JD018658.

Holton, J. R. (1982). The role of gravity wave induced drag and diffusion in the momentum budget of the mesosphere. Journal of the Atmospheric Sciences, 39, 791–799.

Holton, J.R. (1992). An Introduction to Dynamic Meteorology. Academic Press, London.

Houghton, J.T. (1969). Absorption and emission by carbon-dioxide in the mesosphere. Quarterly Journal of the Royal Meteorological Society, 95, 1–20, doi: 10.1002/qj.49709540302.

Houghton, J.T. (2006). The Physics of Atmospheres. Third edition. Cambridge University Press, Cambridge.

Huang, J.Y. (1993). Analysis of Small Scale Gravity Wave Activity in Hydroxyl Airglow. University of Western Ontario.

Imster, E. (2014). Kelvin Helmholtz clouds. http://earthsky.org/constellations/kelvin-helmholzt-clouds.

Innis, J.L., and A.R. Klekociuk. (2006). Planetary wave and gravity wave influence on the occurrence of polar stratospheric clouds over Davis Station, Antarctica, seen in lidar and radiosonde observations. J. Geophys. Res, 111, doi: 10.1029/2006JD007629.

Irving, D., and I. Simmonds. (2015). A Novel Approach to Diagnosing Southern Hemisphere Planetary Wave Activity and Its Influence on Regional Climate Variability. Journal of Climate, 28, 9041–9057, doi: 10.1175/JCLI-D-15-0287.1.

Johnson, N. (1929). Atmospheric oscillations shown by the microbarograph. Quarterly Journal of the Royal Meteorological Society, 55, 19–30.

Jones, W.L. (1969). Ray tracing for internal gravity waves. Journal of Geophysical Research, 74, 2028–2033, doi: 10.1029/JB074i008p02028.

Kaifler, B., F.J. Lübken, J. Höffner, R.J. Morris, and T.P. Viehl. (2015). Lidar observations of gravity wave activity in the middle atmosphere over Davis (69°S, 78°E), Antarctica. Journal of Geophysical Research: Atmospheres, 120, 4506–4521, doi: 10.1002/2014JD022879.

Kalnay, E. (2003). Atmospheric Modeling, Data Assimilation, and Predictability. Cambridge University Press, New York.

Kim, Y.H., C.S. Lee, J.K. Chung, J.H. Kim, and H.Y. Chun. (2010). Seasonal Variations of Mesospheric Gravity Waves Observed with an Airglow All-sky Camera at Mt. Bohyun, Korea (36° N). Journal of Astronomy and Space Sciences, 27, 181–188, doi: 10.5140/JASS.2010.27.3.181.

Kim, Y.J., S.D. Eckermann, and H.Y. Chun. (2003). An overview of the past, present and future of gravity wave drag parametrization for numerical climate and weather prediction models. Atmosphere-Ocean, 41, 65–98, doi: 10.3137/ao.410105.

Kogure, M., T. Nakamura, M.K. Ejiri, T. Nishiyama, M. Tsutsumi, and Y. Tomikawa. (2016). Seasonal and height variation of GW activities in the middle atmosphere over Syowa using a Rayleigh/Raman lidar. 3rd International Antarctic Gravity Wave Instrument Network Workshop, Cambridge.

Lamb, D. (2000). Vertical Forces: The balance of forces used to derive the hydrostatic equation for fluids. http://www.ems.psu.edu/~lno/Meteo431/Vertforc.jpg.

Lamb, H. (1910). On the theory of waves propogated vertically in the atmosphere. Proc. Lond. Math. Soc., 7, 122–141.

Lee, K.M., and D.M. Ryan. (2015). Scale height - A parameter for characterizing atmosphere. The Physics Teacher, 53, 122–123, doi: 10.1119/1.4905820.

Li, J., T. Li, X. Dou, X. Fang, B. Cao, C.Y. She, T. Nakamura, A. Manson, C. Meek, and D. Thorsen. (2017). Characteristics of ripple structures revealed in OH airglow images. Journal of Geophysical Research: Space Physics, 122, 3748–3759, doi: 10.1002/2016JA023538.

Lighthill, J. (1978). Waves in fluids. Cambridge University Press, Cambridge.

Limpasuvan, V., J.H. Richter, Y.J. Orsolini, F. Stordal, and O.K. Kvissel. (2012). The roles of planetary and gravity waves during a major stratospheric sudden warming as characterized in WACCM. Journal of Atmospheric and Solar-Terrestrial Physics, 78–79, 84–98, doi: 10.1016/J.JASTP.2011.03.004.

Lindzen, R.S. (1981). Turbulence and stress owing to gravity wave and tidal breakdown. Journal of Geophysical Research, 86, 9707–9714.

Lindzen, R.S. (1990). Dynamics in Atmospheric Physics: Lecture Notes for an Introductory Graduate-Level Course. Cambridge University Press, Cambridge, Massachussetts.

Lorenz, E.N. (1965). A study of the predictability of a 28-variable atmospheric model. Tellus, 17, 321–333.

Love, P.T., and D.J. Murphy. (2016). Gravity wave momentum flux in the mesosphere measured by VHF radar at Davis, Antarctica. Journal of Geophysical Research: Atmospheres, 121, 12723–12736, doi: 10.1002/2016JD025627.

Lu, X., X. Chu, W. Fong, C. Chen, Z. Yu, B.R. Roberts, and A.J. McDonald. (2015). Vertical evolution of potential energy density and vertical wave number spectrum of Antarctic gravity waves from 35 to 105 km at McMurdo (77.8°S, 166.7°E). Journal of Geophysical Research: Atmospheres, 120, 2719–2737, doi: 10.1002/2014JD022751.

Lu, X., A.Z. Liu, G.R. Swenson, T. Li, T. Leblanc, and I.S. Mcdermid. (2009). Gravity wave propagation and dissipation from the stratosphere to the lower thermosphere. J. Geophys. Res, 114, doi: 10.1029/2008JD010112.

Lynch, P. (2009). Computing tomorrow's weather. Physics World, 22, 38–39.

Lynch, P. (2016). An Artist's Impression of Richardson's Fantastic Forecasting Factory. Weather, 71, 14–18.

Makhlouf, U.B., R.H. Picard, and J.R. Winick. (1995). Photochemical-dynamical modeling of the measured response of airglow to gravity waves: 1. Basic model for OH airglow. Journal of Geophysical Research, 100, 11289, doi: 10.1029/94JD03327.

Mansinha, L., R.G. Stockwell, R.P. Lowe, M. Eramian, and R.A. Schincariol. (1997). Local S-spectrum analysis of 1-D and 2-D data. Physics of the Earth and Planetary Interiors, 103, 329–336, doi: 10.1016/S0031-9201(97)00047-2.

Marks, C.J., and S.D. Eckermann. (1995). A three-dimensional non-hydrostatic ray-tracing model for gravity waves: formulation and preliminary results for the middle atmosphere. Journal of the Atmospheric Sciences, 52, 1959–1984, doi: 10.1175/1520-0469(1995)052<1959:ATDNRT>2.0.CO;2.

Matsuda, T.S., T. Nakamura, M.K. Ejiri, M. Tsutsumi, and K. Shiokawa. (2014). New statistical analysis of the horizontal phase velocity distribution of gravity waves observed by airglow imaging. Journal of Geophysical Research: Atmospheres, 119, 9707–9718, doi: 10.1002/2014JD021543.

Matsuda, T.S., T. Nakamura, M.K. Ejiri, M. Tsutsumi, Y. Tomikawa, M.J. Taylor, Y. Zhao, P.D. Pautet, D.J. Murphy, and T. Moffat-Griffin. (2017). Characteristics of mesospheric gravity waves over Antarctica observed by ANGWIN (Antarctic Gravity Wave Instrument Network) imagers using 3-D spectral analyses. Journal of Geophysical Research: Atmospheres, doi: 10.1002/2016JD026217.

Mbatha, N., V. Sivakumar, H. Bencherif, and S.B. Malinga. (2013). Extracting gravity wave parameters during the September 2002 Southern

Hemisphere major sudden stratospheric warming using a SANAE imaging riometer. Annales Geophysicae, 31, 1709–1719, doi: 10.5194/angeo-31-1709-2013.

McCarthy, D. (2015). Modelling mesopause OH* emissions using a Global Circulation Model. Maynooth University.

McDade, I.C., and E.J. Llewellyn. (1987). Kinetic parameters related to sources and sinks of vibrationally excited OH in the nightglow. Journal of Geophysical Research, 92, 7643–7650, doi: 10.1029/JA092iA07p07643.

McGrath-Spangler, E.L., and A.S. Denning. (2012). Estimates of North American summertime planetary boundary layer depths derived from space-borne lidar. Journal of Geophysical Research, 117, D15101, doi: 10.1029/2012JD017615.

McGuire, R. (2016). MSIS-E-90 Atmosphere Model. http://omniweb.gsfc.nasa.gov/vitmo/msis_vitmo.html.

McIlveen, R. (2010). Fundamentals of Weather and Climate. Oxford University Press, New York.

Medeiros, A.F., J. Fechine, R.A. Buriti, H. Takahashi, C.M. Wrasse, and D. Gobbi. (2005). Response of OH, O2, and OI5577 airglow emissions to the mesosphereic bore in the equatorial region of Brazil. Advances in Space Research, 35, 1971–1975, doi: 10.1016/j.asr.2005.03.075.

Mehta, D., A.J. Gerrard, Y. Ebihara, A.T. Weatherwax, and L.J. Lanzerotti. (2017). Short-period mesospheric gravity waves and their sources at the South Pole. Atmospheric Chemistry and Physics, 17, 911–919, doi: 10.5194/acp-17-911-2017.

Meinel, A., and M. Meinel. (1983). Sunsets, twilights and evening skies. Cambridge University Press, New York.

Meinel, A. (1950). OH Emission Bands in the Spectrum of the Night Sky. The Astrophysical Journal, 111, 555, doi: 10.1086/145296.

Meriwether, J.W., and A.J. Gerrard. (2004). Mesosphere inversion layers and stratosphere temperature enhancements. Reviews of Geophysics, 42, RG3003, doi: 10.1029/2003RG000133.

Mihalikova, M., K. Sato, M. Tsutsumi, and T. Sato. (2016). Properties of inertia-gravity waves in the lowermost stratosphere as observed by the PANSY radar over Syowa Station in the Antarctic. Ann. Geophys, 34, 543–555, doi: 10.5194/angeo-34-543-2016.

Mitchell, N.J., N. Cobbett, A. Gadian, N.P. Hindley, J. Hughes, D. Jackson, J. King, T. Moffat-Griffin, A.C. Moss, A. Ross, S. Vosper, and C.J. Wright. (2016). SG-WEX: The South Georgia Wave Experiment - an overview. 3rd International Antarctic Gravity Wave Instrument Network Workshop, Cambridge.

Moffat-Griffin, T., N. Cobbett, M. Rose, P. Breen, R.E. Hibbins (2016). A ship-borne airglow imager: observing mesospheric gravity waves from the oceans. International Symposium on the Whole Atmosphere, Tokyo.

Moffat-Griffin, T., R.E. Hibbins, M.J. Jarvis, and S.R. Colwell. (2011). Seasonal variations of gravity wave activity in the lower stratosphere over an Antarctic Peninsula station. Journal of Geophysical Research, 116, D14111, doi: 10.1029/2010JD015349.

Moffat-Griffin, T., R.E. Hibbins, K. Nielsen, M.J. Jarvis, and M.J. Taylor. (2008). Observing mesospheric gravity waves with an imaging riometer. Journal of Atmospheric and Solar-Terrestrial Physics, 70, 1327–1335, doi: 10.1016/j.jastp.2008.04.009.

Morris, R.J., D.J. Murphy, R.A. Vincent, D.A. Holdsworth, A.R. Klekociuk, and I.M. Reid. (2006). Characteristics of the wind, temperature and

PMSE field above Davis, Antarctica. Journal of Atmospheric and Solar-Terrestrial Physics, 68, 418–435, doi: 10.1016/j.jastp.2005.04.011.

Murphy, D.J., S.P. Alexander, A.R. Klekociuk, P.T. Love, and R.A. Vincent. (2014). Radiosonde observations of gravity waves in the lower stratosphere over Davis, Antarctica. Journal of Geophysical Research: Atmospheres, 119, 11,973-11,996, doi: 10.1002/2014JD022448.

Murphy, D.J., W.J.R. French, and R.A. Vincent. (2007). Long-period planetary waves in the mesosphere and lower thermosphere above Davis, Antarctica. Journal of Atmospheric and Solar-Terrestrial Physics, 69, 2118–2138, doi: 10.1016/J.JASTP.2007.06.008.

Murphy, D.J., and R.A. Vincent. (2000). Amplitude enhancements in Antarctic MF radar echoes. Journal of Geophysical Research: Atmospheres, 105, 26683–26693, doi: 10.1029/2000JD900510.

Nakamura, T., A. Higashikawa, T. Tsuda, and Y. Matsushita. (1999). Seasonal variations of gravity wave structures in OH airglow with a CCD imager at Shigaraki. Earth, Planets and Space, 51, 897–906, doi: 10.1186/BF03353248.

Nappo, C. J. (2002). An Introduction to Atmospheric Gravity Waves. Academic Press, San Diego.

Newman, P.A., J.A. Pyle, J. Austin, G.O. Braathen, P.O. Canziani, K.S. Carslaw, P.M. de F. Forster, S. Godin-Beekmann, B.M. Knudsen, K. Kreher, H. Nakane, S. Pawson, V. Ramaswamy, M. Rex, R.J. Salawitch, D.T. Shindell, A. Tabazadeh, and D.W. Toohey. (2003). Polar Stratospheric Ozone: Past and Future. Page 3.1-3.104. Scientific Assessment of Ozone Depletion: 2002, Global Ozone Research and Monitoring Project—Report No. 47. World Meteorological Organization, Geneva.

Nielsen, K., M.J. Taylor, R.E. Hibbins, and M.J. Jarvis. (2009). Climatology of short-period mesospheric gravity waves over Halley, Antarctica (76°S, 27°W). Journal of Atmospheric and Solar-Terrestrial Physics, 71, 991–1000, doi: 10.1016/j.jastp.2009.04.005.

Nielsen, K., M.J. Taylor, R.E. Hibbins, M.J. Jarvis, and J.M. Russell. (2012). On the nature of short-period mesospheric gravity wave propagation over Halley, Antarctica. Journal of Geophysical Research, 117, D05124, doi: 10.1029/2011JD016261.

NOAA. (2011). Global Weather. http://www.srh.noaa.gov/jetstream/global/global_intro.htm.

Noel, V., A. Hertzog, H. Chepfer, and D.M. Winker. (2008). Polar stratospheric clouds over Antarctica from the CALIPSO spaceborne lidar. Journal of Geophysical Research, 113, D02205, doi: 10.1029/2007JD008616.

Noel, V., and M. Pitts. (2012). Gravity wave events from mesoscale simulations, compared to polar stratospheric clouds observed from spaceborne lidar over the Antarctic Peninsula. Journal of Geophysical Research, 117, D11207, doi: 10.1029/2011JD017318.

Ortland, D.A., and M.J. Alexander. (2006). Gravity wave influence on the global structure of the diurnal tide in the mesosphere and lower thermosphere. Journal of Geophysical Research, 111, A10S10, doi: 10.1029/2005JA011467.

Pautet, P.D. (2016). Private Communication.

Pautet, P.D. (2018). Private Communication.

Pautet, P.D., M.J. Taylor, J.B. Snively, and C. Solorio. (2018). Unexpected Occurrence of Mesospheric Frontal Gravity Wave Events Over South

Pole (90°S). Journal of Geophysical Research: Atmospheres, 123, 160–173, doi: 10.1002/2017JD027046.

Pautet, P.D., J. Stegman, C.M. Wrasse, K. Nielsen, H. Takahashi, M.J. Taylor, K.W. Hoppel, and S.D. Eckermann. (2011). Analysis of gravity waves structures visible in noctilucent cloud images. Journal of Atmospheric and Solar-Terrestrial Physics, 73, 2082–2090, doi: 10.1016/j.jastp.2010.06.001.

Pautet, P.D., M.J. Taylor, W.R. Pendleton, Y. Zhao, T. Yuan, R. Esplin, and D. McLain. (2014). Advanced mesospheric temperature mapper for high-latitude airglow studies. Applied Optics, 53, 5934–5943, doi: 10.1364/AO.53.005934.

Peterson, A.W., and G.W. Adams. (1983). OH airglow phenomena during the 5-6 July 1982 total lunar eclipse. Applied Optics, 22, 2682–2685.

Piccioni, G., P. Drossart, L. Zasova, A. Migliorini, J.C. Gérard, F.P. Mills, A. Shakun, A. García-Muñoz, N. Ignatiev, D. Grassi, V. Cottini, F.W. Taylor, S. Erard, and the V.V.E. Technical Team. (2008). First detection of hydroxyl in the atmosphere of Venus. Astronomy and Astrophysics, 483, L29–L33, doi: 10.1051/0004-6361:200809761.

Le Pichon, A., J. Vergoz, Y. Cansi, L. Ceranna, and D. Drob. (2010). Contribution of Infrasound Monitoring for Atmospheric Remote Sensing. Pages 629–646 in A. Le Pichon, E. Blanc, and A. Hauchecorne, editors, Infrasound Monitoring for Atmospheric Studies. Springer, New York.

Pickett, H.M., W.G. Read, K.K. Lee, and Y.L. Yung. (2006). Observation of night OH in the mesosphere. Geophysical Research Letters, 33, L19808, doi: 10.1029/2006GL026910.

Ploughonven, R., and F. Zhang. (2014). Internal gravity waves from atmospheric jets and fronts. Reviews of Geophysics, 52, 33–76, doi: 10.1002/2012RG000419.

Pramitha, M., M. Venkat-Ratnam, A. Taori, B.V. Krishna-Murthy, D. Pallamraju, and S. Vijaya-Bhaskar-Rao. (2014). Identification of gravity wave sources using reverse ray tracing over Indian region. Atmospheic Chemistry and Physics Discussions, 14, 19587–19623, doi: 10.5194/acpd-14-19587-2014.

Preusse, P., A. Dörnbrack, S.D. Eckermann, M. Riese, B. Schaeler, J.T. Bacmeister, D. Broutman, and K.U. Grossmann. (2002). Space-based measurements of stratospheric mountain waves by CRISTA 1. Sensitivity, analysis method, and a case study. Journal of Geophysical Research: Atmospheres, 107, CRI 6-1-CRI 6-23, doi: 10.1029/2001JD000699.

Preusse, P., S.D. Eckermann, M. Ern, J. Oberheide, R.H. Picard, R.G. Roble, M. Riese, J.M. Russell, and M.G. Mlynczak. (2009). Global ray tracing simulations of the SABER gravity wave climatology. Journal of Geophysical Research, 114, D08126, doi: 10.1029/2008JD011214.

Pugmire, J.R., M.J. Taylor, and P.D. Pautet. (2014). New measurements of McMurdo gravity wave parameters. 2nd International Antarctic Gravity Wave Instrument Network Workshop, Utah.

Reisin, E.R., J. Scheer, M.E. Dyrland, F. Sigernes, C.S. Deehr, C. Schmidt, K. Höppner, M. Bittner, P.P. Ammosov, G.A. Gavrilyeva, J. Stegman, V.I. Perminov, A.I. Semenov, P. Knieling, R. Koppmann, K. Shiokawa, R.P. Lowe, M.J. López-González, E. Rodríguez, Y. Zhao, M.J. Taylor, R.A. Buriti, P.J. Espy, W.J.R. French, K.U. Eichmann, J.P. Burrows, and C. von Savigny. (2014). Traveling planetary wave activity from mesopause region airglow temperatures determined by the Network for the Detection

of Mesospheric Change (NDMC). Journal of Atmospheric and Solar-Terrestrial Physics, 119, 71–82, doi: 10.1016/J.JASTP.2014.07.002.

Richardson, L.F. (1922). Weather prediction by numerical process. Cambridge University Press, Cambridge.

Rourke, S., F.J. Mulligan, W.J.R. French, and D.J. Murphy. (2017). A climatological study of short-period gravity waves and ripples at Davis Station, Antarctica (68 ° S, 78 ° E) during the (austral winter February-October) period 1999-2013. Journal of Geophysical Research: Atmospheres, doi: 10.1002/2017JD026998.

Sánchez-Lavega, A. (2011). An Introduction to Planetary Atmospheres. CRC Press Taylor and Francis Group, Boca Raton.

Sato, K., S. Watanabe, Y. Kawatani, Y. Tomikawa, K. Miyazaki, and M. Takahashi. (2009). On the origins of mesospheric gravity waves. Geophysical Research Letters, 36, L19801, doi: 10.1029/2009GL039908.

Schmidt, G.A. (2007). The physics of climate modeling. Physics Today, 60, 72–73, doi: 10.1063/1.2709569.

Seinfield, J.H., and S.N. Pandis. (1998). Atmospheric Chemistry and Physics. John Wiley & Sons, Inc., Toronto.

Serreze, M.C. (2011). The Arctic Climate System. http://www.colorado.edu/geography/class_homepages/geog_4271_f11/lectures/week_3.pdf.

Sivjee, G.G. (1992). Airglow hydroxyl emissions. Planetary and Space Science, 40, 235–242, doi: 10.1016/0032-0633(92)90061-R.

Smith, S.M., G. Stober, C. Jacobi, J.L. Chau, M. Gerding, M.G. Mlynczak, J.M. Russell, J.L. Baumgardner, M. Mendillo, M. Lazzarin, and G. Umbriaco. (2017). Characterization of a Double Mesospheric Bore Over Europe.

Journal of Geophysical Research: Space Physics, 122, 9738–9750, doi: 10.1002/2017JA024225.

Snively, J.B., K. Nielsen, M.P. Hickey, C.J. Heale, M.J. Taylor, and T. Moffat-Griffin. (2013). Numerical and statistical evidence for long-range ducted gravity wave propagation over Halley, Antarctica. Geophysical Research Letters, 40, doi: 10.1002/grl.50926.

Song, I.S., C.S. Lee, G. Jee, and J.H. Kim. (2016). Meteor Radar Observations of Vertically-propagating Low-frequency Inertia-gravity waves near the Southern Polar Mesopause Region. 3rd International Antarctic Gravity Wave Instrument Network Workshop, Cambridge.

Song, Y., Y. Zhang, C. Zhou, and Z. Zhao. (2014). Acoustic ray tracing in the atmosphere: with gravitational effect and attenuation considered. Annals of Geophysics, 57, A0542, doi: 10.4401/ag-6474.

Spiegel, E.A., and G. Veronis. (1960). On the Boussinesq Approximation for a Compressible Fluid. The Astrophysical Journal, 131, 442, doi: 10.1086/146849.

Stevens, B., and S. Bony. (2013). Water in the Atmosphere. Physics Today, 29–34.

Stevens, S. (2015). Lenticular Clouds. http://weatherwars.info/wp-content/uploads/2015/06/lenticular-clouds-Google-Search-2015-06-21-22-33-37.jpg.

Stockwell, R.G., and R.P. Lowe. (2001a). Airglow imaging of gravity waves: 1. Results from a small network of OH nightglow scanning imagers.

Stockwell, R.G., and R.P. Lowe. (2001b). Airglow imaging of gravity waves: 1. Results from a small network of OH nightglow scanning imagers. Journal

of Geophysical Research: Atmospheres, 106, 17185–17203, doi: 10.1029/2001JD900035.

Stockwell, R.G., R.P. Lowe, and L. Mansinha. (1996a). Localized cross-spectral analysis with phase-corrected wavelets. Pages 557–564 in H. H. Szu, editor. Proceedings of the SPIE, Volume 2762, p. 557-564 (1996).

Stockwell, R.G., L. Mansinha, and R.P. Lowe. (1996b). Localization of the Complex Spectrum: The S Transform. IEEE transactions on signal processing, 44, doi: 10.1109/78.492555.

Strutt, J.W. (1883). Investigation of the character of the equilibrium of an incompressible heavy fluid of variable density. Proc. Lond. Math. Soc., 14, 170–177.

Summers, M.E., R.R. Conway, D.E. Siskind, M.H. Stevens, D. Offermann, M. Riese, P. Preusse, D.F. Strobel, and J.M. Russell. (1997). Implications of satellite OH observations for middle atmospheric H20 and ozone. Science, 277, 1967–1970.

Suzuki, S., F.J. Lübken, G. Baumgarten, N. Kaifler, R. Eixmann, B.P. Williams, and T. Nakamura. (2013). Vertical propagation of a mesoscale gravity wave from the lower to the upper atmosphere. Journal of Atmospheric and Solar-Terrestrial Physics, 97, 29–36, doi: 10.1016/j.jastp.2013.01.012.

Suzuki, S., K. Shiokawa, K. Hosokawa, K. Nakamura, and W.K. Hocking. (2009). Statistical characteristics of polar cap mesospheric gravity waves observed by an all-sky airglow imager at Resolute Bay, Canada. Journal of Geophysical Research: Space Physics, 114, doi: 10.1029/2008JA013652.

Suzuki, S., M. Tsutsumi, S.E. Palo, Y. Ebihara, M. Taguchi, and M. Ejiri. (2011). Short-period gravity waves and ripples in the South Pole

mesosphere. Journal of Geophysical Research, 116, doi: 10.1029/2011JD015882.

Swenson, G.R., and P.J. Espy. (1995). Observations of 2-dimensional airglow structure and Na density from the ALOHA, October 9, 1993 "storm flight." Geophysical Research Letters, 22, 2845–2848, doi: 10.1029/95GL02795.

Swenson, G.R., and C.S. Gardner. (1998). Analytical models for the responses of the mesospheric OH* and Na layers to atmospheric gravity waves. Journal of Geophysical Research: Atmospheres, 103, 6271–6294, doi: 10.1029/97JD02985.

Swenson, G.R., and S.B. Mende. (1994). OH emission and gravity waves (including a breaking wave) in all-sky imagery from Bear Lake, UT. Geophysical Research Letters, 21, 2239–2242, doi: 10.1029/94GL02112.

Takahashi, T., S. Nozawa, M. Tsutsumi, C. Hall, S. Suzuki, T.T. Tsuda, T.D. Kawahara, N. Saito, S. Oyama, S. Wada, T. Kawabata, H. Fujiwara, A. Brekke, A. Manson, C. Meek, and R. Fujii. (2014). A case study of gravity wave dissipation in the polar MLT region using sodium LIDAR and radar data. Annales Geophysicae, 32, 1195–1205, doi: 10.5194/angeo-32-1195-2014.

Tang, J. (2005). Observational investigations of gravity wave momentum flux with spectroscopic imaging. Journal of Geophysical Research, 110, D09S09, doi: 10.1029/2004JD004778.

Tarasick, D.W., and C.O. Hines. (1990). The observable effects of gravity waves on airglow emissions. Planetary and Space Science, 38, 1105–1119.

Tarasick, D.W., and G.G. Shepherd. (1992). Effects of gravity waves on complex airglow chemistries: 2. OH emission. Journal of Geophysical Research: Space Physics, 97, 3195–3208, doi: 10.1029/91JA02580.

Tateno, S., and K. Sato. (2008). A Study of Inertia-Gravity Waves in the Middle Stratosphere Based on Intensive Radiosonde Observations. Journal of the Meteorological Society of Japan, 86, 719–732.

Taylor, F.W. (2010). Planetary Atmospheres. Oxford University Press, New York.

Taylor, M.J., P.D. Pautet, A.F. Medeiros, R.A. Buriti, J. Fechine, D.C. Fritts, S.L. Vadas, H. Takahashi, and F.T. São Sabbas. (2009). Characteristics of mesospheric gravity waves near the magnetic equator, Brazil, during the SpreadFEx campaign. Annales Geophysicae, 27, 461–472, doi: 10.5194/angeo-27-461-2009.

Taylor, M.J., P.D. Pautet, C. Solorio, Y. Zhao, C. Zamora, W.R. Pendleton, and D.J. Murphy. (2016a). Investigating a Wealth of Mesospheric "Frontal Events" Over Antarctica. 3rd International Antarctic Gravity Wave Instrument Network Workshop, Cambridge.

Taylor, M.J., P.D. Pautet, Y. Zhao, C. Solorio, C. Zamora, and W.R. Pendleton Jr. (2016b). USU activities. 3rd International Antarctic Gravity Wave Instrument Network Workshop, Cambridge.

Taylor, M.J., D.N. Turnbull, and R.P. Lowe. (1995). Spectrometric and imaging measurements of a spectacular gravity wave event observed during the ALOHA-93 Campaign. Geophys. Res. Lett., 22, 2849–2852.

Thompson, W. (1880). On a disturbing infinity in Lord Rayleigh's solution for waves in a plane vortex stratum. Nature, XXIII, 45–46.

Thurburn, J. (2011). Some Basic Dynamics Relevant to the Design of Atmospheric Model Dynamical Cores. Pages 3–27 in P. H. Lauritzen, C. Jablonowski, M. A. Taylor, and R. Nair, editors, Numerical Techniques for Global Atmospheric Models. Springer Berlin Heidelberg, Berlin, Heidelberg.

Trey, F. (1919). Ein Beitrag zum Studium der Luftwogen. Meteor. Zeits, 36, 25–28.

Tsuda, T. (2014). Characteristics of atmospheric gravity waves observed using the MU (Middle and Upper atmosphere) radar and GPS (Global Positioning System) radio occultation. Proceedings of the Japan Academy Series B, 90, 12–27, doi: 10.2183/pjab.90.12.

Vincent, R.A., and A. Hertzog. (2014). The response of superpressure balloons to gravity wave motions. Atmos. Meas. Tech, 7, 1043–1055, doi: 10.5194/amt-7-1043-2014.

Vincent, R.A., and I.M. Reid. (1983). HF Doppler Measurements of Mesospheric Gravity Wave Momentum Fluxes.

Wachter, P., C. Schmidt, S. Wüst, and M. Bittner. (2015). Spatial gravity wave characteristics obtained from multiple OH(3–1) airglow temperature time series. Journal of Atmospheric and Solar-Terrestrial Physics, 135, 192–201, doi: 10.1016/j.jastp.2015.11.008.

Wackter, D. (1976). The structure of atmospheric parameters in wavenumber-space. Colorado State University.

Walterscheid, R.L., J.H. Hecht, L.J. Gelinas, M.P. Hickey, and I.M. Reid. (2012). An intense traveling airglow front in the upper mesosphere-lower thermosphere with characteristics of a bore observed over Alice Springs, Australia, during a strong 2 day wave episode. Journal of Geophysical Research: Atmospheres, 117, n/a-n/a, doi: 10.1029/2012JD017847.

Warner, T.T. (2011). Numerical Weather and Climate Prediction. Cambridge University Press, Cambridge.

Wegener, A. (1906). Studien über Luftwogen (Studies on air waves). Beitr. Physik Freien Atmos., 4, 23–25.

Wilhelmson, B., and M. Ramamurthy. (2010). Jet Stream. http://ww2010.atmos.uiuc.edu/(Gh)/guides/mtr/cyc/upa/jet.rxml.

Wrasse, C.M., T. Nakamura, H. Takahashi, A.F. Medeiros, M.J. Taylor, D. Gobbi, C.M. Denardini, J. Fechine, R.A. Buriti, A. Salatun, E. Achmad, and A.G. Admiranto. (2006a). Mesospheric gravity waves observed near equatorial and low–middle latitude stations: wave characteristics and reverse ray tracing results. Annales Geophysicae, 24, 3229–3240, doi: 10.5194/angeo-24-3229-2006.

Wrasse, C.M., T. Nakamura, T. Tsuda, H. Takahashi, A.F. Medeiros, M.J. Taylor, D. Gobbi, A. Salatun, E. Achmad, and A.G. Admiranto. (2006b). Reverse ray tracing of the mesospheric gravity waves observed at 23°S (Brazil) and 7°S (Indonesia) in airglow imagers. Journal of Atmospheric and Solar-Terrestrial Physics, 68, 163–181, doi: 10.1016/j.jastp.2005.10.012.

Wright, C.J., N.P. Hindley, L. Hoffmann, M.J. Alexander, and N.J. Mitchell. (2017). Exploring gravity wave characteristics in 3-D using a novel S-transform technique: AIRS/Aqua measurements over the Southern Andes and Drake Passage. Atmospheric Chemistry and Physics, 17, 8553–8575, doi: 10.5194/acp-17-8553-2017.

Wright, C.J., N.P. Hindley, and N.J. Mitchell. (2016a). Combining AIRS and MLS observations for three-dimensional gravity wave measurement. Geophysical Research Letters, 43, 884–893, doi: 10.1002/2015GL067233.

Wright, C.J., N.P. Hindley, A.C. Moss, D.C. Fritts, D. Janches, and N.J. Mitchell. (2016b). Multi-instrument gravity-wave measurements over Tierra del Fuego and the Drake Passage – Part 1: Potential energies and vertical wavelengths from AIRS, COSMIC, HIRDLS, MLS-Aura, SAAMER, SABER and radiosondes. Atmospheric Measurement Techniques, 9, 877–908, doi: 10.5194/amt-9-877-2016.

Wright, C.J., M.B. Rivas, and J.C. Gille. (2011). Intercomparisons of HIRDLS, COSMIC and SABER for the detection of stratospheric gravity waves. Atmospheric Measurement Techniques, 4, 1581–1591, doi: 10.5194/amt-4-1581-2011.

Wu, D.L., S.D. Eckermann, D.L. Wu, and S.D. Eckermann. (2008). Global Gravity Wave Variances from Aura MLS: Characteristics and Interpretation. Journal of the Atmospheric Sciences, 65, 3695–3718, doi: 10.1175/2008JAS2489.1.

Yamashita, C., S.L. England, T.J. Immel, and L.C. Chang. (2013). Gravity wave variations during elevated stratopause events using SABER observations. Journal of Geophysical Research: Atmospheres, 118, 5287–5303, doi: 10.1002/jgrd.50474.

Yasui, R., K. Sato, and M. Tsutsumi. (2016). Seasonal and Interannual Variation of Mesospheric Gravity Waves Based on MF Radar Observations over 15 Years at Syowa Station in the Antarctic. SOLA, 12, 46–50, doi: 10.2151/sola.2016-010.

Yue, J., T. Nakamura, C.Y. She, M. Weber, W. Lyons, and T. Li. (2010a). Seasonal and local time variability of ripples from airglow imager observations in US and Japan. Annales Geophysicae, 28, 1401–1408, doi: 10.5194/angeo-28-1401-2010.

Yue, J., T. Nakamura, C.Y. She, M. Weber, and J. Oberheide. (2010b). Seasonal and local time variability of ripples from airglow imager observations in US and Japan. 38th COSPAR Scientific Assembly, Bremen.